

Lecture Notes in Mechanical Engineering

Mokhtar Awang  
Seyed Sattar Emamian  
Farazila Yusof *Editors*

# Advances in Material Sciences and Engineering

 Springer

# **Lecture Notes in Mechanical Engineering**

**Lecture Notes in Mechanical Engineering (LNME)** publishes the latest developments in Mechanical Engineering - quickly, informally and with high quality. Original research reported in proceedings and post-proceedings represents the core of LNME. Volumes published in LNME embrace all aspects, subfields and new challenges of mechanical engineering. Topics in the series include:

- Engineering Design
- Machinery and Machine Elements
- Mechanical Structures and Stress Analysis
- Automotive Engineering
- Engine Technology
- Aerospace Technology and Astronautics
- Nanotechnology and Microengineering
- Control, Robotics, Mechatronics
- MEMS
- Theoretical and Applied Mechanics
- Dynamical Systems, Control
- Fluid Mechanics
- Engineering Thermodynamics, Heat and Mass Transfer
- Manufacturing
- Precision Engineering, Instrumentation, Measurement
- Materials Engineering
- Tribology and Surface Technology

To submit a proposal or request further information, please contact the Springer Editor in your country:

**China:** Li Shen at [li.shen@springer.com](mailto:li.shen@springer.com)

**India:** Dr. Akash Chakraborty at [akash.chakraborty@springernature.com](mailto:akash.chakraborty@springernature.com)

**Rest of Asia, Australia, New Zealand:** Swati Meherishi at [swati.meherishi@springer.com](mailto:swati.meherishi@springer.com)

**All other countries:** Dr. Leontina Di Cecco at [Leontina.dicecco@springer.com](mailto:Leontina.dicecco@springer.com)

To submit a proposal for a monograph, please check our Springer Tracts in Mechanical Engineering at <http://www.springer.com/series/11693> or contact [Leontina.dicecco@springer.com](mailto:Leontina.dicecco@springer.com)

**Indexed by SCOPUS. The books of the series are submitted for indexing to Web of Science.**

More information about this series at <http://www.springer.com/series/11236>

Mokhtar Awang · Seyed Sattar Emamian ·  
Farazila Yusof  
Editors

# Advances in Material Sciences and Engineering

 Springer



*Editors*

Mokhtar Awang  
Department of Mechanical Engineering  
Universiti Teknologi PETRONAS  
Seri Iskandar, Perak, Malaysia

Seyed Sattar Emamian  
Department of Mechanical Engineering  
Universiti Teknologi PETRONAS  
Seri Iskandar, Perak, Malaysia

Farazila Yusof  
Department of Mechanical Engineering  
University of Malaya  
Kuala Lumpur, Malaysia

ISSN 2195-4356

ISSN 2195-4364 (electronic)

Lecture Notes in Mechanical Engineering

ISBN 978-981-13-8296-3

ISBN 978-981-13-8297-0 (eBook)

<https://doi.org/10.1007/978-981-13-8297-0>

© Springer Nature Singapore Pte Ltd. 2020

This work is subject to copyright. All rights are reserved by the Publisher, whether the whole or part of the material is concerned, specifically the rights of translation, reprinting, reuse of illustrations, recitation, broadcasting, reproduction on microfilms or in any other physical way, and transmission or information storage and retrieval, electronic adaptation, computer software, or by similar or dissimilar methodology now known or hereafter developed.

The use of general descriptive names, registered names, trademarks, service marks, etc. in this publication does not imply, even in the absence of a specific statement, that such names are exempt from the relevant protective laws and regulations and therefore free for general use.

The publisher, the authors and the editors are safe to assume that the advice and information in this book are believed to be true and accurate at the date of publication. Neither the publisher nor the authors or the editors give a warranty, expressed or implied, with respect to the material contained herein or for any errors or omissions that may have been made. The publisher remains neutral with regard to jurisdictional claims in published maps and institutional affiliations.

This Springer imprint is published by the registered company Springer Nature Singapore Pte Ltd. The registered company address is: 152 Beach Road, #21-01/04 Gateway East, Singapore 189721, Singapore

# Contents

<b>Effect of Physical Vapour Deposition Coatings on High Speed Steel Single Point Cutting Tool</b> . . . . .	1
R. Ravi Raja Malar Vannan, T. V. Moorthy, P. Hariharan and B. K. Gnanavel	
<b>The Effect of the Gap Distance Between Electrodes on Removal Rate in PMEDM Using FEA</b> . . . . .	7
Mohammed Abdulridha Abbas and Mohd Amri Lajis	
<b>Preliminary Study of Stress Distribution on Modified Femoral Component of Knee Implant at Maximum Flexion Angle</b> . . . . .	17
Rosdayanti Fua-Nizan, Ahmad Majdi Abdul Rani, Mohamad Yazid Din and Suresh Chopra	
<b>Study of CO<sub>2</sub> Solid Formation During Blowdown of Cryogenic CO<sub>2</sub>-CH<sub>4</sub> Distillation Process</b> . . . . .	23
Umar Shafiq, Azmi M. Shariff, Muhammad Babar, Babar Azeem, Abulhassan Ali and Azmi Bustam	
<b>Prediction of Fatigue Failure Location on Lower Control Arm Using Finite Element Analysis (Stress Life Method)</b> . . . . .	33
S. K. Abu Bakar, Rosdi Daud, H. Mas Ayu, M. S. Salwani and A. Shah	
<b>Numerical Investigation of Sand Particle Erosion in Long Radius Elbow for Multiphase Flow</b> . . . . .	41
Muhammad Rehan Khan, H. H. Ya, William Pao and Mohd Amin A. Majid	
<b>Reduction of Non Added Value Activities During Machine Breakdown to Increase Overall Equipment Efficiency</b> . . . . .	51
Shamini Janasekaran and Sheng Hong Lim	

<b>Vibration Analysis Methods for Misalignment and Tolerance Problems in Machine Systems: A Review</b> .....	57
Muhammad Nurshafiq Ramli, Ahmad Majdi Abdul Rani, Nabihah Sallih, Abdul Azeez Abdu Aliyu and T. V. V. L. N. Rao	
<b>Limbs Disabled Needs for an Ergonomics Assistive Technologies and Car Modification</b> .....	67
Salami Bahariah Suliano, Siti Azfanizam Ahmad, Azizan As'arry, Faieza Abdul Aziz, Azizul Rahman Abd Aziz and Ali Ahmed Shokshk	
<b>Effects of Non-neutral Posture and Anthropometry on Heart Rate in Hand Tools Tasks</b> .....	75
Ali Ahmed Shokshk, Siti Azfanizam Ahmad, Faieza Abdul Aziz, Hazreen H. Harith, Azizul Rahman Abd Aziz and Salami Bahariah Suliano	
<b>Determining Optimum Partial Transmission Ratios of Mechanical Driven Systems Using a V-Belt Drive and a Three-Stage Helical Reducer</b> .....	81
Vu Ngoc Pi, Nguyen Khac Tuan, Le Xuan Hung, Nguyen Thi Hong Cam and Tran Thi Phuong Thao	
<b>Determining Optimum Gear Ratios of a Worm—Helical Gearbox for Minimum Acreage of the Cross Section</b> .....	89
Vu Ngoc Pi, Nguyen Khac Tuan, Le Xuan Hung, Nguyen Thi Quoc Dung and Bui Thanh Hien	
<b>A New Study on Calculation of Optimum Partial Transmission Ratios of Mechanical Driven Systems Using a Chain Drive and a Two-Stage Helical Reducer</b> .....	97
Vu Ngoc Pi, Nguyen Khac Tuan and Le Xuan Hung	
<b>A New Study on Determination of Optimum Gear Ratios of a Two-Stage Helical Gearbox</b> .....	107
Vu Ngoc Pi, Nguyen Khac Tuan, Le Xuan Hung and Luu Anh Tung	
<b>Anti-friction Bearing Malfunction Detection and Diagnostics Using Hybrid Approach</b> .....	117
Tamiru Alemu Lemma, Noraimi Omar, Mebrahitom Asmelash Gebremariam and Shazaib Ahsan	
<b>Automated Pipeline Diagnostics Using Image Processing and Intelligent System</b> .....	133
Tamiru Alemu Lemma, Divyeruthra Muniandy and Shazaib Ahsan	
<b>Integrated Safety and Process Economics Approach for Sustainable Process Design of Process Piping</b> .....	145
Muhammad Athar, Azmi M. Shariff and Azizul Buang	

**Optimization of Delignification Process from Red Meranti Wood Sawdust (RMWS) Pretreated with Acidified Sodium Chlorite** . . . . . 155  
 Abdul Rahman Siti Noredyani, Abdul Wahid Zularisam, Ahmad Noormazlinah and Abdul Munaim Mimi Sakinah

**Wrist Twist Working Posture’s Muscles Activity and Potential Energy Analysis via Human Digital Modelling** . . . . . 169  
 Azizul Rahman Abd Aziz, Siti Azfanizam Ahmad, Faieza Abdul Aziz, Siti Anom Ahmad, Ali Ahmed Shokshk and Salami Bahariah Suliano

**Numerical Investigation of Savonius Rotor Elliptical and the Design Modification on a Blade Shape** . . . . . 177  
 Salih Meri AR and Hamidon Bin Salleh

**High Pressure Die Casting Porosity Defect Analysis and Experimental Validation for Power Steering Columns and DVVTs** . . . . . 187  
 M. D. Ibrahim, M. R. Mohamad, L. Roslan, Y. Sunami and S. S. Lam

**Energy Savings in Manufacturing Plant: Pump System Optimization Case Study in Johor and Sarawak, Malaysia** . . . . . 197  
 M. D. Ibrahim, Z. F. Ismail, S. S. Musa and S. S. Lam

**Virtual Reality Training Platform in Onshore Pipeline** . . . . . 207  
 Faieza Abdul Aziz, Adel S. M. A. Alsaed, Shamsuddin Sulaiman, Mohd Khairol Anuar Mohd Ariffin and Abdul Rahman Yahya Al-Arhabi

**Parametric Study of Hydrodynamic Coefficients for Circular Cylinders at Subcritical Reynolds Number** . . . . . 217  
 A. M. Al-Yacouby and M. S. Liew

**Time Step Sensitivity Analysis of a Flow-Driven Savonius Rotor** . . . . . 225  
 Ahmad Zakaria and Mohd Shahrul Nizam Ibrahim

**Biosynthesis of Copper Oxide Nanoparticles Using *Camellia Sinensis* Plant Powder** . . . . . 233  
 Suriani Ibrahim, Nurul Zariyah Jakaria@Zakaria, Shaifulazuar Rozali, Nik Nazri Nik Ghazali, Mohd Sayuti Ab Karim and Mohd Faizul Mohd Sabri

**Two-Dimensional Fast Fourier Transform Analysis of Surface Microstructures of Thin Aluminium Films Prepared by Radio-Frequency (RF) Magnetron Sputtering** . . . . . 239  
 Fredrick M. Mwema, Esther T. Akinlabi and Oluseyi P. Oladijo

**Fractal Analysis of Thin Films Surfaces: A Brief Overview** . . . . . 251  
 Fredrick M. Mwema, Esther T. Akinlabi and Oluseyi P. Oladijo

**Image Segmentation and Grain Size Measurements of Palm Kernel Shell Powder** . . . . . 265  
 Omolayo M. Ikumapayi and Esther T. Akinlabi

<b>Effect of Support Structure Design on the Part Built Using Selective Laser Melting</b> .....	275
Muhammad Rafi Sulaiman, Farazila Yusof and Mohd Fadzil Bin Jamaludin	
<b>A Correlation to Predict Erosion Due to Sand Entrainment in Viscous Oils Flow Through Elbows</b> .....	287
Mysara Eissa Mohyaldinn, Mokhtar Che Ismail and Nurul Hasan	
<b>Reduction of Excessive Flash in Friction Stir Processing of AA1100: An Experimental Observation Study</b> .....	299
Tawanda Marazani, Esther T. Akinlabi and Daniel M. Madyira	
<b>Nonlinear Friction Analysis of a Modified Switching Function Controller in Pre-sliding Regime</b> .....	309
N. A. Rafan, Z. Jamaludin, T. H. Chiew and M. Maharof	
<b>Measurement of Residual Stresses in Aluminium to Copper Friction Stir Spot Welds</b> .....	319
Mukuna Patrick Mubiayi and Esther T. Akinlabi	
<b>Effect of Chip Treatment on Chip-Based Billet Densification in Solid-State Recycling of New Aluminium Scrap</b> .....	327
A. Wagiman, Mohd Sukri Mustapa, S. Shamsudin, Mohd Amri Lajis, R. Asmawi, M. A. Harimon, Farazila Yusof and Mohammed H. Rady	
<b>The Effects of Rotational Tool Speed on Mechanical Properties of Bobbin Friction Stir Welded AA1100</b> .....	337
Siti Noor Najihah Mohd Nasir, Mohammad Kamil Sued and Muhammad Zaimi Zainal Abidin	
<b>Investigation on Oil Absorption and Microstructural Properties of Polyethylene Composites Reinforced with Post-agricultural Waste Fillers</b> .....	343
M. B. Mohd Salahuddin, N. A. Noor Emilia Adila and M. A. T. Intan Syafinaz	
<b>The Analytical Study of Stress Concentration Factor in an Infinite Plate at Various Temperatures</b> .....	353
Nirav P. Patel, Dharmendra S. Sharma and Rahul Singh Dhari	
<b>Performance Evaluation of EFB Biomass Supply Chain for Electricity Power Generation Based on Computer Simulation: Malaysia Case Study</b> .....	363
Seyed Mojib Zahraee, Ainul Akmar Mokhtar, Ali Toloovie and Nurul Afiqah Mohd Asri	

**Effect of Thermal Cycling on Thermal Conductivity of Powder Injection Moulded MWCNT Reinforced Copper Matrix Composites** . . . . . 377  
 Faiz Ahmad, Masdi Mohammad, A. S. Muhsan, Muhammad Ali, A. Naseer, M. Aslam and M. R. R. Malik

**Bending Forces and Hardness Properties of Ti6Al4V Alloy Processed by Constrained Bending and Straightening Severe Plastic Deformation** . . . . . 389  
 Wambura Mwiryenyi Mwita and Esther T. Akinlabi

**Studies on Silica Produced from Original and Firing Rice Husk** . . . . . 399  
 Nur Saadah Zainal, Zaleha Mohamad, Mohd Sukri Mustapa, Nur Azam Badarulzaman and Abdullah Zulfairis Zulkifli

**Industrial Applications of Bamboo in Ghana** . . . . . 409  
 D. R. Akwada and Esther T. Akinlabi

**Mechanical and Physical Properties of Bamboo Species in Ghana** . . . . . 423  
 D. R. Akwada and Esther T. Akinlabi

**In-Process Cooling in Friction Stir Welding of Aluminium Alloys—An Overview** . . . . . 435  
 Olatunji P. Abolusoro and Esther T. Akinlabi

**Experimental Investigation of the Effect of Inclination Angle on Heat Pipe Thermal Performance Using Cu-Nanofluids** . . . . . 445  
 Thaw Zinn Lynn, Aklilu Tesfamichael Baheta and Suleiman Akilu

**Biodegradability Characterization of Cotton Waste Planting Bag Prototype** . . . . . 453  
 Muhammad Farid Shaari, Harris Mubashir Mohamad Isa, Azrin Hani Abdul Rashid, Norshuhaila Mohamed Sunar, Salwa Mahmood, Najib Ismail, Angzzas Sari Mohd Kassim and Noraini Marsi

**Surface Modification of Ti4Al6V Alloy by Laser Cladding with 17-4PH Stainless Steel Powder** . . . . . 465  
 Esther T. Akinlabi and Abiodun Bayode

**Characterisation of Hardened Thermo-Mechanical Treated Reinforcement Bars** . . . . . 473  
 V. Musonda and Esther T. Akinlabi

**Application of Fuzzy Control Charts: A Review of Its Analysis and Findings** . . . . . 483  
 Hidayah Razali, Lazim Abdullah, Termimi Ab Ghani and Nazim Aimran

**Fracturing Parameters in Petroleum Reservoirs and Simulation** . . . . . 491  
 Amani J. Majeed, Ahmed K. Alshara, A. M. Al-Mukhtar and Falah A. Abood

<b>A Modelling of Stereo Matching Algorithm for Machine Vision Application</b> .....	499
Rostam Affendi Hamzah, A. F. Kadmin, S. F. Abd Gani, N. Mohamood, A N. A. Jahari, T. M. F. T. Wook and S. Salam	
<b>Machinability Performance of RBD Palm Oil as a Bio Degradable Dielectric Fluid on Sustainable Electrical Discharge Machining (EDM) of AISI D2 Steel</b> .....	509
Said Ahmad, Richard Ngalie Chendang, Mohd Amri Lajis, Aiman Supawi and Erween Abd Rahim	
<b>Handling Phase Ambiguity in Full Spectrum from FFT</b> .....	519
Nabam Teyi and Sandeep Singh	
<b>A New Model for Predicting Minimum Miscibility Pressure (MMP) in Reservoir-Oil/Injection Gas Mixtures Using Adaptive Neuro Fuzzy Inference System</b> .....	527
M. A. Ayoub, Mysara Eissa Mohyaldinn, Alexy Manalo, Anas. M. Hassan and Quosay A. Ahmed	
<b>Design and Development of Apparatus for Evaluating Galling Resistance Test</b> .....	547
Hemanta Doley, Sandeep Singh and Nabam Teyi	
<b>A Method for the Quantification of Nanoparticle Dispersion in Nanocomposites Based on Fractal Dimension</b> .....	555
K. Anane-Fenin, Esther T. Akinlabi and N. Perry	
<b>Mode I Fracture Toughness of Optimized Alkali-Treated Bambusa Vulgaris Bamboo by Box-Behnken Design</b> .....	565
Siti Amni Roslan, Mohamad Zaki Hassan, Zainudin A. Rasid, Nurul Aini Bani, Shamsul Sarip, Mohd Yusof Md Daud and Firdaus Muhammad-Sukki	
<b>A Preliminary Study of Additional Safety Mechanical Structure for Safety Shoe</b> .....	577
Suhaimi Hassan, Mohd Sallehuddin Yusof, Zaidi Embong, Mohamad Zhairul Iqumal Jumari, Maznan Ismon, Hanis Zakaria, Mohammad Zulafif Rahim, Rosli Ahmad and Engku Mohd Nasri Engku Nasir	
<b>Effect of Flow Regime on Total Interfacial Area of Two Immiscible Fluids in Microchannel Reactor Using VOF Model</b> .....	585
Afiq Mohd Laziz and Ku Zilati Ku Shaari	

**Study on the Wear Influence for Recycled AA6061 Aluminum/ $Al_2O_3$  Utilizing the Face Central-Full Factorial Technique (FCFFT) . . . . . 599**  
Huda M. Sabbar, S. Shamsudin, Mohammed Abdulridha Abbas,  
Muntadher S. Msebawi, Mohd Sukri Mustapa, Mohd Amri Lajis,  
Mohammed H. Rady and Sami Al Alim

**Tensile, Flexural and Fracture Morphological Properties of Recycled Polypropylene (*rPP*) Filled Dried Banana Leaves Fibre (DBLF) Composites: Effects of DBLF Loadings . . . . . 609**  
Thinakaran Narayanan, Jeefferie Abd Razak, Intan Sharhida Othman,  
Noraiham Mohamad, Mohd Edeerozey Abd Manaf,  
Mazlin Aida Mahamood, Hazman Hasib, Mohd Muzafar Ismail  
and Ramli Junid

**Developing a Finite Element Model for Thermal Analysis of Friction Stir Welding (FSW) Using Hyperworks . . . . . 619**  
Bahman Meyghani and Mokhtar Awang



# Effect of Physical Vapour Deposition Coatings on High Speed Steel Single Point Cutting Tool



R. Ravi Raja Malar Vannan, T. V. Moorthy, P. Hariharan  
and B. K. Gnanavel

**Abstract** This Paper presents the investigation of hardness, tool weight loss percentage, surface roughness of High Speed Steel single point cutting tool and Physical vapour deposition coated HSS tool and surface roughness of work piece. The tools with predetermined geometries were analyzed in similar machining conditions. The results identified that the weight loss percentage of the coated tool is less when compared with uncoated tool. Additionally the hardness of the coated tool is greater than uncoated tool, Surface roughness of coated tool is far better than uncoated tool and tool wear is less for coated tool when compared with uncoated tool.

**Keywords** PVD · HSS · TiN · AlCrN · TiAlN

## 1 Introduction

Varieties of machines, equipments and tools are used in the field of mechanical, automobile and manufacturing engineering. The most traditionally used tool is high speed steel (HSS). Titanium Aluminium Nitride (TiAlN/Aluminium Nitride (AlN) multilayer coatings is useful to increase the hardness and its thickness is considerably increased by reducing the flow rate of nitrogen [1]. The Corrosion resistance property is increased by Zinc-Ferrous alloy coatings [2]. The cutting parameters, surface

---

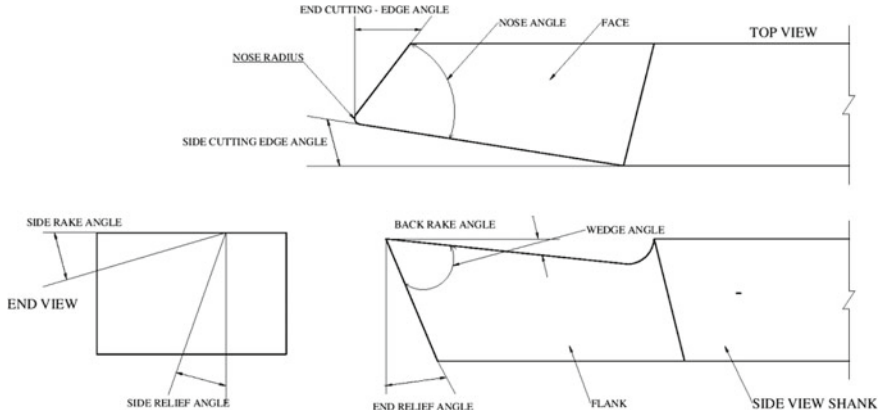
R. Ravi Raja Malar Vannan (✉) · B. K. Gnanavel  
Department of Mechanical Engineering, Saveetha Engineering College, Thandalam 602105, India  
e-mail: [ravirajamalarvannan@saveetha.ac.in](mailto:ravirajamalarvannan@saveetha.ac.in)

B. K. Gnanavel  
e-mail: [hod.mech@saveetha.ac.in](mailto:hod.mech@saveetha.ac.in)

T. V. Moorthy · P. Hariharan  
Department of Manufacturing Engineering, Anna University, Chennai 600025, India  
e-mail: [tvmoorthy1@gmail.com](mailto:tvmoorthy1@gmail.com)

P. Hariharan  
e-mail: [hari@annauniv.edu](mailto:hari@annauniv.edu)

© Springer Nature Singapore Pte Ltd. 2020  
M. Awang et al. (eds.), *Advances in Material Sciences and Engineering*, Lecture Notes in Mechanical Engineering,  
[https://doi.org/10.1007/978-981-13-8297-0\\_1](https://doi.org/10.1007/978-981-13-8297-0_1)



**Fig. 1** Nomenclature of single point HSS cutting tool [8]

finish, tool wear and residual stress were studied [3]. The micro hardness varies with reverence to coating thickness. When compared with uncoated carbide insert, TiN coated carbide insert tool have a longer tool life [4]. The cutting force, surfaces roughness and tool wear were determined [5]. Tool life, flank wear, cutting force and surface roughness were observed [6]. The coatings have been studied in different aspects which help for the modification of surface material, corrosion resistance and wear properties can be improved [7]. In this research work, the characterization of the tool was carried out by PVD Coating on HSS tools.

## 2 Methods

Figure 1 shows the Nomenclature of single point HSS cutting tool. The Physical Vapour Deposition coating process is carried out in high vacuum at pressure ( $2 \times 10^{-4}$  mbar) and at temperature ranges from 150 to 500 °C. Tables 1 and 2 shows the composition and hardness of uncoated HSS single point cutting tool, TiAlN coating on HSS tool, TiN coating on HSS tool, AlCrN coating on HSS tool, (TiN + AlCrN) Bilayer coating on HSS tool and (AlCrN + TiAlN) bilayer coating on HSS tools are used in this experimental work.

The uncoated and coated samples were subjected to an accelerated corrosion testing, which is salt spray test according to ASTM B-117-9 standard. The salt solution of 5 wt% of NaCl is continuously sprayed as a salt mist over the coated surface of the sample at 30° angle held on specimen table. The salt spray test was carried out for 24 h at room temperature. The exposed surface areas of all specimens were 1 cm<sup>2</sup> and the remaining portion except the coated surface was waxed.

Surface roughness of mild steel work-pieces machined by both coated and uncoated tools were determined using Taylor Hobson Talysurf non-contact surface

**Table 1** Element composition for uncoated HSS tool, TiAlN coating on HSS tool, TiN coating on HSS tool, AlCrN coating on HSS tool, (TiN + AlCrN) bilayer coating on HSS tool and (AlCrN + TiAlN) bilayer coating on HSS tool

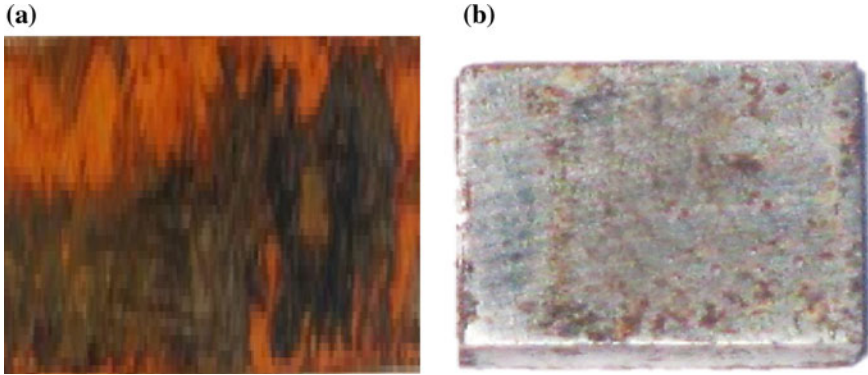
<i>Quantitative results for element composition for uncoated HSS tool</i>									
Elements	C	Mg	Si	V	Cr	Mn	Fe	Mo	W
Weight %	10.71	0.15	0.14	2.14	3.64	0.30	75.00	3.51	4.41
<i>Quantitative results for element composition for TiAlN coating on HSS tool</i>									
Elements	Ti	N	Al	Fe					
Weight%	71.24	3.24	23.81	1.71					
<i>Quantitative results for element composition for TiN coating on HSS tool</i>									
Elements	Ti	N	Al	Fe	Si	Cr	W		
Weight%	85.95	8.37	0.13	3.94	0.15	0.45	1.01		
<i>Quantitative results for element composition for AlCrN coating on HSS tool</i>									
Elements	Al	Cr	N	Fe					
Weight%	42.56	42.18	13.64	1.62					
<i>Quantitative results for (TiN + AlCrN) bilayer coating on HSS tool</i>									
Elements	C	N	Al	Ti	Cr	Fe	W		
Weight%	12.09	1.70	25.78	24.39	33.24	1.41	1.39		
<i>Quantitative results for element composition for (AlCrN + TiAlN) bilayer coating on HSS tool</i>									
Elements	Ti	Al	N	Cr					
Weight%	66.38	29.77	3.28	0.57					

**Table 2** Hardness value in HV 1 kg by using micro hardness tester

Composition	Hardness VHN
Uncoated HSS tool	890
TiAlN coated HSS tool	1249
TiN coated HSS tool	1072
AlCrN coated HSS tool	1060
TiN + AlCrN coated HSS tool	1090
AlCrN + TiAlN coated HSS tool	1250

roughness tester. The surface roughness measurements on bi-layer coated tool and uncoated tool were conducted using Taylor Hobson Talysurf surface roughness tester (ASTMB117).

Hardness test on coated tool and uncoated tools were conducted using Vickers microhardness tester at 1 kg load indentation. The tool wear tests were conducted on bi-layer coated and uncoated tools using weight loss method. The weight loss measurement equipment error is 1 mg. Vickers hardness test was checked in coated and uncoated tool at same loading conditions as per ASTM E384.



**Fig. 2** a Surface corrosion for uncoated HSS tool, b surface corrosion for (AlCrN + TiAlN) bilayer coated HSS tool

### 3 Results and Discussion

Table 1 shows the chemical compositions of uncoated HSS tool, TiAlN coated HSS tool, TiN coated HSS tool, AlCrN coated HSS tool, (TiN + AlCrN) Bilayer coated HSS tool and (AlCrN + TiAlN) bilayer coated HSS tool. There was observed that there was less corrosion in (AlCrN + TiAlN) coated tool when compared with uncoated HSS tool. Figure 2 shows images of the surface corrosion of the uncoated and (AlCrN + TiAlN) coated HSS tools. The coated tool surfaces are corrosion resistant and this is due to the presence of corrosion Prevention elements which are Ti, Al and Cr in the coating material which forms protective oxide layer on the surface.

### 4 Conclusions

In this study TiAlN, TiN, AlCrN, (TiN + AlCrN) and (AlCrN + TiAlN) coatings were successfully performed on HSS single point cutting tool using PVD coating Technique and the following conclusions can be drawn. Surface roughness of the coated tools is found to be better because of the coatings on the tool surface. The surface hardness of the uncoated and coated tools was determined. The coated tools hardness is higher than uncoated HSS tool. It is because of the nitrides present on the coated tool surface. The coated tools have low wear rate because of the hard ceramic material coating on the surface. The (AlCrN + TiAlN) bilayer coating on HSS tool has better corrosion resistance property because of the Protective coating. The mild steel work piece was machined with uncoated and PVD coated HSS tools. The work piece surface roughness is better when machined with coated tools, since the coating

material is acting as lubricant in the dry machining. The protective alumina layer acts as a tribo film during the metal cutting process.

**Acknowledgements** The Authors would like to thank M/S Oerlikon Balzers coating India limited, for their cooperation in performing the experimental works. We are grateful to our Saveetha Engineering College management for acknowledging our research works and encouraging the submission of this paper.

## References

1. Altuncu E, Ustel F (2009) Correlation between sputtering conditions and growth properties of (TiAl)N/AlN multilayer coatings. *Mater Manuf Processes* 24:796–799
2. Venkatakrisna K, Chitharanjan Hegde A (2011) Composition modulated multilayer Zn-Fe alloy coatings on mild steel for better corrosion resistance. *Mater Manuf Process* 337:29–36
3. Saini S, Ahuja IS, Sharma VS (2011) Residual stresses, surface roughness and tool wear in hard turning. *Mater Manuf Process* 584:583–598
4. Sargade V G, Gangopadhyay S, Chattopadhyay AK et al (2011) Effect of coating thickness on the characteristics and dry machining performance of TiN film deposited on cemented carbide inserts using CFUBMS. *Mater Manuf Process* 26:1028–1033
5. EL-Hossainv TM, El-Zoghby AA, Badrc, MA et al (2010) Cutting parameter optimization when machining different materials. *Mater Manuf Process* 335:1101–1114
6. ChangD-Y, Lin S-Y (2012) Tool wear, hole characteristics, and manufacturing tolerance in alumina ceramic micro drilling process. *Mater Manuf Process* 183:306–313
7. Joseph A, Braza F (1989) Review of surface modification technologies II. *Mater Manuf Processes* 3:349–352
8. [www.mfg.mtu.edu](http://www.mfg.mtu.edu). Retrieved 10 Nov 2018

# The Effect of the Gap Distance Between Electrodes on Removal Rate in PMEDM Using FEA



Mohammed Abdulridha Abbas and Mohd Amri Lajis

**Abstract** The numerical investigation using Finite Elements Analysis (FEA) reflects the prediction of the removal rate of the complicated materials in the Electrical Discharge Machining (EDM). Furthermore, it clarifies the ability of the electrothermal energy for the plasma channel to specify behaviors of the removal operation in this environment. One of the significant purposes of using FEA is reduction the experimental cost in both fields of EDM and Powder Mixed-EDM (PMEDM). Therefore, this investigation technique invested in these fields because of the similarity to a large extent between it except for the case of the impedance of the dielectric liquid. The powder additive to this liquid contributes to overcoming the impedance and enhancing the EDM performance. The numerical Kansal's model was used with PMEDM to determine the applied heat flux of the plasma channel between electrodes which require modifying to avoid unstable voltage terminology. At the same time, it is observed a duration the relationship between the spark gap and the voltage of PMEDM system during the pulse. Therefore, this paper will study the effect of the gap distance on the removal rate that is taking place in D2 steel with Chromium Powder Mixed-EDM (CPMEDM) environment. This study depends on the numerical simulation using FEA by modifying Kansal's model to include the spark velocity without relying on the voltage in PMEDM. The results of numerical validation proved during this study shows that the best Material Removal Rate (MRR) is at gap distance = 0.35 mm with the average of error ratio = 6.29%, while the increasing the gap distance must be restricted with equivalent voltage in PMEDM.

**Keywords** Spark channel · Gap distance · Plasma channel · PMEDM simulation

---

M. A. Abbas (✉) · M. A. Lajis

Faculty of Mechanical and Manufacturing Engineering, University Tun Hussein Onn Malaysia (UTHM), Parit Raja, Batu Pahat, Johor, Malaysia  
e-mail: [hd160087@siswa.uthm.edu.my](mailto:hd160087@siswa.uthm.edu.my); [mohd.a.abbas1981@gmail.com](mailto:mohd.a.abbas1981@gmail.com)

M. A. Lajis

e-mail: [amri@uthm.edu.my](mailto:amri@uthm.edu.my)

M. A. Abbas

Engineering Technical College (ETCN), AL-Furat AL-Awsat Technical University (ATU), Main Hilla-Baghdad Road, Kufa, Iraq

© Springer Nature Singapore Pte Ltd. 2020

M. Awang et al. (eds.), *Advances in Material Sciences and Engineering*, Lecture Notes in Mechanical Engineering, [https://doi.org/10.1007/978-981-13-8297-0\\_2](https://doi.org/10.1007/978-981-13-8297-0_2)

## 1 Introduction

High melting temperature and super hardness of advanced materials have hobbled the cutting operation with old machines and reflected unstable conditions in the manufacturing fields related to Airplane and Airspace and other precision fields [1, 2]. The electrical erosion presented a suitable solution for these obstacles by employing Electrical Discharge Machining (EDM) in 1943 to cut these materials [3]. The successive generations of researchers have worked on the development and enhancement of this machine to obtain the best performance. On the other hand, the negative limitations in EDM are the undesired surface quality and the defects in the microstructure of the machined surface. These limitations resulted from applying the highest electric power to overcome impedance in the dielectric fluid which appears during machining with EDM environment. These reasons stimulated the researchers to find the best procedures to reduce or avoid these limitations [4, 5]. Jeswani [6] and Erden [7] confirmed preliminary contribution in this field to improve the efficiency of EDM machine. They added powder particles to the dielectric fluid to conquer the concentrated the spark in a limited region. Besides, the impedance this fluid led to obtaining undesired surface finish with EDM-Environment. Kansal et al. [8] innovated an integrated model with EDM machine known as Powder Mixed-EDM (PMEDM). Consequently, this model catalyzed researchers to develop and activating it over the years.

## 2 Literature Review

An investigation through numerical methods is a vital portion in scientific researches and is a complementary portion to validate experimental cases. It reveals the precision of the scientific and mathematical description with the experimental side. The Finite Elements Method (FEM) is one of the most famous numerical methods that is used by researchers to investigate the PMEDM environment.

Kansal et al. [9] modified the numerical model of EDM and validated a correlation case approximating up to 91% with experimental cases in both EDM and PMEDM for machining D2 steel with or without graphite powder. Jatti and Bagane [10] investigated the removal rate of BeCu alloy using Alumina powder with EDM oil depending on Kansal's model and found the error ratio is equal to 7.8%. Wang et al. [11] through the simulated the plasma channel in Aluminum powder mixed with kerosene oil to erode the Titanium alloy found that the gap distance increases with reducing impedance of the kerosene dielectric fluid. Also, the form of the plasma channel is semi-stable with PMEDM as compared with EDM. Tan and Yeo [12] observed that the validation between the numerical and experimental sides in the Recast Layer Thickness (RLT) is less accurate as compared with the Surface Roughness (SR) during eroded AISI 420 in EDM machine and SiC powder mixed with the dielectric fluid.

The number of studies in the numerical investigation to specify the removal rate by employing FEM with PMEDM is limited. This led to the study of the effect of the gap distance between the copper electrode tool and D2 steel on the removal rate according to the experimental study of Abrol and Sharma [13]. Also, Kansal's model must be modified depending on the description of the voltage required with the spark gap [11]. Depending on the available literature, a gap distance between workpiece and electrode tool in PMEDM will employ in the present study to improve Kansal's model. This improving model leads to avoiding the voltage terminology in Kansal's model. In addition, this model will utilize for validation of the experimental removal rate of D2 steel.

### 3 Traditional Simulation Model

The numerical prediction using Finite Elements Analysis (FEA) is considered a significant objective in the previous studies. The reason attributed to FEA as a numerical technique that has employed to investigate the removal rate of workpiece resulted from the plasma channel. Furthermore, this technique will predict the behavior of parameters during machining in EDM and PMEDM. Therefore, the numerical models presented led to fostering the operation in both environments of EDM and PMEDM by reducing the cost and time produced from the experimental side. The hypotheses of the model proposed by Kansal et al. [9] in PMEDM simulation environment are that the temperature employs both of thermal properties and enthalpy, the thermal expansion and density are not influencing, and the Gaussian distribution represents the heat source. Besides, a behavior of pulse spark is mono, the efficiency of material flushing is 20%, the materials are Isotropic and homogeneous, the materials do not contain any residual stresses before the machining stage, and the heat transferred mode is the transient conduction. This model is no different than EDM numerical model to predict the heat flux of the plasma channel except the new parameter used to interpret the powder frequency or powder concentration in PMEDM [9, 10, 14]. The heat flux  $Q(r)$  of this model can be seen in Eq. (1) which is dependent on Gaussian Distribution and not based on the disk or point heat resource [15–20]:

$$Q(r) = [4.57C_n H_F V I_P / \pi R_{PC}^2] e^{-4.5(r/R_{PC})^2} \quad (1)$$

where:

- $C_n$  Frequency constant or Powder concentration [9, 10].
- $H_F$  Heat fraction constant (9%) [9].
- $V$  Voltage (Volt).
- $I_P$  Pulse current (Amps).
- $R_{PC}$  Plasma channel radius ( $\mu\text{m}$ ).
- $r$  Radial axis ( $\mu\text{m}$ ).



## 4 Problem Statement

The previous researchers have not distinctly identified the voltage term in PMEDM field. Therefore, Some researchers used the term Supply Voltage [21–24] with PMEDM environment, while others defined it as Discharge Voltage [5, 21–23, 25, 26]. The discrepancy between the two terms is not useful with Kansal's model that is depending on voltage as one of its significant parameters. The spark gap as a proposed formula in this study will be avoiding the problem of voltage term in Kansal's model that plays an influential role with the heat distribution of plasma channel. At the same time, this formula will cover the characteristics of the voltage in the gap area.

## 5 Research Contribution

The shallow crater produced by machining the workpiece in PMEDM system has the best performance as compared to pure EDM. This is produced from the distribution of the spark channel over the surface of a workpiece material by increasing the spark distance [25, 27]. Wang et al. [11] proved this interpretation by studying the gap distance characteristics with discharge voltage. Through these results, there appears the need to develop Eq. (1) depending on the role of the gap distance between the electrode tool and workpiece in PMEDM and also to avoid voltage characterization problem. Assuming the pulse duration required for issuing the spark is equivalent the time demanded transmitting the electrons between the workpiece and the electrode tool in PMEDM environment. Therefore, the modification in Kansal's model will be [11]:

$$T_{on} = D_G \sqrt{2m/eV_E} \quad (2)$$

Then:

$$V_E = 2\lambda^2\alpha = 2(D_G/T_{on})^2(m/e) \quad (3)$$

where:

- $V_E$  Equivalent voltage ( $\mu$ Volt).
- $\lambda$  Spark velocity ( $\mu$ m/ $\mu$ s).
- $\alpha$  Spark constant (kg/Coulombs).
- $D_G$  Gap distance between electrode tool and workpiece in PMEDM (mm).
- $T_{on}$  Pulse duration ( $\mu$ s).
- $m$  Electron mass ( $9.10938356 \times 10^{-31}$ ) kg.
- $e$  Elementary charge ( $1.60217662 \times 10^{-19}$ ) Coulombs.

The equivalent voltage ( $V_E$ ) in Eq. 3 depends on the spark velocity ( $\lambda$ ) which is based on the distance between electrodes ( $D_G$ ) in PMEDM and pulse-on-time ( $T_{on}$ ). Equation (3) enhances Eq. (1) by avoiding the problem of voltage terminology and also to numerically study the influence of the spark gap. The redraft of Eq. (1) leads to Eq. (4):

$$Q(r) = [9.14C_n H_F \lambda^2 \alpha I_P / \pi R_{PC}^2] e^{-4.5(r/R_{PC})^2} \tag{4}$$

## 6 Setup the Validation Procedures

In this study, the gap distance will invest to validate MRR in AISI D2 steel using CPMEDM environment based on the investigated results in experimental and numerical sides [11, 13]. Table 1 refers to the number of parameters levels used for the removal rate of this steel.

The gap distance studied between (0.3–0.4 mm) validated the best reduction in impedance in PMEDM especially at range (9–12  $\mu$ s) [11]. Therefore, the intersection between the experimental study results of Abrol and Sharma [13] with results concept relating to gap distance and pulse duration in PMEDM system verified by Wang et al. [11] is at ( $T_{on} = 10 \mu$ s). The experiments showed experimental results for the removal rate at ( $T_{on} = 10 \mu$ s) which is adopted in this research as evident in Table 2 [13].

Table 2 replicates the experiments three times to be the cases of studies (27). Each case from (9) cases will try to validate MRR at gap distance ( $D_G = 30, 35,$  and  $40$  mm). These parameters are used in Eq. (4) to confirm the removal rate at each gap distance. Table 3 illustrates the dynamic equations to investigate these cases.

The methodology of this study can be done depending on the equations in Table 3 with Finite Elements Analysis (FEA) at  $T_{on} = 10 \mu$ s. Thus, the investigation of the removal rate for D2 steel in CPMEDM environment as described in Table 2 will be achieved through replicating the process three times at each gap distance. This methodology will be restricted by the voltage value used in the experimental side according to the study of Abrol and Sharma [13]. Therefore, this value depending on the distances for the spark gap adopted in the present study will confirm by using

**Table 1** Approved parameters for removal rate of AISI D2 in CPMEDM system [13]

Parameter	Unit	Number of level		
		Level (1)	Level (2)	Level (3)
Pulse current (IP)	A	4	6	8
Pulse duration ( $T_{on}$ )	$\mu$ s	10	50	100
Pulse interval ( $T_{off}$ )	$\mu$ s	38	57	85
Powder concentration (PC)	g/L	2	4	6

**Table 2** The experiments performed by Abrol and Sharma at  $T_{on} = 10 \mu s$  [13]

N	IP (A)	Ton ( $\mu s$ )	Toff ( $\mu s$ )	PC (g/L)	MRR ( $mm^3/min$ )
1	4	10	38	2	5.775
2	4	10	57	4	3.653
3	4	10	85	6	2.751
4	6	10	38	2	6.123
5	6	10	57	4	5.329
6	6	10	85	6	3.211
7	8	10	38	2	5.841
8	8	10	57	4	3.322
9	8	10	85	6	3.021

**Table 3** Numerical procedures to simulated PMEDM system

Input equation	Processor domain equation with FEA	Output equation
- Heat flux Eq. (4) - Spark radius Eq. (5) [28]: $R_{PC} = 2040 I_P^{0.43} T_{on}^{0.44}$ (5)	- Governing Eq. (6) [9] $[C_e][T_e] + [D_e][T_e] = [\dot{Q}_{f_e}] + [\dot{Q}_{c_e}]$ (6)	- Crater volume Eq. (7) [10]: $V_c = \frac{\pi}{6} (3 r_c^2 + h^2)$ (7) - MRR Eq. (8) [10]: $MRR = 60 V_c / (T_{on} + T_{off})$ (8)

Eq. (3). Consequently, identification of the best value from  $D_G$  values selected in this study is through obtaining a lower error ratio with MRR without exceeding the value of  $V_E$ .

## 7 Results and Discussion

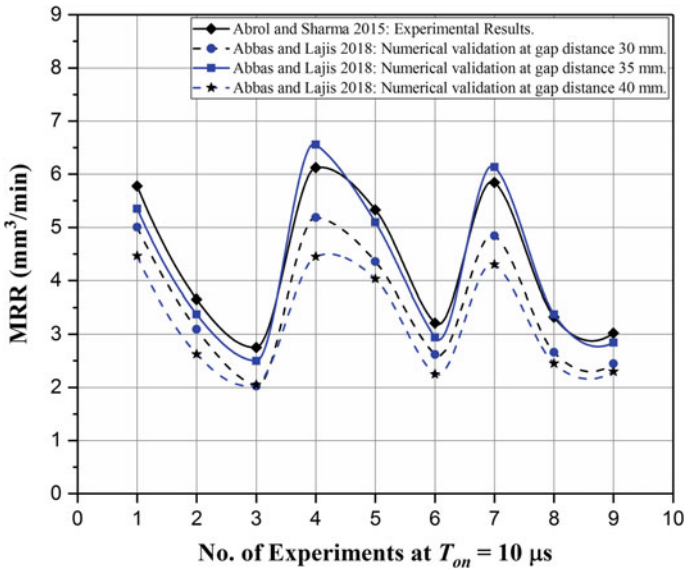
By applying the proposed methodology in this study, the influence of the gap distance between the electrode tool and workpiece on the removal rate of D2 steel numerically in CPMEDM environment is observed. Thus, the validated values of MRR at each gap distance are:

The results as shown in Table 4 indicates the cases that are approaching the numerical prediction of removal rate (MRR) to the experimental outcomes as specified by Abrol and Sharma [13]. These results are indicatives of the success of Eq. (4) which depends on the spark velocity ( $\lambda$ ) instead of the conflicted voltage terminology in Eq. (1). Figure 1 clarifies the numerical validation of MRR cases at each gap distance

**Table 4** Numerical simulation of MRR values depending on FEA at  $T_{on} = 10 \mu s$

No. of validation	Experimental MRR $mm^3/min$ [13]	At $D_G = 0.30$ mm MRR investigation	Error ratio %	At $D_G = 0.35$ mm MRR investigation	Error ratio %	At $D_G = 0.40$ mm MRR investigation	Error ratio %
1	5.775	5.004375	13.34	5.347812	7.39	4.464687	22.68
2	3.653	3.093134	15.32	3.374328	7.62	2.624477	28.15
3	2.751	2.024473	26.40	2.495473	9.28	2.049263	25.50
4	6.123	5.184270	15.33	6.558020	7.10	4.448333	27.35
5	5.329	4.358507	18.21	5.096641	4.36	4.030447	24.36
6	3.211	2.619421	18.42	2.941684	8.38	2.247578	30.00
7	5.841	4.840833	17.12	6.132812	4.99	4.301145	26.36
8	3.322	2.659626	19.93	3.374328	1.57	2.448731	26.28
9	3.021	2.445894	19.03	2.842526	5.90	2.297157	23.96

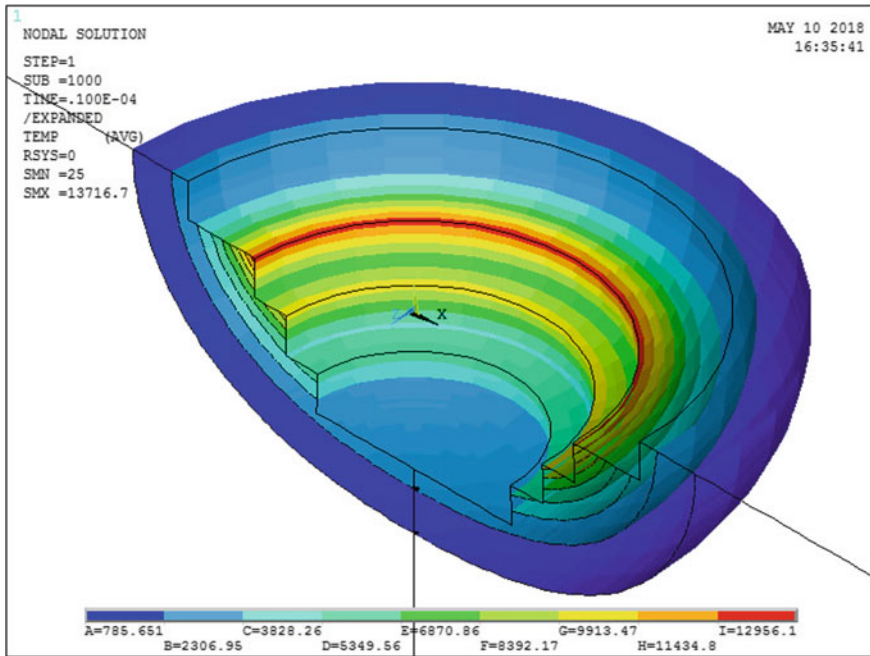
Description: Numerical simulation values predicted for MRR that is validated in this study based on FEA



**Fig. 1** Comparison between numerical validation of MRR in AISI D2 with CPMEDM environment at each gap distance with experimental MRR values

with Fig. 2 which reflects the numerical simulation with FEA, investigated with case No. 10:  $I_p = 4$  A,  $T_{on} = 10 \mu s$ ,  $T_{off} = 38 \mu s$ , and  $P_C = 2$  g/L at gap distance ( $D_G = 0.35$  mm).

The numerical investigation of MRR at ( $D_G = 0.35$  mm) is more accurate as compared with the removal rate investigation performed numerically at ( $D_G = 0.30$  mm)



**Fig. 2** Case validation of MRR No. 10:  $I_p = 4$  A,  $T_{on} = 10$   $\mu$ s,  $T_{off} = 38$   $\mu$ s, an  $P_C = 2$  g/L at gap distance ( $D_G$ ) = 0.35 mm

because of the average of error ratio at ( $D_G = 0.35$  mm) is equal to (6.29393%). These results are consistent with the researchers' view that increased gap distance produces the best performance in the PMEDM system [11, 25, 27]. The growing gap of spark that is approaching ( $D_G = 0.40$  mm) will cause the increase of the average of error rate to be (26.07621%). This deviation may be acceptable with numerical investigation utilizing FEA method, but the equivalent voltage ( $V_E$ ) according to Eq. (3) will constitute a limitation with these results because ( $V_E = 181.94$  V) is at ( $D_G = 0.40$  mm). While at ( $D_G = 0.35$  mm), the removal rate validation is reasonable resulting in generating ( $V_E = 139.29$  V). This outcome is very adjacent to the voltage used in the experimental study that is adopted in this research, where the value of this voltage was up to 135 V [13].

## 8 Conclusions

The numerical simulation performed in this study to validate the removal rate in AISI D2 steel with Chromium Powder Mixed-EDM (CPMEDM) environment at varying distances for the gaps between the electrode tool and the workpiece that have to range (0.3–0.4 mm) comes to the following conclusions:

- i. The numerical simulation with the experimental side for MRR achieved tangible results depending on the new modification formula of Kansal's model that embraces both the spark velocity and the spark constant instead of the unstable voltage term with traditional Kansal's model. This modified model investigated the average of error ratio with experimental cases approaching (18.12, 6.29, and 26.07%) at the gaps distances of (0.30, 0.35, and 0.40 mm) respectively.
- ii. This improved model through the numerical simulation depends on FEA, which proved the increasing of spark gap led to increasing MRR, but this increase of MRR with the equivalent voltage utilized in CPMEMD environment must be restricted. The observation found that the maximum average of error ratio is up to (26.07%) at gap distance of ( $D_G = 0.40$  mm) to obtain the equivalent voltage equal to 181.94 V. Consequently, it did not validate the voltage value used in the experimental study that reaches to 135 V.

These conclusions refer to the active role of the spark gap through the improved Kansal's model in the numerical simulation to validate the removal rate in PMEDM environment. Thus the gap distance is considered as a significant parameter in the *Powder Mixed-Electrical Discharge Machining* (PMEDM) system.

**Acknowledgements** The authors would like to give a special thank to the Ministry of Higher Education Malaysia (MOHE) and Universiti Tun Hussein Onn Malaysia represented by the teams of Precision Machining Research Centre (PREMACH) and Advanced Manufacturing and Materials Centre (AMMC) for their unlimited support to complete this paper.

## References

1. Coldwell H, Woods R, Paul M, Koshy P, Dewes R, Aspinwall D (2003) Rapid machining of hardened AISI H13 and D2 moulds, dies and press tools. *J Mater Process Technol* 135:301–311
2. Koshy P, Dewes RC, Aspinwall DK (2002) High speed end milling of hardened AISI D2 tool steel (~58 HRC). *J Mater Process Technol* 127:266–273
3. Chaudhury P, Samantaray S, Sahu S (2017) Multi response optimization of powder additive mixed electrical discharge machining by Taguchi analysis. *Mater Today Proc* 4:2231–2241
4. Bhattacharya A, Batish A, Kumar N (2013) Surface characterization and material migration during surface modification of die steels with silicon, graphite and tungsten powder in EDM process. *J Mech Sci Technol* 27:133–140
5. Kumar H (2015) Development of mirror like surface characteristics using nano powder mixed electric discharge machining (NPMEDM). *Int J Adv Manuf Technol* 76:105–113
6. Jeswani ML (1981) Effect of the addition of graphite powder to kerosene used as the dielectric fluid in electrical discharge machining. *Wear J* 70:133–139
7. Erden A (1983) Effect of materials on the mechanism of electric discharge machining. *J Eng Mater Technol* 105:132–138
8. Kansal HK, Singh S, Kumar P (2007) Effect of silicon powder mixed EDM on machining rate of AISI D2 die steel. *J Manuf Process* 9:13–22
9. Kansal HK, Singh S, Kumar P (2008) Numerical simulation of powder mixed electric discharge machining (PMEDM) using finite element method. *Math Comput Model* 47:1217–1237
10. Jatti VS, Bagane S (2017) Thermo-electric modelling, simulation and experimental validation of powder mixed electric discharge machining (PMEDM) of BeCu alloys. *Alexandria Eng J*

11. Wang X, Liu Y, Zhang Y, Sun Q, Li Z, Shen Y (2016) Characteristics of plasma channel in powder-mixed EDM based on monopulse discharge. *Int J Adv Manuf Technol* 82:1063–1069
12. Tan PC, Yeo SH (2013) Simulation of surface integrity for nanopowder-mixed dielectric in micro electrical discharge machining. *Metall Mater Trans B Process Metall Mater Process Sci* 44:711–721
13. Abrol A, Sharma S (2015) Effect of chromium powder mixed dielectric on performance characteristic of AISI D2 die steel using EDM. *Int J Res Eng Technol* 4:232–246
14. Izquierdo B, Sanchez JA, Plaza S, Pombo I, Ortega N (2009) A numerical model of the EDM process considering the effect of multiple discharges. *Int J Mach Tools Manuf* 49:220–229
15. Van Dijk FS, Dutre WL (1974) Heat conduction model for the calculation of the volume of molten metal in electric discharges. *J Phys D Appl Phys* 7:899
16. Beck JV (1981) Transient temperatures in a semi-infinite cylinder heated by a disk heat source. *Int J Heat Mass Transf* 24:1631–1640
17. DiBitonto DD, Eubank PT, Patel MR, Barrufet MA (1989) Theoretical models of the electrical discharge machining process. I. A simple cathode erosion model. *J Appl Phys* 66:4095–4103
18. Snoeys R (1971) Investigations of EDM operations by means of thermomathematical models. *Ann CIRP* 20:35–36
19. Jilani ST, Pandey PC (1982) Analysis and modelling of EDM parameters. *Precis Eng* 4:215–221
20. Jilani ST, Pandey PC (1983) An analysis of surface erosion in electrical discharge machining. *Wear* 84:275–284
21. Amorim FL, Dalcin VA, Soares P, Mendes LA (2017) Surface modification of tool steel by electrical discharge machining with molybdenum powder mixed in dielectric fluid. *Int J Adv Manuf Technol* 91:341–350
22. Prakash C, Kansal HK, Pabla BS, Puri S (2016) Multi-objective optimization of powder mixed electric discharge machining parameters for fabrication of biocompatible layer on  $\beta$ -Ti alloy using NSGA-II coupled with Taguchi based response surface methodology. *J Mech Sci Technol* 30:4195–4204
23. Kolli M, Kumar A (2014) Effect of boron carbide powder mixed into dielectric fluid on electrical discharge machining of titanium alloy. *Proc Mater Sci* 5:1957–1965
24. Assarzadeh S, Ghoreishi M (2013) A dual response surface-desirability approach to process modeling and optimization of  $Al_2O_3$  powder-mixed electrical discharge machining (PMEDM) parameters. *Int J Adv Manuf Technol* 64:1459–1477
25. Singh AK, Kumar S, Singh VP (2015) Effect of the addition of conductive powder in dielectric on the surface properties of superalloy Super Co 605 by EDM process. *Int J Adv Manuf Technol* 77:99–106
26. Kumar S, Batra U (2012) Surface modification of die steel materials by EDM method using tungsten powder-mixed dielectric. *J Manuf Process* 14:35–40
27. Shabgard M, Khosrozadeh B (2017) Investigation of carbon nanotube added dielectric on the surface characteristics and machining performance of Ti–6Al–4V alloy in EDM process. *J Manuf Process* 25:212–219
28. Salonitis K, Stournaras A, Stavropoulos P, Chryssolouris G (2009) Thermal modeling of the material removal rate and surface roughness for die-sinking EDM. *Int J Adv Manuf Technol* 40:316–323

# Preliminary Study of Stress Distribution on Modified Femoral Component of Knee Implant at Maximum Flexion Angle



Rosdayanti Fua-Nizan, Ahmad Majdi Abdul Rani, Mohamad Yazid Din and Suresh Chopra

**Abstract** Human knee is an important joint in human body that allows leg movement. However, the cartilage can lose their shape and damage the bone due to illness. Total knee replacement is a medical procedure that replaced the bones with knee implant. However, difference in anatomy between Caucasian and Asian has caused some concern in the fit of the knee implant and most knee implants in the market were not designed for greater flexion ability of Asian population. Hence, a customized femoral component for high flexion application was designed and analysed utilizing DICOM image of MRI scanned knee. Stress distribution analysis was conducted on the femoral component to study the effect of high flexion on the modified femoral component. Preliminary results showed that the stress distribution was relatively higher at smaller contact area. The result concluded that there was a possibility of failure on the modified femoral component due to high stress concentration.

**Keywords** Knee · Replacement · Implant · Prosthesis · Orthopaedic

## 1 Introduction

Human knee is a joint that allows leg movement and functions to support body weight during daily activities. Knee joint consists of several main components which include patella, femur, menisci cartilage, tibia and fibula. The menisci cartilage is located in between femur and tibia bone that functions as protection layer to prevent the

---

R. Fua-Nizan (✉) · A. M. A. Rani  
Mechanical Engineering Department, Universiti Teknologi Petronas, 32610 Bandar Seri Iskandar, Perak, Malaysia  
e-mail: [rosdayanti\\_g03569@utp.edu.my](mailto:rosdayanti_g03569@utp.edu.my)

M. Y. Din  
Orthopaedic Department, Hospital Tuanku Fauziah, Pusat Bandar Kangar, 01000 Kangar, Perlis, Malaysia

S. Chopra  
Orthopaedic Department, Hospital Sultanah Bahiyah, Alor Setar, Perlis, Malaysia



bones from rubbing against each other. Osteoarthritis (OA) on the other hand is an illness that causes the menisci cartilage to lose their shape and texture. Over time, the cartilage will disappear, and bone surfaces will be damaged. Total knee replacement (TKR) is a medical procedure that removes the surfaces of damaged bones and are replaced by knee implant components. Knee implant consists of three components which are the femoral component, tibial insert and tibial component. The manufacturers of the knee implants are from Western and European countries where the implants are available in standard sizes. Due to the difference in bone anatomy between the Caucasian and the Asian [1–3], fit of the implants to Asian patients had become a concern. Knee implant that did not fit properly to the patient's bone cannot restore pre-osteoarthritis knee condition and improve living quality of the patient after TKR [3, 4]. Due to the difference in lifestyle, the maximum flexion ability of the knee for Asian is also higher compared with the Caucasian [5]. Although high flexion knee implant was designed to accommodate higher flexion angle, this design was not able to restore the maximum flexion angle of Asian knee [6–8]. Hence, the objective of this research is to modify and analyse the stress distribution on the femoral component of a knee implant.

## **2 Methodology**

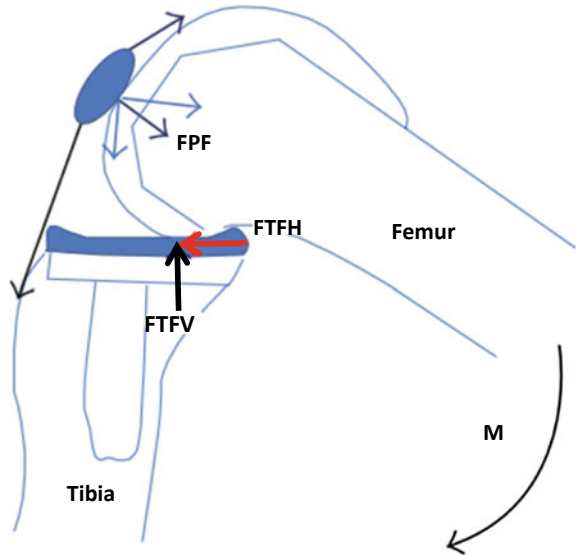
### ***2.1 DICOM Image Reconstruction***

The research started with the acquisition of DICOM images of a female human knee with OA from a hospital. These images were processed by utilizing semi-automatic segmentation system (ITK-Snap) which read and viewed the medical images according to the sequences. The segmentation of the bone began by selecting the segmentation mode and parameters which defined the bone edges from the images. Next, 'seeds' were placed in the image and grown to fill up the bones until the defined edges. Upon completion, the segmentation was stopped manually, and 3D model of the bones was reconstructed in Standard Tessellation Language (STL) format. However, raw 3D model of the bones obtained from the segmentation are comprised of rough edges caused by incomplete 'seed' formation. Due to this reason, meshing was done to improve the bone surface. The meshing system converted the model into a solid body for the ease of modification.

### ***2.2 Knee Bone Modification***

The dimensions of used knee implant were measured and was used as reference for the modification. The dimensions consisted of the resection angles and the thickness of the segments.

**Fig. 1** Forces applied during flexion [10]



The modification of femur bone to femoral component knee implant was conducted by referring to the standard TKR surgical methods. Based on measured resection method, the distal femoral resection angle should be in between  $6^\circ$  and  $7^\circ$  valgus angle [8]. Based on the dimensions acquired, the 3D model of the bone was modified by using computer aided design system (Autodesk Inventor). The modified femoral component consisted of two sides. The first side (A) is the side that connects to the femur bone. This side was modified based on existing knee implant because the resected bone conducted during TKA followed the standard methods developed by the surgeons. The second side (B) on the other hand was the customized component because it was based on the exact bone anatomy of the specific patient.

### 2.3 Stress Analysis

Stress distribution on the femoral component was conducted by utilizing finite element analysis software (ANSYS). The forces applied consists of patellofemoral reaction force ( $F_{PF}$ ), tibiofemoral reaction force in horizontal and vertical direction ( $F_{TFH}$ ,  $F_{TFV}$  respectively), and moment about the knee joint ( $M$ ) [9, 10]. Tibiofemoral reaction force is force exerted by the tibia on the femoral component in horizontal and vertical direction. Patellofemoral reaction force on the other hand is force exerted by the tendons that connect the patellar to femur and tibia bones. The forces are illustrated in Fig. 1.

Based on previous studies, the value of the forces and moment exerted on knee joint are expressed in function of weight and height because load differs in individual with

**Table 1** Mechanical properties of CoCr [15]

Material	Tensile strength (MPa)	Yield strength (MPa)	Density (g/cm <sup>3</sup> )	Young's modulus (MPa)
CoCr	979	752	8.6	7000

different weight even during the similar activities [11]. Due to this reason, the value for tibiofemoral reaction force in vertical and horizontal direction were 2.49 BW and 0.68 BW respectively [10, 12]. The force in patellofemoral joint was 1.9 BW [13] whereas the moment about the knee joint at maximum flexion was 2.2% BW × Ht [14]. These parameters were expressed with function of body weight (BW) and height (Ht). Furthermore, these parameters were measured during maximum flexion activity at average 150.8° flexion angle. The material used for the analysis was cobalt chromium alloy (CoCr), which is a common material used for manufacturing metal knee implant. The mechanical properties of the material are listed in Table 1.

The contact area on the joints need to be considered as well for the analysis because the contact area also changes relatively to the flexion angle [16–19]. Due to this reason, the contact areas for patellofemoral joint and tibiofemoral joint were defined as 362.2 and 15 mm<sup>2</sup> respectively [17, 18].

### 3 Results

The maximum stress distribution on the femoral component at maximum flexion activity was 137.65 MPa. The stress distribution on the femoral component was observed to be concentrated near the edge especially on tibiofemoral joint section. This is because, with increase in flexion angle, contact area decreases, which as a result increases the force applied on the tibiofemoral joint. These results also showed that the stress distribution on the tibiofemoral joint increased as the contact area became smaller. This outcome agrees with studies conducted by another study [20] which as the flexion angle increased, the stress on tibiofemoral joint was concentrated highly on the edge of the femoral condyles. Furthermore, another study conducted also concluded that most of the stresses were concentrated on the femoral component during flexion [10]. However, comparing with a different study [21], high flexion knee implant exhibits lower contact stress on the condylar contact area on the tibial insert. A study was conducted on the shear stress of fixed and mobile bearing type knee implant [22]. The results from this study showed that the maximum stress exerted on both condyles were in between 12 and 14 MPa, which were lower compared to modified femoral component. This comparison also showed that the modified femoral component could experience failure on the tibiofemoral joint during flexion at an angle more than 150°. The results are illustrated in Fig. 2.

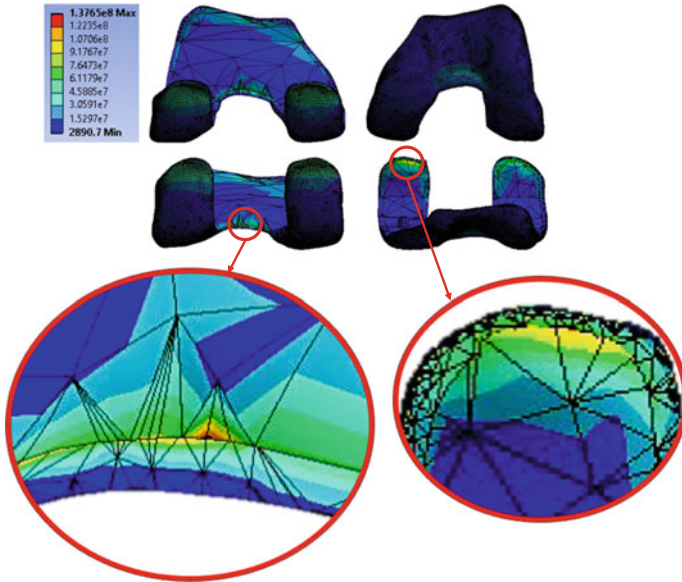


Fig. 2 Stress distribution on the modified femoral component at maximum flexion angle

#### 4 Conclusions

These results showed that the decreased contact area during maximum flexion on the tibiofemoral joint resulted in the increased contact stress. However, the outcomes presented in this study were preliminary results of stress distribution on the customized femoral component knee implant at a specific maximum flexion angle. Due to this reason, the result does not represent stress distribution on the modified femoral component during flexion activity from 0° (full extension) until maximum flexion.

**Acknowledgements** The authors would like to acknowledge the financial support provided by Ministry of Education Malaysia through grant No. FRGS/1/2014/TK01/UTP/02/08.

#### References

1. Yue B, Vadarajan KM, Ai S, Tang T, Rubash HE, Li G (2011) Differences of knee anthropometry between Chinese and white men and women. *J Arthroplasty* 26(1):124–130
2. Chaichankul C, Tanavalee A, Itiravivong P (2011) Anthropometric measurements of knee joints in Thai population: Correlation to the sizing of current knee prostheses. *Knee* 18(1):5–10
3. Ko Y et al (2011) Health-related quality of life after total knee replacement or unicompartmental knee arthroplasty in an urban asian population. *Value Health* 14(2):322–328
4. Xie F et al (2010) Evaluation of health outcomes in osteoarthritis patients after total knee replacement: a two-year follow-up. *Health Qual Life Outcomes* 8:87

5. Acker SM, Cockburn RA, Krevolin J, Li RM, Tarabichi S, Wyss UP (2011) Knee kinematics of high-flexion activities of daily living performed by male muslims in the Middle East. *J Arthroplasty* 26(2):319–327
6. Murphy M, Journeaux S, Russell T (2009) High-flexion total knee arthroplasty: a systematic review. *Int Orthop* 33(4):887–893
7. Fu H, Wang J, Zhang W, Cheng T, Zhang X (2015) No clinical benefit of high-flex total knee arthroplasty: a meta-analysis of randomized controlled trials. *J Arthroplasty* 30(4):573–579
8. Vail TP, Lang JE, Van Sikes C, Chapter 105 surgical techniques and instrumentation in total knee arthroplasty, *Musculoskelet. Key*
9. Dahlkvist NJ, Mayo P, Seedhom BB (1982) Forces during squatting and rising from a deep squat. *Eng Med* 11(012632852):69–76
10. Thambyah A, Fernandez J (2014) Squatting-related tibiofemoral shear reaction forces and a biomechanical rationale for femoral component loosening. *Sci World J* 2014
11. Bergmann G, Bender A, Dymke J, Duda G, Damm P (2016) Standardized loads acting in hip implants. *PLoS One* 11(5)
12. Thambyah A (2008) How critical are the tibiofemoral joint reaction forces during frequent squatting in Asian populations? *Knee* 15(4):286–294
13. Sharma A, Leszko F, Komistek RD, Scuderi GR, Cates HE, Liu F (2008) In vivo patellofemoral forces in high flexion total knee arthroplasty. *J Biomech* 41(3):642–648
14. Nagura T, Dyrby CO, Alexander EJ, Andriacchi TP (2002) Mechanical loads at the knee joint during deep flexion. *J Orthop Res* 20(4):881–886
15. Lu Y et al (2015) Investigation on the microstructure, mechanical property and corrosion behavior of the selective laser melted CoCrW alloy for dental application. *Mater Sci Eng, C* 49:517–525
16. Donahue TLH, Hull ML, Rashid MM, Jacobs CR (2002) A finite element model of the human knee joint for the study of tibio-femoral contact. *J Biomech Eng* 124(3):273
17. Freedman R, Sheehan FT, Lerner AL (2015) MRI-based analysis of patellofemoral cartilage contact, thickness, and alignment in extension, and during moderate and deep flexion. *Knee* 22(5):405–410
18. Thambyah A, Goh JCH, Das De S (2005) Contact stresses in the knee joint in deep flexion. *Med Eng Phys* 27(4):329–335
19. Besier TF, Draper CE, Gold GE, Beaupré GS, Delp SL (2005) Patellofemoral joint contact area increases with knee flexion and weight-bearing. *J Orthop Res* 23(2):345–350
20. Wang J, Tao K, Li H, Wang C (2014) Modelling and analysis on biomechanical dynamic characteristics of knee flexion movement under squatting. *Sci World J* 2014
21. Zelle J, Van der Zanden AC, De Waal Malefijt M, Verdonschot N (2009) Biomechanical analysis of posterior cruciate ligament retaining high-flexion total knee arthroplasty. *Clin Biomech* 24(10):842–849
22. Anuar MAM, Todo M, Nagamine R, Hirokawa S (2014) Dynamic finite element analysis of mobile bearing type knee prosthesis under deep flexional motion. *Sci World J* 2014:6

# Study of CO<sub>2</sub> Solid Formation During Blowdown of Cryogenic CO<sub>2</sub>–CH<sub>4</sub> Distillation Process



Umar Shafiq, Azmi M. Shariff, Muhammad Babar, Babar Azeem, Abulhassan Ali and Azmi Bustam

**Abstract** Solidification of CO<sub>2</sub> is one of the critical issues during blowdown in the cryogenic natural gas distillation process. Cryogenic distillation process for separation of CO<sub>2</sub> from natural gas usually works at low temperature and high pressure that produces higher purity natural gas and CO<sub>2</sub> in the vapor-liquid phase. However, in case there is an emergency, the mixture inside distillation column is passed through blowdown valve for sudden depressurization. This rapid depressurization would cause sudden expansion of CO<sub>2</sub> mixture resulting in a dramatic drop in the fluid temperature that could solidify CO<sub>2</sub> and cause pipe blockage. This solidification phenomenon is not fully understood that makes the solidification of CO<sub>2</sub> during blowdown process difficult to control. Therefore, the research study presents investigations of the thermodynamic study for the depressurization of highly pressurized vessel containing CO<sub>2</sub>–CH<sub>4</sub> binary mixture from cryogenic conditions. Simulation is performed for 20% concentrations of CO<sub>2</sub>–CH<sub>4</sub> mixture over different orifice size e.g. 1.00 and 1.25 mm using BLOWDOWN software package in Aspen HYSYS<sup>®</sup> V 9.0.

## 1 Introduction

In Process plant, particularly in the oil and gas industry, vessels containing gases or flashing liquids are usually operating under pressure. These pressure vessels contain hazardous, flammable or radioactive materials e.g. natural gas, that requires highly safe operating conditions. However, high pressure operations come along with hazards relating to process. Major hazard associated with vessel under pressure is leak or rupture due to accident. Particularly in oil and gas industry, rupture of the pressure

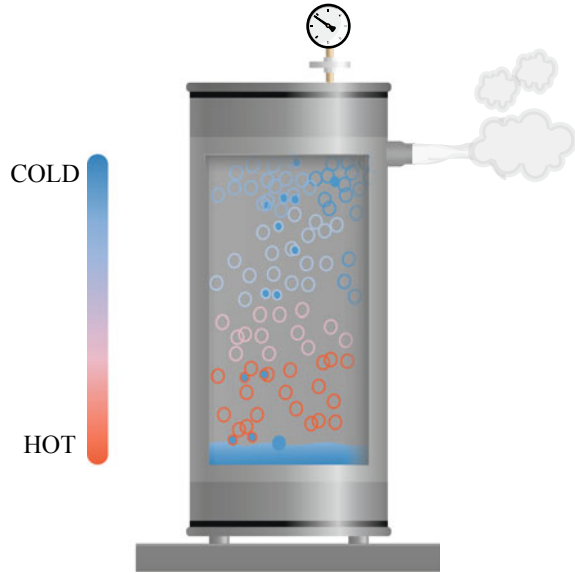
---

U. Shafiq · A. M. Shariff (✉) · M. Babar · B. Azeem · A. Bustam  
CO2 Research Centre (CO2RES), Universiti Teknologi PETRONAS, 32610 Bandar Seri  
Iskandar, Perak, Malaysia  
e-mail: [azmish@utp.edu.my](mailto:azmish@utp.edu.my)

A. Ali  
Department of Chemical Engineering, University of Jeddah, Jeddah, Saudi Arabia

© Springer Nature Singapore Pte Ltd. 2020  
M. Awang et al. (eds.), *Advances in Material Sciences and Engineering*, Lecture Notes in Mechanical Engineering,  
[https://doi.org/10.1007/978-981-13-8297-0\\_4](https://doi.org/10.1007/978-981-13-8297-0_4)

**Fig. 1** Joule-Thomson effect

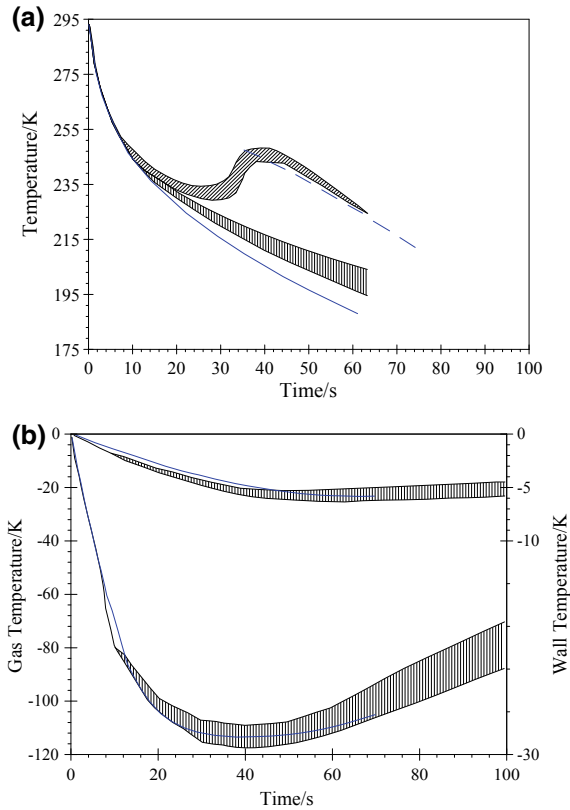


vessel is of higher danger when there is a leakage of flammable mixture. Therefore, to predict the consequences of a leak or rupture of a pipeline or vessel, or to design a controlled pressure release system, a method of predicting the mass efflux is required.

Blowdown of pressure vessel is one of the most prominent techniques used during leak or rupture of a pipeline or vessel. Rapid depressurization of pressure vessels, usually called ‘blowdown’, is a hazardous operation, at least as far as large pressure vessels are concerned. During rapid depressurization the hazard arises following the low temperature generated inside vessel due to Joule-Thomson effect (Fig. 1) [1]. This inevitably leads to a reduction in the temperature of the vessel itself and possibly to a temperature below the ductile-brittle transition temperature of the steel from which the vessel was fabricated [2]. Moreover, in case of cryogenic separation process, another problem associated is the solid formation that can cause blockage. Consequently, the blockage during blowdown in an emergency situation that can lead to further damage. Therefore, it is essential to design such depressurization scenarios that should safely discharge the inventory.

To predict the suitable blowdown scenarios, different models have been developed for the study of depressurization of mixture over time. A tool termed as “BLOW-DOWN” was established and coded by [2, 3]. The tool was validated against experimental data performed for depressurization of vessels containing pure  $N_2$ , 70%  $N_2$ -30%  $CO_2$ . The developed BLOWDOWN tool can predict the dynamic changes of temperatures, pressure and composition, etc. In all the case studies, the BLOW-DOWN tool predicted reasonable understanding of the physical processes occurring and dynamic changes in temperature and pressure as shown in Fig. 2.

**Fig. 2** Dynamic temperature changes during blowdown for **a** 70% N<sub>2</sub>-30% CO<sub>2</sub> mixture and **b** pure N<sub>2</sub>



In this study, BLOWDOWN model is used because it does not assume the thermodynamic equilibrium and can simulate three phases. Density dependency can be modelled using the equation of state (EoS) based upon extended corresponding state principle, which is more accurate than cubic EoS, however, it requires more run-time. Some other significant models are LEKCON [4], SAFIRE [5], OLGA [6], RELEASE [7], PHAST [8], and BLOWSIM [9–11], etc.

The objective of this paper is to describe some of the works performed to predict the behaviour of a vessel during depressurization. The vessel is initially at cryogenic conditions containing binary CO<sub>2</sub>-CH<sub>4</sub> mixture and requires an emergency blowdown. The problem associated with emergency blowdown at cryogenic conditions is that there are chances of vessel rupture as well as dry ice formation because of low temperature generated inside the vessel. Therefore, optimum blowdown parameters are required in order to avoid blockage and rupture of vessel.



## 2 Research Methodology

To overcome issues regarding depressurization, proper assessment of the hazards associated with blowdown of a vessel containing CO<sub>2</sub>–CH<sub>4</sub> mixture, there is a need to be able to predict fluid pressure, temperatures and phase behavior all as a function of time. Subsequently, optimum blowdown time requires a delicate balance between the maximum permissible blowdown time, minimum wall, and fluid temperatures that may be safely considered [12]. The traditional approach has been to overdesign. However, this approach has become less attractive because of the rapidly decreasing profit margins of the oil and gas industry [10]. Thus, for the calculation of optimum blowdown parameters with minimum cost and hazards, two simulation-based case studies were conducted: using 1.00 and 1.25 mm orifice on Aspen HYSYS V9<sup>®</sup>. Both types of simulations were initiated by blowdown from top of the vessel. The aim of the study is to investigate the effect of orifice size and time on the temperature, pressure and phase behavior of binary mixture and evaluate optimum blowdown parameters.

To study the formation of dry ice, the mixture is blown down from cryogenic condition. Since the mixture is already at very low temperature (cryogenic conditions), the Joule-Thomson effect with sudden depressurization causes the spontaneous drop in temperature that leads to the formation of solids. These solid can block the blowdown valve, that can cause further damage because of the increasing pressure inside vessel. Therefore, these case studies helped to observe the solid formation, phase behavior changes with time and orifice size. The mixture inside the vessel was considered to be at –40 °C and 40 bar pressure. The cryogenic conditions helped to observe the worst-case scenario for blowdown of the CO<sub>2</sub> gaseous mixture. The simulation parameters and conditions used for this study are given in Table 1.

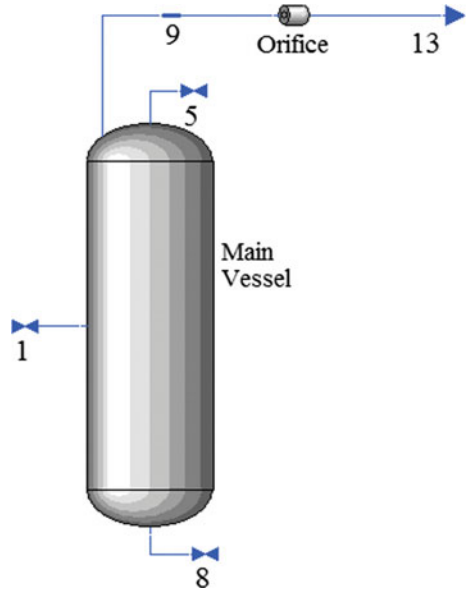
For this study, a 952 mm long with 91.63 mm inner diameter (Fig. 3). The wall thickness of the vessel is 6.7 mm, while the thickness of walls and head of the vessel is constant.

To simulate the process, the BLOWDOWN package in Aspen HYSYS<sup>®</sup> V9 is used as a simulation tool. Peng-Robinson [13] EoS is selected as a property package. After selecting Blowdown utility, blowdown valve is linked to the top of the vessel.

**Table 1** Simulation parameters and conditions

Composition CO <sub>2</sub>	20.0 mol%
CH <sub>4</sub>	80.0 mol%
Initial temperature	–30 °C
Initial pressure	40 bar
Vessel orientation	Vertical
Orifice diameter	1.00 mm (1st case) 1.25 mm (2nd case)
Leakage direction	Top
Ambient temperature	25 °C
Back pressure	1.01325 bar

**Fig. 3** Blowdown process sheet using Aspen HYSYS

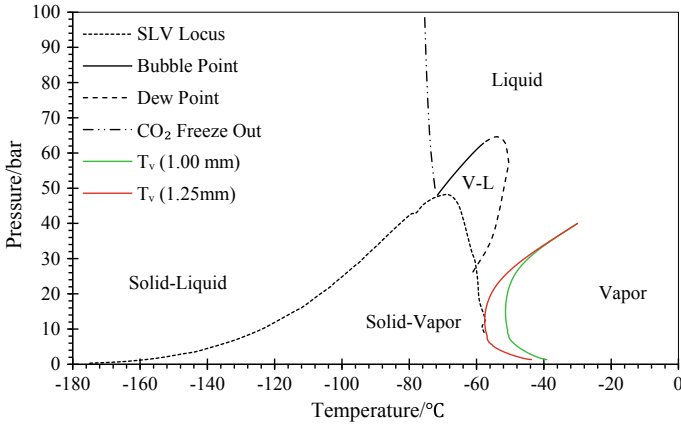


A feed stream at  $-30\text{ }^{\circ}\text{C}$  and 40 bar is connected to the vessel. Vessel conditions and dimensions are defined along with ambient temperature and pressure. First, the blowdown process is converged for 1.25 mm orifice size followed by 1.00 mm. The vessel at high pressure (40 bar) is depressurized to atmospheric pressure with different orifice sizes. It is found that the larger the orifice size, the smaller the depressurization time required to reach the atmospheric pressure.

Dynamic pressure, temperature profiles and phase behavior of mixture during depressurization process is generated. Pressure-time profiles display the trend of the depressurization during blowdown process. Temperature-time profiles are the dynamic temperature transition of vapors inside the vessel. Pressure-Temperature graphs are the phase behavior of binary mixture during the blowdown process. These profiles are generated to observe the solid formation and to calculate suitable orifice size for respective process. To observe the chances of solid formation, frost line for the binary mixture is generated using Aspen HYSYS<sup>®</sup>. This will indicate that the mixture inside the vessel is entering the solid region from vapor-liquid region. To avoid solidification, the mixture should not pass the frost line, otherwise the solid formation starts that may cause the blockage.

### 3 Result and Discussion

Donnelly and Katz [14] and Davis et al. [15] presented explicit data for CO<sub>2</sub> solid formation at different pressures. They presented three-phase locus (SLV Locus) at which all the three phases of CO<sub>2</sub> coexist. The area under the S-L-V curve is the two-

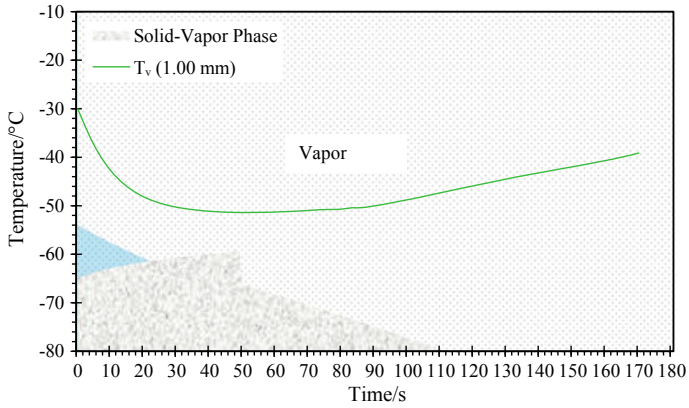


**Fig. 4** Phase behaviour of 20% CO<sub>2</sub>–80% CH<sub>4</sub> mixture during blowdown

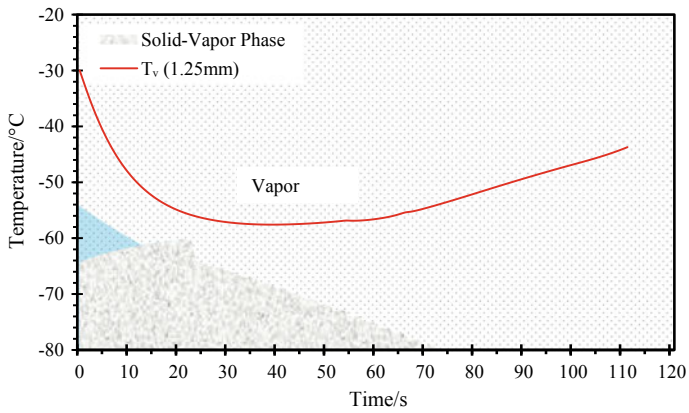
phase S-V region as illustrated in Fig. 4. The SV and SLV Locus are the most critical phases during the depressurization process. Phase behaviour for 20% CO<sub>2</sub>–80% CH<sub>4</sub> mixture during blowdown from 1.00 and 1.25 mm orifice is also outlined in Fig. 4. To study the worst-case scenario for blowdown process, the mixture is blown down from cryogenic conditions (40 bar pressure and –30 °C temperature). These cryogenic conditions will help to overcome the problem related to the solid formation during blowdown process in emergency situations. Initially, the mixture is in vapor phase. Blowdown from 1.00 mm orifice successfully reached minimum pressure without entering the solidification phase as mentioned in Fig. 4. Moreover, this binary mixture remains in vapor phase throughout the process. The vessel with orifice 1.00 mm reaches the minimum pressure in 170 s. However, depressurization using 1.25 mm orifice size can cause the blockage of valve due to chance of solid formation. The minimum temperature reached by the T<sub>v</sub> (1.00 mm) stream is ≈–51 °C, that is higher than the solidification temperature at that pressure.

Similar to Figs. 5, 6 is about dynamic temperature profile for vapor temperature from 1.25 mm orifice. The vessel took 116 s to reach the minimum pressure. However, near 20 s the vapors come closer to the solidification region with the neglectable margin that increases the chances of solid formation, after that the mixture again returned to vapor phase. Therefore, 1.25 mm orifice size is not suitable for 20% CO<sub>2</sub>–80% CH<sub>4</sub> binary mixture blowdown from defined vessel size because there are chances of solid formation.

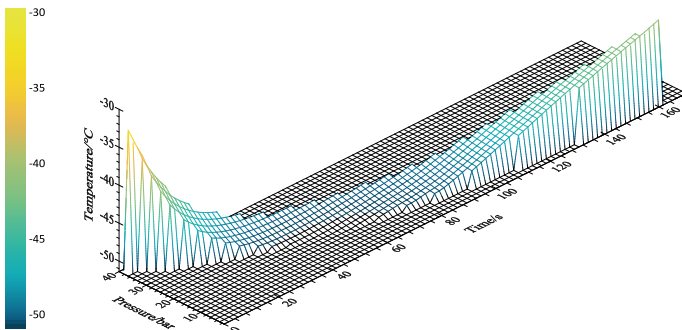
The particular graph in Fig. 7 is three-dimensional representation of how pressure and temperature changes with time when binary mixture is blown down from a 1 mm orifice. It appears that at initial conditions, the temperature first declines till 45 s and afterward shows a gradual increase while pressure constantly decreases throughout the process. Pressure decreases from 40 bar to atm in almost 170 s without solid formation.



**Fig. 5** Main vessel vapor temperature from 1.00 mm orifice



**Fig. 6** Main vessel vapor temperature from 1.25 mm orifice



**Fig. 7** Dynamic temperature-pressure 3D profile for 20% CO<sub>2</sub>-80% CH<sub>4</sub> mixture from 1.00 mm orifice

## 4 Conclusion

In this research paper, a simulation study of depressurization of highly pressurized vessel containing binary mixture is carried out. The aim of this research is to investigate the temperature and pressure changes and phase behavior of binary mixture over different orifice diameters i.e. for 1.00, and 1.25 mm. The results show that the orifice with diameter of 1.00 mm for 20% CO<sub>2</sub>–80% CH<sub>4</sub> can prevent the solidification during depressurization and reduce the chances of accidents. While, other orifice sizes can provoke solidification which may lead to blockage or any accidental event in vessel or process plants. This simulation study requires experimental validation to overview the difference in simulation study with real life problem. In the future, blowdown process can be expanded to planned blowdown in natural gas industry to avoid hazards while shutting down the plant.

**Acknowledgements** The authors would like to extend their most profound gratitude to the CO<sub>2</sub> Research Centre (CO2RES), Universiti Teknologi PETRONAS (UTP), Malaysia, and Hyundai Heavy Industries (HHI), South Korea, for the provision of research grant and on-campus state of the art facilities to accomplish this research.

## References

1. Richardson S, Saville G (1993) Blowdown of vessels and pipelines. In: Institution of chemical engineers symposium series, pp 195–195
2. Haque A, Richardson S, Saville G et al (1990) Rapid depressurization of pressure vessels. *J Loss Prev Process Ind* 3:4–7
3. Richardson S, Saville G (1996) Blowdown of LPG pipelines. *Process Saf Environ Prot* 74:235–244
4. Woodward JL (1990) An integrated model for discharge rate, pool spread, and dispersion from punctured process vessels. *J Loss Prev Process Ind* 3:33–37
5. Cumber P (2001) Predicting outflow from high pressure vessels. *Process Saf Environ Prot* 79:13–22
6. Bendiksen KH, Maines D, Moe R et al (1991) The dynamic two-fluid model OLGA: theory and application. *SPE Prod Eng* 6:171–180
7. Johnson DW, Woodward JL (2000) RELEASE: a model with data to predict aerosol rainout in accidental releases (with CD-ROM) ed
8. Witlox HW, Bowen PJ (2002) Flashing liquid jets and two-phase dispersion: a review prepared by Det Norske Veritas Ltd for the Health and Safety Executive: HMSO
9. Mahgerefteh H, Saha P, Economou IG (2000) Modeling fluid phase transition effects on dynamic behavior of ESDV. *AIChE J* 46:997–1006
10. Mahgerefteh H, Wong SM (1990) A numerical blowdown simulation incorporating cubic equations of state. *Comput Chem Eng* 23:1309–1317
11. Mahgerefteh H, Falope GB, Oke AO (2002) Modeling blowdown of cylindrical vessels under fire attack. *AIChE J* 48:401–410
12. R. Api (1990) Recommended practice 521
13. Peng D-Y, Robinson DB (1976) A new two-constant equation of state. *Ind Eng Chem Fundam* 15:59–64

14. Donnelly HG, Katz DL (1954) Phase equilibria in the carbon dioxide–methane system. *Ind Eng Chem* 46:511–517
15. Davis J, Rodewald N, Kurata F (1962) Solid-liquid-vapor phase behavior of the methane-carbon dioxide system. *AIChE J* 8:537–539

# Prediction of Fatigue Failure Location on Lower Control Arm Using Finite Element Analysis (Stress Life Method)



S. K. Abu Bakar, Rosdi Daud, H. Mas Ayu, M. S. Salwani and A. Shah

**Abstract** Analyzing a structure early in the design cycle gives an automotive industry a huge advantage which can reduce development time and cost. Before a prototype can be built and tested, determination of the critical region of the structure should be achieved and thus the design can be improved. The method involves the study of the fatigue failure location and structural integrity of the lower control arm subjected to the load applied mimicking real condition of the lower control arm operation. The 3D geometry of finite element model is simulated in Autodesk Mechanical Simulation. The finite element analysis (FEA) results are compared to critical distance approach whereby prediction of the fatigue failure is focused on critical location of curve near bushing. Finally, it is concluded that this approach can be considered as an initial process for the design of the high life lower suspension arm.

**Keywords** Fatigue analysis · Fatigue failure · Life cycle

## 1 Introduction

Fatigue analysis can be used to determine the period or time the component can maintain in a given service condition. Kyrre et al. conducted the fatigue life prediction of control arm using finite element analysis of surface topography [1]. Noor et al. did strain analysis on lower control arm where the data were reasonably corrected by the finite element model and helped researchers to identify the exact position where the strain gauges must be fixed [2]. Recently, many analyses and optimization methods and tools for structure design based on FEA have been introduced to biomedical

---

S. K. Abu Bakar · R. Daud (✉) · H. Mas Ayu · M. S. Salwani  
Faculty of Mechanical Engineering and Manufacturing, University Malaysia Pahang, 26600  
Pekan, Pahang, Malaysia  
e-mail: [rosdidaud@ump.edu.my](mailto:rosdidaud@ump.edu.my)

A. Shah  
Faculty of Technical and Vocational, Universiti Pendidikan Sultan Idris, 35900 Tanjung Malim,  
Perak, Malaysia

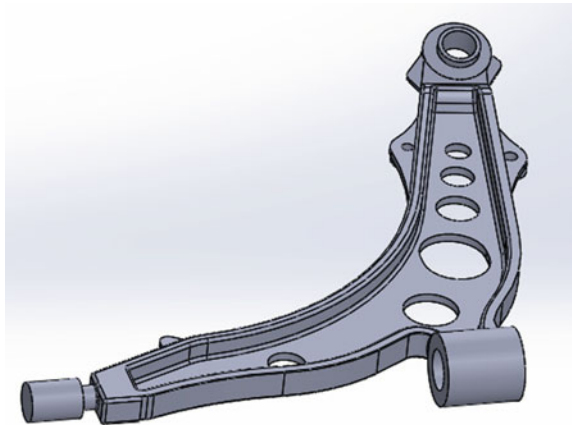
industry [3, 4], so does for automobile industry [5–8]. Bekah et al. investigated car door hinge using FEA and validated the results by experiment [9]. Rahman et al. conducted fatigue life prediction of lower control arm using strain-life approach [10].

The lower control arm was a key part of front suspension which controls the wheel trace and transmits load exerting on the wheel by the road to other parts of the car. When the car was running on the road, the lower control arm was subjected to complex loads alternating with time. Thus, the mechanical performances, usually relating to strength and fatigue life were critical for the safety and reliability of the car. Thus, the aim of the this paper is to show how finite element analysis is helping in complete product development cycle which focus on fatigue failure location and fatigue life prediction of lower control arm using stress-life method. It also can contribute to further research in fatigue failure component that use the theory of critical distance which is considered to be the most effective method in fatigue failure prediction nowadays [11–16].

## 2 Methods

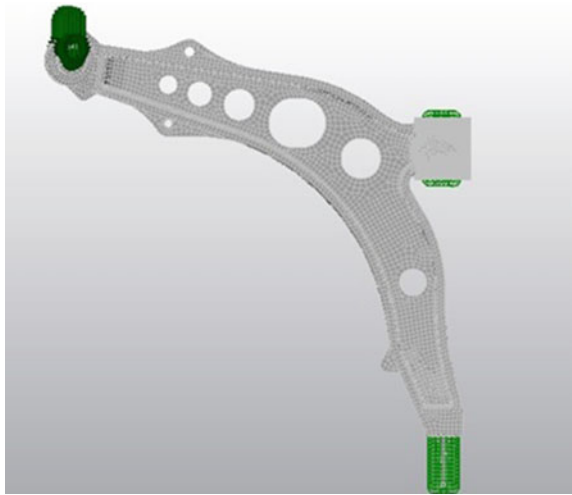
In this study, the method used to predict the fatigue failure location and the life cycle of the lower control arm is made using a standard commercial software package, designed to interface with finite element results to produce post-processed data in the form of contour plots of fatigue life. The software considers all nodes on the surface of the component only, using stress-life data from plain specimens and incorporating a Neuber-type correction for strain-life predictions. The software used is Autodesk Mechanical Simulation while, the 3D geometry of lower control arm is constructed using Solidworks software as shown in Fig. 1.

**Fig. 1** 3D geometry of lower control arm





**Fig. 2** Lower control arm boundary condition



For the finite element analysis (FEA), material that was assigned for the lower control arm (LCA) is ductile cast iron. It is because this material is often used for the automobile’s suspension components. Ductile cast iron is a nodular iron with a fully ferritic matrix. This iron grade’s microstructure is achieved through annealing and offers excellent ductility and impact strength. It has a tensile strength between 310 and 460 MPa.

The load applied to the LCA is mimicking the real condition of the lower control arm operation. Figure 2 shows the boundary condition for the lower control arm where each link has 6 degrees of freedom (3 translation motion and 3 rotation motion). The LCA was loaded with 2363 N at one point only (represented by green arrows in Fig. 2) in the x direction. It was restrained at two points: the bushing and the lowest part. At the front bushing, a rigid restraint (zero displacements) was imposed in y and z directions. At the lowest part, a rigid restraint (zero displacements) was also applied in y and z directions.

For the prediction of the fatigue failure location and the fatigue life of a LCA, an integrated approach between fatigue life analysis and the finite element analysis was done which the S-N curve is the outcome. The S-N curve is usually obtained by plotting the data points on semi-log or log-log paper. The resulting curve could be calculated by mathematical equation as shown below, which relates to the stress amplitude and number of cycles to failure.

$$\sigma_a = \sigma'_f (2N_f)^b \tag{1}$$

where,

$\sigma'_f$  fatigue strength of material.

$b$  fatigue strength exponent.

For iron, fatigue failures with less than  $10^3$  cycles are considered as low cycle fatigue while high cycle fatigue deal with failures more than  $10^3$  cycles. The S-N curve obtained by FE method was then compared with the S-N curve obtained by critical distance approach done by Taylor et al. [17].

### 3 Results and Discussions

For the Stress Maximum Principle, the maximum stress recorded is 212.2695 MPa at the curve near the bushing as shown in Fig. 3.

Based on Fig. 4, we can clearly see that the stress distribution at bushing area is higher than the fillet area. So, we can say that the tendency of fatigue failure to occur is at the bushing area of the lower control arm. In focusing more on the critical location, the maximum stress value of 297.106 MPa is recorded at the bushing curve (Fig. 5). This critical location is quite similar as found by Taylor et al. via experiment [17].

By using stress-life method, the life cycle predicted by FEA is slightly higher compared than critical distance approach results due to the geometry and measuring error during reverse engineering of the lower control arm. This is because, Taylor et al. used critical distance approach based on the dimension of lower control arm directly taken from the 3D scanner. Thus, the dimension is more accurate and additionally, critical distance approach is considered the best method to predict fatigue life cycle. Table 1 shows the life cycles comparison between critical distance and FEA approach. For the critical distance approach, the life cycle is 1210 cycles and FEA recorded

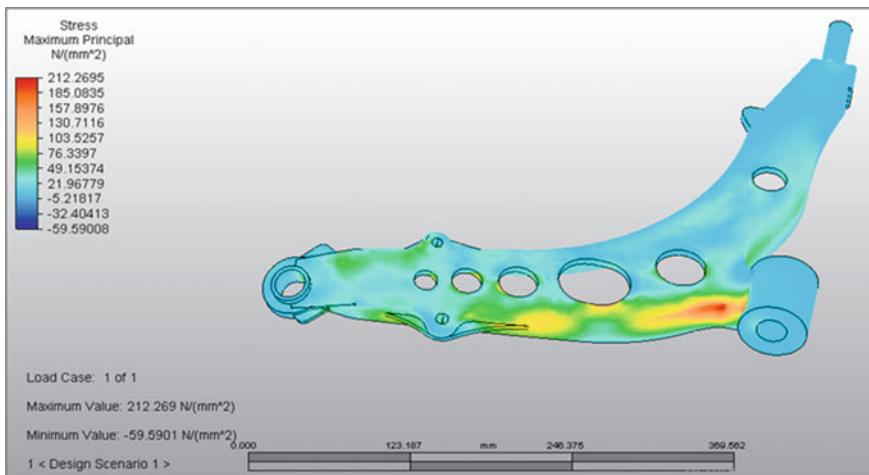


Fig. 3 Maximum stress principle

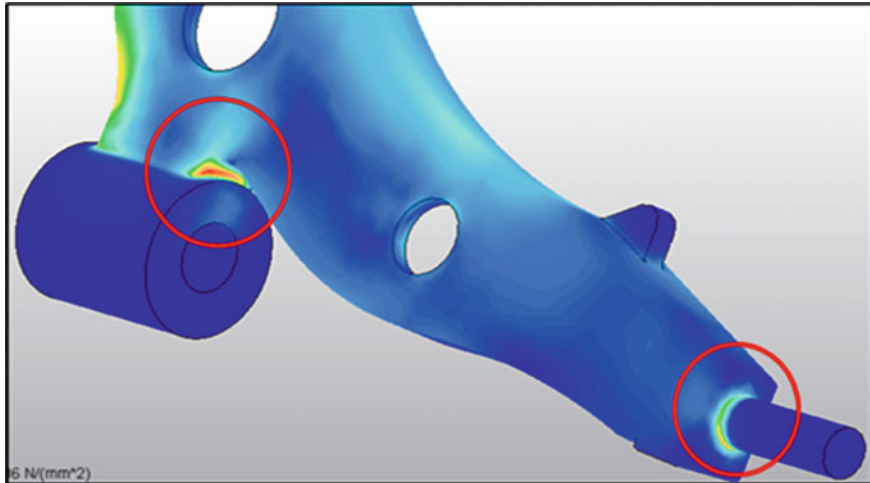


Fig. 4 Maximum stress principle

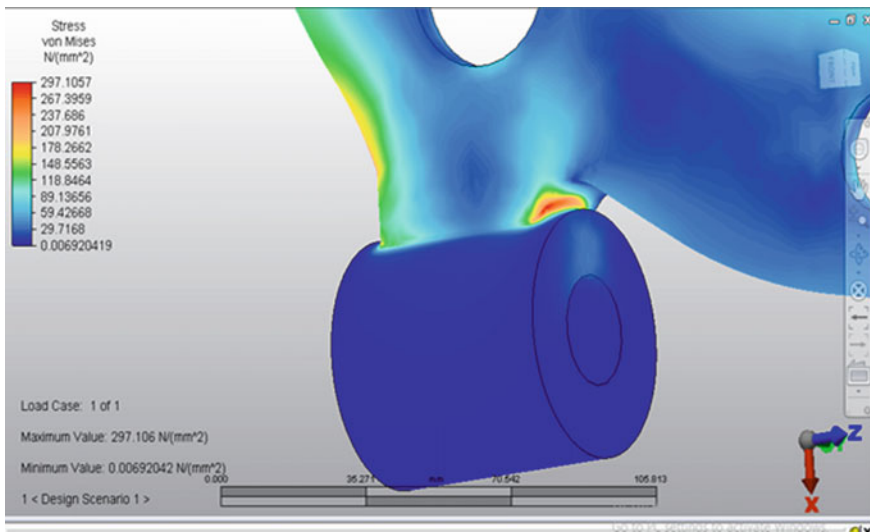


Fig. 5 Showing the stress distribution at the critical location

**Table 1** The life cycles for the finite element analysis and critical distance approach

	Results	
	Critical distance approach [17]	Finite element analysis
Life cycles	1210	1280
Error (%)	5.78%	

life cycles of 1280 cycles. However, the percentage error for the life cycle is 5.78% where the expected error is 10%. Thus, the error is within acceptable tolerances.

## 4 Conclusions

Based on the FEA results performed in this study, the following can be concluded.

- (1) If correct boundary condition is applied on the lower control arm, the location of the fatigue failure can be predicted and the results will be similar with previous experimental results.
- (2) Based on the analysis, prediction of the fatigue failure is focused on critical location of curve near bushing.
- (3) The FEA results can be considered as an initial process for any component design to predict the fatigue failure and the life cycle to minimize the cost and time. You use the above guidelines in conjunction with the two Springer documents, you should be able to prepare you manuscript easily and correctly.

**Acknowledgements** We would like to thank Universiti Malaysia Pahang through research grant RDU1703311 for fully support the facilities and resources for this research.

## References

1. Kyrre SA, Skallerud B, Tveiten WT, Holme B (2005) Fatigue life prediction of machined components using finite element analysis of surface topography. *Int J Fatigue* 27:1590–1596
2. Rahman MM, Noor MM, Kadirgama K, Rejab R (2009) Fatigue life prediction of lower suspension arm using strain-life approach. *Eur J Sci Res* 30:437–450
3. Daud R, Mas Ayu H, Salwani MS, Tomadi SH, Kadir MRA, Raghavendran HB, Kamarul T (2017) Artificial neural network: the alternative method to obtain the dimension of ankle bone parameters. *J Eng Appl Sci* 12:2782–2787
4. Zakaria FA, Daud R, Mas Ayu H, Tomadi SH, Salwani MS, Kadir MRA (2017) The effect of position and different size of radial hole on performance of cannulated pedicle screw. In: *MATEC web of conferences*, vol 108, pp 13001
5. Kang BJ, Sin HC, Kim JH (2007) Optimal shape design of the front wheel lower control arm considering dynamic effects. *Int J Autom Technol* 8:309–317
6. Topac MM, Gunal H, Kuralay NS (2008) Fatigue failure prediction of a rear axle housing prototype by using finite element analysis. *Eng Fail Anal* 16:1474–1482

7. He B, Wang S, Gao F (2010) Failure analysis of an automobile damper spring tower. *Eng Fail Anal* 498–505
8. Rutci A (2015) Failure analysis of a lower wishbone. In: Special issue of the international conference on computational and experimental science and engineering, p 128
9. Bekah S et al (2006) Fatigue life prediction in a door hinge system under uni-axial and multi-axial loading conditions. *Library and Archives Canada = Bibliothèque et Archives Canada*
10. Rahman MM, Ariffin AK, Abdullah S, Jamaludin N (2007) Finite element based durability assessment of a free piston linear engine component. *J Struct Durability Health Monit* 3:1–13
11. Sun S, Yu X, Liu Z, Chen X (2016) Component HCF research based on the theory of critical distance and a relative stress gradient modification. *PLoS ONE* 11(12):e0167722
12. Spaggiari A, Castagnetti D, Dragoni E, Bulleri S (2016) The use of the theory of critical distance and the stress-gradient approach in the fatigue life estimation of notched components. *Proc Inst Mech Eng Part L J Mater Des Appl* 230:735–747
13. Vallellano C, Navarro A, Chaves V (2014) A new proposal of effective stress and critical distance for fatigue at notches. In: MATEC web of conferences, vol 12, p 09002
14. Karakaş Ö, Zhang G, Sonsino CM (2018) Critical distance approach for the fatigue strength assessment of magnesium welded joints in contrast to Neuber's effective stress method. *Int J Fatigue* 112:21–35
15. Majzoobi GH, Azhdarzadeh P (2018) Estimation of axial fretting fatigue life at elevated temperatures using critical distance theory. *Surf Rev Lett* 25(03)
16. Santus C, Taylor D, Benedetti M (2018) Sensibility analysis of the fatigue critical distance values assessed by combining plain and notched cylindrical specimens. *Proc Struct Integrity* 8:67–74
17. Taylor D, Bologna P, Bel Knani K (2000) Prediction of fatigue failure location on a component using a critical distance method. *Int J Fatigue* 22:735–742

# Numerical Investigation of Sand Particle Erosion in Long Radius Elbow for Multiphase Flow



Muhammad Rehan Khan, H. H. Ya, William Pao and Mohd Amin A. Majid

**Abstract** Solid particle erosion is predominant in hydrocarbon production, drilling and minerals processing industries. Erosion may be caused by the impact of particles of various sizes, shapes, and hardness at different velocities and trajectories. Sand particles transported in multiphase flow pipelines pose an erosion threat, which is one of the current flow assurance challenges in hydrocarbon production process. In the midst of them, pipe blockage and erosion issues emerge most important. Erosion is a material removal process which disintegrates material from the flow lines because of continuous sand particle impacts. Eroded pipelines affect operating safety as well as increasing operating cost. Hence, it is vital to comprehend parameters involvement to understand the erosion physics. Recently, computational fluid dynamics (CFD) along with different intrusive and non-intrusive techniques have been widely employed for erosion modeling and failure assessment. In this paper, we highlight the investigation directed to quantify sand particles erosion in long radius elbow configuration for multiphase flow conditions utilizing CFD by implementing empirical and semi-empirical erosion models.

**Keywords** Solid particle erosion · Multiphase · Pipeline · CFD

## 1 Introduction

Erosion is a significant failure mode that can cause failure and malfunctions to parts in equipment, such as hydrocarbon production pipelines, chemical industries, and mineral processing. In an erosion process, erodent particles are transported by a carrier fluid in an operating process, and impact on pipelines and component and wear the surface.

---

M. R. Khan (✉) · H. H. Ya · W. Pao · M. A. A. Majid  
Mechanical Engineering Department, Universiti Teknologi PETRONAS, Bandar Seri, Iskandar,  
Tronoh Perak, Malaysia  
e-mail: [Muhammad\\_15001294@utp.edu.my](mailto:Muhammad_15001294@utp.edu.my)

© Springer Nature Singapore Pte Ltd. 2020  
M. Awang et al. (eds.), *Advances in Material Sciences and Engineering*, Lecture Notes in Mechanical Engineering,  
[https://doi.org/10.1007/978-981-13-8297-0\\_6](https://doi.org/10.1007/978-981-13-8297-0_6)

Erosion is a complicated problem caused by many variables, for example, particle kinematics and particle dynamics characteristics [1, 2]. Various investigations were led to clarify the erosion process. Analyses, for the most part, give constrained information, for example, erosion rate and erosion profile. The constrained information cannot give adequate data to additionally break down the dynamic erosion process.

Anticipating sand particle erosion in the multiphase transporting system is a difficult task. In spite of the considerable number of studies [3–6] that have been done on the investigation of erosion mechanism, the solid particle erosion mechanism is as yet not completely understood. An assortment of erosion prediction models and methodologies have been proposed by researchers [7–10]. However, the accuracy of these models and methodologies are still questionable [11]. The primary objective of this paper is to investigate the accuracy of empirical and semi-empirical erosion models.

To quantify the influence of parameters on the erosion of low stroke flow, different experimental techniques have been designed, such as the Coriolis test [12], direct jet impingement test [13], slurry pot test [14, 15], and flow loop test [16–18]. It is essential to capture those key parameters regulating the observed erosion damages to monitor and avoid excessive erosion damage in the pipeline system. However, the empirical and semi-empirical erosion models defined in literature are derived using direct impact testing condition. In the present study, three most common erosion models are applied using commercial CFD package to quantify induced erosion in long radius elbow configuration. The numerical results are compared with the experimental results extracted by Ronald et al. [19] and shows divergence in the magnitude of induced erosion impact and Oka erosion model is most suitable for quantification of erosion under multiphase conditions as compared to Finnie and Mclaury models which over predicts the erosion rate under multiphase conditions.

## ***1.1 Solid Particle Erosion Models***

Sand particles dispersed in the production of a hydrocarbon fluid, leading to potentially catastrophic failure and equipment malfunction. The magnitude of erosion damage is influenced by a wide range of factors, comprising the properties of the sand particles, carrier fluid characteristics and physical properties of the target material. Numerous sand erosion prediction models, including empirical, semi-empirical, and computational fluid dynamics (CFD), have been developed incorporated with those affecting factors and mechanisms to forecast and to determine the erosion rate, as well as to eliminate the erosion risk in production systems. Some models are based on empirical correlations with laboratory data, and have many simplifying assumptions, while others have built in mechanistic modeling of the different physics and mechanisms of erosion. A review of different models will be further discussed in the consequent section.

Numerous equations have been derived predicated on experimental tests in addition to theoretical erosion equations. In term of semi-empirical models, these models

are similar to empirical models with respect to extrapolation and data requirements, as well as represent physical and erosion phenomena in the equations. Semi-empirical models are some of the most frequently applied models. There are two reasons for this. First of all, uncertainties are anticipated when using those empirical models in the conditions that differ from conducted experimental conditions as they may be valid under certain given conditions. Moreover, empirical models do not solve for sand particle phase. Therefore, the semi-empirical model will overcome those shortcomings. Table 1 summarizes the various empirical and semi-empirical erosion models.

## 2 Computational Fluid Dynamics (CFD) Simulations

The various empirical and semi-empirical erosion models and equations were presented in previous sections. An erosion equation gives an understanding of erosion rate relation for simple geometries. To predict the erosion intensity and damage in the wide range of geometries under different flow conditions, erosion equations should be implemented into CFD codes. Because of the significance of CFD techniques in erosion quantification, a range of studies has been done for complex geometries. For that reason, erosion computational code was developed and integrated with Computational Fluid Dynamic (CFD) software such as FLUENT, CFX, STAR-CCM+. These CFD tools offer the advancement of computational capabilities in providing better accuracy of sand erosion rate and suspected erodent locations.

Pereira et al. [3] utilized the derived model of Grant and Tabakoff to ascertain the erosion intensity of a standard elbow and observed the vee-formed erosion patterns on these elbows. The primary cause of generated vee patterns was sliding impact of the particles at low velocities. A Pereira et al.'s study was extended by Duarte et al. [4] which identified that the mass loading and coupling techniques may essentially alter the erosion pattern of the elbows. Zhang et al. [5] presented a sand erosion probability model to predict erosion of pipe under fully developed flow. Jafari et al. [7] proposed a model to predict erosion by considering the effect of fluctuating velocity of the liquid phase in a horizontal pipe using  $k-\epsilon$  turbulence model and a Discrete Random Walk model.

Zhang and Liu [8] identified the accuracy of turbulence models and concluded that the  $k-\epsilon$  model worked well in modeling the flow field in elbows geometry. In present work, all numerical simulations were performed using  $k-\epsilon$  turbulence model. Erosion of the multiphase flow pipeline bend was simulated using a commercial software package. Assuming that sand particle was introduced at a steady flow condition and entrance length of 1 m and exist length 0.5 m was added to the elbow configuration. The liquid velocity ( $V_L = 0.04$  m/s) and gas velocity ( $V_g = 49$  m/s) were set to obtain multiphase flow condition. The long radius aluminum elbow pipe having an inner diameter of 0.0762 m and the radius of curvature of 0.1143 m geometric configurations were implemented for numerical simulations. The erosion rate is extracted from the simulation for multiphase phase flow conditions. The compu-



**Table 1** Overview of empirical and semi-empirical erosion models

Authors	Models	Descriptions
Finnie [20]	Type: Empirical (Single phase) Equation: $V = K_m \frac{V^2}{p} f(\alpha)$	<ul style="list-style-type: none"> <li>The model is evaluated against the experimental data of micro-cutting mechanism</li> <li>The model developed on assumption that particles fragmentation does not take place during the metal cutting process</li> </ul>
Tabakoff [21]	Type: Empirical (Single phase) Equation: $E = K_1 \left\{ 1 + C_K \left[ K_2 \sin \left( \frac{90}{\beta_0} \beta_1 \right) \right]^2 V_1^2 \cdot \cos^2 \beta_1 \left( 1 - R_1^2 \right) \right. \\ \left. + K_3 (V_1 \sin \beta_1)^4 \right.$	<ul style="list-style-type: none"> <li>Experimentally analyzed the effects of the size, material impact angle, velocity, and concentration of particles on the erosion mechanism</li> <li>A model developed based on analytical approach</li> </ul>
Salama and Venkatesh [22]	Type: Empirical (Single phase) Equation: $ER = s_k \frac{w_p V^2}{D^2}$	<ul style="list-style-type: none"> <li>The model derived from the prediction of penetration rate for elbows and tees configuration</li> <li>A model has been developed for carbon steel materials</li> </ul>
Svedeman and Arnold [23]	Type: Empirical (Multiphase) Equation: $V_e = K_s \frac{D}{\sqrt{w_p}}$	<ul style="list-style-type: none"> <li>Svedeman and Arnold identified the relation for predicting a velocity on the basis of penetration rate</li> </ul>
Shirazi [24]	Type: Semi-Empirical (Multiphase) Equation: $ER = 1.73 \times 10^6 V_1^{1.623}$	<ul style="list-style-type: none"> <li>The model derived to quantify the impact velocity of the particles on the flow line wall</li> </ul>
McLaury [24]	Type: Semi-Empirical (Multiphase) Equation: $ER = F_M F_s F_p F_T / D \left( \frac{D}{D_{ref}} \right)^2$	<ul style="list-style-type: none"> <li>The model derived to study the turbulent fluctuations effect on the erosion intensity for choke geometry</li> </ul>

(continued)

**Table 1** (continued)

Authors	Models	Descriptions
Salama [22]	Type: Empirical (Multiphase) Equation: $ER = \frac{w_p v_p^2 dp}{S_m D^2 \rho_m}$	<ul style="list-style-type: none"> <li>The model derived from Salama and Venkatesh model by introducing multiphase flow</li> </ul>
Oka [25]	Type: Semi-Empirical (Single Phase) Equation: $ER = KH_v^1 \frac{v_p^2}{v} \frac{d^3}{d} \rho_w F(\theta)$	<ul style="list-style-type: none"> <li>The predicted model can be applied for most of the impact angle, particle size, materials, and velocity</li> </ul>
E/CRC [26]	Type: Semi-Empirical (Single Phase) Equation: $ER = C(BH)^{-0.59} F_s V_p^n F(\theta)$	<ul style="list-style-type: none"> <li>The parameters of particles: impact velocity, angle, hardness, and angularity include in the model</li> <li>This model is derived based on sand particles and inconel. Experimentation on the direct impact test</li> </ul>

**Table 2** Summary of erosion parameters under multiphase conditions

	$V_g$ (m/s)	$V_L$ (m/s)	Sand size ( $\mu\text{m}$ )	Max ER (mm/year)	Location ( $^\circ$ )
Experiment [19]	49	0.04	300	89.3	42
Finnie	49	0.04	300	231	40
McLaury	49	0.04	300	597.79	40
Oka	49	0.04	300	103.3	40

tational mesh was generated by ANSYS, 524,000 elements with an element size of 0.003 m were intended to assure the quality. In order to extract erosion rate discrete phase model (DPM) approach was introduced in simulation stages. The parameters used to extract erosion rate of the elbow configurations are listed in Table 2.

### 3 Results and Discussion

Figure 1 shows the erosion rate of the long radius elbow configuration under multiphase flow conditions quantified by three erosion models implemented in CFD and the experimental results extracted by Ronald et al. [19]. It can be seen that the Mclaury erosion model results show large divergence in erosion rate compared to the experimental results. The erosion rate obtained by Mclaury and Finnie model under multiphase conditions over-predicts the erosion rate. Figure 1d shows that the results obtained by the Oka relation are in line with the experimental result with minimum divergence.

Table 2 summarizes the location of maximum erosion region predicted by all three erosion models and result were in line with location obtained by experiment as shown in Fig. 2b. In order to extract erosion under various operating conditions, the more experimental test is needed to further verify the accuracy of erosion models.

### 4 Conclusion

In this paper, we have presented the various investigations that have been conducted to quantify erosion in pipelines, and based on three most common erosion models we drew some main conclusions.

- The liquid-solid-gas erosion mechanism is too complicated than that of liquid-solid induced erosion. The predefined models for erosion quantification and prediction approaches are inadequate because of variations in operating parameters and flow line structural materials leading to a considerable change in erosion damage characteristics.

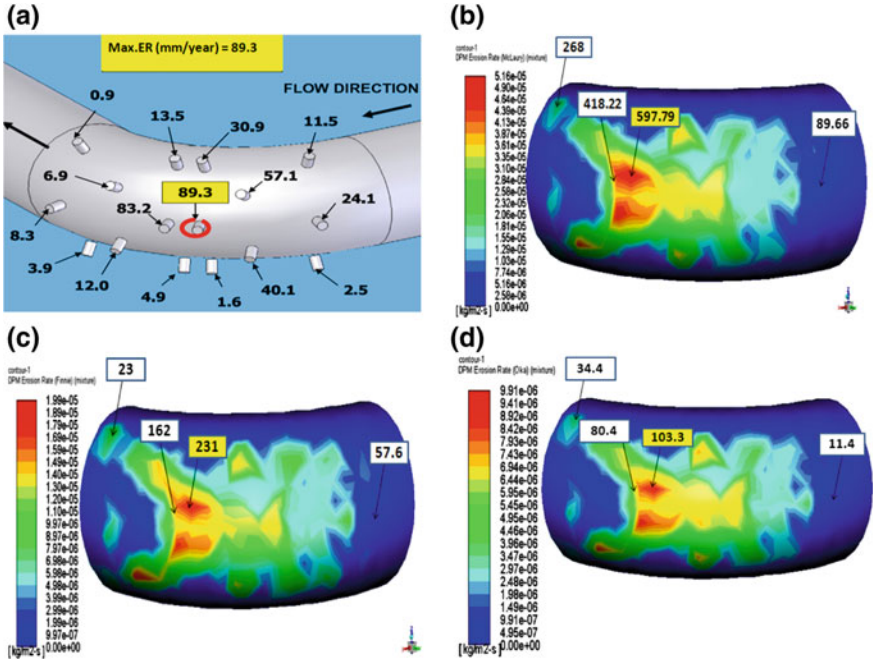


Fig. 1 Comparison of maximum erosion rate ( $\text{Kg/m}^2\text{-s}$ ) or ( $\text{mm/year}$ ) a Experiment [19]. b McLaury model. c Finnie model. d Oka model

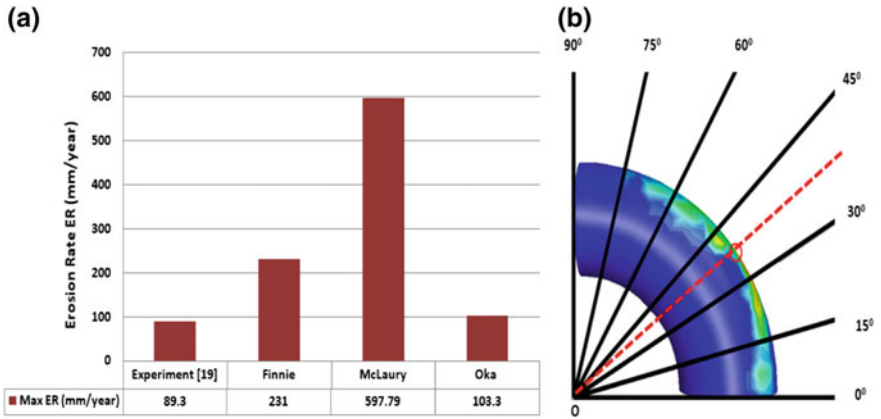


Fig. 2 a Erosion rate obtained with different erosion model. b Location of maximum erosion from a numerical simulation

- The comparison of results in Fig. 2 concludes that Oka's model is quite accurate to capture the location of highest erosion and erosion rate as well as the pattern of the erosion profile under multiphase flow conditions. On the other hand, Finnie and Mclaury model over predicts erosion rate.
- The complexity in modeling flow patterns, as well as particle-particle and particle-fluid interactions in a multiphase carrier fluid, and the difficulty of induced erosion modeling, increase considerably as compared to a single phase flow. Thus, it is vital to understand the deformation due to fluid-solid interactions on pipeline materials by developing a more complex model which includes surface deformation.

**Acknowledgements** The authors acknowledge the support given by the Universiti Teknologi PETRONAS for this research.

## References

1. Nguyen VB, Nguyen QB, Zhang YW, Lim CYH, Khoo BC (2016) Effect of particle size on erosion characteristics. *Wear* 348–349:126–137
2. Yang K, Rong J, Liu CG, Zhao HY, Tao SY, Ding CX (2016) Study on erosion-wear behavior and mechanism of plasma-sprayed alumina-based coatings by a novel slurry injection method. *Tribol Int* 93:29–35
3. Pereira GC, de Souza FJ, de Moro Martins DA (2014) Numerical prediction of the erosion due to particles in elbows. *Powder Technol* 261:105–117
4. Duarte CAR, de Souza FJ, dos Santos VF (2015) Numerical investigation of mass loading effects on elbow erosion. *Powder Technol* 283:593–606
5. Zhang Tan Y (2012) Numerical investigation of location of maximum erosive wear damage in elbow. *Powder Technol* 217:467–476
6. Liu MY, Liu HX, Zhang R (2015) Numerical analyses of the solid particle erosion in elbows for annular flow. *Ocean Eng* 105:186–195
7. Jafari M, Mansoori Z, Saffar Avval M, Ebadi A, Ahmadi G (2014) Modeling and numerical investigation of erosion for gas-solid two-phase flow in a horizontal pipe. *Powder Technol* 267:362–370
8. R Zhang, HX Liu (2014) Numerical simulation of solid particle erosion in a 90-degree bend for gas flow: proceedings of ASME 33rd international conference on ocean, offshore and Arctic Engineering, SanFrancisco, Paper no. OMAE2014-23656
9. Parsi M, Vieira RE, Kesana N et al (2015) Ultrasonic measurements of sand particle erosion in gas dominant multiphase churn flow in vertical pipes. *Wear* 328:413
10. Zhang Jixin (2016) Study on erosion wear of fracturing pipeline under the action of multiphase flow in oil and gas industry. *J Nat Gas Sci Eng* 32:334–346
11. Parsi Mazdak (2014) A comprehensive review of solid particle erosion modeling for oil and gas wells and pipelines application. *J Nat Gas Sci Eng* 21:850–873
12. Lindgren M, Perolainen J (2014) Slurry pot investigation of the influence of erodent characteristics on the erosion resistance of Titanium. *Wear* 321:64–69
13. Zhao Yanlin (2015) Erosion-corrosion behavior and corrosion resistance of AISI 316 stainless steel in flow jet impingement. *Wear* 328–329:464–474
14. Xie Y, Clark HM, Hawthorne H (1999) Modelling slurry particle dynamics in the coriolis erosion tester. *Wear* 225–229:405–416
15. Naz MY (2017) Development of erosion-corrosion mechanisms for the study of steel surface behavior in a sand slurry. *Measurement* 106:203–210

16. Wong CY, Solnordal C, Graham L, Short G, Wu J (2015) Slurry erosion of surface imperfections in pipeline systems. *Wear* 336–337:72–85
17. Vieira RE, Mansouri A, McLaury BS, Shirazi SA (2016) Experimental and computational study of erosion in elbows due to sand particles in air flow. *Powder Technol* 288:339–353
18. Solnordal CB, Wong CY, Boulanger J (2015) An experimental and numerical analysis of erosion caused by sand pneumatically conveyed through a standard pipe elbow. *Wear* 336–337:43–57
19. Vieira RE, Parsi M (2017) Sand erosion measurements under multiphase annular flow conditions in a horizontal-horizontal elbow. *Powder Technol* 320:625–636
20. Finnie L (1995) Some reflections on the past and future of erosion. *Wear* 186–187:1–10
21. Tabakoff GG (1975) Erosion prediction in turbomachinery resulting from environmental solid particles. *J Aircr* 12(5):471–478
22. Salama MM (2000) An alternative to API 14E erosional velocity limits for sand-laden fluids. *J Energy Resour Technol* 122:71–77
23. Svedeman SJ, Arnold KE (1994) Criteria for sizing multi-phase flow lines for erosive/corrosive services. *SPE Prod Facil* 9(1):74–80
24. McLaury BS, Shirazi SA, Shadley JR, Rybicki EF (1996) How erosion corrosion patterns in a choke change as material losses in the choke progress. *Corrosion* 96
25. Oka YI, Matsumura M, Kawabata T (1993) Relationship between surface hardness and erosion damage caused by solid particle impact. *Wear* 162–164:688–695
26. Zhang Y, Reuterfors EP, McLaury BS, Shirazi SA, Rybicki EF (2007) Comparison of computed and measured particle velocities and erosion in water and air flows. *Wear* 263:330–338

# Reduction of Non Added Value Activities During Machine Breakdown to Increase Overall Equipment Efficiency



## Surface Mounting Technology Production Case Study

Shamini Janasekaran and Sheng Hong Lim

**Abstract** Lean manufacturing has been introduced into many industries to increase productivity through reduction of waste. Downtime is one of the contributing factors in determining the production availability time. Changeover time and breakdown failures affect the production available time and this is the main concern in all the manufacturing industries. In this paper, a case study in an electronics assembly line was done to identify the availability time of the operating surface mount technology machine. Reduction in changeover time increased the availability time from the total planned time that leads to increment of overall equipment efficiency from 83.43 to 84.06%. The increment of availability time has increased the performance and overall equipment efficiency from 81.64 to 82.84% and from 64.71 to 66.15% respectively. The increment of overall equipment efficiency increased the production output by 2180 units/month which increased the financial capacity by 545000 MYR/month. The proposed techniques can be used as benchmark to determine the operational decisions made by managements of any manufacturing companies especially in electronics assembly.

**Keywords** Availability · Breakdown · Lean · Manufacturing · OEE

## 1 Introduction

Lean Manufacturing (LM) or simply called as Just-In-Time (JIT) is a tool used to satisfy customer demand on desired output without compromising the quality in effective and economical method. LM can be implemented by identifying the common seven waste (Muda) in the production and eliminating the waste efficiently [1, 2]. LM also can be practiced by emphasizing product flow rather than machine or workstation optimization. Right sizing of productions according to actual demand,

---

S. Janasekaran (✉) · S. H. Lim

Centre for Intelligent Manufacturing Systems, Department of Mechanical Engineering, Faculty of Engineering and Built Environment, SEGi University, Petaling Jaya, Selangor, Malaysia  
e-mail: [shaminijanasekaran@segi.edu.my](mailto:shaminijanasekaran@segi.edu.my)

© Springer Nature Singapore Pte Ltd. 2020

M. Awang et al. (eds.), *Advances in Material Sciences and Engineering*, Lecture Notes in Mechanical Engineering, [https://doi.org/10.1007/978-981-13-8297-0\\_7](https://doi.org/10.1007/978-981-13-8297-0_7)

self-monitoring capabilities of equipment to ensure quality (Jidoka), production flow layout arrangement and implementation of Single Minute Exchange of Die (SMED) which improves setups time for rapid changeovers are some of the techniques used in LM. Usage of kanbans to coordinate the production pull system from the predecessors is a contemporary level in JIT [3, 4]. In implementing LM, the key element is including everyone related in the production and waste elimination. Customers' demand for perfection had urged manufacturers' to be involved in continuous improvements (kaizen) to eliminate waste by sorting Value Added (VA) activity and Non Value Added (NVA) activity. The NVA waste which is a vital obstacle for VA activity is categorized into motion, waiting, overproduction, inventory, defects, over processing and transportation [5, 6]. The ultimate aim of any industries that are introduced to lean management are to have increased productivity, reduced lead time together with cost, and improve quality. However, implementation of lean synchronization has faced resistance due to decrease in productivity as initial setup of lean management consumes time to identify the hidden obstacles. Industries tend to keep wastes along their production flow as waiting in progress (WIP) and inventories. It is important to eliminate them as they incur cost to the final product and contribute to loss of productivity within the premise which can endanger the business' future sustainability [7, 8]. Overall, activities of the manufacturing industry definitely contribute significantly towards improving the economy of many nations, however it is critical for manufacturers to prevent the overuse of as they need to consider its impact on the environment. Any resources that are wasted should be avoided for the development of a particular industry and nation [9].

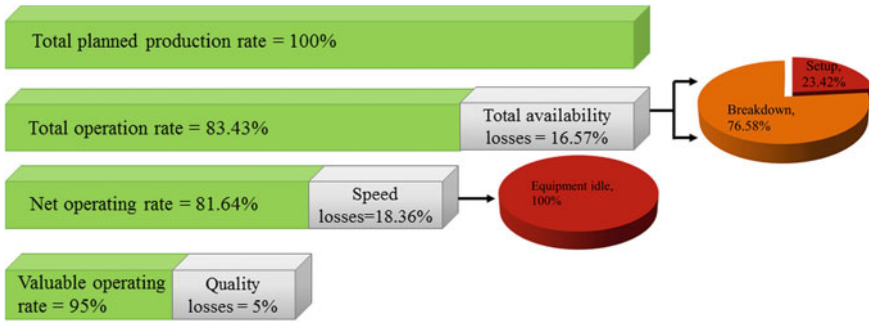
In this case study, motion and waiting time to fix each breakdown have reduced the availability of the machine to work. Motion is described as movement of operators that might look busy but no values are added by the work. Simplification of work surely reduces the motion waste. Meanwhile waiting is measured by equipment or labor efficiency waiting time. It is related to the amount of waiting time for the operators to attend a problem at designated area or machine who were kept busy producing WIP which is not needed at the time [1, 10, 11]. From the previous research done by others [12–14], waste in production has been highlighted but specific studies on motion and waiting time has yet to be conducted and presented clearly. Therefore, this research proposes one of the optimum designs of operators position in aid to improve the overall availability and OEE.

## 2 Experimental Procedure

### 2.1 Overall Equipment Efficiency (OEE)

Overall equipment efficiency (OEE) is a method to measure the effectiveness of equipment operations. It is also a hierarchy of metrics that measure the effectiveness of a manufacturing operation. It is normally based on three criteria; the time the





**Fig. 1** Planned operation rate, actual operation rate, net operating rate and valuable operating rate for an average monthly production in the first quarter of 2018

equipment is available to operate without breakdown, the throughput rate or speed of the equipment and the quality of the product or units or service produced by the equipment. In other words, the OEE is calculated by multiplying the availability rate by performance and multiplied by quality rate [15]. Availability takes into account the down time loss, which includes any events that stop planned production for an appreciable length of time. Availability rate indicates relationship between time and the machine operates theoretically with actual output. The common breakdown observed in this case study were machine breakdowns and waiting for setup or changeover between models. The performance rate is theoretically calculated as the machine is producing at maximum speed during the operation time. However in practical, it does not reach 100% because of certain situations such as operator stopping machines due to waiting for raw materials and removing uncertainty or foreign objects. The same situation occurred in this case study. Lastly, quality rate is determined based on the amount of pieces produced that meets the quality requirement set by the customer or issues raised by the internal quality assurance team [16]. Figure 1 shows the data collected over the first quarter to determine the OEE rate at the surface mount production.

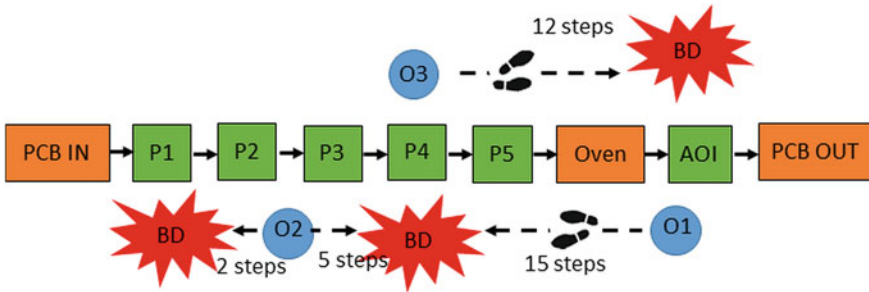
From the data collected, OEE can be calculated using Eq. 1–4 [1]:

$$\begin{aligned}
 \text{Availability}(A) &= \frac{\text{Planned production time} - \text{downtime}}{\text{Planned production time}} \\
 &= \frac{\text{Total operating time}}{\text{Planned production time}} \tag{1}
 \end{aligned}$$

$$\text{Productivity}(P) = \frac{\text{Net operating time}}{\text{Total operating time}} \tag{2}$$

$$\text{Quality}(Q) = \frac{\text{Valuable operating time}}{\text{Net operating time}} \tag{3}$$

$$\text{OEE} = A \times P \times Q \tag{4}$$



**Fig. 2** Value stream mapping of operators’ position rearrangement leading to rapid solving (BD: breakdown, O1: Operator 1, O2: Operator 2, O3: Operator 3, P1–P5: Process 1 to Process 5, AOI: Automated optical inspection)

$$OEE = 83.43\% \times 81.64\% \times 95\% = 64.71\%$$

From the case study, breakdown of the machine contributes to the high losses in OEE percentage. Figure 2 explains the breakdown in detail. The position of operators is reflected on time taken to reach the breakdown area. In the case where breakdown happens at process 1, process 4 and AOI at the same time, operator 2 and operator 3 have to move 36 and 38 steps respectively. From the lean manufacturing prospect, one of the seven wastes is motion. Too many unnecessary movements leads to longer lead time to fix each breakdown and this contributed to the downtime. Breakdowns can happen at any process; therefore movement of operators can make each breakdown repairing taking a longer time.

## 2.2 Research Design

In this specific study, fixing position of operators throughout the operation had reduced the motion involved. The waste of motion had reduced the breakdown time which overall increases the total operation time that leads to increment of availability. Figure 2 shows an option of operators’ position to reduce their movement during breakdown. In this proposal, when there are breakdown at similar processes as before, all the operators can handle breakdown faster than earlier. Operator 1 moves 15 steps towards process 4, operator 2 moves 2 steps to process 1 and operator 3 moves 12 steps to AOI. There are few designs that can be done to minimize the motion.

### 3 Results and Discussion

The reduction in motion had reduced the breakdown time by 5%, which is 0.63% from overall available time. From this data, availability had increased from 83.43 to 84.06%. Using the same technique, the time taken by operators to remove foreign objects during production has also reduced. The reduction of 10% in the speed loss had increased the performance and overall equipment efficiency from 81.64 to 82.84% and from 64.71 to 66.15% respectively. Rearrangement of operators can reduce the motion of the operators to reach each breakdown and eventually it reduces the waiting time of the machine.

The financial benefits and capacity of the OEE increment can be calculated from the added value and throughput per hour. Equations 5 and 6 show the initial calculation on the financial capacities [1].

$$\frac{\text{Added value}}{\text{unit}} = \text{Value of unit produced} - \text{cost of material} \quad (5)$$

If expected throughput is  $y$  products/hour then,

$$\frac{\text{Added value}}{\text{hour}} = \frac{\text{Added value}}{\text{unit}} \times \frac{y \text{ unit}}{\text{hour}} \quad (6)$$

Therefore when OEE is measure at  $k\%$ , the loss per hour of the machine will be calculated as shown in Eq. 7 [1].

$$\text{Losses/hour} = (\text{Added value})/\text{unit} \times (y \text{ unit})/\text{hour} \times (100 - k)\% \quad (7)$$

Each percentage of OEE increment will reduce the loss/hour and through this design proposal the yield is increased by 2180 units/month. By adding the electronics components value for April 2018, the financial capacity can increase by 414200–457800 MYR/month with confidence tolerance of 5%.

### 4 Conclusions

From this case study, the following can be concluded:

- (a) Breakdown of the machine contributes to the largest equipment availability losses up to 76.58%.
- (b) Non value added activities especially motion and waiting time leads to longer breakdown time.
- (c) Position of operators during production can be manipulated to reduce the two mentioned waste.
- (d) Reduction in availability losses leads to increment of 1.44% in OEE.

**Acknowledgements** The fund for this paper was supported by SEGi University, Kota Damansara. We are grateful to the anonymous referees whose comments and suggestions have greatly improved the presentation of the paper.

## References

1. Slack N, Chambers S, Johnston R (2010) Operations management. Pearson education
2. Deshkar A, Kamle S, Giri J, Korde V (2018) Design and evaluation of a Lean Manufacturing framework using Value Stream Mapping (VSM) for a plastic bag manufacturing unit. *Mater Today: Proc* 5 (2, Part 2):7668–7677. <https://doi.org/10.1016/j.matpr.2017.11.442>
3. Munteanu V, Ștefăniță A (2018) Lean Manufacturing in SMEs in Romania. *Procedia—Soc Behav Sci* 238:492–500. <https://doi.org/10.1016/j.sbspro.2018.04.028>
4. Karim R, Rahman CM (2012) A performance analysis of OEE & improvement potential at a selected apparel industry. In: Proceedings of the 6th international mechanical engineering conference and 14th annual paper meet (6IMEC&14APM), 2012. pp 28–29
5. Ghobadian A, Talavera I, Bhattacharya A, Kumar V, Garza-Reyes JA, O'Regan N (2018) Examining legitimatisation of additive manufacturing in the interplay between innovation, lean manufacturing and sustainability. *Int J Prod Econ*. <https://doi.org/10.1016/j.ijpe.2018.06.001>
6. Sundar R, Balaji A, Kumar RS (2014) A review on lean manufacturing implementation techniques. *Procedia Eng* 97:1875–1885
7. Martínez Sánchez A, Pérez Pérez M (2001) Lean indicators and manufacturing strategies. *Int J Oper Prod Manag* 21(11):1433–1452
8. Oliveira J, Sá J, Fernandes A (2017) Continuous improvement through “Lean Tools”: an application in a mechanical company. *Procedia Manuf* 13:1082–1089
9. Muñoz-Villamizar A, Santos J, Viles E, Ormazábal M (2018) Manufacturing and environmental practices in the Spanish context. *J Clean Prod* 178:268–275. <https://doi.org/10.1016/j.jclepro.2018.01.026>
10. Rahani A, Al-Ashraf M (2012) Production flow analysis through value stream mapping: a lean manufacturing process case study. *Procedia Eng* 41:1727–1734
11. Ford AL, Williams JA, Spencer M, McCammon C, Khoury N, Sampson TR, Panagos P, Lee J-M (2012) Reducing door-to-needle times using Toyota’s lean manufacturing principles and value stream analysis. *Stroke:STROKEAHA*. 112.670687
12. Sullivan WG, McDonald TN, Van Aken EM (2002) Equipment replacement decisions and lean manufacturing. *Rob Comput-Integr Manuf* 18(3–4):255–265
13. Poppendieck M (2011) Principles of lean thinking. *IT Manag Sel* 18:1–7
14. Modi DB, Thakkar H (2014) Lean thinking: reduction of waste, lead time, cost through lean manufacturing tools and technique. *Int J Emerg Technol Adv Eng* 4(3):339–344
15. Nayak DM, Vijaya Kumar M, Naidu GS, Shankar V (2013) Evaluation of OEE in a continuous process industry on an insulation line in a cable manufacturing unit. *Int J Innovative Res Sci Eng Technol* 2(5)
16. Dunn T (2014) Manufacturing flexible packaging: materials, machinery, and techniques. William Andrew

# Vibration Analysis Methods for Misalignment and Tolerance Problems in Machine Systems: A Review



Muhammad Nurshafiq Ramli, Ahmad Majdi Abdul Rani, Nabihah Sallih,  
Abdul Azeez Abdu Aliyu and T. V. V. L. N. Rao

**Abstract** Misalignment and tolerance are the most common causes of vibrations in machines. An optimum value of tolerance and alignment are desired for a smooth and clear machine process, but difficult to achieve due to manufacturing, assembly and working constraints of the mechanism. Vibration analysis is a study of repetitive motion, in a certain time interval, which involves mathematical modelling, formulation of governing equations and interpretation of vibration response. Misalignment and tolerance in compliance can result in numbers of failures and safety issues, especially for manually operated machines. These problems need to be diagnosed by using vibration analysis for different purposes such as fault detection, vibration response, research and early prevention. This paper provides an insight into the different available methods and fundamentals of vibration analysis that were used to study these issues in a different situation.

**Keywords** Vibration analysis · Misalignment · Tolerance

## 1 Introduction

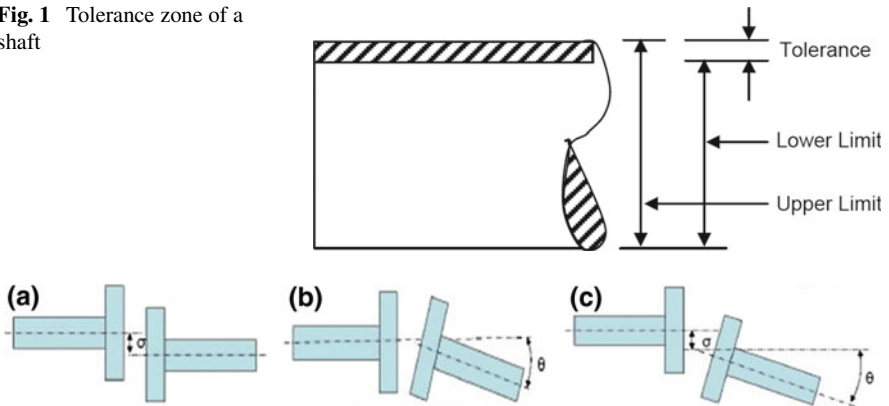
An optimum value of tolerance and alignment are required to ensure machines, especially for the rotating machinery to operate smoothly. Due to manufacturing, assembly and working characteristic of the mechanism, the perfect tolerance size and alignment is difficult to achieve practically [1, 2]. Any small defect in the machine assembly could affect the vibration behavior which can result in crack formation, bend and other types of failures. Tejas et al. claimed that over 70% of vibration problems in rotating machinery are caused by misalignment [2, 3]. Both problems

---

M. Nurshafiq Ramli (✉) · A. M. A. Rani · N. Sallih · A. A. A. Aliyu  
Mechanical Engineering Department, Universiti Teknologi PETRONAS, Seri Iskandar, Malaysia  
e-mail: [muhammad\\_16002673@utp.edu.my](mailto:muhammad_16002673@utp.edu.my)

T. V. V. L. N. Rao  
Department of Mechanical-Mechatronics Engineering, The LNM Institute Technology, Jaipur,  
India

**Fig. 1** Tolerance zone of a shaft



**Fig. 2** Schematic of **a** parallel misalignment **b** angular misalignment and **c** combined alignment at coupling

are the main causes of vibration and require a diagnosis through vibration analysis. Vibration analysis is crucial for machine system and can be used for fault detection, vibration response, research and early prevention [4–8].

Tolerance is the permissible variation in size or dimension of a certain part. A product does not necessarily need to be produced in an exact size. A small size error is allowed such as in clearance fit which allows an air space or a clearance to exist between the assembly parts to maintain a thin film of oil for lubrication. Tolerance is also defined as the amount of the job that is permitted to machine without causing any problems to the assembly process or product function [9]. Figure 1 shows the tolerance zone, which is the difference between the upper limit and the lower limit of the dimensions. Some assembly parts require a large tolerance due to their manufacturing and working characteristics. Such limits may result in a higher vibration response during operation which can lead to machine failure.

Misalignment is a problem where an improper assembly of machine parts and thermal alteration in housing supports cause an irregular vibration behaviour during the machine operation [10]. Tolerance is also one of the factors for misalignment problem as a large tolerance can cause some shaft and hole assemblies to bend or rotate due unbalanced mass. Misalignment is categorized into three different types; parallel, angular and combined misalignments (see Fig. 2). For parallel misalignment, the centre line of both parts is parallel but offset by  $\sigma$  from each other, on the other hand, the parts are assembled at an angle,  $\theta$  to each other are for angular misalignment condition.

Vibration response for the misalignment and tolerance problem is presented in the frequency domain as a series of harmonic against the running speed. These harmonic motions take place due to the strain that occurs in the rotating machine parts.

## 2 Vibration Analysis Methods

Vibration is a repetitive motion of an object for an interval of time. Vibration analysis is a study that involves mathematical modelling, formulation of governing equations and interpretation of the vibration response [11]. The following subsection describes various techniques used for vibration analysis of misalignment and tolerance problem.

### 2.1 Newton-Euler/Newton Dynamic Method

Newtonian-Euler, also known as Newton Dynamic methods, is one of the most common and precise ways of deriving the equation of motion for a vibrating system. Newton-Euler method works well with discrete model of low degree of freedom (DOF) vibrating system. This method transfers all mass ( $m_i$ ) out of their equilibrium position ( $x_i$ ) together with velocities ( $\dot{x}_i$ ) to construct a free body diagram (FBD) of the lumped mass, that indicates the total force ( $F_i$ ) on the mass, refer to Fig. 3 [12].

In linear motion system, if given is the momentum instead of mass  $m_i$ , the Newton equation will apply the momentum and provides the equation of motion of the system as follows:

$$F_i = \frac{d}{dt} p_i = \frac{d}{dt} (m_i v_i) \tag{1}$$

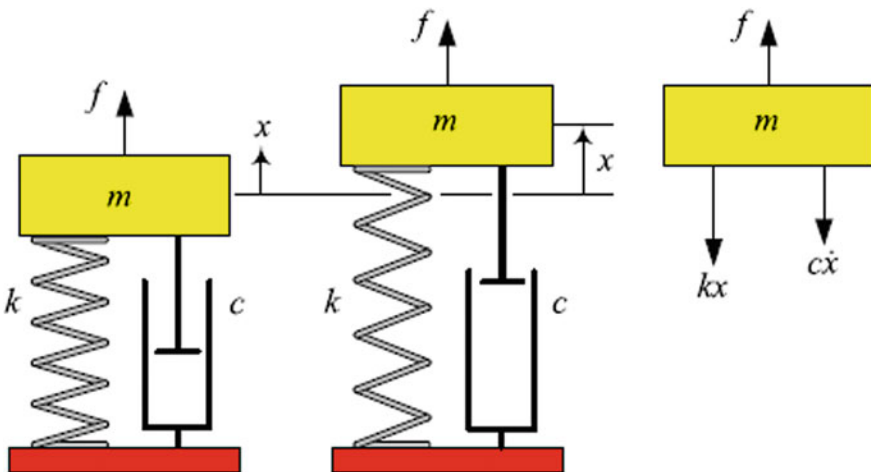


Fig. 3 Free body diagram of one DOF vibrating system

For rotational motion problem such as the rotating shaft in machinery system with mass moment of  $I_i$ , the Euler equation employs the moment of momentum and provides the following equation of motion:

$$M_i = \frac{d}{dt}L_i = \frac{d}{dt}(I_i\omega) \quad (2)$$

The equation of motion generates:

$$ma - cv - kx = f(x, v, t) \quad (3)$$

The Newton equation of motion can also be arranged in second-order derivatives or matrix form and change by either adding or removing parameters, depending on the number forces and DOFs reacting on the model. Ali et al. [13] studied the effect of geometric tolerances on natural frequencies of a rotating shaft system. According to Newton-Euler method, the natural frequencies,  $\omega_n$  were obtained by replacing the mass  $m_i$  with the moment of inertia of the shaft  $J = \frac{1}{2}mR^2$  due to the torsional vibration. They have shown that an increase in geometric tolerances will increase the specific percentage of natural frequencies related to the mode shape.

Another case study related to the misalignment issues is the study of gyroscopic condition, which is the tendency of angular momentum to go to the direction of torque in machine system. Heikkinen et al. [14] published a paper based on the vibration analysis of asymmetric tube roll supported by spherical roller bearings. This research uses the Newton-Euler method by adding gyroscopic parameter into the formulation of equation of motion (4) by using as their equilibrium position.

$$\begin{aligned} & (M_m + M_s \sin 2\Omega t + M_c \cos 2\Omega t)\ddot{q} \\ & + (C + \Omega(G + M_s \sin 2\Omega t + M_c \cos 2\Omega t))\dot{q} \\ & + (K_m + K_s \sin 2\Omega t + K_c \cos 2\Omega t)q \\ & = (Q + Q_c \sin 2\Omega t + Q_s \cos 2\Omega t) \end{aligned} \quad (4)$$

where  $M_m$ ,  $M_s$ ,  $M_c$  are the mean and deviatoric mass matrices of the tube roll,  $C$  is damping matrix,  $G$  is gyroscopic matrix,  $K_m$ ,  $K_s$ ,  $K_c$  are the stiffness matrices,  $Q$  is the external forces, and  $Q_c$  and  $Q_s$  are the force due to unbalance load. The gyroscopic issues had resulted to high vibration when running at twice the rotational speed and the amplitude response from the asymmetric mass and stiffness was less significant. This vibration analysis method was not only limited to specific parameters as in Eq. (3) but flexible when dealing with other additional parameters. The only drawback is when there is an increase in DOF, Newton equation of motion becomes lengthy and complex to formulate.



## 2.2 Lagrange Method

Lagrange method, also known as Lagrange Multiplier, has higher advantages for formulation of governing equation of motion for multi DOF vibrating system due to its generality and simplicity. Lagrange system ( $\mathcal{L}$ ) involves the use of kinetic energy ( $K$ ) and potential energy ( $V$ ) where:

$$\mathcal{L} = K - V \tag{5}$$

By using this method, Newton’s equation of motion can be transformed to

$$\frac{d}{dt} \left( \frac{\partial K}{\partial \dot{q}_r} \right) - \frac{\partial K}{\partial q_r} = F_r \quad r = 1, 2, \dots, n \tag{6}$$

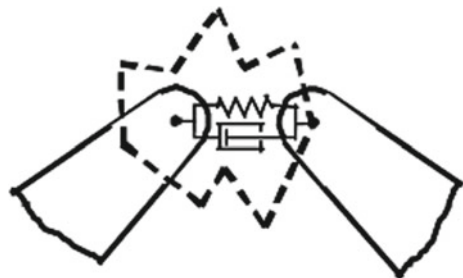
$$F_r = \sum_{i=1}^n \left( F_{ix} \frac{\partial f_i}{\partial q_1} + F_{iy} \frac{\partial g_i}{\partial q_2} + F_{iz} \frac{\partial h_i}{\partial q_n} \right) \tag{7}$$

where, kinetic energy  $K$  can be replaced with  $\mathcal{L}$ , depending on the vibrating system with DOF and is the generalized coordinate of the system. To construct a complete Lagrange equation of motion, the function kinetic and potential energy,  $K$  need to be determined from the parameters of the vibrating system [12].

In machinery tolerance problem, Lagrange method is frequently used in vibration analysis or study of the clearance between the machines parts or components which introduces two or more extra DOF, either in horizontal and vertical motion of noncontact situation, as shown in Fig. 4 [15]. In examples of interrelated dimension chains, such as in manufacturing design, tolerances that are valid within specific range uses high number of DOF. Thus, the use of Lagrange method is preferred by Singh et al. [16].

A study regarding the nonlinear behavior of components in machine system can be considered using the same approach as the joint clearance issues. Malihe et al. [17] used the Lagrange method to impose the in-extensionality gyroscopic constraint ( $G^*$ ), into the Lagrangean system for the nonlinear vibration behavior of the rotating shaft. This nonlinear gyroscopic issue will increase the parameter and DOF of the

**Fig. 4** Revolute clearance joint between two links modelled using spring-damper approach



whole system due to the eccentric position, magnetic load and geometric nonlinearities. Thus, it is shown that this method is suitable when dealing with high DOF due to its flexibility to impose other additional constraints.

### 2.3 Runge-Kutta Ordinary Differential Equation Method

Newton-Euler and Lagrange method were used for formulation of equation of motion for the vibrating system, whereas Runge-Kutta is a technique used to numerically solve the time response of the vibrating system at specific frequency, using the formulated equation of motion [15]. The normal differential equation shown in Eq. (8) can be numerically solved by substituting the given parameter to determine the specific value of the system at an instantaneous condition.

$$\frac{dy}{dx} = f(x, y), y(0) = y_0 \quad (8)$$

In solving vibrations problem, the main ordinary differential equation to solve is the equation of motion. Using Runge-Kutta technique, only the first order ordinary differential equation can be solved. As a result, the equation of motion needed has to be derived from the second order to the first order differential equation [15]. Given an undamped vibrating system of Newton's equation of motion with the value of  $k = 1$  and  $m = 1$ , where:

$$m\ddot{x} - c\dot{x} - kx = f(x, v, t) \quad (9)$$

$$\ddot{x} + x = 0 \quad (10)$$

Then let  $x_1 = x$  and  $x_2 = \dot{x}$ , so the Newton's equation of motion can be rewritten as:

$$\dot{x}_2 = -x_1 \quad (11)$$

From the Eq. (11), the system can be solved using the Runge-Kutta method and other differential equation methods such as Euler method, Heun method, Fehlberg method and integration scheme [18, 19]. Scolastika et al. [18] conducted a comparison on using Runge-Kutta method with forward and central difference methods to solve vibration problems of a story building. They showed that the Runge-Kutta, Euler and Heun methods produced more accurate solution than other finite difference methods.

An example of a case study involved with this method is the effect of different parameter value to the vibration response of the system. Athanasios et al. [20] conducted a research on variable geometry of journal bearing (VGJB) by varying the value of the external damping and stiffness incorporated to the mechanism using

Finite Element Analysis (FEA) and experiment. Runge-Kutta method was preferred compared to Newton or Lagrange due to its capability to numerically solve the vibration response of multiple excitation force acting on different mass body in nonlinear system with different parameters values. It was claimed that the major vibration response work is consumed by the damping force of the bearing system. The results showed that the vibration response of the VGJB decreased at resonance by 70% when compared to that of conventional journal bearing. Thus, this method is very good to numerically solve problem when dealing with multiple parameter values and often closely related to FEA.

## 2.4 *Fourier Transform Method*

Fourier transformed a technique used to transform the signal analysis from time-based domain to frequency-based domain. This method is different from the previous technique as it is mainly used for signal visualization. This method works by decomposing the signal into sinusoidal waves at different frequency whereas the main output is the amplitude to the frequency graph. There are two different types of Fourier Transform:

### 2.4.1 **Fast Fourier Transform (FFT)**

FFT converts the time waveform into its sinusoidal component. Abhijet et al. [3] claimed that FFT is advantageous in diagnosing a variety of vibration related to problems in a rotary machinery which generates the spectrum  $F(\omega)$  that includes the signal's constituent frequencies and the time function  $f(t)$ :

$$F(\omega) = \int_{-\infty}^{\infty} f(t) \cdot e^{-i\omega t} \cdot dt \quad (12)$$

The major drawback of FFT is that it not capable to provide information of the time dependence for spectrum of a signal examined. Thus, some information is missing when an event takes place because it can only detect the oscillations of the system. A study on vibration response of misalignment motor issues using FFT algorithm shows that FFT only uses data from one coordinate direction (z/y-direction) and the sampled part transducer data is needed to put direct and quadrature to the signal input. Thus, it cannot show the relative coordinates between Y and Z spectral components. In addition, the output signal is subjected to change from Y to Z and Z to Y precessions [2].

### 2.4.2 Short-Time Fourier Transform (STFT)

Normally, Fourier transform cannot analyze the non-stationary subject but using STFT, the signal will be divided into several sections, which is called as windowing, and is assumed to be stationary. In STFT, a finite-time window is examined once at a time. It separates the input into multiple sinusoidal waves of different frequencies and identifies their respective amplitude response, thus giving out more information of the signal in their respective frequencies, as compared to the FFT [21]. Other advantages of STFT are that the method is simpler with low cross term interference and it requires low computation ability. STFT performs the above procedure to analyze the non-stationary signal using the following Eq. (13).

$$STFT_x^w(\tau, f) = \int_{-\infty}^{+\infty} x(t)w^*(t - \tau)e^{-j2\pi ft} dt \quad (13)$$

The drawback of using STFT is that the size time window must remain the same for all frequencies because this method cannot work properly for high frequency components in a short time and low frequencies component at a long-time interval [22]. A study of piston scratching fault on vibration behavior of IC engine were conducted by Moosavin et al. [22] by using the STFT method to analyze the vibrating system of healthy and faulty conditions of IC engine due to scratch of the piston which was caused by an interference tolerance of the engine cylinder. The usage of STFT method is more beneficial compared to FFT as it gives the result of level of the vibration response and the time of the occurrence in the engine body. These are important information for engineers to optimize the fault from the designed product.

## 3 Conclusions

Different vibration analysis methods have their own advantages and drawbacks when dealing with tolerance and misalignment problem, in specific machine parts. For example, Newton-Euler method can be chosen in solving theoretical vibration problem with low DOF and low parameter constraint, whereas Lagrange method is more suitable and favorable for system with higher DOF. As for Runge-Kutta method, it is used to determine the time response given specific frequency by numerically solving the specific equation of motion, which is proven useful when dealing with accuracy and FEA of the solution for vibrating system. Meanwhile, Fourier Transform is different from the parameter and DOF related equation. This method is a signal analysis that analyzes the spectrum behavior and converts the signal from time to frequency domain. Conventional FFT has a critical drawback on the amount of information provided compared to STFT, where the method of windowing is used to get more response information in their respective frequencies. Selection of suitable methods is critical because these methods produce different outcomes to the applied system. A

combination of vibration analysis method also can be used to solve certain tolerance and misalignment problems. For instance, the usage of Lagrange method is critical when dealing with a problem that focuses on formulating the equation of motion and high DOF, then the usage of Runge-Kutta method to numerically solve the generated equation of motion to validate the vibration response value of the system. Thus, the proper selection of analysis method in different situations is important to produce the right outcomes of the vibrating system.

**Acknowledgements** The author hereby acknowledges the financial support from Universiti Teknologi PETRONAS (UTP), Malaysia under Graduate Assistance (GA) Scheme and the Prototype Research Grant Scheme (PRGS), 0153AB-L47.

## References

1. Erkaya S (2018) Experimental investigation of flexible connection and clearance joint effects on the vibration responses of mechanisms. *Mech Mach Theory* 121:515–529
2. Patel TH, Darpe AK (2009) Experimental investigations on vibration response of misaligned rotors. *Mech Syst Signal Proc* 23:2236–2252
3. Gajjal ASSY (2016) A review on vibration analysis for misalignment of shaft in rotary system by using discrete wavelet transform. *Int J Res Mech Eng* 03:5
4. Mansour A, Mekki OB, Montassar S, Rega G (2018) Catenary-induced geometric nonlinearity effects on cable linear vibrations. *J Sound Vib* 413:332–353
5. Logan D, Mathew J (1996) Using the correlation dimension for vibration fault diagnosis of rolling element bearings—I. Basic concepts. *Mech Syst Signal Proc* 10:241–250
6. Mishra C, Samantaray AK, Chakraborty G (2017) Ball bearing defect models: a study of simulated and experimental fault signatures. *J Sound Vib* 400:86–112
7. Mishra AKDA (2015) Computation effort and effect of signal processing techniques in condition monitoring and fault diagnosis of machine. *Int J Adv Res Electr Electron Instr Eng* 4:7
8. Xue S, Howard I (2018) Torsional vibration signal analysis as a diagnostic tool for planetary gear fault detection. *Mech Syst Signal Proc* 100:706–728
9. Metrology and Instrumentation (2012) IGNO University, Ed., ed 2012
10. Lee YS, Lee CW (1999) Modelling and vibration analysis of misaligned rotor-ball bearing systems. *J Sound Vib* 224:17–32
11. Rao SS (2011) *Mechanical Vibrations*. University of Miami, PEARSON
12. Jazar RN (2013) “Advance Vibration” in advance vibration a modern approach. vol XVI, p 696, ed: Springer, 2013
13. Ansarifard AA, Jaamialahmadi A (2014) An investigation the effects of geometric tolerances on the natural frequencies of rotating shafts. *J Appl Comput Mech* 1:103–111
14. Heikkinen JE, Ghalamchi B, Viitala R, Sopanen J, Juhanko J, Mikkola A et al (2018) Vibration analysis of paper machine’s asymmetric tube roll supported by spherical roller bearings. *Mech Syst Signal Proc* 104:688–704
15. Ambrosio PFJ (2004) Revolute joints with clearance in multibody system. *Comput Struct* 82:11
16. Singh PK, Jain SC, Jain PK (2005) Advanced optimal tolerance design of mechanical assemblies with interrelated dimension chains and process precision limits. *Comput Ind* 56:179–194
17. Eftekhari M, Rahmatabadi AD, Mazidi A (2018) Nonlinear vibration of in-extensional rotating shaft under electromagnetic load. *Mech Mach Theory* 121:42–58
18. Radityani SLR, Mungkasi S (2017) Finite difference and Runge-Kutta methods for solving vibration problems. *J Phys Conf Series* 909:012044

19. Salahshoor E, Ebrahimi S, Maasoomi M (2016) Nonlinear vibration analysis of mechanical systems with multiple joint clearances using the method of multiple scales. *Mech Mach Theory* 105:495–509
20. Chasalevris A, Dohnal F (2015) A journal bearing with variable geometry for the suppression of vibrations in rotating shafts: simulation, design, construction and experiment. *Mech Syst Signal Proc* 52–53:506–528
21. Wald R, Khoshgoftaar T, Sloan JC (2011) Fourier transforms for vibration analysis: a review and case study. In: 2011 IEEE international conference on information reuse and integration, pp 366–371
22. Moosavian A, Najafi G, Ghobadian B, Mirsalim M (2017) The effect of piston scratching fault on the vibration behavior of an IC engine. *Appl Acoust* 126:91–100

# Limbs Disabled Needs for an Ergonomics Assistive Technologies and Car Modification



**Salami Bahariah Suliano, Siti Azfanizam Ahmad, Azizan As'arry, Faieza Abdul Aziz, Azizul Rahman Abd Aziz and Ali Ahmed Shokshk**

**Abstract** Over the years, designers have developed various assistive technologies and introduced numbers of modifications in an effort to bring limbs disabled person to mobile. This paper dealt with the survey outcome from 30 independent limbs disabled drivers in Selangor, Malaysia. The main objective of this survey is to find the real need of limbs disabled in respect to any activities related to car driving as a driver enter, drive and exit the car. At the present time, the car's interior is equipped with few assistive technologies and modification available to be installed ranging from hand to foot and also to those with or without wheelchair users according the typo of limbs disabilities. The main components evaluated during the survey include five aspects of ergonomics, namely safety, ease of use, comfort, productivity and performance, and aesthetics. The Likert scale (1 to 5) was used as the rating score given for each question within the components. From the survey, it was found that interior part such as handling, upholstery, and steering is in high need to be ergonomically redesigned.

**Keywords** Limbs disabled · Redesign · Interior car · Ergonomics · Inclusive design

## 1 Introduction

The automotive industry has been facing new challenges and economic limitations [1], where one such challenge is determining the needs of the inclusive group to produce an inclusive design. Inclusive design helps to identify needs or requirements for the group of people with or without functional limitations that will improve their driving quality [2] as well as an important approach to ensure needs of users with various physical, cognitive, and sensory ability limitation were included and met [3]. In a way, the design made is “design for all”.

---

S. B. Suliano (✉) · S. A. Ahmad · A. As'arry · F. A. Aziz · A. R. A. Aziz · A. A. Shokshk  
Department of Mechanical and Manufacturing, Universiti Putra Malaysia, Serdang, Malaysia  
e-mail: [salami.suliano@gmail.com](mailto:salami.suliano@gmail.com)

© Springer Nature Singapore Pte Ltd. 2020  
M. Awang et al. (eds.), *Advances in Material Sciences and Engineering*, Lecture Notes in Mechanical Engineering,  
[https://doi.org/10.1007/978-981-13-8297-0\\_9](https://doi.org/10.1007/978-981-13-8297-0_9)

Medical condition accompanied by physical impairments and relative individual functional performance (which varies depending on personal characteristics) are often the reasons that cause challenge in assessing driving abilities of disabled [4]. In addition, the ability to drive independently was found to be an important aspect especially for persons with disabilities for activities of daily life [5]. For improvement of quality of life, majority of disabled is driving an adapted or modification car as a most important means of independency [6] on access to personal vehicular transportation [7]. Modification or assistive driving has led to improvement for limbs disabled driver. Moreover, assistive driving can easily be found in most countries [5]. This is proven by the availability of modification introduced in previous studies.

Ordinary primary car or standard in market car are equipped with an ordinary control; steering, accelerator and pedal which are designed in a way to provide feedback to drivers. For example, steering and pedal are designed for a rotational distribution of control towards drivers hand and feet. However, there are certain points or types of disabilities that limit the driver from driving a conventional control car [6]. Having modification of adaptive equipment are said to be a proven process for maintaining freedom on the road for the disabled [8]. With adaptation, it meets user's needs in a different way as well as allowing the disabled who cannot drive before, to drive more easily and independently [9]. In general, the usefulness of an adaptation or modification depends on several factors as considered by Scherer [10], Thorkildsen [11], and Batavia et al. [12].

In Malaysia, most of modifications made were based on references of modified personal car without a clear measure of needs of limbs disabled. It was found that only standard of procedure focuses on medical examination and suggestion of modification that can be done at any registered workshop under Road Transport Department (RTD) after health pre-driving assessment is available for reference. Therefore, this study intends to analyse the needs of limbs disabled, covering driver's area of car interior design.

## 2 Methods

A set of questionnaire consisting of demographic of respondents, details of respondents, interior car modification and in-vehicle ergonomics experience was asked. Respondents were customers from FARESH MOTOR Sdn. Bhd. in Kuala Lumpur and students and staff from Industrial Training and Rehabilitation Centre (PLPP) in Bangi, Selangor. Participation was voluntary, and approval was received from Universiti Putra Malaysia Ethical Committee.

The conducted study involved 30 Malaysian independent upper limb or lower limb or combined limb disabled drivers as respondents in this study is covering the driver's interior area only. The questionnaire was composed of 4 major sections where the final section is the most crucial one which is on ergonomics elements. A normality checking and descriptive analysis has been carried out for this survey output. The



answers were tabulated using a commercial program, Statistical Package for Social Sciences (SPSS) and results were expressed as frequencies (mode) and percentages.

### 3 Results and Discussions

#### 3.1 Respondent Characteristics

A total of 55 questionnaires were sent out, in which 30 disabled completed the survey. The survey was based on 30 respondents who drove independently with or without modification. Table 1 includes part of the demographics, type of disability,

**Table 1** Respondents characteristics

Respondent demographic	N	(%)
<i>Gender</i>		
Male	26	(87%)
Female	4	(13%)
Respondent details	N	(%)
<i>Type of disabilities</i>		
Upper limb disabled	4	(13%)
Lower limb disabled	18	(60%)
Combined limb disabled	8	(27%)
<i>Needs of special equipment</i>		
Yes	16	(53%)
No	14	(47%)
<i>Negative symptoms</i>		
Upper limb	4	(13%)
Lower limb	11	(37%)
Both limb	7	(23%)
None	8	(27%)
<i>Modification made</i>		
Right pedal to left pedal	8	(27%)
Pedal to Joystick	1	(3%)
Pedal to hand control	6	(20%)
Seat height adjustment	3	(10%)
Pedal height adjustment	1	(3%)
Signals to push button	1	(3%)
Other	2	(7%)
No modification	8	(27%)

**Table 2** Likert scale scoring for Ergonomics section

Section		Level of score	Likert scale
A	Car interior	NE-LE-N-E-VE	1-2-3-4-5
B	Safety [13]	VD-D-N-E-VE	1-2-3-4-5
C	Comfort [18], [20]	VU-U-N-C-VC	1-2-3-4-5
D	Ease of use [9], [21]	VD-D-N-E-VE	1-2-3-4-5
E	Productivity and performance [13]	VD-D-N-E-VE	1-2-3-4-5
F	Aesthetics [22]	VNI-NI-N-I-VI	1-2-3-4-5

Very comfortable (VC); Very easy (VE); Neutral (N); Uncomfortable (U); Very difficult (VD); Difficult (D); Very uncomfortable (VU); Very ergonomics (VE); Easy (E); Very important (VI); Less ergonomics (LE); Important (I); Not important (NI); Not ergonomics (NE); Ergonomics (E); Very not important (VNI); Comfortable (C)

need of special equipment to travel, negative symptoms while traveling and type of modification made onto their vehicles. The male as displayed in table recorded as the majority (87%) respondents in the study while only 13% female drivers were involved. As to add more, 53% of the respondents needed special equipment to be mobile such as wheelchair, crutches and artificial upper and lower limb, while 73% respondents need assistive technologies and modification to be able to drive car.

### 3.2 Ergonomic Friendly Car for Disabled

One of the studies once claimed that “transportation is a heart of society grand challenge” in which it simplified movements, increased level of commute, improved economics as well as public health [13]. It is significant to ensure ergonomics is injected in order to improve safety, efficiency, and comfort through design [13]. Therefore, it is imperative that everyone with vehicle in daily life observes an adequate ergonomics requirement to improve safety and minimize risk [14]. In addition, several studies have shown the effects of ergonomics on better quality [7, 15–17]. Ergonomics in design has a dependent and interaction on arrangement between man and machine [18]. When ergonomics factor is taken into account, the human capabilities and limitations of certain designs are taken into consideration [19]. In considering design of an ergonomics car, there are five aspects of ergonomics as listed in Table 2B–F.

These five factors were used in the questionnaire in order to identify the weaknesses of current interior design in order to identify the most appropriate improvement to fulfill the disabled needs. Likert scale was used in the ergonomics Section (5-point scale) as shows in Table 2. For section A, B, C, D, and E, high mode or high frequencies of selection of low level score indicates attention is needed for further ergonomics improvement. Meanwhile opposite concepts falls for section F as the level of scoring is in different direction.

**Table 3** Ergonomics need for limb disabled as per level scoring based

Section A	Mode	Level of scores
Handle (Door)	9	LE
Handle (Surrounded)	9	LE
Pedals	9	LE
Egress	10	LE
Section C	Mode	Level of scores
Opening door from inside	9	U
Lower back support	9	U
Section E	Mode	Level of scores
Operate navigation while driving	8	D
Section F	Mode	Level of scores
Upholstery (bottom)	12	I
Upholstery (back)	11	I
Handle	13	VI
Steering trim	11	I
Gear knob trim	11	I

Table 3 shows the response on ergonomics need of a limb disabled person towards basic works and part of their vehicles which scores high mode as outcome. Table 3, section A, lists common surrounded parts and equipment in car interior that received high mode and less ergonomics scores such as handle at the door, handle at surrounding, pedals and egress. Table 3, section C, E, F are lists of segregated highlighted elements from five ergonomics aspects as discussed in Table 2. “The feeling uncomfortable while opening door from inside” and “lower back support” also recorded high mode with low level scores by respondents (section C). This shows that at certain situations, respondents have an inconvenient experience while opening door, seating position (section C) and also difficulty in operating navigator devices while driving (section E). In Table 3, (section F) illustrate a high mode score for critical elements of Aesthetics with important and very important scores level was upholstery (bottom), upholstery (back), handle, steering trim and gear knob trim.

It is interesting to see that limb disabled drivers did not raise any issue in safety and ease of use (section B and Section D) even though it affects the controlling action especially in unknown road condition and weather. A similar response from few respondents was received where they did not take safety into consideration (e.g. not fastening seat belt) or did not have a hard time to operate interior devices, but they actually got used with what they have through daily practices. They tend not to consider further adjustment although they are driving with or without any pain or symptoms chronicled.

## 4 Conclusions

In conclusion, the result from the study conducted on Malaysia limb disabled drivers was presented. The results concluded that certain major needs to be taken into consideration to redesign interior part of driver's area in order to achieve ergonomic friendly car for limb disabled driver. These include handle at the door and surrounded area, pedals, egress, upholstery (back) and upholstery (bottom). Besides, some elements with high mode and high score should also be considered. Although some of the responses given by respondents were not highlighted, they still need to be used as a measure in developing solution in regards to the needs of limbs disabled. By considering the findings of the study, a solution will be developed to redesign disabled friendly car that is more ergonomic. As this is an ongoing project, the final outcome is expected to be able to improve the driving experience, in particular to limbs disabled drivers.

**Acknowledgements** This research has been supported by Grant Putra (GP-IPS) from Universiti Putra Malaysia. The authors would like to acknowledge Road Transport Department Malaysia, Social Welfare Department, FARESH MOTOR Sdn. Bhd., and Industrial Training and Rehabilitation Centre (PLPP) who provided insight, expertise and documentation that greatly guided the research.

## References

1. Bhise VD (2012) Ergonomics in automotive design process. CRC Press, Florida
2. Karali S (2015) Vehicle ergonomics and older drivers
3. Persad U, Langdon P, Clarkson J (2006) Exploring user capabilities and health
4. Greve JMDA, Santos L, Alonso AC et al (2015) Driving evaluation methods for able-bodied persons and individuals with lower extremity disabilities: a review of assessment modalities. *Clinics* 70:638–647
5. Dahuri MKAM, Hussain MN, Yusof NFM et al. (2017) Factors, effects, and preferences on vehicle driving modification for the Malaysia independent disabled. 1:103–110
6. Peters B, Ostlund J (2005) Joystick controlled driving for drivers with disabilities
7. Roosmalen L, Paquin GJ, Steinfeld AM (2017) Quality of life technology: the state of personal transportation. *Phys Med Rehabil Clin* 21:111–125
8. NHTSA (2015) Adapting motor vehicles for people with disabilities
9. Field M, Jette A (2007) the future of disability in America. The National Academies Press, Washington
10. Scherer MJ (2005) Living in the state of stuck: how assistive technology impacts the lives of people with disabilities. Brookline Books, Cambridge, MA
11. Thorkildsen R (1994) Research synthesis on quality and availability of assistive technology devices, Washington, DC
12. Batavia AI, Hammer GS (1990) Toward the development of consumer-based criteria for the evaluation of assistive devices. *J Rehabil Res Dev* 27:425–436
13. Woodcock A (2012) New insights, new challenges; Person centred transport design. *Work* 41:4879–4886
14. Recovre (2017) Vehicle ergonomics. <https://www.recovre.com.au/vehicle-ergonomics/>
15. Zare M, Croq M, Hossein AF et al (2016) Does ergonomics improve product quality and reduce costs? a review article. *Hum Factors Ergon Manuf* 26:205–223

16. Keates S, Clarkson J (2003) Countering design exclusion. Inclusive design: design for the whole population, pp 438–453, Springer London, London
17. Khoo SL, Tiun LT, Lee LW (2013) Unseen challenges, unheard voices, unspoken desires: experiences of employment by Malaysians with physical disabilities. *Kaji Malaysia* 31:37–55
18. Haug E, Trameeon A, Allain JC et al (2001) Modelling of ergonomics and muscular comfort. *KSME Int J* 15:982–988
19. Samuji MSBM (2009) Development of ergonomics passenger car driver seat concept design
20. Giacomini J, Quattrocolo S (1997) An analysis of human comfort when entering and exiting the rear seat of an automobile. *Applied Ergonomics* 28(5–6):397–406
21. Waller S, Cardoso C, Clarke S et al (2007) Inclusive design toolkit. Engineering Design Centre, University of Cambridge, Cambridge
22. Liu Y (2000) Engineering aesthetics and ergo-aesthetics: theoretical and methodological foundations. In *Industrial Engineering-Theory and Practice*, pp 1–12

# Effects of Non-neutral Posture and Anthropometry on Heart Rate in Hand Tools Tasks



Ali Ahmed Shokshk, Siti Azfanizam Ahmad, Faieza Abdul Aziz, Hazreen H. Harith, Azizul Rahman Abd Aziz and Salami Bahariah Suliano

**Abstract** The use of hand tools in industry is one of the many risky issues for musculoskeletal disorders. Working postures during handling tools assumed may be reiterated several times a day, every day for several years and can be predicted to affect the musculature of the workers. Using physiological demands to assess coordinated posture and anthropometry in manual handling tools has not received much attention in literature. Therefore, the aim of this research is to study the effects of combined postures of trunk and shoulder besides the individual's anthropometry on heart rate in vertical drilling task. Ten male students participated in this experiment and ANOVA (Analysis of variance) was used to analyse the data. The results showed that shoulder flexion and trunk inclining forward have a significant effect on heart rate ( $P < 0.01$ ). Also, the anthropometric in terms of individual's weight and max grip strength has a negative correlation with heart rate ( $R^2 = 0.46$  and  $0.13$  respectively).

**Keywords** Heart rate · Posture · Anthropometry · Hand tool

## 1 Introduction

Hand handling tools are common in performing activities such as maintenance, assembly of cars, electricity works, construction, health care and agriculture. Musculoskeletal disorders (MSD), such as back pain, are the most common work-related injuries in manual hand-handling tasks. Many researches have revealed that such diseases occur mainly because of excessive efforts or through repetitive/prolonged work positions [1]. US companies have spent billions of dollars on lost productivity because of bone-related musculoskeletal disorders. This can be expressed financially through compensation, insurance bills, legal claims and disability, as well as the hiring

---

A. A. Shokshk (✉) · S. A. Ahmad · F. A. Aziz · A. R. A. Aziz · S. B. Suliano  
Mechanical and Manufacturing Engineering, Universiti Putra Malaysia, Selangor, Malaysia  
e-mail: [alishokshok@yahoo.com](mailto:alishokshok@yahoo.com)

H. H. Harith  
Biological and Agricultural Engineering, Universiti Putra Malaysia, Selangor, Malaysia

© Springer Nature Singapore Pte Ltd. 2020  
M. Awang et al. (eds.), *Advances in Material Sciences and Engineering*, Lecture Notes in Mechanical Engineering,  
[https://doi.org/10.1007/978-981-13-8297-0\\_10](https://doi.org/10.1007/978-981-13-8297-0_10)

and training of new workers [2]. In a recent investigation into Malaysian industrial workers by Zein et al. [3] found that the most challenging postures practiced by Malaysian industrial workers are moderate bending forward trunk and shoulder flexion at chest level. Thus, the main goal of the physiological assessment is to design tasks so that the physiological response of the body is within acceptable limits [4].

Awkward posture is a significant deviation in the joint from the neutral body position. When a worker uses different parts of the body and the back is twisted or bent backward or forward, this awkward posture increases stress as well as reduces performance [5]. Static postures (or “static loading”) refer to the physical effort in which the same position is maintained during a particular work. This overload puts heavier loads or forces on the muscles and tendons, leading to fatigue because static work inhibits the blood movement required to carry nutrients to the muscles and remove the waste from muscle metabolism. Examples of static postures are keeping tools that cannot be put in place, keeping the arms up out to perform tasks or standing in one place for long periods. Much of the available literature on posture deals with self-evaluation and have neglected the effect of the combination of different postures [6]. Some authors have mainly been interested in the effect of the posture on certain physiological factors, such as hand holding strength, muscle activity, and heartbeat [7, 8]. All of these research support the fact that working in a non-neutral posture raises physiological stress. However, these studies have used different evaluation methods as they have conflicting results with respect to the amount of stress produced in different coordinated positions. In trunk posture, several studies have agreed that bending the back forward has a significant effect on heartbeat, self-perception and muscular activity [9–11]. These results are similar to those reported by [6] who observed that the discomfort was the least, and heartbeat was the highest when the angle of back and shoulder flexion were  $45^\circ$  as a combined posture. Also in shoulder flexion, Lee [12] revealed that postures of shoulder flexion  $0^\circ$  with elbow flexion  $90^\circ$  have an excellent ability. Also, Brookham et al. [13] found that the shoulder flexion of  $60^\circ$  and rotation of hand inside  $-45^\circ$  are the most powerful posture. In addition, Sasikumar and Lenin [14] noted that drilling with extending hand in or above the head makes the stress highest. Assessing non-neutral postures and anthropometric effects in hand tools on physiological demands have not received much attention in the literature. Therefore, the aims of this study are to determine the effect of shoulder flexion, trunk bending forward and anthropometry on heart rate in vertical drilling task.

## 2 Materials and Methods

Ten students of men with mean age and body mass index (BMI) of  $23.3 \pm 0.67$  and  $23.24 \pm 1.93$  from the Faculty of Engineering of University Putra Malaysia volunteered to participate in the study. Participants should not have a history of health problems and injuries, especially in the hands and trunk. They were provided



**Fig. 1** Coordinated postures of shoulder and trunk

with information about the purpose, methods, demands, discomforts, and possible outcomes of the study.

Equipment used in this research were Actiheart kit (Cambridge Neuro-technology, Cambridge, UK) that would be put on the subject chest to record the heart rate. Also, anthropometric measuring set including the goniometer to measure the angle of deviation from neutral posture, weighing scale, tailor’s measuring tape, and hydraulic hand dynamometer. Cordless power hand drill and drill platform were used to carry on the experiment.

All the subjects were involved in six subtasks with different coordinated postures to drill 30 holes in each (Two seconds as a repetitive cycle time after finishing each hole and five minutes rest between the subtasks). The coordinated postures were shoulder flexion angles ( $0^\circ$ ,  $45^\circ$  and  $90^\circ$ ) and trunk inclination angles ( $0^\circ$ ,  $20^\circ$ ). These postures are represented S0T0, S0T20, S45T0, S45T20, S90T0 and S90T20 as independent variables (S = shoulder; T = trunk) (see Fig. 1). The anthropometry in terms of subject’s weight and max grip strength were treated as demographic variables. The dependent variable were heart rate, which were recorded during conducting of the drilling in each subtask. All subjects used the same drill tool, the drill work piece was plywood, and the diameter of hole was 6 mm as a fixed variables.



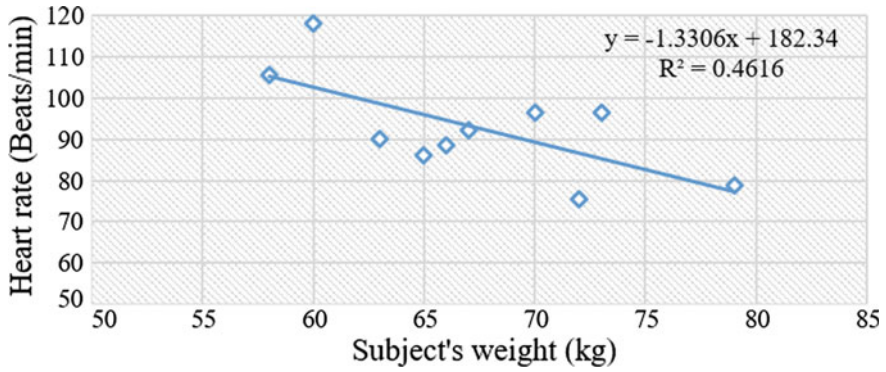


Fig. 2 Subject's weight versus mean of heart rate of all subtasks

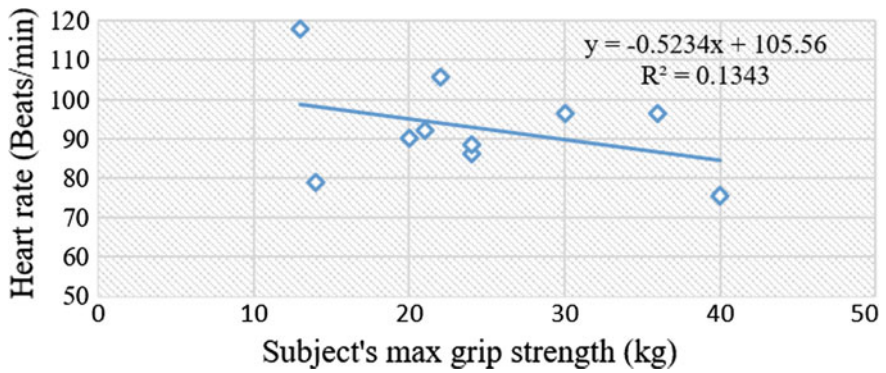


Fig. 3 Subject's max grip strength versus mean of heart rate of all subtasks

### 3 Results and Discussions

Figure 2 shows the relation between weights of subjects and the mean of heart rate for all sub-tasks for each subject. The graph showed that the heart rate is inversely proportional to the weight of subjects ( $R^2 = 0.46$ ). The bigger subjects showed the stable heart rate during drilling task compared to the smaller ones. In contrast, these results is conflicted by Hills et al. [15] who revealed that bigger individuals need more energy requirement than smaller ones.

Figure 3 shows the relation between max grip strength of subjects and the mean of heart rate for all sub-tasks for each subject. There was a negative correlation ( $R^2 = 0.13$ ). This is due to the balance energy attained by the bigger subject compared to the smaller subject. No relation was found between the other demographic factors and heart rate in this study.

Figure 4 shows the mean of heart rate of subjects versus working in the six coordinated postures of shoulder and trunk. The heart rate increases with the increase

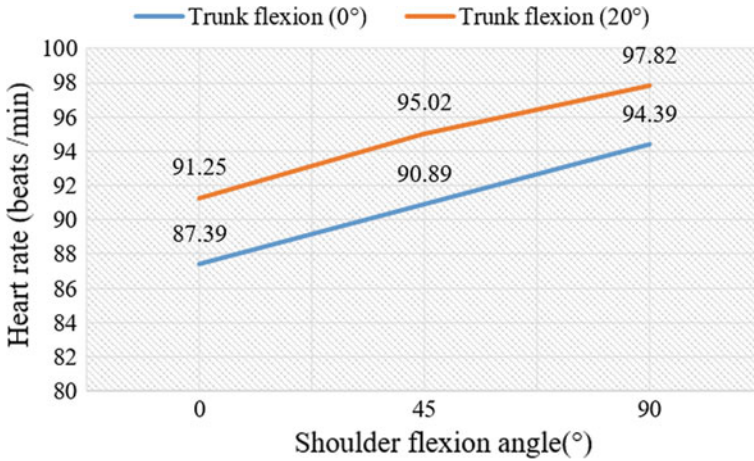


Fig. 4 Postures versus mean of heart rate

of shoulder and trunk above the neutral posture. Working in posture S0T0 had the least mean of heart rate (87.388 beats/min), whereas the posture S90T20 was the highest mean of heart rate (97.817 beats/min). Also, working in posture S0T20 and posture S90T0 had an approximately the same heart rate as well as postures S45T20 and S90T20 as interaction postures. The general linear model of repeated measures ANOVA (Analysis of variance) was used to analyse the data. The differences between the means are statistically significant for shoulder flexion [ $F(2, 18) = 11.4, P = 0.001$ ] and trunk bending forward [ $F(1, 9) = 19.08, P = 0.002$ ].

These results agree with the studies of Sasikumar and Lenin [14] whereby the working where the shoulder is at the chest level gives the highest stress, and with Lee [12] who found that working in posture of shoulder flexion (0°) and elbow flexion (90°) have the maximum individual holding capability. Furthermore, this finding agreed with the study of Damecour et al. [10] who found that trunk inclining forward had a significant effect on heart rate and muscle contraction. Also these finding is consistent with De et al. [16] who approved that working with trunk flexion (0°) is the optimum posture. In contrast, these finding is not consistent with Brookham et al. [13] who revealed that shoulder flexion of 60° and internal rotation of -45° is an outstanding posture. Also, it is contrary to that Lim et al. [6], who revealed the excellent posture is when the trunk and shoulder flexion are 45°.

## 4 Conclusions

This study was done to determine the effect of coordinated postures and the anthropometry in hand tools tasks on heart rate. Specifically, this study strived to determine the effects of shoulder flexion, trunk bending and anthropometry on heart rate. The

results indicated that the heart rate increased with the increase of shoulder and trunk flexion with statistically significant results. Working in neutral posture had the least heart rate whereas working with shoulder flexion 90° and trunk bending 20° had the highest heart rate. The combined postures between shoulder and trunk produced different heart beats. Anthropometry has also a significant effect on heart rate. Individuals who have higher weight and stronger grip strength have less heart rate. This is attributed to bigger and stronger individuals exert less effort to overcome the hard situations compared to smaller and weaker ones. Therefore, training and exercises are important for workers to overcome the awkward situations in hand tools works. These findings are important to design workplaces. The limitation of this research is the differences in physiological responses for individuals in the same loads. Further investigation should be carried out for the analysis of heart rate responses for different combined postures for lower and upper limbs in hand tools tasks.

## References

1. Basahel AM (2014) Impacts of postural stress and assembling task workload interactions on individual performance by Saudis. *Int J Curr Eng Tech* 4:3359–3369
2. Alzuheri A, Luong L, Xing K (2010) Ergonomics design measures in manual assembly work. ICESMA, Sharjah, UAE 1–6
3. Zein RM, Halim I, Azis NA et al (2015) A survey on working postures among Malaysian industrial workers. *Procedia Manufact* 2:450–459
4. Dempsey PG (1998) A critical review of biomechanical, epidemiological, physiological and psychophysical criteria for designing manual materials handling tasks. *Ergonomics* 41:73–88
5. Lei L, Dempsey PG, Xu J-G et al (2005) Risk factors for the prevalence of musculoskeletal disorders among Chinese foundry workers. *Int J Ind Ergonom* 35:197–204
6. Lim C-M, Jung M-C, Kong Y-K (2011) Evaluation of upper-limb body postures based on the effects of back and shoulder flexion angles on subjective discomfort ratings, heart rates and muscle activities. *Ergonomics* 54:849–857
7. Farooq M, Khan AA (2014) Effects of shoulder rotation combined with elbow flexion on discomfort and EMG activity of ECRB muscle. *Int J Ind Ergonom* 44:882–891
8. Khan AA, Khan Z, Mukarram M (2013) Effect of elbow flexion on grip strength in vertical and horizontal directions. *J Hum Ergol* 42:13–22
9. Chung MK, Lee I, Yeo YS (2001) Physiological workload evaluation of screw driving tasks in automobile assembly jobs. *Int J Ind Ergonom* 28:181–188
10. Damecour C, Abdoli-Eramaki M, Ghasempoor A et al (2010) Comparison of two heights for forward-placed trunk support with standing work. *Appl Ergon* 41:536–541
11. Saha D, Gard S, Fatone S et al (2007) The effect of trunk-flexed postures on balance and metabolic energy expenditure during standing. *Spine* 32:1605–1611
12. Lee TH (2017) The effects of arm posture and holding time on holding capability and muscle activity. *Int J Occup Saf Ergon* 23:410–414
13. Brookham RL, Wong JM, Dickerson CR (2010) Upper limb posture and submaximal hand tasks influence shoulder muscle activity. *Int J Ind Ergonom* 40:337–344
14. Sasikumar R, Lenin K (2016) Assessing the influence of hand-arm posture on mechanical responses of the human hand during drilling operation. *Int J Adv Manuf Technol* 1–4:1–10
15. Hills AP, Mokhtar N, Byrne NM (2014) Assessment of physical activity and energy expenditure: an overview of objective measures. *Front Nutrition* 1:5
16. De S, Sengupta P, Maity P et al (2011) Effect of body posture on hand grip strength in adult Bengalee population. *J Physiother Phys Rehabil* 7:79–88

# Determining Optimum Partial Transmission Ratios of Mechanical Driven Systems Using a V-Belt Drive and a Three-Stage Helical Reducer



Vu Ngoc Pi, Nguyen Khac Tuan, Le Xuan Hung, Nguyen Thi Hong Cam and Tran Thi Phuong Thao

**Abstract** This paper presents a new study on the calculation of optimum partial transmission ratios of mechanical drive systems using a V-belt drive and a three-stage helical reducer. In the optimization study, the objective function of the optimization problem is to find the minimum acreage of system cross section. Besides, the design equation for pitting resistance of gear sets was investigated and equations on moment equilibrium condition of a mechanic system including a V-belt drive and a three-stage helical reducer and their regular resistance condition were considered. Based on the results of the optimization problem, equations for calculating the optimal partial ratios of the V-belt drive and three stages of the reducer were proposed. Using these models, the partial ratios can be calculated accurately and simply.

**Keywords** Transmission ratio · Optimal reducer design · V-belt drive · Three-stage helical reducer

## 1 Introduction

In optimization design of a mechanical system which used a reducer, the determination of the optimum partial transmission ratios is a very important task. This is because the size, the mass and the cost of the system mainly depend on the partial ratios. Subsequently, the calculation of optimum partial ratios of a mechanical system has been subjected to many studies.

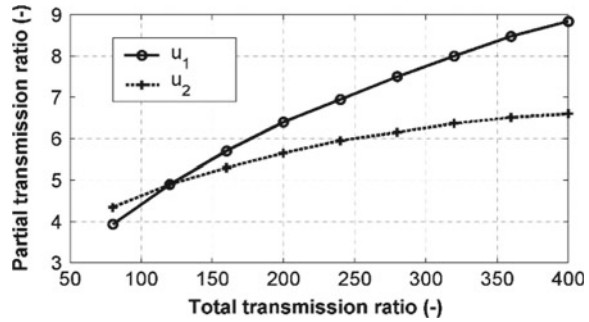
Until now, the gear ratios have been found through different methods and usually for multi-stage reducers. The optimum gear ratios were determined for two-stage

---

V. N. Pi (✉) · L. X. Hung · N. T. H. Cam · T. T. P. Thao  
Mechanical Engineering Faculty, Thai Nguyen University of Technology, Thai Nguyen City,  
Vietnam  
e-mail: [vungocpi@tnut.edu.vn](mailto:vungocpi@tnut.edu.vn)

N. K. Tuan  
Automotive and Power Machinery Faculty, Thai Nguyen University of Technology, Thai Nguyen  
City, Vietnam

**Fig. 1** Gear ratios versus the total transmission ratio [1]



reducers [1–4], three-stage reducers [4–8], and four-stage reducers [4, 8, 9]. Also, they were found by the graph method [1, 2, 4], by “the practical method” [2] or by the model method [5–9].

Using the graph method, the gear ratios of a reducer were determined graphically. For instance, the gear ratios of the first and the second stage of a three-stage helical reducer can be determined based on the graph in Fig. 1 [1]. Using the “practical method”, the gear ratios can be found from the practical data. For example, from the data of reducer factories, it was noted that the weight of two-stage reducer is at minimum if the ratio of center distance of the second stage to that of the first stage is from 1.4 to 1.6 [2]. Based on that, the optimum gear ratios were presented in the tabulated form. Using model method, the gear ratios can be determined in models for different objectives. The objective can be the minimum volume of gears [4], the minimum reducer cross section [5], the minimum mass of gears [6, 9], the minimum length of the reducer [7] and the minimum reducer mass [8].

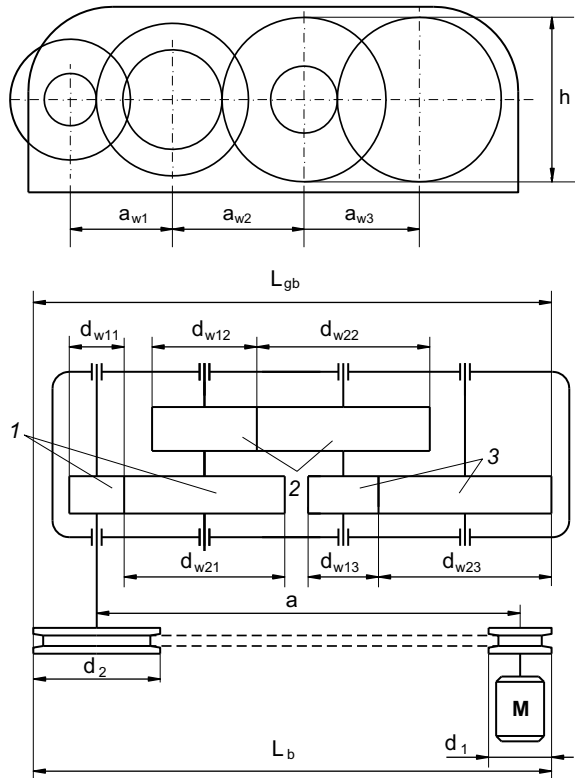
Recently, there have been studies on the calculation of the optimum gear ratios of a mechanical system which consists of a V-belt drive [10, 11] or a chain drive [12] and a two-stage reducer. The objective used in this study is the minimum height of the system including the reducer and the V-belt drive or the chain drive.

This paper introduces a study for optimum determination of the partial transmission ratios for a driven system using a V-belt drive and a three-stage helical reducer. In the study, the objective of the optimization problem is to find the minimum acreage of system cross section.

## 2 Optimization Problem

In this study, the objective of the optimization problem is to find the optimum partial transmission ratios for getting the minimum acreage of cross section of a mechanical driven system using a V-belt drive and a two-stage helical reducer. From Fig. 2, the acreage of cross section of the system can be determined as:

Fig. 2 Calculation schema



$$A = L_{\max} \cdot h_{\max} \tag{1}$$

In which,

$$L_{\max} = \max(L_{gb}, L_b) \tag{2}$$

$$h_{\max} = \max(d_2, d_{w21}, d_{w22}, d_{w23}) \tag{3}$$

Wherein,  $L_{gb}$  and  $L_b$  are determined as (see Fig. 2):

$$L_{gb} = d_2/2 + a_{w1} + a_{w2} + a_{w3} + d_{w23}/2 \tag{4}$$

$$L_b = d_1/2 + a + d_2/2 \tag{5}$$

In the above equations,  $a_{w1}$ ,  $a_{w2}$  and  $a_{w3}$  are the center distance of the first, the second and the third step, respectively;  $d_2$ ,  $d_{w21}$ ,  $d_{w22}$  and  $d_{w23}$  are the diameter of the driven pulley of the V-belt drive, the driver gear of the first, the second and the third step, respectively.

The diameter of the drive pulley of V-belt drive can be determined as:

$$d_1 = d_2/[u_b \cdot (1 - \varepsilon)] \quad (6)$$

Substituting (6) into (5) gives

$$L_b = d_1/2 + a + d_2/2 \quad (7)$$

With a reducer, the driven diameters of the first, the second and the third stage can be determined by the following equations [13]:

$$d_{w21} = 2 \cdot a_{w1} \cdot u_1/(u_1 + 1) \quad (8)$$

$$d_{w22} = 2 \cdot a_{w2} \cdot u_2/(u_2 + 1) \quad (9)$$

$$d_{w23} = 2 \cdot a_{w3} \cdot u_3/(u_3 + 1) \quad (10)$$

From (2), (3), (4), (7), (8), (9) and (10) the following equations are given:

$$L_{\max} = f(d_2, a_{w1}, a_{w2}, a_{w3}, u_b, u_1, u_2) \quad (11)$$

$$h_{\max} = f(d_2, a_{w1}, a_{w2}, a_{w3}, u_1, u_2) \quad (12)$$

Thus, the optimization problem is defined as

$$\text{minimize } A = L_{\max} \cdot h_{\max} \quad (13)$$

With the following constraints:

$$\begin{aligned} 1 &\leq u_b \leq 6 \\ 1 &\leq u_1 \leq 9 \\ 1 &\leq u_2 \leq 9 \\ 1 &\leq u_3 \leq 9 \end{aligned} \quad (14)$$

It can be seen from Eqs. (11), (12), (13) and (14) that in order to solve the optimization problem, it is necessary to determine the driven pulley diameter, the center distances of the first, the second and the third stages.

## 2.1 Determining the Driven Pulley Diameter $d_2$

From the tabulated data to determine the allowable power of a V-belt drive [13], the following regression equation (with the determination coefficient  $R^2 = 0.9156$ ) to determine the driver diameter  $d_1$  was found:

$$d_1 = 269.7721 \cdot [P_1]^{0.7042} / v^{0.5067} \quad (15)$$

Also, the peripheral velocity of the belt can be determined as follows:

$$v = \pi \cdot d_1 \cdot n_1 / 60000 \quad (16)$$

From Eqs. (15) and (16), the driving pulley diameter is calculated by the following equation:

$$d_1 = 1093.8 \cdot [P_1]^{0.7923} / n_1^{0.6369} \quad (17)$$

Besides, the driven pulley diameter can be determined by using the equation in [13]:

$$d_2 = u_b \cdot d_1 \cdot (1 - \varepsilon) \quad (18)$$

Substituting (17) into (18) gives

$$d_2 = 1093.8 \cdot u_b \cdot (1 - \varepsilon) \cdot [P_1]^{0.7923} / n_1^{0.6369} \quad (19)$$

In which,  $\varepsilon$  is slippage coefficient and  $\varepsilon = 0.01 \dots 0.02$  [13];  $u_b$  is the transmission ratio of the V-belt drive;  $[P_1]$  is the allowable power of the drive (kW);  $[P_1]$  is determined as:

$$[P_1] = n_1 \cdot [T_1] / (9.55 \cdot 10^6) \quad (20)$$

Choosing  $\varepsilon = 0.015$  and substituting it and (20) into (19) gives:

$$d_2 = 0.0032 \cdot u_b \cdot n_1^{0.1554} \cdot [T_1]^{0.7923} \quad (21)$$

wherein,  $[T_1]$  is the permissible torque on the driving shaft;  $[T_1]$  can be determined from permissible torque on the output shaft  $[T_{out}]$  by:

$$[T_1] = [T_{out}] / (u_t \cdot \eta_t) \quad (22)$$

In Eq. (22),  $u_t$  is the total transmission ratio of the system;  $\eta_t$  is the total efficiency of the system:



$$\eta_t = \eta_d \cdot \eta_{br}^2 \cdot \eta_o^3 \quad (23)$$

In which,  $\eta_d$  is V-belt efficiency ( $\eta_d = 0.956 \dots 0.96$  [13]);  $\eta_{br}$  is helical gear transmission efficiency ( $\eta_{br} = 0.96 \dots 0.98$  [13]);  $\eta_o$  is the efficiency of a bearing pair ( $\eta_o = 0.99 \dots 0.995$  [13]). Choosing  $\eta_d = 0.955$ ,  $\eta_{br} = 0.97$  and  $\eta_o = 0.992$  [13] and substituting (23) into (22) gives

$$T_1 = 1.14 \cdot T_{out}/u_t \quad (24)$$

## 2.2 Determining the Center Distance of the First and the Second Stage

Theoretically, the center distance of the first stage is determined as [13]:

$$a_{w1} = K_a \cdot (u_1 + 1) \cdot \sqrt[3]{T_{11} \cdot k_{H\beta} / ([\sigma_H]^2 \cdot u_1 \cdot \psi_{ba1})} \quad (25)$$

In which,

- $K_{H\beta}$  is the contact load ratio for pitting resistance; for the first stage of a three-stage helical reducer  $k_{H\beta} = 1.02 - 1.28$  [13]; it is chosen as  $k_{H\beta} = 1, 1$ ;
- $[\sigma_H]$ -allowable contact stress (MPa); In practice,  $[\sigma_H] = 350 \dots 410$  (MPa); it is chosen as  $[\sigma_H] = 380$  (MPa);
- $k_a$  is material coefficient; Because of the gear material is steel,  $k_a = 43$  [13];
- $\psi_{ba1}$  is coefficient of wheel face width of the first stage; for a three-stage helical reducer  $\psi_{ba1} = 0.3$ .

Substituting above values into Eq. (25) gets:

$$a_{w1} \approx 1.2639 \cdot (u_1 + 1) \cdot \sqrt[3]{T_{11}/u_1} \quad (26)$$

Calculating in the same way and with the note that the coefficient of wheel face width for the second and the third stage  $\psi_{ba2} = 0.35$  and  $\psi_{ba3} = 0.4$ , the center distance of the second stage  $a_{w2}$  and the third stage  $a_{w3}$  are calculated by (Fig. 3):

$$a_{w2} \approx 1.2006 \cdot (u_2 + 1) \cdot \sqrt[3]{T_{12}/u_2} \quad (27)$$

$$a_{w3} \approx 1.483 \cdot (u_3 + 1) \cdot \sqrt[3]{T_{13}/u_3} \quad (28)$$

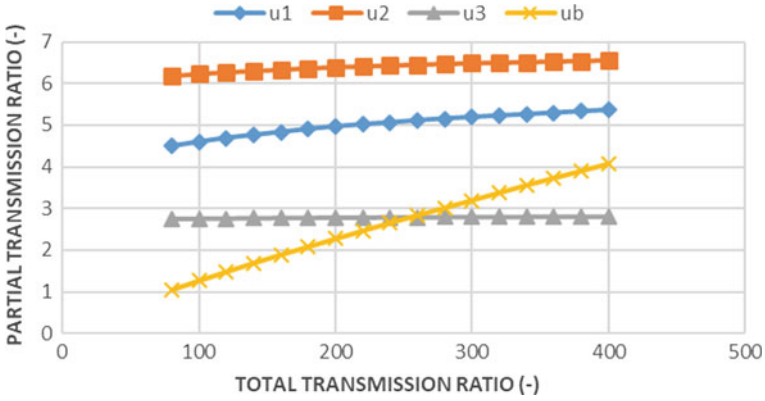


Fig. 3 Partial ratios versus total ratio (With  $T_r = 107 \text{ Nmm}$ )

### 3 Results and Discussions

Based on Eqs. (13) and (14), a computer program was conducted in order to find the optimum partial transmission ratios to get the minimum acreage of system cross section. The data used in the program was:  $u_t = 80 \dots 400$ ;  $T_{out} = 10^6 \dots 10^7$ .

From the results of the optimization program, three following regression equations were found:

- For calculation of the optimum transmission ratio of the V-belt drive (with the coefficient of determination is  $R^2 = 0.9758$ ):

$$u_b = 4.5042 \cdot [T_{out}]^{-0.3133} \cdot u_t^{0.8273} \tag{29}$$

- For calculation of the optimum gear ratio of the first stage of the reducer (with  $R^2 = 0.9764$ ):

$$u_1 = 0.0805 \cdot [T_{out}]^{0.2158} \cdot u_t^{0.1189} \tag{30}$$

- For calculation of the optimum gear ratio of the second stage of the reducer (with  $R^2 = 0.9734$ ):

$$u_2 = 1.7188 \cdot [T_{out}]^{0.0688} \cdot u_t^{0.0379} \tag{31}$$

After having  $u_b$ ,  $u_1$  and  $u_2$ , the gear ratio of the third stage of the reducer is determined by the following equation:

$$u_3 = u_t / (u_1 \cdot u_2) \tag{32}$$

## 4 Conclusions

A study on determination of optimum partial transmission ratios of a mechanical drive system using a V-belt drive and a three-stage helical reducer to get the minimum cross-sectional acreage was conducted.

Models for determination of the optimum partial transmission ratios of the V-belt drive and the reducer were introduced in order to get the minimum cross-sectional acreage of the system.

The partial transmission ratios of the V-belt drive and the reducer can be found simply by using explicit models.

**Acknowledgements** The work described in this paper was supported by Thai Nguyen University of Technology for a scientific project.

## References

1. Kudreavtev VN, Gierzaves IA, Glukharev EG (1971) Design and calculus of gearboxes. Mashinostroenie Publishing, Sankt Petersburg (in Russian)
2. Milou G, Dobre G, Visa F, Vitila H (1996) Optimal design of two step gear units, regarding the Main Parameters, VDI Berichte No 1230, p 227
3. Pi VN (2001) A method for optimal calculation of total transmission ratio of two step helical gearboxes. In Proceedings of the national conference on engineering mechanics. Ha Noi, p 12
4. Petrovski AN, Sapiro BA, Saphonova NK (1987) About optimal problem for multi-step gearboxes (in Russian). Vestnik Mashinostroenie, No. 10, p 13
5. Pi VN, Tuan NK (2016) Optimum determination of partial transmission ratios of three-step helical gearboxes for getting minimum cross section. J Environ Sci Eng A 5:570–573
6. Pi VN, Binh D, Dac VQ, Phan QT (2006) Optimal calculation of total transmission ratio of three-step helical gearboxes for minimum mass of gears (In Vietnamese). J Sci Technol 6 Eng Univ p 91
7. Pi VN (2008) A new study on optimal calculation of partial transmission ratio of three-step helical reducers. In: The 3rd IASME/ WSEAS international conference on continuum mechanics. Cambridge, UK, p 23
8. Romhild I, Linke H (1992) Gezielte Auslegung Von Zahnradgetrieben mit minimaler Masse auf der Basis neuer Berechnungsverfahren. Konstruktion 44:229–236
9. Pi VN (2008) Optimal determination of partial transmission ratios for four-step helical gearboxes with first and third step double gear-sets for minimal mass of gears. In: Applied computing conference (ACC' 08), Istanbul, Turkey, May 27–30
10. Pi VN, Binh D, Dac VQ, Phan QT (2015) A new study on optimum determination of partial transmission ratios of mechanical driven systems using a V-belt and two-step helical gearbox. Vietnam Mech Eng J 10:123
11. Pi VN, Cam NTH, Tuan NK (2016) Optimum calculation of partial transmission ratios of mechanical driven systems using a V-belt and two-step bevel helical gearbox. J Environ Sci Eng A 5:566
12. Pi VN, Thao TTP, Tuan DA (2017) Optimum determination of partial transmission ratios of mechanical driven systems using a chain drive and two-step helical gearbox. J Environ Sci Eng B 6:80
13. Chat T, Van Uyen L (1998) Design and calculus of mechanical transmissions (in Vietnamese). Educational Republishing House, Hanoi

# Determining Optimum Gear Ratios of a Worm—Helical Gearbox for Minimum Acreage of the Cross Section



Vu Ngoc Pi, Nguyen Khac Tuan, Le Xuan Hung, Nguyen Thi Quoc Dung and Bui Thanh Hien

**Abstract** This paper presents a study on the optimal determination of gear ratios of worm-helical gearboxes. In this study, the acreage of the cross section of the gearbox was chosen as the objective function of the optimization problem. Furthermore, the design equations for pitting resistance of the worm and the gear set were considered. In addition, equations on moment equilibrium condition of a mechanic system including two-gear unit of the gearbox and their regular resistance condition were analysed. From the results of the optimization problem, equations for determining the optimum partial ratios of the two stages of the gearbox were proposed. Based on these models, the partial ratios are calculated accurately and simply.

**Keywords** Gear ratio · Optimum gearbox design · Worm-helical gearbox

## 1 Introduction

Up to now, in the optimization gearbox design, many studies have concentrated in optimum determination of the gear ratio of the gearbox. This is because the gear ratio is the decisive factor for the size and mass of the gearbox. For worm-helical gearboxes, there have been several ways to determine the gear ratios.

For a two-stage worm gearbox, in order to get the reasonable housing structure of the gearboxes, the gear ratios can be calculated by the following equations [1, 2]:

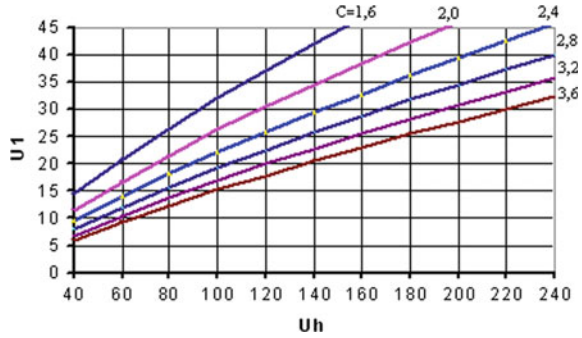
$$u_1 \approx u_2 \approx \sqrt{u_h} \quad (1)$$

---

V. N. Pi (✉) · L. X. Hung · N. T. Q. Dung · B. T. Hien  
Mechanical Engineering Faculty, Thai Nguyen University of Technology, Thai Nguyen City,  
Vietnam  
e-mail: [vungocpi@tnut.edu.vn](mailto:vungocpi@tnut.edu.vn)

N. K. Tuan  
Automotive and Power Machinery Faculty, Thai Nguyen University of Technology, Thai Nguyen  
City, Vietnam

**Fig. 1** Transmission ratio of worm gear unit versus the total transmission ratio [5]



Also for this type of gearbox, Milou et al. [3] proposed “a practical method” for determining the gear ratios. In their report, it was noted that the mass of gearboxes could be smallest if the ratio of two center distances  $a_{w2}/a_{w1}$  arranged from 1.8 to 2. Based on that, the optimum gear ratios for two-stage worm gearboxes are the total ratios from 315 to 2500 can be selected from tabulated data. Besides, Vu et al. [4] reported that the optimum gear ratio of the second stage of a two-stage worm gearbox is  $u_2 \approx 30.97$  when the objective is the gearbox structure reasonable.

For worm–helical gearboxes, the gear ratios of the helical gear unit can be determined by the following formula, identified from an actual experience [1]:

$$u_2 = (0.03 - 0.06)u_h \tag{2}$$

The above calculation is quite simple. However, in many cases it may lead to the gearbox structure unreasonableness. In order to ensure the effectiveness of oil lubrication for both stages of the gearbox, Trinh Chat [5] presented a graph which can be used to determine the gear ratio of the worm gear unit from the total transmission ratio of the gearbox (Fig. 1). It can be seen that, the determination of the gear ratio of the worm gear  $u_1$  by using the graph in Fig. 1 is quite complicated. In addition, in order to determine  $u_1$ , the user must select the coefficient  $c$  (with  $c = 1.3$  to  $1.6$ ) so it is very complicated and the result cannot reach the optimum values. To exclude these points, Pi and Dac [6] presented a study to determine of the optimum gear ratios of the gearbox with the same objective as in [5]. In this study, the optimum gear ratio of the helical gear unit is calculated as follows [6]:

$$u_2 = 6.86 \cdot \psi_{ba2}^{1/2} \tag{3}$$

In which,  $\psi_{ba2}$  is the coefficient of wheel face width ( $\psi_{ba2} = 0.3 \dots 0.4$ ).

Additionally, for worm–helical gearboxes, Pi et al. [7] conducted a study to find the optimum gear ratios in order to get the minimum gearbox length. It was noted that the optimum gear ratio of the helical gear unit  $u_2$  was the allowable maximal transmission ratio of it ( $[u_{2max}] = 8 \dots 10$ ).

From the above analysis, it is clear that, until now there have been many studies on the optimum determination of the gear ratios of worm gearboxes. However, there is still a lack of a study in which the objective is the minimum acreege of the cross section. This paper presents a study for determining optimum gear ratios of worm-helical gearboxes with this objective.

## 2 Optimization Problem

The objective of the optimization problem is to determine the optimum gear ratios in order to get the minimum acreege of cross section of a worm-helical gearbox. From Fig. 2, the acreege of cross section of the gearbox is determined as:

$$A = L \cdot h \tag{4}$$

where,

$$L = \frac{d_{w21}}{2} + a_{w2} + \frac{d_{w22}}{2} \tag{5}$$

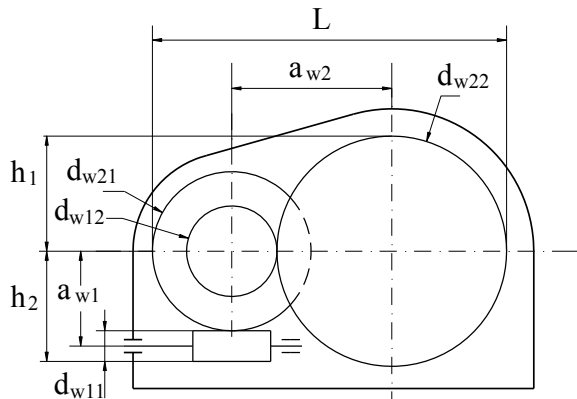
$$h = \max h_1 + \max h_2 \tag{6}$$

In which,  $h_1$  and  $h_2$  are determined as (see Fig. 2):

$$h_1 = \max\left(\frac{d_{w21}}{2}; \frac{d_{w22}}{2}\right) \tag{7}$$

$$h_2 = \max\left(\frac{d_{w11}}{2} + a_{w1}; \frac{d_{w22}}{2}\right) \tag{8}$$

Fig. 2 Calculation schema



In the above equations,  $a_{w1}$  and  $a_{w2}$  are the center distances of the first and the second stages, respectively;  $d_{w11}$  and  $d_{w21}$  are the pitch diameters of the worm and the worm gear;  $d_{w22}$  is the pitch diameter of the driven gear of the helical gear unit.

With the worm gear unit, we have [8]:

$$d_{w21} = m \cdot z_2 = \frac{2 \cdot a_{w1}}{z_2 + q} \cdot z_2 \quad (9)$$

where,  $q$  is the worm pitch diameter coefficient;  $q = (0.25 \dots 0.3) \cdot z_2$  [8]. Choosing  $q = 0.275 \cdot z_2$  and substituting it into (9) gets

$$d_{w21} = 1.5686 \cdot a_{w1} \quad (10)$$

For the worm gear unit, we also have:

$$d_{w11} = m \cdot q = \frac{2 \cdot a_{w1}}{z_2 + q} \cdot q \quad (11)$$

From (11) and with  $q = 0.275 \cdot z_2$  we get:

$$d_{w11} = 0.4314 \cdot a_{w1} \quad (12)$$

For the helical gear unit, the driven diameters can be determined as [8]:

$$d_{w22} = 2 \cdot a_{w2} \cdot u_2 / (u_2 + 1) \quad (13)$$

From (4), (5), (6), (7), (10), (12) and (13) the following equations are given:

$$A = f(a_{w1}, a_{w2}, u_2) \quad (14)$$

Thus, the optimization problem is defined as:

$$\text{minimize } A = L \cdot h \quad (15)$$

With the following constraints

$$\begin{aligned} 8 &\leq u_1 \leq 60 \\ 1 &\leq u_2 \leq 9 \end{aligned} \quad (16)$$

From (14), (15) and (16), it is clear that to solve the optimization problem, it is necessary to calculate the center distances of the worm gear set  $a_{w1}$  and the helical gear set  $a_{w2}$ .

## 2.1 Determining the Center Distance of the Worm Gear Set

Based on the design equation for pitting resistance of the worm gear set, the center distance of it  $a_{w1}$  (mm) can be calculated by [8]:

$$a_{w1} = (z_2 + q) \sqrt[3]{\left(\frac{170}{z_2 \cdot [\sigma_H]}\right)^2 \cdot \frac{T_{21} \cdot K_H}{q}} \quad (17)$$

Choosing  $q = 0.275 \cdot z_2$  as above, Eq. (17) can be rewritten as:

$$a_{w1} = 60.168 \cdot \sqrt[3]{K_H \cdot [T_{21}]/[\sigma_H]^2} \quad (18)$$

where,  $T_{21}$  is the torque on the wheel (Nmm); with the worm-helical gearbox,  $T_{21}$  is calculated by:

$$T_{21} = T_{out} / (\eta_g \cdot \eta_b^3 \cdot u_2) \quad (19)$$

In which,  $T_{out}$  is the output torque (Nmm);  $\eta_{hg}$  is the helical gear transmission efficiency ( $\eta_{hg} = 0.96 \dots 0.98$  [8]);  $\eta_b$  is the transmission efficiency of a pair of rolling bearing ( $\eta_b = 0.99 \dots 0.995$  [8]). Choosing  $\eta_{hg} = 0.97$ ,  $\eta_b = 0.992$  and substituting them into (19) gives:

$$T_{21} = 1.056 \cdot T_{out} / u_2 \quad (20)$$

$K_H$  is the load factor;  $K_H = 1.1 \dots 1.3$  [8]; Choosing  $K_H = 1.2$  we have

$$a_{w1} = 56.6203 \cdot \sqrt[3]{T_{21}/[\sigma_H]^2} \quad (21)$$

In which,  $[\sigma_H]$  is the allowable contact stress (N/mm<sup>2</sup>);  $[\sigma_H]$  depends on the wheel material. If the wheel material is tin less bronze or soft grey iron, from the tabulated data in [8], the following regression equation was found (with the determination coefficient  $R^2 = 0.9906$ ) for determination of the allowable contact stress:

$$[\sigma_H] = 5.0515 \cdot v_{sl}^2 - 49.742 \cdot v_{sl} + 189.9 \quad (22)$$

In which,  $v_{sl}$  is the slip velocity;  $v_{sl}$  can be calculated as [8]:

$$v_{sl} = 0.0088 \cdot \sqrt[3]{P_1 \cdot u \cdot n_1^2} \quad (23)$$

If the wheel material is tin bronze,  $[\sigma_H]$  is determined by [8]:

$$[\sigma_H] = K_{HL} \cdot v_{sl} \cdot [\sigma_{H0}] \quad (24)$$



In which,  $[\sigma_{H0}]$  is the allowable contact stress when the stress change cycle is  $10^7$ :

$$[\sigma_{H0}] = (0.7 \dots 0.9) \cdot \sigma_t \quad (25)$$

where,  $\sigma_t$  is the tensile stress (N/mm<sup>2</sup>);  $\sigma_t = 260$  if  $v_{sl} = 5 \dots 8$ ;  $\sigma_t = 230$  if  $v_{sl} = 8 \dots 12$  and  $\sigma_t = 285$  if  $v_{sl} = 8 \dots 25$ .

$K_{HL}$  is the service life ratio;  $K_{HL}$  is determined by:

$$K_{HL} = \sqrt[8]{10^7 / N_{HE}} \quad (26)$$

In which  $N_{HE}$  is the equivalent loading cycle number for the worm-wheel teeth for the whole lifetime of the gearing:

$$N_{HE} = 60 \cdot n_2 \cdot t_{\Sigma} \quad (27)$$

where,  $t_{\Sigma}$  is the service lifetime of the gearing (h);  $n_2$  is rotational frequencies of the wheel (rpm);

## 2.2 Determining the Center Distance of the Helical Gear Set

The center distance of the helical gear set can be calculated by [8]:

$$a_{w2} = K_a \cdot (u_2 + 1) \cdot \sqrt[3]{\frac{T_{12} \cdot k_{H\beta}}{[\sigma_H]^2 \cdot u_2 \cdot \psi_{ba}}} \quad (28)$$

where,

- $K_{H\beta}$  is the contact load ratio for pitting resistance; for the first stage of a two-stage helical reducer  $k_{H\beta} = 1.02 - 1.28$  [8]. Therefore, we can choose  $k_{H\beta} = 1, 1$ ;
- $[\sigma_H]$ -allowable contact stress (MPa); In practice,  $[\sigma_H] = 350 \dots 410$ (MPa) and we can chose  $[\sigma_H] = 380$ (MPa);
- $k_a$  is the material coefficient; As the gear material is steel,  $k_a = 43$  [8];
- $\psi_{ba}$  is the coefficient of wheel face width; for the helical gear of the gearbox we can get  $\psi_{ba} = 0.3$  [8].

Substituting the above values into (28) gets:

$$a_{w2} \approx 1.2639 \cdot (u_2 + 1) \cdot \sqrt[3]{\frac{T_{12}}{u_2}} \quad (29)$$

where,  $T_{12}$  is the torque on the driver gear of the helical gear set (Nmm);  $T_{12}$  is determined by:

$$T_{12} = T_{out} / (\eta_g \cdot \eta_b^2 \cdot u_2) \tag{30}$$

Choosing  $\eta_{hg} = 0.97$ ,  $\eta_b = 0.992$  as in Sect. 2.1 and substituting them into (30) gives:

$$T_{12} = 1.0476 \cdot T_{out} / u_2 \tag{31}$$

### 3 Results and Discussions

From Eqs. (15) and (16), a computer program was conducted to determine the optimum gear ratios to obtain the minimum acreage of the cross section of the gearbox. The data used in the optimization program were:  $u_t = 50 \dots 300$ ;  $T_{out} = 10^5 \dots 1.6 \cdot 10^6$ .

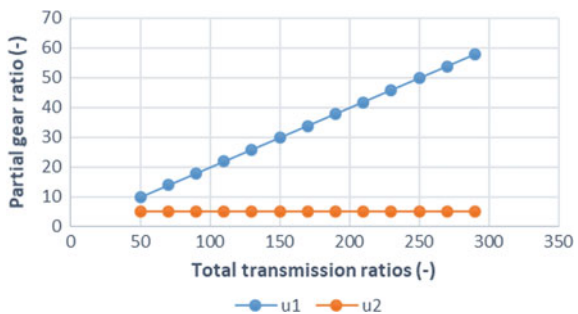
Figure 3 shows the relation between the gear ratios and the total ratio of the gearbox. It was found that with the same output torque of gearbox  $T_{out}$ , when the total ratio is increased, the gear ratio of the helical gear set do not change whereas the gear ratio of the worm gear set is increased linearly. This is because the worm gear set can reach a large transmission ratio with its small size while the helical gear set cannot. Therefore, the gear ratio of the second stage needs to be kept constant in order to reduce the size of the gearbox (see Eq. (29)).

From the results of the optimization program, the following regression equations (with the coefficients of determination  $R^2 = 0.9349$ ) was found to determine the optimum gear ratio of the worm gear set:

$$u_1 = 6.9279 \cdot 10^{-4} \cdot T_{out}^{0.4166} u_t \tag{32}$$

After having  $u_1$ , the gear ratio of the helical gear set is calculated by  $u_g = u_t / u_1$ .

**Fig. 3** Partial ratios versus total ratio, (With  $T_{out} = 106$  Nmm)



## 4 Conclusions

The minimum cross-sectional acreage of a worm helical gearbox can be obtained by using optimum gear ratios when designing.

Models for determination of optimum gear ratios of a worm helical gearbox to get the minimum cross-sectional acreage of the gearbox were proposed.

The gear ratios can be calculated simply by using explicit models.

**Acknowledgements** The work described in this paper was supported by Thai Nguyen University of Technology for a scientific project.

## References

1. Hiep Nguyen Trong, Van Lam Nguyen (1979) Design of machine elements (in Vietnamese). Educational Republishing House, Hanoi
2. Trenapski CA, Trekharev GA (1984) Design of mechanical transmission system. Mashinostroenie Publishing, Moskova (in Russian)
3. Miloiu G, Dobre G, Visa F, Vintila H (1996) Optimal design of two step gear units, regarding the main paramaters. VDI BERICHTE, 1230:227–244
4. Pi Vu Ngoc, Dac Vu Quy (2007) Calculation of total transmission ratio of two step worm reducers for the best reasonable gearbox housing structure (in Vietnamese). J Sci Technol Thai Nguyen University 1(41):65–69
5. Chat T (1993) Some problems of kinematics calculation of transmission mechanics system (in Vietnamese). In: Proceedings of the national conference on engineering mechanics, vol. 2. Hanoi, pp 7–12
6. Pi VN, Dac VQ (2005) Optimal calculation of total transmission ratio of worm-helical gear reducers. J Sci Technol-Thai Nguyen University, 1(4):36
7. Pi VN, Dac VQ (2007) Optimal calculation of partial transmission ratios of worm-helical gear reducers for minimal gearbox length. J Sci Technol Technical Universities 61:73–77
8. Chat T, Van Uyen L (2007) Design and calculus of mechanical transmissions systems (in Vietnamese), vol 1. Educational Republishing House, Hanoi

# A New Study on Calculation of Optimum Partial Transmission Ratios of Mechanical Driven Systems Using a Chain Drive and a Two-Stage Helical Reducer



Vu Ngoc Pi, Nguyen Khac Tuan and Le Xuan Hung

**Abstract** This article introduces a new study on the optimal calculation of partial transmission ratios of mechanical drive systems using a chain and a two-stage helical reducer. In the study, the dimension of the cross section of the system was chosen as the objective function of the optimization problem. Also, the design equation for pitting resistance of a gear set was investigated and equations on moment equilibrium condition of a mechanic system including a chain and a two-stage helical reducer and their regular resistance condition were analyses. From the results of the study, models for determining the optimal partial ratios of the chain and two stages of the reducer were proposed. Using these models, the partial ratios can be calculated accurately and simply.

**Keywords** Transmission ratio · Reducer design · Chain drive · Two-step helical reducer

## 1 Introduction

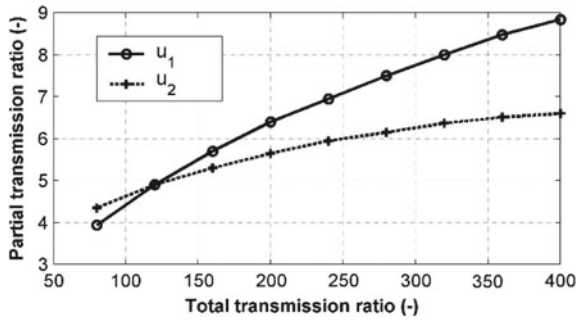
Up to now, in optimization design of a mechanical driven system, many studies have concentrated in optimum determination of the gear ratios of the reducer in the system. The reason of that is the gear ratios strongly affect the size, the dimension, the mass as well as the cost of the reducer.

---

V. N. Pi (✉) · L. X. Hung  
Mechanical Engineering Faculty, Thai Nguyen University of Technology, Thai Nguyen, Vietnam  
e-mail: [vungocpi@tnut.edu.vn](mailto:vungocpi@tnut.edu.vn)

L. X. Hung  
e-mail: [lexuanhung@tnut.edu.vn](mailto:lexuanhung@tnut.edu.vn)

N. K. Tuan  
Automotive and Power Machinery Faculty, Thai Nguyen University of Technology, Thai Nguyen, Vietnam  
e-mail: [tuannkc@tnut.edu.vn](mailto:tuannkc@tnut.edu.vn)



**Fig. 1** Transmission ratio of step 1 and 2 versus the total transmission ratio [1]

In previous researches, the gear ratios have been determined for two-stage reducers [1–4], three-stage reducers [4–8], and four-stage reducers [4, 8–10]. Also, the gear ratios have been found by different methods. They were found by graph method [1, 2, 4], by “practical method” [2] or by model method [5–10].

The oldest method for determining the partial ratios is the graph method. In this method, the gear ratios can be found graphically. For example, for a three-stage helical reducer, the gear ratios of the first and second stages can be determined by the graph in Fig. 1 [1].

The “practical method” was introduced by G. Milou et al. [2]. In this method, the gear ratios are determined based on the practical data. For example, from the data of reducer factories, it was noted that the total weight of two-stage reducer is minimal if the ratio of center distance of the second to the first stage is in the range of 1.4–1.6 [2]. Based on that, the optimum gear ratios were proposed.

Model method is the most common and effective method for calculation of gear ratios. In this method, models for determining the gear ratios have been proposed for different objectives. The objectives in the previous studies were the minimal volume of gears [4], the minimum cross section of the reducer [5], the minimum reducer length [7], the minimum mass of gears [6, 9, 10], or the minimum total reducer mass [8].

Recently, the gear ratios of a mechanical system used a chain [11, 12] or a chain drive [13] and a two-stage reducer. However, in these studies, the objective was the minimum height of the system including the reducer and the chain of the chain drive.

The optimum design of the conventional chain drive is also considered. For instance, for improving the efficiency of the cycling, in [14] proposed the optimum speed ratio for the chain drive of the tricycle.

This paper presents a study for optimum determining partial transmission ratios and for driven systems using a chain drive and a two-stage helical reducer with the objective is the minimum system cross-sectional dimension.

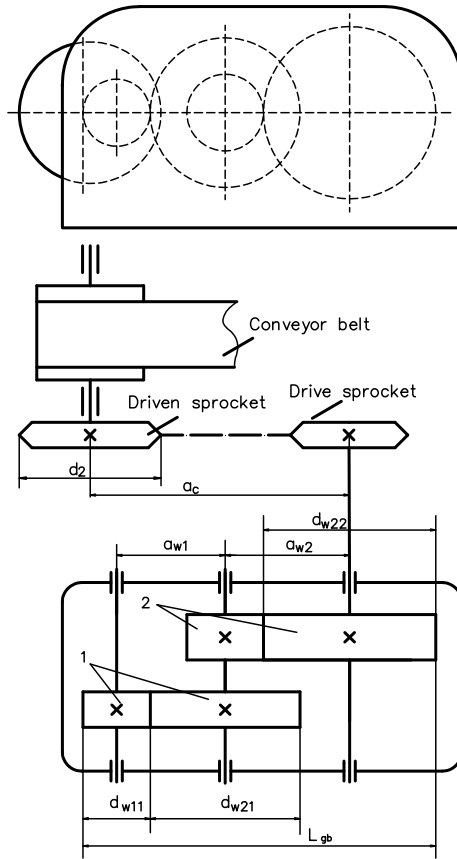


Fig. 2 Calculation schema

## 2 Optimization Problem

The objective of the optimization problem is to find the optimum partial transmission ratios for getting the minimum acreage of cross section of a mechanical driven system using a chain drive and a two-stage helical reducer. For this mechanical system (Fig. 2), the acreage of cross section of it can be calculated by the following equation:

$$A = L_{\max} \cdot h_{\max} \tag{1}$$

In which,

$$L_{\max} = \max(L_{gb}, L_c) \tag{2}$$

$$h_{\max} = \max(d_2, d_{w21}, d_{w22}) \quad (3)$$

where,  $L_{gb}$  and  $L_c$  are determined as (see Fig. 2):

$$L_{gb} = \frac{d_{w11}}{2} + a_{w1} + a_{w2} + \frac{d_{w22}}{2} \quad (4)$$

$$L_c = \frac{d_{w22}}{2} + a_c + \frac{d_2}{2} \quad (5)$$

In the above equations,  $a_c$ ,  $a_{w1}$  and  $a_{w2}$  are the center distance of the chain drive, the first and the second step, respectively;  $d_2$ ,  $d_{w21}$  and  $d_{w22}$  is the diameter of the driven sprocket of the chain drive, the driver gear of the first and the second step, respectively.

For the first and the second-stage of the gearbox, the driven and driver diameters can be determined as [15]:

$$d_{w21} = 2 \cdot a_{w1} \cdot u_1 / (u_1 + 1) \quad (6)$$

$$d_{w11} = d_{w21} / u_1 \quad (7)$$

$$d_{w22} = 2 \cdot a_{w2} \cdot u_2 / (u_2 + 1) d_{w11} = d_{w21} / u_1 \quad (8)$$

From (2), (3), (4), (5), (6), (7) and (8) the following equations are given:

$$L_{\max} = f(d_2, a_{w1}, a_{w2}, u_1, u_2) \quad (9)$$

$$h_{\max} = f(d_2, a_{w1}, a_{w2}, u_1, u_2) \quad (10)$$

Thus, the optimization problem is defined as:

$$\text{minimize } A = L_{\max} \cdot h_{\max} \quad (11)$$

With the following constraints

$$\begin{aligned} 1 &\leq u_c \leq 6 \\ 1 &\leq u_1 \leq 9 \\ 1 &\leq u_2 \leq 9 \end{aligned} \quad (12)$$

From (9), (10) and (11), it is clear that for solving the optimization problem it is necessary to calculate the driven sprocket diameter  $d_2$ , the center distance of the first stage  $a_{w1}$ , and the center distance of the second stage  $a_{w2}$ .

## 2.1 Determining the Driven Sprocket Diameter $d_2$

The pitch diameter of the driven sprocket can be determined as [15]:

$$d_2 = d_1 \cdot u_c \quad (13)$$

In which,  $d_1$  is the pitch diameter of the drive sprocket;  $d_1$  is calculated by [15]:

$$d_1 = p / \sin(\pi/z_1) \quad (14)$$

where,

$z_1$ —the number of teeth of the drive sprocket and it is calculated by [13]:

$$z_1 = 32.4 - 2.4 \cdot u_c \quad (15)$$

$p$ —the chain pitch (mm);  $p$  can be determined from the design power capacity  $P$  which is determined by the following equation [15]:

$$P = P_1 \cdot k \cdot k_z \cdot k_n \quad (16)$$

In which,  $P_1$  is the power rating (kW) of the chain drive;  $P_1$  is determined as:

$$P_1 = \frac{T_1 \cdot n_1}{9.55 \times 10^6} \quad (17)$$

where,  $n_1$  is the revolution of the drive sprocket (rpm):

$$n_1 = n_m / u_g \quad (18)$$

$$T_1 = T_{out} \cdot \eta_c \cdot \eta_b \quad (19)$$

In the above equations,  $\eta_c$  is the efficiency of the chain drive ( $\eta_c = 0.95 \div 0.97$  [15]);  $\eta_b$  is the efficiency of a pair of bearings ( $\eta_b = 0.99 \div 0.995$  [15]);  $T_1$  and  $T_{out}$  are the torque on the drive and the output torque (Nmm).

$k$ ,  $k_z$  and  $k_n$  are coefficients determined as [15]:

$$k = k_d \cdot k_p \cdot k_c \cdot k_{adj} \cdot k_{lub} \cdot k_{con} \quad (20)$$

$$k_z = 25/z_1 \quad (21)$$

$$k_n = n_{01}/n_1 \quad (22)$$

In Eqs. (20), (21) and (22),  $k_d$ ,  $k_p$ ,  $k_c$ ,  $k_{adj}$ ,  $k_{lub}$  and  $k_{con}$  are coefficients which take into account the influences of shock factor, the drive position, the center distance



of the drive, the possibility of adjusting the center distance, the lubrication and the operating conditions, respectively;  $n_{01}$  is tabulated number of teeth of the drive sprocket.

## 2.2 Determining the Center Distance of the First and the Second Stage

The center distance of the first stage can be calculated by [15]:

$$a_{w1} = K_a \cdot (u_1 + 1) \cdot \sqrt[3]{\frac{T_{11} \cdot k_{H\beta}}{[\sigma_H]^2 \cdot u_1 \cdot \psi_{ba1}}} \quad (23)$$

where,

- $K_{H\beta}$  is contact load ratio for pitting resistance; for the first stage of a two-stage helical reducer  $k_{H\beta} = 1.02 \div 1.28$  [15]. Therefore, we can chose  $k_{H\beta} = 1.1$ ;
- $[\sigma_H]$ -allowable contact stress (MPa); In practice,  $[\sigma_H] = 350 \dots 410$  (MPa) and we can chose  $[\sigma_H] = 380$  (MPa);
- $k_a$  is material coefficient; As the gear material is steel,  $k_a = 43$  [15];
- $\psi_{ba}$  is coefficient of wheel face width; for the for the first stage of a two-stage helical reducer  $\psi_{ba} = 0.3$ .

Substituting the above values into (23) gets:

$$a_{w1} \approx 1.2639 \cdot (u_1 + 1) \cdot \sqrt[3]{\frac{T_{11}}{u_1}} \quad (24)$$

Considering that the coefficient of wheel face width for the second stage  $\psi_{ba} = 0.35$  and calculating in the same way, the center distance of the second stage is determined as:

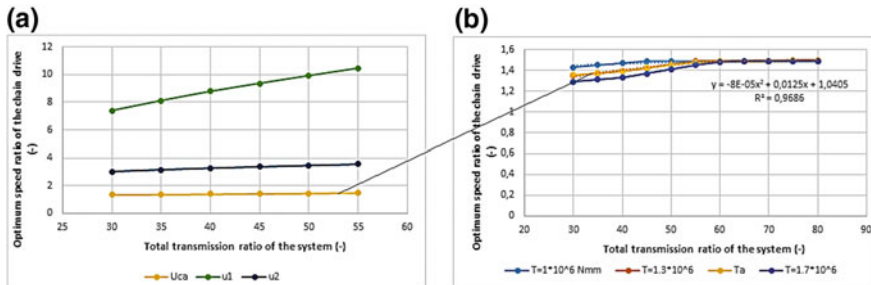
$$a_{w2} \approx 1.2006 \cdot (u_2 + 1) \cdot \sqrt[3]{\frac{T_{12}}{u_2}} \quad (25)$$

## 3 Results and Discussions

From Eqs. (11) and (12), a computer program was built for finding the optimum partial transmission ratios in order to get the minimum dimension of the cross section of the system. The following data was used in the optimization program:  $u_t = 30 \dots 80$ ;  $T_{out} = 10^6 \dots 10^7$ ;  $k_d = 1$ ;  $k_p = 1$ ;  $k_c = 1$ ;  $k_{adj} = 1$ ;  $k_{lub} = 1$  and  $k_{con} = 1.25$ .

**Table 1** Optimum gear ratios of the chain drive

$u_t$	$u_x$ when $T_{out} = 10^6x$										
	1	1.3	1.7	1.8	2	2.3	2.6	3	5	7	10
30	1.43	1.35	1.29	6	6	6	6	6	6	6	6
40	1.47	1.39	1.33	6	6	6	6	6	6	6	6
50	1.49	1.46	1.36	6	6	6	6	6	6	6	6
60	1.49	1.49	1.39	6	6	6	6	6	6	6	6
70	1.49	1.49	1.41	6	6	6	6	6	6	6	6
80	1.49	1.50	1.43	6	6	6	6	6	6	6	6



**Fig. 3** Optimum partial ratios versus total ratio

Table 1 shows the optimum values of speed ratio of the chain drive with different values of the total ratio of the system and the output torque. Besides, Fig. 3a presents the relation between the optimum partial ratios (including the gear ratio of the first stage  $u_1$ , the gear ratio of the second stage  $u_2$  and speed ratio of the chain drive  $u_c$ ) and the total ratios of the system. Also, the relation between the optimum speed ratio of the chain drive  $u_c$  and the total ratio  $u_t$  is shown in Fig. 3b.

From Table 1, it is observed that with large values of the output torque of the system ( $T_{out} \geq 1.8 \times 10^6$  (Nmm)), the optimum gear ratio of the chain drive is equal 6. Otherwise, the small values of the output torque ( $T_{out} < 1.8 \times 10^6$  (Nmm)), the small optimum gear ratios of the chain drive (less than 1.5). Also, the optimum gear ratio when  $T_{out} < 1.8 \times 10^6$  can be calculated by the following equation (with  $R^2 = 0.9686$ —see Fig. 3b):

$$u_c = -8 \cdot 10^{-5} \cdot u_t^2 + 0.0113 \cdot u_t + 1.0775 \tag{26}$$

From the data of the program, the following equations (with the coefficients of determination of both equations are  $R^2 = 1$ ) were found for determining the optimum gear ratios of the reducer:

$$u_1 = 0.9365 \cdot u_{gb}^{0.667} \tag{27}$$

$$u_2 = 1.0678 \cdot u_{gb}^{0.333} \quad (28)$$

Equation (26) is used to calculate the gear ratio of the chain drive  $u_c$ . After having  $u_c$ , the total ratio of the reducer is calculated by  $u_{gb} = u_t/u_c$  and the partial gear ratios of the reducer  $u_1$  and  $u_2$  can be determined by Eqs. (27) and (28) respectively.

## 4 Conclusions

The minimum cross-sectional acreage of a mechanical drive system using a chain drive and a two-stage helical reducer can be obtained by designing with optimum partial gear ratios which found from optimization program.

From the results of the optimization problem, models for determining the partial gear ratios of the chain drive and the gear-stages were proposed in order to get the minimum cross-sectional dimension of the system.

The partial gear ratios of the chain drive and the reducer can be calculated merely by using explicit models.

**Acknowledgements** The work described in this paper was supported by Thai Nguyen University of Technology for a scientific project.

## References

1. Kudreavtev VN, Gierzaves IA, Glukharev EG (1971) Design and calculus of gearboxes. Mashinostroenie Publishing, Sankt Petersburg (in Russian)
2. Milou G, Dobre G, Visa F, Vitila H (1996) Optimal design of two step gear units, regarding the Main Parameters. VDI Berichte No 1230, p 227
3. Pi VN (2001) A method for optimal calculation of total transmission ratio of two step helical gearboxes. In: Proceedings of the national conference on engineering mechanics, Ha Noi, p 12
4. Petrovski AN, Sapiro BA, Saphonova NK (1987) About optimal problem for multi-step gearboxes. Vestnik Mashinostr 10:13. (in Russian)
5. Pi VN, Tuan NK (2016) Optimum determination of partial transmission ratios of three-step helical gearboxes for getting minimum cross section. J Environ Sci Eng A 5:570–573
6. Pi VN, Binh ND, Dac VQ (2006) Phan Quang The, Optimal calculation of total transmission ratio of three-step helical gearboxes for minimum mass of gears. J Sci Technol 6 Eng Univ 91
7. Pi VN (2008) A new study on optimal calculation of partial transmission ratio of three-step helical reducers. In: The 3rd IASME/WSEAS international conference on continuum mechanics, Cambridge, UK, p 23
8. Romhild I, Linke H (1992) Gezielte Auslegung Von Zahnradgetrieben mit minimaler Masse auf der Basis neuer Berechnungsverfahren. Konstruktion 44:229–236
9. Pi VN (2008) Optimal determination of partial transmission ratios for four-step helical gearboxes with first and third step double gear-sets for minimal mass of gears. Applied Computing Conference (ACC' 08), Istanbul, Turkey, May 27–30
10. Hung LX, Pi VN, Du NV (2009) Optimal calculation of partial transmission ratios of four-step helical gearboxes with second and fourth-step double gear-sets for minimal mass of gears. In:

The international symposium on mechanical engineering (ISME), Ho Chi Minh city, Vietnam, 21–23, September

11. Pi VN, Thao TTP, Thao LTP (2015) A new study on optimum determination of partial transmission ratios of mechanical driven systems using a V-belt and two-step helical gearbox. Vietnam Mech Eng J 10:123
12. Pi VN, Cam NTH, Tuan NK (2016) Optimum calculation of partial transmission ratios of mechanical driven systems using a V-belt and two-step bevel helical gearbox. J Environ Sci Eng A 5:566
13. Pi VN, Thao TTP, Tuan DA (2017) Optimum determination of partial transmission ratios of mechanical driven systems using a chain drive and two-step helical gearbox. J Environ Sci Eng B 6:80
14. Chetan AS, Mahalle AK (2012) Design optimization of speed ratio for conventional chain drive used in tricycle. Int J Innovative Technol Exploring Eng 1(1):40–43
15. Chat T, Le Van Uyen D (1998) Design and calculus of mechanical transmissions. Educational Republishing House, Hanoi. (in Vietnamese)

# A New Study on Determination of Optimum Gear Ratios of a Two-Stage Helical Gearbox



Vu Ngoc Pi, Nguyen Khac Tuan, Le Xuan Hung and Luu Anh Tung

**Abstract** This paper presents a new study on the optimum determination of gear ratios of a two-stage helical gearbox. In this study, in order to find the optimum gear ratios of the gearbox, the acreage of the cross section of the gearbox was chosen as the objective function of the optimization problem. Besides, the effects of input parameters including the total gearbox ratio, the wheel face width coefficient, the output torque and the allowable contact stress were considered. To evaluate the effect of these factors on the optimum gear ratios, an “experiment” was designed and a computer program was built to perform the “experiment”. From the results of the study, models for calculation of the optimum gear ratios of a two-stage helical gearbox were proposed. Using these models, the gear ratios can be determined accurately and simply.

**Keywords** Gear ratio · Optimum gearbox design · Helical gearbox

## 1 Introduction

In gearbox design, the calculation of the gear ratios is a very important task. This is because the gear ratios strongly affect the dimension, the mass, and the cost of a gearbox. Consequently, optimum determination of the gear ratios has been considered in many researches.

For a two-stage helical gearbox, Kudreavtev et al. [1] introduced a graph (Fig. 1) to determine the gear ratio of the first stage. It can be seen that the determination of the gear ratio of the first stage  $u_1$  by using the graph in Fig. 1 is quite complicated.

---

V. N. Pi (✉) · L. X. Hung · L. A. Tung  
Mechanical Engineering Faculty, Thai Nguyen University of Technology, Thai Nguyen, Vietnam  
e-mail: [vungocpi@tnut.edu.vn](mailto:vungocpi@tnut.edu.vn)

N. K. Tuan  
Automotive and Power Machinery Faculty, Thai Nguyen University of Technology, Thai Nguyen, Vietnam

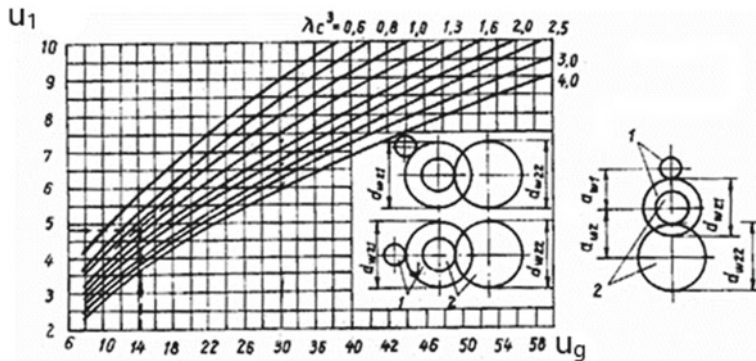


Fig. 1 The gear ratio of the stage 1 versus the total gearbox ratio [1]

Also, to find  $u_1$ , we must select the coefficient  $\lambda c^3$  (with  $\lambda c^3 = 0.6-4$ ) so it is very complicated and the result cannot reach to optimum values.

Additionally, to determine the gear ratios of this gearbox type, Milou et al. [2] proposed “a practical method”. In this method, the gear ratios were found from practical data. For example, based on the data from reducer factories, it was reported that the two-stage gearbox weight is minimum if the ratio of two center distances  $a_{w2}/a_{w1}$  ranged from 1.4 to 1.6 [2]. Based on that, the optimal gear ratios were introduced in the tabulated form.

The most common method to find optimum gear ratios of two-stage helical gearboxes is the model method. In this method, models for calculation of optimum gear ratios will be used for different objectives. The objective can be the minimum volume of gears [3], the minimum gearbox mass [4], the minimum cross section dimension of the gearbox [5], the minimum mass of gears [6], and the minimum gearbox length [7].

This paper presents a new study to determine the gear ratios of a two-stage helical gearbox in which the objective is the minimum gearbox cross-sectional acreage. Also, the influence of input parameters on the optimum gear ratios was investigated.

## 2 Optimization Problem

The objective of the optimization problem is to determine the optimum gear ratios in order to get the minimal acreage of cross section of a two-stage helical gearbox. From Fig. 2, the acreage of cross section of the gearbox can be calculated as:

$$A = L \cdot h \tag{1}$$

In which,  $L$  and  $h$  are determined as (see Fig. 2):

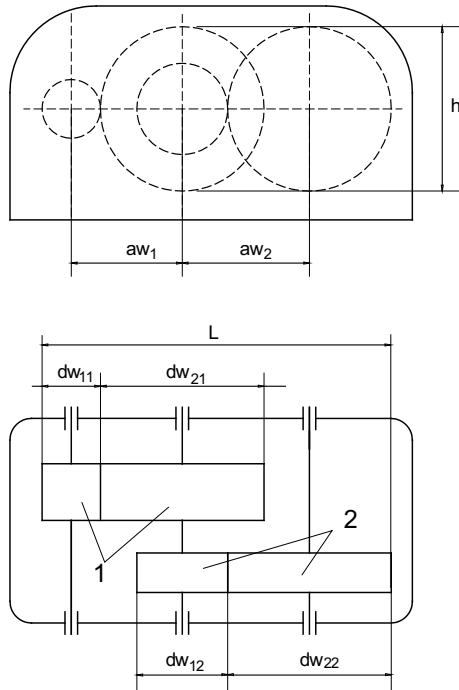


Fig. 2 Calculation schema

$$L = d_{w11}/2 + a_{w1} + a_{w2} + d_{w22}/2 \tag{2}$$

$$h = \max(d_{w21}, d_{w22}) \tag{3}$$

In the above equations,  $a_{w1}$  and  $a_{w2}$  are the center distance of the first and the second stage;  $d_{w11}$ ,  $d_{w21}$  and  $d_{w22}$  are pitch diameters (mm) of the first and the second stage, respectively.

For a two-stage gearbox, the diameters  $d_{w11}$ ,  $d_{w21}$  and  $d_{w22}$  can be determined as [8]:

$$d_{w11} = 2 \cdot a_{w1} / (u_1 + 1) \tag{4}$$

$$d_{w21} = 2 \cdot a_{w1} \cdot u_1 / (u_1 + 1) \tag{5}$$

$$d_{w22} = 2 \cdot a_{w2} \cdot u_2 / (u_2 + 1) \tag{6}$$

Also, for a two-stage gearbox we have:

$$u_2 = u_g / u_1 \tag{7}$$

where,  $u_g$  is the total gearbox ratio;  $u_1, u_2$  are the gear ratios.

From (2), (3), (4), (5) and (6) the following equations are given:

$$L = f(a_{w1}, a_{w2}, u_1, u_g) \quad (8)$$

$$h = f(a_{w1}, a_{w2}, u_1, u_g) \quad (9)$$

Thus, the optimization problem is defined as

$$\text{minimize } A = L \cdot h \quad (10)$$

With the following constraints

$$5 \leq u_g \leq 30 \quad (11)$$

From (8), (9) and (10), it is clear that in order to solve the optimization problem, it is necessary to determine the center distances of the first stage  $a_{w1}$  and the second stage  $a_{w2}$ .

## 2.1 Determining the Center Distance of the First Stage

The center distance of the first stage  $a_{w1}$  is calculated by [8]:

$$a_{w1} = K_a \cdot (u_1 + 1) \cdot \sqrt[3]{\frac{T_{11} \cdot k_{H\beta}}{[\sigma_H]^2 \cdot u_1 \cdot \psi_{ba1}}} \quad (12)$$

In which,

- $K_{H\beta}$  is contact load ratio for pitting resistance; for the first stage of a two-stage helical gearbox  $k_{H\beta} = 1.02 \div 1.28$  [8]. Therefore, we can chose  $k_{H\beta} = 1.1$ ;
- $[\sigma_H]$ -allowable contact stress (MPa); In practice,  $[\sigma_H] = 350 \dots 410$  (MPa);
- $k_a$  is material coefficient; As the gear material is steel,  $k_a = 43$  [8];
- $\psi_{ba}$  is coefficient of wheel face width; for the for the first stage of a two-stage helical gearbox  $\psi_{ba1} = 0.3 \dots 0.35$ ;

From the moment equilibrium condition of a two-stage helical gearbox and their regular resistance condition, the following equation can be used:

$$T_{out} = T_{11} \cdot \eta_{hg}^2 \cdot \eta_{be}^3 \cdot u_g \quad (13)$$

wherein,  $\eta_{hg}$  is helical gear transmission efficiency ( $\eta_{hg}$  is from 0.96 to 0.98 [2]);  $\eta_{be}$  is transmission efficiency of a pair of rolling bearing ( $\eta_{be}$  is from 0.99 to 0.995 [2]). Choosing  $\eta_{hg} = 0.97$  and  $\eta_{be} = 0.992$  [8] gives



$$T_{11} = 1.0887 \cdot T_{out}/u_g \quad (14)$$

Substituting (14) and  $k_{H\beta} = 1.1$  into (12) gets:

$$a_{w1} = 45.6634 \cdot (u_1 + 1) \cdot \sqrt[3]{\frac{T_{out}}{[\sigma_{H1}]^2 \cdot u_1 \cdot u_g \cdot \psi_{ba1}}} \quad (15)$$

## 2.2 Determining the Center Distance of the Second Stage

The center distance of the second stage  $a_{w2}$  is calculated by [8]:

$$a_{w2} = K_a \cdot (u_2 + 1) \cdot \sqrt[3]{\frac{T_{12} \cdot k_{H\beta}}{[\sigma_H]^2 \cdot u_2 \cdot \psi_{ba2}}} \quad (16)$$

Also, for the second stage, we have

$$T_{out} = T_{12} \cdot \eta_{hg} \cdot \eta_{be}^2 \cdot u_2 \quad (17)$$

Choosing  $\eta_{hg} = 0.97$  and  $\eta_{be} = 0.992$  as in Sect. 2.1 gives

$$T_{12} = 1.0476 \cdot T_{out}/u_2 \quad (18)$$

Substituting (18),  $k_a = 43$  and  $k_{H\beta} = 1.1$  (as in Sect. 2.1) into (16) gets:

$$a_{w2} = 45.0814 \cdot (u_2 + 1) \cdot \sqrt[3]{\frac{T_{out}}{[\sigma_H]^2 \cdot u_2^2 \cdot \psi_{ba2}}} \quad (19)$$

## 2.3 Experimental Work

To investigate the effect of input parameters on the optimum gear ratios, an “experiment” was designed and conducted. For the design of the experiment, a 2-level full factorial design was selected. Table 1 shows 5 input parameters which were selected for the exploring. Therefore, the design was arranged with  $2^5 = 32$ , which is the number of experiments. To conduct the experiment, a computer program was built based on Eqs. (10) and (11). The various levels of input parameters and the results of the output of the computer program (the optimum gear ratio of the first stage  $u_1$ ) are presented in Table 2.

**Table 1** Input parameters

Factor	Code	Unit	Low	High
Total gearbox ratio	$u_g$	–	5	30
Coefficient of wheel face width of stage 1	$x_{ba1}$	–	0.3	0.35
Coefficient of wheel face width of stage 2	$x_{ba2}$	–	0.35	0.4
Allowable contact stress	AS	MPa	350	410
Output torque	$T_{out}$	Nmm	$10^5$	$10^6$

**Table 2** Experimental plans and output response

Std-order	Run-order	Center Pt	Blocks	$u_g$	$x_{ba1}$	$x_{ba2}$	AS (MPa)	$T_{out}$ (Nm)	$u_1$
28	1	1	1	30	0.35	0.35	410	1000	9.53
14	2	1	1	30	0.3	0.4	410	100	8.66
13	3	1	1	5	0.3	0.4	410	100	2.62
32	4	1	1	30	0.35	0.4	410	1000	9.11
30	5	1	1	30	0.3	0.4	410	1000	8.66
6	6	1	1	30	0.3	0.4	350	100	8.66
3	7	1	1	5	0.35	0.35	350	100	2.88
27	8	1	1	5	0.35	0.35	410	1000	2.88
...									
20	31	1	1	30	0.35	0.35	350	1000	9.53
8	32	1	1	30	0.35	0.4	350	100	9.11

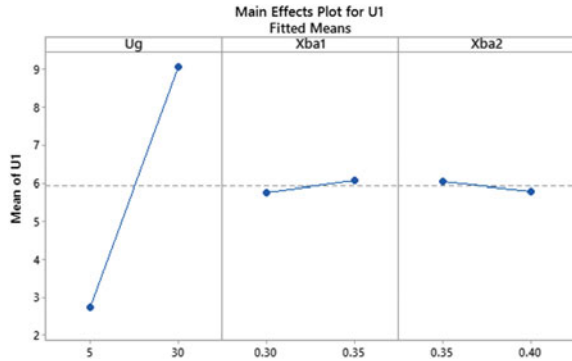
### 3 Optimization Results and Discussions

To visualize the effect of input parameters on the response and to evaluate of the relative strength of the effect, a graph of the main effect of each parameter is plotted in Fig. 3. From Fig. 3, it is clear that the optimum gear ratio of the first stage  $u_1$  increases significantly with the increase of the total gearbox ratio  $u_g$ . Besides, it is also effected by the coefficient of wheel face width of the first and the second stages ( $\psi_{ba1}$  and  $\psi_{ba2}$ ). In addition, it is found that the allowable contact stress and the output torque do not affect the optimum gear ratio.

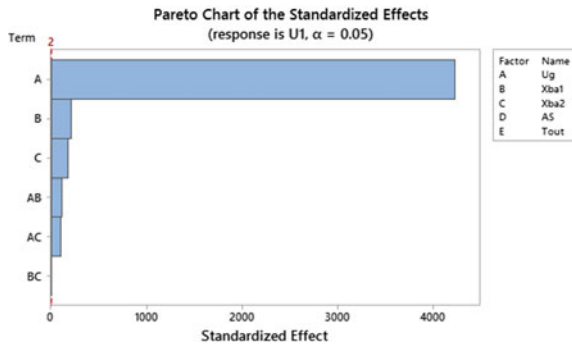
Figure 4 shows the Pareto chart of the standardized effects from the largest effect to the smallest effect. According to the chart, the bars that represent parameters including the total gearbox ratio (factor A), the coefficient of wheel face width of the first and the second stages (factors B and C) and the interactions between them (AB and AC) cross the reference line. Therefore, these factors are statistically significant at the 0.05 level with the response model.

Theoretically, the Pareto chart cannot show which effects increase or decrease the response. Therefore, the Normal Plot of the standardized effects (Fig. 5) is used for that. From Fig. 5, it is found that the total gearbox ratio is the most significant factor

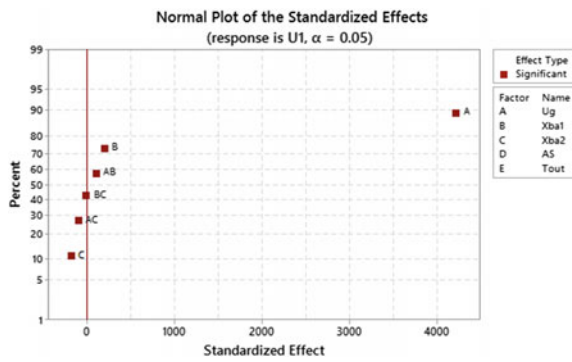
**Fig. 3** Main effects plot for optimum gear ratio of stage 1



**Fig. 4** Pareto chart of the standardized effects



**Fig. 5** Normal plot for  $u_1$



for the optimum gear ratio of the first stage. Also, the total gearbox ratio and the coefficient of wheel face width of the first stage have a positive standardized effect. If they change from the low level to the high level of the factors, the optimum gear ratio of the first stage increases. Besides, the coefficient of wheel face width of the second stage has a negative standardized effect. When it increases, the optimum gear ratio decreases.

Coded Coefficients						
Term	Effect	Coef	SE Coef	T-Value	P-Value	VIF
Constant		5.91875	0.00075	7891.67	0.000	1.00
Ug	6.33750	3.16875	0.00075	4225.00	0.000	1.00
Xba1	0.302500	0.151250	0.000750	201.67	0.000	1.00
Xba2	-0.262500	-0.131250	0.000750	-175.00	0.000	1.00
Ug*Xba1	0.162500	0.081250	0.000750	108.33	0.000	1.00
Ug*Xba2	-0.142500	-0.071250	0.000750	-95.00	0.000	1.00
Xba1*Xba2	-0.007500	-0.003750	0.000750	-5.00	0.000	1.00
Model Summary						
	S	R-sq	R-sq(adj)	R-sq(pred)		
	0.0042426	100.00%	100.00%	100.00%		

**Fig. 6** Estimated effects and coefficients for  $u_1$

Figure 6 shows the estimated effects and coefficients for  $u_1$ . As in Fig. 6, factors which have a significant effect on a response have P-values lower than 0.05 are the total gearbox ratio  $u_g$ , the coefficient of wheel face width of the first and the second stage ( $\psi_{ba1}$  and  $\psi_{ba2}$ ) and their interactions. As a result, the relation between the optimum gear ratio and significant effect factors can be described by the following equation:

$$u_1 = 0.2545 \cdot u_g + 3.75 \cdot \psi_{ba1} + 0.69 \cdot \psi_{ba2} + 0.26 \cdot u_g \cdot \psi_{a1} - 0.228 \cdot u_g \cdot \psi_{ba2} - 6 \cdot \psi_{ba1} \cdot \psi_{ba2} + 0.736 \quad (20)$$

As seen in Fig. 6, the high values of adj-R<sup>2</sup> and pred-R<sup>2</sup> indicate that the estimated model (Eq. 20) fit the experimental data very well.

Equation (20) is used to calculate the gear ratio of the first stage  $u_1$ . After having  $u_1$ , the total ratio of the second stage is calculated by  $u_2 = u_g/u_1$ .

## 4 Conclusions

The minimum cross-sectional acreage of a two-stage helical gearbox can be obtained by determination of optimum gear ratios of the gearbox.

Models for calculation of the optimum gear ratios of a two-stage helical gearbox to get the minimum cross-sectional acreage of the gearbox were proposed.

By using explicit models, the optimum gear ratios of the gearbox can be calculated accurately and simply.

**Acknowledgements** The work described in this paper was supported by Thai Nguyen University of Technology for a scientific project.

## References

1. Kudreavtev VN, Gierzaves IA, Glukharev EG (1971) Design and calculus of gearboxes. Mashinostroenie Publishing, Sankt Petersburg. (in Russian)
2. Milou G, Dobre G, Visa F, Vitila H (1996) Optimal design of two step gear units, regarding the Main Parameters. VDI Berichte No 1230, p 227
3. Petrovski AN, Sapiro BA, Saphonova NK (1987) About optimal problem for multi-step gearboxes. Vestnik Mashinostr 10:13. (in Russian)
4. Romhild I, Linke H (1992) Gezielte Auslegung Von Zahnradgetrieben mit minimaler Masse auf der Basis neuer Berechnungsverfahren. Konstruktion 44:229–236
5. Pi VN (2001) A method for optimal calculation of total transmission ratio of two step helical gearboxes. In: Proceedings of the national conference on engineering mechanics, Ha Noi, pp 12–15
6. Pi VN, Dac VQ (2004) A new and effective method for optimal calculation of total transmission ratio of two step helical gearboxes. School of computational sciences and engineering: theory and applications, March 3–5, Ho Chi Minh City, pp 103–106
7. Pi VN (2008) A new study on optimal calculation of partial transmission ratios of two-step helical gearboxes. In: 2nd WSEAS international conference on computer engineering and applications (CEA'08) Acapulco, Mexico, January 25–27, 2008, pp 162–165
8. Chat T, Le Van Uyen D (1998) Design and calculus of mechanical transmissions. Educational Republishing House, Hanoi. (in Vietnamese)

# Anti-friction Bearing Malfunction Detection and Diagnostics Using Hybrid Approach



Tamiru Alemu Lemma, Noraimi Omar,  
Mebrahitom Asmelash Gebremariam and Shazaib Ahsan

**Abstract** Antifriction bearings are widely used in the industries especially in aircraft, machine tool, and construction industry. It holds and guides moving parts of the machine and reduces friction and wear. As they are one of the riskiest components in the rotating machinery, it puts challenges on the bearing health condition monitoring. The defects found in the bearings can lead to malfunctioning of the machinery and impact the level of production. This paper presents detection technique and diagnosis of bearing defects using a novel hybrid approach (continuous wavelet transform, Abbott–Firestone parameter, and artificial neural network). The vibration signals were obtained from Case Western Reserve University. MATLAB is used to analyse the vibration signals, test, and train the required models according to the chosen model structure. Various statistical features are extracted from the time domain namely kurtosis, skewness, root mean square, standard deviation, crest factor, and Abbott parameters to analyse and identify the bearing fault. The results demonstrate that the proposed method is effective in identifying the bearing faults.

**Keywords** Antifriction bearing · Rotating machinery · Condition monitoring · Detection · Diagnosis · Vibration · ANN · Wavelet · Abbott parameter

## 1 Introduction

Antifriction bearings are designed to support moving machine parts such as the rotating shafts and they have the potential to reduce friction effectively. They minimize the friction by eliminating any possible sliding between bearing surfaces and replacing all contacts with rolling interfaces. The bearing is also known as rolling contact

---

T. A. Lemma (✉) · N. Omar · S. Ahsan  
Department of Mechanical Engineering, Universiti Teknologi PETRONAS, 32610 Seri Iskandar,  
Perak, Malaysia  
e-mail: [tamiru.lemma@utp.edu.my](mailto:tamiru.lemma@utp.edu.my)

M. A. Gebremariam  
Faculty of Manufacturing, University Malaysia Pahang, Pekan, Malaysia

© Springer Nature Singapore Pte Ltd. 2020  
M. Awang et al. (eds.), *Advances in Material Sciences and Engineering*, Lecture Notes in Mechanical Engineering,  
[https://doi.org/10.1007/978-981-13-8297-0\\_15](https://doi.org/10.1007/978-981-13-8297-0_15)

bearing. It can be divided into two different designs, which are ball bearings and roller bearings. The bearings are mostly used in automobile, automatic production machinery and high-speed engines due to their capacity and reliability of carrying load. Thus, it is safe to say that in majority of machines, bearings are among the most essential components.

In most of the manufacturing company or any commercial industry, if there is an unexpected downtime due to mechanical failures, it will lead to a big impact on the company especially on the economic side. Example causes of mechanical failures are improper lubrication, misalignments, bearings faults and gearbox failure. However, several researches show that bearing malfunctioning is one of the main reasons why rotating equipment fails. Most of the bearing failures are not correlated with the end of its useful life but it can be caused by poor handling and installation, harsh operating conditions, material fatigue, lubrication or even contamination problems. Failure of bearings will not directly cause the machinery to breakdown, but it will persist overtime and cause a severe failure. Therefore, it is important to detect any early warning sign before the equipment failed.

Mostly damaged bearings are not equated with the end of its useful life, a large number of bearings fail too early while in service due to heavier loading that has exceeded the prescribed limit, inadequate lubrication, incorrect assembly or handling, ineffective sealing and incorrect fit [1]. When the rolling elements in the bearing roll over the flaw, they will generate vibration signal which frequency might be correlated to rotational speed of the supported shaft. The frequencies associated with flaws in the cage, internal and external races, and on one of the bearing balls, are given by Eqs. (1), (2), (3), and (4), respectively.

$$\text{Train or Cage Frequency: FTF} = \frac{f_r}{2} \left\{ 1 - \frac{d}{D} \cos \varnothing \right\} \quad (1)$$

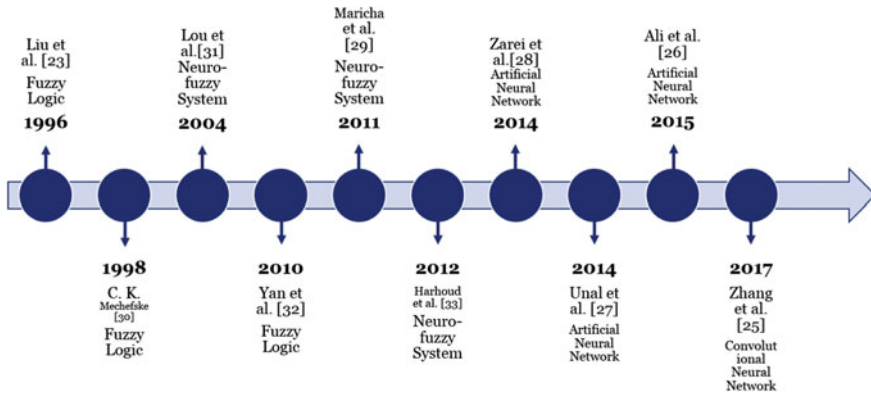
$$\text{Ball Pass Frequency Inner Race: BPFI} = n \frac{f_r}{2} \left\{ 1 + \frac{d}{D} \cos \varnothing \right\} \quad (2)$$

$$\text{Ball Pass Frequency Outer Race: BPFO} = n \frac{f_r}{2} \left\{ 1 - \frac{d}{D} \cos \varnothing \right\} \quad (3)$$

$$\text{Ball Spin Frequency: BSF} = D \frac{f_r}{2d} \left\{ 1 - \left( \frac{d}{D} \cos \varnothing \right)^2 \right\} \quad (4)$$

where  $d$  is the ball diameter,  $D$  is the pitch diameter,  $n$  is the number of balls,  $f_r$  is the rotational frequency, and  $\varnothing$  is the contact angle. These formulas are the kinematic frequencies assuming no slippage.

With today's advanced technology and an efficient diagnostics system, it is possible to recognize these primitive faults before destructive failure happened. The technique is called as condition monitoring. It plays an important role to maintain the efficiency and effectiveness of the machine at an optimal level. Condition monitoring means to monitor, determine, and understand the state of the machine in operation. If there is a sudden change in the machine behaviour, it is likely an indica-



**Fig. 1** Timeline for intelligent system-based bearing fault detection and diagnostics research

tive of a developing failure. Hence, an efficient and effective condition monitoring is very critical in an industry. The most commonly used condition monitoring technique for fault detection in rotating machine is vibration analysis. The vibration spectrum will be interpreted and analysed using hybrid approach to detect and diagnose the bearing faults.

Many researches have been carried out to improve the technology on bearing fault detection. There is wide range of methods for bearing fault detection based on vibration analysis ranging from Fast Fourier transform (FFT), short-time Fourier transform (STFT), Wigner-Ville Distribution (WVD) [2], wavelet transform [3], singular value decomposition (SVD), Hidden Markov Model (HMM) [4], medium entropy deconvolution (MED), spectral kurtosis (SK), experimental data analysis (EDA) [11], neural network [6], fuzzy logic [7] and spectral analysis [8]. To improve the accuracy and precision of the bearing fault diagnosis, there is an alternative solution using the artificial intelligence approach. Various studies have been carried out and a lot of researchers have brought new strategies in view of the artificial intelligent techniques. The timeline for intelligent system-based bearing fault detection and diagnostics research is illustrated in Fig. 1.

The main purpose of this paper is to establish an understanding on the signatures of possible causes of bearing failures using hybrid approach (continuous wavelet transforms and Abbott–Firestone parameters) and develop a diagnostic system that can be applied in the field. This will help to improve the bearing life and carry out preventive maintenance. To our knowledge, such a hybrid approach has not been reported before.



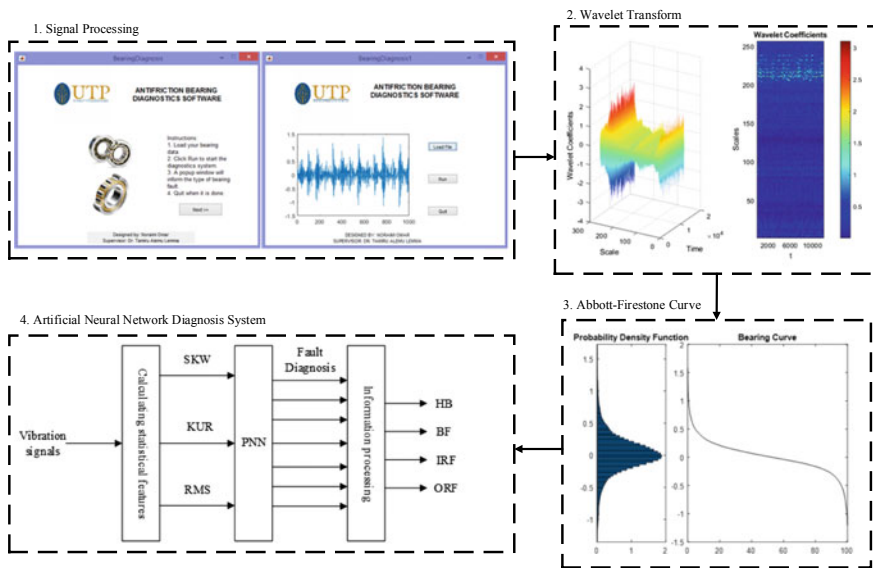


Fig. 2 Flowchart for bearing detection and diagnostics system

## 2 Methodology

There are five important steps involved in fault detection and diagnostics of anti-friction bearings using our proposed hybrid approach, as shown in Fig. 2: signal processing, wavelet transform, Abbott-Firestone curve, and artificial neural network. The description of each step is provided as follows:

- Step 1: The raw vibration signals obtained from the vibrating system is processed to capture the relevant information or also known as feature extraction. The current study uses time-domain analysis to calculate the diagnostics indicator.
- Step 2: New method is applied in the present paper where the vibration signals is directly feed into the Continuous Wavelet Transform (CWT) and the results is presented as a 3D pattern of the CWT coefficients.
- Step 3: From the wavelet coefficients obtained in previous step, all those values will be aggregated into cumulative density function and the associated parameters are computed. This step will produce what is called as Abbott-Firestone curve or bearing area curve. The same curve will be further processed to generate Abbott parameter.
- Step 4: The computed Abbott parameters is then plotted and tend to capture them into the artificial neural network. In this stage, the classification of the bearing fault can be determined.

**Table 1** Diagnostics indicators

Name	Formula	Name	Formula
Standard deviation	$\sigma = \sqrt{\frac{1}{n} \sum_{i=1}^n (k_i - \bar{k})^2}$	Moment	$k_s = \left( \frac{1}{n} \sqrt{\sum_{i=1}^n k} \right)^2$
Kurtosis	$k_{kur} = \frac{1}{n} \sum_{i=1}^n \frac{(k_i - \bar{k})^4}{\sigma^4}$	Peak-to-peak	$k_{p2p} =  k_{max} - k_{min} $
Root mean square	$k_{rms} = \sqrt{\frac{1}{n} \sum_{i=1}^n k^2}$	Peak to RMS	$k_{peak.to.rms} = \frac{ k_{max} }{k_{rms}}$
Skewness	$k_{skew} = \frac{1}{n} \sum_{i=1}^n \frac{(k_i - \bar{k})^3}{\sigma^3}$	Waveform factor	$k_{wave} = \frac{k_{rms}}{ k }$
Square mean root	$k_s = \left( \frac{1}{n} \sqrt{\sum_{i=1}^n k} \right)^2$	Impulse factor	$k_{impulse} = \frac{k_{max}}{ k }$

$\bar{k}$  is the mean

## 2.1 Signal Processing

Suitable feature extraction strategies highlight the essential distinctive attributes of the data, while at the same time disregards all kinds of unimportant characteristics, for example, the noise. The common parameters computed in the time domain include the root mean square (RMS), kurtosis, skewness, and crest factor. In the present paper, the features are extracted from time domain.

The time domain parameters can viably show early faults happening in rotating machinery. These indicators can be good indicators for monitoring the bearing health. Here, there are ten of them which are generally used for the fault diagnosis of rotating machinery, as shown in Table 1.

Each of the diagnostic indicators has distinctive critical degrees to distinguish the bearing fault, though all represent defect data of the bearing. Thus, the selected features used in this paper are RMS, skewness, kurtosis, standard deviation, and crest factor.

## 2.2 Continuous Wavelet Transform

Wavelet transform has turned out to be one of the developing and quick advancing numerical and signal processing instruments for its numerous distinct benefits. Wavelet investigation is fit for uncovering parts of information that other signal analysis methods might miss, similar to patterns, breakdown points and discontinuities in higher subsidiaries. Moreover, because it bears an alternate perspective of information than those displayed by traditional approaches, wavelet investigation can

frequently denoise a signal without measurable deterioration [9]. As such, it is an effective means to interpret a nonstationary signal.

The CWT of  $x(t)$ , represented by  $(W_\varphi^x)(a, b)$ , is the convolution of the signal  $x(t)$  with wavelet  $\varphi_{a,b}(t)$  and integrated over the interval  $[-\infty, +\infty]$  [10]. It is given by:

$$(W_\varphi^x)(a, b) = \frac{1}{\sqrt{a}} \int_{-\infty}^{\infty} x(t) \varphi\left(\frac{t-b}{a}\right) dt \quad (5)$$

where  $a > 0$  and  $b$  are scale and shift parameters, respectively.  $\varphi(t)$  represents the mother wavelet. Typical mother wavelets include Mexican hat, Morlet, Gaussian derivative, Shanon, and Daubechies. Whenever ‘ $a$ ’ decreases, the wavering turns out to be more intense and shows high-recurrence nature. Likewise, when ‘ $a$ ’ increases, the motions wind up drawn out and demonstrate low-recurrence nature. The size ‘ $a$ ’ is thought to be confined to  $R^+$ , though easily understood as a corresponding of frequency.

For a known  $(W_\varphi^x)(a, b)$  and constant  $C_\varphi$ , the original signal can be constructed by applying the inverse transform, which is given by the equation

$$x(t) = \frac{1}{C_\varphi} \int_0^\infty \left\{ \int_{-\infty}^{\infty} (W_\varphi^x)(a, b) \varphi\left(\frac{t-b}{a}\right) db \right\} \frac{da}{a^2} \quad (6)$$

where  $C_\varphi$  is the constant parameter that relies upon  $\varphi(t)$ . Based on  $C_\varphi$ , the admissibility condition is given by Eq. (7).

$$C_\varphi = \int_{-\infty}^{\infty} \frac{|\varphi(\omega)|^2}{\omega} d\omega < \infty \quad (7)$$

where  $\varphi(\omega) = \int_{-\infty}^{\infty} \varphi(t) e^{-i\omega t} dt$ . If the mother wavelet satisfies Eq. (7), then any function  $x(t) \in L^2(\mathbb{R})$  satisfies Eq. (6). As such, the continuous wavelet transform based on  $\varphi(t)$  is invertible.

### 2.3 Abbott-Firestone Parameter

The wavelet coefficients obtained from the vibration signals are transformed to Abbott parameters. The latter is normally used to measure wear occurrence, for example, lubrication impact, bearing materials, or the texture of the surface [11]. The Abbott parameters are tabulated in Table 2. All the parameters depend on the  $F(x)$  equation that represents the best-fitted line computed from the “linear part” of  $A(x)$ , the Abbott curve equation.  $F(x)$  is the straight line equation that best adjusts the linear part of the Abbott curve, and we define  $c1 = F(0)$  and  $c2 = F(100)$ .

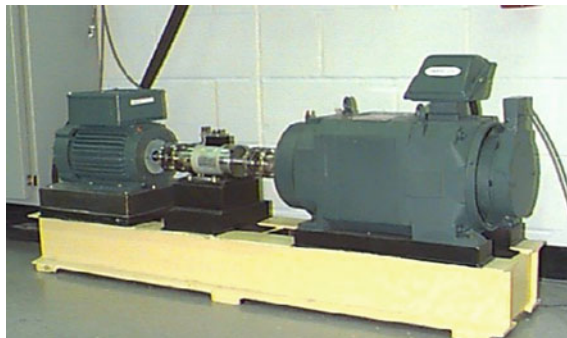
**Table 2** Definition of Abbott parameters [11]

Definition		Formula
Quantity of solid peaks	$A_1$	$A^{-1}(c_1) \int_0^{A^{-1}(c_1)} (A(x) - c_1) dx$
Quantity of solid valleys	$A_2$	$A^{-1}(c_2) \int_{A^{-1}(c_2)}^{100} (A(x) - A(100)) dx$
Threshold as the minimal AHD	$M_{r1}$	$A^{-1}(c_1)$
Threshold as the maximal AHD	$M_{r2}$	$A^{-1}(c_2)$
Kernel or core roughness depth	$R_k$	$c_1 - c_2$
“Reduced” height peak amplitude	$R_{pk}$	$A(0) - c_1$
“Reduced” height valley amplitude	$R_{vk}$	$c_1 - A(100)$

### 3 Results and Discussion

The bearing fault data set is obtained from Case Western Reserve University. The information set is collected from the test stand as indicated in Fig. 3, where it comprises of a 2 hp motor, a dynamometer, a torque transducer, and control hardware. The bearing signals are extracted using sampling rate of 12,000 samples per second through accelerometer, which were connected to the housing. As shown in Table 3, these signals were measured under 0, 1, 2, and 3 hp engine load with the engine speed of 1797, 1772, 1750, and 1730 rpm respectively.

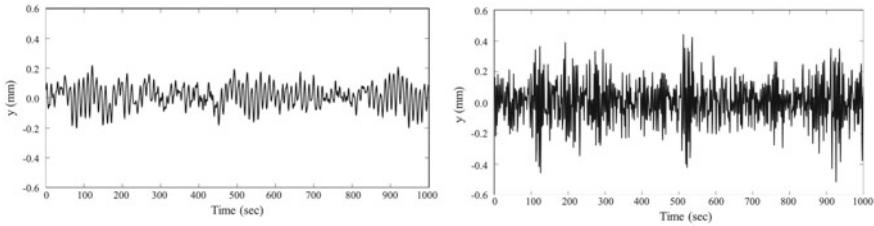
The bearings utilized as part of this study are deep groove ball bearings which were made by SKF. The diameter measurements of the inside, outside, thickness, ball, and pitch of the tested bearings are 0.9843, 2.0472, 0.5906, 0.3126, and 1.537 in. respectively.



**Fig. 3** Bearing test stand

**Table 3** Summary of bearing fault data arrangement

Fault position	Motor load (hp)	Fault diameter (in.)
Inner race	0, 1, 2, 3	0.007, 0.014, 0.021
Ball	0, 1, 2, 3	0.007, 0.014, 0.021
Outer race (at 3:00)	0, 1, 2, 3	0.007, 0.021
Outer race (at 6:00)	0, 1, 2, 3	0.007, 0.014, 0.021
Outer race (at 12:00)	0, 1, 2, 3	0.007, 0.021

**Fig. 4** **a** Signal from healthy bearing for 0 hp and 1797 rpm. **b** Signal from bearing with inner race fault for 0 hp and 1797 rpm

The deformity sizes were 0.007, 0.014, and 0.021 in. Healthy bearing, bearing with inner race fault, outer race fault bearing, and bearing with ball defect are the four sets of data that were obtained from the experimental set up.

Figure 4a, b illustrates the characteristics waveforms of the vibration signal evaluated from the test bearing: healthy bearing and bearing with inner ring defect, respectively. There is a major difference in the vibration amplitude of a healthy bearing and a defect bearing. The amplitude of the vibration of a damage bearing inner ring is much higher compared to a normal healthy bearing. The spikes in the waveform as presented in Fig. 4b indicate the impact between a ball and a crack inside the bearing.

Figures 5 and 6 represent some plots of the calculated values of RMS, kurtosis, skewness, and crest factor. Windows are applied to the time waveform to shape the spectrum and reduce errors. It can be observed that for the faulty bearing, the values of the indicators are slightly more than the normal bearing. The crest factor has high value due to the increasing peaks in the time domain signal. Kurtosis value describes the impulsive shape of the time signal while the negative values of the skewness points out the malfunctioning of the bearing since it is not symmetrical.

Figure 7a, b show the vibration signal and their standard deviation of a normal bearing. The range of the normal bearing amplitude is  $-0.25$  to  $0.25$  mm and  $0.05$  to  $0.08$  of standard deviation. However, comparing the value to a bearing with inner race fault, as illustrated in Fig. 8a and b, the amplitude of the vibration signal is higher with the range from  $-2$  to  $2$  mm and the standard deviation varies from  $0.27$  to  $0.34$ .

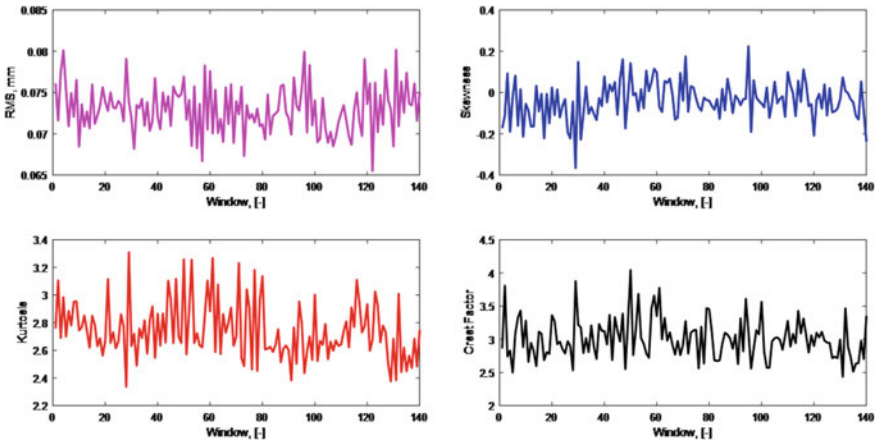


Fig. 5 Diagnostics indicator for healthy bearing (0 hp, 1797 rpm)

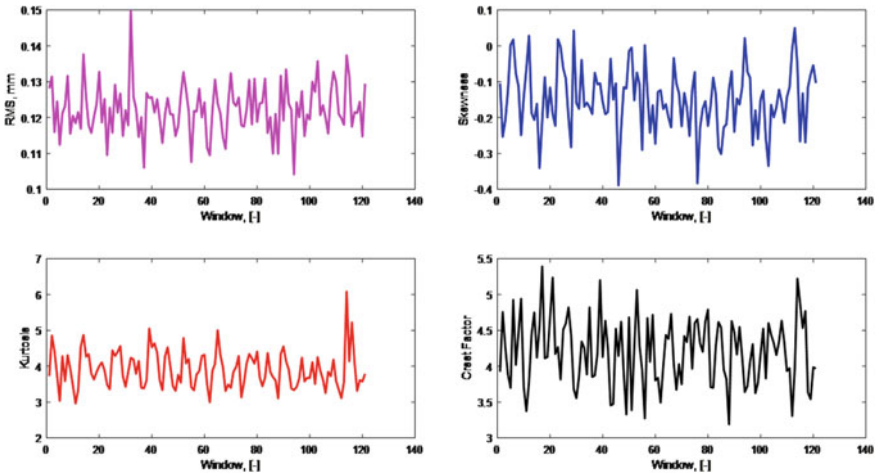


Fig. 6 Diagnostics indicator for bearing with inner race fault (0 hp, 1797 rpm)

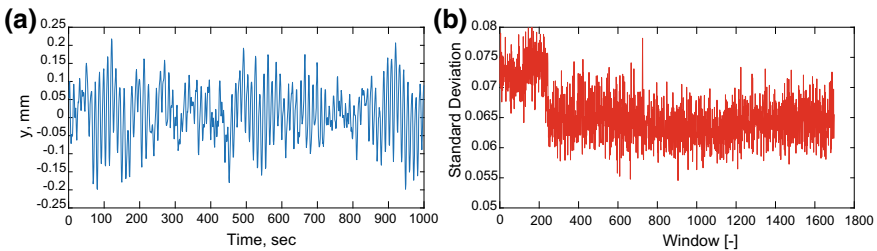
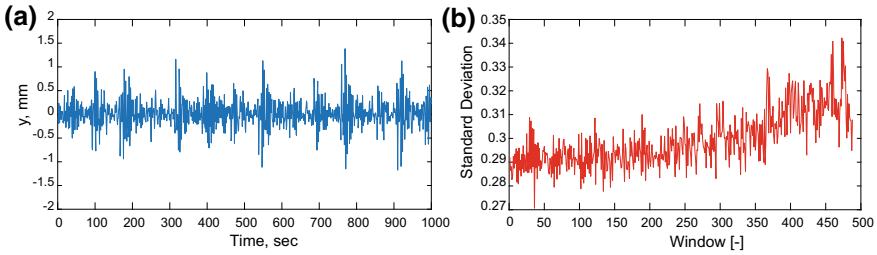
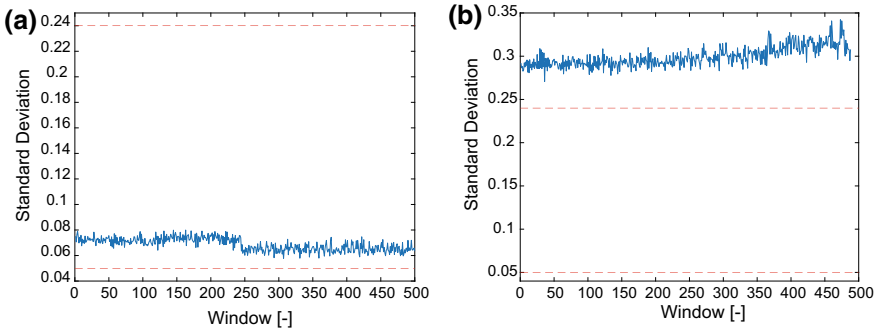


Fig. 7 a Overall vibration signal of healthy bearing b standard deviation for healthy bearing



**Fig. 8** **a** Overall vibration signal of inner race fault bearing **b** standard deviation for inner race fault bearing

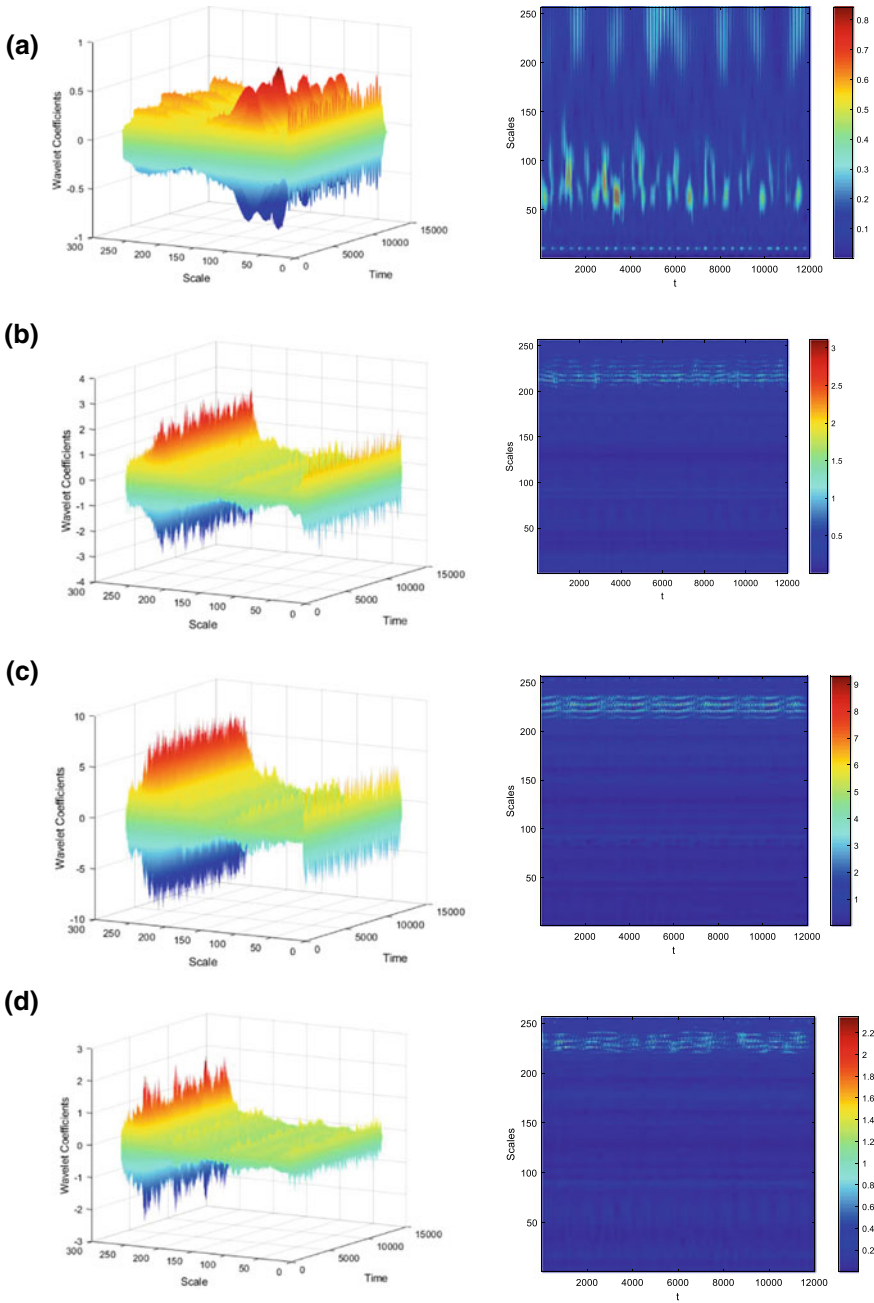


**Fig. 9** **a** Standard deviation for healthy bearing with threshold line **b** standard deviation for inner race fault with threshold line

Referring to Fig. 9, the two horizontal lines represent the threshold value of the standard deviation. The threshold value is defined at the range of 0.05–0.24. Any points located outside of this band will be considered as faulty.

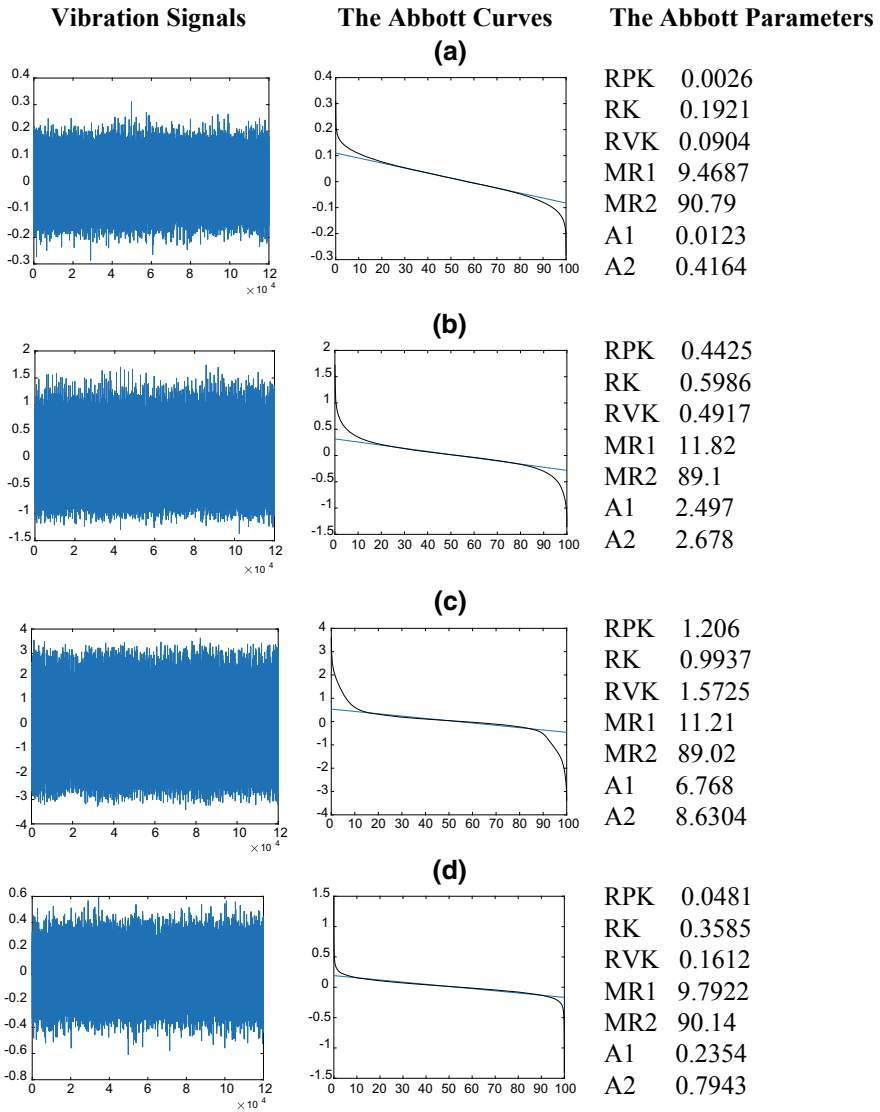
The statistical features used for fault diagnosis in this paper are extracted from vibration signals in both time domain and frequency domain. To get more bearing information and avoid misclassification of the bearing fault, wavelet-based feature extraction is also used. The continuous wavelet coefficients of the signals are calculated using complex Morlet wavelets. The three-dimensional plots between relative wavelet energy, scale, and time for different type of bearing fault are as shown in Fig. 10. It is observed that outer race fault has the highest magnitudes of the coefficient value, followed by inner race fault and ball fault. The lowest wavelet coefficient magnitude is the no fault bearing. The magnitudes are depending on the frequency of the vibration signals, higher frequency will result in high magnitudes of wavelet coefficients at a particular scale.

After applying the wavelet transform and obtained the wavelet coefficients, the magnitudes will be aggregated into cumulative density function. It is obtained by integrating the profile length, in this case the vibration signals. The cumulative density function of the profile permits the estimation of the Abbott-Firestone parameters.



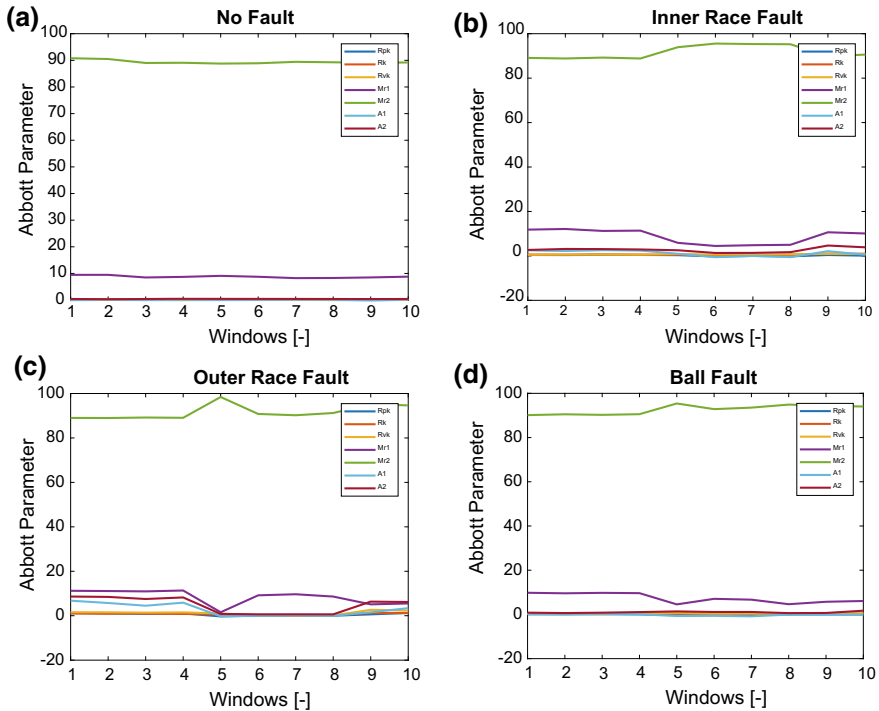
**Fig. 10** Wavelet coefficients for **a** healthy bearing **b** inner race fault bearing **c** outer race fault bearing **d** ball fault bearing





**Fig. 11** Abbott parameter for **a** healthy bearing **b** inner race fault bearing **c** outer race fault bearing **d** ball fault bearing

Using the formula stated in Table 2, the associated parameters can be calculated (see Fig. 11). The vibration signals and the corresponding bearing curve are shown in Fig. 11. The cumulative probability is divided into three parts which include Rk, Rpk, and Rvk at 40% of the tangent of the density function.



**Fig. 12** Plot of the Abbott parameter for **a** healthy bearing **b** bearing with inner race fault **c** bearing with outer race fault **d** bearing with ball fault

Rk is the central portion, whereas Rpk defines upper portion and Rvk is the under portion of Rk area. They are determined by constructing a horizontal line from the crossing point of tangent line to the vertical axis. The Mr1, Mr2, A1, and A2 parameters portray the level of peak and valley that offer details on the peak and valley density of the surface.

The distinction amongst Rpk and Rvk parameters give the characteristic of the surface’s topology where valleys are marked compared to the peaks. The higher the estimation of Mr2, the lower the valleys density is. The calculated Abbott parameters are plotted as shown in Fig. 12. It is obvious that the values of the parameters for bearing with outer race faults are higher compared to the other three conditions of bearing.

To diagnose the defects in the antifriction bearings, a new hybrid approach has been developed. It is based on the statistical analysis which involves the signal processing, the continuous wavelet transforms, followed by the Abbott-Firestone parameters, and pattern classification techniques such as artificial neural network. By using the vibration signals obtained from the CWRU with different types of bearing faults, the diagnostic system was tested and evaluated.

**Table 4** Performance of the proposed approach

Dataset	Cross-entropy	Percentage error (%)
Training	6.3964	0
Testing	11.553	0
Validating	11.607	0

There are three chosen statistical features extracted from the vibration signals namely kurtosis, skewness, and the root mean square which corresponds to the different types of bearing faults. The vibration data set consists of 4000 samples of four operating condition (healthy bearing, inner race fault, outer race fault, and ball fault). Each of the fault consists of 1000 samples with 700 for training, 150 for testing, and 150 for validating.

The computed Abbott parameter is combined with the statistical diagnostic indicators to evaluate the proposed method. The classification of the bearing fault is done by using the neural network pattern recognition tool in MATLAB. The model has 10 inputs: Rpk, Rk, Rvk, Mr1, Mr2, A1, A2, skewness, kurtosis, and RMS, and four outputs: healthy bearing, inner race fault bearing, outer race fault bearing, and ball fault bearing.

To identify the four types of bearing fault, binary encoding format is used as the fault outputs. The four-digit output target nodes are distinguished as (1 0 0 0) for healthy bearing, (0 1 0 0) for inner race fault, (0 0 1 0) for bearing with outer race fault, and (0 0 0 1) for bearing with ball fault.

The hidden layer used in the network is 10 and the iteration stopped at 87 when it reached the minimum gradient. The results indicate that the proposed method can diagnose the bearing faults. The training, testing, and validating success show 100%. Meanwhile, the average error measurement is  $6.22 \times 10^{-7}$ . The details of the cross-entropy and percentage error for each data set are tabulated in Table 4. Minimizing Cross-Entropy results in good classification. The lower the values, the better the results will be. On the other hand, the percentage error indicates the fraction of samples which are misclassified. A value of 0 tabulated as such in Table 4 means there is no misclassifications.

## 4 Conclusions

The objective of this paper is to develop a detection technique and diagnosis of bearing defects using the hybrid approach. The conclusions that can be made from this research are as follows:

- Using hybrid approach to diagnose the bearing fault is the best idea since it can accommodate huge information.
- The outcomes of the analysis demonstrate that the new method is efficient and capable to analyse and classify the bearing fault.

Future work will consider further tests to make the proposed method applicable in the field.

**Acknowledgements** The authors would like to thank Universiti Teknologi PETRONAS for the resources provided for the research. The authors are also grateful to CWR for generously sharing the vibration data.

## References

1. Syed Zeashan SA, Prashanth Pai M (2016) Antifriction bearing diagnostics in a manufacturing industry—A case study. *J Mech Eng Autom* 6(5A):58–62
2. Gupta P, Pradhan MK (2017) Fault detection analysis in rolling element bearing: a review. *Mater Today Proc Part A* 4(2):2085–2094
3. Boudiaf A, Djebala A, Bendjma H, Balaska A, Dahane A (2016) A summary of vibration analysis techniques for fault detection and diagnosis in bearing. In: 8th International conference on modelling, identification and control (ICMIC), IEEE, pp 37–42
4. Xu H, Fan Y, Wu J, Gao Y, Yu Z (2015) Bearing fault diagnosis method based on singular value decomposition and hidden Markov model. In: 27th Chinese control and decision conference (CCDC), IEEE, pp 6355–6359
5. Amarnath M, Shrinidhi R, Ramachandra A, Kandagal SB (2004) Prediction of defects in antifriction bearings using vibration signal analysis. *J Inst Eng (India), Part MC, Mech Eng Div* 85:88.
6. Zhang W, Peng G, Li C (2017) Bearings fault diagnosis based on convolutional neural networks with 2-D representation of vibration signals as input. In: *MATEC web of conferences*, vol 95, p 13001: EDP Sciences
7. Geropp B, Schneider S, Seeliger A (1997) Automatic diagnosis of antifriction bearings using vibration analysis and fuzzy-logic. *IFAC Proc Volumes* 30(18):965–970
8. Taylor JI (1980) Identification of bearing defects by spectral analysis. *J Mech Des* 102(2):199–204
9. Kumar HS, Pai PS, Sriram NS, Vijay GS (2013) ANN based evaluation of performance of wavelet transform for condition monitoring of rolling element bearing. *Procedia Eng* 64:805–814
10. Sharma R, Kumar A, Kankar PK (2014) Ball bearing fault diagnosis using continuous wavelet transforms with modern algebraic function. Springer, New Delhi, India, pp 313–322
11. Bigerelle M, Alain I (2007) A numerical method to calculate the Abbott parameters: a wear application, pp 1319–1334

# Automated Pipeline Diagnostics Using Image Processing and Intelligent System



Tamiru Alemu Lemma, Divyeruthra Muniandy and Shazaib Ahsan

**Abstract** Due to many drawbacks such as human error, tremendous energy and time consumption in traditional method of pipeline inspection, this paper proposes an automated pipeline diagnostic using image processing and intelligent system. The primary focus of the developed system is underwater pipeline network due to higher inaccessibility and defect rate. Comparatively, many methods were used in image processing along the years and Convolutional Neural Network (CNN) was identified as the most effective method for this case study based on the literature review. Narrowing down into CNN context, the author has identified and compared the mean accuracy of transfer learning process of two pre-trained convolutional neural networks which were also the winners of ImageNet Large Scale Visual Recognition Challenge (ILSVRC) for the year 2012 and 2014. They are known as AlexNet and GoogLeNet. This was done by initially modelling pipes with various defects in CATIA and surface recording was simulated similar to ROV recording. Then these videos were automatically converted into image frames, pre-processed and fed into system as training material. After sufficient training, the system was able to detect and distinguish the pipeline defects. GoogLeNet was identified as the network with the highest mean accuracy of 99.87%, hence was finalised as the systems network architecture. MATLAB 2017b was used to develop the system. To further evaluate the performance of the system, a mini lab rig was set up replicating underwater environment with pipeline models with dents, holes and cracks. Similarly, the inspection videos were recorded and the system was able to detect and distinguish the defects on the pipeline alongside their location and percentage coverage with mean accuracy of 99.87% as well, proving the functionality of the system in real condition. The mechanical properties of the pipelines and characterisation of pipeline defects were also reviewed thoroughly before developing the inspection system.

**Keywords** Pipeline diagnostics · Convolution neural network · Video processing · Image processing · Intelligent systems

---

T. A. Lemma (✉) · D. Muniandy · S. Ahsan  
Department of Mechanical Engineering, Universiti Teknologi PETRONAS, 32610 Seri Iskandar,  
Perak, Malaysia  
e-mail: [tamiru.lemma@utp.edu.my](mailto:tamiru.lemma@utp.edu.my)

© Springer Nature Singapore Pte Ltd. 2020  
M. Awang et al. (eds.), *Advances in Material Sciences and Engineering*, Lecture Notes in Mechanical Engineering,  
[https://doi.org/10.1007/978-981-13-8297-0\\_16](https://doi.org/10.1007/978-981-13-8297-0_16)

## 1 Introduction

Deep-water pipeline or subsea pipelines are located beyond water depths and all activities inclusive of servicing, maintaining and inspection are remotely controlled (IMR). The typical characteristics of deep-water pipelines system are high wall thickness, high insulation, extreme operating and ambient external pressure, significant geohazard and slug formation etc. Relatively, there are many factors addressed that promote degradation and deterioration of these pipelines. They are from three main categories; environmental, internal process and chemical processes. Environmental factor's contributors are uncertainty and geological occurrence of the pipeline base such as plate tectonics at sea bed while internal process consists of corrosion, solid deposition, erosion, pressure gradient drop, deformation leakage etc. Lastly, biological degradation, deposition of anions and cations, and sacrificial degradation are chemical process factors. Other factors such as improper usages and deposition of anchors too lead to most of the deep-water pipeline deterioration.

Acknowledging the importance of pipeline systems and numerous factors attributing to its deterioration and degradation, it is unerring to emphasize a proper inspection system. Planned inspection campaigns are integral part of IMR strategy aiming to monitor pipeline system integrity over time and to monitor the impact of the subsea and production environments on the pipeline. Routine inspection might be an indicator for more specific investigation or specialist techniques. The usual deep-water pipeline physical inspection is split into internal and external locations to pipelines. Pigging and Remotely operated underwater vehicle (ROV)/Autonomous underwater vehicle (AUV) methods are typical internal and external physical monitoring method. Permanent methods are also becoming more common and inspection frequency is determined from risk-based techniques.

Justification for proceeding with this project is done by acknowledging numerous problems faced by the industry due to conventional pipeline diagnostics. Traditionally, skilled human inspectors manually inspect the pipelines either by walk-down or from videos recorded by Underwater Water Vehicles. This however poses so many drawbacks. Considering pipeline system usually composed of long and complicated pipeline networks, it requires a tremendous amount of time, labour and cost to inspect them manually which relatively reduces the productivity, quality and accuracy of the inspection. The inspectors are at risk of committing human errors due this fatigue while analysing lengthy videos. Hence, if longer time is taken to preserve the quality and accuracy, production cost will be at rise. The link between the collected information and mechanical problems is also left to the expert to identify and diagnose. The purpose of this project is to establish an automated mechanism concentrating more on the mechanical integrity of the pipelines.

The automated diagnosis system utilizes CNN for image processing. Many fields have been utilizing deep learning networks for object detection and classification e.g. facial recognition in Facebook and Apple Gadgets. Traditional machine learning depends on shallow nets which revolve around single input and output with at most one hidden layer. If a network is configured with more than three layers, it is

considered as deep learning network. In this type, every layer of nodes is trained to detect a cluster of features depending on previous layer's output. Advancement of neural network enables detection of more complex features as they are able to aggregate and recombine features from all the previous layers. Most importantly, deep learning network is capable of processing unlabelled and unstructured data. Hence, deep learning network is the best means of image clustering and object detection which is a perfect fit for the system development.

## 2 Literature Review

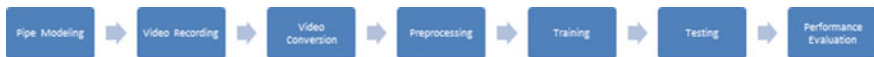
There were many researches that have done image processing and defect detection dating as early as the 90s and experiments with various advancements in computer technology are still ongoing. Petraglia [1] is among the recent ones who used CNN to classify underwater pipeline events and compared their accuracy with MLP based on wavelet features which were about 93.2 and 91.2% on average respectively. Random Forest classifier is one of many new attempts which was able to distinguish faults in 88% of the overall image frames in CCTV acquired images of waste water pipeline in research done by Myrans [2]. Besides, there are other edge detection methods namely Susan Edge Detection by Wang and Su [3], and Canny Edge Detection by Mashford [4–6], which had an accuracy of about 99%. Abdel-Qader [7], who compared it with Fourier Higher Transform and Sobel Gradient, later proved FHT to have the highest reliability. Mashford [4–6, 8] has also done various image segmentations by Support Vector Machine while Iyer and Sinha's [9] work using morphological segmentation gained huge limelight. Lastly Kaseko et al. [10], Osama Moselhi and Tariq Shehab-Eldeen [11–13] can be considered pioneers in image processing for defect detection and they have also used neural classifiers. Even though there were various methods developed, CNN was chosen to process the image for the system. This is because they have various advantages such as ruggedness to shift and distortion in images, fewer memory requirements, easy training, able to process large data without manual labelling and has high accuracy. Hence, it serves as an appropriate image processing medium for underwater environment due to their harsh environment and long pipeline configurations.

Narrowing down to CNN, various deep CNN were compared. ImageNet project is a huge visual database project designed for visual object recognition software research. An annual software (ILSVRC) is conducted by ImageNet project where software programs are evaluated based on their capability in object detection and image classification. They were LeNet [14], AlexNet [15], ZFNet [16], GoogleNet [17], VGGNet [18] and ResNet [19]. Finally, AlexNet and GoogleNet were chosen to be compared in the project due the availability of pretrained model and memory requirement for transfer learning in MATLAB 2017b.

### 3 Methodology

The overall project algorithm is represented by Fig. 1. Initially, 15 pipes were modelled in Computer Aided Three-dimensional Interactive Application (CATIA) with various defect configuration and coverage. The defects modelled were two types of corrosion and cracks, holes, breakage and pitting. Later, these models were recorded through screen video recording application. These videos were converted into image frames by algorithm developed in MATLAB 2017b and saved in a specific folder named accordingly. This folder is then used as a training source for both developed AlexNet and GoogLeNet system. In pre-processing stage, a number of images in each folder are computed and displayed. The folder names serve as categories in which the images will be classified. Then these images are read one by one, converted to RGB images and then resized according to the requirement of the CNN network. Then the sets are split into training and validation data. The split is randomized to avoid biasing the results. These training sets are then processed by the system. Prior to training of the system, Parallel Computing Toolbox, Neural Network Toolbox, and all the pre-trained networks models were downloaded and installed in MATLAB 2017b. First, the GPU capability is computed, and the algorithm is allowed to continue if it is more than 3 as training on a GPU requires a CUDA-enabled GPU with compute capability 3.0 or higher. The details of the hardware setup used by the author to model the system is shown in Table 1. The CNN network was specified to be used alongside with the required the mini batch sizes, maximum epochs, initial learn rate, verbose frequency, validation data and validation frequency. Layers of the CNN network was also connected according to requirement of the chosen network for transfer learning process. After sufficient training, the system was tested by feeding videos of various pipe models and the results were plotted. The accuracy of the CNN networks was compared to finalise the system architecture.

After finalising the CNN architecture to be used, the system is further developed with the ability to identify location of the defects and percentage of defect coverage. Then the system is tested with actual steel pipes which were defected in prior. The defects were holes with constant diameter, dents and corrosion. The steel pipes were placed in the dark box filled with water to represent dark environment of underwater



**Fig. 1** Project algorithm

**Table 1** Hardware setup

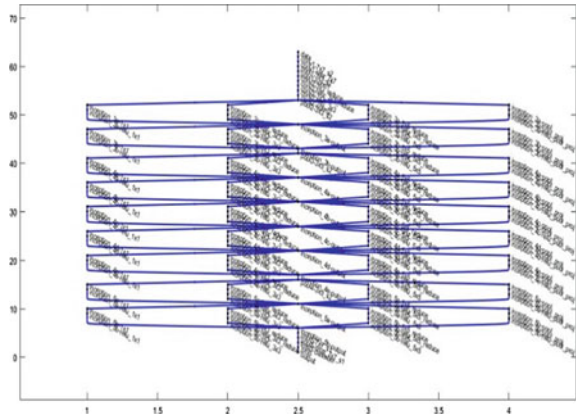
CPU	Intel Core i5-3337U CPU 1.80 GHz
The number of CPU cores	3
Memory size	8 GB
Operation system	Windows 10



**Fig. 2** Performance evaluation setup



**Fig. 3** Layer graph



**Table 2** Camera specification

Features	Specification
Megapixels	14
Video capture resolution	4 K
Remote operation	Wifi and Infrared

pipeline system. Then an automated dolly with camera attached which was connected by wireless network to the computer was placed in the same box. The setup is shown in Fig. 2 and specification in Table 2. The dolly then moves along the pipes recording the surface defects replicating ROV. Then the videos were converted and used as training and validation data for the system.

### 4 Results

Comparing the accuracy of the system developed using AlexNet and GoogLeNet as shown in Table 3, GoogLeNet was finalised as system architecture.

GoogLeNet used in this application has a total of 144 layers. To retrain the network, the last three layers have been removed which serve the purpose of combining features extracted into class probabilities and labels. Three new layers were added to layer graph namely, fully connected layer, a softmax layer, and a classification output layer. The layer graph at this stage is shown in Fig. 3. The last of the transferred layers are then connected to the new layers and ensured to be connected correctly by plotting the new layer graph as shown in Fig. 4. The visualization of weight of the first CNN layer is represented in Fig. 5. The smoothness and less noise visualization of the weight represent good convergence of the network (Fig. 5).

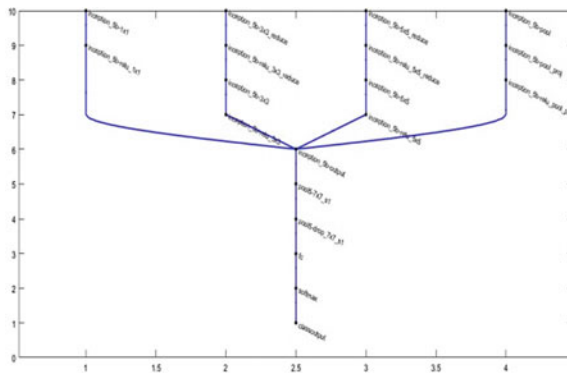
The result acquired using the system for the CAD pipe models were plotted. Figure 6 shows the defects detected in each image frame while Fig. 7 shows percentage of coverage of each defect detected on the pipe.

Finally, the system is developed into a user-friendly application with the ability to evaluate defect location and calculate the percentage of the defect coverage. GUI of the application is shown in Fig. 8. The application has four tabs namely, 'Input', 'Result: Location', 'Results: Percentage' and 'Results: Details'. The 'Input Tab' is where all the information are filled and chosen for the diagnostics. In this tab, the 'Staff ID' column is to fill the details of the user using the application and 'Line Number' is to identify the pipe being diagnosed. 'Pipe Length' and 'Frame Rate' requires details of total length of the diagnosed pipe and frame rate set of the video source defect which is used to estimate the location of the defects. 'Department'

**Table 3** Mean accuracy of the systems developed

Networks	Mean accuracy (%)
AlexNet	84.0
GoogLeNet	99.87

**Fig. 4** Layer graph after connecting to new layers



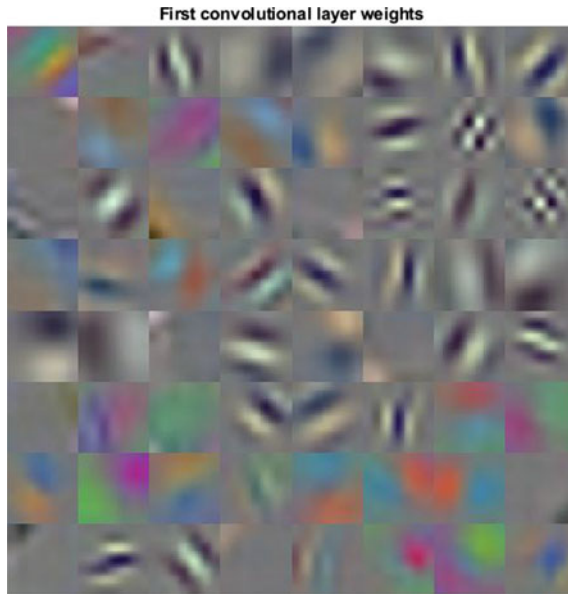


Fig. 5 First convolutional layer weights

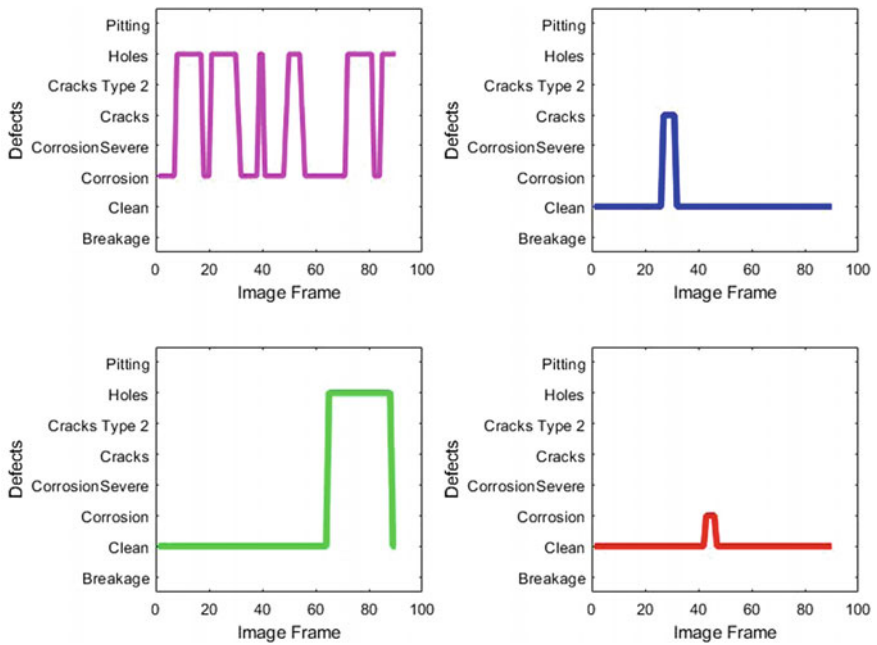


Fig. 6 Plots of defect detection on pipeline model

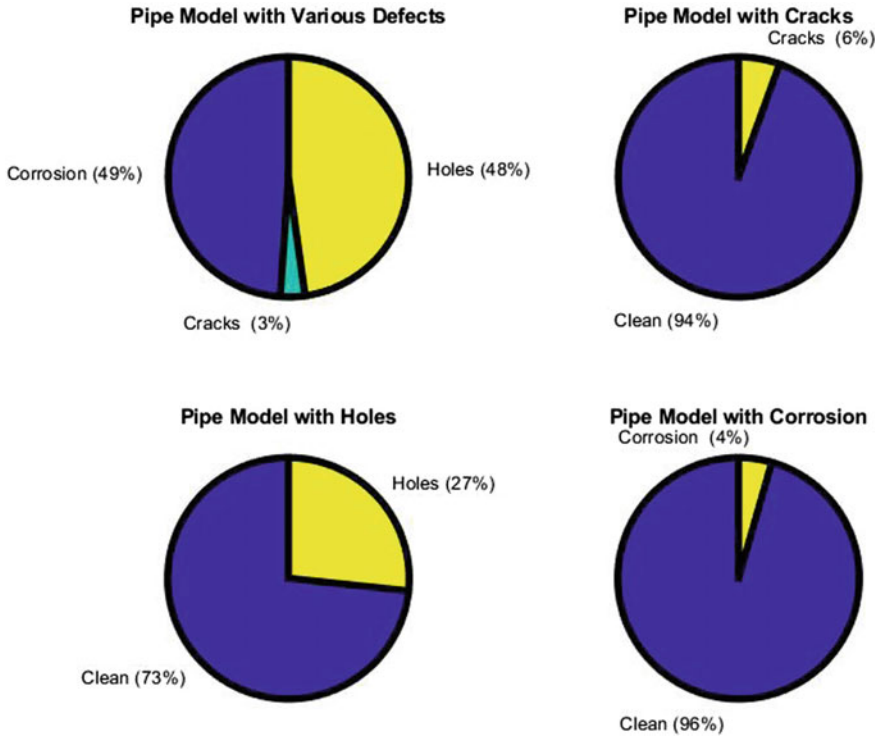


Fig. 7 Percentage of defect coverage of the pipe models

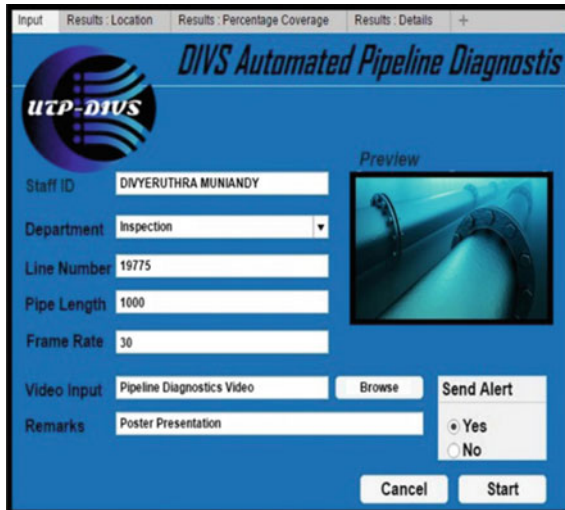


Fig. 8 GUI of the application

**Table 4** Configuration of steel pipes

No.	Configuration
1	Clean, corrosion, clean, dents, clean, holes and clean.
2	Corrosion, clean, corrosion, dents, corrosion, holes, corrosion
3	Dents, clean, dents, corrosion, dents, holes, dents
4	Holes, clean, holes, corrosion, holes, dents, holes

is the section where user selects the department they are representing for the diagnostics purpose whilst the rest of the unselected departments will receive a copy of diagnostics report only if ‘Yes’ is selected for ‘Send Alert’ option. In ‘Video Input’ section, users can browse their folders to select the video file they want. The opened folders only show files which are in video format. To ensure the right videos are being uploaded, the ‘Preview’ pane plays the video once the video file is selected. The ‘Start’ button initiates the diagnostics and ‘Cancel’ buttons halts the process. ‘Result: Location’ is the tab where the plots of defects detected, and their location are shown whilst ‘Results: Percentage’ shows the percentage of defect coverage. The last tab has details of the diagnostics.

The performance of the application was evaluated with feeding videos of equi-length steel pipes arranged to have various configuration of defects as shown in Table 4. The defects were holes, corrosion and dents. Based on the literature review, even though there are many types of defects haunting pipeline industry, it is safe to conclude that there are only 4 major types of defects namely, cracks, dents, corrosion and mechanical damage. So, the defects included in this performance evaluation are able to generalize and proof the ability of the system to detect and distinguish the wider range of defects.

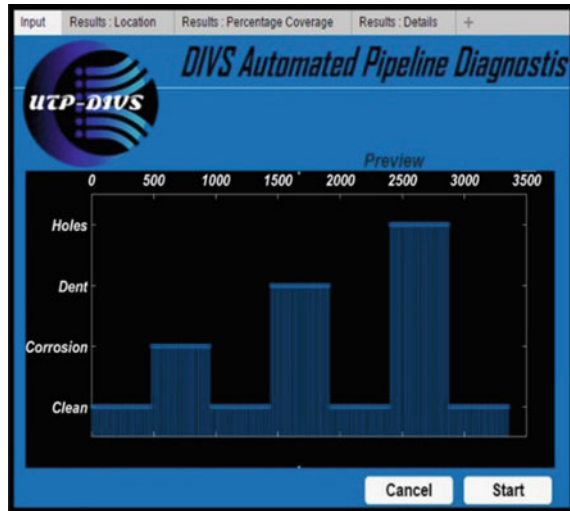
The defect location detected for configuration 1 and configuration 2 are shown in Figs. 9 and 10, respectively. The percentage coverage for all cases in Table 4 are shown in Fig. 11.

The plots have shown no error or variance in distinguishing the defects and identifying the accurate location and percentage every time the videos are fed for analysis. Hence, the repeatability of the result acquired for all the steel pipe defect configuration has proven the precision and reliability of the system. GoogLeNet has also ensured the accuracy of the detection is also on check ensuring the system is highly suitable to replace the current manual diagnostics system. Many limitations and challenges posed by manual diagnostic system can be avoided using this system;

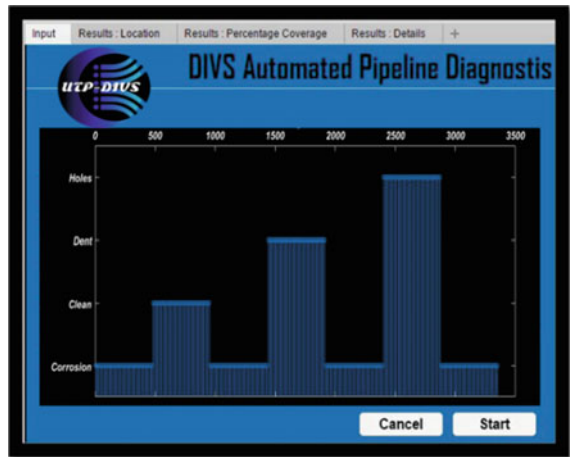
(i) High time consumption to analyse the ROV videos

- Subsea pipelines are usually long and huge. To fully analyse their surface based on the videos, it will require tremendous amount of time. With the rate of detection the automated system has, the defect can be detected quickly and the repair team can be alerted as soon as possible. This could prevent time allocation for further aggravation of the defects.

**Fig. 9** Location of defect detected in performance evaluation for configuration 1



**Fig. 10** Location of defect detected in performance evaluation for configuration 2



- (ii) High energy consumption to analyse the ROV videos
  - Engineers need to carefully assess the videos and distinguish the defects. They too are forced to constantly organize the data, update the repair team and be aware of the pipeline activity around the clock. This may cause fatigue among the inspectors. However, with this system, it can be programmed to be running all the time, organize and present the data suitably whilst updating the repair team in case of any serious detection.
- (iii) High memory requirement for continuous data storage

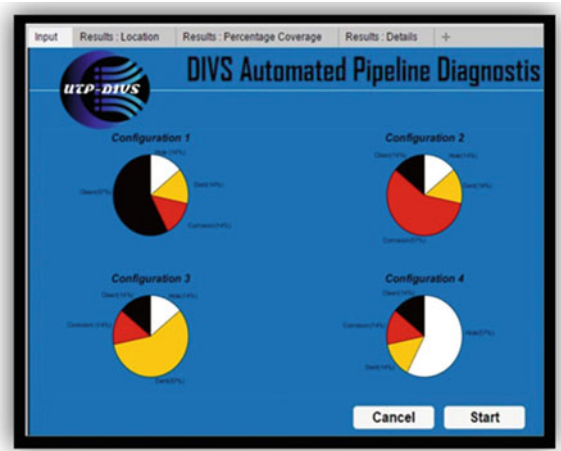


Fig. 11 Percentage of coverage in performance evaluation for all configurations

- Currently, the ROV requires huge amount of memory to store the surface inspection recording of the long pipelines. With this system, the data can be updated to the detection system concurrent with the recording process. However, this requires strong internet connection between the ROV and the receiver or inspection panel.

(iv) Complex data transmission system

- Traditionally, engineers need to update several departments after every inspection process, namely repair and maintenance team, production team and health, safety and environment team. This process is highly tedious. However, with this system, notifications can be programmed to be sent to all the required department automatically.

## 5 Conclusion and Recommendations

All objectives were achieved. An automated pipeline diagnostic system was invented with the ability to distinguish and detect defect with accuracy of 99.87%. The system was just tested with three defects to generalize and prove the ability of the system to detect defects and it can be trained to detect wider range of defects. Besides, for maximum efficiency of the system, it is recommended to use high quality camera and higher GPU configuration. For future work, extensive research regarding causes of defects should be done and added as preventive mechanism to the system to further increase the productivity of the pipeline industry.

**Acknowledgements** The authors are very grateful for the developers of AlexNet and GoogLeNet network who made their models available for public use.

## References

1. Petraglia F, Gomes JGR (2017) Classification of underwater pipeline events using deep convolutional neural networks
2. Myrans J, Kapelan Z, Everson R (2016) Automated detection of faults in wastewater pipes from CCTV footage by using random forests. *Proc Eng* 154:36–41
3. Wang Y, Su J (2014) Automated defect and contaminant inspection of HVAC duct. *Autom Constr* 41:15–24
4. Mashford J, Rahilly M, Lane B, Marney D, Burn S (2014) Edge detection in pipe images using classification of haar wavelet transforms. *Appl Artificial Intell* 28(7):675–689
5. Mashford J, Rahilly M, Davis P, Burn S (2010) A morphological approach to pipe image interpretation based on segmentation by support vector machine. *Autom Constr* 19(7):875–883
6. Mashford J, Marlow D, Burn S (2009) An approach to pipe image interpretation based condition assessment for automatic pipe inspection. *Adv Civ Eng* 2009
7. Abdel-Qader I, Abudayyeh O, Kelly ME (2003) Analysis of edge-detection techniques for crack identification in bridges. *J Comput Civ Eng* 17(4):255–263
8. Mashford JS, Rahilly M, Davis P (2008) An approach using mathematical morphology and support vector machines to detect features in pipe images. In: *Computing: techniques and applications, 2008, DICTA'08. Digital image, 2008*, pp 84–89. IEEE
9. Iyer S, Sinha SK (2005) A robust approach for automatic detection and segmentation of cracks in underground pipeline images. *Image Vis Comput* 23(10):921–933
10. Kaseko MS, Lo Z-P, Ritchie SG (1994) Comparison of traditional and neural classifiers for pavement-crack detection. *J Transp Eng* 120(4):552–569
11. Moselhi O, Shehab-Eldeen T (2000) Classification of defects in sewer pipes using neural networks. *J Infrastruct Syst* 6(3):97–104
12. Shehab-Eldeen T, Moselhi O (2003) Automated inspection of utility pipes: a solution strategy for data management. NIST Special Publication SP, pp 531–536
13. Moselhi O, Shehab-Eldeen T (1999) Automated detection of surface defects in water and sewer pipes. *Autom Constr* 8(5):581–588
14. Yu O, Wang H, Chen P, Wei Z (2014) Mixed pooling for convolutional neural networks. In: *International conference on rough sets and knowledge technology, 2014*, pp 364–375. Springer, Berlin
15. Krizhevsky A, Sutskever I, Hinton GE (2012) Imagenet classification with deep convolutional neural networks. In: *Advances in neural information processing systems, 2012*, pp 1097–1105
16. Zeiler MD, Fergus R (2014) Visualizing and understanding convolutional networks. In: *European conference on computer vision, 2014*, pp 818–833. Springer, Berlin
17. Szegedy C, Liu W, Jia Y, Sermanet P, Reed S, Anguelov D, Erhan D, Rabinovich A. (2014) Going deeper with convolutions. Technical report. arXiv: 1409.4842
18. Chatfield K, Lempitsky VS, Vedaldi A, Zisserman A (2011) The devil is in the details: an evaluation of recent feature encoding methods. *BMVC* 2(4):8
19. He K, Zhang X, Ren S, Sun J (2016) Deep residual learning for image recognition. In: *Proceedings of the IEEE conference on computer vision and pattern recognition, 2016*, pp 770–778



# Integrated Safety and Process Economics Approach for Sustainable Process Design of Process Piping



Muhammad Athar, Azmi M. Shariff and Azizul Buang

**Abstract** Inherent safety is termed as the best approach of process safety which aids in creating sustainable process designs at the preliminary design stage. However, the available inherent safety techniques for process designs do not contemplate the nature of individual process equipment and process economics for the purpose. Consequently, an innovative approach is consolidated in this work to cover the gaps for the process piping, which is one of the most failing process equipment in the industry. The method consists of streams indexing section to identify critical pipes followed by risk estimation and analysis section to make the decision about safety for the critical process pipes. For unacceptable risk, the process conditions can be moderated as per the inherent safety concept. The critical process streams are analyzed again for risk acceptability and continued until the risk is acceptable. The use of inherent safety principle would change the process economics and can be compared with the base case to recognize the improvement. Conclusively, the resulted process design has the features of acceptable risk and enhanced process economics.

**Keywords** Inherent safety · Preliminary design · Process economics · Safety index · Sustainability

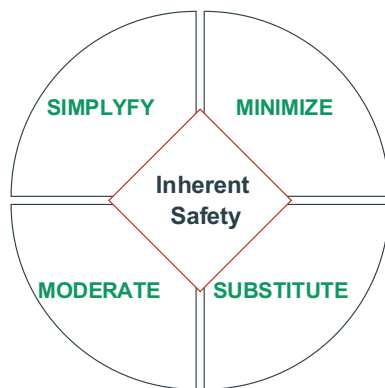
## 1 Introduction

For safety enhancement in chemical process industries, four methodologies are adopted namely inherent, passive, active, and procedural [1]. Among these, inherent and passive schemes are considered as better options. A process is termed as inherently safer if the hazards related to either chemicals or process are minimized or completely eradicated [2]. However, inherent safety benefits can be maximized by implementation at the earlier design stages [3]. Furthermore, it aids the designer

---

M. Athar · A. M. Shariff (✉) · A. Buang  
Centre of Advanced Process Safety (CAPS), Universiti Teknologi PETRONAS, 32610 Bandar,  
Seri Iskandar, Perak Darul Ridzuan, Malaysia  
e-mail: [azmish@utp.edu.my](mailto:azmish@utp.edu.my)

© Springer Nature Singapore Pte Ltd. 2020  
M. Awang et al. (eds.), *Advances in Material Sciences and Engineering*, Lecture Notes in Mechanical Engineering,  
[https://doi.org/10.1007/978-981-13-8297-0\\_17](https://doi.org/10.1007/978-981-13-8297-0_17)



**Fig. 1** Inherent safety concepts [3]

such that there is no need of external safety system. Moreover, the implementation of the inherent safety concept tends to minimize the capital and operational costs [4]. In practice, most of the traditional safety studies are performed once the process design is finalized. At this point, the remaining three strategies are engaged to control the risk [5]. Additionally, any modification in the process at this stage would incur extra capital in comparison to the design modification at the early design stages [6]. Therefore, the inherent safety concept of process safety is capable of providing sustainable process design, as it tends to either minimize or remove the root cause of hazards associated with materials and process. There are four main principles for inherent safety; as demonstrated in Fig. 1 [3].

The quantification of the inherent safety has always been the biggest challenge and has been resolved by comparing various design options to select the safer one. For this purpose, a number of inherent safety methods have been presented, and most of these methods rely upon indexing approach for inherently safer process route selection [7]. These include inherent safety index (ISI), integrated inherent safety index (I2SI) and process route index (PRI) [7–9].

Process design in the modern era is focusing on conflicting objectives involving safety, economics, and environment [10], and multi-objective optimization (MOO) is considered as the best option [11] for a trade-off among these conflicting objectives [12]. A lot of research has been performed to integrate safety with process economics. Initial works include the Pareto type curve for investment purposes by exploiting accident scenarios [13] and extended decision making procedure for investment [14]. There are other methodologies in the literature, which target either a specific process or section of the process. These include multi-objective optimization study for the supply chain network of bio-refineries [15], quantification of the risk in storage facilities and relevant economics aspects [16] and quantitative risk assessment (QRA) strategy for minimization of risk for storage facilities [11].

In the above-mentioned research works, none of the technique is applicable for the inherently safer design of process piping by considering the nature of equipment

and process economics collectively. Subsequently, this work proposes a method for the sustainable process design of process piping at the preliminary design stage by focusing at the aforementioned gaps. In this method, individual process piping in the chemical process is analysed and ranked using the relative ranking indexing followed by the risk assessment and analysis for the safety aspect. For the unacceptable risk, inherent safety theme is engaged to modify the design followed by the comparison of the revised process economics with the base case to quantify the improvement.

## 2 Methodology

The framework to reduce the fire risk from the leakage of process piping up to the acceptable range using inherent safety ideology and relevant changes in process economics is given in Fig. 2. The framework is comprised of different sections including the indexing part for process piping ranking, risk estimation and analysis section, inherent safety utilization segment and process economics component. For indexing, the flow related issues have been used for its significance in process piping accidents [17], and at this stage, process streams are the alternative of process pipes. The parameters for flow behavior are estimated using the relative ranking concept [18], via the newly proposed index namely process stream characteristic index (PSCI), as below:

$$PSCI = A \times (I_p \times I_T \times I_\rho \times I_v \times I_e \times I_{FL}) \tag{1}$$

Individual indices in Eq. (1) can be estimated using the following generic relationship:

$$I_{Parameter} = \frac{\text{Parameter value of individual stream}}{\text{Average parameter value of all streams}} \tag{2}$$

This indexing would aid the process designer to rank the process streams and recognize the critical one. For the critical process streams, fire risk is assessed and analysed. The risk can be computed through:

$$\text{Fire Risk} = \text{Consequences of Fire} \times \text{Probability of Fire} \tag{3}$$

The necessary equations of fire consequences are estimated by Eqs. (4)–(7) [19], while the fire frequency can be estimated using Eq. (8) [20].

Estimation of flammable mass

$$m_v = C_D A_h \sqrt{\gamma \rho p \left( \frac{2}{\gamma + 1} \right)^{\frac{\gamma+1}{\gamma-1}}} \tag{4}$$

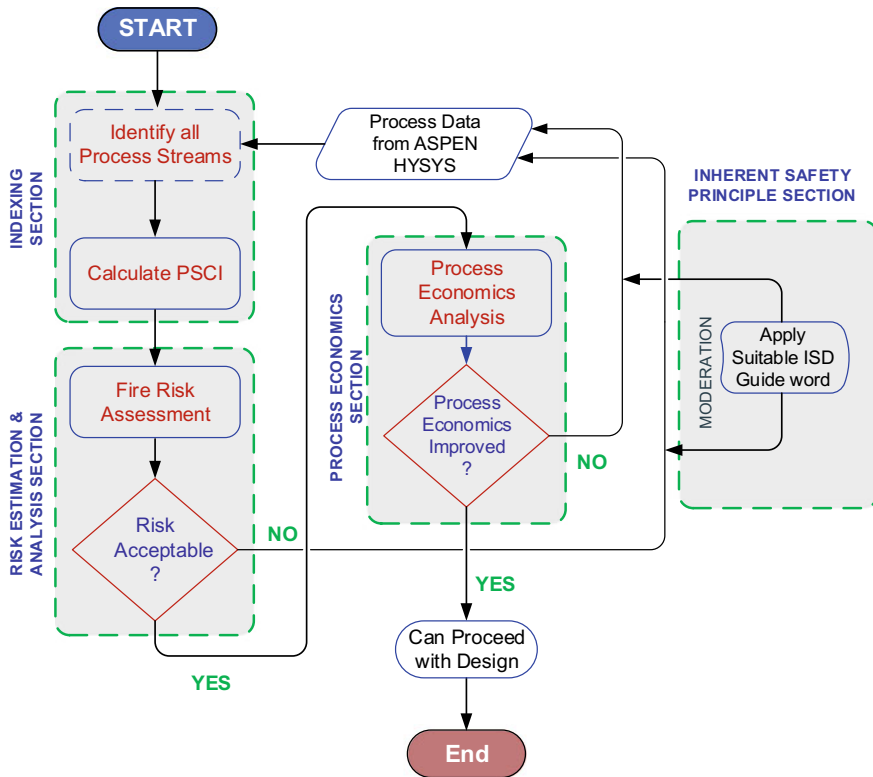


Fig. 2 Framework for integrated safety and economics approach for process piping design

Height of flame

$$\frac{L}{d} = \frac{15}{C_T} \sqrt{\frac{M_a}{M_f}} \tag{5}$$

Point view source factor

$$F = \frac{1}{4 \pi x^2} \tag{6}$$

Radiation intensity at the point of interest

$$E_r = \tau_a \eta m \Delta H_c F_p \tag{7}$$

Fire frequency

$$f = [f_{IL} \times P_{imm,ign}] + \left[ \begin{array}{c} f_{IL} \times (1 - P_{imm,ign}) \times \\ (P_{del,ign}) \times (1 - P_{exp/g/ign}) \end{array} \right] \quad (8)$$

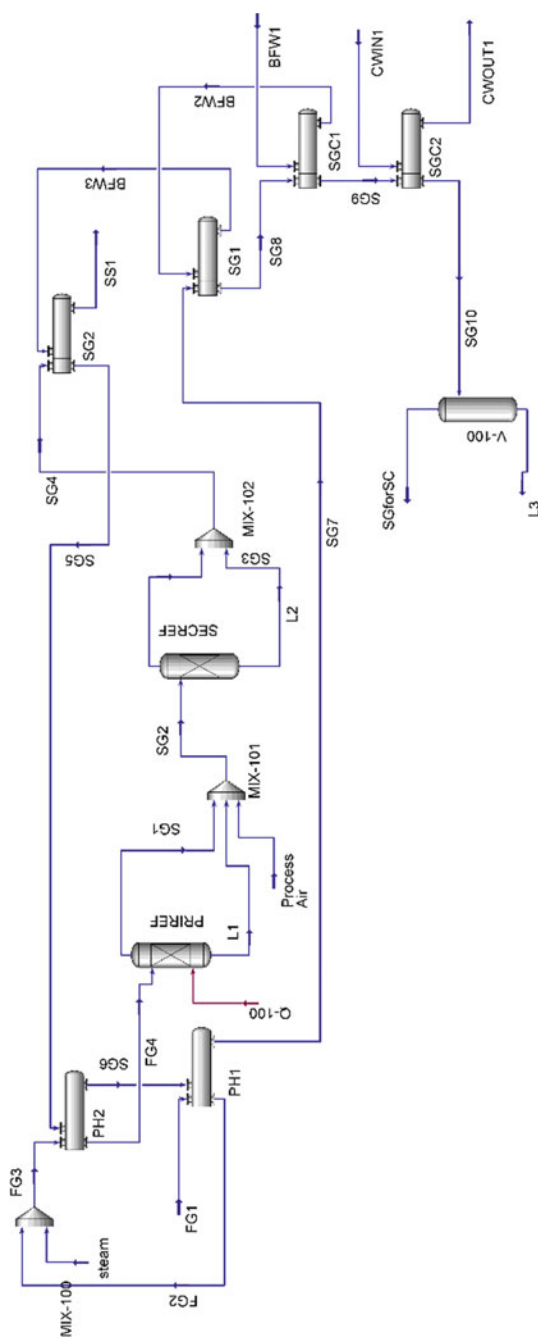
Fire consequences and frequencies are readily discussed in the literature [21, 22], and the risk is ranged from 1 to 36 using the magnitudes of radiation and frequency [23]. The risk range is grouped into three regions, i.e., 1–8 is acceptable, 9–24 is tolerable and 25–36 is unacceptable. The tolerable risk is defined as the residual risk after employment of all cost-effective actions. For the unacceptable risk, the process is modified through inherent safety concept of moderation, which is coupled with process conditions.

Lastly, the process economic analysis is involved in the framework, for which energy requirements and product quantity can be obtained from ASPEN HYSYS. Both risk and process economics parameters can be plotted against the modifications and this can help to identify the suitable conditions for the process streams. For the unacceptable risk of the critical process stream, the above-mentioned inherent safety principle is used, and the loop starts again and continues until the risk is acceptable. For the modified design, process economic analysis is performed by comparing the process duty and product flow rate of modified and base case process conditions. With the improved process economics i.e., less process duty and enhanced product amount, the loop would finish. On the contrary aspect, a further modification is required in the process until risk and process economics criteria are satisfied.

### 3 Results and Discussions

The design of process piping using the integrated safety and economics framework is demonstrated using the natural gas steam reforming loop. The preheated natural gas is mixed with steam and in the first reactor an endothermic reaction takes place, usually named as a primary reformer, to produce carbon monoxide and hydrogen. At the same time, an exothermic reaction also occurs to produce carbon dioxide and hydrogen. As a result of these reactions, a mixture of hydrogen, carbon monoxide, carbon dioxide and water is obtained. However, a substantial amount of methane in natural gas is still unconverted, for which a high-temperature reactor is engaged, termed as a secondary reformer, and heat required from the reaction is provided by the addition of air. The outlet of the secondary reformer is cooled, and the gas mixture is separated from the water contents. This gas mixture is enriched in hydrogen and nitrogen with a significant amount of carbon dioxide and can be used for making various chemical products.

The simulation of the steam reforming process is available in Fig. 3, which has been simulated using the Peng Robinson equations of state, and there are 26 process streams. The PSCI concept has been applied to all process streams and the critical streams are identified based on the PSCI. Sub-indices for PSCI have been calculated for all streams, and the individual variables have shared in the magnitude of PSCI.



**Fig. 3** Process simulation of steam reforming process from natural gas

**Table 1** PSCI values of critical process streams

Process stream	$I_e$	$I_p$	$I_T$	$I_\rho$	$I_{FL}$	$I_v$	PSCI
SG4	1.0453	0.7260	2.3416	0.0241	2.1710	0.2735	0.2538
SG3	1.0453	0.7260	2.3416	0.0241	2.1710	0.2735	0.2538
SG10	1.0453	0.6169	0.0720	0.1196	2.1710	1.8556	0.2238
SG5	1.0453	0.7259	1.6810	0.0309	2.1710	0.2206	0.1885
SG1	1.6093	0.7260	1.9403	0.0251	1.4180	0.2223	0.1794

The PSCI and relevant individual indices for critical process streams are provided in Table 1 and it is recognized that all critical streams are in the syn. gas (SG) loop. Among the SG loop, SG1 is the exit stream of primary reformer, SG3 is the exit stream of secondary reformer, SG4, SG5 and SG10 streams are associated with heat exchanger network used for cooling of synthesis gas. The PSCI concept is used to represent the mutual influence of all variables in the flow. The PSCI values are observed with small magnitude, therefore, PSCI values are magnified using factor value 10. In the steam reforming process, streams SG4 and SG3 are identified as the most critical streams. A few other streams have also been included in the critical streams list as mentioned in Table 1, while others have fewer chances of damage due to leakage.

For the identified critical streams, the fire risk is estimated, which in turn is dependant upon the fire consequences and the frequency. These two parameters are calculated using the above-mentioned equations. Consequences are estimated for a leakage hole of 25 mm. A few other assumptions have been made using the literature criteria [19], i.e. dimensions of pipe as 100 mm diameter and 5000 mm length, the maximum distance of interest as 2 m, the height of pipe from the ground as 5 m and relative humidity 50%. Only the risk for streams SG10 and SG5 is acceptable, whereas, the others have a tolerable risk. Although, the risk is tolerable, however, the radiation intensity is a bit high which needs to be minimized.

For the minimization of the radiation intensity, inherent safety principle moderation is applied to the process conditions. Iteration method is implemented for moderation of process conditions. After each moderation, fire risk is estimated and analysed for acceptability. After each moderation, the process economic analysis is also performed and compared with the base case to materialize the improvement in the process economics. For critical streams mentioned in Table 1, radiation intensity, fire frequency, process duty and product amount for initial condition and modified conditions are depicted in Fig. 4. Analysing the results for acceptable risk of all critical streams and improved process economics, new process conditions are identified for steam reforming process, delineated in Table 2.

After the modification, the risk for all critical streams is acceptable, as the mass released and the radiation intensity of these streams is considerably reduced. Furthermore, a slight reduction in the frequency of fire is observed for all streams except the stream SG1, which experiences a substantial decrease to minimize the risk. The mod-

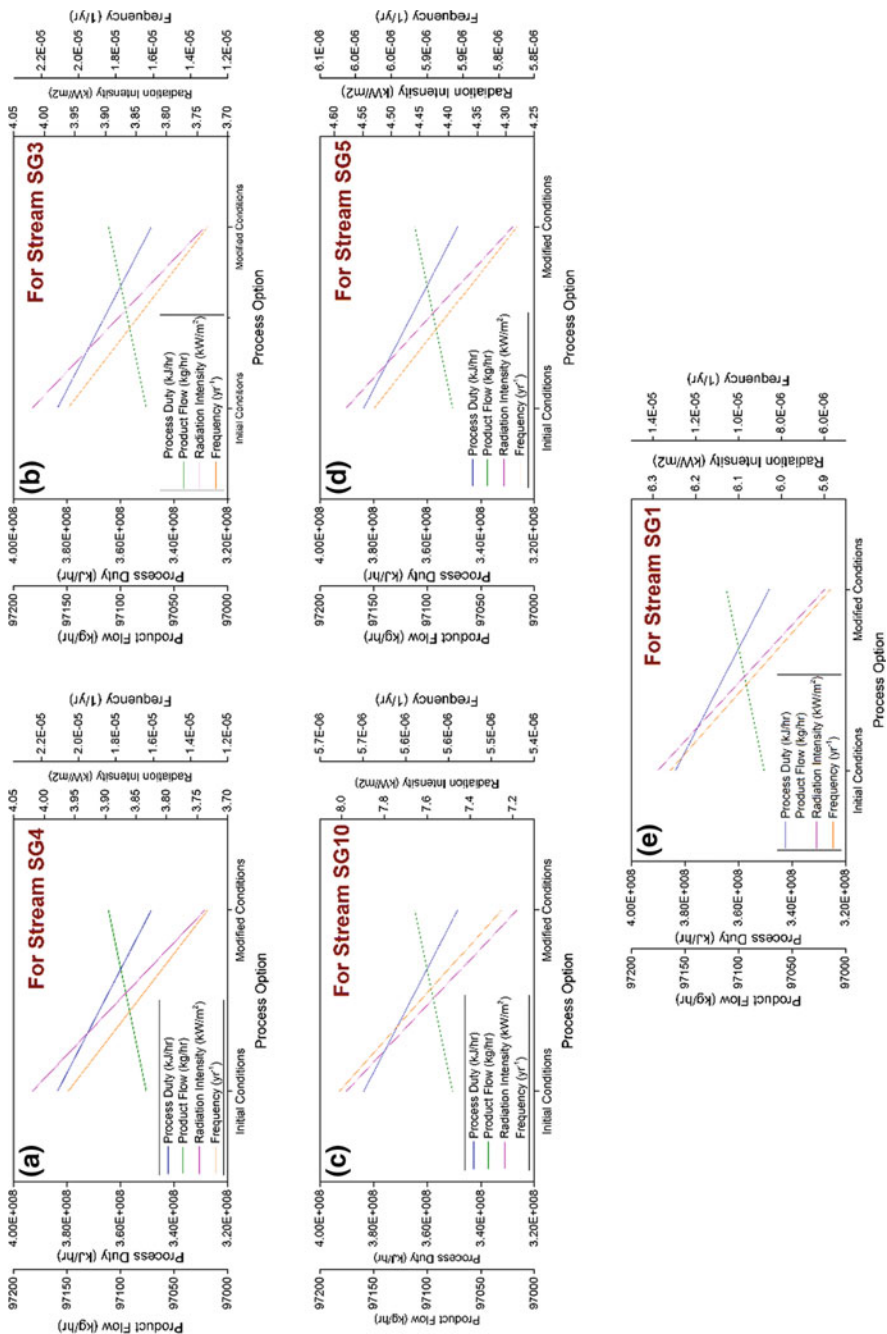


Fig. 4 Risk and process economics parameters of critical process streams



**Table 2** Initial and final process conditions for critical streams

Stream name	Original pressure (kPa)	Modified pressure (kPa)	Original temperature (°C)	Modified temperature (°C)
SG4	3530	3177	975.1	900.3
SG3	3530	3177	975.1	900.3
SG10	3000	2700	30	30
SG5	3530	3177	700	630
SG1	3530	3177	808	727.2

ified process conditions have contributed to minimizing the fire radiation intensity and process duty because of moderated process conditions, while the product amount is increased, as observed in Fig. 4. The moderated conditions have not affected the reaction in reformers, whereas it has favored the thermodynamic separation of the gas mixture from the water and improved the gas purity slightly. The moderation of process conditions has also released the duty load on cooling water requirements and the primary reformer by 26 and 3.3% respectively. Therefore, the process of duty observes a smooth and significant decline of 9.6% overall.

Overall, the risk is reduced for all critical streams with fractional improvement in product amount and a significant reduction in process duty. In the future, more case studies can be executed to further improve the proposed approach. In this context, the moderated process conditions have altered the rating of the process vessels and piping, which would minimize the installation cost. This aspect is not in the scope of current work, however, it can be integrated into future works.

## 4 Conclusion

To obtain the economic and inherently safer sustainable process design for process piping at the preliminary design stage, a new method is proposed in this work. The indexing method is engaged to rank the pipes in the process to recognize the critical ones. These critical process pipes are then studied through fire risk estimation and analysis. For the unacceptable risk, the process conditions are moderated, and risk is estimated again for risk acceptability confirmation. Moreover, the engagement of inherent safety principle in the process design would alter the process duty and product amount, which is compared with the base case to identify the improvement. The design is finalized once the risk is acceptable for all critical process streams and process economics depicts betterment using inherent safety guide word.

**Acknowledgements** The authors would like to show gratitude to Universiti Teknologi PETRONAS, Malaysia for providing research facilities and funding to make this research feasible.

## References

1. Hendershot DC (2010) A summary of inherently safer technology. *Process Saf Prog* 29:389–392
2. Eini S, Abdolhamidzadeh B, Reniers G, Rashtchian D (2015) Optimization procedure to select an inherently safer design scheme. *Process Saf Environ Prot* 93:89–98
3. Center for Chemical Process Safety, CCPS (2010) *Inherently safer chemical processes: a life cycle approach*, 2 edn. Wiley
4. Hendershot DC (2000) Process minimization: making plants safer. *Chem Eng Prog* 96(1), 35–40
5. Shariff AM, Zaini D (2010) Toxic release consequence analysis tool (TORCAT) for inherently safer design plant. *J Hazard Mater* 182:394–402
6. Ashford NA, Zwetsloot G (2000) Encouraging inherently safer production in European firms: a report from the field. *J Hazard Mater* 78:123–144
7. Leong CT, Shariff AM (2009) Process route index (PRI) to assess level of explosiveness for inherent safety quantification. *J Loss Prev Proc Indus* 22:216–221
8. Heikkilä AM (1999) *Inherent safety in process plant design: an index-based approach*. VTT Technical Research Centre of Finland
9. Khan FI, Amyotte PR (2005) I2SI: a comprehensive quantitative tool for inherent safety and cost evaluation. *J Loss Prev Proc Indus*. 18:310–326
10. Ramzan N, Witt W (2006) Methodology for decision support among conflicting objectives using process simulators. *Comput Aided Chem Eng* 21:415–420
11. Bernechea EJ, Arnaldos J (2014) Optimizing the design of storage facilities through the application of ISD and QRA. *Process Saf Environ Prot* 92:598–615
12. Ramzan N, Naveed S, Feroze N, Witt W (2009) Multicriteria decision analysis for safety and economic achievement using PROMETHEE: a case study. *Process Saf Prog* 28:68–83
13. Kim D, Ko D, Kim J, Park M, Moon I (2004) Automatic accident scenario generation and multiobjective optimization for safety-related decision making in chemical processes. In: *European symposium on computer aided process engineering-14 meeting*. Lisbon, Portugal
14. Kim D, Kim J, Moon I (2006) Integration of accident scenario generation and multiobjective optimization for safety-cost decision making in chemical processes. *J Loss Prev Proc Indus* 19:705–713
15. El-Halwagi AM, Rosas C, Ponce-Ortega JM, Jiménez-Gutiérrez A, Mannan MS, El-Halwagi MM (2013) Multiobjective optimization of biorefineries with economic and safety objectives. *AIChE J* 59:2427–2434
16. Bernechea EJ, Viger JA (2013) Design optimization of hazardous substance storage facilities to minimize project risk. *Saf Sci* 51:49–62
17. Kidam K, Hurme M (2013) Analysis of equipment failures as contributors to chemical process accidents. *Process Saf Environ Prot* 91:61–78
18. Shariff AM, Leong CT, Zaini D (2012) Using process stream index (PSI) to assess inherent safety level during preliminary design stage. *Saf Sci* 50:1098–1103
19. Center for Chemical Process Safety, CCPS (2010) *Guidelines for chemical process quantitative risk analysis*. Center for Chemical Process Safety, AIChE2000
20. Moosemiller M (2011) Development of algorithms for predicting ignition probabilities and explosion frequencies. *J Loss Prev Proc Indus* 24:259–265
21. Shariff AM, Wahab NA (2013) Inherent fire consequence estimation tool (IFCET) for preliminary design of process plant. *Fire Saf J* 59:47–54
22. Shariff AM, Zaini D (2013) Inherent risk assessment methodology in preliminary design stage: a case study for toxic release. *J Loss Prev Proc Indus* 26:605–613
23. Athar M, Shariff AM, Buang A, Shaikh MS, See TL (2019) Inherent safety for sustainable process design of process piping at the preliminary design stage. *J Cleaner Prod* 209:1307–1318

# Optimization of Delignification Process from Red Meranti Wood Sawdust (RMWS) Pretreated with Acidified Sodium Chlorite



Abdul Rahman Siti Noredyani, Abdul Wahid Zularisam, Ahmad Noormazlinah and Abdul Munaim Mimi Sakinah

**Abstract** Delignification is a process to remove the lignin content from lignocellulosic biomass to increase hydrolysis efficiency. In other word, the process ensures cellulose parts are more accessible. In the present research, there are two objectives; (i) to optimize the operating parameters of acidified sodium chlorite pretreatment for delignification of RMWS, and (ii) to characterize the RMWS used as feedstock. The two significant variables, reaction temperature and ratio of sodium chlorite to sawdust were optimized using response surface methodology and experiments were performed according to a central composite experimental design in order to enhance the delignification process as well as holocellulose recovery. The experimental design was expressed based on preliminary work and screening process using the combined severity, which ranged from 0.76 to 1.64 for chlorite solution and temperature range from 65 to 85 °C. The experimental results showed the most optimal condition of acidified pretreatment of RMWS was 1.42 for the ratio of sodium chlorite to RMWS at an optimal temperature at 70 °C, resulted with 97% of lignin removal. These results are important for further treatment to finally extract the cellulose.

**Keywords** Red Meranti Wood Sawdust (RMWS) · Acidified sodium chlorite · Delignification · Respond surface methodology (RSM) · Lignin removal

## 1 Introduction

As the world's most abundant renewable lignocelluloses resources for second generation biofuels, there has been an increasing interest in biomass for past three decade as a sustainable alternative platform to fossil energy carriers for production of bio-based

---

A. R. Siti Noredyani · A. W. Zularisam · A. M. Mimi Sakinah (✉)  
Faculty of Engineering Technology, Universiti Malaysia Pahang, Gambang, Pahang, Malaysia  
e-mail: [mimi@ump.edu.my](mailto:mimi@ump.edu.my)

A. Noormazlinah  
Faculty of Chemical & Natural Resources Engineering, Universiti Malaysia Pahang, Gambang, Pahang, Malaysia

chemicals, biomaterials and other added-value products including cellulose [1, 2]. There are four types of lignocellulosic biomass, including forestry residuals, dedicated crops, agricultures residuals, and waste and residual. Malaysia's forest plays an important role, as a feeder to provide feedstock especially logs to the timber industry. The total land area in Malaysia is 32.9 M ha, of which 55.3% was under natural and plantation forest cover in 2008, with total up for Peninsular Malaysia; 5.9 M ha, Sarawak; 8 M ha and Sabah; 4.3 M ha [3]. Under the Third Industrial Master Plan (IMP3 2006–2020), in two years forward, the annual exports of the timber industry are targeted to achieve *RM53B* by 2020. When this target was achieved, the abundance of sawdust will arise, and the economical disposal of sawdust is a problem of growing concern to the wood industries. Sawdust, is are composed of wood's fine particle and by-product of woodworking processes, for example milling, sanding, sawing, planning and drilling.

Lignocellulosic biomass in forestry residue is mostly contained of three major components, which are cellulose (40–50%), hemicellulose (20–30%) and lignin (10–25%) [4]. Cellulose, as major component in residual biomass, is considered as the most robust candidate for displace fossil fuel based polymers attributable to its eco-friendly properties like sustainability, non-food material, bio-compatibility and biodegradability [5, 6]. There have been a number of longitude studies involving this kind of resources especially for forestry residues that have been reported to play an important role in the transformation to a more sustainable society, which contributes up to 50% world biomass resources, aside, they are being carbon neutral [7, 8]. In this context, the concepts of bio-refineries are supposed to improve economic impacts by utilization of renewable biomass, together with the positive effects to environment to reduce greenhouse gas (GHG) emission and also as an alternative disposal method because of their large availability, which may contribute to serious environmental problems due to land use and open burning [9]. The normal extraction of logging residues from logging and sawmill will leave at least 20% of remaining by-products containing of chips, bark and sawdust at the clear-felled area [10]. As a raw material, sawdust residue from wood especially from Red Meranti Wood is widely harvested and available worldwide with low cost and high potentials for industrial scale industries. Cellulose, as a major component of sawdust which is encapsulated by lignin-hemicellulose matrix makes it robust or recalcitrance from crystallinity of its bonding which may affect potential applications [11, 12]. Delignification process is a pretreatment to disrupt and to expose its complex lignin structure to achieve the main objectives; to recover as many cellulose from residue RMWS biomass. The aim of this work was to optimize the operating parameters of acidified sodium chlorite pretreatment for delignification of RMWS and to characterize its lignocellulosic contents. The effectiveness of lignin removal during the pretreatment is a successful downstream process.

## 2 Materials and Method

### 2.1 Raw Material

Red Meranti Wood Sawdust (RMWS) was collected from local sawmill (Kilang Papan Sg. Charu Sdn. Bhd), and used as a raw material for cellulose recovery. These Red Meranti trees were harvested from Sg Lembing forest area before being sent to the nearby sawmill plant. RMWS was screened to remove outsized particles and then, sun dried. The dried Red Meranti Wood sawdust was passed through to a particle size of 0.5 mm before dried in an oven for 24 h at temperature 45 °C (Vibratory Sieve Shaker AS 200 Basic, Retsch, Germany). The dried samples were kept (sealed plastic sheet) at room temperature until next procedure. The quantification of lignocellulosic RMWS composition was done to determine the main structural constituent using standard methods and chlorite delignification method [13–17].

### 2.2 Pretreatment of Acidified Sodium Chlorite

The acidified NaClO<sub>2</sub> treatment consists of two steps. The RMWS (500 mg) was delignified with 25% NaClO<sub>2</sub> adjusted with glacial acetic acid with fixed ratio 0.6 to RMWS for 6 h of total pretreatment time at certain temperatures. The water insoluble solids (WIS) or known as holocellulose was separated by filtration from the light yellow suspension, washed with plentiful amount of distilled water until close to neutral (~pH 7) and dried at 45 °C for 24 h. The WIS were analysed for Lignin Klason and the recoveries of solid fraction were determined as a percentage of the solid recovery or known as Holocellulose recovery, calculated as shown at Eq. (1) [18, 19]. These analyses were used to measure the effectiveness of delignification pretreatment on RMWS. The previous study have reported the highest holocellulose yield was achieved with acidified sodium chlorite delignification compared with sodium hydroxide extraction and alkaline hydrogen peroxide extraction [20].

$$\text{HC recovery (Yield), \%} = 100 \frac{(\text{Amount of dry solid recovered after reaction, g})}{\text{Initial amount of dry solids, g}} \quad (1)$$

### 2.3 Klason-Lignin Characterisation

The percentage of lignin removal was measured as a response in this study. From Eq. (2), Klason lignin, also known as acid-insoluble lignin (AIL) analysis was used to analyse the lignin content left after delignification reaction [15, 21]. Firstly, 0.3 g from 13 runs of delignified sample of RMWS was weighed (in duplicate) and 3 ml

**Table 1** Levels of parameters condition variables tested in the CCD

Factor	Symbols		$-\alpha$	$-1$	$0$	$+1$	$+\alpha$
	Coded	Actual					
Ratio NaClO <sub>2</sub> to RMWS	A	a	0.76	0.98	1.2	1.42	1.64
Temperature	B	b	65	70	75	80	85

of strong H<sub>2</sub>SO<sub>4</sub> of 72% solution was added for hydrolysis in water bath for 1 h at 30 °C. Then, the solution was diluted with 84 ml deionized water to obtain 3% of H<sub>2</sub>SO<sub>4</sub> and heated in autoclave at 121 °C for 1 h. The autoclaved hydrolysis solution was vacuum filtered and washed with hot water. The acid insoluble residues were dried at 105 °C until a constant weight was achieved.

$$\text{Lignin removal, \%} = 100 \frac{(\text{Delignify RMWS, g} - \text{Klason Lignin residue, g})}{\text{Delignify RMWS, g}} \quad (2)$$

## 2.4 Design of Experiment

In order to optimize the process, a central composite design (CCD) was employed along with two different parameters to design the best combination of parameters. According to the CCD, the pretreatment of RMWS with acidified NaClO<sub>2</sub> was calculated using an experimental design ( $\alpha = 2$ ). The ratio NaClO<sub>2</sub> to sawdust (0.7–1.64) and temperature (65–85 °C) were selected as independent variables (parameters), keeping the pretreatment time at 6 h and fixed ratio of acetic acid to sawdust as 0.6. A total of 13 experiments including 5 centres of the domain selected for each factor (75 °C and 1.2 ratio 25% NaClO<sub>2</sub> to RMWS) were performed in random order. Table 1 displays the coded and actual levels of both, the pretreatment temperature and the number of ratio of 25% NaClO<sub>2</sub> to RMWS. The experimental data were analysed by the statistical software Design Expert 7.1, Stat-Ease, Inc., Minneapolis, USA.

## 3 Results and Discussion

### 3.1 Lignocellulosic Composition of Red Meranti Wood Sawdust

These analyses are important for measuring the theoretical yield in polysaccharides and for calculating the reactivity of components present in this lignocellulosic biomass. The main lignocellulosic composition of RMWS is showed in Table 2. The

**Table 2** Lignocellulosic composition of Red Meranti Wood Sawdust

Composition	% Total dry weight <sup>a</sup> (w/w) ± SD <sup>a</sup>		
	Rafiqul and Sakinah (2012)	Siti Sabrina and Sakinah (2017)	In this study
Total solid	n/a	96.11 ± 0.02	91.12 ± 0.19
Moisture	n/a	3.89 ± 0.02	8.88 ± 0.19
Ash	0.43 ± 0.04	0.16 ± 0.06	0.25 ± 0.02
Extractives	3.08 ± 0.05	4.40 ± 0.04	2.065
Holocellulose	n/a	72.60 ± 0.52	73.52
Hemicellulose	30.64 ± 0.07	24.88 ± 0.57	34.08
α-Cellulose	41.06 ± 0.03	47.72 ± 0.05	39.44
Lignin	25.22 ± 0.05	27.75 ± 2.02	27.00

<sup>a</sup>Standard deviation (Duplicate)

total solid and moisture content were measured using natural convection heating or drying oven (Memmert GmbH, Germany). The results for both were based on dry matter (DM) basis. The ash content of RMWS was measured as the residue remaining after calcination at 575 °C for 3 h to burn off all the carbon [22]. Extractives were calculated by extracting untreated RMWS (2 g) with Ethanol-Toluene solution (160 ml), using a Soxhlet tool ( $v = 250$  ml) for 6 h (about 16 extraction cycles) [23]. The major lignocellulosic composition of RMWS (hemicellulose, cellulose and lignin) were analysed according to the standard methods. [15–17, 22, 24]. The high content of cellulose (39.44%) in RMWS contributes this kind of biomass suitable for cellulose recovery.

### 3.2 Holocellulose Recovery and Lignin Removal

After pretreatment of delignification of RMWS using the acidified sodium chlorite, the holocellulose (HC) was recovered as shown in Table 3. Subsequently, the Klason lignin analysis was done to calculate the effectiveness of delignification reaction to RMWS and then, calculated as the percentage of lignin removal as Eqs. (1) and (2) above. The results for holocellulose recovery (%) and lignin removal (%) was summarize in the Table 3. From these data, run 5 was found as the highest percentage of HC and the lowest one was run 6. On the contrary, the observed difference between both runs for lignin removal was presented Run 6 was the highest on the percentage of lignin removal. This finding revealed that the delignification reaction at Run 6 was almost complete, with 97.33% of lignin was removed from RMWS. The results differ with run 5, which higher impurities in HC, it was recovered. There are several explanations for these result, which clearly indicated that the optimization of the pretreatment process condition had a synergetic effect on the overall process

**Table 3** Experimental design for acidified NaClO<sub>2</sub> pretreatment of delignification RMWS

Run	Holocellulose	Temperature, °C		SC <sup>a</sup> : RMWS <sup>b</sup>		Lignin
	Recovery (%)	Coded	Real	Coded	Real	Removal (%)
12	86.40	-1	70	-1	0.98	85.33
10	84.80	-1	70	1	1.42	96.67
13	89.60	1	80	-1	0.98	88.00
2	86.80	1	80	1	1.42	88.00
5	91.80	0	75	-2	0.76	81.33
8	81.20	0	75	2	1.64	93.33
9	89.36	-2	65	0	1.20	90.00
3	82.46	2	85	0	1.20	90.67
1	82.60	0	75	0	1.20	94.67
11	82.20	0	75	0	1.20	93.33
6	79.60	0	75	0	1.20	97.33
4	83.60	0	75	0	1.20	93.33
7	83.00	0	75	0	1.20	96.67

including *HC* yield and lignin removal process, as mentioned by [25]. When there are impurities in *HC* means that the reaction was not entirely successful and need subsequent extractions or processes have to carry out in order to obtain free-lignin holocellulose [20]. The other reason is because of the glycoside bounds with acidic cleavage [26].

### 3.3 Screening of Parameters

Prior studies that have noted the importance of optimization of pretreatment because woody biomass as RMWS is harder to treat as compared to grass biomass, revealed that the extent of cross-linking and the phenyl content lignin found in wood is far more complex than that of grassy substrates [27]. To enhance the reaction in delignification of RMWS with optimization process, process screenings were performed earlier using a 2<sup>5-1</sup> fractional factorial analysis to evaluate significant parameters within designated values, then, to be optimised using central composite design. In previous research, there are a number of parameters that need to be considered while employing a pretreatment of RMWS (delignification), before it is used to recover the cellulose as a final product [28]. These parameters include the ratio of CH<sub>3</sub>COOH to RMWS, the ratio of NaClO<sub>2</sub> to RMWS, reaction time and temperature with average percentage of lignin removal from total run of 61.67%. In this study, only temperature and the ratio of NaClO<sub>2</sub> to RMWS were recognized as parameters that have significant effect on lignin removal from RMWS at 99.63% confidence level. As a result, two variables



were chosen as parameters to be optimised, with temperature at 75 °C at 1.2 ratio of NaClO<sub>2</sub> to RMWS were selected as center point in this study.

Central composite design (CCD) was applied to predict the optimum parameters conditions for enhancement of delignification reaction of RMWS, with the different combination of temperature and amount of NaClO<sub>2</sub> conditions involved. The percentage of lignin removal was calculated as the response (Table 3). The CCD used in this study is generated a polynomial regression equation which allowed determination of levels of both parameters to be carried out with the interrelation between each parameter evolved simultaneously [29].

### 3.4 Model Fitting and Analysis of Variance (ANOVA)

By using Design Expert software, version 7.1.6 (Stat-Ease Inc, USA), the experimental plan generated as tabulated in Table 3 were designated to evaluate the suitable model for the response using the fit summary collects the important statistics used to identify which model to suggest for detailed study. The suggested model should be considered a good starting point for the model fitting [30]. According to fit summary reports (Tables 4 and 5), the quadratic model was adequately significant to appoint the percentage of lignin removal as a response and was observed by Fisher's statistical test (*F*-test) and the coefficient of determination, *R*<sup>2</sup>.

Sequential model sum of squares started with mean and addition term with linear, two factor interactions, quadratic, and cubic were implemented and *F* statistic value was calculated. According to the fitted model (Table 4), the addition of significant terms with value of *p* are less than 0.05, which clearly indicated that the quadratic model is significant, fits the conditions to be chosen to fit response, supported with

**Table 4** Sequential model sum of squares

Source	Sum of squares	df <sup>a</sup>	Mean square	<i>F</i> value	<i>p</i> -value Prob > <i>F</i>
Mean versus Total	1.087 × 10 <sup>5</sup>	1	1.087 × 10 <sup>5</sup>		
Linear versus Mean	105.89	2	52.94	3.10	0.0894
2FI versus Linear	32.15	1	32.15	2.09	0.1821
Quadratic versus 2FI	100.47	2	50.24	9.27	0.0108
Cubic versus Quadratic	7.49	2	3.74	0.62	0.5770
Residual	30.43	5	6.09		
Total	1.090 × 10 <sup>5</sup>	13	8381.69		

<sup>a</sup>Degree of freedom

**Table 5** Lack of fit test

Source	Sum of squares	df <sup>a</sup>	Mean square	F value	p-value
Linear	$1.087 \times 10^5$	6	26.11	7.52	0.0356
2FI	105.89	5	24.90	7.17	0.0397
Quadratic	32.15	3	80.01	2.31	0.2182
Cubic	100.47	1	16.55	4.77	0.0944
Pure error	7.49	4	30.47		

<sup>a</sup>Degree of freedom

Mason et al. [31]. The lack of fit test is considered as insignificant in lack of fit ( $p$ -value  $> 0.1$ ) [30, 31]. Stated to tables Table 5, the computed  $P$ -Value for quadratic is 0.2182, considered as insignificant condition. Based on these results (Tables 4 and 5), it is concluded that quadratic model was the sufficient model it a good starting point for the model fitting. The value of regression coefficient interrelation with the parameters and response are designed as the 2nd order polynomial equation in coded form as shown in Eqs. (3) and (4).

- i. Percentage of lignin removal,  $Y$  (coded):

$$Y(\text{coded}) = 94.39 + 2.94A - 0.39B - 2.83AB - 1.98^2 - 1.22B^2 \quad (3)$$

- ii. Percentage of lignin removal,  $y$  (actual):

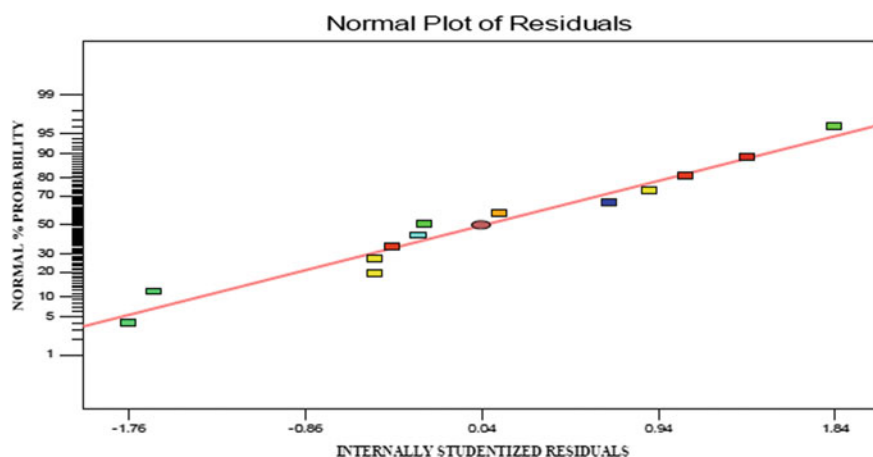
$$y(\text{actual}) = -482.22 + 304.68a + 10.36b - 2.58ab - 40.83ab^2 - 0.049b^2 \quad (4)$$

According to the Table 6, the values of Prob  $> F$  for that model are less than 0.05, which showed that the model is significant. In addition, the main effect of sodium chlorite concentration (in term of ratio) are significant model terms, whereas the main effect of temperature ( $B$ ) is insignificant model term for delignification reaction of RMWS. The coefficient of determination ( $R^2$ ) for this model is 0.8628. This  $R^2$  value is relatively close to 1, which is acceptable. In particular, this implies that 86.28% of total variations in the delignification method is explained by the fitted models (Eqs. 3 and 4). The predicted  $R^2$  (0.2428) is acceptable justification with the adjusted  $R^2$  (0.7648) which explains the correlation between both values from the model. Table 6 showed the adequate precision greater than 4 (10.601), which means adequate model discrimination. The normal probability residual points (Fig. 1) apparently follow a straight line which shows the errors are scattered at normal plot (adequacy of the least square fit). The plot of the residual versus the predicted response (Fig. 2) displays a random distribution and considered the model suggested is adequate and free from any destructions assumption (independence variance & constant variance).

**Table 6** ANOVA table and summary of fit for optimization of delignification RMWS

Source	Sum of squares	df <sup>a</sup>	Mean square	F value	p-value
Model	238.51	5	47.70	8.81	0.0063
A-Ratio SC to RMWS	104.08	1	104.08	19.21	0.0032
B-Temperature	1.81	1	1.81	0.33	0.5814
AB	32.15	1	32.15	5.93	0.0450
A <sup>2</sup>	89.49	1	89.49	16.52	0.0048
B <sup>2</sup>	34.38	1	34.38	6.35	0.0398
Residual	37.92	7	5.42		
Lack of fit	24.04	3	8.01	2.31	0.2182
Pure error	13.88	4	3.47		
Cor total	276.42	12			
Std. Dev	2.33	Adj R-squared			0.7648
Mean	91.44	Pred R-squared			0.2428
R-squared	0.8628	Adeq precision			10.601

<sup>a</sup>Degree of freedom



**Fig. 1** Normal probability plots of residual

### 3.5 Optimisation of Parameters

The effect between amount of sodium chlorite (in term of ratio, *A*) and temperature (*B*) on delignification process of RMWS at contact amount of acetic acid (0.6) and time (6 h) were analyzed using simulated interaction plot and three-dimensional response surface plot which are illustrated in Fig. 3. As shown in Table 6 and Fig. 3, the interaction effect between both parameters has a *p*-value < 0.05, representing that

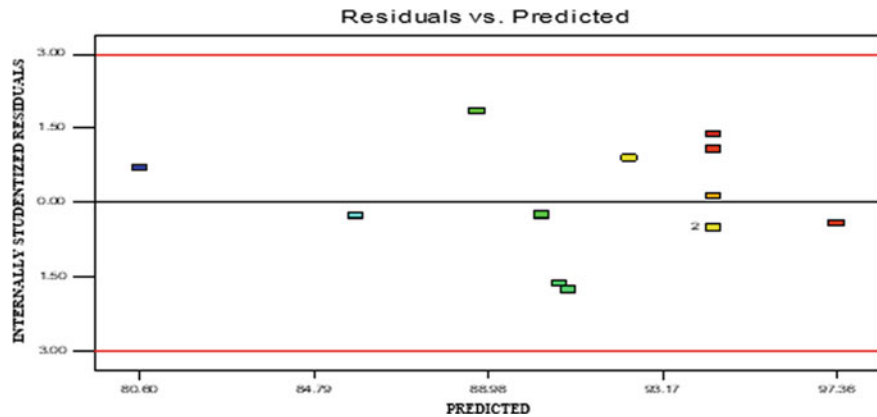
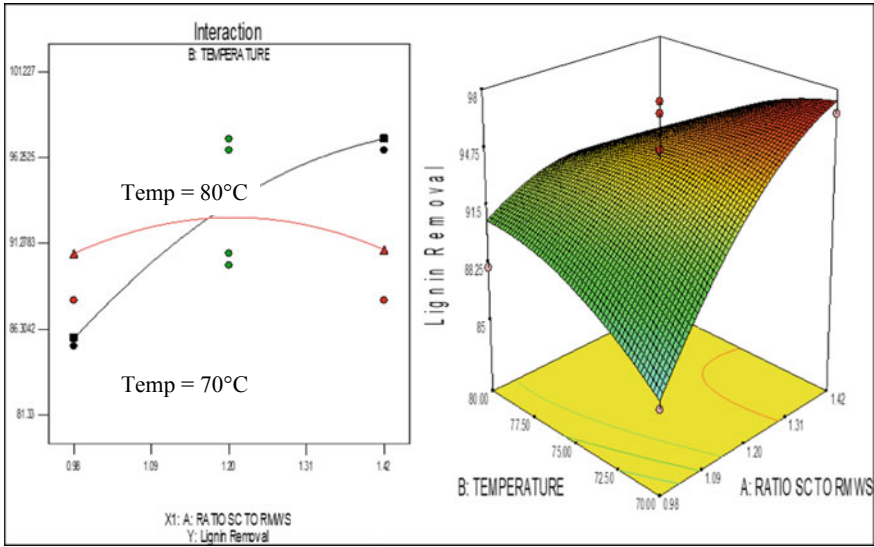


Fig. 2 Plot of residual versus predicted response for lignin removal (%) for lignin removal (%)

the interaction is significant to the response. Based on Fig. 3, a notable and constant improvement in the percentage of lignin removal is observed for the increase of the amount of sodium chlorite from ratio 0.96–1.42 at temperature condition 70 °C. However, at higher temperature condition (80 °C), a result is also observed where the percentage of lignin removal decreased slightly from ratio 1.2–1.42 of *SC* to *RMWS*. These results probably indicate that the process of delignifying the *RMWS* keep on increasing at increment of concentration (1.2–1.42; ratio *SC* to *RMWS*) under temperature condition 70 °C. This finding supports previous research from Nadia Rabetafika et al. [20] and Kumar et al. [18], which showed the acidified  $\text{NaClO}$  pretreatment is the best at 70 °C compared with other pretreatment. From the result, there is slight decrement of lignin removal at 80 °C, which assume it reach the optimal condition. Rabemanolontsoa and Saka [32] have recently mentioned that the concentrated acid allows to obtain high yield of product with lower temperature less than 100 °C.

### 3.6 Model Validation and Model Confirmation Testing

For this study, numerical optimization was conducted based on the regression models with the aim to achieve maximum desirability for lignin removal using response surface analysis. A desirability of response variable used into a specific value ranging from 0 (completely undesirable response) to 1 (most desirable response) [30]. Three proposed optimum conditions were chosen that directed to maximum response (lignin removal, %) with higher desirability factors (1,0.933 and 0.988). Validation experiments were performed at three suggested optimum conditions (for validation of model) and three confirmation runs from the design of experiments setting to



**Fig. 3** 3D interaction graph and response surface plot for the effects of ratio SC to RMWS (a) and temperature (b)

validate these conditions. According to the Eqs. (5) and (6) by Zularisam et al. [33], the error and residual were calculated.

$$Residual = (Actual\ value - Predicted\ value) \tag{5}$$

$$Error, \% = 100 \frac{(Actual\ value)}{Predicted\ value} \tag{6}$$

In order to validate the reliability of the models, a series of additional experiments were run (Table 7) and estimating the percentage of lignin removal from Eqs. (3) and (4). Based on Table 7, the first three conditions which were recommended by the Design Expert software, while the other two conditions were among the preparation conditions which were applied previously. From the results, the percentage error between the actual and predicted value ranging from 0.935 to 1.035%, which implied that the produced models were accurately sufficient because the error were less than 5%. Thus, the models were successfully validated.

Furthermore, Table 7 also exposed the results of confirmation testing consist of suggested level of critical parameters and the most constructive setting from design of experiment. Based on the validation results, the optimal value for percentage of lignin removal was chosen with parameters 1.42 of NaClO<sub>2</sub> to RMWS temperature 70 °C with the response resulted in the actual (97%) and predicted (97.36%), at 95% of confidence interval (CI). Concisely, the percentage error between both value was 0.996%, which found to be very close to the predicted value. Thus, the model

**Table 7** Results of model validation and model confirmation testing for percentage of lignin removal

Validation of models					
<i>Parameter</i>					
Ratio SC to RMWS	Temperature (°C)	Actual	Predicted	Residual	Error (%)
1.42	70	95.0	97.36	2.36	0.976
1.42	72	90.67	96.96	6.29	0.935
1.42	75	95.67	95.36	0.31	1.003
1.64	75	95.67	92.38	3.29	1.035
1.2	75	97.33	94.39	2.94	1.031
<i>Model confirmation testing</i>					
1.42	70	97.0	97.36	0.36	0.996

was successfully validated and verified that model was adequate to the experimental data. Accordingly, the selected optimal condition was the most suitable and could be achieved using response surface methodology (RSM). These results of this study are in agreement with Nadia Rabetafika et al. [20] findings that proved acidified NaClO<sub>2</sub> pretreatment contributed to low content of lignin which were explained by the cleavage of ester linkages between lignins and hemicelluloses during the extraction process.

## 4 Conclusions

- The aim of acidified NaClO<sub>2</sub> pretreatment of RMWS was to remove as much lignin in order to recover as many cellulose from this feedstock. Therefore, the pretreatment was optimized by maximizing the delignification process in holocellulose recovery.
- According to the central composite design, the optimal conditions were found at 70 °C and 1.42 of NaClO<sub>2</sub> to RMWS, with predicted value obtained by the model for lignin removal (%) was 97.36. The optimal conditions were experimentally repeated and resulted as 97% of lignin removal from RMWS. These results are important for further treatments to eliminate hemicellulose in order to extract cellulose as a final product.

**Acknowledgements** This research was supported by internal grants, Universiti Malaysia Pahang, RDU1703325 and PGRS1803111.

## References

1. Popa VI (2018) Biomass for fuels and biomaterials. In *Biomass as renewable raw material to obtain bioproducts of high-tech value*. Elsevier, pp 1–37
2. Watkins D, Hosur M, Tcherbi-narteh A, Jeelani S (2014) Extraction and characterization of lignin from different biomass resources. *Integr Med Res* 4:26–32
3. Malaysia Timber Industrial Board: National Timber Industry Policy. Ministry of Plantation Industries and Commodities Malaysia
4. Iqbal HMN, Kyazze G, Keshavarz T (2013) Advances in the valorization of lignocellulosic materials by biotechnology: an overview. *BioResources* 8(2):3157–3176
5. Ahn Y, Hu DH, Hong JH, Lee SH, Kim HJ, Kim H (2012) Effect of co-solvent on the spinnability and properties of electrospun cellulose nanofiber. *Carbohydr, Polym*
6. Mohammadinejad R, Karimi S, Irvani S, Varma RS (2005) Plant-derived nanostructures: types and applications. <http://xlink.rsc.org/?DOI=C5GC01403D>
7. Putro JN, Soetaredjo FE, Lin S-Y, Ju Y-H, Ismadji S (2016) Pretreatment and conversion of lignocellulose biomass into valuable chemicals. *RSC Adv* 6:46834–46852
8. Fernandes MC, Ferro MD, Paulino AFC, Mendes JAS, Gravitis J, Evtuguin DV, Xavier AMRB (2015) Enzymatic saccharification and bioethanol production from *Cynara cardunculus* pretreated by steam explosion. *Bioresour Technol* 186:309–315
9. Romero I, López-Linares JC, Moya M, Castro E (2018) Optimization of sugar recovery from rapeseed straw pretreated with FeCl<sub>3</sub>. *Bioresour Technol* 268:204–211
10. Nilsson B, Se L (2016) Extraction of logging residues for bioenergy: effects of operational methods on fuel quality and biomass losses in the forest. Linnaeus University Press
11. Isikgor FH, Becer CR (2015) Lignocellulosic biomass: a sustainable platform for the production of bio-based chemicals and polymers. *Polym Chem* 6:4497–4559
12. Studer MH, DeMartini JD, Davis MF, Sykes RW, Davison B, Keller M, Tuskan GA, Wyman CE (2011) Lignin content in natural *Populus* variants affects sugar release. *Proc Natl Acad Sci* 108:6300–6305
13. Sukri SSM, Sakinah AM (2018) Production of high commercial value xylooligosaccharides from Meranti wood sawdust using immobilised xylanase. *Appl Biochem Biotechnol* 184(1):278–290
14. Sluiter A, Ruiz R, Scarlata C, Sluiter J, Templeton D, Sluiter A, Ruiz R, Scarlata C, Sluiter J, Templeton D (2008) Determination of extractives in biomass laboratory analytical procedure (LAP) Issue date : 7/17/2005. Determination of Extractives in Biomass Laboratory Analytical Procedure (LAP)
15. Sluiter A, Hames B, Ruiz R, Scarlata C, Sluiter J, Templeton D, Nrel DC (2011) Determination of structural carbohydrates and lignin in biomass determination of structural carbohydrates and lignin in biomass
16. Sluiter A, Hames B, Hyman D, Payne C, Ruiz R, Scarlata C, Sluiter J, Templeton D, Nrel JW (2008) Determination of total solids in biomass and total dissolved solids in liquid process samples. National Renewable Energy Laboratory 9
17. Wise LE, Maxine M, D'Addieco AA (1946) Chlorite holocellulose, its fractionation and bearing on summative wood analysis and on studies on the hemicelluloses. *Tech Assoc Pulp Pap Ind* 29:210–218
18. Kumar R, Hu F, Hubbell CA, Ragauskas AJ, Wyman CE (2013) Comparison of laboratory delignification methods, their selectivity, and impacts on physiochemical characteristics of cellulosic biomass. *Bioresour Technol* 130:372–381
19. Duret X, Fredon E, Masson E, Desharnais L, Gérardin P (2013) Optimization of acid pretreatment in order to increase the phenolic content of *Picea abies* bark by surface response methodology. *BioResources*
20. Nadia Rabetafika H, Bchir B, Blecker C, Paquot M, Wathelet B (2014) Comparative study of alkaline extraction process of hemicelluloses from pear pomace
21. ASTM D1106-96 (2001) Standard test method for acid-insoluble lignin in wood

22. Han JS, Rowell JS (2008) Chemical composition of fibers. *Cellulose* 283:83–134
23. Technical Association of Pulp and Paper Industry (2007) TAPPI: TAPPI T 204 cm-07—Solvent extractives of wood and pulp
24. Winandy JE, Rowell RM (2005) Chemistry of wood strength. In: *Handbook of wood chemistry and wood composites*
25. Kumar AK, Sharma S (2017) Recent updates on different methods of pretreatment of ligno-cellulosic feedstocks : a review. *Bioresour Bioprocess*
26. Gierer J (1986) Chemistry of delignification. *Wood Sci Technol* 20:1–33
27. Ververis C, Georghiou K, Christodoulakis N, Santas P, Santas R (2004) Fiber dimensions, lignin and cellulose content of various plant materials and their suitability for paper production. *Ind Crops Prod* 19:245–254
28. Abdul Rahman, SN, Mimi Sakinah A (2018) Influenced factors in the delignification process of Red Meranti wood sawdust. *J Chem Eng Ind Biotechnol Open Access* 3:26–36
29. Brahim M, Boussetta N, Grimi N, Vorobiev E, Zieger-Devin I, Brosse N (2017) Pretreatment optimization from rapeseed straw and lignin characterization. *Ind Crop Prod* 95:643–650
30. Anderson MJ, Whitcomb PJ, Kraber SL, Adams W (2009) *Stat-ease handbook for experimenters*. Stat-Ease, Inc
31. Mason RL, Gunst RF, Hess JL (2015) *Statistical design and analysis of experiments—with applications to engineering and science*, 2nd edn
32. Rabemanolontsoa H, Saka S (2016) Various pretreatments of lignocellulosics
33. Zularisam AW, Ismail AF, Salim MR, Sakinah M, Matsuura T (2009) Application of coagulation-ultrafiltration hybrid process for drinking water treatment: optimization of operating conditions using experimental design. *Sep Purif Technol*



# Wrist Twist Working Posture's Muscles Activity and Potential Energy Analysis via Human Digital Modelling



Azizul Rahman Abd Aziz, Siti Azfanizam Ahmad, Faieza Abdul Aziz, Siti Anom Ahmad, Ali Ahmed Shokshk and Salami Bahariah Suliano

**Abstract** Pronation and supination are a pair of unique movements possible only at the to flip the palm either facing superiorly (supination) or inferiorly (pronation). Muscles in the forearm work together by pulling on the radius bone of the forearm. This posture was concerned in work ergonomics assessments but still was not clarified about the postures variety. The objective of this research is to evaluate the postures variance range via kinesiology variables. A digital male human model was developed according to the Malaysian population anthropometry data with AnyBody Modelling System (AMS). The model was simulated with the constraints of static wrist pronation and supination postures for 30 min duration at a constant elbow flexion  $90^\circ$  (neutral) and  $0^\circ$  for both wrist flexion abduction to find the muscles activity and potential energy differences across the range of motion. The simulation result showed that co-contraction occurred between agonist and antagonist muscles on dynamic balance pronation movement (postures) act in a non-proportionate relationship. The other 2 outputs of maximum muscles activity and potential have been analyzed to generate the statistical risk index across the movement variety based on the outputs range. It is concluded that wrist twist postures range of motion varies by both muscles activity and potential energy which can be used to differentiate the posture's angles.

**Keywords** Wrist twist · Pronation · Supination · Muscles activity · Potential energy

## 1 Introduction

Pronation and supination is a process of rotating the forearm or palm along a range. In working posture practices, the palm used to handle manual operation is required to be held at certain angles. Prolong postures held will cause musculoskeletal dis-

---

A. R. A. Aziz (✉) · S. A. Ahmad · F. A. Aziz · S. A. Ahmad · A. A. Shokshk · S. B. Suliano  
Faculty of Engineering, Universiti Putra Malaysia, Serdang, Malaysia  
e-mail: [azizulrahman86@gmail.com](mailto:azizulrahman86@gmail.com)

© Springer Nature Singapore Pte Ltd. 2020  
M. Awang et al. (eds.), *Advances in Material Sciences and Engineering*, Lecture Notes in Mechanical Engineering,  
[https://doi.org/10.1007/978-981-13-8297-0\\_19](https://doi.org/10.1007/978-981-13-8297-0_19)

orders (MSDs) which contribute to injury. In 1984, a study focusing on a 66 years old female case to diagnose the method for injury treatment has summarized that stress occurrence at the joint caused by the muscles activity or contraction did affect the injury [1]. Ergonomics had taken the initiative in preventing MSDs by developing ergonomics assessments. An ergonomics assessment named Rapid Upper Limb Assessment (RULA) was developed by Lynn Mcatamney in 1993 to evaluate the individual worker's exposure to ergonomic risk factors [2]. The risk was then indexed with numbers to differentiate the postures possibilities for MSDs. This assessment also had included wrist pronation as a posture to be assessed. Interest in correlating muscles activity and working posture have been drawn by Fountain in 2003 [3]. The author has conducted an experiment in testing RULA risk scores compared with muscles activity by using electromyography (EMG) measurement. 20 subjects, each performed a 30 min typing task in three working postures differentiated by RULA's scoring system. Tested muscles were trapezius, deltoid, biceps brachii and forearm extensor. It has claimed that there is no statistical significance in the root-mean-squared amplitude in the signals measurement which has raised the curiosity to investigate the wrist twist or supination posture by muscles activity and energy expenditure.

## 2 Postures Kinesiology Review

This research has included the kinesiology viewpoints on human postures. The upturned study was conducted to identify the wrist pronation posture kinesiological aspects to be comprised in this research including postures definition, the muscles involve and the range of motion (ROM). The subject posture itself is a term used to describe a position of the body or the arrangements of body parts. Working postures represent required static kinematic positioning of the worker's overtime in completing the tasks. Postures are as a type of movement named dynamic balance where constant antagonistic pair muscle contractions are required to maintain a certain position [4]. From the static posture definition, antagonistic pair or prime mover muscles of wrist pronation movement has been identified and mapped in Table 1 [5]. The joint proximal radioulnar has been identified as the joint correspond for the wrist pronation movement. The posture accepted ranges is 80° pronation and 80° supination [6]. Table 1 shows the mapped kinesiological aspects of wrist pronation posture or twist as assessed in RULA.

## 3 Methodology

This research analysis was conducted with human digital modeling by AnyBody Modelling System (AMS) to simulate a Malaysian male digital model towards correlating the muscles activity and the potential energy changes across the pronation

**Table 1** Pronation supination prime mover muscles and kinesiology mapping

Rapid upper limb assessment			Kinesiology		
Description	Range	Score	Joint	ROM	Prime mover muscles
Wrist is pronated/supinated (twisted)	Mid-range	+1	Radioulnar	0–80	Pronator quadratus Pronator Teres
	End-range	+2		0–80	Biceps brachii Supinator

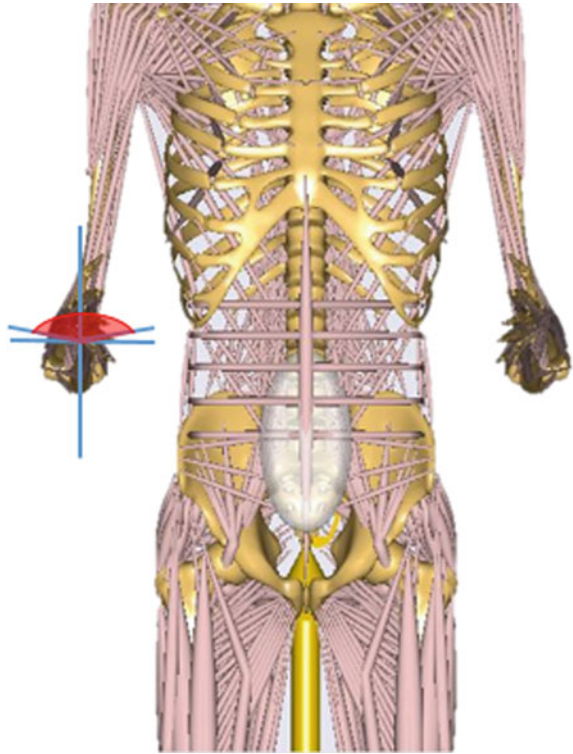
and supination postures. The Malaysian male anthropometry data from [7] has been used as the references in the AMS model scaling. The average weight of 67.35 kg and height 172.02 cm with BMI 22.76 has been identified and used for the model scaling. This average data was gathered from 150 males ranging from age of 18 to 24 years old. The template of standing man provided by AMS has been used as the initial setup for the human digital model preparation. This model was then scaled with average Malaysian male data mentioned to configure a specific Malaysian male model as the research subject. The scaling process was calculated automatically by the AMS with the standard scaling script for body’s dimensions estimation including segment’s length and mass as referred [8].

This model was then modified at the radiohumeral (elbow) and radiocarpal (wrist) joints deflection as the simulation constraint. The elbow deflection was set up at 90° flexion and 0° for both wrist flexion and abduction condition while performing the wrist pronation simulation. This elbow flexion constraint was based on the neutral posture stated in the ergonomic report [9]. Wrist pronation and supination postures were adjusted by the proximal radioulnar joint symmetrically for both the right and left hand. The simulation duration was set to a 30 min constant for all tested angles. The range of tested postures angles was as referred to identified ROM from the review stated above which are 80° for maximum pronation and 80° for maximum supination. The simulation output data were collected with the angles interval increment of 10° each testing. The epoch for output data collection was set to 5 min which make 7 output data per posture’s angle simulation. Figure 1 shows the tested proximal radioulnar joint adjustment.

## 4 Result and Discussion

This research outputs concerned were the specific posture potential energy in calorie and the muscles activity which include antagonistic pair and maximum muscles activity. Muscles activity was analyzed in the maximum voluntary contraction percentage (%MVC) unit or the activation level compared to the maximum capacity of specific muscles. 30% of MVC level has been recognized as a high intensity for

**Fig. 1** Pronation supination mannequin adjustment



muscles activation as referred in human physiology study [10]. The negative sign in the x-axis plots stands for supination angle deflection.

#### ***4.1 Postures Potential Energy***

The postures potential energy output was a measurement affected by postures specific mass positioning against the gravity which indicates the energy required to uphold the postures specific angle deflection. Figure 2 shows the distribution of potential energy across a deviation of pronation angles along the ROM.

The scattered data has been tested for the statistical significance using a P-value. The plot has given a P-value 1.0978E-08 which is less than 0.05 and proceeded with relationship or model determination. The model or equation for the posture data has been developed using spreadsheet trendline identification. Equation (1) shows the trendline of pronation postures and deflection angle relationship and the mod output legend shows the value gained by the equation with 1° accuracy. The output value was then used to find maximum and minimum value and used to generate a statistical index level of low (<33.3%), medium (33.3–66.7%) and high (>66.7%).

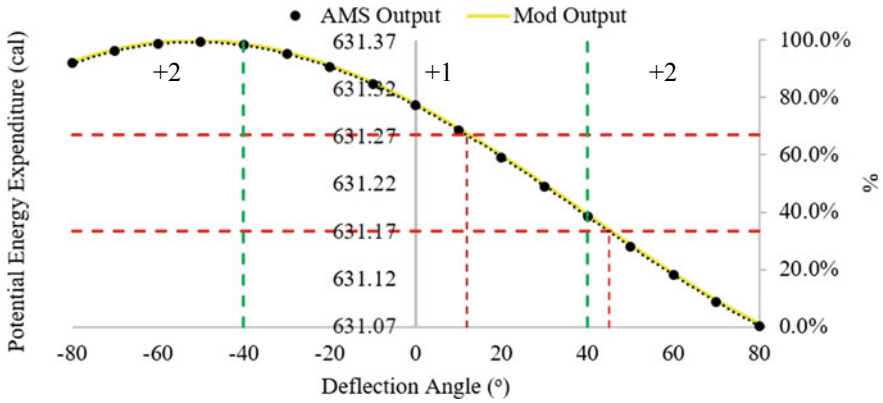


Fig. 2 Postures potential energy expenditure

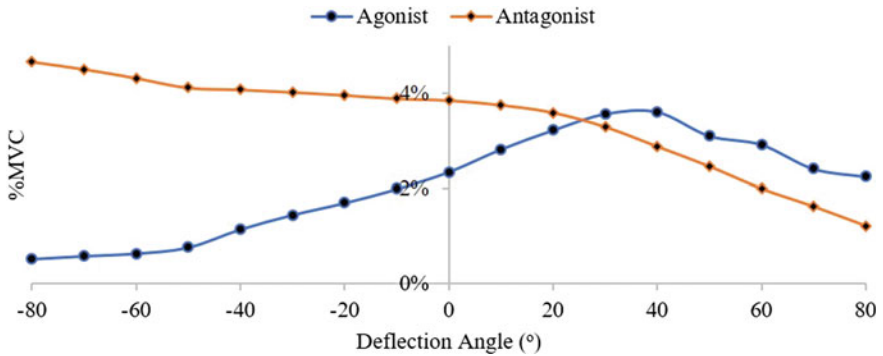


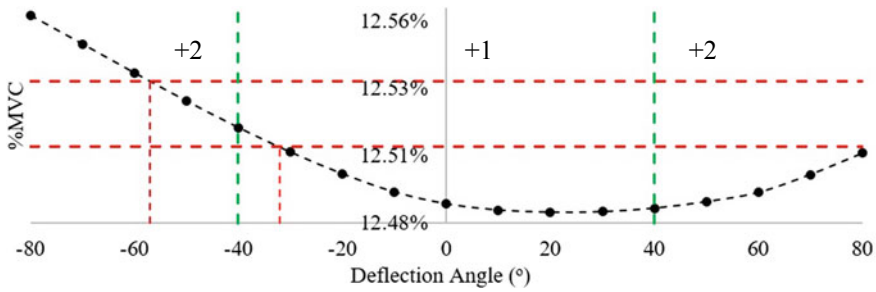
Fig. 3 Postures antagonistic pair muscles activity

$$y = 3.957E - 10x^4 + 1.097E - 07x^3 - 1.718E - 05x^2 - 2.426E - 03x + 631.3 \tag{1}$$

### 4.2 Postures Muscles Activity

The data of 30 min postures simulation have been averaged to select a representative value for the specific posture muscles activity. The first output was the antagonistic pair muscles activity for each specific posture tested shown in Fig. 3. Another muscles activity concerned was the maximum muscles activity shown in Fig. 4 comparing all muscles included in the model during specific posture simulation.

Shown in Fig. 3 the co-contraction mechanism where both functioning muscles were activated at certain magnitude during specific postures uphold. This result has answered the insignificant statistical claimed [3] where individual muscles activity



**Fig. 4** Postures maximum muscles activity

measurement cannot be compared to workers perceived discomfort. Subsequently, the P-value test on maximum muscles activity variable has given 0.0004 P-value but not been proceeded with the trendline or equation development since the variable result did not originate from the same entity. However, the maximum and minimum values extracted from the variable were also used to generate the statistic index range to classify postures angle maximum stress. The variables levels were shown in Figs. 2 and 4 by horizontal red dashed line. These levels were developed from the maximum and minimum range value within the ROM. Both variables change collaboratively in the trend with perceived discomfort as noted in RULA, except at the 40° pronation angle where both variables show low level but RULA has scored it as +2 (high). This condition may require higher precision in the statistic index for further justification. However, these results have indicated that these 2 variables were posture's measurable kinesiology parameters affecting the worker's postures discomfort level.

## 5 Conclusion

From the discussion, it can be concluded that the postures risk index or scores in RULA which were generated from perceived discomfort were influenced by both muscles activity (stress) and energy expended (fatigue). Other than that, wrist twist or pronation variation has been clarified regarding posture's specific angle deflection along the ROM with maximum stress and fatigue tendency variables. These 2 kinesiological variables appear to be appropriate as a magnitude reference for posture's risk index justification.

**Acknowledgements** This research was supported by Universiti Putra Malaysia. We thank our colleagues from ICMPE who provided insight and expertise that greatly assisted the publication

## References

1. McCoy GF, Graham HK, Beverland DE (1984) Isolated injury to the distal radioulnar joint. Case report and cadaver study. *Ulster Med J* 53:155–158
2. McAtamney L, Nigel Corlett E (1993) RULA: a survey method for the investigation of work-related upper limb disorders. *Appl Ergon* 24:91–99
3. Fountain LJ (2003) Examining RULA's postural scoring system with selected physiological and psychophysiological measures. *Int J Occup Saf Ergon* 9:383–392
4. Collie B, Mix C (2011) Kinesiology: The Study of Human Motion, <http://www.hawaiianshirtray.com/anatomy-physiology/kinesiology-study-human-motion/>. Accessed 7 May 2018
5. TechMeAnatomy (2015) The radioulnar joints, <http://teachmeanatomy.info/upper-limb/joints/radioulnar-joints/>. Accessed 7 May 2018
6. Department of Social and Health Service (2003) Range of joint motion evaluation chart
7. Karmegam K, Sapuan SM, Ismail MY et al (2011) Anthropometric study among adults of different ethnicity in Malaysia. *Int J Phys Sci* 6:777–788
8. Winter DA (2009) Biomechanics and motor control of human movement
9. Susan M Moore, Janet Torma-Krajewski, LJS (2011) Report of investigations 9684: practical demonstrations of ergonomic principles. Pittsburgh
10. Place N, Bruton JD, Westerblad H (2009) Mechanisms of fatigue induced by isometric contractions in exercising humans and in mouse isolated single muscle fibres. *Clin Exp Pharmacol Physiol* 36:334–339

# Numerical Investigation of Savonius Rotor Elliptical and the Design Modification on a Blade Shape



Salih Meri AR and Hamidon Bin Salleh

**Abstract** The Savonius turbine has advantages over its counterpart of other species Vertical Axis Wind Turbine, which has a speed-start at the lowest wind speed, but its main problem is a negative torque on the return blade. In this paper, the focus is on reducing this problem and upgrading the performance of the Savonius turbine. The design of the blade shape has been modified to obtain optimal responses (maximum power factor and maximum torque factor). The behaviour of wind energy was studied through a change in the shape of an elliptical blade for the concave side to a wavy surface to the purpose of increasing the area exposed to the thrust force and also to increase the positive torque. Four vertical channels were also created for each blade and parallel to the turbine shaft to reduce the air pressure on the convex side of the blade and thus reduce the negative torque on the same side. The results obtained by numerical testing using the CFD-FLUENT ve 16.1 program are the maximum value of the power coefficient equals 0.276, compared with the experimental test maximum power coefficient of the classical form of the elliptical form 0.25.

**Keywords** Savonius rotor · CFD-Fluent · Design modification · Coefficient of power

## 1 Introduction

As a result of the increasing rise in the prices of fuel and its polluting emissions of the atmosphere, researchers have tended to pay attention to green technology, especially wind energy to generate electric power and to move away from the generators of electric power that works with oil [1].

---

S. Meri AR (✉)

Faculty of Mechanical and Manufacturing Engineering, University Tun Hussein Onn Malaysia (UTHM), Parit Raja, Batupahat, Johor, Malaysia  
e-mail: [almerly123@gmail.com](mailto:almerly123@gmail.com)

S. Meri AR · H. Bin Salleh

Iraqi Cement State Company, Ministry of Industry and Minerals, Baghdad, Iraq

© Springer Nature Singapore Pte Ltd. 2020

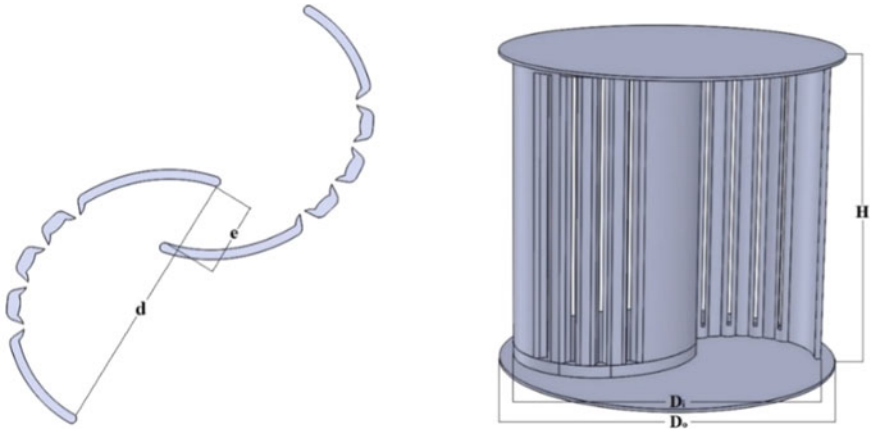
M. Awang et al. (eds.), *Advances in Material Sciences and Engineering*, Lecture Notes in Mechanical Engineering, [https://doi.org/10.1007/978-981-13-8297-0\\_20](https://doi.org/10.1007/978-981-13-8297-0_20)



Wind turbines are devices that utilize wind energy and convert them into electrical or mechanical power. They are divided into two groups depending on the direction of the axis of rotation with the wind direction, namely the horizontal axis wind turbines and vertical axis wind turbines. The vertical axis wind turbine is a device relatively small in size and does not require routers because it receive wind in all directions, therefore can be used in urban areas for electric power generation, and have the installation costs and components are lower compared to the first type [2]. Savonius is the first to invent a wind-powered system in 1920; therefore, it is called as his name (Savonius), which is based on the principle of drag. Since a non-complex design consists of two semi-circular blades that are similar to the letter “S”, the manufacturing is simple and low-cost. It also has a low-speed start and a low noise level. From that period, increased attention to the development of the Savonius system and to consider the engineering parameters of the effect on the efficiency of turbine performance (such as TSR-tip speed ratio ( $\lambda$ ), the ratio of height H to diameter D, overlap ratio  $e/d$ , the shape of a blade) [3, 4]. The main problem that reduces the efficiency of the Savonius turbine is the negative torque confrontation the rotor on the convex blade, therefore, the design of the blade shape has attracted the greatest interest of researchers. Study of the effect of the geometry parameter (shape of the blade) of the Savonius type was the focus on decrease the negative torque and to obtain the highest of the performance than the other types. The increases in power coefficients for each type were (blade shape of the classic Savonius 4.2%), (blade shape of the Benesh rotor 11.1%), (blade shape of the elliptical rotor 22.8%) and (blade shape of the Developer Bach rotor 31.6%) [5].

Three-dimensional experimental tests were carried out for the design of the Savonius rotor by means of venting and covering in the blade, which is intended to create different pressure on both sides of the feather. The validation of the two tests showed positive results in improved performance compared to the conventional rotor [6]. Others also studied the effect of the overlap ratio between blades of the rotor. The optimal overlaps ratio are at a range of 0–0.15 [7, 8].

Some literary verifications were found focussing on the change in the form of the blade of the Savonius rotor such as the classical Savonius rotor [9], Bach [10, 11], the modified rotor of Bach type [5, 12], Banish [12] and the twisted blade [13]. There is an evidence for preliminary studies of the elliptic shape with the possibility of using in the application of rotor Savonius which showed that the elliptical rotor of the concave side of the increase in the total pressure and the tip losses is less compared to the classic rotor [10]. These features encourage a comprehensive study focuses geometry parameters for the Savonius turbine with the aim of reaching the design of Savonius elliptical rotor optimization by following up the previous numerical and experimental investigations.



**Fig. 1** Model of a new Savonius elliptical rotor

**Table 1** Description of geometric parameters

Geometric parameter	Value (mm)	Geometric parameter	Value
Chord length $d$	115	Overlap ratio $e/D_i$	0.15
Rotor diameter $D_i$	200	Aspect ratio $H/D$	1
End plate diameter $D_o$	220	No. of blade	2
Height of the blade $H$	200	No. of channels	8

## 2 Problem Statement

The main problems affecting the performance of the Savonius rotor are negative torque which intercepts the movement of the rotor blades from the convex side. Therefore, the goal of this study is to rely on the blade shape of the elliptical type after verification of the experimental results of the research Sanusi et al. [15] using numerical tests (CFD-FLUENT) ve. 16.1. Then, the study develops and improves the performance of the Savonius rotor to obtain the highest coefficient of power through the creation of four vertical and parallel channels of the axis of rotation for each blade and appropriate entry angles of the convex blade to reduce the negative torque of the rotor and to reduce the load on the axis of rotation caused by a force of thrust on the rotor as shown in Fig. (1) and Table (1) illustrates the geometric parameters.

### 3 Numerical Investigation

In this study, the focus will be on three non-dimensional entities used globally that are depended on to extract the performance coefficient of the Savonius turbine. First: the power coefficient  $P_f$  describes the energy conversion efficiency of the turbine, second: the torque coefficient  $T_f$  is a non-dimensional representation of rotor torque, which is proportional to power produced, and third: the tip speed ratio is defined as the ratio of the blade tip speed (TSR or  $\lambda$ ) to the free-stream wind speed  $V$  [14].

$$P_f = \frac{\text{Output (power turbine)}}{\text{Input (power available)}} \quad (1)$$

$$P_{\text{available}} = \frac{1}{2} \rho A V^3 \quad (2)$$

$$P_{\text{turbine}} = \frac{2 \pi N T}{60} = T \omega \quad (3)$$

$$\text{TSR} = \frac{\omega R}{V} = \lambda \quad (4)$$

$$T_f = \frac{T}{\frac{1}{2} \rho A r V^2} \quad (5)$$

$$P_f = \frac{T \omega}{\frac{1}{2} \rho A V^3} = \frac{T}{\frac{1}{2} \rho A R V^2} \frac{\omega R}{V} = C_T \lambda \quad (6)$$

where  $P$  is the power,  $T$  is the rotational torque,  $N$  is the revolution per minute (rpm),  $\omega$  is the rotating speed of rotor (rad/s),  $\rho$  is the air density (kg/m<sup>3</sup>),  $A$  is the swept area of the turbine (m), and  $R$  is the rotor reduce.

The experimental results were investigated numerically of the researchers Sanusi et al. [15] using the program (CFD-FLUENT) for Savonius elliptical rotor, made of aluminium material with an overlap ratio between the blades is 0.15 and aspect ratio ( $D/H = 1$ ). The experimental test used an open system wind tunnel and depended on wind speed inlet (5.999 m/s). The maximum power coefficient obtained by the researchers was  $P_{fmax} = 0.25$ . The parameters that affect the performance for Savonius turbine are the presence of an overlap ratio between the two blades, the ratio of the rotor diameter to the height, the shape of the blade (control of the blade arc), the number of rotor blades, add or not adding the end plate, number of stages and angle twisting of the blade. The improvement in the ratio of the rotor to height increases the turbine performance [16]. The end plates in the Savonius rotor are fixed at the top and bottom of the turbine and the particular thickness has an effective increase in the coefficient of power [6], which makes control of the flow and its concentration on the concave blade better [17]. The overlap ratio between the blades rotor has a shown importance and through previous studies in increasing and improving the efficiency of the turbine, it allows the gap to reduce the pressure to the return blade on the suction side [18]. Therefore, the interference ratio was studied by many researchers as it is significant in improving the performance of Savonius turbines [19, 20].

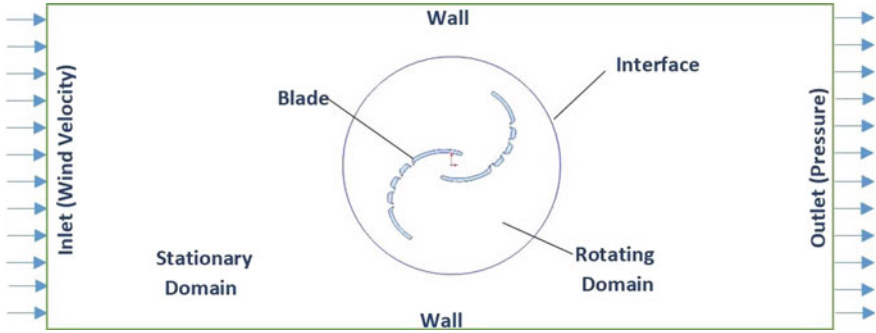


Fig. 2 Computational domain and boundary conditions

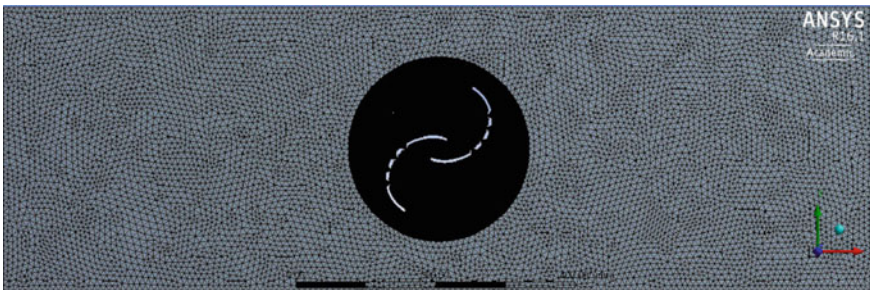


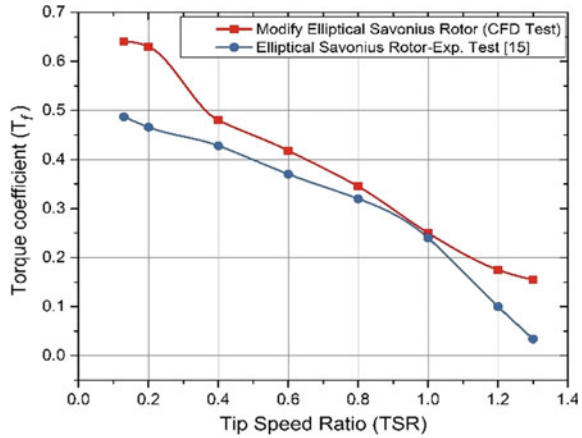
Fig. 3 Computational grid (ANSYS Mesh)

### 4 Results and Discussion

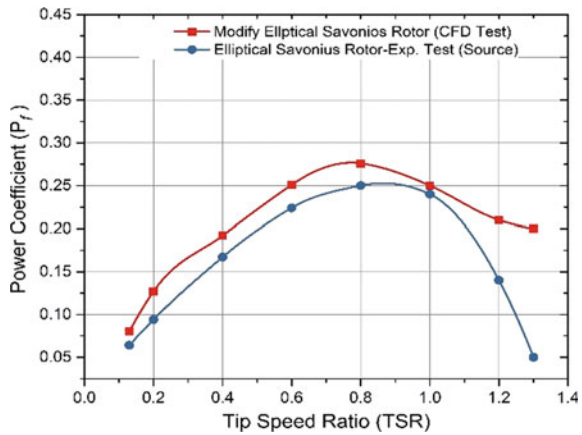
The length of the analytical domain was 120 cm in parallel to the wind flow and 40 cm in the vertical direction of the wind, based on the measurement of the wind tunnel test section of the aerodynamic laboratory in University Tun Hussein Onn Malaysia (UTHM). The numerical test of the Savonius turbine consists of the analysis domain represented by the rectangle form and the modified rotor design is a circular shape centred in the centre as shown in Fig. 2. In this paper, to generate a grid for two-dimensional numerical analysis of the study, where the grid is created for the test model by the most important part (ANSYS Mesh) in the numerical analysis program (CFD-Computational fluid dynamics). The total number of elements and nodes were obtained with 80,000 and 40,000 respectively after finding the best reference values for Skewness, which reached a maximum value at 0.45 as shown in Fig. 3.

The flow around the Savonius rotor is assumed to be unsteady and turbulent, operating at a free stream wind speed of 5.999 m/s. With the SST  $k-\omega$  turbulence model [21], at  $V = 5.999$  m/s, 2D simulations (transient time) are carried out on modifying elliptical Savonius wind turbine with blade overlap ratio (0.15). The torque coefficient ( $T_f$ ) and the power coefficient ( $P_f$ ) obtained are shown in Figs. 4 and 5, respectively.

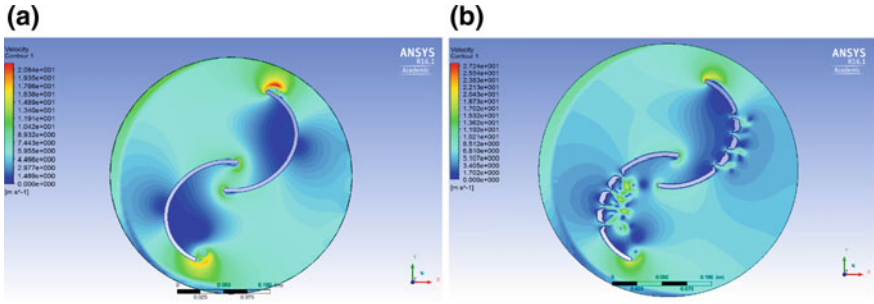
**Fig. 4** Torque coefficients  $T_f$  obtained using CFD analysis



**Fig. 5** Power coefficients  $P_f$  obtained using CFD analysis



The variation of  $T_f$  show the effect of rotational speed on the torque generated by the turbine. It indicates that gradual decrease in the generated torque increases the rotational speed of the turbine. This phenomenon is analogous to the electrical loading on the turbine, where with the gradual application of the electrical load, the turbine torque increases, which in turn, reduces the rotational speed of the turbine. In this process, to modify elliptical Savonius wind turbine with blade overlap ratio (0.15), the highest  $P_f$  of (0.276) is obtained at  $TSR = 0.8$  with the assumption the density of air is  $1.185 \text{ kg/m}^3$  at  $25 \text{ }^\circ\text{C}$  and  $1 \text{ atm}$ .



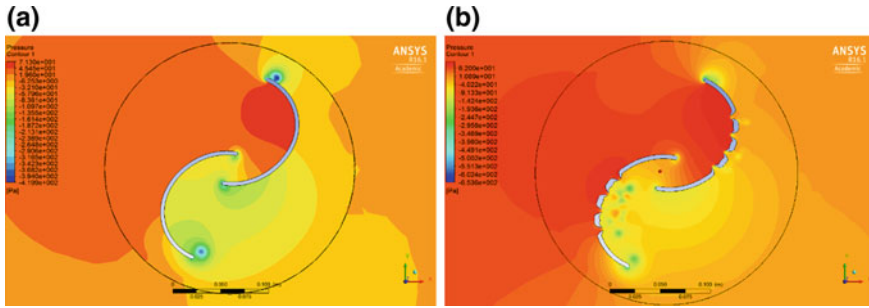
**Fig. 6** Velocity contours: **a** Conventional Savonius elliptical rotor. **b** New Savonius elliptical rotor

### 4.1 Velocity Contours

Figure 6a, b shows the distribution of velocity contours through the Savonius rotor for a conventional elliptical rotor and new Savonius elliptical rotor (modified design) so that the maximum speed and minimum values are represented as red and blue colour respectively. As shown in Fig. 6b, the speed goes up near the side of the concave blade and less to the convex blade side of the rotor. Therefore, the distribution of the velocity around the rotor blades is better because the loss of the tip speed is lower for the modified Savonius turbine compared to the conventional elliptical turbine. There is a significant decrease in negative torque on the convex side of the rotor due the holes vent (4 channels) on the convex side of the blade, and the wind power conservation from loss through the distribution of air on the internal surface curves in a homogeneous manner and also because of its small holes vent on the concave feather side making the wind velocity difference is clear as shown in Fig. 6b.

### 4.2 Pressure Contours

Figure 7. At part (a) and (b) show the distribution of pressure contours around the Savonius rotor for the conventional elliptical rotor and new Savonius elliptical rotor (modified design). All pressure lines on the XY are shown at wind speed (5.999 m/s) with the best tip value (0.8) at maximum power coefficient. The maximum and minimum pressure values are red and blue, respectively, it notes that the amount of pressure applied to the convex blade side of the modified design is decreased due to the presence of ventilation holes (4 channels) along the blade, as shown in Fig. 7b. Resulting in lower wind flow resistance on the surface of the convex blade as well as negative torque values compared to the convex blade surface of the classical elliptical Savellius turbine.



**Fig. 7** Pressure contours: (a) Conventional Savonius elliptical rotor. (b) New Savonius elliptical rotor

## 5 Conclusion

Within the framework of this study, a numerical simulation was carried out to investigate of experimental results a two-dimensional by the program CFD-Fluent of the Savonius elliptical turbine with an overlap ratio (0.15) at the speed of the wind flow (5.999 m/s). The objective of the current study is to develop and improve the performance of the Savonius elliptical rotor to obtain the highest coefficient of power through the creation of four vertical and parallel channels of the axis of rotation for each blade and appropriate entry angles of the convex blade. It works to reduce of the pressure on the return blade from the convex side and will also reduce the negative torque of the turbine. The results obtained the maximum power coefficient  $P_{fmax}$  (0.276) compared with the conventional elliptical Savonius turbine which reaches the maximum power coefficient  $P_{fmax}$  (0.25) [15] for this study. Therefore it is hoped for this numerical study that be useful can future research in experimental tests.

**Acknowledgements** The authors would like to express special thanks to the research team of Energy and Thermofluid Engineering in Faculty of Mechanical and Manufacturing Engineering, University Tun Hussein Onn Malaysia (UTHM) and Iraqi Cement State Company, Ministry of Industry and Minerals, Baghdad, Iraq for their financial and moral support in accomplishing this work.

## References

1. Mohammadi M, Lakestani M, Mohamed MH (2018) Intelligent parameter optimization of Savonius rotor using artificial neural network and genetic algorithm. *Energy* 143:56–68
2. Yang B, Lawn C (2011) Fluid dynamic performance of a vertical axis turbine for tidal currents. *Renew Energy* 36(12):3355–3366
3. Vicente J, Antonio H, Prisco A (2012) A review on the performance of Savonius wind turbines. *Renew Sustain Energy Rev* 16(5):3054–3064

4. Al-Kayiem H, Bhayo BA, Assadi M (2016) Comparative critique on the design parameters and their effect on the performance of S-rotors. *Renew Energy* 99:1306–1317
5. Roy S, Saha UK (2015) Wind tunnel experiments of a newly developed two-bladed Savonius-style wind turbine. *Appl Energy* 137:117–125
6. Plourde BD, Abraham JP, Mowry GS, Minkowycz WJ (2012) Simulations of three-dimensional vertical-axis turbines for communications applications. *Wind Eng* 36(4):443–453
7. El-askary WA, Nasef MH, Abdel-hamid AA, Gad HE (2015) Journal of Wind Engineering Harvesting wind energy for improving performance of Savonius rotor. *J Wind Eng Ind Aerodyn* 139:8–15
8. Nasef MH, El-askary WA, Abdel-hamid AA, Gad HE (2013) Journal of Wind Engineering Evaluation of Savonius rotor performance: Static and dynamic studies. *J Wind Eng Ind Aerodyn* 123:1–11
9. Shaughnessy BM, Probert SD (1992) Partially-blocked Savonius rotor. *Appl Energy* 43(4):239–249
10. Kacprzak K, Liskiewicz G, Sobczak K (2013) Numerical investigation of conventional and modified Savonius wind turbines. *Renew Energy* 60:578–585
11. Ushiyama I, Nagai H (1988) Optimum design configurations and performance of Savonius rotors. *Wind Eng* 12(1):59–75
12. Roy S (2014) Aerodynamic performance evaluation of a novel savonius0style wind turbine through unsteady simulations and wind tunnel experiments
13. Grinspan AS, Saha UK (2005) Experimental investigation of twisted bladed Savonius wind turbine rotor. *Int Energy J* 5
14. MacPhee D, Beyene A (2012) Recent advances in rotor design of vertical axis wind turbines. *Wind Eng* 36(6):647–665
15. Sanusi A, Soeparman S, Wahyudi S, Yuliati L (2017) Performance analysis of a combined blade savonius wind turbines. *Int J Fluid Mach Syst* 10(1):54–62
16. Akwa JV, Vielmo HA, Petry AP (2012) A review on the performance of Savonius wind turbines. *Renew Sustain Energy Rev* 16(5):3054–3064
17. Mohamed MH, Janiga G, Pap E, Thévenin D (2011) Optimal blade shape of a modified Savonius turbine using an obstacle shielding the returning blade. *Energy Convers Manag* 52(1):236–242
18. Roy S, Saha UK (2013) Computational study to assess the influence of overlap ratio on static torque characteristics of a vertical axis wind turbine. *Procedia Eng* 51:694–702
19. Roy S, Saha UK (2013) Review on the numerical investigations into the design and development of Savonius wind rotors. *Renew Sustain Energy Rev* 24:73–83
20. Akwa JV, da Silva Júnior GA, Petry AP (2012) Discussion on the verification of the overlap ratio influence on performance coefficients of a Savonius wind rotor using computational fluid dynamics. *Renewable Energy* 38(1):141–149
21. Saha UK, Alom N (2017) GT2017-64137 arriving at the optimum overlap ratio for an elliptical-bladed. pp 1–10



# High Pressure Die Casting Porosity Defect Analysis and Experimental Validation for Power Steering Columns and DVVTs



M. D. Ibrahim, M. R. Mohamad, L. Roslan, Y. Sunami and S. S. Lam

**Abstract** This paper presents a research study conducted in a local automotive component manufacturer that produces aluminium alloy of Power Steering Column and Dynamic Variable Valve Timing (DVVTs) for local and global markets. The die casting defects that are caused by molten metal during mould filling include gas porosity, shrinkage porosity and air entrapment. However, the control of casting defects has been based on the experience of die casting engineers and trial and error experiments. Trial and error experiments are time consuming and costly which eventually leads to high rate of rejection. This paper presents some numerical simulations which analyzed the filling flow of molten metal, metal solidification behavior and porosity prediction through changes during the heat transfer process from liquid form to solid form using a 3-D computer numerical simulation. The numerical simulation replicated the actual condition of parameter setting on the die casting machine, mould's gating, runner, air vents and cooling design. The numerical result is validated through comparisons with observations made on experimental casting. Results showed a significant confidence in the ability of casting numerical simulation to predict porosity. A location of shrinkage porosity is accurately predicted through significant correlations between numerical simulation of mould filling and casting solidification behaviour. This research will enhance the efficiency of the mass production of die casting the industry with the understanding of porosity defect analysis and its solution, which traditionally relies on trial and error methods, in a way early in its stages of die casting mould and process parameter design.

**Keywords** Die casting · Porosity · ADC12 · CFD · Experimental analysis

---

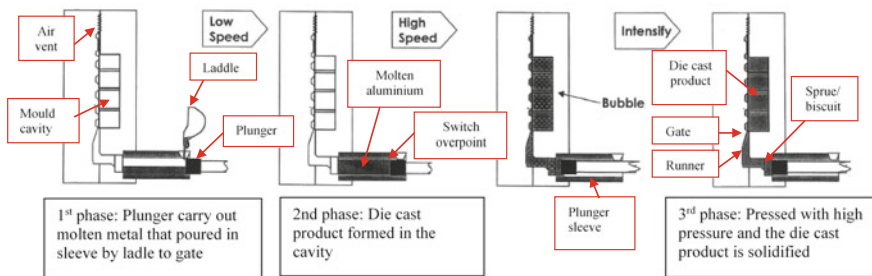
M. D. Ibrahim (✉) · M. R. Mohamad · L. Roslan  
Department of Mechanical and Manufacturing Engineering,  
Universiti Malaysia Sarawak, Kota Samarahan, Sarawak, Malaysia  
e-mail: [imdania@unimas.my](mailto:imdania@unimas.my)

Y. Sunami  
Department of Mechanical Engineering, Tokai University, Kanagawa, Japan

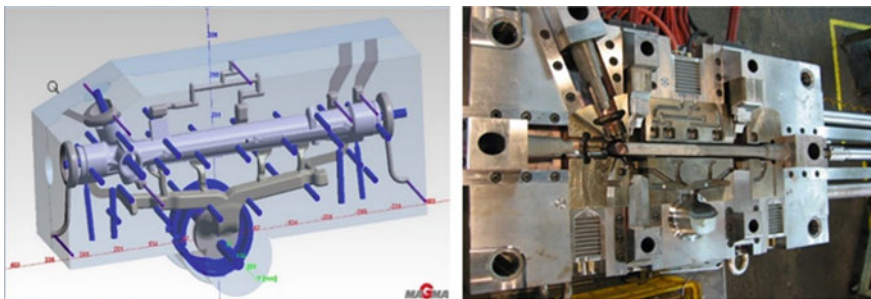
S. S. Lam  
School of Ocean Engineering, Universiti Malaysia Terengganu,  
Kuala Nerus, Terengganu, Malaysia

# 1 Introduction

Common practice of die caster in Malaysia was based on trial and error on innovation and modifications of a die casting mould design to overcome the porosity problem. Generally, experiences from past project are used for future projects applications. As the die castings processes and the die cast products get more and more complex, it became too difficult to still maintain the trial and errors methodology. This situation leads to a lot of wastage of die casted products and production time. The North American Die Casting Association (NADCA) [1] has defined die casting as: A manufacturing process for producing accurately dimensioned, sharply defined, smooth or textured-metal part. It is accomplished by forcing molten under high pressure into reusable metal dies or moulds. High pressure die casting process consists of three main phases as illustrated in Fig. 1. In this study, a computer simulation software of Magmasoft© is used to predict the porosity of the Power Steering Column and DVVTs (Daihatsu Valve Variable Timing) die cast products. In casting simulation, the mould filling and solidification analysis is done by using an algorithm or program based on finite volume method. The simulation programs are also based on Finite Element Analysis of 3-D models of castings. The casting model has to be created using a solid modelling system and imported into the simulation program



**Fig. 1** High pressure die casting process phases [1]

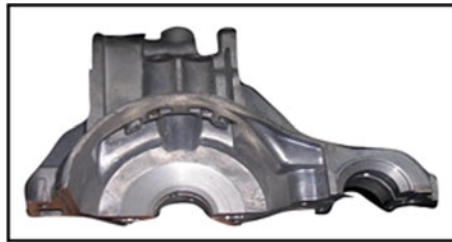


**Fig. 2** The 3-D geometry model of power steering column layout resembles the actual mould condition. Mould dimension is 1117 mm (length) × 650 mm (width) × 650 mm (thickness)

[3]. The numerical input data replicates an actual process parameter, gate and runner design and mould construction. The geometry comparison can be seen in Fig. 2. The simulation result is then validated through an experiment analysis on the actual die casting machine and die casting mould. The accuracy of the prediction porosity is then being compared with the actual porosity found on die cast parts.

## 2 Case Study: Die Cast Automotive Product of Power Steering Column and DDVTs Engine Component

The objective of this simulation is to validate the accuracy of numerical prediction for porosity formation in the die cast product of Power Steering Column and DVVTs as shown in Figs. 3 and 4. These die cast products were chosen because these automotive product require a very high-quality standard and a safety parts for the automotive component. The DVVTs diecast parts control the amount of fuel injected to the combustion compartment of the engine. The Power Steering Column parts control a system that helps in steering the wheels. Any failure on these parts will cause a disaster to the engines and vehicles. In a worst case scenario, fatality may occur if the products failed. The numerical result are then being compared with actual casting parts that is produced during experimental analysis.



**Fig. 3** The diecast of DVVTs



**Fig. 4** The diecast of power steering column

### 3 High Pressure Die Casting Filling and Flow Simulation Model Formulation

The mathematical model and numerical simulation of molten metal in high pressure die casting are more likely belong to casting filling process. This casting filling process is an unsteady flow of incompressible viscous liquid with free surface [8]. This casting filling process can be described by continuity equation, momentum conservation equation, energy equation and volume of fluid-function equation [2, 4, 5, 8].

#### A. Continuity Equation

$$D = \frac{\partial u}{\partial x} + \frac{\partial v}{\partial y} + \frac{\partial w}{\partial z}$$

where  $D$  is the divergence;  $u$ ,  $v$ , and  $w$  are the components of velocity vector in  $x$ ,  $y$ ,  $z$  direction of  $\text{ms}^{-1}$ .

### 4 Heat Transfer in High Pressure Die Casting Model Formulation

In casting process, there are temperature gradients where heat flows from hot regions to cold regions. The heat transfer modes are through conduction in the mould and the solidified casting. In actual die casting processes, the mould cooling system is also important for the casting solidification process to occur efficiently. The heat transfer during casting filling process can be described by the rate of equation of the following Fourier's Law, Heat Diffusion Equation and Newton's Law of Cooling, respectively [2, 4, 8].

#### A. Rate Equation: Fourier's law

$$q_x^n = -\lambda \frac{dT}{dx} \quad \text{or} \quad \frac{q_x}{A} = -\lambda \frac{\Delta T}{\Delta x}$$

where  $q^n$  is the heat flux,  $\text{W/m}^2$ ;  $q$  is the heat rate,  $\text{W}$ ;  $A$  is the area normal to flow,  $\text{m}^2$ ;  $\lambda$  is the thermal conductivity,  $\frac{\text{W}}{\text{mK}}$ ;  $T$  is the temperature,  $\text{K}$  and  $x$  is the distance,  $\text{m}$ .

#### B. Heat Diffusion Equation

$$\rho C_p \frac{\partial T}{\partial t} = \lambda \left( \frac{\partial^2 T}{\partial x^2} + \frac{\partial^2 T}{\partial y^2} + \frac{\partial^2 T}{\partial z^2} \right) + \dot{q}$$

where  $\dot{q}$ ; is the heat rate per unit volume;  $\rho$  is the density  $\left(\frac{\text{kg}}{\text{m}^3}\right)$ ;  $C_p$  is the specific heat  $\left(\frac{\text{kJ}}{\text{kg K}}\right)$ ,  $K$  and  $\lambda$  is the thermal conductivity,  $\frac{\text{W}}{\text{mK}}$  and  $T$  is the temperature.

C. Newton’s Law of Cooling

$$q^n = \frac{q}{A} = h(T_1 - T_2)$$

where  $q^n$  is the heat flux,  $\frac{\text{W}}{\text{m}^2}$ ;  $q$  is the heat rate,  $\text{W}$ ;  $A$  is the area,  $\text{m}^2$ ,  $h$  is the heat transfer coefficient,  $\frac{\text{W}}{\text{m}^2 \text{K}}$  and  $(T_1 - T_2)$  is the temperature difference across the boundary,  $\text{K}$ .

## 5 Formulation of Die Casting Porosity Defect Prediction Model

The mathematical model to predict porosity evolution during solidification was first proposed by Kubo and Pehlke in [5]. In this simulation, the model is used to predict the flow pattern and temperature distribution in the mould cavity during casting solidification and mould filling [6, 7]. The results of temperature distribution and mould filling in the casting model are combined to make porosity predictions. The Basic Equations for porosity prediction are presented in the following Continuity Equation and Equation of Motion [2, 5, 8].

A. Motion Equation

$$u = -\frac{k}{uf_L} (\nabla P_s + \rho_L g)$$

where  $u$  is the interdendritic flow velocity vector,  $k$  is the permeability of the medium,  $f_L$  is the volume fraction of liquid,  $\text{m}^3$ ,  $P_s$  is the shrinkage pressure,  $\text{Pa}$ ,  $\rho_L$  is the density of liquid,  $\left(\frac{\text{kg}}{\text{m}^3}\right)$  and  $g$  is the acceleration due to gravity,  $\text{ms}^{-2}$ . The permeability is defined as [2, 4].

$$k = \frac{f_L^3 d_2^2}{180(1 - f_L)^2}$$

where  $d_2$  is the secondary dendrite arm spacing.

**Table 1** The process parameters used on high pressure die casting machine

Description	DVVTs	Power steering column
Aluminium alloys	ADC12	ADC12
Low speed plunger velocity (1st phase) ( $\text{ms}^{-1}$ )	0.2	0.2
High speed plunger velocity (2nd phase) ( $\text{ms}^{-1}$ )	3.5	3.3
High speed velocity switch over point (mm)	375	390
Metal pressure (3rd phase) (bar)	900	800
Molten metal temperature ( $^{\circ}\text{C}$ )	675	650
Mould temperature fixed and moving half ( $^{\circ}\text{C}$ )	$150 \pm 10$	$150 \pm 10$
Mould materials (steel)	H13	H13
Cycle time (s)	55	60
Mould cooling time (s)	9	10

## 6 The High Pressure Die Casting Process Parameters

The actual casting products were casted using cold chamber high pressure die casting machine. The product is being examined by a cross cut at the location where the porosity has been predicted in the simulation. This is to verify and validate the simulation results. The process' actual setting parameters used on casting machine and in the simulation for DVVTs and Power Steering Column is shown in the Table 1.

## 7 Results and Discussions

Die casting simulation were conducted using numerical commercialized software. In this simulation, several important information, were obtained from the simulation filling, solidification and porosity prediction result. The information from the simulation filling results are metal turbulence, smooth filling, air inclusion, entrapment and the last area to be filled in the casting. The information from the simulation solidification results are the last area of solidification and hotspot area in the casting. The information from the simulation porosity prediction results are all types of porosity. The most important point in the casting is the porosity defect. High volume production and very near net shape make the process very attractive, but the reputation of die castings as having high porosity has heavily restricted the use of the process.

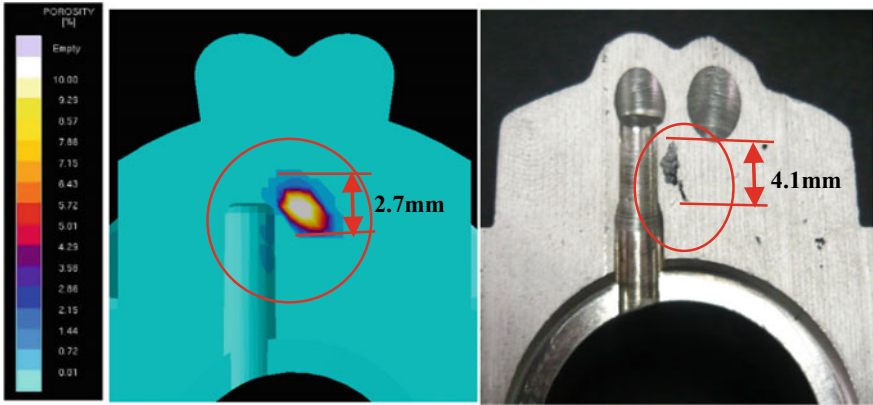


Fig. 5 Location 1, comparison between model and actual cross cut die casted DVVTs products



Fig. 6 Location 2, comparison between model and actual cross cut die casted power steering column products

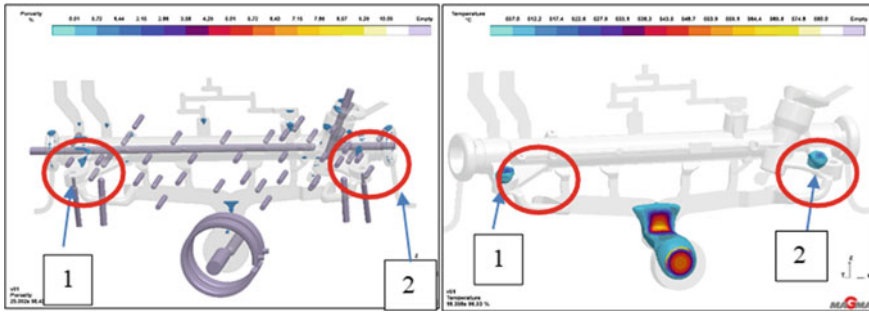
Porosity is one of the biggest problems in the die casting [1]. Porosity was predicted by a porosity simulation at several locations as shown in Figs. 5 and 6. According to the results, the average porosity fraction was between 5–10%. The validation of simulation result is verified through actual casting produced from the experiment on the die casting shop floor. The casting part is examined through a cross cut of casting component at the area porosity and has been predicted by a simulation. These phenomena can be seen from the right-hand side of Figs. 5 and 6. This verifies the result from simulation where it matches with the die casted part.

## 8 Shrinkage Porosity and Casting Solidification Behavior Correlation

In high pressure die casting, there are two major internal types of porosity. It is shrinkage porosity and gas porosity. Gas and shrinkage porosity require almost completely opposite actions for corrections, hence an engineer doing troubleshooting must first identify the type of porosity, otherwise the corrective actions are likely to be little or no value [1]. It is very important for the simulation result to be able to give information so that shrinkage porosity and gas porosity can be differentiated. This will save a lot of very expensive trial and error. Shrinkage porosity occurs because most of the casted metals will occupy less space when they change state. Shrinkage porosity wherever it occurs, will always be at the last point to solidify. This will also be the hottest point in that region of the castings [1]. In the porosity simulation, the results only predicted the location of porosity that might happen in the casting. The results are unable to provide information whether it was a gas porosity or a shrinkage porosity.

In this study, the result of simulation porosity prediction was compared with a casting solidification simulation to identify the type of porosity. Based on the solidification simulation of Power Steering Column, the location of the last point area at castings to solidify was observed and detected. The results matched with the location of porosity predicted by simulation of porosity on the castings as shown in Fig. 7. Most of the casting part has completely solidify after 18 s of molten injected into the mould except at the two areas indicated in blue colour in the same figure. These localized areas temperature is still high, between 507 and 530 °C. By comparing the simulation results from solidification and porosity, there was a significant correlation between the last point at cast to solidify with a shrinkage porosity. From the actual experimental data in Fig. 7, specifically at location 1 and 2, it was found that the porosity predicted by the simulation was found in an agreement with the area where the last point at casting solidifies Taking this correlation, the porosity can be considered as shrinkage porosity. Furthermore, the cross cut of location 2 result has irregular shapes and rough structured shape, shown previously in the most right figure in Fig. 6. The shrinkage porosity can be identified at casting as an irregular and rough dendritic structured shapes compared to gas porosity where it has a round shape [9, 10]. This information is beneficial to the casting engineer and designer to distinguished between porosity caused by gas and porosity caused by shrinkages. This is so that an effective corrective action can be done successfully in a shorter time frame and at a lower cost because it can be detected early, during its simulation stages.





**Fig. 7** Result from simulation shows porosity at casting location 1 and 2 matches the location of last point of power steering column cast to solidify

## 9 Conclusions

This paper concludes that the results of numerical simulation showed the porosity prediction on the die casted DVVTs and Power Steering Column matches the data from experimental analysis. However, the size of porosity prediction through simulation is fairly acceptable compared to the actual size found on the castings surface. The mould filling simulation is useful for casting engineer and designer to accurately design runner system, air vent and overflows without the need of expensive trial and error experiment on the production line. The solidification simulation is capable to determine the last point on casting to solidify. This will give an accurate information whether the porosity was caused by a gas porosity or shrinkage porosity. As result, casting engineers are able to do corrective action effectively. Through the information obtained from the numerical simulation and experimental data, the proposed methods to reduce shrinkage porosity are by using metal savings, squeeze pins and super cooling [1, 9].

## References

1. Wallace WG (1997) Die castings defect—causes and solution. NADCA Publication
2. Magma Engineering Asia Pacific Pte Ltd (2000) 2nd Asia-Pacific MAGMASOFT user group meeting Jun 21st–23rd. MAGMASOFT Manual, pp 13–27
3. Chavan SV, Tavildar RK (2014) Casting defect analysis and optimization using computer aided casting simulation technique. *Int J Innovative Res Sci Eng Technol* 3:1–5
4. Incropera FP, Dewitt DP (1985) *Fundamental of heat and mass transfer*. Wiley, pp 491–949
5. Kubo K, Phelke R (1985) Mathematical modeling of porosity formation in solidification. *Met Trans B* 16B:359–366
6. Wannarumon S, Grande MA (2009) Comparisons of computer fluid dynamic software programs applied to jewelry investment casting process. *World Acad Sci Eng Technol* 55
7. Boydak Ö, Savaş M, Ekici B (2016) A numerical and an experimental investigation of a high-pressure die-casting aluminum alloy. *Int J Metalcast* 10(1):56–69

8. Ibrahim MD, Rahman MRA, Khan AA, Mohamad MR, Suffian MSZM, YunosYS, Mohtar MZ (2017) Effect of mold designs on molten metal behaviour in high-pressure die casting. In: Journal of physics: conference series, vol. 822, no. 1. IOP Publishing, p 012029
9. Kirkman S (1997) Die cast problem solving. NADCA Publication, pp 43–86
10. Cambell J (2003) The new metallurgy of cast metals casting, 2nd edn. Butterworth Heinemann, pp 178–227

# Energy Savings in Manufacturing Plant: Pump System Optimization Case Study in Johor and Sarawak, Malaysia



M. D. Ibrahim, Z. F. Ismail, S. S. Musa and S. S. Lam

**Abstract** This paper presents a preliminary analysis of energy usage and energy savings opportunities in two targeted manufacturing plants, Plant A and Plant B by optimizing their pump systems. Plant A is a manufacturer of Examination Nitrile Powder Free Glove, located in Johor, meanwhile Plant B is a cement manufacturing plant located in Sarawak, Malaysia. Pumping System Assessment Tools (PSAT), is used to assess the efficiency of pumping system operations and to assist in preliminary assessments on the efficiency of the pumping system operation. Annual savings potential for the existing performance of the system can be compared with the optimal condition that is suggested by the PSAT database. Annual savings potential for Plant A is found to be USD 4000, meanwhile for Plant B, annual savings potential that can be saved is up to USD 24,100. For effective implementation, the system's pressure drops can be improved to ensure the pump achieves its best efficiency point, (BEP).

**Keywords** Energy savings opportunity · Pump system · Pump system optimization

## 1 Introduction

From 2010 to 2030, world marketed energy consumption is projected to increase by 33%. In 2030, total world energy use rose from 82,919 Zetawatt (ZW) in 1980 to 116,614 ZW in 2000 and is expected to reach up to 198,654 ZW [1]. The contribution

---

M. D. Ibrahim (✉) · Z. F. Ismail (✉) · S. S. Musa  
Department of Mechanical and Manufacturing Engineering, Universiti  
Malaysia Sarawak, Kota Samarahan, Sarawak, Malaysia  
e-mail: [imdaniel@unimas.my](mailto:imdaniel@unimas.my)

Z. F. Ismail  
e-mail: [zalkhafarhah@gmail.com](mailto:zalkhafarhah@gmail.com)

S. S. Lam  
School of Ocean Engineering, Universiti Malaysia Terengganu,  
Kuala Nerus, Terengganu, Malaysia

© Springer Nature Singapore Pte Ltd. 2020  
M. Awang et al. (eds.), *Advances in Material Sciences  
and Engineering*, Lecture Notes in Mechanical Engineering,  
[https://doi.org/10.1007/978-981-13-8297-0\\_22](https://doi.org/10.1007/978-981-13-8297-0_22)

of industrial sector has been significant, among all the various sectors contributing to greenhouse gas emission, GHG. As reported through a previous study, 10–30% of GHG emissions can be reduced by implementation of a few energy savings options with little or no cost to the industrial sector [2]. The major equipment or drive in a building or plant can reduce energy consumption. It is also estimated that by making use of energy efficient motors in a system, this significant amount of energy can be saved by using better motor loading percentages [3].

In 2011 to 2030, China's cement industry, current energy and carbon dioxide (CO<sub>2</sub>) emission have been analyzed for cement production in different levels. Under the best practice scenarios, the results show potential for cumulative final energy savings of 27.1–37.5 Exajoules, EJ, and energy emission reductions by 1.2 Gigatonnes CO<sub>2</sub> [4]. By 2035, under technical diffusion scenario, eighteen energy efficient technologies result in 25% savings for electricity and 9% savings for fuels, where this has been proved by the study for cement industry in Taiwan [4]. As this industry is the second most energy-intensive user in the country, it is important to understand its promising potentials for energy efficiency improvements. Energy savings by using modified split pump system shows promising result, where it shows that this energy solution as calculated and analyzed by Levelized Cost of Energy (LCOE), is competitive with current retail prices of electricity in the European market. Depending on the considered of hybrid energy solution, the calculated LCOE ranges from 0.440 up to 0.194 USD/kWh [5]. Similarly, most of the plants especially petroleum or chemical plants are committed in reducing energy consumption in terms of thermal, electrical and mechanical in the process equipment used. In most machine such as pumps, fans, compressors and blowers, throttling valves, dampers and adjustable guide vanes are causing mechanical and fluid energy to be dissipated or wasted. Foretold strategies for energy can be applied in the machineries in the rubber industries, which can save a significant amount of energy and some utility bills [6]. 10% of electricity consumption can be reduced by combining or selecting motor savings strategically which is also equal to around 38% of CO<sub>2</sub> emission reductions [7].

In this study, targeted factories use pump to supply cooled water for machine and process. Failure of the pump will cause stoppage of the machine and the worst will cause defect to the production output, thus affecting the quality of the product. In order to adjust the system back to its initial designed best efficiency, current condition of system needs to be monitored. Through optimization of the system, the plant will reduce its baseline consumption, thus, will increase the productivity of the plant.

## 2 Methods

In this study, the targeted factories were approached through walkthrough audit and data collection, to estimate energy usage and energy savings by energy-using equipment or processes for different energy savings measures.

Pumping System Assessment Tools (PSAT) provided by the United Nations Industrial Development Organization is used to analyze the pump system in this study.

PSAT is used to assess the efficiency of pumping system operations. The system uses achievable pump performance data from Hydraulic Institute standards and motor performance data from the Motor Master and database to calculate the potential energy and associated cost savings. The output of the PSAT can estimate pump and motor efficiencies, calculate annual energy usage and energy costs for existing and optimal equipment, potential annual energy savings, and its optimization rating. Data for the current condition of the system has been collected and analyzed.

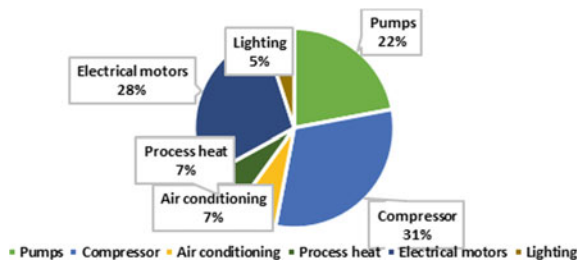
### 3 Findings

Figure 1 shows the energy consumption in Plant A. From the graph, it can be observed that, pumping system is one of the main drives in Plant A which has contributed to the significant energy usage. Thus, in this study, pump has been targeted to reduce the energy consumption of the plant. Graph in Fig. 1 shows that compressor has the highest contribution of the total consumption of the plant with 31%, followed by electrical motors with 28%, pumps with 22% and followed by process heat, air conditioning and lighting. The percentage of energy consumption by the main drive is calculated by considering the specification of the machine, total units of the machine and plant total consumption for year 2016.

Figures 2 and 3 show the targeted pump system diagram in Manufacturing Plant A and location for the targeted pump system. The chiller system supports the plant to supply chilled water to the production line. For glove industry, cooled water is important to ensure the efficiency of the process until final product is made. Figure 4 shows PSAT result in Plant A. It shows that the current pump efficiency is 60.6% as shown at the upper right side (yellow column) of the figure. The database suggests that the system can be operated up to 82.9% as stated in optimal column side, which means the system can run in a more efficient condition than its current state. Figures 5 and 6 show pump head calculation for both conditions A and B.

The flow rate of the pump can be changed to see the difference in the head so that the plot can be constructed. Optimization of the system is important as the efficiency usually drops due to ageing, changes in the process and improper utilization. This will contribute to reliability issue for the system, therefore the current condition

**Fig. 1** Energy consumption in Manufacturing Plant A



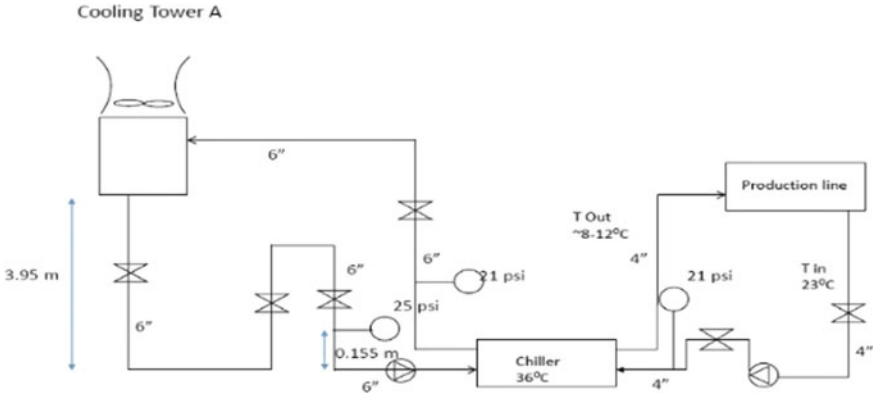


Fig. 2 Targeted pumping system diagram in Plant A

Fig. 3 Targeted pump in Plant A



needs to be monitored to adjust the system back to its best efficiency point. Figure 7 shows the pump curve of the targeted pump, plotted based on current condition.

From the graph, it can be seen that the system should be operated at 80% efficiency (flow rate of about 58 L/s) but the curve shows that the pump is currently operated at 60% region (flow rate of 45 L/s). The pump is operating off from its best efficiency point (BEP) as it should be. From this condition, it can be said that the pump will have reliability issues, which may lead to vibration problems, and shorter lifespan. When the pump operates at flow which is less than the flow designated BEP, this will also induce cavitation, vibration, impeller damages, suction and discharge recirculation to the pump system.

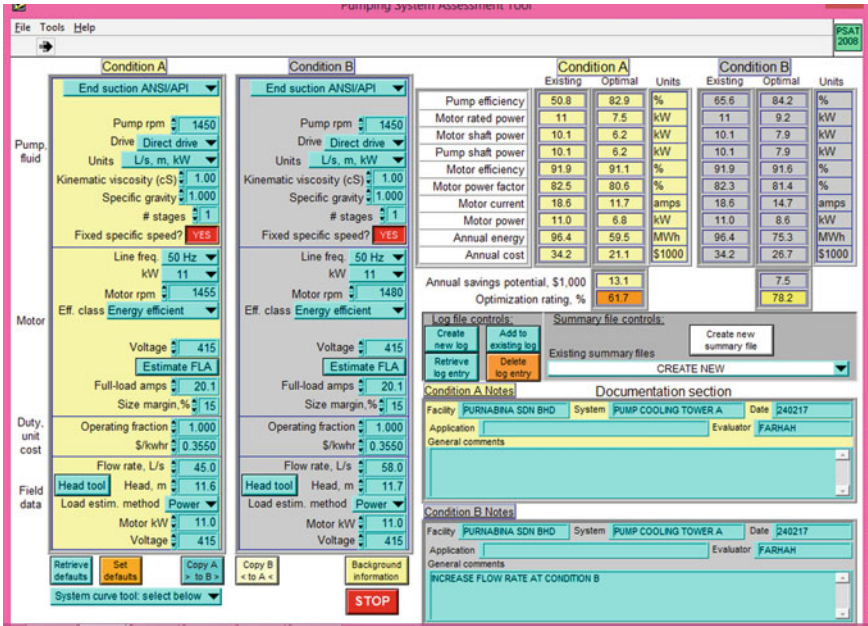


Fig. 4 PSAT result for Manufacturing Plant A

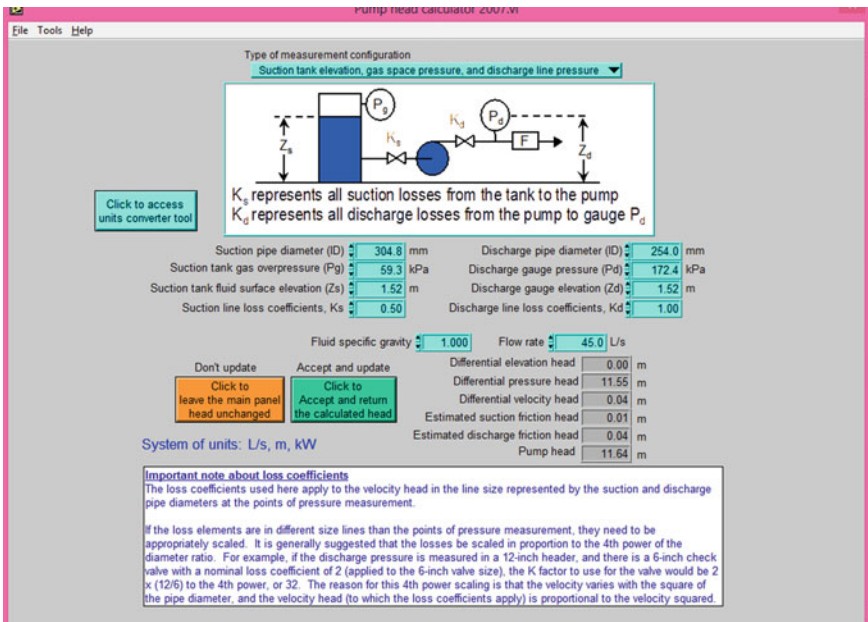


Fig. 5 Pump head for condition A



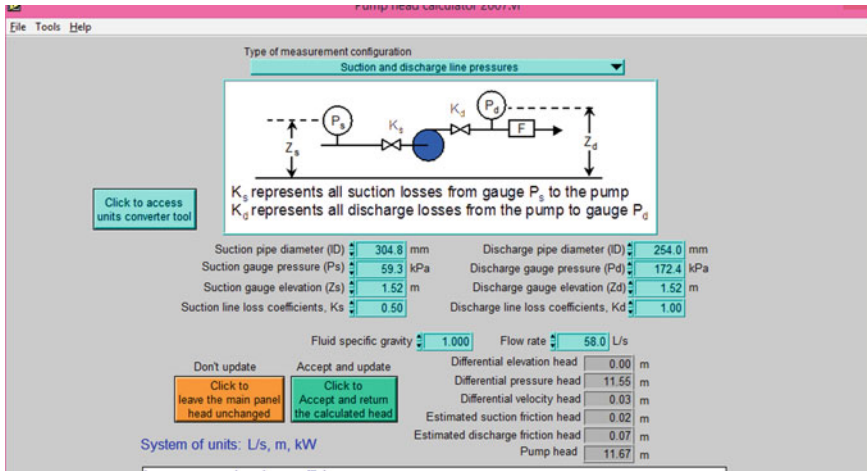


Fig. 6 Pump head for condition B

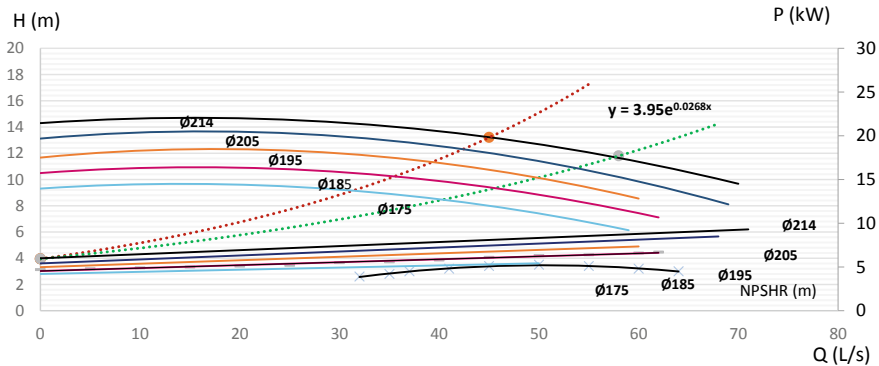


Fig. 7 Pump curve of targeted pump Plant A

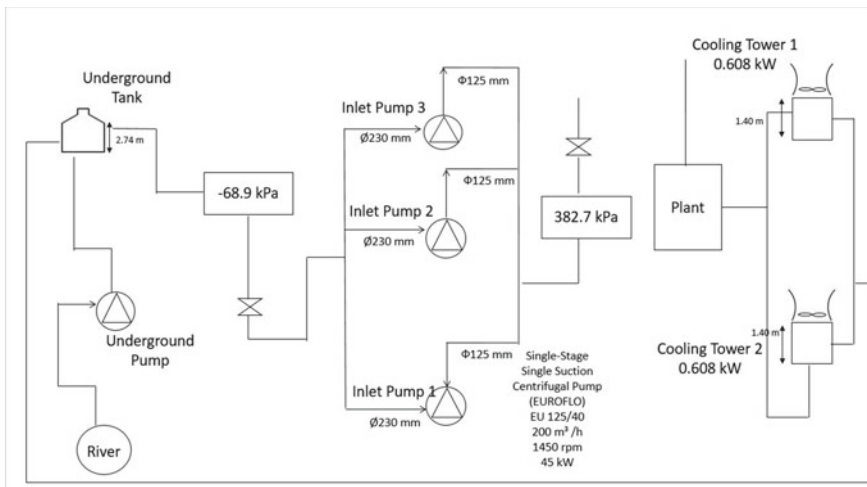
This research study has been carried out in another manufacturing plant located in Sarawak. Same approach was used in this case study. Figures 8 and 9 show targeted pumping system diagram in Plant B. The cooling system is important to the plant as it supplies cooled water to support other machineries like compressor, bearing equipment, cooling tower conditioning, hydraulic oil station and etc. [4].

Pump system of the plant is analyzed by using PSAT. From the results, it shows that the current pump efficiency is 59.5%, shown at the upper right side (yellow column) of the Fig. 10. The database suggests that the system can be operated up to 79.4% as stated in optimal column side, which means the system can run in a more efficient condition than its current state. The proposed system optimizations are the management of Plant B can survey at the market for centrifugal pump with 37 kW motor power, 31.7 kW pump and motor shaft and motor current at 60.6 A to get the





**Fig. 8** Targeted pump in Plant B



**Fig. 9** Targeted pumping system diagram in Plant B

optimal pump efficiency which is at 79.4%. Furthermore, the potential annual savings for the plant is about MYR 96,300 per year or USD 24,100. The annual energy for Plant B also can also be saved from 394.2 to 295.5 MWh. The current annual cost for the selected centrifugal pump is MYR 385,300 per year and if they change the motor and pump to the suggested optimal condition, they will get the annual cost at MYR 289,000 per year. The management can replace the current large pump with a smaller pump available in the market to get more efficient pump system. Otherwise, they can also consider trimming the pump impeller instead of changing the pump

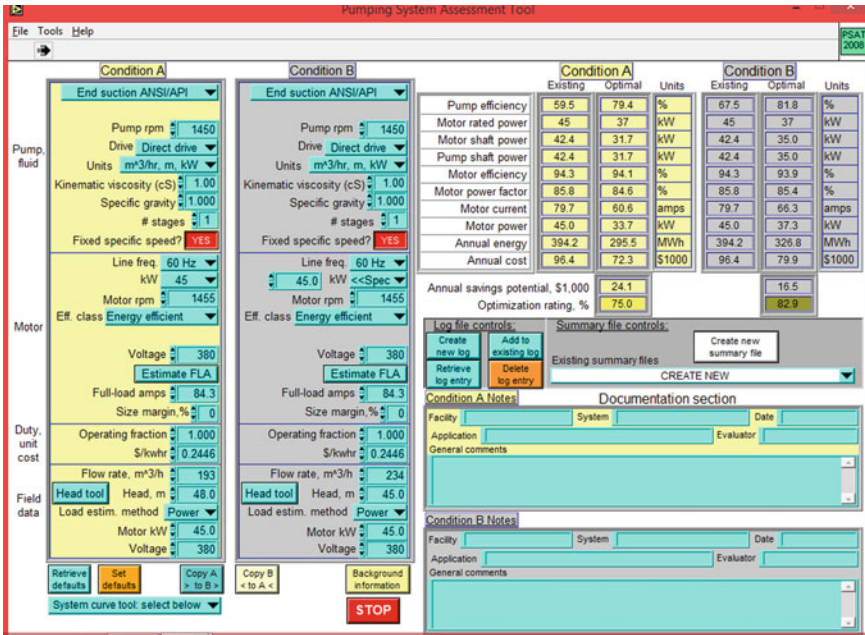


Fig. 10 PSAT result for Manufacturing Plant B

with the new one. Operation of the pump at reduced speed eliminated much of the throttling losses.

From Fig. 10, it shows that from condition A, optimization rating of the system is 75.0%. If the flow rate of the pump is increased from 193 to 234 m<sup>3</sup>/h as shown in Figs. 11 and 12, the optimization can be achieved up to 81.8% compared to current condition (shown in right hand side of the previous figure of Fig. 10 in condition B, grey column). The flow rate of the condition B is inserted in pump head calculation as shown in comparison in Figs. 11 and 12 previously. Thus, the flow rate of the pump can also be changed to see the difference in the pump head. Result shows that the percentage obtained from optimization rating for the pump system running is approximately 75.0%, meanwhile the database suggested that the optimal condition for the system that it can be operated is around 81.8%. It can be concluded that the pump system efficiency can be increased more than 5% from its current operating condition. Figure 13 shows the installation of flow meter at targeted pump to determine its flow rate to obtain the data before been analyzed by PSAT, on-site.

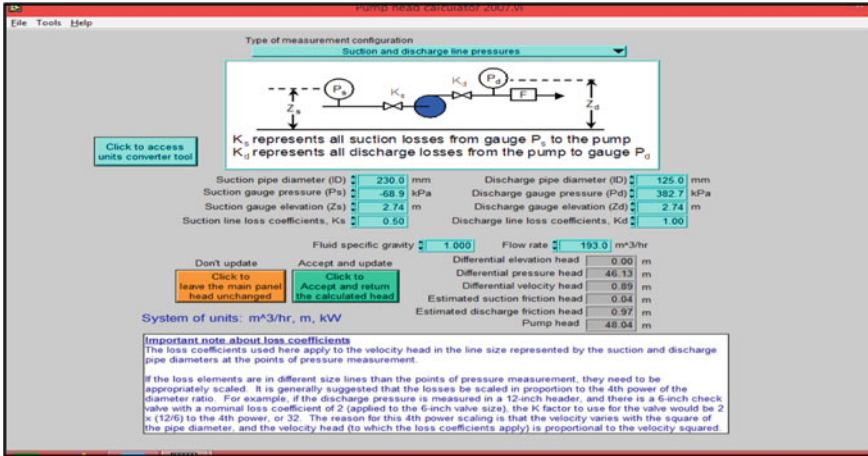


Fig. 11 Pump head for condition A

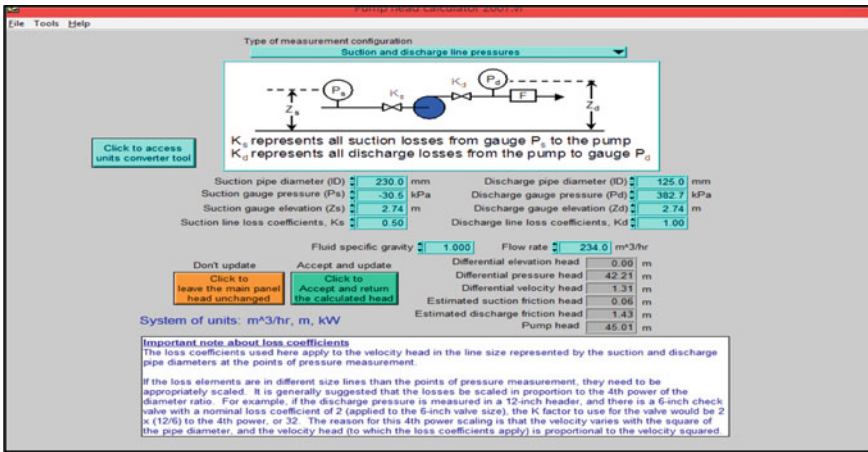


Fig. 12 Pump Head for condition B



Fig. 13 Installation of flow meter to calculate the flow rate of the pump

## 4 Conclusions

This paper investigates the amount of energy that can be saved through optimization of the pump system. The system can be optimized by returning the flow rate of the pump to its designed state to gain better pump efficiency. Based on the results, 13,983.6 kg CO<sub>2</sub> of emission can be reduced from the system improvement in manufacturing of Plant A, meanwhile 126,665.4 kg CO<sub>2</sub> can be reduced from manufacturing of Plant B. Emission of CO<sub>2</sub> still can be reduced without considering the change of the pump size used. Flow rate of the pump can be improved by maintaining the cleanliness of the pipeline and ensuring that there is no friction or blockage in the flow.

This can be done by maintaining the service of the pipeline and minimizing the choking from any unnecessary valves. Thus, the system can be operated in its optimum condition. This implies that systems had improved and there is a potential of saving energy for the system. Future works can be implemented by trimming the impeller to a lower diameter, whereby there will be less power needed to transfer the fluid in the pump, thus increasing the pump efficiency. Improving the pump system as one of the major drives in plant will automatically reduce the total consumption of the plant, therefore reducing the CO<sub>2</sub> emission.

**Acknowledgements** This research was funded by “Low Carbon Organizations Through System Optimization for UNIMAS, Manufacturing Industries and SMEs,” Special FRGS 2016 Cycle, Grant No: F02/SpFRGS/1537/2017, RM20,500, Jan 2017–Dec 2018, in progress.

## References

1. Abdelaziz EA, Saidur R, Mekhilef S (2011) A review on energy saving strategies in industrial sector. *J Renew Sustain Energy Rev* 15:150–168
2. Ghaddar N, Mezher T (1999) Modeling of current and future energy intensity and greenhouse gas emissions of the lebanese industrial sector, assessment of mitigation options. *J Appl Energy* 63:53–74
3. Saidur R (2009) Energy consumption, energy savings, and emission analysis in Malaysian office buildings. *J Energy Policy* 37:4104–4113
4. Ke J, Zheng N, Fridley D et al (2012) Potential energy savings CO<sub>2</sub> emissions reduction of China’s cement industry. *Energy Policy* 45:739–751. <https://doi.org/10.1016/j.enpol.2012.03.065>
5. Nizetic S, Papadopulus AM, Tina GM et al (2017) Hybrid energy scenarios for residential applications based on the heat pump split air conditioning units for operations in the Mediterranean climate conditions, energy and buildings. *J Renew Sustain Energy Rev* 140:110–120
6. Saidur R, Mekhilef S (2010) Energy use, energy savings and emission analysis in the Malaysian rubber producing industries. *J Appl Energy* 87:2746–2758
7. Tanoto Y (2012) Electricity energy saving assessment for induction motors towards sustainable energy practice in indonesian small and medium industry. *J Appl Mech Mater* 229–232:1090–1094

# Virtual Reality Training Platform in Onshore Pipeline



Faieza Abdul Aziz, Adel S. M. A. Alsaeed, Shamsuddin Sulaiman,  
Mohd Khairol Anuar Mohd Ariffin and Abdul Rahman Yahya Al-Arhabi

**Abstract** This paper reviews the possibility to implement Virtual Reality (VR) training platform for maintenance in oil and gas industry. All major oil and gas companies in recent years have advocated design and develop Virtual Maintenance training system for the greater benefit of the humanity and the environment focusing on sustainable development. Oil and gas industry often requires people to work in hazardous environments, these environments are constantly increasing in size and complexity as companies look for new more cost effective ways of doing training and maintenance. Therefore the application of Virtual Reality may allow the new workers to practice and become familiar with the real work using Virtual Environment before performing the real tasks.

**Keywords** Virtual reality · Maintenance · Training · Oil · Generator

## 1 Introduction

Thermoelectric generators (TEGs) have been actively used to regenerate the useful energy from the waste heat and the spread of the application has been increased from microwatts to kilowatts [1]. Oil and gas industry has been a key commodity in today's world. Continuous technology revolution and inventions created high competitive environment for all the industries. Thus, industries and investors have to adapt to the novel technology and innovations to increase their productivity and product quality while minimizing the operational cost and lead time [2].

Thus, implementation of VR technology in training enables an inexpensive, yet significant training environment to be created. In VR training platform, a 3D model is used for interaction and learning purposes. This eliminates the use of plain docu-

---

F. Abdul Aziz (✉) · A. S. M. A. Alsaeed · S. Sulaiman · M. K. A. M. Ariffin · A. R. Y. Al-Arhabi  
Department of Mechanical and Manufacturing Engineering, Faculty of Engineering, Universiti  
Putra Malaysia, 43400 UPM Serdang, Selangor, Malaysia  
e-mail: [faieza@upm.edu.my](mailto:faieza@upm.edu.my)

ments, blueprints and fixed videos, making way for significant and effective training communication among the workers [3].

This research paper focuses on removal and installation of pipes in onshore pipeline of thermoelectric generators (TEGs). Due to the high temperature circulation in the block valve station, the pipes require frequent maintenance activities, where at minimum, the removal and installation of pipes occur within two months' time. According to a study [4] the manual maintenance training is equivalently risky as the actual work environment onshore. The training could turn into a devastating incident and which leads to property damage and loss of life, due to the mistake of trainee. Thus, VR training platform approach is expected to remove the risk present in the current training method and provide an interactive 3D VR based training simulators for workers in TEGs removal and installation of pipes.

## 2 Oil and Gas Industry in Middle East

Middle East LNG is the largest industrial enterprise and it attracts huge foreign direct investment. Besides that, it is among the most modern LNG station in the world. The strategic location of Middle East LNG plant enables it to actively intrude in the markets of Asia, Europe and the Americas. There are various types of facilities and processes that natural gas goes through to obtain the final product. The final product should be free from carbon dioxide, water and mercury.

Middle East LNG plants are associated with advanced facilities and technologies to cater the huge demand. For example, in Yemen LNG, their main pipeline has the capacity of supplying 1.140 million SCf/d of natural gas from the reservoir to the LNG plants. The production capacity of the LNG plant in Yemen is responsible in fulfilling the sale demands in Asian, European and American markets [5].

### 2.1 Theory of Thermoelectric Generator Operation

TEG generates electrical power via the direct conversion of heat energy to electrical energy. The generated electrical power will be directed to the load in a circuit. Despite the variance in temperature, the process of electrical power generation continues as two dissimilar materials are combined and heated. Figure 1 shows LNG Terminals scattered across Middle East Countries. Figure 2 is the illustration of TEG and how the electrical power is generated.

The temperature difference and therefore the amount of power produced, solely depends on the fuel supply rate to the burner. It is also influenced by the amount of cooling supply from ambient air. The physical size data of TEG is as illustrated in Table 1.

In the context of maintenance, TEG is highly reliable as it requires relatively little maintenance activities. Yet, it still requires periodic maintenance checks to ensure



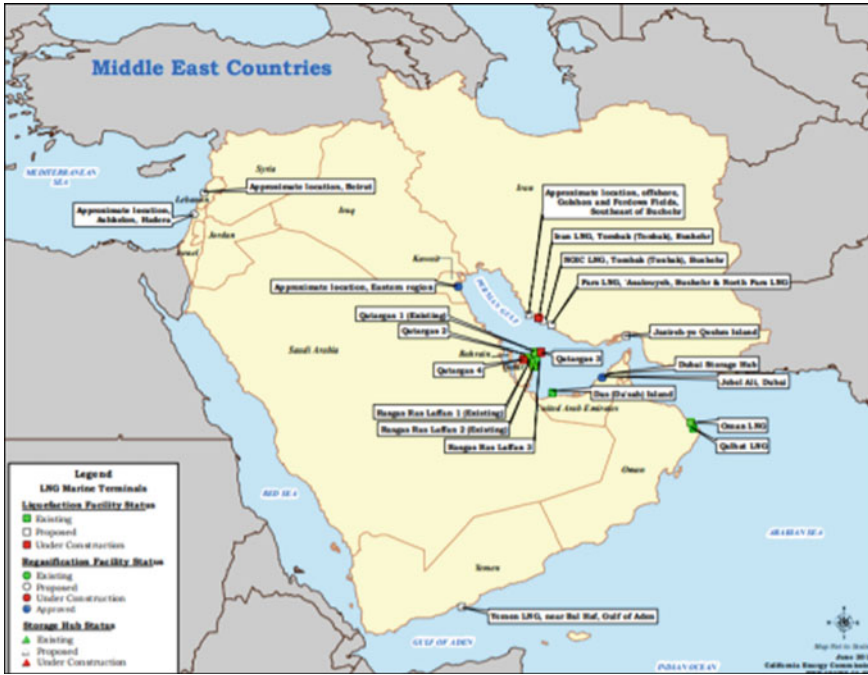


Fig. 1 Middle East Countries LNG Terminals

Table 1 Physical size of thermoelectric generator TEG

Physical size data		
Diameter of top	155 cm	61 in.
Overall height	102 cm	40 in.
Length of lower cabinet	46 cm	18 in.
Width of lower cabinet	46 cm	18 in.
Height of lower cabinet	44 cm	17 in.
Weight (less power conditioner)	83 kg	183 lb

abruption free operation of TEF throughout the year, meeting the capability of and capacity of the TEG. On annual basis, it is necessary to perform power check, to determine if the system is operating at accurate power setting for the current ambient conditions.

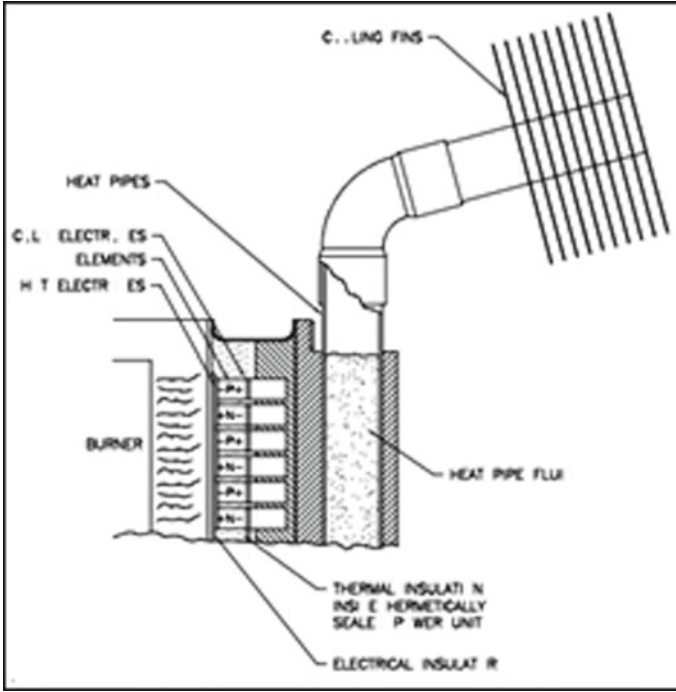


Fig. 2 Illustration of TEG

## 2.2 Maintenance of Cooling System in Onshore Pipeline

Cooling system of the heat pipes consists of 12 set of heat pipes (Fig. 3) and they are hermetically sealed. It contains a specific amount of fluid in equilibrium with its vapor. The heat pipe is filled with methanol and heat is absorbed by the liquid fill, causing it to vaporize. Vapor moves up to the heat pipe till the finned section to condense the vapor. As the ambient temperature varies, the cooling effect on the heat pipe also varies. Greater cooling effect is attained at significantly cooler ambient air.

Figure 4 shows the cut away of the heat pipe. The heat pipe is inspected during the TEG operation. There are two methods of inspecting the heat pipes.

### 2.2.1 Method 1

The first method is to inspect the ability of heat pipe to warm up. If the heat pipe is not able to warm up to 50 mm from the tip, it shall be inspected by using Method 2. During the cold weathers or windy conditions, it is difficult to conduct inspection via Method 1. Even though Method 1 is less accurate, it does not require any additional equipment to conduct the inspection.



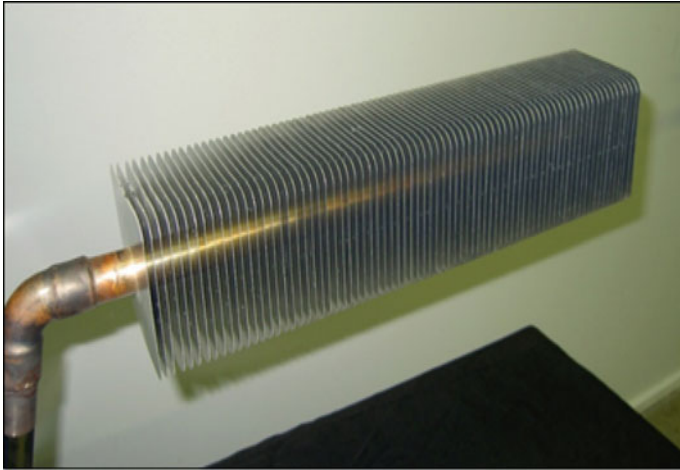


Fig. 3 Heat pipe

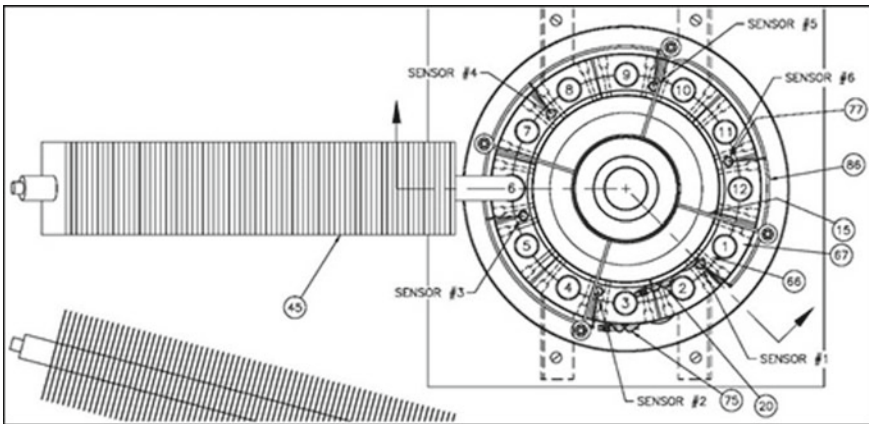


Fig. 4 Cut away of heat pipe Middle East Countries LNG Terminals

### 2.2.2 Method 2

This method requires thermocouple meter and a 50 mm probe with 5 mm or lesser diameter. The thermocouple meter is able to read temperatures up to 150 °C with accuracy level of  $\pm 1$  °C. The method involves the temperature profile of heat pipe condenser tube for analysis as a good heat pipe generates constant temperature profile. Before conducting the inspection, technicians need to ensure the TEG operation hour is more than an hour.

The inspection procedure begins with the temperature profile from the third and fourth fin, from inside, at the bottom surface of the tube. Readings were taken every

50 mm (2 in.) along the Condenser Tube. All readings should be within 5 °C (9 °F) of each other up to the end of the finned section of the Condenser Tube. If the temperature profile drops by more than 5 °C (9 °F) along the finned section, more readings are required to be taken to locate the point where the temperature drops. If this point is within 7 fins of the last fin on the Condenser Tube, or all the readings were within 5 °C (9 °F) of each other, the heat pipe is working well. This method is more accurate and reliable when compared to Method 1.

Commonly, for both methods, it is not advised to conduct heat pipe inspection if the heat pipe is physically damaged or no longer operable. The replacement of heat pipe is done by certified technician only.

### 3 Virtual Reality

#### 3.1 *Attributes of Virtual Reality (VR)*

##### 3.1.1 Immersion

Immersion is a key feature of VR technology. This terminology describes the feeling of a VR user, that his virtual environment is real. A high degree of immersion is equivalent to a realistic or “believable” virtual environment [6]. The term “Immersion” could also be defined as the sensation of being immersed within a virtual environment (VE) [7].

There are several factors which detract from the experience of immersion. They are indicated as: Feedback Lag, Narrow field-of-view, a monoscopic view and low display resolution in order of significance [6]. In addition, the factor of feedback lag is considered as the most important effect with regard to immersion effectiveness, which is represented in related psychological experiments.

Much of the discussion emphasized the significance of fidelity of a virtual environment and visual ‘immersion’ of the user (e.g. by using a head mounted display or CAVE display system) and assessment of how well these support user performance in VR/VE tasks [8, 9].

Uses of immersive VR for training workers in industrial processes have been suggested in the literature. It is reported [10] that an immersive VE for training in manual assembly operations [10] and a virtual machine shop are part of a planning and training tool for machining processes [10] such as: machine tool setup and NC part program execution. In addition, [11] reported in 2006 that a VE was developed to support training in manual welding processes using immersive VR [11].

However, due to various aspects of VR environments that need further research and development, e.g. representation speed, presence, real-time interaction and response, realistic visualization and expensive costs, full immersive VR simulation systems are rarely employed in real industry [12]. The lowest level of VR systems are desktop systems which provide only a monitor-based viewing of virtual objects. The features

of desktop, non-immersive VR systems are far from the possibility of immersive VR technologies, but the main advantage of desktop systems is that standardized computer techniques can be applied [13].

As a result, desktop, non-immersive VR systems have greater applicability for industrial uses compared to immersive VR technologies. The advantage of desktop-based VR systems is to provide a standardized method to support most common computers even including the lowest level of monitor-based computers and this may help to spread the VR application in industry.

### 3.1.2 Presence

While immersion is an objective measure, presence is the subjective sense of being in the virtual environment (VE). Presence requires a self-representation in the VE. For instance: a virtual body (often, only the hand is represented in the VE, since the whole body is not tracked). Presence also requires that participants can identify the movements of a virtual body representing his/her movements [6].

In addition, Sheridan defined presence as the sense of being physically present with the visual, auditory, or force displays generated by the computer [14]. However, a study [15] addressed a simpler definition to the whole concept by introducing that presence as the “feeling of” being in an environment. Another researcher [15] also proposed that if a feeling of presence is not high, then users become detached from the environment, thus resulting in a decrease of performance [15]. This may be true but other factors can also affect performance, like frame-rate, the screen resolution or the VE layout itself [16].

### 3.1.3 Interaction

Interaction is described as any action of the user aiming to modify or probe the virtual environment [6]. In order to achieve a good degree of immersion, it is necessary to develop interaction techniques that are as intuitive as possible. Conventional interaction devices such as key board, mouse and tablet are employed with most VR applications are not adequate enough for natural interaction.

The main drawback of these is their low number of input dimensions, maximally 2. However, a new advanced device allows 6 or more dimensions that allow efficient, natural interaction techniques (Fig. 5).

### 3.1.4 Autonomy

Autonomy reflects the extent to which the environments function on their own, without (and sometimes in spite of) user input. Systems with low autonomy, like many tutorials and practice programs, stayed dormant until students enter an answer to a question or click on a navigation icon. Autonomous environments, on the other



Fig. 5 Advanced inventions to support VR interaction

hand, follow their own goals, evolve and develop whether the user does anything or not. Real-time simulations and many games fall into this category.

#### 4 Advantages and Diadvantages of VR

One major advantage of using virtual reality to teach objectives is that it is highly motivating. An investigation by [17] of the attitude of education students towards virtual reality as a tool in the educational process, and towards virtual learning environments on specific disciplines, found that students had a favorable attitude towards virtual reality in the educational process.

VR grabs and holds the attention of students. This has been documented in the reports of a number of research studies. Students find it exciting and challenging to walk through an environment in three dimensions, interact with an environment, and create their own three dimensional (3D) worlds.

Virtual reality can more accurately illustrate some features, processes, and so forth than by other means. VR allows extreme close-up examination of an object. VR gives the opportunity for insights based on new perspectives. Looking at the model of an object from the inside or the top or bottom shows areas never seen before.

The disadvantages of using virtual reality are primarily related to cost, the time necessary to learn how to use hardware and software, possible health and safety effects, and dealing with possible reluctance to use and integrate new technology into a course or curriculum. As with all new technologies each of these issues may fade as time goes by and virtual reality becomes more commonly used in areas outside of education.

## 5 Summary

This is an on-going project and the breakdown of the project for the design and development of virtual maintenance training system was divided into different phases. The first phase includes documentation of conceptual design, training function and the process of designing and development of VR app and second phase is focused on testing and evaluating the effectiveness of developed virtual training app for heat pipe removal and installation in pipeline of oil and gas industry. The third phase is the comparison between the process performance data, such as time data, recorded during an immersive process execution. Validation will be performed on the developed VR maintenance training platform based on aspects of functionality, reliability, usability, efficiency, maintainability and portability.

**Acknowledgements** The project was funded by International grant—Kuwait PIPPT vote no. 6387700.

## References

1. Montecucco A, Siviter J, Knox AR (2014) The effect of temperature mismatch on thermoelectric generators electrically connected in series and parallel. *Appl Energy* 123:47–54
2. Ji P, Choi AC, Tu L (2002) VDAS: a virtual design and assembly system in a virtual reality environment. *Assembly Autom* 4:337–342
3. Oliveira DM, Cao SC, Hermida XF, Rodríguez FM (2007) Virtual reality system for industrial training. In: *IEEE International Symposium on Industrial Electronics*, June 2007. *ISIE 2007*. IEEE, pp 1715–1720
4. Pantelidis VS (2009) Reasons to use virtual reality in education and training courses and a model to determine when to use virtual reality. *Themes Sci Technol Educ* 2(1–2):59–70
5. Lecuyer P, Martinot B, Meyer E, Thibaut E (2011) Yemen LNG-starter/helper application of VSI+ induction motors for 4 LNG compressor lines (2 LNG trains). In: *Proceedings of the Petroleum and Chemical Industry Conference Europe Conference (PCIC EUROPE)*, June 2011. IEEE, pp 1–7
6. Dai F (1998) Introduction—beyond walkthroughs. In: *Virtual reality for industrial applications*. Springer, Berlin, pp 1–9
7. Vince J (1995) *Virtual reality systems*. Pearson Education India
8. Chryssolouris G, Karabatsou V, Mavrikios D, Fragos D, Pistiolis K, Petrakou E (2000) A virtual environment for assembly design and training. *33rd International CIRP Seminar on Manufacturing Systems*, Stockholm, Sweden, pp 326–330
9. Pausch R, Proffitt D, Williams G (1997) Quantifying immersion in virtual reality. In: *Proceedings of the 24th annual conference on Computer graphics and interactive techniques*, August 1997, pp 13–18
10. Chryssolouris G, Mavrikios D, Fragos D, Karabatsou V, Pistiolis K (2002) A novel virtual experimentation approach to planning and training for manufacturing processes—the virtual machine shop. *Int J Comput Integr Manuf* 15(3):214–221
11. Mavrikios D, Karabatsou V, Fragos D, Chryssolouris G (2006) A prototype virtual reality-based demonstrator for immersive and interactive simulation of welding processes. *Int J Comput Integr Manuf* 19(03):294–300

12. Li Q, Chen X, Cobb S, Eastgate R (2005) Virtual reality applications in fixture assembly and interactive simulation. In: Proceedings of the 11th Annual Conference of the Chinese Automation and Computing Society in the UK (CACSUUK05), Sheffield, UK, 10 September 2005, pp 183–188
13. Jezernik A, Hren G (2003) A solution to integrate computer-aided design (CAD) and virtual reality (VR) databases in design and manufacturing processes. *Int J Adv Manuf Technol* 22(11–12):768–774
14. Sheridan TB (1992) Defining our terms. *Presence: Teleoperators Virtual Environ* 1(2):272–274
15. Steuer J (1992) Defining virtual reality: dimensions determining telepresence. *J Commun* 42(4):73–93
16. Griffiths GD (2001) Virtual environment usability and user competence: the Nottingham Assessment of Interaction within Virtual Environments (NAIVE) tool. Doctoral dissertation, University of Nottingham
17. Shinomiya Y, Nomura J, Yoshida Y, Kimura T (1997) Horseback riding therapy simulator with VR technology. In: Proceedings of the ACM symposium on Virtual reality software and technology, September 1997. ACM, pp 9–14

# Parametric Study of Hydrodynamic Coefficients for Circular Cylinders at Subcritical Reynolds Number



A. M. Al-Yacouby and M. S. Liew

**Abstract** Vortex induced vibrations of circular structures are well known phenomena in many fields of engineering applications. Up to now, most of the experimental investigations are conducted at low Reynolds Numbers. In this study, the hydrodynamic forces and flow around smooth circular cylinders at subcritical Reynolds ( $Re$ ) Number was investigated experimentally in the wave basin. The objective of this study is to conduct a parametric study and determine the important parameters affecting drag coefficient ( $C_D$ ) and lift coefficient ( $C_L$ ). The model tests were conducted in the offshore engineering laboratory at Universiti Teknologi PETRONAS (UTP), Malaysia, using rigid vertical cylinders with various outer diameter  $D_o = 27, 34, 42$  and  $48$  mm. The range of  $Re$  Number achieved in the wave basin varied from  $3.19E+03$  to  $2.83E+04$  which covers the subcritical flow regime. Generally, the values of  $C_D$  determined experimentally varied between 1.12 and 1.23, while the values of  $C_L$  varied between 0.23 and 0.36. The range of these force coefficients are comparable with the recommended values of drag and lift coefficients available in the literature for the similar flow regime.

**Keywords** Drag coefficient · Lift coefficients · Circular cylinders · Subcritical Reynolds Number

## 1 Introduction

Flow around circular cylinders, is a challenging classical problem encountered in many fields of engineering applications related to fluid mechanics. For instance, bridge piers, chimneys, high rise buildings are some examples of engineering applications where circular cylinders are interacting with the incident flow. Many offshore structures such as jacket platforms, jackup, tension-leg platforms, semi-submersibles,

---

A. M. Al-Yacouby (✉) · M. S. Liew  
Civil and Environmental Engineering Department, Universiti  
Teknologi PETRONAS, 32610 Bandar Seri Iskandar, Perak, Malaysia  
e-mail: [ahmad.alyacouby@utp.edu.my](mailto:ahmad.alyacouby@utp.edu.my); [aalyacouby@gmail.com](mailto:aalyacouby@gmail.com)

© Springer Nature Singapore Pte Ltd. 2020  
M. Awang et al. (eds.), *Advances in Material Sciences  
and Engineering*, Lecture Notes in Mechanical Engineering,  
[https://doi.org/10.1007/978-981-13-8297-0\\_24](https://doi.org/10.1007/978-981-13-8297-0_24)

marine pipelines, conductors and production risers contain elements with cylindrical shapes. As the exploration of oil and gas has moved from shallow water to the deep sea, the safety of production risers becomes increasingly important, as fatigue damage caused by Vortex Induced Vibration (VIV) of risers play a crucial importance role in the design of production risers [1]. Despite its simple geometry, flow past a circular cylinder is considered to be an essential starting point for better understanding of more complex flows [2]. The complication of the flow around circular cylinders is mainly associated with the boundary layer, the separated and reattached shear layer and wake interference [3]. Thus, the complex physics of flow around circular cylinders and its real-life engineering applications have attracted the attention of many scientists and engineers for over a century, leading to many successful theoretical and experimental contributions. The review of the literature indicates that several successful studies have been conducted on flow around circular cylinders such as Roshko [4], Morcovin [5], Williamson [6], Achenbach [7] and Bearman [8]. However, only very limited papers addressed the parametric studies in details. Thus, the objective of this study is to conduct a parametric study and determine the important parameters that affect drag ( $C_D$ ) and lift ( $C_L$ ) coefficients. This paper is organized into the following sections. In Sect. 2, the theoretical formulation is briefly presented, In Sect. 3, the experimental set up is presented. Section 4 contains the test results and the investigation of dynamic characteristics of the cylinders and the validation of the results. Finally, some conclusions are drawn in Sect. 5.

## 2 Theoretical Formulations

The dynamics of a circular cylinder subjected to flow induced vibration can be described by a damped spring-mass system with a single degree of freedom in the direction of the imposed harmonic external force [9, 10]. A circular cylinder subjected uniform flow can also be described as a two-degree of freedom system where the structure is allowed to vibrate in the  $x$  and  $y$  directions. In the following sections, important parameters related to flow around circular cylinders, are briefly discussed.

### 2.1 Solution to Vibration Equation

The basic differential equation of motion describing the dynamic and vibration of structures is as follows:

$$m \ddot{y}(t) + c \dot{y}(t) + ky(t) = F(t) \quad (1)$$

In which  $m$  is the total mass of the system,  $-ky$  is the spring force,  $k$  is the spring constant,  $y(t)$  is the displacement of the structure,  $c \dot{y}$  is the damping force in which



$c$  is the viscous damping,  $\ddot{y}$  is the acceleration,  $F(t)$  is the force on the structure and  $t$  is the time. The dot above the symbols indicates differentiation with respect to time [11]. The response of the cylinder  $y(t)$  can be set to be  $y(t) = A \sin(\omega_0 t)$ , where  $A$  is the amplitude of excitation and  $\omega_0 = \sqrt{k/m}$  represents the still water Eigen frequency. Thus, differentiating the response  $y(t)$  with respect to time ( $t$ ) gives  $\dot{y}(t) = \omega_0 A \cos(\omega_0 t) \Rightarrow \ddot{y} = -\omega_0^2 A \sin(\omega_0 t)$ .

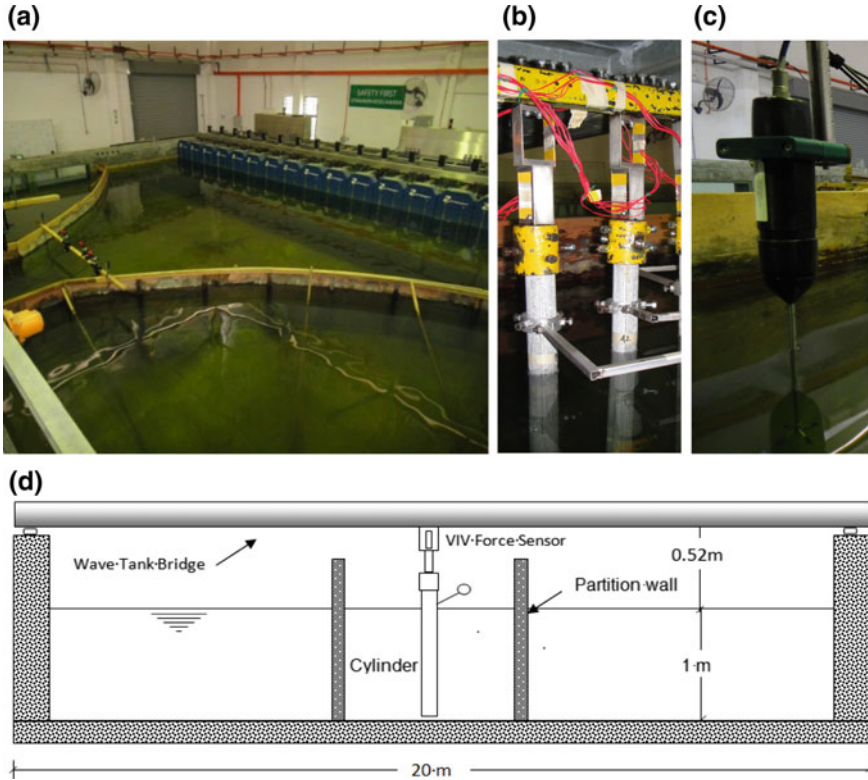
### 3 Experimental Description

Figure 1 shows the wave tank in which the model tests were conducted. The model consists of vertical cylinders made of galvanized steel, flexibly fixed at the top as cantilever beam. The cylinders have a total length  $L = 1.32$  m, with outer diameter,  $D_o = 27, 34, 42$  and  $48$  mm and wall thickness  $t = 2.5$  mm. The wetted length is  $0.98$  m, giving an aspect ratio  $L/D_o = 27.5\text{--}48.9$ . Instead of using the conventional spring setup adopted in VIV model tests, a force sensor was developed custom-made for this purpose (refer to Fig. 1b). The force sensor has  $2$  mm thick walls and acts as spring, allowing the cylinder to oscillate. The top part of the sensor permits motions in  $x$  direction and the bottom part of the sensor acts as a spring permits motion in the  $y$  direction. Thus the model responses in  $x$  and  $y$  direction are ensured and captured. The mass of the pipe  $m$  varied from  $2.5$  to  $4.8$  kg,  $m^* = m/m_d$  in which  $m$  is the mass of the cylinder and  $m_d$  is the mass of the displaced fluid. The displaced mass can be calculated as  $m_d = \pi \rho D^2 L/4$ , where  $\rho$  is the density of the fluid ( $1000$  kg/m<sup>3</sup>).

Furthermore, as the maximum current velocity inside the wave tank was limited to  $0.123$  m/s, and the intention of the experimental study was to investigate the response of the cylinders at subcritical to high  $Re$  Number and the geometry of the wave basin was modified. To achieve higher  $Re$  number using small models, fluid velocity has to be increased, and thus the shape of the wave tank was modified by constructing temporary walls inside the wave tank to form a test section of  $2$  m  $\times$   $3$  m within the wave tank. The optimum layout of the test section and the general layout of the wall configuration were determined using CFD simulations. The effects of walls on the current velocity were analysed using three different CFD proposals. The optimum layout which gives the highest flow velocity was adopted and constructed as the best wall configuration for VIV model tests.

### 4 Parametric Study of a Single Cylinder in Current

The total forces acting on a smooth circular cylinder subject to current can vary with the cylinder diameter, current velocity,  $Re$  Number and the reduced velocity. As the effect of cylinder diameter on the total forces is well established, it is obvious that increasing the cylinder diameters will definitely increase the hydrodynamic forces.



**Fig. 1** Details of model setup: **a** Wave tank, **b** Cylinders fitted with force sensors, **c** Velocity meter, **d** Cross sectional view of the test section

Thus, in the present study, cylinders with relative outer diameters  $D/d = 0.027, 0.034, 0.042$  and  $0.048$  were investigated. The important parameters that can affect the in-line and cross-flow forces and the force coefficients are discussed in the following sections.

### **4.1 Variation of in-Line and Cross-Flow Forces with Current Velocity**

The variation of in-line and cross-flow forces with respect to flow velocities are presented in Figs. 2 and 3 respectively. The plots indicate that increasing the current velocity has a major influence on the measured hydrodynamic forces. The in-line forces varied from 0.071 to 3.47 N, while the cross-flow forces varied from 0.0149 to 0.577 N. From the graphs depicted in Figs. 2 and 3, one can observe that the effect of relative cylinder diameter ( $D/d$ ) on in-line and cross flow forces is very similar to that

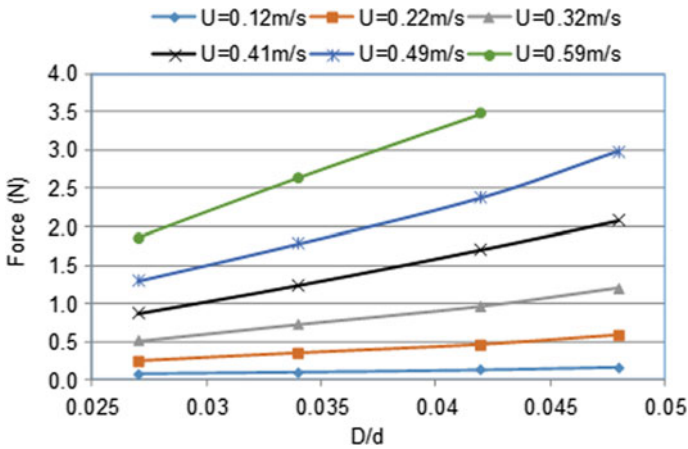


Fig. 2 Variation of in-line force with relative cylinder diameters at different flow velocities

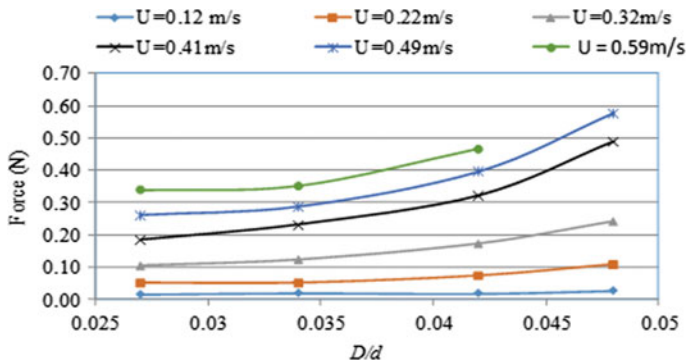


Fig. 3 Variation of cross-flow forces with relative cylinder diameters at different flow velocities

of flow velocities. The plot indicates that the recorded forces increased proportionally with the increasing relative cylinder diameters ( $D/d$ ) as well as with the increased current.

#### 4.2 Variation of in-Line and Cross-Flow Forces with Re Number

$Re$  Number is an important parameter used to present test results pertaining to VIV as the  $Re$  is a function of cylinder diameter, current velocity and kinematic viscosity of the fluid. The variations of in-line and cross-flow forces with  $Re$  Number for different relative cylinder diameters are presented in Figs. 4 and 5 respectively. The

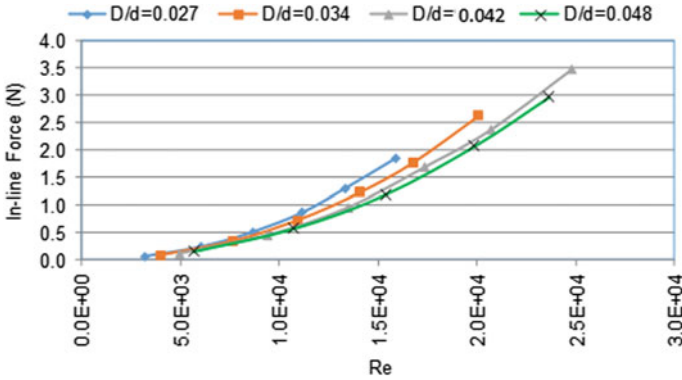


Fig. 4 Variation of in-line forces with  $Re$  for  $D/d = 0.027, 0.034, 0.042$  and  $0.048$

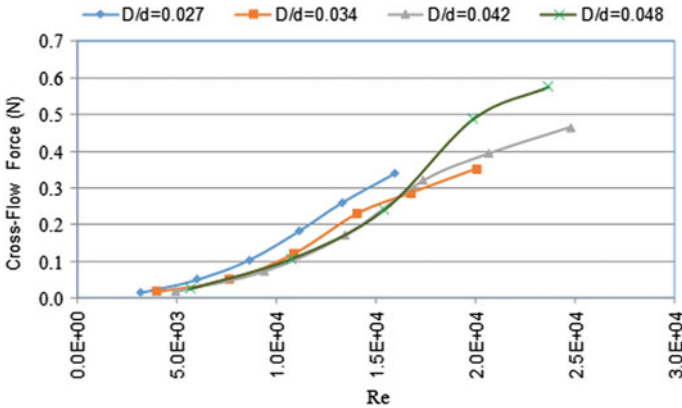


Fig. 5 Variation of cross-flow forces with  $Re$  for  $D/d = 0.027, 0.034, 0.042$  and  $0.048$

graphs show that the range of  $Re$  Number covered in this study varies from  $3.19E+03$  to  $2.83E+04$ , which corresponds to the subcritical flow regime characterized with transition in shear layers. The variation of in-line and cross-flow forces with  $Re$  indicates that these forces increased proportionally with the increasing  $Re$  Number.

### 4.3 Variation of $C_D$ and $C_L$ with $Re$ Number

When a cylinder is exposed to flow with  $Re > 40$  the vortex shedding developed in the wake of the cylinder become time dependent [12], and the drag and lift forces can be estimated as  $C_D = F_D/0.5\rho DLU^2$  and  $C_L = F_L/0.5\rho DLU^2$  respectively. Figure 6 shows the variation of  $C_D$  with  $Re$  Number. The values of drag coefficients for all the different cylinders almost follow the same pattern with respect to  $Re$  Number.

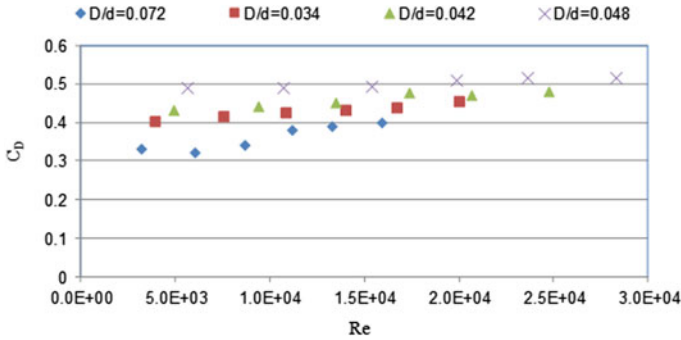


Fig. 6 Variation of  $C_D$  with Re for  $D/d = 0.027, 0.034, 0.042$  and  $0.048$

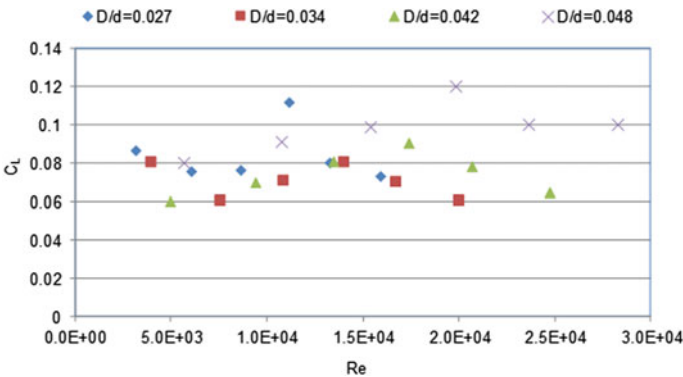


Fig. 7 Variation of  $C_L$  with Re Number for  $D/d = 0.027, 0.034, 0.042$  and  $0.048$

Generally, the range of  $C_D$  Number varied from 0.3 to 0.5 depending on the cylinder diameter and the flow regime. Similarly, the values of  $C_L$  for smooth cylinders with different outer diameters are presented in Fig. 7. The trend of the graph indicates that the values of  $C_L$  are slightly fluctuating as compared to the drag coefficients. But generally, all the four cylinders have shown a consistent trend. The range of  $C_L$  coefficients determined experimentally varied from 0.06 to 0.12. The values of  $C_D$  and  $C_L$  are in good agreement with the published studies available in the literature. For comprehensive studies on variation of  $C_D$  and  $C_M$  with  $Re$  Number, one can refer to Zdravkovich [13] and Sumer and Fredsøe [12].

### 5 Concluding Remarks

The flow around smooth circular cylinders at  $Re$  Number range varied from  $3.19E+03$  to  $2.83E+04$  was investigated experimentally in the wave basin, and the findings

were validated using numerical and experimental data available in the literature. The cylinder specimens used in this research have outer diameter  $D_o = 27, 34, 42$  and  $48$  mm. By comparing the results with the previously published results for the same flow regime, the main findings are as follows:

- The values of  $C_D$  determined experimentally varied between 1.12 and 1.23, while the values of  $C_L$  varied between 0.23 and 0.36. The range of these force coefficients are comparable with the recommended values of drag and lift coefficients available in the literature for the similar flow regime.
- The comparison of the parametric study with the previously published results in the same flow regime shows a good agreement. Therefore, this parametric study appears to be suitable for better understanding the fundamentals of flow structure interactions at subcritical flow regime.

**Acknowledgements** The authors would like to gratefully acknowledge their gratitude to YUTP for funding the presentation of this paper at the conference using YUTP-FRG Project (015LC0-008) and Universiti Teknologi PETRONAS for the supports.

## References

1. Trim AD, Braaten H, Lie H, Tognarelli MA (2005) Experimental investigation of vortex-induced vibration of long marine risers. *J Fluids Struct* 21(3):335–361
2. Zdravkovich M (1997) Flow around circular cylinders. Fundamentals, vol 1. Oxford University Press, New York
3. Ye, H., D. Wan (2017) Benchmark computations for flows around a stationary cylinder with high Reynolds numbers by RANS-overset grid approach. *Appl Ocean Res*
4. Roshko A (1961) Experiments on the flow past a circular cylinder at very high Reynolds number. *J Fluid Mech* 10(3):345–356
5. Morkovin M (1964) Flow around circular cylinders. A kaleidoscope of challenging fluid phenomena. In: ASME Symposium on Fully Separated Flows. ASME, New York
6. Williamson CH (1996) Vortex dynamics in the cylinder wake. *Annu Rev Fluid Mech* 28(1):477–539
7. Achenbach E (1968) Distribution of local pressure and skin friction around a circular cylinder in cross-flow up to  $Re = 5 \times 10^6$ . *J Fluid Mech* 34(4):625–639
8. Bearman P (1969) On vortex shedding from a circular cylinder in the critical Reynolds number regime. *J Fluid Mech* 37(3):577–585
9. Thomson WT (1965) Vibration theory and applications. Prentice-Hall
10. Chakrabarti SK (1987) Hydrodynamics of offshore structures. WIT press
11. Sumer BM (2006) Hydrodynamics around cylindrical structures. World Scientific
12. Sumer BM, Fredsøe J (2010) Hydrodynamics around cylindrical structures. Advanced Series on Ocean Engineering. World Scientific
13. Zdravkovich M (2003) Flow around circular cylinders, vol 1. Fundamentals. *J Fluid Mech* 350:377–378

# Time Step Sensitivity Analysis of a Flow-Driven Savonius Rotor



Ahmad Zakaria and Mohd Shahrul Nizam Ibrahim

**Abstract** The difficulty in choosing the right combination of time step and time increment in simulating a flow-driven rotating rotor is largely attributed to the wind speed dependent time constant which is defined as the elapsed time for the rotor to reach its stable rotational speed. Therefore, a combination of time step and time increment for one wind speed may not work for other wind speeds. A CFD sensitivity analysis of a Savonius rotor is conducted in this study in order to improve its simulation accuracy in predicting the rotor rotational speed by manipulating the time step for a wind speed range of 2–6 m/s. An optimum combination of time step and time increment for minimum error for first are obtained by CFD analysis. Based on a reference parameter of 6 m/s wind speed, other time step for 2, 3, 4 and 5 m/s wind speeds were calculated using the number of revolutions required to reach a steady state rotational speed. The resulted rotational speeds generated were then compared with the actual experiment in an open circuit wind tunnel. It is observed that the rotor only starts to rotate just after zero-time step and gradually accelerates until it reaches a constant rotational speed. Consequently, higher time step is required for low speeds and the converse is true for the high speeds. Lower time step can result in non-convergence solution. The result shows that the predicted RPM of Savonius rotor can be made close to the experimental data at the expense of higher computing time. Accuracy of predicted RPM is within 5% as compared to 20% without sensitivity analysis.

**Keywords** Time step · Sensitivity analysis · Flow-driven · Savonius

---

A. Zakaria (✉) · M. S. N. Ibrahim  
Numerical Simulation Lab, Universiti Kuala Lumpur  
Malaysia Italy Design Institute, Kuala Lumpur, Malaysia  
e-mail: [dzakaria@unikl.edu.my](mailto:dzakaria@unikl.edu.my)

© Springer Nature Singapore Pte Ltd. 2020  
M. Awang et al. (eds.), *Advances in Material Sciences and Engineering*, Lecture Notes in Mechanical Engineering,  
[https://doi.org/10.1007/978-981-13-8297-0\\_25](https://doi.org/10.1007/978-981-13-8297-0_25)

225

## 1 Introduction

Savonius rotors are characterized by its simplicity in design and ease of manufacture. They are widely used in low wind power density regions like Malaysia. Their main advantages over to the horizontal axis wind turbine have been discussed in [1]. The performance of a Savonius rotor can be improved by several methods. These include the addition of the end plate on both ends, aspect ratio (height to diameter ratio), bucket spacing and overlap, number of bucket, and rotor staging design [2]. Various rotor profiles such as semi-circular, twisted, air foil shape, multiple miniature semi-circular and a few more have been suggested by previous researcher in order to increase the Savonius rotor performance [3]. A similar improved performance can be achieved by adding a fin on the rotor blade [4].

Prior to implementation, Savonius rotor's performance can be evaluated by Computational Fluid Dynamic (CFD) analysis. However, the accuracy of such a study is highly dependent on the correct computational parameter, such as azimuthal increment, domain size and number of the turbine revolutions to reach convergence [1]. Grid convergence analysis is very crucial to ensure better rotor torque prediction [5]. A sensitivity analysis is usually performed to determine parameters affecting its output of interest. The values determined can be used as guidelines for others to use.

To date, most analyses on wind turbines are performed in conjunction with the sliding mesh method where a known angular velocity is applied to the rotor during simulation. The optimum rotation speed is then obtained by varying the tip speed ratio (TSR). This study on the other hand uses a flow driven approach in which the rotor is defined as a rigid body. Hence, the rotor is driven by the incoming wind speed due to the net torque generated by angular velocity and moment of inertia. A two bladed Savonius rotor with  $180^\circ$  twist angle was employed as a case study. The main objective was to study the sensitivity in variations of time step on the accuracy of rotational speed of the rotor by using commercial computation fluid dynamic code, AcuSolve.

## 2 Savonius Rotors

A two-bladed Savonius rotor with  $180^\circ$  twist angle used is shown in Fig. 1. The rotor height is 1.0 m and its diameter is 0.5 m.

The rotor is designed to rotate in counter-clockwise (CCW) direction. The basic parameter of the Savonius rotor is given in Table 1.

The ABS prototype model for the experiment was fabricated by using 3D printer. The end plates are made of 0.002 m thick  $\times$  0.55 m diameter Aluminium, thus giving a total weight of the rotor assembly of about 4.0 kg.



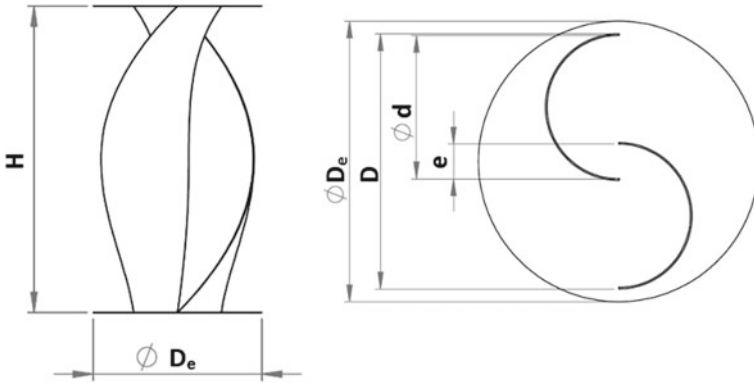


Fig. 1 Savonius rotor parameter

Table 1 Basic parameters of Savonius rotor

Parameter	Value
Overlap ratio, $\delta = e/d$	0.242
Rotor thickness	0.003 m
End plate diameter, $D_e$	1.1 D
End plate thickness	0.002 m

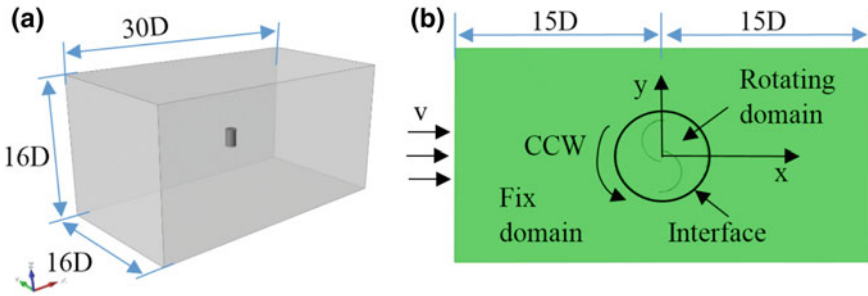
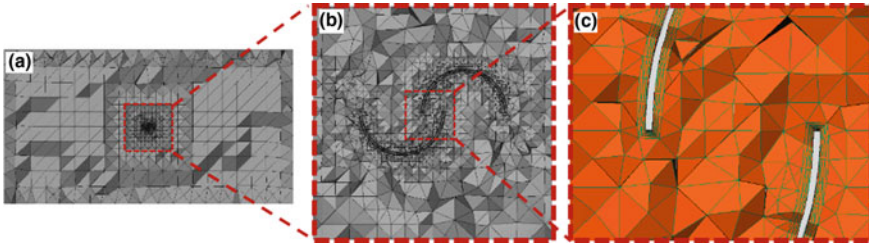


Fig. 2 a 3D domain dimension, b boundary condition

### 3 Computational Domain and Boundary Condition

Figure 2 shows the three-dimensional (3D) computational domain used in this study. The domain size is  $16 D \times 16 D \times 30 D$  (where  $D = 0.5 \text{ m}$ ). The rotor is positioned at the middle of the computational domain to ensure the free stream flow does not disturb the induction field in front of the rotor. The flow will decelerate to lower velocity than the free stream velocity in induction field. This location is also to provide a sufficient distance for turbine wake generations [1].



**Fig. 3** Meshing condition: **a** 3D domain z-axis cross-section, **b** rotating region, **c** boundary layer meshing

### 3.1 Mesh Generation

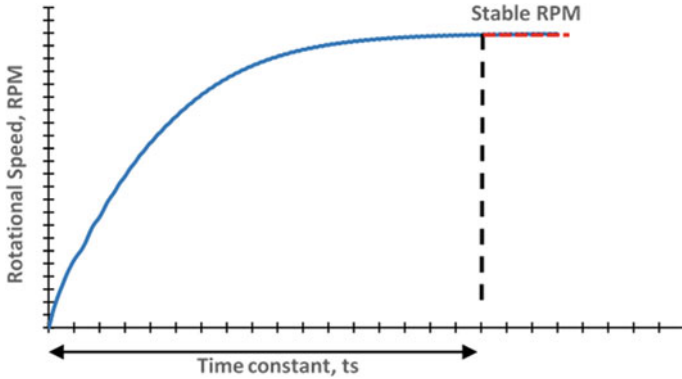
The 3D tetrahedral mesh of 0.05 m around the rotor was created in the computational domain. The rotor surface was fine meshed to 0.01 m with three boundary layers created around the rotor. The cross section of mesh around the rotor is shown in Fig. 3. The denser mesh around the rotor with an addition of boundary layer will improve the accuracy of Savonius rotor torque prediction [6]. A total number of 1,339,710 elements are generated based on the setup parameter.

### 3.2 Boundary Condition and Time Step Calculation

Non-slip boundary condition is applied to the rotor surface. The inlet boundary condition is set to Cartesian velocity on x-axis based on computational domain axis. No boundary conditions are applied to the interface between the rotating domain and fixed domain to allow the transport of flow properties between two domains. The wall boundary condition is set to slip boundary condition. Turbulence model Spalart-Almaras (SA) was selected due to low wind speed operations as suggested by [7].

In the case of a sliding mesh approach, the time step can be estimated by assuming the stable rotational speed is achieved at the beginning of simulation. Hence time step can be calculated by knowing the number of rotor's revolutions before it reaches a stable condition. Typical number of revolution to reach a steady state is between 20 and 30 [1]. On the contrary, a flow driven method as shown in Fig. 4, the rotor will gradually start to rotate just after zero-time step. It will then accelerate until it reaches its stable rotational speed in unit rotation per minute (RPM) indicated by the red dashed line. Minimum time to reach this situation is defined as time step or time constant ( $T_s$ ). Since  $T_s$  is a function of wind speed, it can therefore be estimated by conducting an experiment involving various wind speeds.

The optimum combination of time step and time increment obtained from previous work [8, 9] is used in this study. The best combination of time step = 7000 and time



**Fig. 4** Rotational speed versus time constant in a flow-driven simulation

**Table 2** Time step for specified wind speed

Wind speed, m/s	Time step
2	21,000
3	14,000
4	10,500
5	8400

increment = 0.0015 s give an output rotational speed closer to the actual experiment. These two parameters are termed as the reference values. The following equations are used to generate other time steps for each wind speed.

$$T_{xref} = T_{sref} \times \Delta t \tag{1}$$

$$S = T_{xref} \times V \tag{2}$$

$$N = \frac{S}{2\pi R} \tag{3}$$

$$T_{x=2,3,4,5} = \frac{S}{V} \tag{4}$$

$$T_{s=2,3,4,5} = \frac{T_{x=2,3,4,5}}{\Delta t} \tag{5}$$

where  $T_{xref}$  is total simulation time for reference wind speed,  $T_{sref}$  is reference time step,  $\Delta t$  is time increment,  $S$  is distance travelled for reference wind speed,  $V$  is wind velocity,  $N$  is total number of revolution for stable RPM,  $R$  is rotor radius,  $T_{x=2,3,4,5}$  is simulation time for 2, 3, 4 and 5 m/s wind speed and  $T_{s=2,3,4,5}$  is time step for each wind speed.

The generated time steps for all wind velocities are given in Table 2.

## 4 Results and Discussion

### 4.1 Accuracy of RPM Prediction at Specified Wind Speed

The result of simulated rotational speed of Savonius rotor at different wind speed is shown in Fig. 5. Low wind speeds require longer time step to reach its stable RPM. Similarly, time step required is reduced with the increasing wind speed. Any attempts to use smaller than minimum time step will result in non-convergence solution and poor RPM prediction. This analysis also shows that by using time increment of 0.0015 s, its computational time will be much longer for lower wind speed. It is also observed that at 2 m/s wind speed, the computational time is 93 h. On the contrary it took only 37 h of computational time for 5 m/s wind speed using 16 core machine. Overall accuracy of rotor RPM prediction is shown in Fig. 6. It clearly demonstrates improvement in terms of accuracy after sensitivity analysis done. The overall difference percentage is about 10% as compared to the results obtained without sensitivity analysis of 20% [8].

Figure 6 shows the numerical study result at various wind speed and percent different from the experimental data. The result shows close relationship between the numerical study result and experimental data. With exception of 2 m/s, the error in RPM prediction results for other wind speeds is below 5%.

As stated in Sect. 3.2, a transient flow field is captured in the flow-driven approach. Hence the time step cannot easily be predicted. In this case, the minimum number of rotor revolution (N) to reach a steady state RPM is about 40. If  $N = 20\text{--}30$  as suggested in the literature [1] is used, this will result in non-convergence solution.

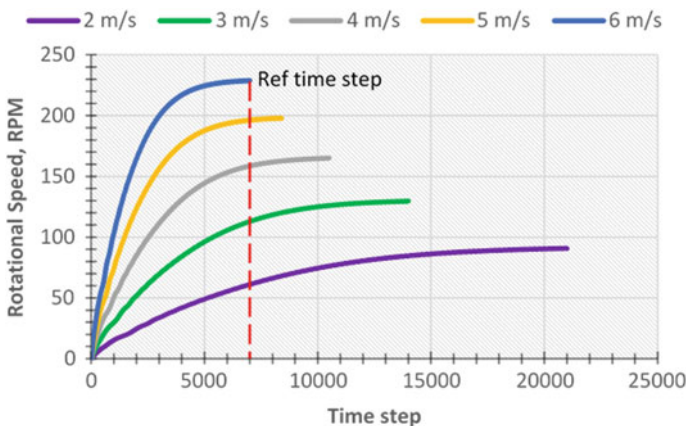


Fig. 5 Time step required to reach stable RPM for different wind speeds

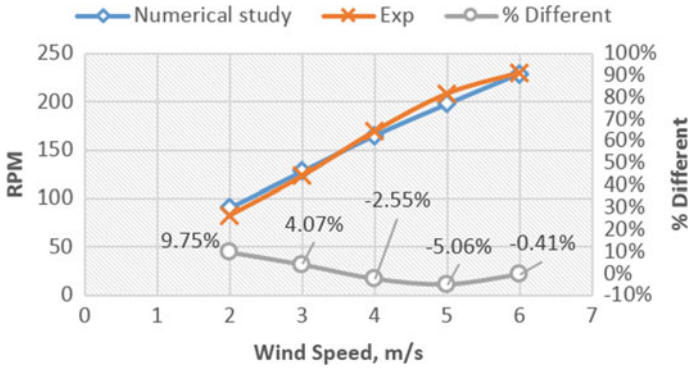


Fig. 6 Savonius rotor RPM prediction at various wind speed

### 5 Conclusions

In this study, a procedure for performing sensitivity analysis of a flow-driven rotating body has been developed. Without the sensitivity analysis, the error in RPM prediction is about 20%. However, with the additional sensitivity analysis done, this error has been reduced to about 5%. It should be noted that time step should properly be selected to ensure convergence and good accuracy.

It is also admitted that similar results could be obtained by the sliding mesh approach. However as mentioned by [8], the flow driven method adopted this study has an edge in terms ease of bench marking against the wind tunnel experimental data in which tip speed ratio (TSR) cannot be implemented in the later. Although the time taken for the analysis is quite high, it can be justified with the availability of affordable higher cores machine.

**Acknowledgements** The authors would like to acknowledge the Malaysian Electricity Supply Trust Account (AAIBE) through the Ministry of Energy, Green Technology and Water Malaysia (KeTTHA) for funding this research.

### References

1. Rezaeiha A, Montazeri H, Blocken B (2018) Towards accurate CFD simulation of vertical axis wind turbine at different tip speed ratios and solidities: guidelines for azimuthal increment, domain size and convergence. *Energy Convers Manag* 156:301–316
2. Pamungkas SF, Wijayanto DS, Saputro H et al (2018) Performance ‘S’ type Savonius wind turbine with variation of fin addition on blade. In: *IOP Conference Series: Materials Science and Engineering*, vol 288
3. Akwa JV, Vielmo HA, Petry AP (2012) A review on the performance of Savonius wind turbines. *Renew Sustain Energy Rev* 16(5):3054–3064
4. Alom A, Saha UK (2018) Four decades of research into the augmentation techniques of Savonius wind turbine rotor. *J Energy Resour Technol* 140(5):050801-1–050801-14

5. Shaheen M, El-Sayed M, Abdallah S (2015) Numerical study of two-bucket Savonius wind turbine cluster. *J Wind Eng Ind Aerodyn* 137:78–89
6. Sharma S, Sharma RK (2016) Performance improvement of Savonius rotor using multiple quarter blades—a CFD investigation. *Energy Convers Manag* 127:43–54
7. Tian W, Song B, Vanzwieten J et al (2015) Computational fluid dynamics prediction of a modified Savonius wind turbine with novel blade shapes. *Energies* 8(8):7915–7929
8. Zakaria A, Ibrahim MSN (2018) Analysis of Savonius rotor performance at low speeds using numerical study. 1st International Joint Conference on Advanced Manufacturing Technology & Simulation (IJCAMTS 2018), 8–9 August, UiTM Shah Alam, Malaysia
9. Zakaria A, Ibrahim MSN, Dezfouli MMS (2018) Comparison of different techniques for modelling and an ultra-low speed vertical wind turbine. NAFEMS 18 UK Conference, 17–18 July, Milton Keynes

# Biosynthesis of Copper Oxide Nanoparticles Using *Camellia Sinensis* Plant Powder



Suriani Ibrahim, Nurul Zariyah Jakaria@Zakaria, Shaifulazuar Rozali, Nik Nazri Nik Ghazali, Mohd Sayuti Ab Karim and Mohd Faizul Mohd Sabri

**Abstract** In this study, copper oxide nanoparticles were prepared by green approach using solution cast method. The mixture of green tea aqueous acts as a bio-reducing agent and copper nitrate is used as metal sources. The copper ions ( $\text{Cu}^{2+}$ ) were reduced by polyphenol in green tea aqueous extract to form copper oxide nanoparticles. The FTIR spectra shown C–H peak represent polyphenol chemical bonding in green tea aqueous solution. As the weight of tea increases, the content of polyphenol in green tea also increases. The structure and morphology of the synthesized copper oxide nanoparticles were characterized using Field Emission Scanning Electron Microscopy (FESEM) and X-Ray diffraction (XRD). The size of the particles was found to be in the range of 100–200 nm. The formation rate of copper oxide nanoparticles is higher as the concentration of polyphenols increases. The optimum copper oxide nanoparticles with the smallest particles size was produced with the amount of 20 g of green tea.

**Keywords** Biosynthesis · *Camellia sinensis* · Copper oxide · Nanoparticles

## 1 Introduction

Copper oxide nanoparticles (CuO NPs) are widely used in various industrial applications including semiconductor devices, sensor, medicine, solar energy and catalyst. The properties of these copper nanoparticles are mostly dependent to the material size, morphology, and the specific surface area of the material, which strongly depend on the preparation method [1]. Smaller size and great porosity that exist in the nanoparticles are capable of performing a higher reaction yield. The usage of copper oxide nanoparticles in various applications has led to numerous studies

---

S. Ibrahim (✉) · N. Z. Jakaria@Zakaria · S. Rozali · N. N. N. Ghazali · M. S. A. Karim · M. F. M. Sabri  
Department of Mechanical Engineering, Faculty of Engineering, University of Malaya, 50603 Kuala Lumpur, Malaysia  
e-mail: [sue\\_83@um.edu.my](mailto:sue_83@um.edu.my)

© Springer Nature Singapore Pte Ltd. 2020  
M. Awang et al. (eds.), *Advances in Material Sciences and Engineering*, Lecture Notes in Mechanical Engineering, [https://doi.org/10.1007/978-981-13-8297-0\\_26](https://doi.org/10.1007/978-981-13-8297-0_26)

of different synthesis method for copper nanoparticles [2, 3]. In achieving a more convenient and less toxic disposal, eco-friendly approach is becoming favourable. The common synthesis procedure will yield to toxic chemical and high in cost [4]. Sometimes, the chemical by-product itself will drain into the soil and water that results in contamination that often leads to mutagens and serious health hazards.

Biosynthesis of nanoparticles by plant has currently received more attentions as it is a suitable alternative compared to chemical and physical methods. Previously, there are multiple studies that have been done on synthesis of the copper oxide nanoparticles by using different plant extract such as from *Carica papaya*, *Azadirachta indica* (Indian Lilac), *Hibiscus rosa-sinensis* (Chinese hibiscus), *Murraya koenigii* (Curry Tree), *Moringa oleifera* (Drumstick Tree) and *Tamarindus indica* (Tamarind tree) [5]. The extract from the plants may act as reducing and capping agent for the nanoparticles synthesis. Different parts of plants such as the leaves, stems, seeds and fruits could be used in the synthesis as the plants exhibit combinations of metabolites [6]. Terpenoids, polyphenols, sugars, alkaloids, phenolic acids and proteins play an important role as the reducing agent in the synthesis [7]. For example, the polyphenolic compounds could release reactive hydrogen atoms that could reduce the metal ions to form nanoparticles.

Thus, in this study, an eco-friendly approach of copper oxide nanoparticle is developed by using plant extract of tea extract aqueous (*Camellia sinensis*). Afterwards, the CuO NPs were tested for the present of ions metal after the characterization test. Besides that, canesis tea has a higher polyphenols contents compared to others fruits like apples [8].

## 2 Methods

### 2.1 Materials

The main material used in this research is the tea powder from plant *Camellia sinensis* obtained from a local store.

### 2.2 Preparation of Tea Extract

The tea extract solutions were prepared by adding 20, 30 and 40 g of the green tea powder into the beaker followed by 200 ml of deionized water. The solution was mixed at 350 rpm for about 2 h. After that, the samples were left for a while to allow the water and the tea to completely dissolve. The samples obtained were filtered and then were kept at 4 °C for further use. The copper nitrate solutions were prepared by using the same technique and stirred at 350 rpm. In this study, the concentration of the copper nitrate solution is 0.5 M.

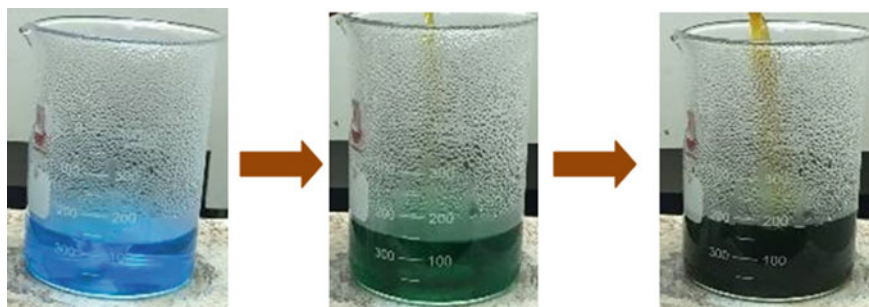


### 2.3 *Copper Oxide Nanoparticles*

The synthesis process starts with stirring and heating of the copper nitrate solution vigorously at 350 rpm until the copper nitrate were completely dissolved. Subsequently, 100 ml of 20 g of tea extract solution was slowly added. The solution was heated at 90 °C and stirred for about one hour. The colour changes gradually from sea blue to brownish, which was indicating the formation of the copper oxide nanoparticles as showed in Fig. 1. After one hour, the mixture was cooled at room temperature. The process was repeated but with different concentrations of tea extracts solution. The precipitates obtained were filtered and rinsed with ethanol. Then, the process is continued by purification of the sample by rinsing the precipitates with distilled water. To remove the moisture from copper oxide nanoparticles, the particles were dried in a conventional oven at 90 °C for 5 h.

### 2.4 *Characterization of Nanoparticles*

It is necessary to characterize the properties of the copper nanoparticles in order to understand the effect of experimental parameter. FESEM with 2 kV was used to determined morphology of the nickel oxide nanoparticles. Energy Dispersive X-ray Spectrometry (EDX) is a microanalysis technique that is used to validate and confirm the existence of copper oxide element in the nanoparticles.



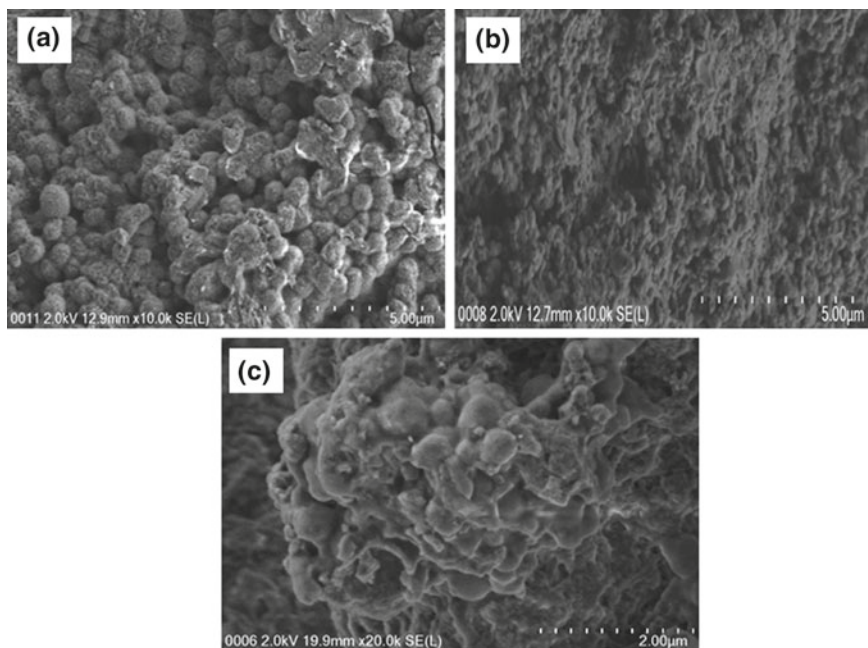
**Fig. 1** Colour changing during biosynthesis of copper oxide nanoparticles

### 3 Results and Discussion

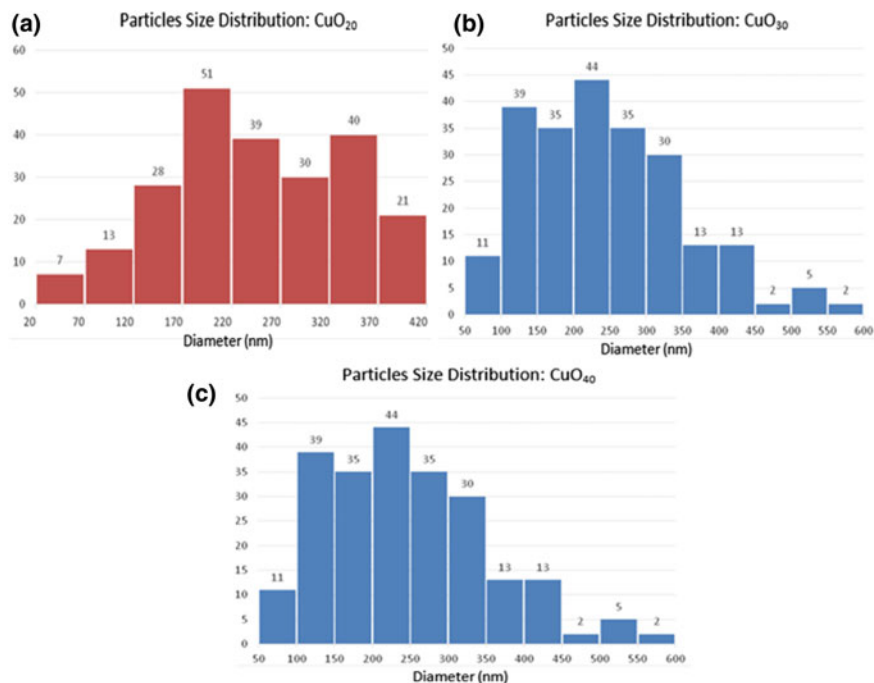
#### 3.1 Morphology Studies

The physical properties of biosynthesized copper oxide nanoparticles can be observed by FESEM and the FESEM images were shown in Fig. 2. The biosynthesized CuO NPs were spherical in shape. It shows that when higher the concentration of tea extract solutions used, the more the aggregation can be observed. Based on Fig. 3, the mean diameter for the CuO NPs obtained were 391.43, 243, and 230.74 nm for CuO<sub>20</sub>, CuO<sub>30</sub> and CuO<sub>40</sub> respectively. Although the synthesis of CuO<sub>20</sub> exhibits a larger average size, the nanoparticles are well dispersed and distributed compared to others.

The chemical compositions for all CuO NPs were illustrated in Table 1. It shows that copper and oxygen are present in the finished product. It also can be observed when the concentration of phenolic compound increases, the copper content in the sample will decrease.



**Fig. 2** FESEM images for **a** CuO<sub>20</sub>, **b** CuO<sub>30</sub> and **c** CuO<sub>40</sub>



**Fig. 3** Copper oxide nanoparticles particle size distribution for **a** CuO<sub>20</sub>, **b** CuO<sub>30</sub> and **c** CuO<sub>40</sub>

**Table 1** Chemical composition for synthesized copper oxide nanoparticles

Copper oxide nanoparticles	Copper, %	Oxygen, %
CuO <sub>20</sub>	18.98	32.85
CuO <sub>30</sub>	13.77	36.23
CuO <sub>40</sub>	11.54	34.62

## 4 Conclusions

Copper oxide nanoparticles were successfully synthesized using the biosynthesis method. Tea solution extract was used as a bio-reducing agent. Reduction of metal salt occurred due to the presence of phenol compound in the tea aqueous extract. The biosynthesized copper oxide nanoparticles have different sizes from the FESEM images with 391.43, 243 and 230.74 nm for CuO<sub>20</sub>, CuO<sub>30</sub> and CuO<sub>40</sub> of the tea aqueous extract.

**Acknowledgements** This work was supported by the University of Malaya with Grant no. BK063-2016 and RF025A-2018. The authors also would like to express appreciation to Department of Mechanical Engineering, University of Malaya technical staffs for their assistance.

## References

1. Aparna Y, Enkateswara Rao K, Subbarao P (2012) Synthesis and characterization of CuO nanoparticles by novel sol gel method. In: International Conference on Environment Science and Biotechnology, vol 48. <https://doi.org/10.7763/IPCBE>
2. Din MI, Rehan R (2017) Synthesis, characterization, and applications of copper nanoparticles. *J Anal Lett* 50:50–62
3. Ibrahim S, Charinpanitkul T, Kobatake E et al (2016) Nanowires nickel oxide and nanospherical manganese oxide synthesized via low temperature hydrothermal technique for hydrogen peroxide sensor. *J Chem*, Article ID 9138961
4. Gudikandula K, Maringanti SC (2016) Synthesis of silver nanoparticles by chemical and biological methods and their antimicrobial properties. *J Exp Nanosci* 11:714–721
5. Rajendran A, Siva E, Dhanraj C et al (2018) A green and facile approach for the synthesis copper oxide nanoparticles using *Hibiscus rosa-sinensis* flower extracts and its antibacterial activities. *J Bioprocess Biotech* 8:1–4
6. Kuppusamy P, Yusoff MM, Maniam GP et al (2016) Biosynthesis of metallic nanoparticles using plant derivatives and their new avenues in pharmacological applications—an updated report. *Saudi Pharm J* 24:473–484
7. Mohamad NAN, Arham NA, Jai J et al (2014) Plant extract as reducing agent in synthesis of metallic nanoparticles: a review. *Adv Mater Res* 832:350–355
8. Claudine M, Augustin S, Christine M et al (2004) Polyphenols: food sources and bioavailability. *Am J Clin Nutr* 79:727–747

# Two-Dimensional Fast Fourier Transform Analysis of Surface Microstructures of Thin Aluminium Films Prepared by Radio-Frequency (RF) Magnetron Sputtering



Fredrick M. Mwema, Esther T. Akinlabi and Oluseyi P. Oladijo

**Abstract** The purpose of this article is to illustrate the use of two-dimensional fast Fourier transform (2D-FFT) algorithm to describe the properties of aluminium thin films. To do so, the microstructures of thin Al films deposited on stainless steel substrates through radio-frequency (RF) magnetron sputtering are analysed using two-dimensional fast Fourier transform (2D-FFT) algorithm. Field emission scanning electron microscope (FESEM) and atomic force microscope (AFM) images obtained on the surfaces of the films are taken through different image analysis processes. The power spectra are described in terms of spatial frequencies, wavelengths and light intensities in the reciprocal space for both SEM and AFM images. The results of power spectra obtained from FESEM and AFM micrographs are compared for two different cases—films deposited at 200 and 300 W at the same substrate temperature (100 °C). We observe that the 2D-FFT analysis of both SEM and AFM methods can describe (in more details) the distribution of surface structures in thin aluminium films.

**Keywords** Atomic force microscopy (AFM) · Aluminium thin films · Image analysis · Fast Fourier transform (FFT) · Field emission electron microscopy (FESEM) · Sputtering

---

F. M. Mwema (✉) · E. T. Akinlabi · O. P. Oladijo  
Department of Mechanical Engineering Science, University of Johannesburg,  
Auckland Park Campus, Johannesburg 2006, South Africa  
e-mail: [fredrick.mwema@dkut.ac.ke](mailto:fredrick.mwema@dkut.ac.ke)

O. P. Oladijo  
Department of Chemical, Materials and Metallurgical Engineering, Botswana  
International of Science and Technology, Private Bag, 16, Palapye, Botswana

© Springer Nature Singapore Pte Ltd. 2020  
M. Awang et al. (eds.), *Advances in Material Sciences  
and Engineering*, Lecture Notes in Mechanical Engineering,  
[https://doi.org/10.1007/978-981-13-8297-0\\_27](https://doi.org/10.1007/978-981-13-8297-0_27)

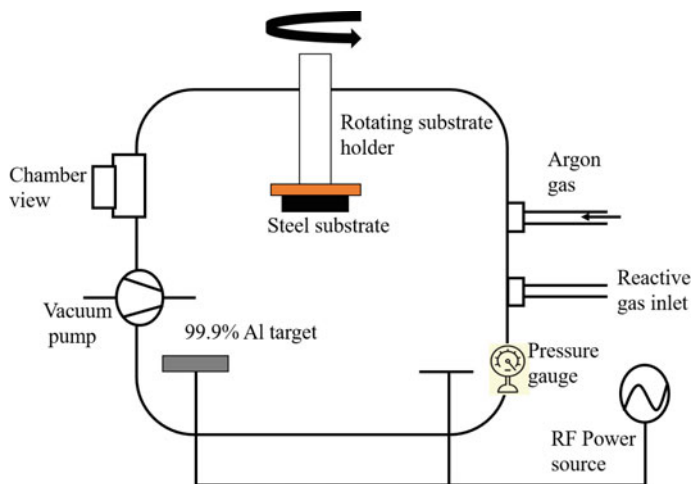
## 1 Introduction

Surface microstructures of thin films are usually obtained through various microscopic techniques, including scanning electron, transmission electron and atomic force microscopes. The characterization of the structural properties of the thin films, therefore, depends on image analysis of the captured micrographs [1]. In materials engineering, image analysis is the extraction of the physical information from a micrograph, and it involves both qualitative and quantitative approaches depending on the type of information required. In surface engineering, researchers are interested in morphology, texture, defects, grain orientation and size evolution during film growth [2]. The homogeneity and distribution of surface structures (roughness) are also important aspects in thin films microscopy. An extensive literature on microscopic analyses of thin aluminium films is readily available [2]. Through different microscopic techniques, as reported in literature, a conceptual model for the evolution of porosity across the interface of aluminium/substrate films has been described [2]. The development of the structural zone models (SZM) for thin film growth is based on microscopic analyses [3]. Most of the microstructural analyses reported in the literature on Al films rely on visual/qualitative examination of the micrographs although some studies have tried to report on the quantitative results of Al films. However, most of these studies have reported porosity using the percentage (area fraction) method of image analysis. Other studies have used statistical techniques such as Gaussian distribution to report on the distribution of sizes of the surface structures in thin films from atomic force microscopy (AFM) [4]. Line profile extraction that measures the lateral and height sizes of surface structures especially in AFM micrographs has also been reported [5]. Quantitative image analysis derives some of the most important parameters for detailed description of the films' structural properties. As such, to build into the existing quantitative methods, the present work illustrates the use of two-dimensional fast Fourier transform (2D-FFT) algorithm to analyse both SEM and AFM micrographs of thin aluminium films sputtered on stainless steel substrates. The overall aim is to show that 2D-FFT analysis can satisfactorily describe the structural properties of thin films from SEM and AFM micrographs.

## 2 Methods

The thin aluminium films were prepared by radio-frequency (RF) magnetron sputtering equipment whose schematic is illustrated in Fig. 1. The equipment consists of the sputtering chamber and human interface control unit. It has the capacity of sputtering with two targets and up to four substrates per run.

The sputtering system consists of a substrate heater control to regulate and monitor the temperature of the substrate and an automatic chamber vacuuming system, which includes a turbo pump, barometer and gas valves, which can reduce the system

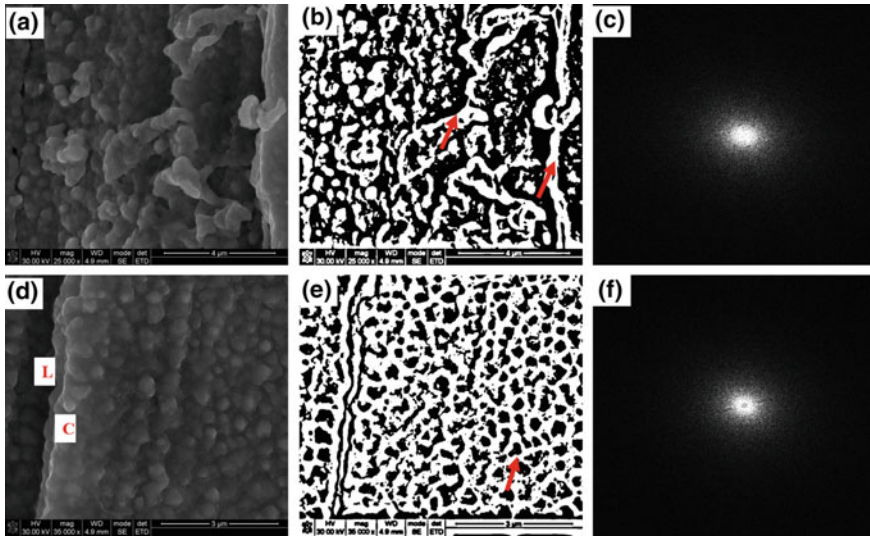


**Fig. 1** A schematic illustration of magnetron sputtering system. The system also consists of electron beam evaporation and thermal spray techniques and control unit

pressure to the order of  $10^{-6}$  mbar. The films, in this case, were prepared on stainless steel substrates at RF powers of 200 and 300 W for 2 hours at a substrate temperature of 100 °C. The 99.99% purity Al target of 75 mm diameter and 3 mm thickness was used. The argon flow rate was maintained at 12.0 sccm throughout the experiment. The Al-coated samples were then allowed to cool inside the sputtering chamber for close to 12 h after which they were sliced into 10 mm × 10 mm for SEM and AFM microscopy imaging. Scanning electron microscopy was undertaken using field emission scanning electron microscopy (FESEM) whereas the atomic force microscopy (AFM) imaging was undertaken using Veeco Dimension 3100 facility in tapping mode in the air and at room temperature. The obtained micrographs were taken through image analysis process.

### 3 Results and Discussions

Figure 2 shows the FESEM micrographs of thin aluminium films deposited on 316L stainless steel substrates at 200 W and substrate temperature of 100 °C. Figure 2a and d show the micrograph taken at magnifications of 25000× and 35000× respectively. At lower magnification (25000×), the microstructure shows highly interconnected structures of aluminium films. The interconnection is well illustrated by the processed image as indicated by red arrows in Fig. 2b. As seen, the microstructure appears as a layer-by-layer structure of aluminium films growing from the substrate towards the surface.

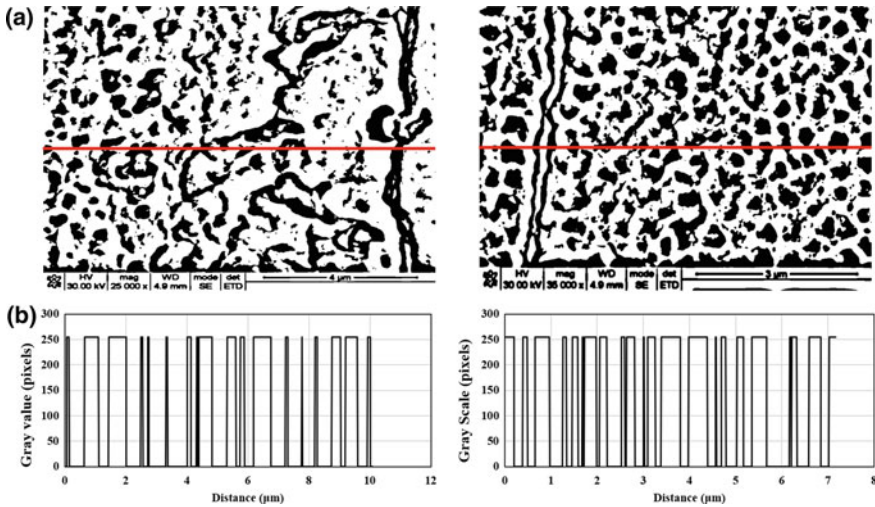


**Fig. 2** FESEM micrographs of thin aluminium films on stainless steel at magnifications (a) 25000 $\times$  and (d) 35000 $\times$  and their corresponding processed images (b) and (e) and 2D-FFT power spectral (c) and (f). The red arrows in (b) and (e) indicate the interconnected paths between the aluminium structures. L and C in (d) indicate layered and chocolate-like structures respectively

Further magnification of the interconnected structures reveals ‘bubble chocolate’ morphologies (labelled C in Fig. 2d) containing aluminium structures layered and aligned on top of each other. The structure appears as bands indicated as L layered on each other from the substrate to the top surface of the film. This observation is an indication of the epitaxial growth of aluminium films during magnetron sputtering on stainless steel substrate at 100 °C. The processed image (Fig. 2e) of the microstructure shows highly interconnected paths between adjacent layers of the films. These paths can be interpreted as the porosity which occurs during formation and growth of thin aluminium films as reported in the literature [3]. The paths appear mostly on the surface of the film and are caused by oxidation which occurs mostly during the cooling of the aluminium films inside the sputtering chamber. The evolution of porosity on the surface of aluminium films deposited through physical vapor deposition methods has been detailed in literature [2] and usually appears as interconnected paths as observed in this case.

Figure 2c and f show the corresponding two-dimensional fast Fourier transforms of the micrographs. The central region of 2D-FFT spectrum provides the most important information about the peaks in the real images [6]. At lower magnification (25000 $\times$ ), the radius of the light intensity at the centre of the power spectrum is larger than at higher magnification (35000 $\times$ ), which can be attributed to the larger interconnected aluminium structures and porous paths indicated by the red arrows in the processed image. This observation indicates the essence of using the images of two different magnifications in this case since different magnifications show various information



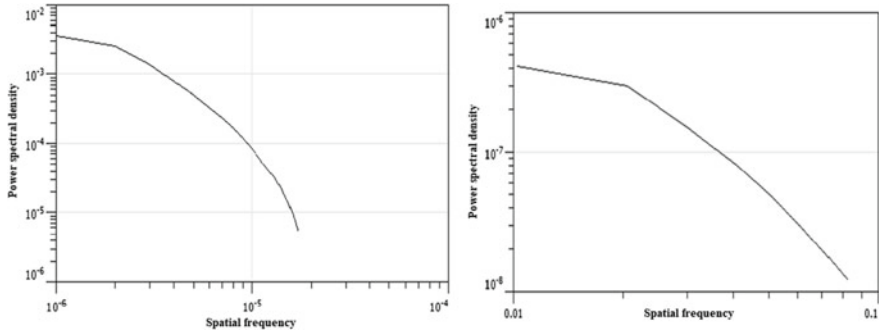


**Fig. 3** Gray level signals along the red lines of the micrographs in Fig. 2a and d

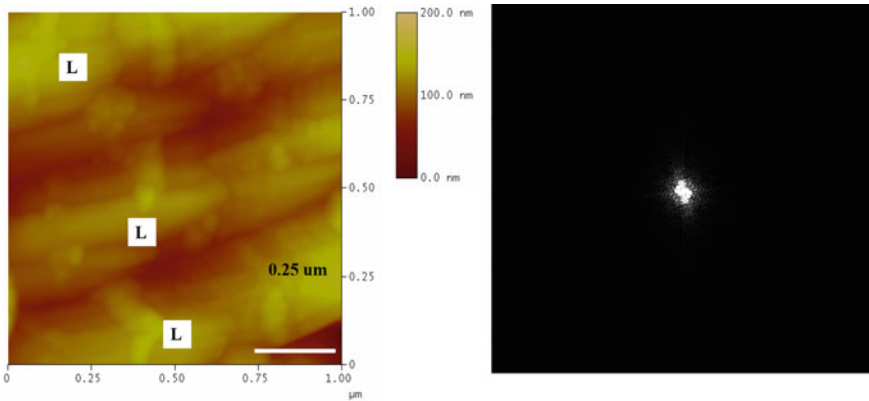
regarding the microstructure. The 2D-FFT in Fig. 2f can be used to explain the distribution and density of the layered and ‘chocolate-like’ structures indicated as L and C respectively. The smaller size of the central region at a magnification of  $35000\times$  indicates finer and closed packed particles of aluminium within the different layers. The few traces of high-frequency values appearing on the radial spectrum are due to the presence of small spaces/voids exposing the substrate (which means that the film is not laterally uniform and has not fully covered the substrate surface).

Figure 3 shows the grey scale values along the red lines of the processed image of the FESEM micrographs in Fig. 2a and d. As shown, a high grey value represents the aluminium structures whereas the low values indicate the interconnected porous paths and aluminium-free (spaces/voids) substrate surfaces. The grey scale images can be used to show the visual distribution of the aluminium structures, and in this case, the frequency of fluctuations of the grey values indicate a high degree of non-homogeneity especially at low magnification ( $25000\times$ ). The log-log plot of the power spectrum density (PSD) versus spatial frequency of the 2D-FFT analysis is represented in Fig. 4. The PSD profile at lower magnification is a characteristic of randomly distributed structures in the micrograph whereas at higher magnification, the profile indicates the periodic behavior of the structures. At higher magnifications, in fact, the particles of the film appear periodically aligned along the length of the substrate although with occasional spaces exposing the surfaces of the substrate. These observations agree with the FESEM results, which show that the microstructure consists of largely interconnected paths and aluminium structures and voids thereby, indicating that the film microstructure is non-homogeneous.

The 2D AFM image for the thin films deposited at 200 W and substrate temperature of  $100\text{ }^{\circ}\text{C}$  and its corresponding 2D-FFT spectrum is shown in Fig. 5. The advantage



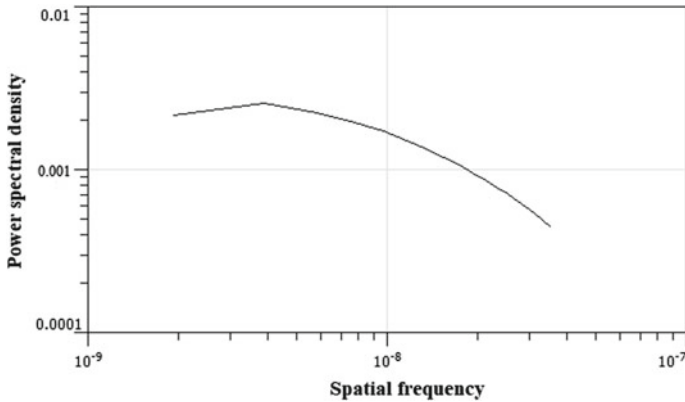
**Fig. 4** The corresponding power spectral density versus spatial frequency of 2D-FFT analysis of micrographs shown in **a** left-hand and **b** right-hand graphs



**Fig. 5** AFM micrograph (scan size 1  $\mu\text{m} \times 1 \mu\text{m}$ ) and the corresponding 2D-FFT analysis of thin aluminium films deposited on stainless steel substrates at 200 W at a substrate temperature of 100  $^{\circ}\text{C}$

of AFM is that it gives very high magnifications of the structures; in this case, up to nanoscale levels. There are observable features on the surface topography which can be related to the FESEM micrographs. Layers (indicated as L in the AFM image) are visible with the interconnected paths between adjacent layers (appearing darker in the image) as earlier observed at 35000 $\times$  of FESEM micrograph.

The 2D-FFT spectrum of the AFM image shows a tiny central peak, indicating the presence of very fine features. There is the formation of very small aluminium structures (with well-defined boundaries) as earlier observed in the FESEM at the magnification of 35000 $\times$ . The peaks in the 2D-FFT image represent the layered structures of the film and the interconnected paths whereas the high-frequency values indicate the well-defined fine particles of the films. The presence of high-frequency values on the radius of the spectrum is an indication of the tiny spaces/voids within

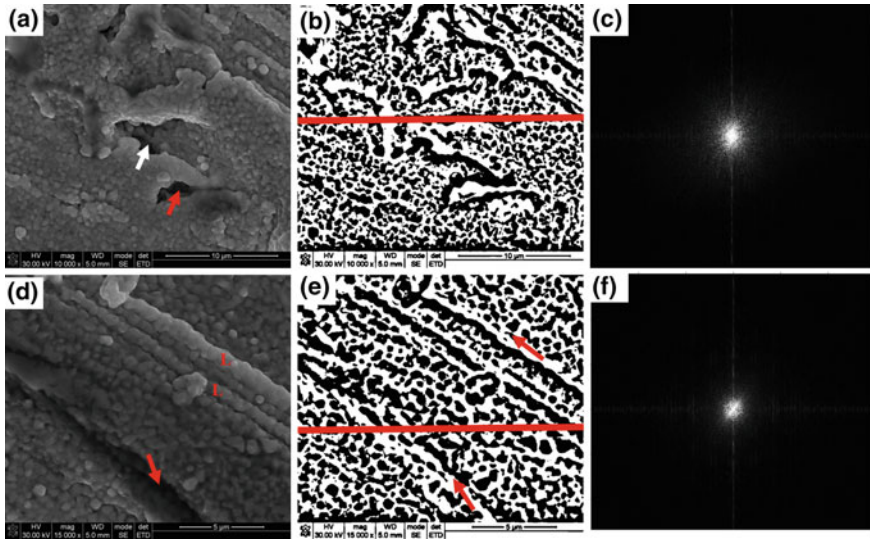


**Fig. 6** Power spectral density profiles of the AFM image of thin aluminium films deposited on stainless steel substrates at 200 W and substrate temperature of 100 °C

the surface of the film. The spaces are an indication that some surfaces of the substrate were not coated during the sputtering process.

Figure 6 shows the PSD profile for the AFM topography. Such profiles from AFM micrographs can be used to describe the lateral distribution of surface structures. The profile (Fig. 6) is a characteristic of random surfaces. At very higher magnifications, the AFM probe can detect the atomic levels of the surface structures, which mostly for a sputtering process are likely to follow a pattern resulting in a periodic surface [7]. The region of the white noise (low spatial frequency) indicates a uniform distribution of the structures. However, in this case, the profile is dominated by the power law gradient, which indicates lateral non-homogeneity of the surface structures. The non-uniformity is due to the presence of the interconnected pores and lateral spaces within the aluminium microstructures observed in the FESEM micrographs.

Figure 7 shows the FESEM micrographs of aluminium films deposited at 300 W and a substrate temperature of 100 °C. The microstructure consists of nearly uniformly distributed morphology of aluminium films on the surface of the substrate at both magnifications. There are fewer voids and interconnected paths (indicated by red and white arrows in Fig. 7a and c and the processed images) than observed at 200 W in Fig. 2. At RF power of 300 W, the density of ions in the sputtering plasma is higher than at 200 W and therefore the sputtering yield is increased leading to densification of the films, which results in more uniform coating of the substrate with less voids within the surface of the film [8–11]. The grey scale values plotted against arbitrary distances along the processed images (Fig. 8) reveal an alternating fluctuation in the aluminium film structures and voids/interconnected spaces. The 2D-FFT power spectra of the FESEM images reveal some noises in the high frequency regions (as seen in Fig. 7c and f). The observation can be attributed to the occasional interconnected paths appearing between the very fine structures of aluminium layers (indicated as L in Fig. 7d). The 2D-FFT spectra for both images



**Fig. 7** FESEM micrographs of thin aluminium films deposited on stainless steel substrate at RF power of 300 W and a substrate temperature of 100 °C. The images were taken at (a) 1000× and (b) 15000× to reveal the important features of the microstructure. The corresponding processed (b) and (e) and 2D-FFT images are shown. The red arrows indicate voids (aluminium-free spaces exposing the substrate) while white arrows indicate paths (pores) within the aluminium structures

are symmetrical indicating the level of homogeneity of the sizes and distribution of the films' structures. The PSD profiles of these images are shown in Fig. 9, and they represent the periodic distribution of the surface features. For both magnifications, the profile is characterized by the non-fluctuating region at low spatial frequencies and the highly correlated region at high frequencies.

Figure 10 represents the AFM micrograph of the thin films deposited at 300 W and substrate temperature of 100 °C and its corresponding 2D-FFT spectrum. As shown, the topography consists of well-distributed structures of aluminium films (brighter regions) with a few voids (dark regions). The 2D-FFT of the AFM micrograph shows a nearly oval central region with random peaks along the fast scan direction of the AFM probe (Y-direction in the 2D-FFT image). This observation indicates that there are fine structures entangled in larger structures within the surface microstructure. The PSD profile of the AFM micrograph shown in Fig. 11 indicates the periodic behaviour of the surface topography and is comparable to the profiles illustrated in Fig. 9.

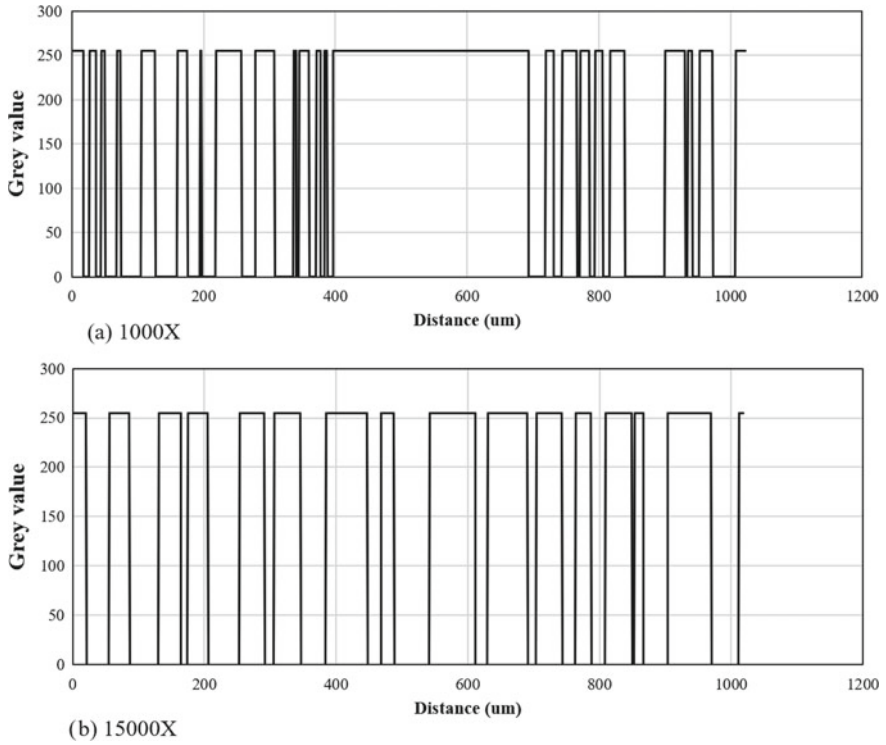


Fig. 8 The grey scale values along the red lines indicated in images in Fig. 7

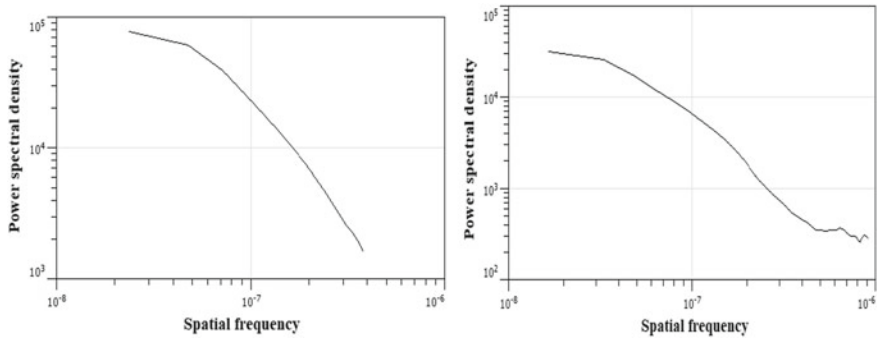
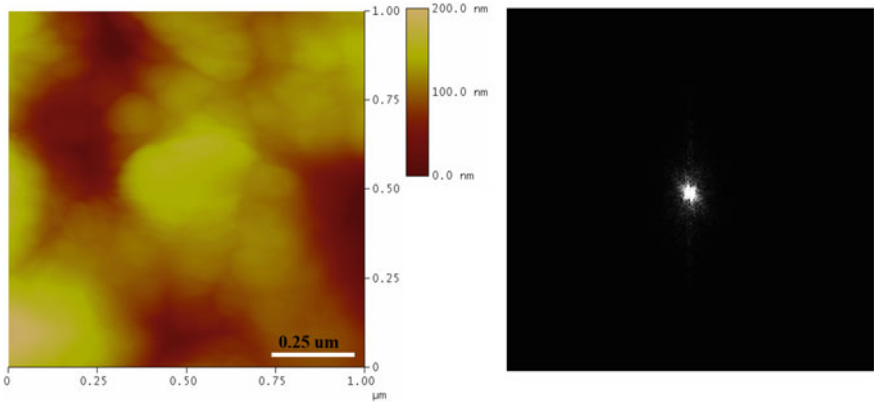
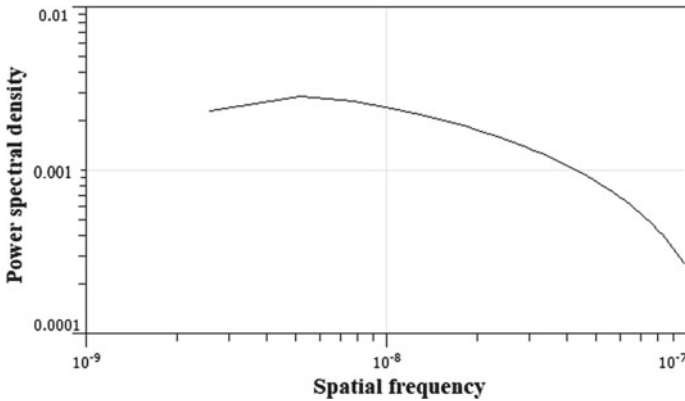


Fig. 9 Power spectral density profiles for 2D-FFT analysis of micrographs shown in Fig. 7



**Fig. 10** AFM micrograph and corresponding 2D-FFT spectrum for the thin aluminium film deposited at RF power of 300 W and a substrate temperature of 100 °C



**Fig. 11** Power spectral density profiles of the AFM image of thin aluminium films deposited on stainless steel substrates at 300 W and a substrate temperature of 100 °C

## 4 Conclusions

In this article, two-dimensional fast Fourier transform analysis of SEM and AFM micrographs of thin aluminium films prepared by RF magnetron sputtering was illustrated. Aluminium films prepared at 200 and 300 W at 100 °C were used as a case study to explain how this technique can be used to characterize the properties of the films. For SEM images, two different magnifications were chosen for consistency purposes of the observations and computations. From the study, the following conclusions can be drawn:

- From the SEM and AFM micrographs, aluminium films deposited through sputtering grow through layer-by-layer mechanism thereby forming thin films. However,

during the film growth, interconnected and porous paths (as illustrated by the processed images) are formed. The 2D-FFT spectra for SEM and AFM micrographs in all cases correlated well with the film growth mechanism during sputtering.

- The power spectral density profiles of SEM micrographs, for all the cases considered, were comparable to those of the AFM micrographs and both profiles depicted the similar behaviour of the thin films.

The two-dimensional fast Fourier transform technique is therefore recommended for detailed microstructural analysis of field emission scanning electron microscope (FESEM) and atomic force microscope (AFM) images of thin aluminium and other films.

**Acknowledgements** The authors of this article would like to acknowledge University Research Committee (URC), University of Johannesburg, South Africa for sponsoring the PhD candidate working on magnetron sputtering of thin films. Mr. Maphane of Botswana International University of Science & Technology (BIUST), Botswana and MMU staff at the University of Witwatersrand (Wits), South Africa are also acknowledged for assisting on Magnetron sputtering and AFM/FESEM facilities respectively.

## References

1. Zhu J, Balieu R, Lu X et al (2018) Microstructure evaluation of polymer-modified bitumen by image analysis using two-dimensional fast Fourier transform. *Mater Des* 137(5):164–175
2. Mwema FM, Oladijo OP, Akinlabi SA et al (2018) Properties of physically deposited thin aluminium film coatings: a review. *J Alloy Compd* 747:306–323
3. Petrov I, Barna PB, Hultman L et al (2003) Microstructural evolution during film growth. *J Vac Sci Technol, A* 21:S117
4. Aqil M, Azam M, Aziz M et al (2017) Deposition and characterization of molybdenum thin film using direct current magnetron and atomic force microscopy. *J Nanotechnol* 2017:1–10
5. Mwema FM, Oladijo OP, Sathiaraj TS et al (2018) Atomic force microscopy analysis of surface topography of pure thin aluminium films. *Mater Res Express* 5(4):1–15
6. Cao Y, Dong S, Liang Y et al (2007) Study the order of morphology self-assembled triblock copolymer thin films by FFT of the AFM Images. In: *First international conference on integration and commercialization of micro and nanosystems, Parts A and B*, pp 1181–1184
7. Ţălu S, Bramowicz M, Kulesza S et al (2018) Topographic characterization of thin film field-effect transistors of 2,6-diphenyl anthracene (DPA) by fractal and AFM analysis. *Mater Sci Semicond Process* 79(144–152):13
8. Wang LF, Wu ZY, Meng ZJ (2011) Magnetron sputtering yield and relative factors. *Adv Mater Res* 361–363:1655–1663
9. Simon AH (2018) Sputter processing. In: *Handbook of thin film deposition*, Elsevier, pp 195–230
10. Wasa K, Hayakawa S (1992) *Handbook of sputter deposition technology*. Noyes Publications, New Jersey
11. Mwema FM, Oladijo OP, Akinlabi ET (2018) Effect of substrate temperature on aluminium thin films prepared by RF-magnetron sputtering. *Mater Today* 5(9/3):–20473

# Fractal Analysis of Thin Films Surfaces: A Brief Overview



Fredrick M. Mwema, Esther T. Akinlabi and Oluseyi P. Oladijo

**Abstract** The concept of fractals has been widely accepted in various fields for studying natural or random phenomena. Most specifically, in surface engineering and thin films, fractal analysis is used to investigate the self-affine nature and scaling characteristics of surfaces to understand the physical processes of creating the surfaces. Various methods have been applied in the fractal analysis of thin films, some of which include autocorrelation, height-height correlation, power spectral density functions, triangulation, and box counting among others. From these methods, it is possible to compute the roughness characteristics such as roughness exponent, correlation length, fractal dimension, Hurst exponent, etc. Fractal dimension is the key parameter used to understand the roughness properties of the films. In this article, we have summarised some of the key results on the fractal analysis of thin films, and it has been noted that fractal characteristics depend on the thin films' deposition processes. The interrelationships among the fractal parameters and surface morphology of the films are unpredictable, and therefore fractal analysis should be undertaken for each new type of thin films.

**Keywords** Atomic force microscope · Autocorrelation · Fractals · Roughness · Self-affine · Thin films

---

F. M. Mwema (✉) · E. T. Akinlabi · O. P. Oladijo  
Department of Mechanical Engineering Science, University of Johannesburg, Johannesburg 2006,  
South Africa  
e-mail: [fredrick.mwema@dkut.ac.ke](mailto:fredrick.mwema@dkut.ac.ke)

O. P. Oladijo  
Department of Chemical, Materials and Metallurgical Engineering, Botswana University of  
Science and Technology, Private Bag 16, Palapye, Botswana

© Springer Nature Singapore Pte Ltd. 2020  
M. Awang et al. (eds.), *Advances in Material Sciences  
and Engineering*, Lecture Notes in Mechanical Engineering,  
[https://doi.org/10.1007/978-981-13-8297-0\\_28](https://doi.org/10.1007/978-981-13-8297-0_28)

251



# 1 Introduction

## 1.1 Background

The concept of fractals has been accepted to describe most natural systems and currently finding extensive application in the characterisation of surfaces [1, 2]. In most cases, random systems such as surface microscopy behave like fractals, i.e. their geometrical units resemble one another at all scales (at both low and high magnification similar features are identified) [3–5]. It, therefore, means that fractals are not sensitive to the scale of resolution and fractal analysis can be used to extract more information about a surface as compared to the conventional statistical methods [6]. The concept of fractals in thin film structures was clearly described, for the first time, in 1985 by Yehoda and Messier [7]. They argued that the presence of low-density regions (network of voids) of films microstructures was the reason for the fractal behaviour of thin films. In thin film surfaces, fractal dimension is used as an analytical index to measure how the morphological features vary on scaling [2]. The fractal analysis provides information on roughness exponent, correlation length, shift (or lattice size) and pseudo-topothesy besides the fractal dimension of thin films [8]. These parameters offer a detailed description of spatial patterning, segmentation, texture and lateral roughness of the surface morphology [9]. As such extensive literature exists on fractal analysis of surfaces of thin films [10–19] and several methods of fractal analysis, have been developed. The objective of this paper is to provide a very short overview of the most commonly used methods and summarize some of the published results of fractal analysis of thin films. The article may assist researchers expecting to use these methods in thin film imaging applications.

## 1.2 A Review of Common Fractal Analysis Methods

### 1.2.1 Autocorrelation Function

The autocorrelation function (ACF) shows the dependence of a signal on its own at different time shifts. In thin films, ACF describes the self-affine characteristics of surfaces and is used to derive fractal parameters such as roughness exponent, correlation length and fractal dimension (D) [12]. From various literatures [20, 21], the autocorrelation function ( $A(r)$ ) along the direction of fast scan (x-direction) is expressed in terms of height function  $z(i, j)$  as follows.

$$A(r = ld) = \frac{1}{m(m-l)w^2} \sum_{j=1}^m \sum_{i=1}^{m-l} z(i+l, j)z(i, j) \quad (1)$$

where  $d$  is the horizontal distance between two adjacent image features and  $l$  is the preceding feature of the point ( $m$ ) of interest.

### 1.2.2 Height-Height Correlation Function

Various researchers have used height-height correlation function ( $H(r)$ ) to illustrate the self-affine and mounded characteristics of surfaces of thin films [1, 6, 12, 13]. Mathematically, one-dimensional  $H(r)$  of the  $m \times m$  area of surface micrograph in the direction of the fast scan of the AFM probe is given as follows [22].

$$H(r = ld) = \frac{1}{m(m-l)} \sum_{j=1}^m \sum_{i=1}^{m-l} [z(i+l, j) - z(i, j)]^2 \tag{2}$$

A bi-logarithmic plot of  $H(r)$  versus  $r$  reveals two regimes as described by Yadav et al. [12] and it has been shown that the fractal dimension ( $D$ ) is determined by fitting a power law within the linear region (small values of  $r$ ) of the plot whereas roughness exponent, correlation lengths and Hurst exponents are determined by best-curve at the nonlinear region (large values of  $r$ ). Detailed applications of  $H(r)$  are reported elsewhere [1, 12, 20].

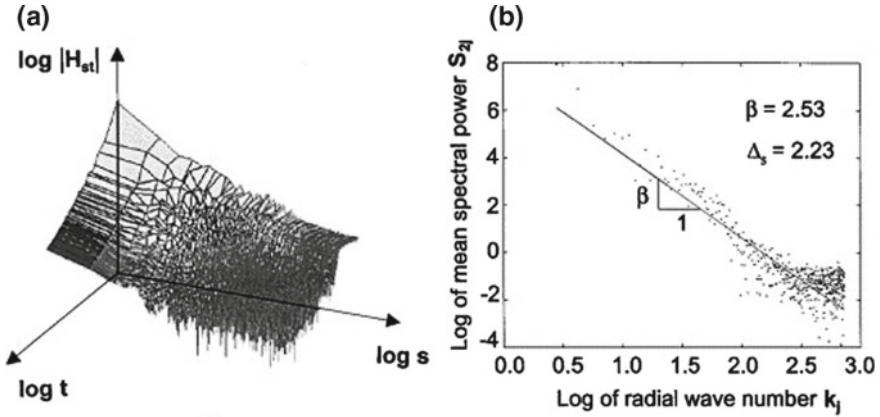
### 1.2.3 Power Spectral Density Function

The power spectral density function uses a fast Fourier transform algorithm of the height functions ( $H_{st}$ ) of the surface as shown in the logarithmic diagram in Fig. 1a. The fractal dimension is computed as a function of the average power ( $S$ ) of the height spectra over the area under study and is determined as follows [23].

$$S = \frac{1}{l^2 N_j} \sum_1^{N_j} |H_{st}|^2 \tag{3}$$

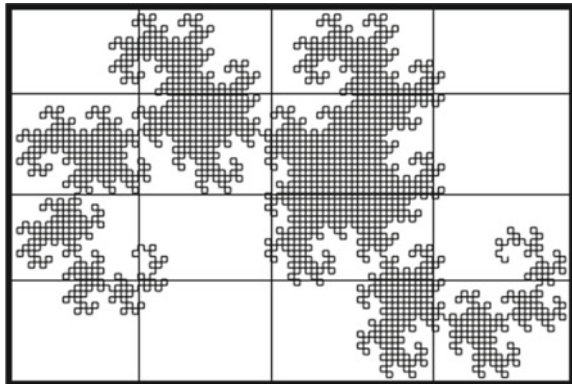
where  $N_j$  is the number of points within the digital area whose linear size is defined by  $l$ . Within the highly correlated region (self-affine surfaces),  $S$  obeys the power law in the form  $S = k_j^{-\beta-1}$  where,  $k_j$  is the radial spatial frequency and the slope of the curve in Fig. 1b is defined by  $\beta$  [24]. From this method,  $D$  can be determined as follows.

$$D = \frac{7 - \beta}{2} \tag{4}$$



**Fig. 1** Illustrating the spectral determination of the fractal dimension through (a) fast Fourier transform of surface and (b) the double log plot of power versus spatial frequency (adapted from Carpinteri et al. [23] with permission from Elsevier, copyright order number 501448072)

**Fig. 2** Illustrating the box-counting method for dragon curve fractals. In this method,  $N$  is the number of the boxes and  $h$  is the length scale (size of each box)



**1.2.4 Box-Counting Method**

In this method, the fractal features are covered with a single box, which is subsequently divided into four quadrants. Each of the quadrants is further divided into four quadrants, and this is repeated in a loop until the minimum size of each box is equal to the resolution of the data [25, 26]. Then for each case, the number of boxes ( $N$ ) covering the fractal features are counted, and its logarithm is plotted versus the size of boxes ( $h$ ). The fractal dimension ( $D$ ) is determined from the maximal slope coefficient of the double log plot defined as follows [25, 27, 28]. The method is illustrated in Fig. 2.

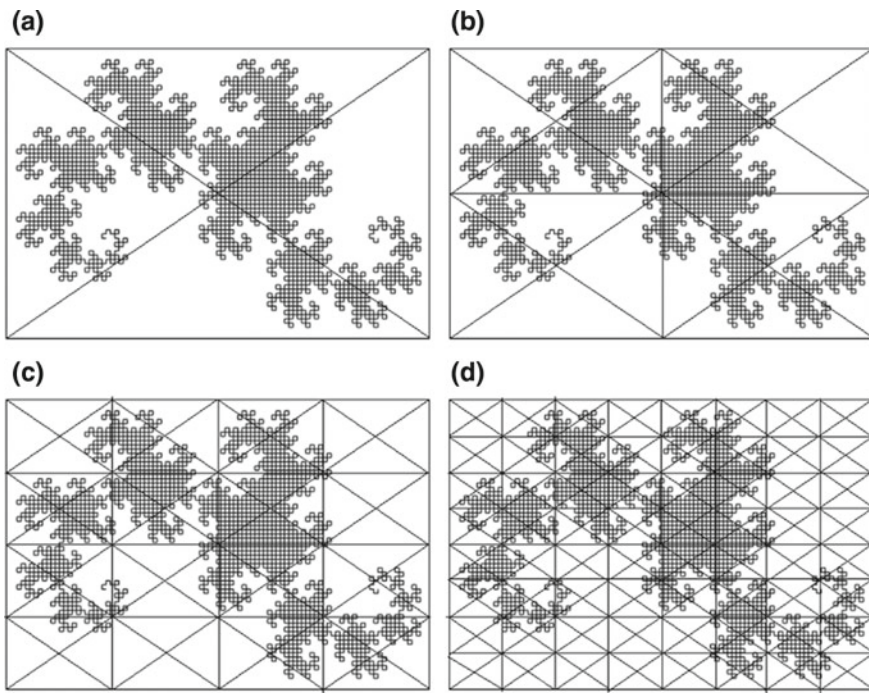
$$D = \lim_{h \rightarrow 0} - \frac{\log N(h)}{\log h} \tag{5}$$

### 1.2.5 Triangulation Method

The computation of  $D$  in triangulation method (as known as prism counting) is based on approximating the area of the surface using successive pyramids and computing their lateral regions as illustrated in Fig. 2 [23, 29]. The area under study is covered by a square patch, and then one pyramid on the four angles of the square is created (Fig. 3a). The square is further subdivided into four quadrants, and then on each quadrant, a pyramid is created so that a total of 8 pyramids are generated (Fig. 3b).

The procedure is repeated to generate 16 pyramids (Fig. 3c), 32 pyramids (Fig. 3d) and so forth until the base length of each pyramid ( $r$ ) is equal to the resolution of the digital data of the image. The apparent area ( $A$ ) of each prism is then computed for each  $r$ . The slope of the bi-logarithmic plot of  $r$  versus  $A$  is used to compute  $D$  as follows [23].

$$D = 2 - \lim_{r \rightarrow 0} - \frac{\log A(r)}{\log r} \tag{6}$$



**Fig. 3** Triangulation fractal dimension scheme of the dragon curve fractal. The **a**, **b**, **c**, **d** represents the repetitive steps followed in constructing the pyramids for each rectangular space occupied by the fractal features

## 2 Overview of Published Literature

There is considerable published literature on the fractal analysis of thin films. The general observation from literature is that fractal methods provide a detailed description of the microstructure and evolution of the physical structures during thin film deposition. Through, fractal methods, the evolution of surface complexity of structure with the deposition parameters has been detailed [1, 13, 17, 24, 30]. The fractal dimension has been shown to increase/decrease with the substrate temperature, power and films' thickness [1, 31, 32]. In a recent study, the effect of deposition time on the sputtering of Ti thin films on glass substrate was reported and shown that the fractal dimension increases with the deposition time [33]. Țălu et al. [34] reported on the variation of fractal dimension of Ni–C prepared through the combination of radio frequency sputtering and plasma enhanced chemical vapor deposition (PEVD) techniques at varying times of 7, 10, 13 min on silicon and glass substrates. The highest fractal dimension was obtained at 10 min while the lowest obtained at 13 min of deposition. The fractal dimension has also been shown to decrease with increase in PEVD deposition pressure [35]. The power spectral density of 10 and 20 nm gold thin films has been reported [36]. The effect of annealing temperatures on the fractal properties of ITO thin films deposited by electron beam evaporation has been reported [37, 38]. Using height-height correlation method, Raoufi et al. [37] reported that fractal dimension of ITO films increases with the annealing temperature. Similar results were reported for the same films using power spectral density method [3]. In a similar study, Raoufi [38] reported that the lower annealing temperature, the slower the decrease of the fractal dimension. The fractal dimension of AlN epilayers sputtered on alumina was shown to increase with the substrate temperature [31]. The effect of deposition power and substrate temperature of Al thin films on steel substrates has been described by power spectral density function [24, 30]. The relationship between the statistical and fractal measurements of thin films has also been reported by various researchers [14, 24, 30, 39]. The general finding from these reports is that there is no direct relationship between root mean square and average roughness and fractal dimension.

Table 1 provides a summary of some of the fractal methods used in thin film analysis. The results of the correlation among the properties, deposition methods/parameters and fractal characteristics of the thin films are also included in Table 1.

## 3 Conclusions

Fractal techniques offer powerful tools for characterisation and segmentation of surface structures of thin films. The fractal dimension is the basic measure of irregularity and discontinuities of the surface properties. Various methods have been used for computation of fractal dimension of thin films some of which include, autocorrelation, height-height correlation functions, power spectrum and box counting methods.

**Table 1** Selected published articles and key results on the fractal analysis of thin films

Author/year	Description of the publication	Fractal analysis method(s) used	Findings and inferences
Yadav et al. [12]/2014	Fractal characteristics of LiF thin films deposited through electron beam evaporation at 77, 300 and 500 K substrate temperatures were reported	Height-height autocorrelation	The lateral correlation lengths, roughness exponents and fractal dimensions were computed. The fractal dimension decreased with increasing substrate temperature and roughness. The surfaces of LiF films were shown to be self-affine
Yadav et al. [13]/2017	The study investigated the fractal properties of ZnO prepared by atom beam sputtering on Si at varying deposition angles- 20°, 30°, 40°, 60°, 75°	Higuchi's algorithm	Fractal dimension and Hurst exponent were determined. The highest fractal dimensions were reported at 30° and 60° while the lowest at 75°. The highest Hurst exponent was determined at 75°. The surfaces were said to be self-affine
Yadav et al. [1]/2012	The fractal and multifractal analysis were performed on electron beam prepared LiF thin film surfaces at different thicknesses (10, 20 and 40 nm)	Autocorrelation, height-height correlation and multifractal detrended fluctuation analysis (MFDFA)	The lateral correlation length and fractal dimensions were seen to increase with film's thickness; whereas the roughness exponent decreased with the thickness of the film
Buchko et al. [40]/2001	The study reports on the fractal analysis of protein polymer films prepared through electrostatic atomization and gas evolution foaming. The films were prepared at different polymer concentration (1.6–2.4 wt%), the electric field (3–6 kV/cm), deposition separation (1–2 cm) and time (1–10 s)	Power spectral density	The fractal dimensions were computed as 2.7 for fibre-only films and 2.025 for fiber + bead films. For the bead-only film, the fractal dimension value did not have any physical meaning

(continued)

**Table 1** (continued)

Author/year	Description of the publication	Fractal analysis method(s) used	Findings and inferences
Dallaeva et al. [31]/2014	The fractal analyses of AlN epilayers prepared through magnetron sputtering at varying substrate temperatures of 1000, 1300 and 1500 K are reported. The films were deposited on Al <sub>2</sub> O <sub>3</sub> substrates	Morphological envelopes (cube counting method)	The fractal dimension was computed and shown to increase with a deposition temperature of the substrate
Arman et al. [41]/2015	Fractal analysis of AFM micrographs of Cu films deposited on Si and glass substrates was reported. The films were prepared through DC magnetron sputtering at different thicknesses (5, 25 and 50 nm)	Autocorrelation function, Box (cube) counting and power spectral density methods	The fractal dimensions were computed and were shown to decrease with the increase in the thickness of the film. The results show that sputtered Cu thin films are self-affine and can be characterised through fractal methods
Țălu et al. [42]/2018	The fractal nature of oxidised CdTe surfaces was investigated using AFM	Autocorrelation, height-height and power spectral density functions	The micromorphology description based on the various fractal techniques was satisfactory to describe the surface oxidation of CdTe
Țălu et al. [43]/2016	Surface analysis of Cu/Co nanoparticles prepared by DC magnetron sputtering on Si was undertaken under various power and deposition times	Autocorrelation function	Evolution of correlation lengths, pseudo-topothesy and fractal dimensions with various deposition parameters were reported
Țălu et al. [44]/2016	Fractal analysis of gold nanoparticles in carbon film deposited through rf magnetron sputtering was reported. The sputtering was undertaken under varying power (80–120 W)	Autocorrelation and height-height (structural) functions	Fractal dimensions, pseudo-topothesy and corner frequency, were computed as a function of the sputtering power. There were no proportional relationships among fractal dimension, pseudo-topothesy and roughness

(continued)

**Table 1** (continued)

Author/year	Description of the publication	Fractal analysis method(s) used	Findings and inferences
Yadav et al. [6]/2015	Fractal and multifractal analysis of BaF <sub>2</sub> thin films deposited on Si by electron beam evaporation. The surfaces of the films were irradiated at different ions/cm <sup>2</sup>	Autocorrelation, multifractal and power spectral density functions	Lateral correlation lengths, power spectral density, roughness exponent and fractal dimensions were computed
Hosseinpanahi et al. [45]/2015	The paper reported on the fractal and multifractal analysis of CdTe films deposited on glass substrates by sputtering at varying times of 5, 10 and 15 min and at a constant power of 30 W	Detrended fluctuation analysis (DFA) and MF DFA	Multifractal parameters and Hurst exponent were computed. The Hurst exponent was shown to be higher than 0.5, indicating a positive correlation and multifractal nature of the films
Nasehnejad et al. [46]/2017	Dynamic scaling analysis of electrodeposited silver thin films is reported. The films were prepared at varying thicknesses (80, 150, 220, 320, 600 and 750 nm)	Power spectral density, height-height correlation	Roughness exponent, power spectrum and correlation functions were computed. The power spectral density and correlation functions were seen to increase with the film thickness indicating dynamic scaling of the films. The roughness characteristics were observed to also increase with film's thickness
Raoufi [38]/2009	The fractal analysis of ITO films prepared through electron beam evaporation was undertaken. The analysis was done on as-deposited, annealed samples (200 and 300 °C)	Box-counting method	Fractal dimension was computed for the three AFM micrographs, and higher values were determined on the as-deposited sample. The fractal dimension was shown to decrease with an annealing temperature of the ITO thin films

(continued)



**Table 1** (continued)

Author/year	Description of the publication	Fractal analysis method(s) used	Findings and inferences
Raoufi [3]/2010	A power spectral density analysis was reported for electron beam evaporated ITO thin films annealed at various temperatures. The annealing temperatures varied as 0, 250, 350 and 450 °C	Power spectral density function	The fractal dimensions and slope of the inverse power law were computed. The fractal dimension and roughness were seen to increase with annealing temperature whereas the slope decreased with the annealing temperature
Douketis et al. [47]/1995	The fractal characteristics of vacuum-deposited films at 100 and 300 K were investigated	Cube counting, triangulation and power spectrum analyses	For the three methods, fractal dimension was computed and averaged. The highest value of fractal dimension was shown to correspond to films with high roughness
Țălu et al. [48]/2018	The study investigated the fractal character of ITO deposited by DC magnetron sputtering under different sputtering chamber conditions (O <sub>2</sub> , N <sub>2</sub> and H <sub>2</sub> gases)	Autocorrelation function	Fractal dimension and pseudo topothesy were computed and shown to vary with different deposition conditions
Mwema et al. [24]/2018	A power spectral density analysis was undertaken on Al thin films deposited on stainless and mild steel substrates at 150 and 200 W	Power spectral density function	Correlation length, roughness exponent, fractal dimension and Hurst exponent were determined. The fractal characteristics were seen to evolve with the substrate type and rf power
Li et al. [49]/2000	The fractal model was developed to study the self-affine nature of Co-based thin films	Variation-correlation function	The fractal dimension and correlation length were calculated. The fractal dimension was shown to decrease with an increase in surface roughness. The lowest fractal length was reported at the lowest surface roughness

The advantage of these techniques over the statistical techniques of surface analysis of thin films is that they describe the lateral development of the surface features rather than just the vertical features. Through fractal analysis, researchers can deeply understand the growth and scaling of thin films during deposition at various process parameters and techniques. Despite the extensive use of fractal methods, there has been no much efforts to determine the best technique for analysing thin films. Future researches on fractal studies, therefore, should undertake comparative studies of the behaviour of different techniques on the morphological data to determine the suitable algorithm for specific films. There is also increasing application of multifractal analysis for films' surfaces exhibiting multifractal behaviours.

**Acknowledgements** The authors wish to acknowledge the University Research Committee (URC), University of Johannesburg, South Africa for financing the Ph.D. researcher working on thin film processing.

## References

1. Yadav RP, Dwivedi S, Mittal AK, Kumar M, Pandey AC (2012) Fractal and multifractal analysis of LiF thin film surface. *Appl Surf Sci* 261:547–553
2. Valle F, Brucale M, Chiodini S, Bystrenova E, Albonetti C (2017) Nanoscale morphological analysis of soft matter aggregates with fractal dimension ranging from 1 to 3. *Micron* 100:60–72
3. Raoufi D (2010) Fractal analyses of ITO thin films: a study based on power spectral density. *Phys B Condens Matter* 405(1):451–455
4. Barrera E, Gonzalez F, Rodriguez E, Alvarez-Ramirez J (2010) Correlation of optical properties with the fractal microstructure of black molybdenum coatings. *Appl Surf Sci* 256(6):1756–1763
5. Mandelbrot BB (1985) Self-affine fractals and fractal dimension. *Phys Scr* 32:257–260
6. Yadav RP, Kumar M, Mittal AK, Pandey AC (2015) Fractal and multifractal characteristics of swift heavy ion induced self-affine nanostructured BaF<sub>2</sub> thin film surfaces. *Chaos Interdiscip J Nonlinear Sci* 25(8):83115
7. Yehoda JE, Messier R (1985) Are thin film physical structures fractals? *Appl Surf Sci* 22–23(2):590–595
8. Feng F et al (2018) Surface scaling analysis of textured MgO thin films fabricated by energetic particle self-assisted deposition. *Appl Surf Sci* 437:287–293
9. Jing C, Tang W (2016) Ga-doped ZnO thin film surface characterization by wavelet and fractal analysis. *Appl Surf Sci* 364:843–849
10. Kong YL, Muniandy SV, Sulaiman K, Fakir MS (2017) Random fractal surface analysis of disordered organic thin films. *Thin Solid Films* 623:147–156
11. Dinner O, Paz Y, Grader GS (2018) Orthogonal fractal growth of CsI domains forming a ladder-like structure. *Thin Solid Films* 661:108–115
12. Yadav RP, Kumar M, Mittal AK, Dwivedi S, Pandey AC (2014) On the scaling law analysis of nanodimensional LiF thin film surfaces. *Mater Lett* 126:123–125
13. Yadav, RP et al (2017) Effect of angle of deposition on the Fractal properties of ZnO thin film surface. *Appl Surf Sci* 416:51–58
14. Țălu S, Stach S, Sueiras V, Ziebarth NM (2015) Fractal analysis of AFM images of the surface of Bowman's membrane of the human cornea. *Ann Biomed Eng* 43(4):906–916
15. Tokas RB, Jena S, Thakur S, Sahoo NK (2016) Effect of angle of deposition on micro-roughness parameters and optical properties of HfO<sub>2</sub> thin films deposited by reactive electron beam evaporation. *Thin Solid Films* 609:42–48

16. Senthilkumar M, Sahoo NK, Thakur S, Tokas RB (2005) Characterization of microroughness parameters in gadolinium oxide thin films: a study based on extended power spectral density analyses. *Appl Surf Sci* 252(5):1608–1619
17. Țălu S et al (2017) Application of Mie theory and fractal models to determine the optical and surface roughness of Ag–Cu thin films. *Opt Quantum Electron* 49(7):1–15
18. Wang Y, Xu KW (2004) Characterization of surface morphology of copper tungsten thin film by surface fractal geometry and resistivity. *Thin Solid Films* 468(1–2):310–315
19. Roy A, Sundaravel B, Batabyal R, Dev BN (2012) Fractal pattern formation in thermal grooving at grain boundaries in Ag films on Si(111) surfaces. *Thin Solid Films* 520(15):5086–5090
20. Nečas D, Klapetek P (2013) One-dimensional autocorrelation and power spectrum density functions of irregular regions. *Ultramicroscopy* 124:13–19
21. To, TBT, de Sousa, VB, Aarão Reis, FDA (2018) Thin film growth models with long surface diffusion lengths. *Phys A Stat Mech Appl*
22. Nečas D, Klapetek P (2012) Gwyddion: an open-source software for SPM data analysis. *Cent Eur J Phys* 10(1):181–188
23. Carpinteri A, Chiaia B, Invernizzi S (1999) Three-dimensional fractal analysis of concrete fracture at the meso-level. *Theor Appl Fract Mech* 31(3):163–172
24. Mwema FM, Oladijo OP, Sathiaraj TS, Akinlabi ET (2018) Atomic force microscopy analysis of surface topography of pure thin aluminium films. *Mater Res Express* 5(4):1–15
25. Starodubtseva MN, Starodubtsev IE, Starodubtsev EG (2017) Novel fractal characteristic of atomic force microscopy images. *Micron* 96:96–102
26. Klinkenberg B (1994) A review of methods used to determine the fractal dimension of linear features. *Math Geol* 26(1):23–46
27. Starodubtseva MN, Kuznetsova TG, Chizhik SA, Yegorenkov NI (2007) Atomic force microscopy observation of peroxynitrite-induced erythrocyte cytoskeleton reorganization. *Micron* 38(8):782–786
28. Annadhasan A (2012) Methods of fractal dimension computation. *IRACST Int J Comput Sci Inf Technol Secur* 2(1):2249–9555
29. Torkhov NA, Bozhkova VG, Ivonin IV, Novikov VA (2009) Determination of the fractal dimension for the epitaxial n-GaAs surface in the local limit. *Semiconductors* 43(1):33–41
30. Mwema FM, Oladijo OP, Akinlabi ET (2018) Effect of substrate temperature on aluminium thin films prepared by RF-magnetron sputtering. *Mater Today Proc.* 5(9):20464–20473
31. Dallaeva D, Țălu S, Stach S, Skarvada P, Tomanek P, Grmela L (2014) AFM imaging and fractal analysis of surface roughness of AlN epilayers on sapphire substrates. *Appl Surf Sci* 312:81–86
32. Țălu S, Stach S, Raoufi D, Hosseinpanahi F (2015) Film thickness effect on fractality of tin-doped In<sub>2</sub>O<sub>3</sub> thin films. *Electron Mater Lett* 11(5):749–757
33. Astinchap B (2019) Fractal and statistical characterization of Ti thin films deposited by RF-magnetron sputtering: the effects of deposition time. *Optik (Stuttg)* 178:231–242
34. Țălu S et al (2016) Micromorphology and fractal analysis of nickel–carbon composite thin films. *J Mater Sci: Mater Electron* 27(11):11425–11431
35. Țălu S et al (2015) Microstructure and tribological properties of FeNPs@a-C: H films by micromorphology analysis and fractal geometry. *Ind Eng Chem Res* 54(33):8212–8218
36. Dash P et al (2009) Surface roughness and power spectral density study of SHI irradiated ultra-thin gold films. *Appl Surf Sci* 256(2):558–561
37. Raoufi D, Kiasatpour A, Fallah HR, Rozatian ASH (2007) Surface characterization and microstructure of ITO thin films at different annealing temperatures. *Appl Surf Sci* 253(23):9085–9090
38. Raoufi D (2009) Morphological characterization of ITO thin films surfaces. *Appl Surf Sci* 255(6):3682–3686
39. Stach S et al (2017) 3-D surface stereometry studies of sputtered TiN thin films obtained at different substrate temperatures. *J Mater Sci: Mater Electron* 28(2):2113–2122
40. Buchko CJ, Kozloff KM, Martin DC (2001) Surface characterization of porous, biocompatible protein polymer thin films. *Biomaterials* 22(11):1289–1300

41. Arman A, Țălu S, Luna C, Ahmadpourian A, Naseri M, Molamohammadi M (2015) Micro-morphology characterization of copper thin films by AFM and fractal analysis. *J Mater Sci: Mater Electron* 26(12):9630–9639
42. Țălu S, Pratap R, Sik O, Sobola D, Dallaev R (2018) How topographical surface parameters are correlated with CdTe monocrystal surface oxidation. *Mater Sci Semicond Process* 85:15–23
43. Țălu S et al (2016) Microstructure and micromorphology of Cu/Co nanoparticles: surface texture analysis. *Electron Mater Lett* 12(5):580–588
44. Țălu S et al (2016) Gold nanoparticles embedded in carbon film: micromorphology analysis. *J Ind Eng Chem* 35:158–166
45. Hosseinpanahi F, Raoufi D, Ranjbarghanei K, Karimi B, Babaei R, Hasani E (2015) Fractal features of CdTe thin films grown by RF magnetron sputtering. *Appl Surf Sci* 357:1843–1848
46. Nasehnejad M, Nabiyouni G, Shahraki MG (2017) Dynamic scaling study of nanostructured silver films. *J Phys D Appl Phys* 50(37)
47. Douketis C, Wang Z, Haslett ZL, Moskovits M (1995) Fractal character of cold-deposited silver films determined by low-temperature scanning tunneling microscopy. *Phys Rev B: Condens Matter* 51(16):11022–11031
48. Țălu S et al (2018) Micromorphology analysis of sputtered indium tin oxide fabricated with variable ambient combinations. *Mater Lett* 220:169–171
49. Li JM, Lu L, Su Y, Lai MO (2000) Self-affine nature of thin film surface. *Appl Surf Sci* 161(1):187–193

# Image Segmentation and Grain Size Measurements of Palm Kernel Shell Powder



Omolayo M. Ikumapayi and Esther T. Akinlabi

**Abstract** Image segmentation is one of the essential tools to determine the foreground from background and at the same time enhance visual perception for better understanding through image manipulation. It is very useful for pattern recognition and image processing. This enables users to determine the high quality and high resolutions of the final result of the analysis. In this present study, PKS-Powder has been characterized with the use of Scanning Electron Microscopy (SEM), and Energy Dispersive X-ray (EDX) analyses. Digital Vibratory milling machine was employed for the mechanical milling at the time interval of 0, 10, 15 and 20 min. ImageJ software was employed for image processing by sectioning an image into various regions using thresholding segmentation method. It was revealed that at 0 min (i.e. 300  $\mu\text{m}$  sieved), it has the highest mean area value of 127.169  $\mu\text{m}^2$  and area standard deviation of 4,091.487  $\mu\text{m}^2$  with the least value of a number of particle size distribution of 458  $\mu\text{m}$ . In contrast, 20 min milled has the lowest values for mean area and area standard deviation of 52.913  $\mu\text{m}^2$  and 795.413  $\mu\text{m}^2$  respectively with the highest number of particle size distribution of 1,315  $\mu\text{m}$ . It was observed that milling time increases the number of particle sizes distributions and reduces the area of particle size. EDX analysis revealed that Ca, Al, Si, Fe, C, K, and O are the main elemental constituents of PKS-powder.

**Keywords** Palm kernel shell · Image segmentation · SEM-EDX · Milling

---

O. M. Ikumapayi (✉) · E. T. Akinlabi  
Department of Mechanical Engineering Science, University of Johannesburg, Auckland Park  
Kingsway Campus, Johannesburg 2006, South Africa  
e-mail: [oikumapayi@uj.ac.za](mailto:oikumapayi@uj.ac.za)

E. T. Akinlabi  
Department of Mechanical Engineering, Covenant University, Ota, Nigeria  
[etakinlabi@uj.ac.za](mailto:etakinlabi@uj.ac.za)

© Springer Nature Singapore Pte Ltd. 2020  
M. Awang et al. (eds.), *Advances in Material Sciences and Engineering*, Lecture Notes in Mechanical Engineering,  
[https://doi.org/10.1007/978-981-13-8297-0\\_29](https://doi.org/10.1007/978-981-13-8297-0_29)

265

## 1 Introduction

Nowadays, the use of bio-waste materials especially agro-waste has been a subject of interest, not only for scientific and technological point of view but also for socio-economic benefits in terms of employment, revenue generation such as exportation to other countries, as well as environmental issues [1–3]. Palm Kernel Shell (PKS) has been utilized in several applications today in form of macro-, micro- and nano-particles. Despite being bio-waste materials that pose a nuisance to the environment, its applications have made it be environmentally friendly and at the same time, is cost effective. Palm kernel shell is that hard part that enclosed and houses the nut of palm kernel fruit (*Elaeis guineensis*) [3, 4] (see Fig. 1). The processing of PKS involving the crushing of the palm kernel seed into different sectional sizes and then remove the nut within it and the left over as waste product is known as palm kernel shell. Several residues and waste products can be obtained from the process of removing and extracting freshly ripe and fleshy palm fruits from the bunch either at the mills or at home. These residues can be in form of empty fruit bunches (EFB), fibres, palm kernel shells as well as liquid waste in form of sewage (palm oil mill effluent, POME) with various usage, amongst which are preventing the attack of fibres from pest and insect. Other applications is found in weaving of baskets, as fuel for domestic use.

PKS is a bio-waste material from the processing of palm kernel fruit oil and has been progressively used in the various applications for environmental and technical benefits varying from water purification, additives, and reinforcements in building technology [5], aggregates, energy generation and fuel. It was noted that a greater use of this bio-waste material is mostly pronounced in the concrete application for structural components, water detoxifier and in the making of brakes in automotive parts. It has been established that in order to increase the environmental sustainability of by-product waste materials, there must be effective management. However, to reduce landfill during construction process using waste materials such as PKS, there must be effective strategies to waste management, this will eventually bring clean, sustainable and green construction [6]. It was also established that a large amount of PKS residues are left over during the process of oil palm production and as such



**Fig. 1** a Palm kernel fruits, b palm kernel shell, c pulverised PKS

posed environmental challenges since it was discharged untreated. On this note, effective utilization of PKS is required to curb this menace. At present, the most utilization of PKS has been traced to boiler fuel in direct-fired systems to generate steam, nevertheless, there is still an under-utilization of this bio-waste material [7].

Several researchers have done a tremendous study using PKS in Macro, Micro, and Nano level to conduct various experiments [7]. However, there is an area that is still left blank that the researchers are yet to address which is the motive behind this investigation. PKS has been utilized in the area of reinforcement in cement, concretes [8], composites in polymers, metals, and ceramics by various researchers. It has been utilized as fuel generation [9], carbon additives [10, 11] and pyrolysis up till today. Pyrolysis of PKS was characterized and to be used for washing medium and pre-treatment process [12]. Its usefulness has also been extended to water treatment in terms of Activated Carbon (AC) [13]. AC was produced from PKS and used as an adsorbent to remove pollutants from the aqueous phase. Production of AC from PKS was established which was used to remove colorants from the body of water with the help of activating agent called  $ZnCl_2$  [8, 14]. Literatures revealed that about 34.5% PKS is estimated from a single palm kernel fruit and the disposal of this biomass material waste has been a major environmental issue as reported [3, 15–17]. Palm kernel fruits, palm kernel shell as well as pulverized palm kernel shell are depicted in Fig. 1a–c respectively.

## 2 Materials and Methods

### 2.1 Material Collection and Processing

About 50 kg of palm kernel shell (PKS) used for this research work was collected from a local palm oil processing mill located at Ota, Ogun State Nigeria. The PKS was first sorted by removing any appearance of nuts and other extraneous materials, after which it was then washed with soap and rinsed with sufficient water to remove dirt, dust or any other impurities and free it from foreign materials. It was then air-dried naturally under the sun for 48 h. In order to ensure total dryness, it was further dried in an electric oven set at 50 °C for another 24 h before it was finally crushed using digitalised vibratory disc milling machine.

### 2.2 Vibratory Disc Milling Machine (VDMM)

A Digital Vibratory Disc Grinding Mill Lab Pulveriser (740 × 740 × 950 mm) with Machine Model 2MZ-200 supplied by FTLAB Technology has 2 pieces of bowl with a capacity of 200 g per bowl, feed size of less than 15 mm, pulverize time of 3–5 min or more depends on the nature of the materials, while the operating voltage

of 380 V/50 Hz, motor capacity of 1.5 KW with rotational speed of 940 rpm; was employed to carry out dry mechanical milling (DMM) at varying processing time of 10, 15 and 20 min which enables the reduction in particle size from micron to near-nano levels for palm kernel shell powder. The machine was thoroughly washed, dried and cleaned with acetone before and after use to remove any contaminants that may be present. 40 g of PKS-Powder sample was charged into each bowl and then set for running. The machine was interrupted every 5 min of operation in order to avoid a rise in temperature and at the same time to limit adherence of the powder within the container walls, the cooling interval before the next running was 30 min.

### **2.3 Microstructural Characterization**

The milled and unmilled PKS-P were analyzed through various microstructural characterization processes. For this study, the Scanning Electron Microscopy (SEM), Energy Dispersive X-ray (EDX), X-Ray Diffraction (XRD), and X-Ray Fluorescence (XRF) were used. The processes involved are discussed as follows.

#### **2.3.1 Scanning Electron Microscope (SEM)**

TESCAN model, type VEGA 3 LMH with model number VG9731276ZA and the following details 50/60 Hz, 230 V and 1,300 VA is the type of SEM machine that was employed for the studies. In order to have the sample more conductive and to have better resolution, the samples were sputter coated with a thin layer of carbon just before the scanning electron microscope analyses coupled with Energy Dispersive Spectrometer (EDS) analyses. The beam intensity used in the analysis is 14 and the accelerating voltage used is 20 kV, all micrographs were taken at SEM magnification of 500 $\times$  except the unmilled PKS-P which was taken at 56 $\times$  SEM MEG. The particle size and surface of Palm kernel Shell Powder (PKS-P) were analyzed at different milling times and the unmilled samples were also analyzed by SEM—this was taken as the sieved size of 300  $\mu\text{m}$  according to ASTM standard. The micrographs of different milling time were taken at 10, 15 and 20 min at 100  $\mu\text{m}$ .

#### **2.3.2 Energy Dispersive X-Ray Spectroscopy (EDXS)**

The elemental compositions of palm kernel shell powder as analysed by EDXS is depicted in Table 1.



**Table 1** The EDX shows elemental compositions of PKS-P

Element	Composition (wt%)
C	64.4
O	34.1
Si	0.9
Al	0.2
Fe	0.2
Ca	0.1
K	0.1

**Table 2** The chemical composition analysis of PKS-P using XRF

Chemical formula	PKS-P (%)
MgO	0.667
Al <sub>2</sub> O <sub>3</sub>	4.921
SiO <sub>2</sub>	46.23
K <sub>2</sub> O	4.254
SO <sub>3</sub>	2.257
CaO	4.786
Fe <sub>2</sub> O <sub>3</sub>	31.013
P <sub>2</sub> O <sub>5</sub>	2.448
TiO <sub>2</sub>	0.218
Cr <sub>2</sub> O <sub>3</sub>	0.267
MnO <sub>2</sub>	0.088
Na <sub>2</sub> O	1.32

### 2.3.3 X-Ray Fluorescence (XRF) Analysis

In this research, PHILIPS PW1404 X-Ray Fluorescence (XRF) Spectrometer is used to carry out the chemical composition of PKS-P when sieved with 300  $\mu\text{m}$  ASTM standard sieve and the outcome of the analysis is presented in Table 2.

### 2.3.4 Image Thresholding

Otsu's method [18] was used for image thresholding. The technique is a nonparametric as well as unsupervised thresholding technique, which selects optimum thresholds from a maximization of the intraclass variance of binary images. The global optimal threshold value was obtained for the SEM images. To determine whether the milling time has a significant effect on the microstructure, three time-steps were chosen for the experiment on the palm kernel shell powder (PKS-P).

### 3 Results and Discussion

#### 3.1 Image Analysis

The SEM images of PKS-P are originally obtained in 758 by 753 pixels dimension. The images were cropped into 747 by 747 pixels. SEM images obtained were binary images with the palm kernel powder being of white in column 2, which is a processed image and green intensity in column 3 in thresholding Images and red intensity in column 4 in particle size analysis; and the sputtering giving black shades in column 2 and 3 which are processed and thresholding images and white in column 4 in particle size analysis. Hence, an image complementing process is essential. The resulting cropped image was complemented, such that white and black, green and black as well as red and white are reversed in the binary images. This makes the PKS-P the regions of interest other than the black spots signifying the sputtering. Actual size of the particles was obtained using ImageJ software, the result of the processed, thresholding and particle size analysis results are presented in Fig. 2. The mean areas of the particle sizes, standard deviation, minimum and maximum areas of the particle sizes are presented in Table 3.

Figure 2a–t contains the Original Images from 0, 10, 15 and 20 min milling time as well as processed images, thresholding images and particle size measurements of the same milling time. This has been grouped into four columns i.e. columns 1–4. Column 1 represents the Original Image from 300  $\mu\text{m}$  down to 20 min milled.

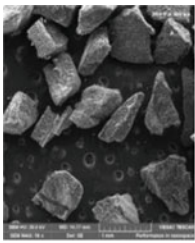

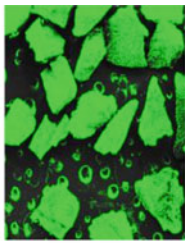
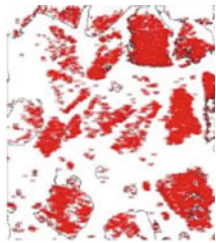
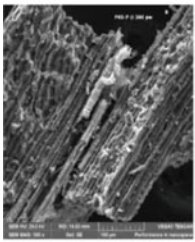
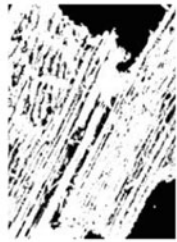
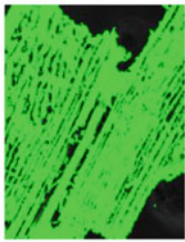
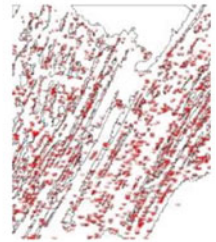
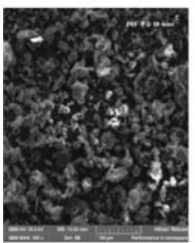

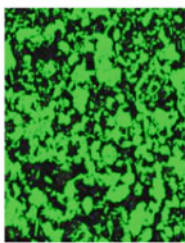
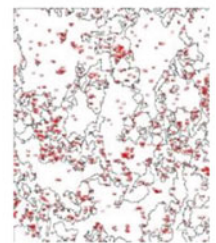
Figure 2a, e, I, m, q in column 1 is the original images before the actual processing takes place for unmilled (300  $\mu\text{m}$  sieved), 0, 10, 1 and 20 min respectively. There was a gradual reduction in the area of the particle from column 1 down the column (Fig. 2a–q) which was also evident in Table 3 as the number of particle sizes increase down the column 1.

Figure 2b, f, j, n, r are the processed Images from Original Images which appeared in binary images by segmentation. The foreground is the white pixel (i.e. PKS-P) and the background is the black pixel (i.e. sputtering).

Figure 2c, g, k, o, s are the thresholding images from the processed images where the foreground is a green pixel which replaced the white pixel in the processed images but still maintained the background which is a black pixel.

**Table 3** Measurements of particle size area of PKS-P at unmilled and varying milling time

Milling time (mins)	Mean area ( $\mu\text{m}^2$ )	STD area ( $\mu\text{m}^2$ )	Min. area ( $\mu\text{m}^2$ )	Max. area ( $\mu\text{m}^2$ )	No. of particle sizes ( $\mu\text{m}$ )
0	127.169	4091.487	0.291	166,163.117	458
10	97.163	1964.954	0.304	55,425.272	839
15	62.687	1431.954	0.295	47,156.624	1167
20	52.913	795.413	0.287	26,131.384	1315

Column 1 for Original Images	Column 2 for Processed Images	Column 3 for Thresholding Images	Column 4 for Particle sizes analysis
			
(a) Original micrograph at 1 mm of 300 $\mu\text{m}$ sieved	(b) Processed Image at 1 mm of 300 $\mu\text{m}$ sieved	(c) Thresholding Image at 1 mm of 300 $\mu\text{m}$ sieved	(d) Particle Size Analysis at 1 mm of 300 $\mu\text{m}$ sieved
			
(e) Original micrograph at 100 $\mu\text{m}$ of 300 $\mu\text{m}$ sieved	(f) Processed Image at 100 $\mu\text{m}$ of 300 $\mu\text{m}$ sieved	(g) Thresholding Image at 100 $\mu\text{m}$ of 300 $\mu\text{m}$ sieved	(h) Particle Size Analysis at 100 $\mu\text{m}$ of 300 $\mu\text{m}$ sieved
			
(i) Original micrograph at 100 $\mu\text{m}$ of 10 mins milled	(j) Processed Image at 100 $\mu\text{m}$ of 10 mins milled	(k) Thresholding Image at 100 $\mu\text{m}$ of 10 mins milled	(l) Particle Size Analysis at 100 $\mu\text{m}$ of 10 mins milled

**Fig. 2** SEM images of PKS-powder at various milling time of 0, 10, 15 and 20 min taking at 500 $\times$  MAG

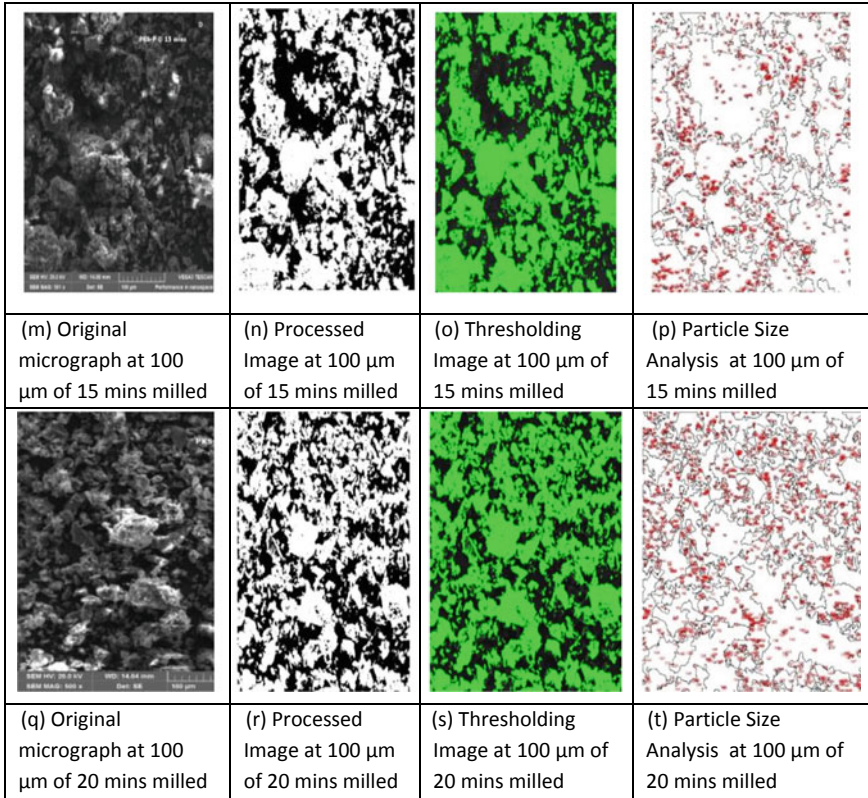


Fig. 2 (continued)

Figure 2d, h, l, p, t are the measured images for particle size analysis taken at (300 μm sieved), 0, 10, 1 and 20 min. It was observed in Table 3 that there was an increased in the number of particle sizes from 458 μm at 0 min to 1,315 μm at 20 min milled. This suggests that there was a significant influence of milling on the PKS-P.

## 4 Conclusion

The method used in this work permitted the manipulations of micrographs in order to have a true representation of the Powder distribution and at the same time distinguishing foreground from background. Image processing analysis was investigated in this research through thresholding segmentation at varying milling times ( $t = 0, 20, 40, 60$  min). It was revealed in the study that progressive milling leads to an increase in particle size distributions and decrease in the area of particle size as

noted in Table 3. It was revealed that at 0 min (i.e. 300  $\mu\text{m}$  sieved), the highest mean area value of 127.169  $\mu\text{m}^2$  and area standard deviation of 4091.487  $\mu\text{m}^2$  with least value of a number of particle size distribution of 458  $\mu\text{m}$  were observed. In contrast, 20 min milled has the lowest values for mean area and area standard deviation of 52.913  $\mu\text{m}^2$  and 795.413  $\mu\text{m}^2$  respectively with the highest number of particle size distribution of 1315  $\mu\text{m}$ . It was observed that milling time increases the number of particle sizes distributions and reduces the area of particle size. EDX analysis revealed as showed in Fig. 1 that Ca, Al, Si, Fe, C, K, and O are the main elemental constituents of PKS-powder. Applications of PKS-Powder are rooted in many areas such as reinforcements in building and concretes applications, fillers, energy generation and fuel, additives, activated carbon as well as water purification. PKS-powder can also finds its near future applications in reinforcement of metal, ceramics and polymers composites most especially in the friction stir processing and welding.

## References

1. Dagwa IM, Builders PF, Achebo J (2012) Characterization of palm kernel shell powder for use in polymer matrix composites. *Int J Mech Mechatron Eng* 12(4):88–93
2. Olutoge FA, Quadri HA, Olafusi OS (2012) Investigation of the strength properties of palm kernel shell ash concrete. *Eng Technol Appl Sci Res* 2(6):315–319
3. Ikumapayi OM, Akinlabi ET (2018) Composition, characteristics and socioeconomic benefits of palm kernel shell exploitation—an overview. *J Environ Sci Technol* 11(6):1–13
4. Peter Ndoke NDOKE (2006) Performance of palm kernel shells as a partial replacement for coarse aggregate in asphalt concrete. *Leonardo Electr J Pract Technol* 5(9):145–152
5. Wang P, Zhang J, Shao Q, Wang G (2018) Physicochemical properties evolution of chars from palm kernel shell pyrolysis. *J Therm Anal Calorim* 133(3):1–10
6. Khankhaje E, Rafieizonooz M, Salim MR, Mirza J, Salmiati, Hussin MW (2017) Comparing the effects of oil palm kernel shell and cockle shell on properties of pervious concrete pavement. *Int J Pavement Res Technol* 10(5):383–392
7. Huang Y et al (2018) Relevance between chemical structure and pyrolysis behavior of palm kernel shell lignin. *Sci Total Environ* 633:785–795
8. Hamada HM, Jokhio GA, Yahaya FM, Humada AM, Gul Y (2018) The present state of the use of palm oil fuel ash (POFA) in concrete. *Constr Build Mater* 175:26–40
9. Bediako M, Gawu SK, Adjaottor AA, Solomon Ankrah J, Atiemo E (2016) Analysis of co-fired clay and palm kernel shells as a cementitious material in Ghana. *Case Stud Constr Mater* 5:46–52
10. Fono-Tamo RS, Idowu OO, Koya FO (2014) Development of pulverized palm kernel shells based particleboard. *Int J Mater Mech Eng* 3(3):54
11. Fono-Tamo RS, Koya OA (2017) Influence of palm kernel shell particle size on fade and recovery behaviour of non-asbestos organic friction material. *Procedia Manuf* 7:440–451
12. Hidayu AR, Muda N (2016) Preparation and characterization of impregnated activated carbon from palm kernel shell and coconut shell for CO<sub>2</sub> capture. *Procedia Eng* 148:106–113
13. Edmund CO, Christopher MS, Pascal DK (2014) Characterization of palm kernel shell for materials reinforcement and water treatment. *J Chem Eng Mater Sci* 5(1):1–6
14. García JR, Sedran U, Zaini MAA, Zakaria ZA (2017) Preparation, characterization, and dye removal study of activated carbon prepared from palm kernel shell. *Environ Sci Pollut Res* 1–10
15. Singh RP, Ibrahim MH, Esa N, Iliyana MS (2010) Composting of waste from palm oil mill: a sustainable waste management practice. *Rev Environ Sci Biotechnol* 9(4):331–344

16. Mgbemena CO, Mgbemena CE, Okwu MO (2014) Thermal stability of pulverized palm kernel shell (PKS) based friction lining material locally developed from spent waste. *ChemXpress* 5(4):115–122
17. Anyaoha KE, Sakrabani R, Patchigolla K, Mouazen AM (2018) Evaluating oil palm fresh fruit bunch processing in Nigeria. *Waste Manag Res* 36(3):236–246
18. Otsu N (1979) A threshold selection method from gray-level histograms. *IEEE Trans Syst Man Cybern* 9(1):62–66

# Effect of Support Structure Design on the Part Built Using Selective Laser Melting



Muhammad Rafi Sulaiman, Farazila Yusof and Mohd Fadzil Bin Jamaludin

**Abstract** Support structures are needed to successfully build parts using Selective Laser Melting (SLM) in order to support overhanging surfaces to disperse process heat, minimize geometrical deformation induced by residual stresses and hold the work piece in its place. These structures need extra post-processing time for their removal and are often massive. Reduce in amount of support structures would significantly decrease finishing efforts and manufacturing costs. The design of support structure can influence the manufacturability of more complex metal parts, energy and material utilization. In this research, it focuses on finding the design of support structure which can reduce deformation of the resulting print part with lowest volume of material used and easy to be removed during post processing. Experimental result revealed that change in design and parameter of support structure and sample orientation influence the amount of deformation, build time and support removability.

**Keywords** Additive manufacturing · Support structure design

## 1 Introduction

Additive manufacturing (AM) is a general term used to describe a process that creates three-dimensional object in which sequential layers of material are formed under computer control to build the object. Layer fabrication process is key in building parts using AM. The process starts with depositing thin layers of material, one on top of another. The part is built by repeating the fabrication process from bottom to top. Literally any shape that can be modelled on a Computer Aided Design (CAD)

---

M. R. Sulaiman · F. Yusof (✉)

Department of Mechanical Engineering, Faculty of Engineering, University of Malaya, 50603 Kuala Lumpur, Malaysia  
e-mail: [farazila@um.edu.my](mailto:farazila@um.edu.my)

F. Yusof · M. F. B. Jamaludin

Department of Mechanical Engineering, Centre of Advanced Manufacturing and Material Processing, University of Malaya, 50603 Kuala Lumpur, Malaysia

© Springer Nature Singapore Pte Ltd. 2020

M. Awang et al. (eds.), *Advances in Material Sciences and Engineering*, Lecture Notes in Mechanical Engineering, [https://doi.org/10.1007/978-981-13-8297-0\\_30](https://doi.org/10.1007/978-981-13-8297-0_30)

275



system can be constructed using this technique, including geometric shapes that is impossible to be manufactured using conventional techniques. SLM technique is one of the AM processes that builds prototype parts by depositing and melting metal powder layer by layer. It is one of the additive manufacturing technologies enabling building components from metallic powders [1, 2]. Although SLM is a relatively new technology, the Rapid Prototyping (RP) based SLM process challenges the traditional material removal processes.

Many AM-produced parts can be supported by their surrounding materials such as the powder in the Selective Laser Sintering (SLS), sheet lamination processes and Powder Bed Fusion (PBF). However, several other AM processes, such as extrusion-based systems and direct printing, are not be able to be supported by surrounding materials. Extra supports are required for overhanging structures and to attach the part to the build plate. In some cases with large distortion, such as when using Powder Bed Fusion (PBF) process for metal in SLM, supports are needed in order to release the heat, resist distortion and prevent the work piece from moving from original place [3]. Support structures are needed to be removed before the finishing process takes place.

The number of support structures that need to be used is determined through the design of a part. Compare to other AM processes, SLM has the most difficulty to remove the supports as they are solid metal. The main restriction on designing part geometries in AM is the need of support structures because support placement is equally as important as the part design. Some of the major concerns in metal Powder Bed Fusion (PBF) processes such as SLM are distortion and high residual stresses. Due to concentrated heating of laser irradiation, phase transformation and complex thermal cause stress to be generated. In addition, frequent thermal contraction and expansion of the earlier hardened layers during the process produce considerable stress gradients and thermal stress that can exceed the yield strength of the material [4]. Residual stresses can lead to initiate fracture, part distortion, and unwanted reduction in strength of the part [5].

It is significant to make the first layer without distortion on the powder bed in creating parts with overhanging parts because the primary powders do not restrict the distortion [6]. Thermal stress can cause huge deformations to the part and can lead to build failure due to delamination of the part from the base plate. Thermal stress can also encourage cracks during processing before the part is finished being built. The need for support structures is described as one of the limitations of the SLM process because it severely limits the geometries that the processes can make and adds significant cost and time to production [7].

The major work of post-processing in SLM is support removal and finishing. There are two types of support materials: (a) rigid structures which are built and designed to support the part being built to a build plate (synthetic support), and (b) powder which surrounds the part as a naturally-occurring by-product of the build process (natural supports) [8]. In SLM, the nearby powder acts as a natural support and provides support for the part during build process. The loose powder can simply be removed from the part in SLM. In most cases, extra synthetic support structures need to be designed and fabricated to decrease deformation caused by thermal stress.



This type of support structure needs to be removed from the part during SLM post processing. Surface finishing is usually required after support removal.

The rule of thumb for good SLM support structure design is that it should be the minimum amount of supports which avoids the risk of fabrication failure. A good support design should also achieve the following important functions: restraining the part to a maximal amount of distortion and keeping the part from crashing into the blade, avoiding breaking of the support structure, anchoring the floating sections and overhanging introduced during the building process to the platform, raising the part off the platform for easy removal, and reinforcing thin and tall parts during the build to prevent them from bending by the forces of the blade [9]. Too many supports increase the amount of material used and leads to an increase in difficulty for removing supports. The surface with the lowest requirement for finishing is a good option for the bottom surface since the surface attached to the support structure will have poor surface finish after removal of the support structure. So, a good support strategy should also avoid interfering with key geometrical features.

In light of this, the present study investigates the effect of support structure design on part built using selective laser melting by determining the best support structure in term of build time, support removability, and amount of deformation.

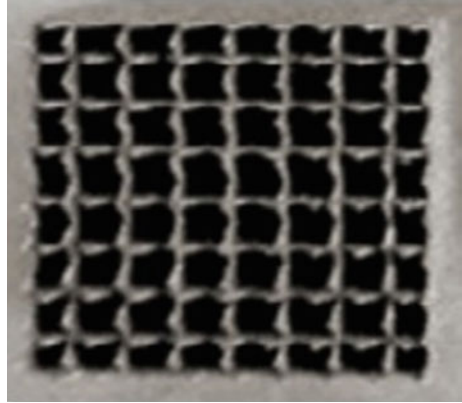
## 2 Experimental Procedure

### 2.1 Design of Support Structure

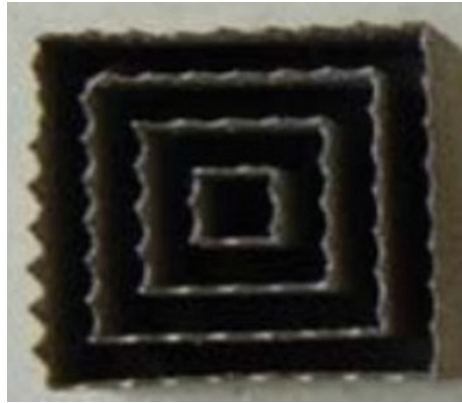
Magics software (from Materialise, Belgium) and AutoFab (from Marcam, Germany—Now acquired by Materialise, Belgium) have functions to generate support structures manually or automatically. It allows users to choose orientation of the 3D model to attach to the support structure. Types and parameters of the support structure are also flexible for the user to select. The user can modify and tune the support structure for special features to optimize the design. Magics software support generation module provides a broad range of support structure types including block, line, point, web, contour, gusset, combi, volume, and cone support structure. In this study, the researchers focus on block and contour type of support structure because both are suitable for large surface. Figures 1 and 2 show the block and contour type of support that are used in this experiment.

The parameters of support structure that are changed is hatching distance for block type of support structure while for contour type of support structure, it is contour offset. Block support are made with a grid of X and Y lines which are separated at a certain distance (X Hatching and Y Hatching) as in Fig. 3. While in Fig. 4, it shows the contour offset value in contour support that indicates the offset from one contour to the other. The default value in magics software for hatching distance and contour offset is 1.5 mm. To avoid failure during build process, both hatching distance and contour offset value are set to range only 20% (0.3 mm) from the default value which

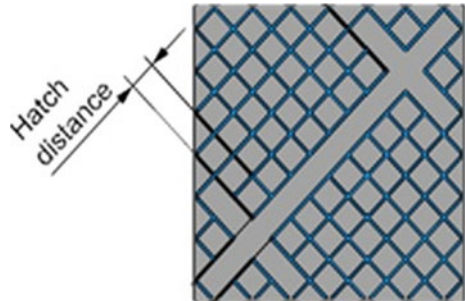
**Fig. 1** Block type of support structure



**Fig. 2** Contour type of support structure

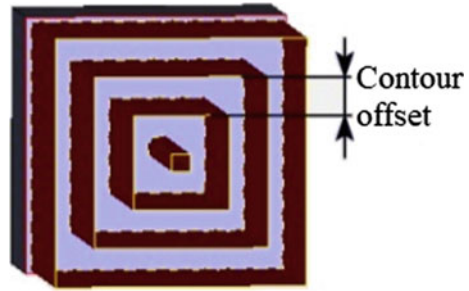


**Fig. 3** Hatching distance in block support

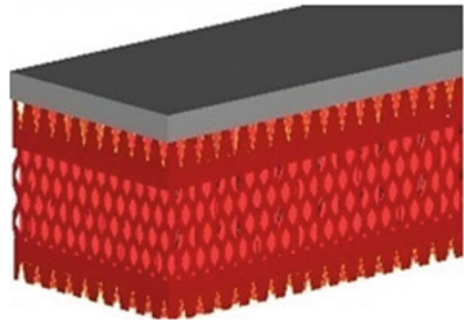


is 1.2 and 1.8 mm. Another parameter that is tested in this experiment is whether the support is perforated or fragmented as shown in Figs. 5 and 6. The wall of support are perforated and fragmented to allow the removal of excess powder and make the process of support removal easier [10, 11].

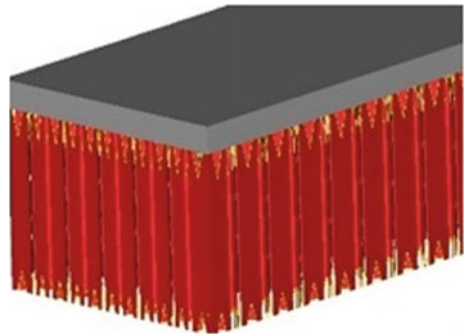
**Fig. 4** Contour offset in contour support



**Fig. 5** Perforation type of support



**Fig. 6** Fragmentation type of support



The parameters of 24 samples produced in this experiment were summarized in Table 1. Sample 1–12 use overhanging part as in Fig. 7 while sample 13–24 use incline angle part as in Fig. 8. The cantilever part was chosen to study the efficiency of the support structure and to collect enough data on cantilever deformation while the incline angle part is chosen to study the effect of angle on performance of support structure. Since sample 1–12 (overhanging) and 13–24 (incline angle) are using similar support parameter but the only thing different is the sample part, the first 2 types of test which is build time evaluation and support removability are carried out only for the first 12 samples (overhanging) while deformation analysis are carried out for all 24 samples.

**Table 1** Support structure parameter

Sample number	Type of part	Support type	Hatching distance	Contour offset	Perforation/fragmentation
1	Overhanging	Block	1.2	–	Perforation
2	Overhanging	Block	1.2	–	Fragmentation
3	Overhanging	Block	1.5	–	Perforation
4	Overhanging	Block	1.5	–	Fragmentation
5	Overhanging	Block	1.8	–	Perforation
6	Overhanging	Block	1.8	–	Fragmentation
7	Overhanging	Contour	–	1.2	Perforation
8	Overhanging	Contour	–	1.2	Fragmentation
9	Overhanging	Contour	–	1.5	Perforation
10	Overhanging	Contour	–	1.5	Fragmentation
11	Overhanging	Contour	–	1.8	Perforation
12	Overhanging	Contour	–	1.8	Fragmentation
13	Incline angle	Block	1.2	–	Perforation
14	Incline angle	Block	1.2	–	Fragmentation
15	Incline angle	Block	1.5	–	Perforation
16	Incline angle	Block	1.5	–	Fragmentation
17	Incline angle	Block	1.8	–	Perforation
18	Incline angle	Block	1.8	–	Fragmentation
19	Incline angle	Contour	–	1.2	Perforation
20	Incline angle	Contour	–	1.2	Fragmentation
21	Incline angle	Contour	–	1.5	Perforation
22	Incline angle	Contour	–	1.5	Fragmentation
23	Incline angle	Contour	–	1.8	Perforation
24	Incline angle	Contour	–	1.8	Fragmentation

## 2.2 Manufacturing Process

All experiments are conducted using SLM 280 HL machine. The open software architecture and integrated SLM Build Processor offer the ability to adjust whether system parameters run standard builds or optimized to meet strict production requirements and gain a competitive lead. The whole process is done in inert gas atmosphere and closed-loop powder handling. The material used to print the part is AISi10Mg.

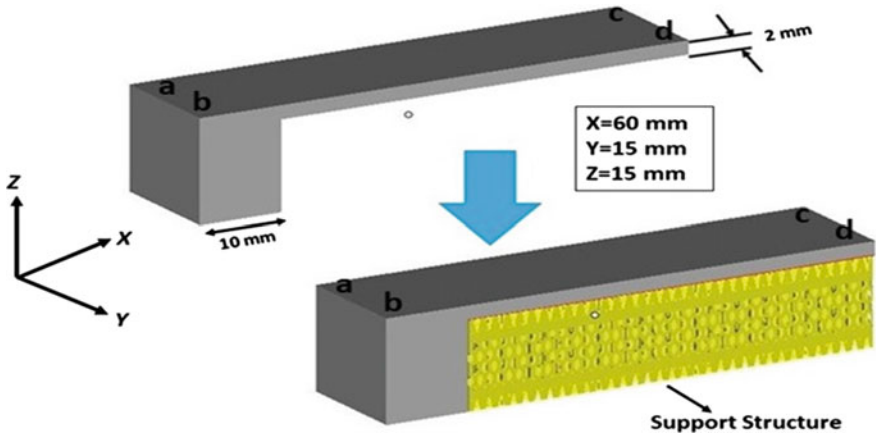


Fig. 7 CAD geometry of overhanging part

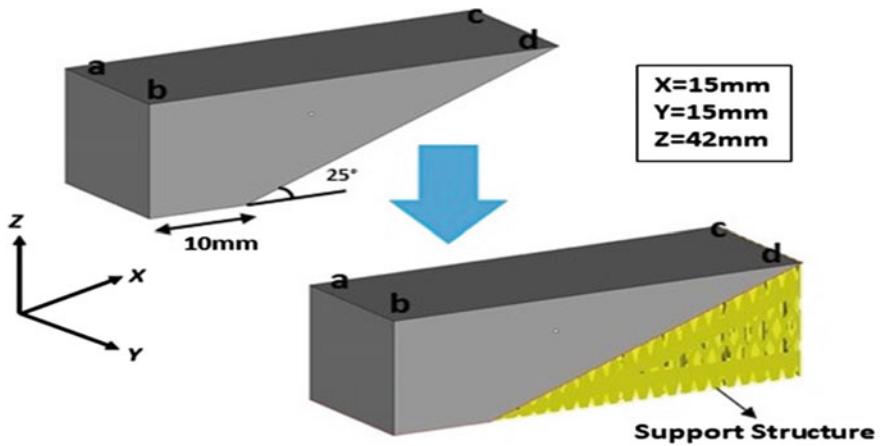


Fig. 8 CAD geometry of incline angle part

### 2.3 Measurement and Analysis

Build time of support structure is evaluated through the date obtained from Magics software. Post processing to remove support structure is done manually using Multi Cutter. The level of removability (hard or easy) recorded during the post processing of samples. Lastly, the deformation analysis is carried to differentiate the amount of trapped stresses that are released through longitudinal deformation. This deformation is an indication of the quantity of residual stresses present in the part. Dimensional inspection was conducted by attaching dial indicator on grinding machine to get the value of z-axis to see the part deformation. The value of z-axis in upward direction was used to indicate the performance of the created supports. Since the parts were

still attached to build platform, the flatness of the build plate was measured first to avoid wrong measurement of the results. The build plate was grinded using NAGACHI PRECISION Grinding Machine until flatness value of the plate was less than  $50\ \mu\text{m}$ . The heights of 4 points were measured on the top part surface. These points were denoted with the letters a, b, c, d in Figs. 7 and 8. Measurement points “a” and “b” were located on the edge of part surface attach to build plate while the points “c” and “d” were located on the edge of overhang surface. Using measurement results for each sample, amount of deformation graphs was generated to provide better interpretation of the results.

### 3 Results and Discussion

#### 3.1 Build Time

Table 2 gives the build time that are required to build each sample part individually based on magics software. Since all samples used in this experiment have similar dimension, the difference in build time is because of the different type and parameter of the support structure. The build time is directly proportional to the amount of material used to create the support which means the higher the build time, the higher the cost to build part is; because more materials are used to build the part. From Table 2, it is noticed that even though all samples have different support parameters, the build time different is not significant. The biggest difference of build time is only 3 s because the height of support structure is only 13 mm. However, in real manufacturing situation, the part that are built is bigger which require larger support structure which will give more significant in build time. The data from Table 2 also show that in block type support structure, when the hatching distance becomes bigger the build time becomes less. For example, in sample 13, 15 and 17 which have value of hatching distance of 1.2, 1.5 and 1.8 mm respectively, the build time increases 1 s every time the hatching distance is increasing. However, it is different in contour type support structure where even though the hatching distance is increasing, the build time remains the same. For example, in sample 7, 8, 9, 10, 11, and 12, the build time remaining maintained at 46 min and 56 s even though the hatching distance is increasing from 1.2 to 1.8 mm. Even though the build time is not changing, it does not mean the part has same build time, but it is because the difference between each sample part build time is less than one second. The contour type support structure does not have a significant difference in build time compared to block type support structure even though the hatching distance is changing because the air gap in contour type support structure is bigger compared to block type of support structure as in Figs. 1 and 2.

**Table 2** Build time of support structure from magics 19 software

Sample number	Build time (min)
1	46 min 59 s
2	46 min 59 s
3	46 min 58 s
4	46 min 58 s
5	46 min 58 s
6	46 min 58 s
7	46 min 56 s
8	46 min 56 s
9	46 min 56 s
10	46 min 56 s
11	46 min 56 s
12	46 min 56 s

**Table 3** Removability evaluation of support structure

Sample number	Removability score
1	1
2	2
3	1
4	2
5	1
6	2
7	2
8	3
9	2
10	3
11	2
12	3

3 easy to remove, 2 average, 1 hard to remove

### 3.2 Support Removability

As we can see in Table 3, the easiest support structures to be removed is sample 8, 10 and 12. Sample 8, 10 and 12 are built using contour type support structure with outside wall fragmented while the hardest support structures to be removed are sample 1, 3 and 5. Sample 1, 3 and 5 are built using block type support structure with different hatching distance and outside wall is perforated. From sample 1, 3 and 5, it is also known that the lower the hatching distance, the harder it is to remove it.

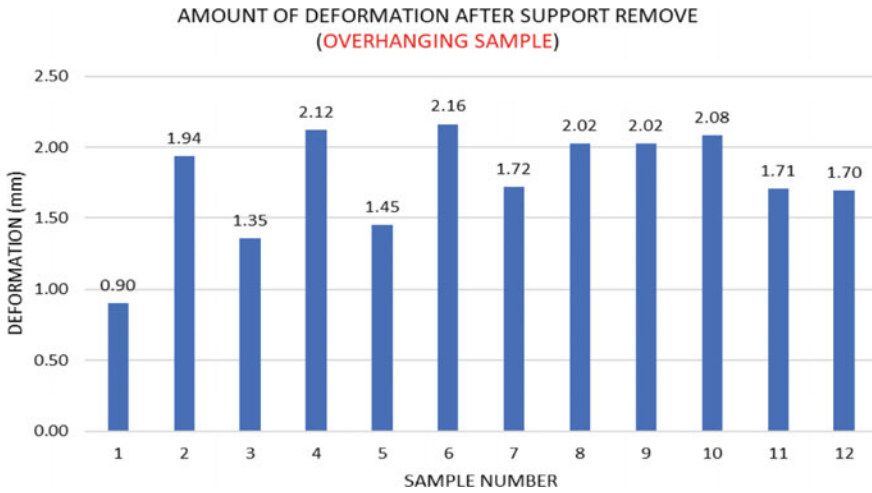


Fig. 9 Amount of deformation after support remove for overhanging sample

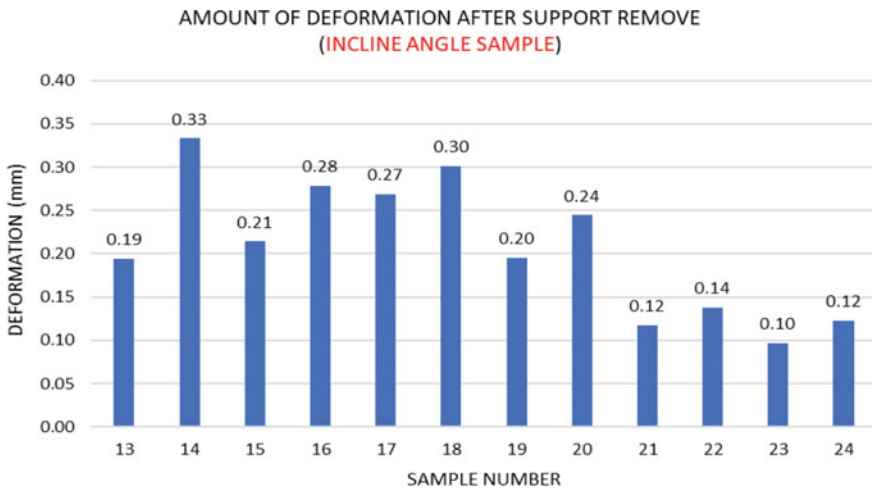


Fig. 10 Amount of deformation after support remove for incline angle sample

### 3.3 Deformation Analysis After Support Remove

Once the supports is removed from sample, point a, b, c and d are measured and presented into form of graph for easier comparison. The points (a, b) are added and divided by 2 to find the average of height for each end of overhanging sample. The same processes were also done to point (c, d) to find the average. Then the average height of (c, d) are minuses by average height of (a, b) to find the amount of deformation as shown in Figs. 9 and 10.



From the graph in Fig. 9, we can see that the lowest amount of deformation is for sample 1 with only 0.90 mm of deformation. Sample 1 is built using block type support structure with perforation outer wall and the hatching distance is 1.2 mm. If we compare the amount of deformation for sample 1, 3, 5 and 2, 4, 6 we can conclude that the lower the hatching distance, the lower the deformation that occurred. The highest deformation occurs to sample 6 with 2.16 mm of deformation. Sample 6 is built using block type of support structure with fragmentation outer wall and the hatching distance is 1.8 mm.

From the graph in Fig. 10, we can see that the lowest amount of deformation is for sample 23 with only 0.10 mm of deformation. Sample 23 is built using contour type support structure with perforated outer wall and the contour offset is 1.8 mm. Meanwhile the highest deformation occurs to sample 14 with 0.33 mm of deformation. Sample 14 is built using block type support structure with fragmented outer wall and the hatching distance is 1.2 mm. If we compare the highest deformation in overhanging sample which is 2.16 mm with incline angle sample which is only 0.10 we can conclude that the angle orientation of the part also affects in reducing amount of deformation.

## 4 Conclusion

This study shows the effect of changing support structure parameter on part built using Selective Laser Melting (SLM) machine. Overhanging and incline angle type of sample part are used to evaluate performance of support structure in term of build time, support removability and amount of deformation. From discussion, few conclusions can be made regarding the parameter of support structure. First, change in support structure design give significant effect on amount of deformation. Second, the lower the hatching distance and contour offset the lower the amount of deformation. Third, different in sample orientation give effect on amount of deformation. Fourth, build time is not significant for small area of support structure. Fifth, for easier support removability is by using contour type of support structure with fragmentation outer wall. Sixth, for lower amount of deformation is by using block type of support structure with perforation outer wall.

**Acknowledgements** We would like to express our gratitude to the Ministry of Education for providing Fundamental Research Grant Scheme (FRGS) with project number of FP062-2015A for funding this project.

## References

1. Strano G et al (2013) Surface roughness analysis, modelling and prediction in selective laser melting. *J Mater Process Technol* 213(4):589–597
2. Wohlers T, Caffrey T (2013) Additive manufacturing: going mainstream. *Manuf Eng* 151(6):67–73
3. Järvinen J-P et al (2014) Characterization of effect of support structures in laser additive manufacturing of stainless steel. *Phys Procedia* 56:72–81
4. Wang D et al (2013) Research on the fabricating quality optimization of the overhanging surface in SLM process. *Int J Adv Manuf Technol* 65(9–12):1471–1484
5. Mercelis P, Kruth J-P (2006) Residual stresses in selective laser sintering and selective laser melting. *Rapid Prototyp J* 12(5):254–265
6. Matsumoto M et al (2002) Finite element analysis of single layer forming on metallic powder bed in rapid prototyping by selective laser processing. *Int J Mach Tools Manuf* 42(1):61–67
7. Mumtaz K, Vora P, Hopkinson N (2011) A method to eliminate anchors/supports from directly laser melted metal powder bed processes. In: *Proceedings of the solid freeform fabrication symposium, 2011*, Sheffield
8. Gibson I, Rosen D, Stucker B (2015) *Direct digital manufacturing*. In: *Additive manufacturing technologies*. Springer, pp 375–397
9. Hussein A et al (2013) Advanced lattice support structures for metal additive manufacturing. *J Mater Process Technol* 213(7):1019–1026
10. Venuvinod P, Ma W (2004) *Rapid prototyping: laser-based and other technologies*. Springer (Optics, Kluwer)
11. Swaelens B, Pauwels J, Vancraen W (1997) Method for supporting an object made by means of stereolithography or another rapid prototype production method. Google Patents

# A Correlation to Predict Erosion Due to Sand Entrainment in Viscous Oils Flow Through Elbows



Mysara Eissa Mohyaldinn, Mokhtar Che Ismail and Nurul Hasan

**Abstract** The entrainment of sand particles in fluids flowing through horizontal or vertical pipes is frequently occurring during oil and gas production and transportation. Consequently, sand impingement on the internal walls of pipes and fittings leads to continuous eroding and wall thinning of these fittings. One of the practices followed to avoid erosion is by early prediction of erosion rate and controlling the flow parameters to be within a pre-specified safe operation limit. The prediction can be conducted using empirical correlations, semi-empirical models, or computational fluid dynamics (CFD) simulation. Direct impingement model (DIM) is a semi-empirical model that processes high accuracy result than the empirical correlations and involves inclusion of the effect of viscosity. DIM, however, was found more complicated than empirical correlations as it involves numerical solution of the equation of particles motion. It is desired, therefore, to develop a model that processes the features of both empirical (i.e. easy use) and semi-empirical (i.e. high accuracy) models. In this paper, a correlation has been proposed for prediction of sand erosion in elbows due to entrainment of sand in oils. The correlation has been developed by mean of comparison of results from the empirical Salama model with results from DIM for oil with different viscosities. As a result, the viscosity was incorporated into Salama model and the applicability of it is extended to oil flow. The new model was validated against results from the DIM model as well as published experimental data. The new model was found to perform better than the original Salama model for viscous oil.

**Keywords** Sand erosion · Semi-empirical · Prediction · Flow

---

M. E. Mohyaldinn (✉)

Petroleum Engineering Department, Universiti Teknologi PETRONAS, 31750 Bandar Seri Iskandar, Tronoh, Perak, Malaysia  
e-mail: [mysara.eissa@utp.edu.my](mailto:mysara.eissa@utp.edu.my)

M. C. Ismail

Mechanical Engineering Department, Universiti Teknologi PETRONAS, 31750 Bandar Seri Iskandar, Tronoh, Perak, Malaysia

N. Hasan

Petroleum and Chemical Engineering, Universiti Teknologi Brunei, Gadong, Brunei Darussalam

© Springer Nature Singapore Pte Ltd. 2020

M. Awang et al. (eds.), *Advances in Material Sciences and Engineering*, Lecture Notes in Mechanical Engineering, [https://doi.org/10.1007/978-981-13-8297-0\\_31](https://doi.org/10.1007/978-981-13-8297-0_31)

287

## 1 Introduction

The entrainment of sand particles in fluids flowing through horizontal or vertical pipes is frequently occurring during oil and gas production and transportation. In conventional oil production, sand is produced with oil and gas from a sandstone reservoir under certain conditions; such conditions include unconsolidated formation, high water cut, and high pressure drop. In unconventional oil or crude bitumen, which is a mixture of sand, bitumen, and water; sand is produced with a very high volume fraction [18].

The entrainment of sand in fluids causes wear of pipes and fittings through which it flows, due to the impingement of sand particles on internal surfaces. The severity of the wear depends on many factors that are related to the fluid, sand particles, and target material.

The erosion rate for a material used in any flow process can be determined either by field or laboratory tests under simulated conditions or be calculated using a selected mathematical or computational model, provided that the noteworthy flow parameters are included in the model. Although field and laboratory tests guarantee more accurate results than modeling, it is more costly, difficult, and time consuming than prediction using mathematical and computational tools. Modeling the erosion, on the other hand, requires proper selection of the model that is suitable for the specified process, and provides accepted accuracy. For erosion, the models in the open literature can be grouped into three categories, namely CFD models, semi-empirical models, and empirical models [9]. In the empirical methods, erosion is predicted for a component (most probably elbow or tee) by using the fluid velocity (no particles or bubbles tracking). The methods are commonly based on simple empirical correlations that predict erosional velocity (the velocity above which erosion occurs) and erosion rate, and are more applicable to gas flow where the dispersed phase (particles or bubbles) is assumed to be almost flowing at the same mean velocity of the fluid. The erosional velocity is usually predicted using the American Petroleum Institute Recommended Practice equation (API RP 14 E) [1], which is a simple equation that equates the erosional velocity with the ratio of a material-dependent constant to the square root of fluid density. This form makes the equation questionable on the ground of overlooking of some important factors such as particles size and shapes, component geometries, and fluid viscosity. It follows that other empirical models have been proposed to replace the API RP 14E equation. Examples of empirical equations for sand erosion rate prediction are those proposed by Salama and Venkatesh [15] and Salama [14]. Salama model [14] has the advantage over Salama and Venkatesh model due to its incorporation of the effect of two-phase mixture density and particle size. This model has further been examined by Mysara and others by comparison with published data [8] and three new models are produced from it and proposed for prediction of erosion rate for fluids based on gas-liquid-ratio.

Throughout the previous attempts, there is a big gap in the literature for including viscosity in the empirical correlation. As a matter of fact, the experimental investigations of the effect of viscosity on erosion rate is limited [13]. The significance of the

dependency of erosion rate on viscosity has been highlighted by some researchers but with limited results, high discrepancy of the findings, and at conditions mostly different with those faced in oil and gas operations. Saleh and his co-workers [16] have used mixtures of glycerin and distilled water of various concentrations at room temperature of 30 °C to study the effect of viscosity on cavitation erosion. Their results, however, were predominately in qualitative analysis using scanning electron photomicrographs and no quantitative results were presented for the viscosity effect. Okita et al. [12] studied the effect of viscosity on erosion rate using a jet impingement tester which is believed not to generate a real simulated conditions as those encountered during flow in piping, especially with regards to viscosity impact. A finding that there is ore related to flow in pipes has been presented by Huang et al. [3], who concluded a reduction of erosion rate by 10% when viscosity is increased 2 by folds from 1 mPa s to around 2 mPa s. However, recently Kesana et al. [4], also examined erosion at the same two values of viscosity (1 and 10 mPa s), hey concluded that no clear relationship between wear and viscosity. The latest study conducted by Sadighian [13] concluded that at low range of viscosities, erosion rate decreases with the increase of viscosity, while at higher range of viscosities, erosion rate increases with viscosity. Although Ardalan's study is the latest and most comprehensive one, the number of experimental measurements conducted to investigate the effect of viscosity is limited, and hence their finding in this regards cannot be generalized. Therefore, no erosion-viscosity correlation was presented as part of Ardalan's study to be used for future prediction of erosion rate.

In this paper, Salama model is modified to increase its accuracy and extend its applicability to viscous oil flow. The reason for that is because Salama model is a simple model that can be used for routine sand erosion prediction. Salama model is very easy to use if compared with semi-empirical and CFD [20] methods but the original form of Salama model shows less accuracy for viscous liquids as viscosity is not included in the model.

## 2 Methodology

In this work, Salama model, an easy to use empirical model but less accurate when applied for viscous fluids, has been improved by including the effect of viscosity, which is missing in the original model. The viscosity parameter has been incorporated into Salama model following comparison with CFD [19] model, Direct Impingement Model (DIM), and published experimental data.

Salama model was developed through numerous tests that were carried out using water and nitrogen gas. Since water and gas viscosities are almost constant, therefore the viscosity parameter has not been included in the equation. Salama, however, expected that higher viscosity will result in reduction of erosion rate [11, 8, 14, 15].

The direct impingement model (DIM) is a semi-empirical model developed by University of Tulsa to predict erosion in elbows and tees [5]. The model assumed that particles velocity changes within an identified distance (so-called stagnation

zone). A simplified form of the equation of particles motion can be solved within the stagnation zone to calculate the particles terminal (impingement) velocity (the velocity at which the particles hit the internal surface of the tee or elbow) [6, 7, 17]. In this work, the simplified equation of particles motion has been solved numerically following the method proposed by University of Tulsa to calculate the [10]. The calculated terminal velocity was then used to perform erosion calculations.

In addition to the empirical and semi-empirical model deliberated above, erosion due to sand entrained in oil flowing through a 2-in. elbow has been performed using Fluent 6.0 discrete phase model (DPM). The discrete phase model (DPM) in Fluent has been used to track the particles and to simulate the erosion rate. In DIM, the dispersed phase is tracked using Lagrangian method, which solves the equation of force balance on particles.

### 3 Results and Discussion

Firstly, published measured data sets from Salama [14] and Shirazi et al. [17] were used to assess the accuracy of Salama and DIM. The results shown in Fig. 1, indicate that the erosion rate values predicted by Salama model overestimates the corresponding measured values. The average absolute error was found to be 41.7% (details are found in [9]).

On the other hand, DIM reveals better agreement with the measured data as indicated by Fig. 2. Although DIM model marginally underestimates the measured

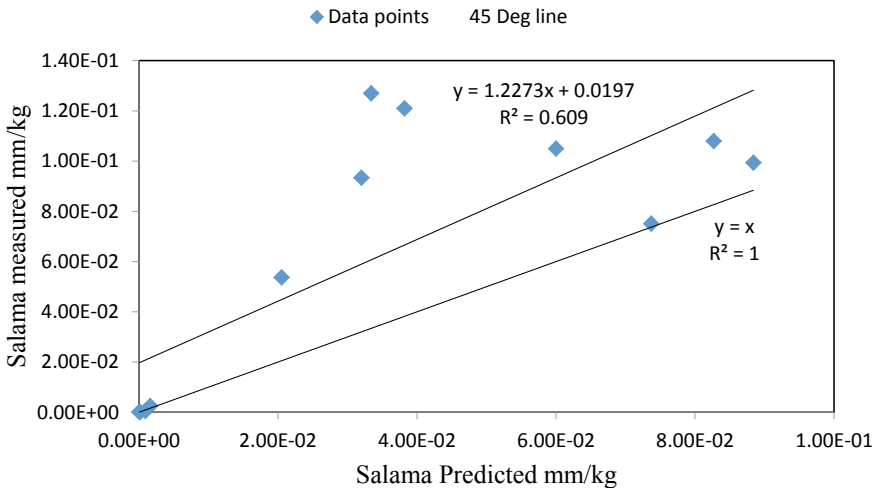


Fig. 1 Comparison of Salama model with measured data

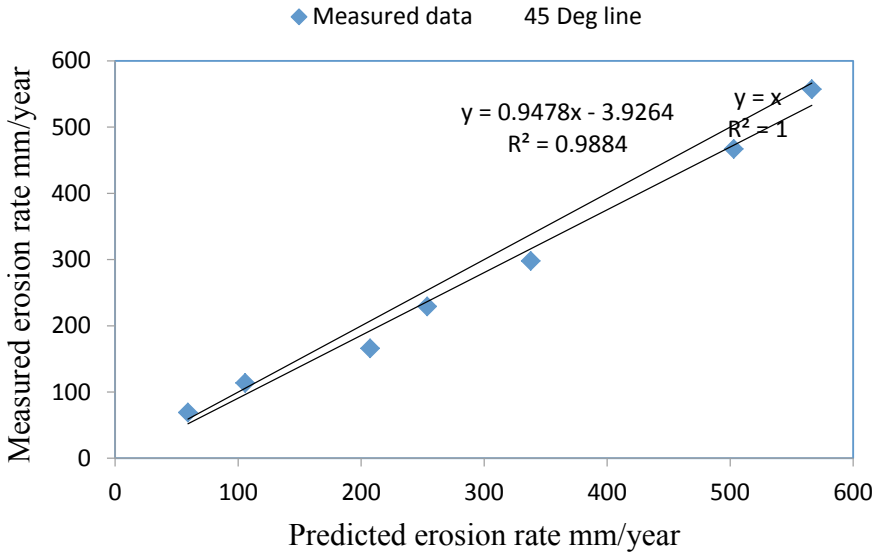


Fig. 2 Validation of direct impingement model

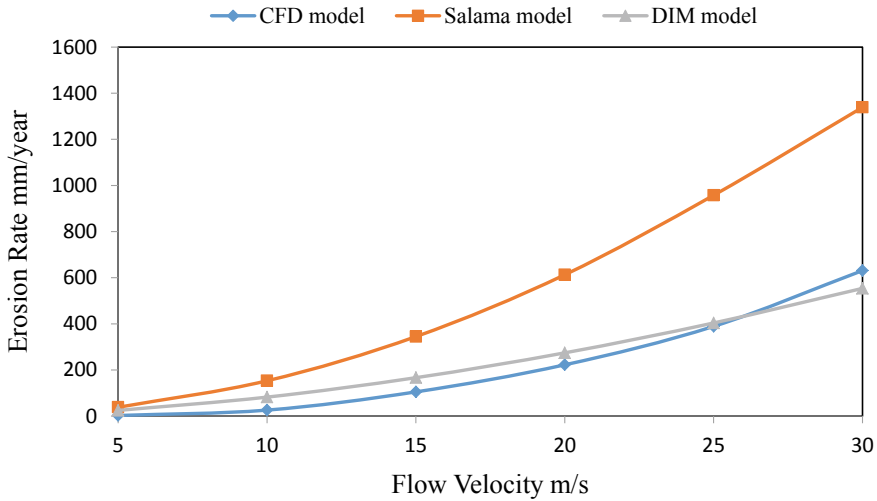
data, its accuracy can be considered as adequate (with only 7.33% average absolute error).

For further assessment, both models have been compared with CFD predicted erosion rates at the same flow characteristics (input data). The comparison result is shown in Fig. 3. More details about the model geometry, the boundary conditions, and other input data used in the CFD simulation can be found in [11].

Figure 3 underpins the results obtained above as it shows more deviation of Salama model predicted values than DIM predicted values from the CFD results. The deviation of Salama model from the CFD results has been reported previously by other researchers. In instance [2], documented better agreement of the DIM model than Salama model with CFD model when compared erosion rate in a 2-in. elbow.

### 3.1 Extension of Salama Model to Oils Flow

In this section, the procedure followed to improve Salama model by incorporating fluid viscosity effect is outlined. A modified model that combines both the ease of Salama model as well as the accuracy of DIM model is presented here. We believed that this model will be a reliable tool for easy calculation of erosion rate due to sand-oil flow in elbow.



**Fig. 3** Comparison of results of Salama, DIM, and CFD models

*Development of the model*

To incorporate viscosity in Salama model, similar input data was assumed for an oil with varied viscosity values. Erosion rates were predicted by Salama model and compared with those predicted by DIM at the same input data (Table 1).

As shown, Salama model predicts erosion rate values greater than zero for all non-zero flow velocities, while DIM model predicts zero erosion rates as long as flow velocity is lower than the erosional velocity. The erosional velocity (in m/s) was found to proportionally relate to viscosity  $\mu$  (in pa s) (Eq. 1).

$$V_{el} = 1227\mu \tag{1}$$

When velocity is greater than erosional velocity, the erosion rate calculated by Salama model is found to be greater than those predicted by DIM model until the velocity reaches another critical value (we referred to as abnormal velocity). The abnormal velocity is also found proportionally related to viscosity (Eq. 2).

$$V_{ab} = 3081\mu \tag{2}$$

Based on that, the following model (Eq. 3) was developed as an improvement of Salama model:

$$E_m = \begin{cases} 0 & V < V_{el} \\ A_l E_s - B_l & V_{el} \leq V \leq V_{ab} \\ A_u E_s - B_u & V \geq V_{ab} \end{cases} \tag{3}$$



**Table 1** Comparison of Salama and DIM results for oil with different viscosity

V (m/s)	Erosion rate (mm/year)				V (m/s)	Erosion rate (mm/year)				
	Salama		DIM			Salama		DIM		
	0.002 (Pa s)	0.005 (Pa s)	0.009 (Pa s)	0.009 (Pa s)		0.002 (Pa s)	0.005 (Pa s)	0.009 (Pa s)	0.009 (Pa s)	
0	0	0	0	0	20	0.72	2.28017	1.16562	0.009 (Pa s)	0.33348
1	0.0018	0	0	0	21	0.7938	2.52771	1.34667	0.009 (Pa s)	0.42601
2	0.0072	0	0	0	22	0.8712	2.78608	1.53957	0.009 (Pa s)	0.53089
3	0.0162	0.0015	0	0	23	0.9522	3.0551	1.74412	0.009 (Pa s)	0.64801
4	0.0288	0.01373	0	0	24	1.0368	3.33462	1.96008	0.009 (Pa s)	0.77726
5	0.045	0.04358	0	0	25	1.125	3.62451	2.18728	0.009 (Pa s)	0.91851
6	0.0648	0.09165	0.00053	0	26	1.2168	3.92462	2.42554	0.009 (Pa s)	1.07162
7	0.0882	0.15706	0.00357	0	27	1.3122	4.23482	2.67468	0.009 (Pa s)	1.23645
8	0.1152	0.23885	0.01329	0	28	1.4112	4.555	2.93454	0.009 (Pa s)	1.41283
9	0.1458	0.33613	0.03365	0	29	1.5138	4.88504	3.20497	0.009 (Pa s)	1.60062
10	0.18	0.4482	0.06702	0	30	1.62	5.22484	3.48584	0.009 (Pa s)	1.79967
11	0.2178	0.57442	0.11448	0.00189	31	1.7298	5.5743	3.777	0.009 (Pa s)	2.00982
12	0.2592	0.71428	0.17633	0.00565	32	1.8432	5.93334	4.07833	0.009 (Pa s)	2.23095
13	0.3042	0.86734	0.25258	0.01383	33	1.9602	6.30181	4.38972	0.009 (Pa s)	2.4629
14	0.3528	1.0332	0.34298	0.02857	34	2.0808	6.67965	4.71104	0.009 (Pa s)	2.70554
15	0.405	1.21151	0.44726	0.05181	35	2.205	7.06678	5.04221	0.009 (Pa s)	2.95875
16	0.4608	1.40197	0.56507	0.08506	36	2.3328	7.46311	5.38308	0.009 (Pa s)	3.2224
17	0.5202	1.60431	0.69612	0.12935	37	2.4642	7.86858	5.73358	0.009 (Pa s)	3.49637
18	0.5832	1.81827	0.84008	0.18527	38	2.5992	8.28309	6.09361	0.009 (Pa s)	3.78055

where

$E_m$ : the modified erosion rate (expressed as mass loss rate) (mm/kg)

$E_s$  is the erosion rate (expressed as mass loss rate) predicted by Salama model (mm/kg)

$A_l$ ,  $B_l$ ,  $A_u$  and  $B_u$  are viscosity dependent constants (Eq. 4):

$$\begin{aligned} A_l &= -47.06\mu - 1.522 \\ B_l &= 0.001\mu + 2E - 06 \\ A_u &= -175.6\mu + 3.556 \\ B_u &= 0.006\mu - 1E - 05 \end{aligned} \quad (4)$$

For more details about the model development [9].

The new model was employed to Visual Basic 6 to develop a computational package. The flow chart of the program shown in Fig. 4.

### 3.2 Validation of the New Model

The new model is recommended for application to oil with viscosities exceeding 0.001 Pa s (1 cp). The validation of the model was conducted in two steps. The first step is comparison with DIM model (erosion rate prediction from the two models at the same input data). Figure 5 indicates excellent agreement between the two models.

The second step is validation with published measured data. Due to a lack of sufficient measured data, limited data from Shirazi et al. [17] was utilized for validation. Data is for clay-water mud with 6 cp (0.006 Pa s) viscosity and 68.7 b/ft<sup>3</sup> (1101 kg/m<sup>3</sup>) density, flowing at 31 ft/s (9.45 m/s) in 2-in. (0.05 m) elbow. The entrained sand is 350-micron sand particles flows with sand flow rate of 1754 ft<sup>3</sup>/day (131720 kg/day (assuming sand density of 2650 kg/m<sup>3</sup>)). The reported measured erosion rate is 4238 mil/year (105.95 mm/year).

The calculation from the original Salama model and the modified Salama model (listed below) revealed more accuracy of the new model as compared with the original one.

- The predicted erosional velocity = 7.362 m/s
- The abnorm predicted al velocity = 18.486
- The erosion rate by the modified Salama 116.8 mm/year
- The erosion rate by Salama the original model = 249.3 mm/year.

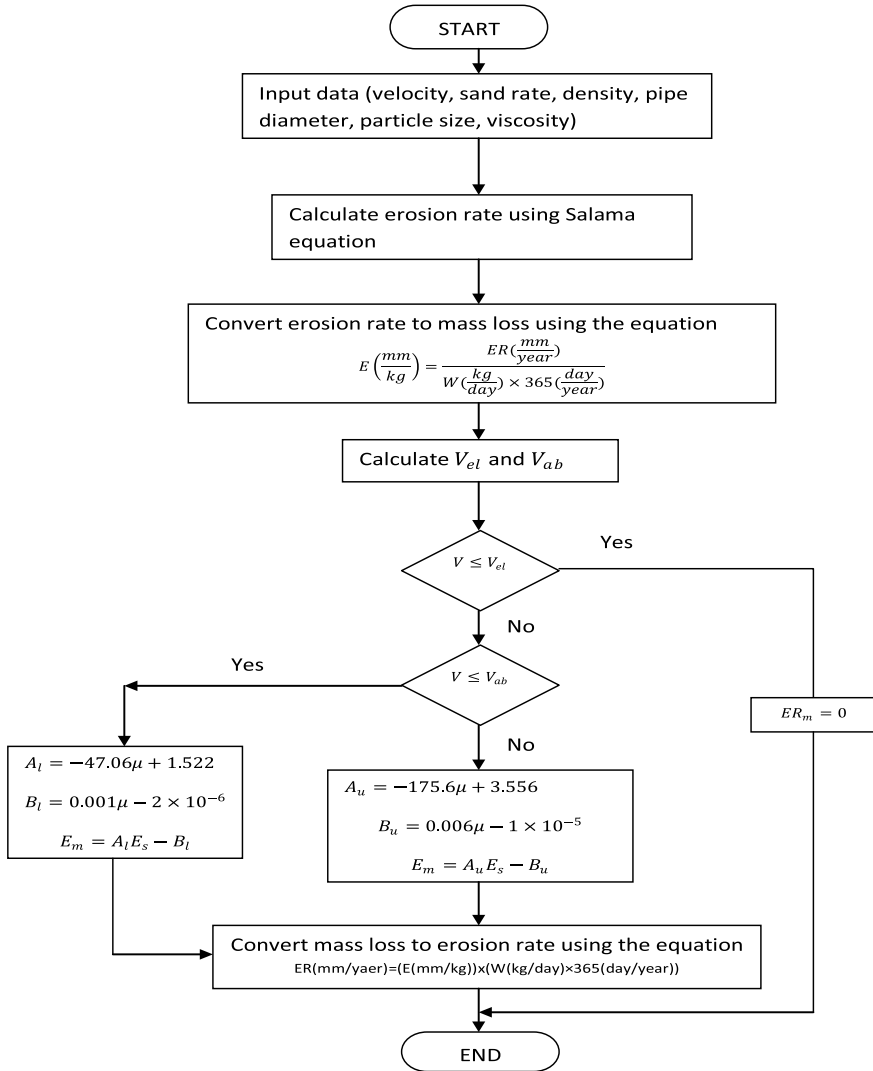
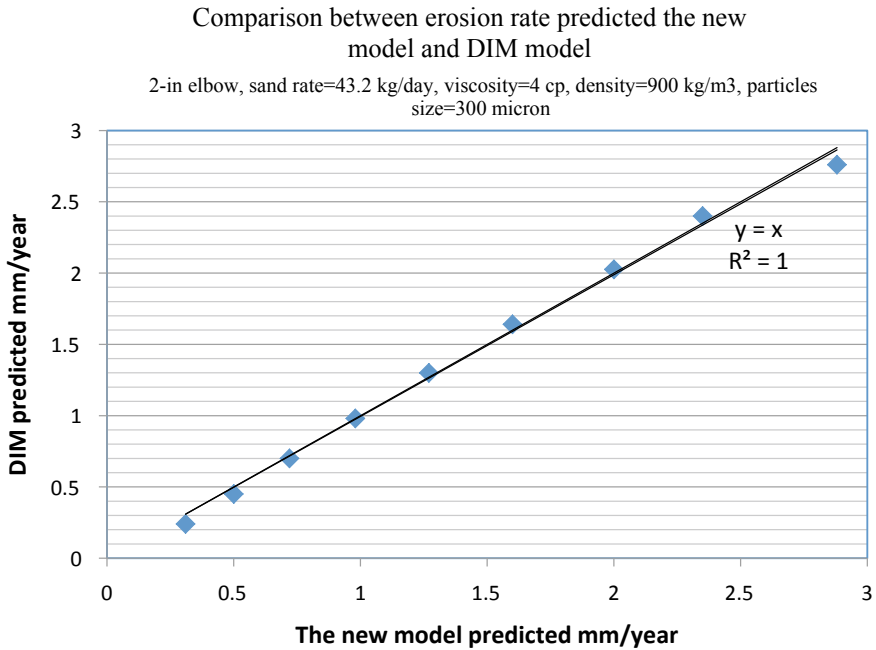


Fig. 4 Flow chart of calculation procedure using the new model

## 4 Conclusions

Comparison of Salama model and the DIM model with CFD results and experimental data show good accuracy of the DIM model and a lack of accuracy of Salama model. A new model was developed by comparison of results from Salama model with results from the DIM model for oil with different viscosities. Unlike the original Salama model, the developed model predicts non-zero erosion rate only for velocities



**Fig. 5** Comparison of new model with the DIM model

greater than a critical value referred to as erosional velocity, which is directly related to viscosity. The developed model combines the simplicity of Salama model and the accuracy of the DIM model. The validation of the model with results from the DIM model and published experimental data indicates good accuracy.

**Acknowledgements** The authors would like to thank Petroleum Engineering Department at University of Khartoum for supporting this work.

## References

1. API (1991) API RP 14 E Recommended Practice for Design and Installation of Offshore Production Platform Piping Systems. Retrieved from Washington DC
2. Barton NA (2003) Erosion in elbows in hydrocarbon production system: review document, Research Report 115, HSE, ISBN 0 7176 2743 8
3. Huang C, Minev P, Luo J, Nandakumar K (2010) A phenomenological model for erosion of material in a horizontal slurry pipeline flow. *Wear* 269(3):190–196. <https://doi.org/10.1016/j.wear.2010.03.002>
4. Kesana NR, Throneberry JM, McLaury BS, Shirazi SA, Rybicki EF (2013) Effect of particle size and liquid viscosity on erosion in annular and slug flow. *J Energy Resour Technol* 136(1):012901–012910. <https://doi.org/10.1115/1.4024857>

5. McLaury BS (1996) Predicting solid particle erosion resulting from turbulent fluctuations in oilfield geometries. Ph.D. thesis, University of Tulsa
6. McLaury BS, Shirazi SA (1999) Generalization of API RP 14E for Erosive Service in Multi-phase Production. Paper presented at the SPE 56812, Houston, Texas
7. McLaury BS, Shirazi SA, Shadley, Rybicki E (1996) Modelling erosion in chokes. Paper presented at the ASME FED, San Diego
8. Mohyaldinn ME, Ismail MC, Ayoub M, Mahmood SM (2016) Examination and improvement of Salama model for calculation of sand erosion in elbows. Paper presented at the international conference of integrated petroleum engineering and geosciences
9. Mohyaldinn ME (2011) Development and validation of computational models for sand erosion and corrosion predictions in pipes and fittings. Ph.D., Universiti Teknologi PETRONAS
10. Mohyaldinn ME, Elkhatib N, Hamzah R, Ismail MC (2009) A computational code for sand erosion prediction in elbows and tees: an improvement to the direct impingement model to account for temperature dependence. *J Corros Mater* 35
11. Mohyaldinn ME, Elkhatib N, Ismail MC (2011) Evaluation of different modelling methods used for erosion prediction. Paper presented at the NACE Shanghai 2011
12. Okita R, Zhang Y, McLaury BS, Shirazi SA (2012) Experimental and computational investigations to evaluate the effects of fluid viscosity and particle size on erosion damage. *J Fluids Eng* 134(6):061301–061313. <https://doi.org/10.1115/1.4005683>
13. Sadighian A (2016) Investigating key parameters affecting slurry pipeline erosion. University of Alberta
14. Salama MM (2000) An alternative to API 14E erosional velocity limits for sand-laden fluids. *J Energy Res Technol* 122:71–77
15. Salama MM, Venkatesh ES (1983) Evaluation of erosional velocity limitations in offshore gas wells OTC. Paper presented at the 15th Annual OTC, Houston, Texas
16. Saleh B, El-Deen AE, Ahmed S (2011) Effect of liquid viscosity on cavitation damage based on analysis of erosion particles. *J Eng Sci* 39(2):327–336
17. Shirazi SA, McLaury BS, Shadley JR, Rybicki EF (1995) Generalization of the API RP 74E guideline for erosive services. *J Pet Technol (SPE No. 28518):693–698*
18. Tian B (2007) Mechanistic understanding and effective prevention of erosion-corrosion of hydrotransport pipes in oil sand slurries. M.Sc., University of Calgary
19. Witt P, Khan MNH, Brooks G (2007) CFD modelling of heat transfer in supersonic nozzles for magnesium production. Paper presented at the TMS Annual Meeting
20. Zhalehrajabi E, Rahmanian N, Hasan N (2014) Effects of mesh grid and turbulence models on heat transfer coefficient in a convergent–divergent nozzle. *Asia-Pacific J Chem Eng* 9(2):265–271. <https://goo.gl/uNz2jm>

# Reduction of Excessive Flash in Friction Stir Processing of AA1100: An Experimental Observation Study



Tawanda Marazani, Esther T. Akinlabi and Daniel M. Madyira

**Abstract** Friction stir processing (FSP) has proven to be a powerful emerging surface engineering technology for modifying metal surfaces and their bulk properties to desired forms. As a variant of friction stir welding (FSW), FSP borrows its principles of functionality from FSW. FSP technology is highly dependent on careful selection of process parameters. Its key parameters include tool rotational speed, traverse speed, tool tilt angles, axial force, tool and process design as well as base metal properties. Formation of excessive flash is a common FSP parametric challenge which needs to be studied. In this work, build-up of mass flash was experimentally observed and controlled by varying process tool tilt angle and the rotational during FSP of AA1100. The process was conducted using H13 tool steel cylindrical tool with a shoulder diameter of 21 mm with a 7 mm cylindrical threaded pin, at constant traverse speed of 20 mm/min at tilt angles varying from 0° to 3°, rotational speeds of 500 to 1500 rpm for unreinforced process and 2100–2800 rpm for reinforced process, at constant plunge depth of 0.2 mm, and traverse force of 11.2 kN. Results obtained from the physically examined FSP'ed samples show that excessive flash was generated for tilt angles from 0° to 2° as a result of limited under-shoulder space for flow of the plasticized material and the front tip of the tool digging into the base metal ejecting material from the processed zone. Massive flash reduction was observed at 2.5°. A further improvement of flash reduction was witnessed at 3° tilt angle but with reduced shoulder-to-base metal areal contact due to too much raised tool front.

**Keywords** AA1100 · Excessive flash reduction · Experimental study · Friction stir processing · Plasticized metal flow

---

T. Marazani (✉) · E. T. Akinlabi · D. M. Madyira  
Department of Mechanical Engineering Science, University of Johannesburg,  
Auckland Park Kingsway Campus, Johannesburg, South Africa  
e-mail: [tmtmarazani@gmail.com](mailto:tmtmarazani@gmail.com)

© Springer Nature Singapore Pte Ltd. 2020  
M. Awang et al. (eds.), *Advances in Material Sciences and Engineering*, Lecture Notes in Mechanical Engineering,  
[https://doi.org/10.1007/978-981-13-8297-0\\_32](https://doi.org/10.1007/978-981-13-8297-0_32)

# 1 Introduction

Friction stir processing (FSP) is a recently developed surface engineering tool which draws its functionality from the principles of friction stir welding (FSW) [1, 2]. The technique was developed for localized modification of materials, mostly light metals, through friction and severe plastic deformation (SPD) to yield desired microstructural refinement usually of ultrafine grain (UFG) structure for the improvement of grain size based attributes [3–6]. FSP differs with FSW in that, it simply does modification of either the surface or in-volume properties of the metal [7, 8], it does not join metal plates together which is the major role of the latter [9]. FSP highly depends on careful selection of process parameters, tool design, type of reinforcement particles, its method of delivery and containment, the base metal to be processed and the design of the process, that is whether it is single pass or multi-pass [10–15]. These factors do not function as standalone parameters but in combinations and a deeper understanding of how they interact is highly indispensable to every successful FSP engineer.

FSP uses a specially designed non-consumable shouldered and pinned tool which is rotated and plunged into the metal plate until the tool shoulder reaches the desired plunge depth [16] during what is known as the plunging or plunging or dwell period [17, 18]. This generates frictional heating at the point beneath the tool shoulder causing superplastic deformation of the base metal which results in material breaking, heating, softening and consequently complex material mixing within the processed zone as the tool traverse in the desired direction [19–22]. If second phase nano particles are impregnated onto the surface by either pasting, drilling hole or grooving, this normally results in improved mechanical properties [23].

FSP is mainly used in modifying aluminium (Al) based alloys for applications which include production of surface composites, powder metallurgy homogenization, micro-forming or modification of microstructure for metal matrix composites (MMCs) and property improvement in cast Al alloys [24]. FSP has been conducted on Al/SiC composites [25], AA-2024 T351 [26], aluminium-magnesium alloy [27], AA7075 [16], AA6056 [28], Al–Mg alloy AA5086 [15], 7050-T7451 [14], AA2024/Al<sub>2</sub>O<sub>3</sub> [29], AA 6063 [24], WC/AMCs [30] and many others. The resulting improved properties from these studies include hardness, tensile strength, wear, corrosion resistance, elimination of casting defects and refined microstructures, strength, ductility, fatigue and enhanced formability [18].

Process parameters that govern FSP have been widely studied [28], and these include tool rotation speed, traverse speed, tool shoulder, tool pin, shoulder surface design, tool tilt angle and number of passes [29]. These parameters determine the amount of heat generated and the extent of plastic deformation and material mixing. The generated heat should be optimal as either insufficient or excessive heat leads to formation of defects. Longitudinal grooves or wormholes also known as cavities which arise as a result of high traverse speed, insufficient heat and insufficient forging pressure tunnel, pinholes, cracks and mass or excessive flash during FSP have been presented as common FSP defects. Mass flash was reported to be caused by excessive



**Fig. 1** H13 tool steel FSP threaded cylindrical pin tool

**Table 1** FSP parameters

Process	Tool tilt angle (degrees)	Rotational speed (rpm)	Traverse speed (mm/min)	Plunge depth (mm)	Traverse force (kN)
Unreinforced	2	500–1500	20	0.2	11.2
Reinforced	0–3	2100–2800	20	0.2	11.2

heat input, but in the views of the researchers, the parameters that lead to excessive heat are the causes of mass flash. Apart from being a defect, excessive flash constitutes unaccounted material removal or loss. It is formed from material ejected from the processed zone. The subject of flash formation and reduction during FSP has hardly been studied and reported. The purpose of the current work is to study mass flash formation during FSP of AA1100 and develop ways of containing it within practically reasonable limits.

## 2 Experimental Design

AA1100 plates used in this work had dimensions  $250 \times 130 \times 6$  mm, length, width and thickness respectively. For the reinforced processes, the plates had a groove each of size of  $225 \times 2 \times 3.5$  mm, length, width and depth respectively in which 17-4PH stainless steel powder reinforcements were compacted using a pinless H13 tool steel cylindrical tool before FSP. Unreinforced processes were done on plane base metal with no groove. FSP was conducted using H13 tool steel cylindrical tool (Fig. 1) with a shoulder diameter of 21 mm, a 7 mm cylindrical threaded pin, of pin length 5.5 mm. Table 1 summarises the FSP parameters employed in this work. The process was conducted using the ETA Friction Stir Welding Numerical Controlled Manual Machine. The job setup with the compacted reinforcements is shown in Fig. 2.





Fig. 2 Job setup with compacted 17-4 PH reinforcements

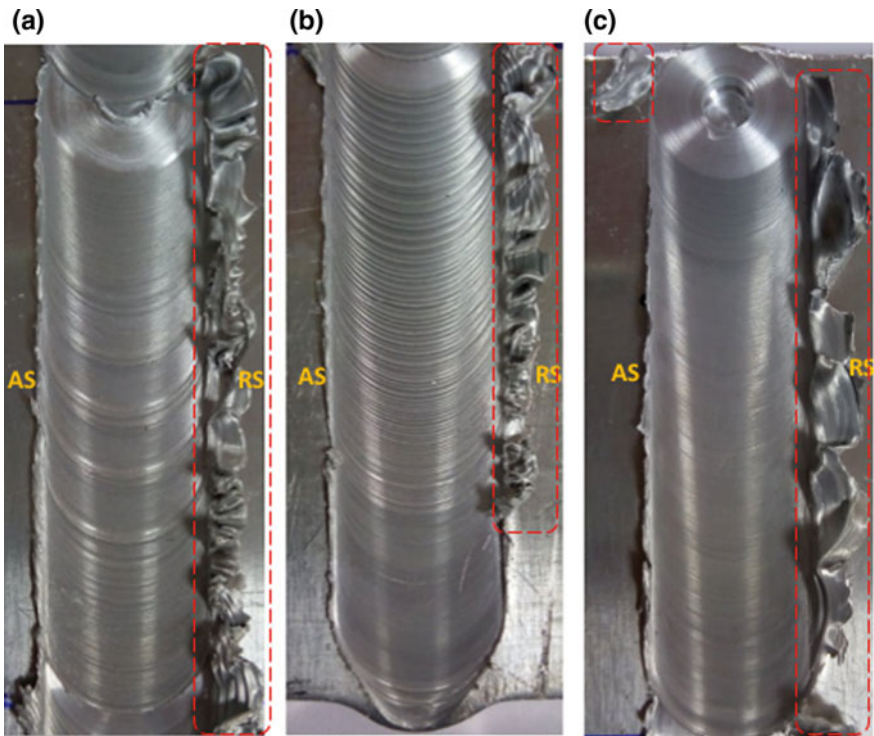


Fig. 3 Excessive flash (red dots) images on unreinforced FSP'ed AA1100: a at 500 rpm; b at 900 rpm; and c at 1500 rpm, at 2°, 20 mm/min travel speed and 11.2 kN traverse force

### 3 Results and Discussion

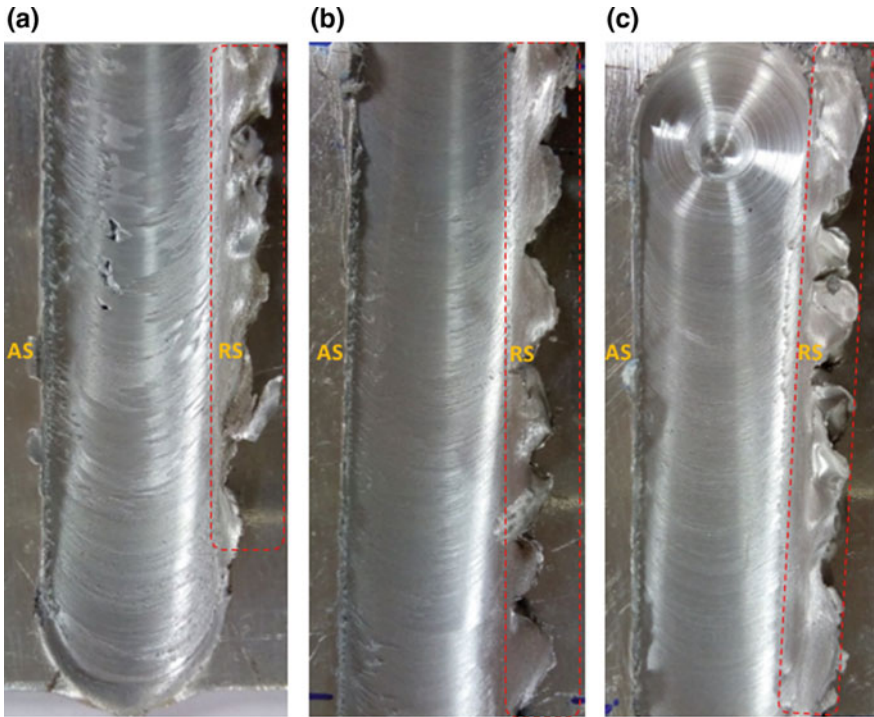
*Preliminary unreinforced processing done at 2°.* FSP was conducted on the AA1100 base metal without a groove and with no reinforcements. The machine spindle was set to a tilt angle of 2° and the process was carried out at unreinforced variables as shown in Table 1. At his setting, for all chosen rotational speeds 500, 900, and 1500 rpm, excessive flash was generated on the retreating side for the whole length of the processed track while the advancing side showed no flash. The unreinforced FSP images are shown in Fig. 3. The coiled excessive flash was untwined and measured and recorded an average width of 9 mm and an average thickness of 0.17 mm. The advancing side is clear of flash. For one processed sample with an effective processed length of 75 mm, this yielded a material volumetric loss of 114.75 mm<sup>3</sup> which translated to 0.31875 g of material removal since the density of AA1100 is 0.0027 g/mm<sup>3</sup>. For the 3 process A, B and C, of an effective processing length of 225 mm, this yielded a material volume loss of 344.25 mm<sup>3</sup> and thus a mass of 0.929475 g.

*Reinforced processing done at 0°.* Images for processing conducted at 0° are shown in Fig. 4 where it is evident that excessive flash was generated on the retreating side. The coiled excessive flash was untwined and measured and recorded an average width of 9 mm and an average thickness of 0.17 mm. The advancing side is clear of flash. 17-4 PH SS powder hardened the ejected mass flash and made it very hard to uncoil for width and thickness measurement. The flash from the three processes was then removed using a side cutter and weighed on a high accuracy mini digital jewellery weighing scale with an accuracy of 0.01 g, and recorded a mass of 1.221 g.

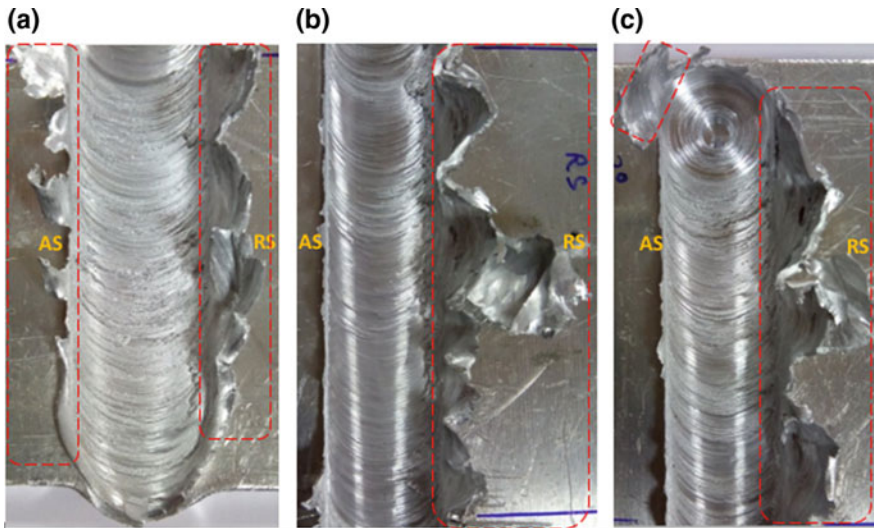
*Reinforced processing done at 2°.* Figure 5 shows images for processing conducted with reinforcements at 2°. Excessive flash was generated at the retreating side. The flash was observed to be ejected out of the processed zone during FSP. The flash was coiling around the tool but got deposited onto the retreating side. The image conducted at 2100 rpm also shows excessive flash but not as much as the one on the retreating side. As a result of the mixing with the 17-4 PH SS powder, the ejected mass flash was very hard to uncoil for width and thickness measurement. It was carefully removed using a side cutter and weighed on a high accuracy mini digital jewellery weighing scale with an accuracy of 0.01 g, and recorded a mass of 2.574 g.

*Reinforced processing done at 2.5°.* Images for processing conducted at 2.5° are shown in Fig. 6. From the images, it can be seen that mass flash was remarkably reduced to reasonable levels. Very small spatters of less than an average of 2 mm measured offset from the shoulder track were measured on both the advancing and retreating sides. This was noticed for all processes conducted using the whole range of rotational speeds. The small flash spatters were chipped off and weighed and yielded 0.318 g of material loss.

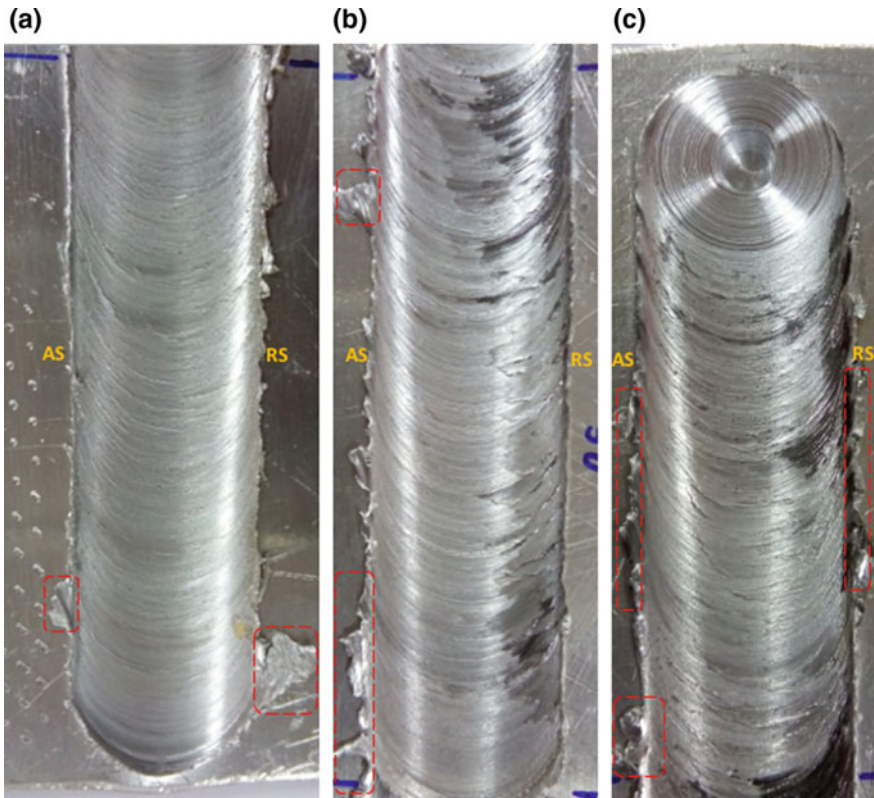
*Reinforced processing done at 3°.* Images for FSP conducted at 3° are shown in Fig. 7. Remarkable reduction of mass flash can be observed from the images. Flash spatters of less than an average of 2 mm measured offset from the shoulder track on both the advancing and retreating sides were recorded for the whole range of



**Fig. 4** Excessive flash (red dots) images on reinforced FSP'ed AA1100: **d** at 2100 rpm; **e** at 2450 rpm; and **f** at 2800 rpm, at 0°, 20 mm/min travel speed and 11.2 kN travel force



**Fig. 5** Excessive flash (red dots) images on reinforced FSP'ed AA1100: **g** at 2100 rpm; **h** at 2450 rpm; and **i** at 2800 rpm, at 2°, 20 mm/min travel speed and 11.2 kN traverse force



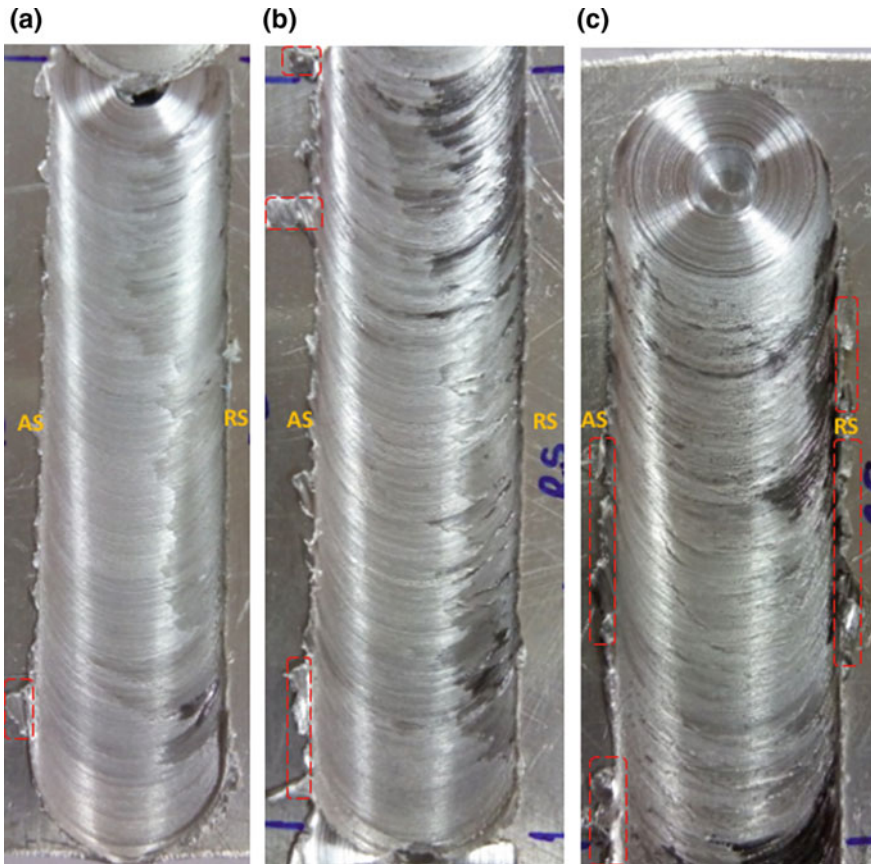
**Fig. 6** Small flash spatters (red dots) images of reinforced FSP'ed AA1100: **j** at 2100 rpm; **k** at 2450 rpm; and **l** at 2800 rpm, at 2.5°, 20 mm/min travel speed and 11.2 kN traverse force

rotational speeds. The flash spatters were carefully chipped off weighed and yielded 0.263 g of material loss.

## 4 Conclusions

A total of 18 samples were FSP'ed and were physically examined for mass flash during FSP. Excessive flash was generated at tool tilt angles of 0°–2° due to lack of space for the containment of the plasticised material under the flat surfaced shoulder. Material loss due to excessive flash is one of the FSP limitations. 17-4 PH powder has the potential to enhance hardness and wear properties of AA 1100. Tilt angles of 2.5° and 3° massively reduced excessive flash generation since they allowed the flow of the plasticized material under the flat shoulder surface. Further increase of tool tilt beyond 3° reduces shoulder-base metal contact which requires increased





**Fig. 7** Small flash spatters (red dots) images of reinforced FSP'ed AA1100: **m** at 2100 rpm; **n** at 2450 rpm; and **o** at 2800 rpm, at 3°, 20 mm/min travel speed and 11.2 kN traverse force

plunge depth. Controlled variation of tool tilt angle played a very important role in the successful reduction of excessive flash.

## References

1. Kiran AU, Pravala EK (2017) Experimental investigations on tribological properties of 6061-T6 Al alloy by via friction stir processing. *Int J Adv Eng Manag Sci (IJAEMS)* 3(10):995–1000
2. García-Vázquez F, Vargas-Arista B, Muñiz R, Ortiz JC, García HH (2017) The role of friction stir processing (FSP) parameters on TiC reinforced surface Al7075-T651 aluminum alloy. *Corporación Mexicana de Investigación en Materiales—COMIMSA*. Saltillo, México 21(4):508–516
3. Chainarong S, Muangjunburee P, Suthummanon S (2014) Friction stir processing of SSM356 aluminium alloy. In 12th Global Congress on Manufacturing and Management, GCM 2014,

## Thailand

4. Węglowski M (2014) Microstructural characterisation of friction stir processed cast AlSi9Mg aluminium alloy. *Arch Foundry Eng* 14(3):75–78
5. Sairam SGNV, Madhu S (2015) A review on friction stir processing on aluminum based materials. *Int J Appl Eng Res* 10(33):25462–25467
6. Chan CY (2011) A doctoral thesis: friction stir processing of aluminium-silicon alloys. University of Manchester, London
7. Miranda RM, Gandra J, Vilaça P (2013) Surface modification by friction based processes. In: *Morden surface engineering treatments*, Lisbon, INTECH, 2013, pp 1–20
8. Kumar VM, Kumar RS, Vishnuadhithya U, Raj SJP, Kumar PS, Franklin SB (2017) Fabrication of aluminum surface composite by friction stir processing—a review. *SSRG Int J Mech Eng (ICET'17)* 17:15–19
9. Zhang YN, Cao X, Larose S, Wanjara P (2012) Review of tools for friction stir welding and processing. *Can Metall Q* 51(3):250–261
10. Akinlabi ET, Mahamood RM, Ogunmuyiwa E (2014) Process parameters influence on wear resistance behaviour of friction stir processed Al-TiC composites. *Adv Mater Sci Eng* 2014:1–12
11. Amirtharaj D, Rajamurugan G, Sivachidambaram S, Dinesh D (2015) Effect of tool geometry on surface modification of aluminium 6063 by friction stir processing. *J Eng Appl Sci, ARPN* 10(12):5391–5394
12. Cartigueyen S, Mahadevan K (2014) Study of friction stir processed zone under different tool pin profiles in pure copper. *IOSR J Mech Civil Eng (IOSR-JMCE)* 70(3):6–12
13. Wadekar W, Soladhra R, Barkade H, Thombare N (2017) A review on friction stir technology. *Int Conf Ideas, Impact Innov Mech Eng (ICIIME 2017)* 5(6):1542–1549
14. Yang W, Ding H, Mu Y, Li J, Zhang W (2017) Achieving high strength and ductility in double-sided friction stir processing 7050-T7451 aluminum alloy. *Mater Sci Eng, A* 707:193–198
15. Nadammal N, Kailas SV, Szpunar J, Suwas S (2018) Development of microstructure and texture during single and multiple pass friction stir processing of a strain hardenable aluminium alloy. *Mater Charact* 140:134–146
16. Navaser M, Atapour M (2017) Effect of friction stir processing on pitting corrosion and intergranular attack of 7075 aluminum alloy. *J Mater Sci Technol* 33:155–165
17. Akinlabi ET, Akinlabi SA (2016) Effect of rotational speed on joint integrity of friction stir lap welded aluminium. In: *Proceedings of the world congress on engineering 2016, vol II. (WCE 2016)*, London, UK
18. Gnanavel JPL, Vijayan S (2017) Friction stir processing of magnesium alloys—review. *J Chem Pharm Sci* 7:121–126
19. Hariharan R, Golden Renjith Nimal RJ (2014) Friction stir welding of dissimilar aluminium alloys (6061&7075) by using computerized numerical control machine. *Middle-East J Sci Res* 20(5):601–605
20. Vepakomma H (2006) Masters thesis: three dimensional thermal modeling of friction stir processing. Florida State University, Florida, USA
21. Anglada CS (2006) A final degree project: friction stir processing, a new microstructure improvement technique. Universitat de Girona, Spain
22. Langlade C, Roman A, Schlegel D, Gete E, Noel P, Folea M (2017) Influence of friction stir process parameters on surface quality of aluminum alloy A2017. In: *International conference on computing and solutions in manufacturing engineering, CoSME'16, Belfort Cedex*
23. Sun N, Apelian D (2014) Friction stir processing of aluminum cast alloys for high performance applications. *JOM* 63(11):44–50
24. Kumar S (2016) Ultrasonic assisted friction stir processing of 6063 aluminum alloy. *Arch Civil Mech Eng* 16:473–484
25. Izadi H, Nolting A, Munro C, Bishop DP, Plucknett KP, Gerlich AP (2013) Friction stir processing of Al/SiC composites fabricated by powder metallurgy. *J Mater Process Technol* 213:1900–1907

26. John J, Shanmughanatan SP, Kiran MB (2018) Effect of tool geometry on microstructure and mechanical properties of friction stir processed AA2024-T351 aluminium alloy. *Mater Today Proceedings* 5:2965–2979
27. Khodabakhshi F, Simchi A, Kokabi AH, Švec P, Simančik F, Gerlich AP (2015) Effects of nanometric inclusions on the microstructural characteristics and strengthening of a friction-stir processed aluminum–magnesium alloy. *Mater Sci Eng, A* 642:215–229
28. Hannard F, Castin S, Maire E, Mokso R, Pardoën T, Simar A (2017) Ductilization of aluminium alloy 6056 by friction stir processing. *Acta Mater* 130:121–136
29. Moustafa EB, Mohammed S, Abdel-Wanis S, Mahmoud T, El-Kady E (2017) Surface composites defects of Al/Al<sub>2</sub>O<sub>3</sub> Metal matrix fabricated by friction stir. *J Mater Sci Surf Eng* 5(2):524–527
30. Huang G, Hou W, Shen Y (2018) Evaluation of the microstructure and mechanical properties of WC particle reinforced aluminum matrix composites fabricated by friction stir processing. *Mater Charact* 138:26–37

# Nonlinear Friction Analysis of a Modified Switching Function Controller in Pre-sliding Regime



N. A. Rafan, Z. Jamaludin, T. H. Chiew and M. Maharof

**Abstract** Highly nonlinear effect in motion accuracy is commonly referred as quadrant glitches which occurred at a quadrant. The abnormal spikes that occur at each quadrant is the friction to be compensated which due to reversal motion for continuous movement while machining process. Friction that focuses at point of reversal motion behaves as switching line in pre-sliding regime. The magnitude of glitches is higher at low velocity. Thus, a design of switching function in pre-sliding regime is necessary to overcome nonlinear friction effect. This paper analyzes experimentally the performance of switching function model namely Pseudo-like-curve-slip (PLCS) model. The controllers involved in this analysis are cascade P/PI controller and sliding mode controller (SMC) which is combined accordingly. The results show that PLCS model with feedforward combining with cascade P/PI controller performed better than SMC combination.

**Keywords** Friction model · Pre-sliding regime · Quadrant glitch · Sliding mode controller · Cascade controller

## 1 Introduction

Until recent years, many researches have focused on reducing errors and designing robust controller accordingly in pre-sliding friction. Pre-sliding regime is where displacement is a function of motion. Within the time interval for velocity reversal, there is a sudden change of torque. Normally this situation leads to system chattering

---

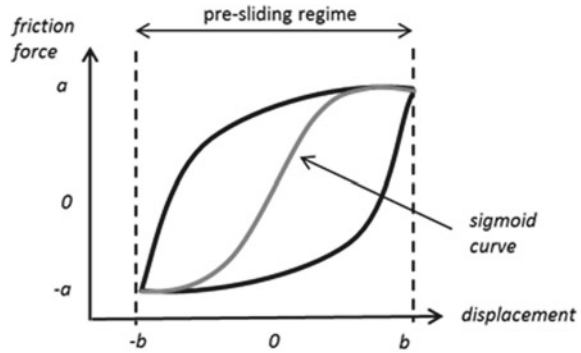
N. A. Rafan (✉) · Z. Jamaludin · M. Maharof  
Fakulti Kejuruteraan Pembuatan, Universiti Teknikal Malaysia  
Melaka, 76100 Durian Tunggal, Melaka, Malaysia  
e-mail: [aidawaty@utem.edu.my](mailto:aidawaty@utem.edu.my)

T. H. Chiew  
Tunku Abdul Rahman University College, Jalan Genting Kelang,  
Setapak, 53300 Kuala Lumpur, Malaysia

© Springer Nature Singapore Pte Ltd. 2020  
M. Awang et al. (eds.), *Advances in Material Sciences  
and Engineering*, Lecture Notes in Mechanical Engineering,  
[https://doi.org/10.1007/978-981-13-8297-0\\_33](https://doi.org/10.1007/978-981-13-8297-0_33)



**Fig. 1** Sigmoid curve at pre-sliding regime



due to the discontinuity. A sigmoid function is introduced to overcome the issue where it is expected to make ideal continuous motion between sliding regime [1].

Sigmoid function is located at pre-sliding regime which behaves as switching line to connect both sliding regime. Figure 1 shows sigmoid curve function at pre-sliding regime.

In pre-sliding regime, friction behaves as a hysteresis function of displacement with non-local memory behaviour. It is dependent to the displacement. Sigmoid function is widely used as basis of neural network and sliding mode control [2–4]. Estimating sigmoid function, displacement of a sinusoidal excitation of the system is evaluated as elementary slip block and spring in Generalized Maxwell Slip model.

In classical design of sliding mode control, a sigmoid function is implemented to reduce chattering in system. Tjahjowidodo [5] suggested sigmoid function in compensation model to control discontinuity around zero position error. When modeling a sigmoid function, Park [1] stated that  $\alpha$ , is the slope of the sigmoid function, with scaling factor and a bias for adjusting the magnitude of the function.

Another study of the sigmoid function in modeling showed that suitable numbers of sigmoid function are important. Shang et al. [6] found that higher number of the sigmoid function improved accuracy but it become more complicated. A broader perspective has been adopted by Piatkowski who introduced sigmoid like curve to compensate pre-sliding friction. A sigmoid like curve has the shape as the letter S [2].

A friction compensation model is intended to reduce errors in pre-sliding regime as well as to reduce chattering for linear and circular motion. The uncompensated friction lead to the positioning errors while machining process. Therefore, this paper presents the friction model design and performance analysis with different controllers applied at one time of experimentation. The results provide effectiveness of modified switching function in pre-sliding regime.

This paper is organized as follows. Section II provides an overview of nonlinear effect in motion accuracy. Section III describes the controller design applied in experimental work and friction compensation model design. Section IV discusses

on experimental results and analysis. Finally, Section V concludes the finding and gives recommendation for future works.

## 2 Nonlinear Effect in Motion Accuracy

During circular cutting test analysis, spikes are observed at quadrant of circular motion. The quadrant is referred as motion reversal of axes during circular motion. The quadrant spikes are caused by highly nonlinear friction phenomenon at low velocity while performing motion reversal [7]. It is also known as quadrant glitch.

Quadrant glitch is identified as nonlinear effect in motion accuracy with large tracking error, undesired stick slip motion and limit cycles due to nonlinear behavior of Coulomb friction [8, 9]. The spikes are caused by stiction and depends on feed speed [10]. Quadrant glitches can be reduced at lower feed rate and speed of machine tool. Besides, smaller radius of circular motion has lead to smaller quadrant glitches [11]. The magnitude of glitches is measured from contour error at 90-degree interval based on circular tests. Figure 2 illustrates quadrant glitches measured by contour roundness test measurement.

Quadrant glitches is the magnitude of contour error occurred at each quadrant of circular motion. Contour error is the difference between actual circle and reference circle which is tabulated according to circular angle (00–3600) as shown in Fig. 3.

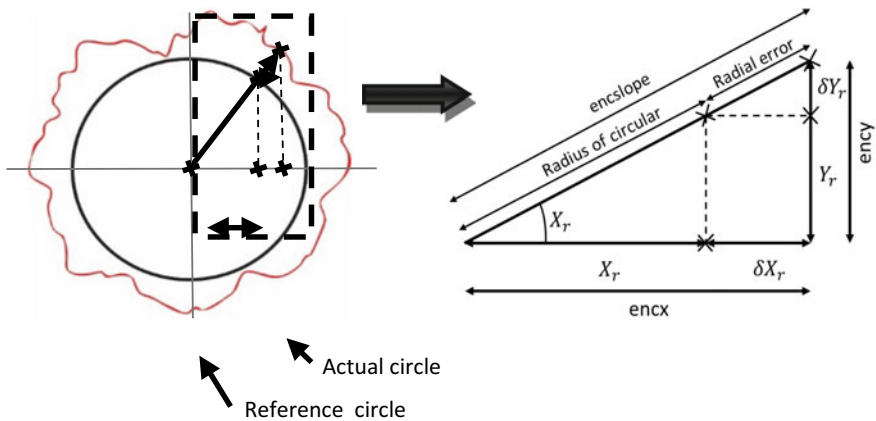


Fig. 2 Quadrant glitches measured by contour roundness test measurement

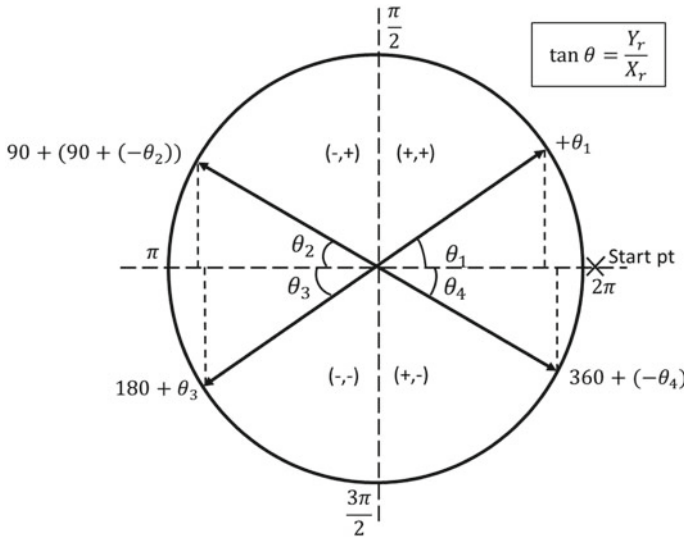


Fig. 3 Contour error

### 3 Methodology

#### 3.1 Controller Scheme

The controller applied to evaluate controlled system behaviour is cascade P/PI controller and Sliding Mode Controller (SMC).

A cascade P/PI position controller consists of a Proportional (P) plus Integral (I) velocity control loop and a Proportional (P) position control loop. The control performance of a cascade P/PI controller could be further enhanced with velocity feedforward, applied at velocity loop of the cascade P/PI position controller and a friction model. Figure 4 shows control scheme of the cascade P/PI position controller configuration with friction model based feedforward.

Parameters applied for cascade P/PI controller is tabulated in Table 1.

XY milling positioning table which consists of motor is defined as a second order sliding mode controller (SMC) [12]. In sliding mode controller (SMC), tracking error input signal is a difference between measured position signals with reference input signal. Trajectories of motion is driven to reach sliding surface designed which is called as reaching phase. Ideal sliding motion is to ensure trajectories maintained at sliding surface causes fast switching function.

The general form of the sliding surface:

$$s(e, \dot{e}) = \left( \frac{d}{dt} + \lambda \right)^{n-1} e \quad \text{where } \lambda > 0 \tag{1}$$

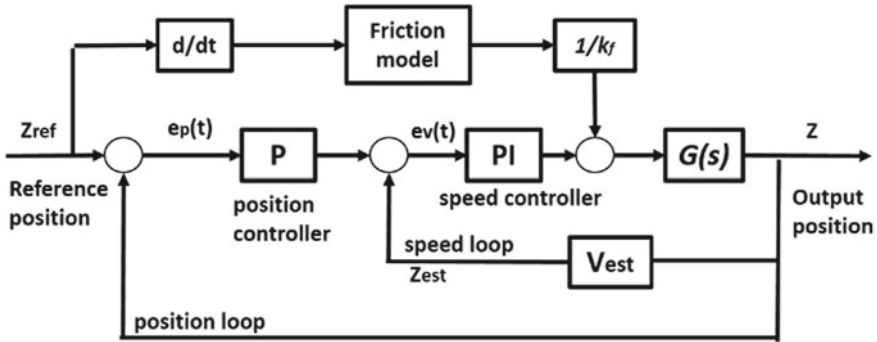


Fig. 4 Cascade P/PI position control scheme with friction model based feedforward

Table 1 Parameters of cascade P/PI controller

Parameter	X axis	Y axis
Source of input signal	Cosine wave	Sine wave
Amplitude (mm)	30	30
Bias	0	0
Frequency (rad/s)	$f * 2 * \pi$	$f * 2 * \pi$
Phase (rad)	$\pi/2$	0
Sample time, Ts	1/2000	1/2000
Kp of position controller	282	282
Kp of velocity controller	0.009505	0.9523
Ki of velocity controller	0.007594	0.7609
Velocity (mm/s)	2	2

$$\text{Position error, } e(t) = y(t) - r(t) \tag{2}$$

where,  $y(t) = z(t)$  is actual position and  $r(t) = Z_{ref}(t)$  is reference position.

The plant transfer function for the table relating the amplifier voltage to the encoder position is given as follows:

$$\text{(x-axis) } \frac{y(s)}{u(s)} = \frac{67940}{s^2 + 155.1s + 53.81} \tag{3}$$

$$\text{(y-axis) } \frac{y(s)}{u(s)} = \frac{69380}{s^2 + 144.8s + 166.3} \tag{4}$$

where,  $y(s)$  is encoder position in mm and  $u(s)$  is voltage input in volts.

The differential equation representing this transfer function is referred as second order model as (5) and (6) with parameters shown in Table 2.

$$\text{(x-axis) } \ddot{y} + 155.1\dot{y} + 53.81y = 67940u \tag{5}$$

**Table 2** Parameters for SMC controller

Parameter	Gain (K)	Lamda ( $\lambda$ )	Delta ( $\delta$ )
X-axis	0.10	50	5
Y-axis	0.09	100	5

$$(y\text{-axis}) \quad \ddot{y} + 144.8\dot{y} + 166.3y = 69380u \tag{6}$$

At the moment of ideal sliding motion, the followings are true:

$$n = 2; \text{ order of SMC} \tag{7}$$

$$s(e, \dot{e}) = \dot{e} + \lambda e \quad \text{where } \dot{e} = \dot{y} - \dot{r} \tag{8}$$

$$\dot{s}(\dot{e}, \ddot{e}) = \ddot{e} + \lambda \dot{e} = 0 \quad \text{where } \ddot{e} = \ddot{y} - \ddot{r} \tag{9}$$

$$\text{Thus, } \ddot{e} = -\lambda \dot{e} \tag{10}$$

$$\text{where, } \ddot{y} = \ddot{e} + \ddot{r} \tag{11}$$

In order to satisfy the sliding condition where trajectories remain at sliding surface, a discontinuous term across the surface is added such that,

$$u = u_{equivalent} - k \cdot sgn(s) \tag{12}$$

where *sgn* is signum function,

$$sgn(s) = \begin{cases} +1 & \text{for } s > 0 \\ -1 & \text{for } s < 0 \end{cases} \tag{13}$$

Parameters applied for SMC controller for x and y axis is shown in Table 2.

### 3.2 Friction Compensation Model

The ideal sigmoid curve that smoothly connected between sliding regimes is referred for better tracking accuracy [13]. The sigmoid-like curve is a curve of S placed in pre-sliding regime to exhibit smoothness behaviour in reversal motion.

In pre-sliding regime, a stick and slip of N-elementary friction model is parallel connected. Each elementary is identified as asperity that stick and slip [14]. Based on Generalized Maxwell Slip (GMS) model, the dynamic behavior of elementary slip block and spring is described as below [15–17].

$$\frac{dF_i}{dt} = k_i v \quad (14)$$

$$\frac{dF_i}{dt} = \text{sign}(v) \cdot C \cdot \left( \alpha_i - \frac{F_i}{s(v)} \right) \quad (15)$$

Equation (14) shows elementary friction force,  $F_i$  is proportional to the deflection of asperity,  $k_1 v$  when asperity is stick where  $k_i$  is the stiffness of asperity. The elementary friction model is remained in stick until equals to the maximum force,  $W$  where the elementary is about to slip. The number of elementary friction force allocates the total number of memory location of hysteresis.

Equation (15) shows elementary friction force,  $F_i$  is slipping when force,  $W_i = \alpha_i s(v)$  where  $\sum \alpha_i$  is equal to Stribeck force.

Measured friction force during spring elementary state is grouped into three main elements which are: (i) switching function (ii) constant force and (iii) friction caused by Stribeck curve towards viscous friction [7, 17].

The total friction force  $F$  is the summation of the output of all elementary state models and viscous term  $\sigma$ .

$$F(v) = \sum_{i=1}^N F_i(v) + \sigma \cdot v(t) \quad (16)$$

The friction compensation model is designed as Pseudo-Like-Curve-Slip (PLCS) model. A classical sigmoid function is replaced at switching function which is commonly applied as switching function in sliding mode controller (SMC) design.

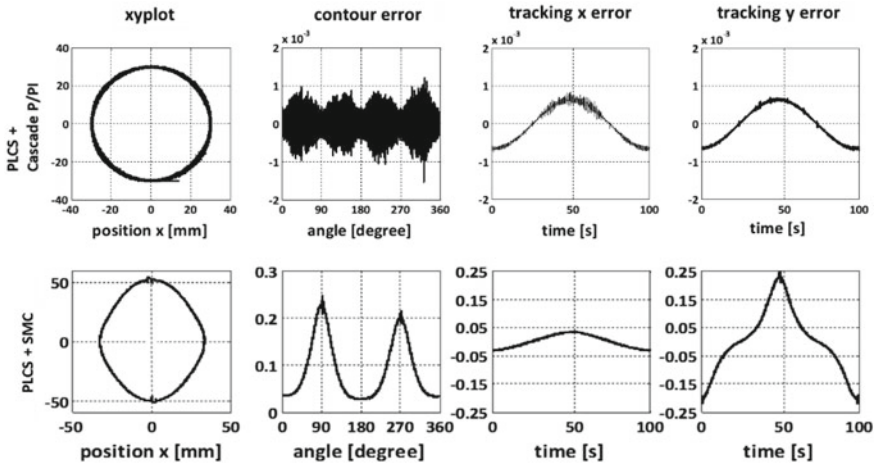
$$\frac{dF_i}{dt} = \left( \frac{v}{|v| + \delta} \right) \cdot C \cdot \left( \alpha_i - \frac{F_i}{s(v)} \right) \quad (17)$$

where  $v$  is velocity and  $\alpha_i$  is normalized sustainable maximum friction force of each element during sticking and  $s(v)$  is Stribeck curve.

## 4 Results and Discussions

The system involves a Panasonic MSMD 022G1U AC servomotor and attached with an incremental encoder with resolution of 0.0005 mm/pulse accordingly. Each axis of test setup applies a sinusoidal signal of amplitude 30 mm and a frequency of 0.01061 Hz.

Experimental result is analysed based on root-mean-square error (RMSE) and contour error. A percentage reduction on magnitude of quadrant glitches at  $0^\circ$ ,  $90^\circ$ ,  $180^\circ$  and  $270^\circ$  in angle are also analysed in order to evaluate the performance of PLCS model to the different controllers.



**Fig. 5** Comparison tracking errors and contour errors between cascade P/PI controller and SMC controller for PLCS model

**Table 3** Comparison errors of PLCS model applied with cascade P/PI controller and SMC controller

Controller	Contour error ( $\mu\text{m}$ )		Radial tracking error ( $\mu\text{m}$ )	
	RMSE	Max error	RMSE at X	RMSE at Y
Cascade P/PI	0.217	1.20	0.542	0.000495
SMC	110	247	21.8	109

Figure 5 illustrates tracking and contour errors between applied cascade P/PI controller and SMC controller. The resulting plot shows that PLCS model with applied SMC controller showed less chattering compared to cascade P/PI controller. The effect of sigmoid function at switching function in pre-sliding combined with SMC controller which is good at switching phase provide better chattering reduction. However, the position error of y axis led to higher RMSE and contour error. The overall tracking performance was poorly affected when applied with SMC controller because SMC controller design mainly focused on control law and switching phase design accuracy, hence reducing chattering.

Table 3 shows RMSE and contour error of PLCS model applied with cascade P/PI controller and SMC controller. The RMSE of applied PLCS model with SMC exhibited larger position and contour error affected from higher position error of y-axis.

Figure 6 shows comparisons of percentage error reduction in term of quadrant glitches for PLCS model applied with cascade P/PI controller and SMC controller. The tabulated results indicate that PLCS model gives better reduction when applied with cascade P/PI controller compared to SMC controller. The percentage error

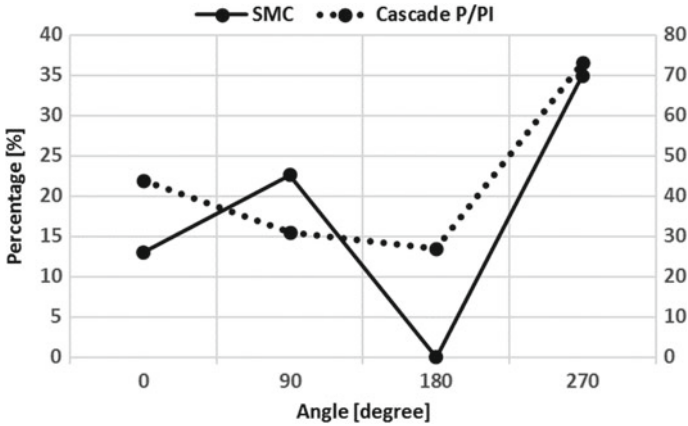


Fig. 6 Percentage error reduction of PLCS model using cascade P/PI controller and SMC controller

reduction is in a range of 30–70%. Meanwhile, applied PLCS model with SMC controller provides 13–35% of error reduction. Based on the result obtained, PLCS model is performed well with cascade P/PI controller in pre-sliding regime at low velocity.

### 5 Conclusion

This paper presents experimental results of modified switching function model namely PLCS model when applied with different controllers at one time. The experiments are conducted with PLCS model applied with cascade P/PI controller and PLCS model applied with SMC controller respectively. The results are based on reversal motion of a ball screw driven positioning table at low velocity. Based on the performance analysis of PLCS model, the results show that PLCS model with feedforward are capable to reduce quadrant glitches as well as tracking error better with cascade P/PI controller compared to SMC controller at low velocity. Quadrant glitches reduction referred to reduction in nonlinear effect in motion accuracy, hence indicating that PLCS model is able to improve smoothness behavior in pre-sliding regime.

**Acknowledgements** This research was supported financially by Universiti Teknikal Malaysia Melaka (UTeM) with research grant PJP/2018/FKP(1C)/S01581.



## References

1. Park EC, Lim H, Choi CH (2003) Position control of X-Y table at velocity reversal using presliding friction characteristics. *IEEE Trans Control Syst Technol* 11(1):24–31
2. Piatkowski T (2014) GMS friction model approximation. *Mech Mach Theory* 75:1–11
3. Rafan NA, Jamaludin Z, Tjahjowidodo T, Chey L, Chiew T (2012) Theoretical analysis of friction compensation using sliding mode control. *Appl Mech Mater* 231:2385–2388
4. Muñoz D, Sbarbaro D (2000) An adaptive sliding-mode controller for discrete nonlinear systems. *IEEE Trans Ind Electron* 47(3):574–581
5. Tjahjowidodo T (2012) Geometric nonlinear equivalence of frictional systems for compensation. *Int Conf Noise Vibr Isma I*:985–1000
6. Shang W, Cong S, Zhang Y (2008) Nonlinear friction compensation of a 2-DOF planar parallel manipulator. *Mechatronics* 18(7):340–346
7. Jamaludin Z, Van Brussel H, Swevers J (2008) Quadrant glitch compensation using friction model-based feedforward and an inverse-model-based disturbance observer. In 2008 10th IEEE international workshop on advanced motion control, pp 212–217
8. Yao J, Yang G, Jiao Z, Ma D (2013) Adaptive robust motion control of direct-drive DC motors with continuous friction compensation. *Abstr Appl Anal* 2013:1–14
9. Ko RC, Good MC (2005) Improving contour accuracy of machine tools using an integral-gain scheduler. *Proc Inst Mech Eng Part I J Syst Control Eng* 219(7):511–518
10. Tung ED, Urushisaki Y, Tomizuka M (1993) Low velocity friction compensation for machine tool feed drives. In Proceedings of American control conference, pp 1932–1936
11. Kaneko S, Sato R, Tstusumi M (2008) Mathematical model of linear motor stage with nonlinear friction characteristics. *J Adv Mech Des Syst Manuf* 2(4):675–684
12. Milosavljevic C, Drazenovic BP, Veselic B (2013) Discrete-time velocity servo system design using sliding mode control approach with disturbance compensation. *IEEE Trans Ind Inform* 9(2):920–927
13. Rafan NA, Jamaludin Z, Heng CT (2016) Investigation on tracking performance of adaptive friction compensation using cascade P/PI controller at low velocity. In: 2016 international conference on computer and communication engineering, pp 149–154
14. Lampaert V, Al-Bender F, Swevers J (2003) A generalized Maxwell-slip friction model appropriate for control purposes. In: 2003 IEEE International Workshop on Workload Characterization, vol 4, pp 1170–1177
15. Lampaert V, Swevers J, Al-bender F (2002) Experimental comparison of different low-velocity tracking. In: 10th mediterranean conference on control and automation
16. Jamaludin Z, Van H, Pipeleers G, Swevers J (2008) Accurate motion control of xy high-speed linear drives using friction model feedforward and cutting forces estimation. *CIRP Ann Manuf Technol* 57:403–406
17. Jamaludin Z, Van Brussel H, Swevers J (2009) Friction compensation of an XY feed table using friction-model-based feedforward and an inverse-model-based disturbance observer. *IEEE Trans Ind Electron* 56(10):3848–3853

# Measurement of Residual Stresses in Aluminium to Copper Friction Stir Spot Welds



Mukuna Patrick Mubiayi and Esther T. Akinlabi

**Abstract** Friction stir spot welding (FSSW) technique was used to join aluminium (AA1060) to copper (C11000). The effect of process parameters on the residual stress and the full width at half maximum was studied. A copper ring was observed on both sides of the keyhole in all the fabricated FSS Welds. The surface morphology of the copper rings was examined using a scanning electron microscope; while the residual stresses were measured using the non-destructive X-ray diffraction method. The copper ring dimension in all the fabricated FSS Welds increased with the variation of the tool shoulder plunge depths; nevertheless, the welds fabricated at 1200 rpm rotation speed displayed a decrease in the dimension of the formed copper ring. In the analysed samples only compressive residual stresses were observed and highest residual stress of  $-116.8$  MPa was obtained on the formed copper ring of the spot welds fabricated at a rotation speed of 800 rpm and 0.5 mm tool shoulder plunge depth. The presence of higher residual stress on the copper rings was due to the extrusion of copper into the aluminium sheet. Additionally, the intensity of all the peaks for the fabricated spot welds decreased in comparison to the peaks generated by the aluminium and copper base materials. Furthermore, the tool shoulder plunge depth affected the full width at half the maximum (FWHM).

**Keywords** Aluminium · Copper · Copper ring · Friction stir spot welding · Residual stress

## 1 Introduction

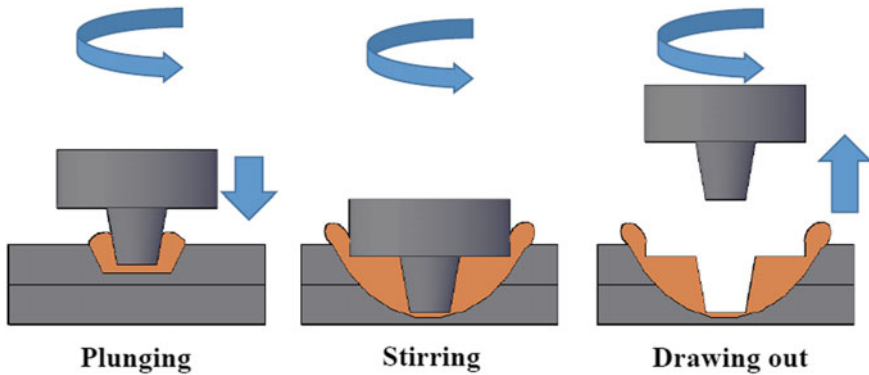
Materials joining friction stir welding (FSW) was developed in 1991, and it has been recognized as a reliable solid-state joining method. Friction stir spot welding (FSSW) is an alternative to friction stir welding, and it is an alternative joining procedure for

---

M. P. Mubiayi (✉) · E. T. Akinlabi  
Department of Mechanical Engineering Science, University of Johannesburg, Kingsway Campus,  
Auckland Park, Johannesburg 2006, South Africa  
e-mail: [patrickmubiayi@gmail.com](mailto:patrickmubiayi@gmail.com)

© Springer Nature Singapore Pte Ltd. 2020  
M. Awang et al. (eds.), *Advances in Material Sciences and Engineering*, Lecture Notes in Mechanical Engineering,  
[https://doi.org/10.1007/978-981-13-8297-0\\_34](https://doi.org/10.1007/978-981-13-8297-0_34)

319



**Fig. 1** A diagram showing the different stages of the friction stir spot joining procedure

resistance welding [1]. For the two welding methods, a rotating non-consumable tool is plunged into the materials to be joined. Figure 1 displays a schematic diagram of the FSSW technique. FSW and FSSW welding methods are being used in various sectors, and these sectors include automotive and aerospace. Hence, it is of importance to understand the different characteristics of these materials' behaviours include mechanical properties. Residual stresses in materials especially in joined dissimilar materials are among these essential mechanical properties. Residual stresses are the stresses that are still present in a material after manufacturing and processing in the absence of thermal gradients or external forces. There are many different methods to measure the residual stress for components and these methods include non-destructive method such as X-ray diffraction and neutron diffraction methods [2]. Various studies have been carried out by many researchers on the residual stresses in FS Welded structures [3–7].

Bach et al. [3] measured the residual stress distribution of AA 2024 T3 FS Welded using the non-destructive neutron diffraction technique. They used two sets of samples named, the welded plate and the hammer peened plate. They observed that the residual stresses on the as-welded are better than those found in the hammer peened samples at every slit depth.

A cut-compliance technique was used to measure the residual stress intensity factor  $K_{Ires}$  on FS Welded AA 2024-T351 sheets [4]. Fratini et al. [4] found that the  $K_{Ires}$  profile for friction stir welding decreased up to a lowest at around 9 mm away from the welding centreline; then, rose to a positive maximum closer to the retreating side. Additionally, the maximum residual stress was found in the advancing side, and the distribution was quite symmetrical [4]. Ma et al. [5] successfully joined AA 2195-T8 sheets using FSW and utilised the non-destructive neutron diffraction method to measure the residual stresses. They investigated the effect the specimen dimensions on residual stress profiles, and three specimens of different dimensions were utilised in their study.

The residual stresses obtained on the X-direction have a double peak tensile residual stress field of similar form in all the fabricated three specimens. They further stated that the maximum residual stress (tensile) parallel to the fabricated joint ranged from 120 MPa (biggest specimen) to 47 MPa (smallest specimen). Far-off the joint line at the notch tip, the minimum residual stress ranged from around  $-130$  MPa (biggest specimen) to  $-20$  MPa (smallest specimen) compression values. A synchrotron X-ray diffraction method was used to measure the residual stress distribution in FS Welds of AA7449 [6]. Altenkirch et al. [6] investigated the effect of tensioning on the residual stresses. They observed that the application of tensioning stress decreased the tensile magnitude of the final measured residual stresses by modifying the stress accumulation path [6].

The effect of the variation of the welding parameters on the residual stress profiles in the FS Welds of AA5083-H321 was investigated by Lombard et al. [7]. They used a synchrotron X-ray diffraction technique.

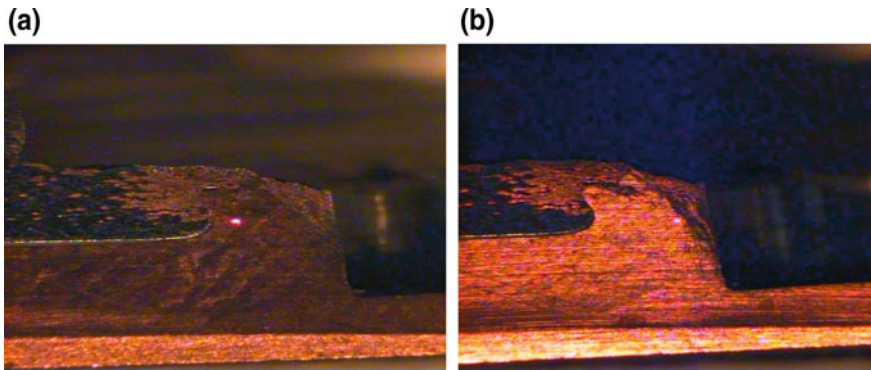
They mostly observed tensile residual stresses in the weld area, with balancing compressive stresses in the base material.

More recently, Sun et al. [8] used friction stir welding (FSW) technique to weld hot rolled AA7050-T7651 sheets of 6.35 mm thickness using a conventional tool, different downforce and comparing the obtained results to the welds fabricated using a stationary shoulder friction stir welding (SSFSW). They observed that by reducing the tool downforce, the shoulder input power decreases, nonetheless a negligible decrease in the weld zone (WZ) microhardness and the residual stresses peak was seen. On the other hand, in contrast, the stationary shoulder led to a much more significant increase in the minimum WZ microhardness and a substantial reduction in the peak tensile residual stresses [8]. And this was obtained by using a similar input power used with the conventional tool.

In the current study, the X-ray diffraction method was used to measure the residual stresses on FSS Welded AA1060/C11000. Furthermore, the effects of process parameters namely rotation speed and tool shoulder plunge depth on the formation of a copper ring and the full width at half maximum are also studied.

## 2 Methods

A 3 mm thick pure aluminium (AA1060) and pure copper (C11000) sheets were joined using FSSW in a 30 mm overlap configuration using H13 tool steel (50-52 HRC). A tool having a flat pin and flat shoulder was employed. A pin of 4 mm (length), 5 mm (diameter) and 15 mm shoulder diameter was used. 800 and 1200 rpm rotation speeds, 0.5 and 1 mm shoulder plunge depths while keeping a constant dwell time of 10 s were used. The samples are coded as XXX\_X, the first part depicts the rotation speed and the second part the shoulder plunge depth. The formation of copper rings on both sides of the keyhole was studied using a scanning electron microscope (SEM), a TESCAN Vega TC was used. The non-destructive X-ray diffraction (XRD) technique was employed to measure the residual stress dis-



**Fig. 2** The position of the residual stress measurement **a** in the copper ring and **b** in the stir zone

tribution in the produced FSS Welded sheets. A BRUKER AXS was used to measure the residual stress. Figure 2a, b depicts the residual stress measurements position in the stir zone (SZ) and the copper ring of the fabricated friction stir spot welds.

### 3 Results and Discussions

A keyhole was present in all the fabricated friction stir spot welds, and copper rings were observed on both sides of all the friction stir spot welds [9], the copper rings which can also be called hooks [10], are extruded copper material penetrating into the Al sheet. This was also observed by Ozdemir et al. [11]. Figure 3 shows the copper rings with different dimensions and the keyholes in the fabricated friction stir spot welds.

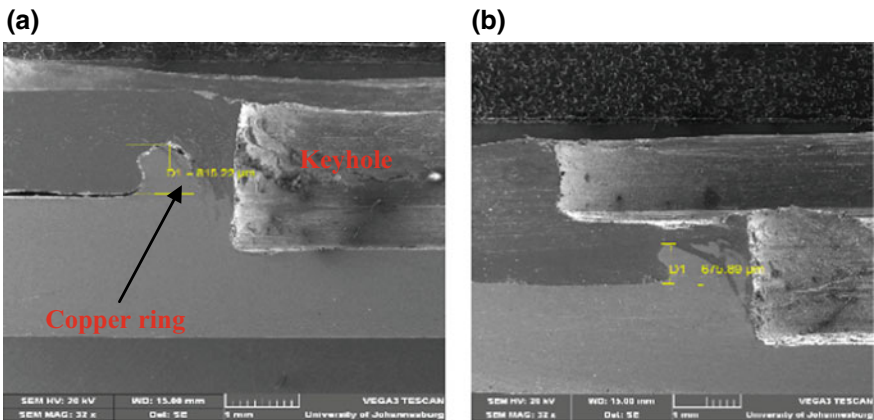
Additionally, Heideman et al. [9] also reported on the presence of the copper ring with different dimensions in all the produced friction stir spot welds. They explained that the copper rings formed are made of the copper (Cu) base material extruded in the aluminium (Al) sheet and the copper rings were also observed in this study. Heideman et al. [9] further said that while the copper base material was moving and diffusing into the aluminium base material, the aluminium was not diffusing or being pushed into the formed copper ring [9].

The dimensions of the copper ring seen on the produced FSS Welds using different FSSW process parameters are shown in Fig. 4. Furthermore, in this study, a reduction in the thickness of the sheets in all the fabricated FSS Welds was further observed. Ozdemir et al. [11] further indicated that the penetration length of the copper material into the aluminium material was about half of the aluminium sheet thickness, but this was not in agreement with the results obtained in the current study. The copper penetration length into the aluminium was investigated in the present study.

It was observed that the dimension of the copper ring increases with the increment of the tool shoulder plunge depth, except for the FSS Welds fabricated at 1200 rpm rotation speed, where a decrease was observed. This indicates that the spot welds produced at high rotation speed display an increment in the dimension of the copper ring and a reduction when the shoulder plunge depth of the tool is increased to 1 mm. Heideman et al. [9] indicated in their study that, the copper ring caused interlocking between the two sheets (copper and aluminium), which helped the two sheets to stick together during tensile testing and this resulted in reaching higher strength before failure [9].

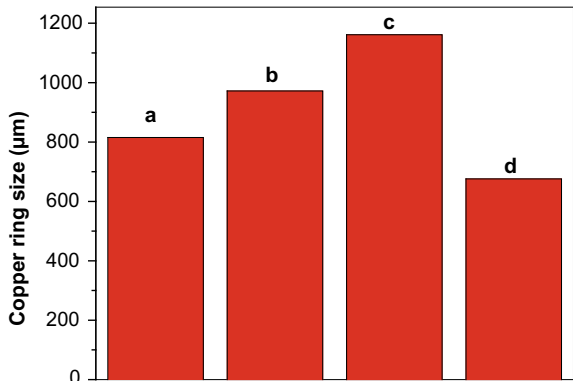
The measured residual stresses in the SZ (one measurement) and on the copper ring (three measurements) of the FSS Welds are shown in Fig. 5.

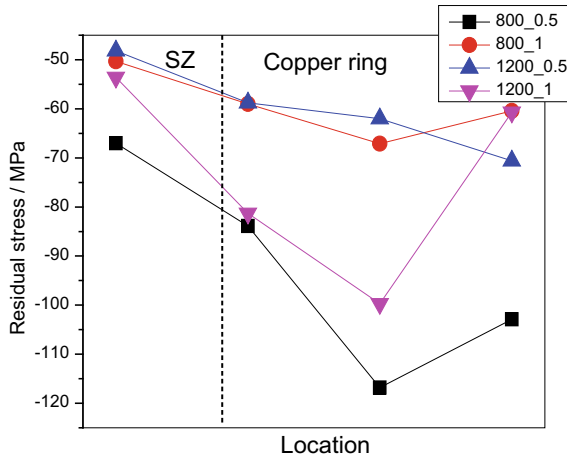
Residual stresses of  $-67$  and  $-50.3$  MPa were obtained in the stir zone (SZ) of the spot weld produced at a rotation speed of 800 rpm and the tool shoulder plunge depths of 0.5 and 1 mm, respectively. On the other hand, the welds fabricated



**Fig. 3** Copper ring dimension of the FSS Welds fabricated: **a** 800 rpm, 0.5 mm and **b** 1200 rpm, 1 mm

**Fig. 4** The dimensions of copper rings at different process parameters, **a** (800\_0.5), **b** (800\_1), **c** (1200\_0.5) and **d** (1200\_1)



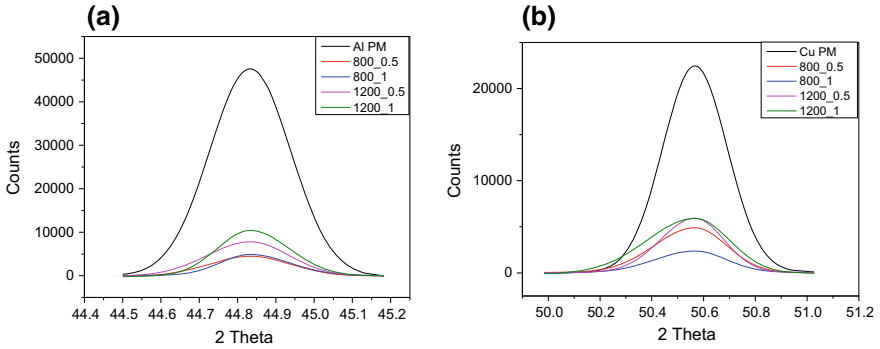


**Fig. 5** Measured residual stress obtained on the stir zone and on the copper ring of the FSS Welds fabricated at different process parameters

at 1200 rpm rotation speed using 0.5 and 1 mm tool plunge depths exhibited an increment. The residual stresses obtained were  $-48.2$  and  $-53.6$  MPa. This indicates that the residual stresses were affected by the tool shoulder plunge depths. Furthermore, no trend was observed on the variations in the residual stresses when the tool shoulder plunge depth was varied. The maximum measured residual stress of  $-116.8$  MPa was observed on the copper ring of the friction stir spot weld fabricated at 800 rpm rotation speed and with a tool shoulder plunge depth of 0.5 mm. It can be further said that the extrusion of the copper material (placed at the bottom) into the aluminium material (placed on top) was the cause of high values of residual stress measured in the copper ring. Figure 6a, b depicts the X-ray diffraction of Al and Cu peaks utilized to measure the full width at half maximum (FWHM) of different FSS Welded samples. A diffraction peak from both base materials was chosen, viz.  $44.83^\circ$  (200) and  $50.57^\circ$  (200) (2 Theta) for Al and Cu, respectively.

It was observed that the intensity of all the peaks decreases in comparison to the peaks generated by the base materials for the same peak position, and it was further observed that those peaks were broadened, as displayed in Fig. 6. This indicates that the joining process parameters created stress in the produced FSS Welds. Vashista and Paul [12] reported that not only microstrains but also small grains can broaden the peaks. It was seen that welding parameters affect the peaks position compared to the peaks generated from the base materials. The diffraction peaks of the Al had a higher shift than the Cu diffraction peaks, and this can be due to their different properties, including the melting point. The FWHM values are display in Table 1.

It was observed that the FWHM increases at rotation speed of 800 rpm, 0.5 mm shoulder plunge depth, and then it decreases when the tool shoulder plunge depth is increased to 1 mm. It was further observed that when the rotation speed is increased, the full width at half maximum (FWHM) also increases.



**Fig. 6** X-ray diffraction peaks of **a** Al and **b** Cu used to measure the FWHM of the fabricated FSS Welds depicting the variation of the intensity of the peak intensity and the widths

**Table 1** Depicts the variation full width at half maximum (FWHM)

Sample name	FWHM
Copper PM	0.29271
800_0.5	0.36551
800_1	0.32128
1200_0.5	0.33443
1200_1	0.33662
Aluminium PM	0.24875
800_0.5	0.3594
800_1	0.26731
1200_0.5	0.31654
1200_1	0.29351

Additionally, when 1 mm tool shoulder plunge depth is used, the FWHM decreases. This shows that the tool shoulder plunge depth affects the FWHM. The Al diffraction peaks shifted more than that of the Cu diffraction peaks; this can be due to the different properties exhibited by the two parent materials.

## 4 Conclusions

In this study, AA1060 and C11000 sheets were spot welded by using the FSSW method. The results are summarised as follow:

- A copper ring was observed on both sides of the keyhole for all the produced FSS Welds. This could mean that the extrusion of copper into aluminium resulted in the presence of a copper ring which could be the reason for the presence of residual stresses in all the produced FSS Welds.



- It was observed that the residual stresses measured in the copper ring were higher compared to the residual stresses values in the SZ. The spot weld produced at the rotation speed of 800 rpm and 0.5 mm tool shoulder plunge depth exhibited the highest residual stresses of  $-116$  MPa which was measured in the copper ring. This is due to the extrusion of copper into the aluminium sheet and which resulted in the presence of residual stress in the formed copper ring.
- It was further observed that the intensity of all the selected diffraction peaks was lower when compared with the diffraction peaks generated by the copper and aluminium parent materials.
- The tool shoulder plunge depths namely 0.5 and 1 mm were found to affect the full width at half maximum (FWHM).

**Acknowledgements** The authors acknowledge the financial support from the University of Johannesburg.

## References

1. Badarinarayan H (2009) Fundamentals of friction stir spot welding. Missouri University of Science and Technology
2. Rossini NS, Dassisti M, Benyounis KY, Olabi AG (2012) Methods of measuring residual stresses in components. *Mater Des* 35:572–588
3. Bach M, Merati A, Gharghoury M (2014) Effects of fatigue on the integrity of a friction stir welded lap joint containing residual stresses. *Adv Mater Res* 996:794–800
4. Fratini L, Pasta S, Reynolds AP (2009) Fatigue crack growth in 2024-T351 friction stir welded joints: longitudinal residual stress and microstructural effects. *Int J Fatigue* 31:495–500
5. Ma YuE, Staron P, Fischer T, Irving PE (2011) Size effects on residual stress and fatigue crack growth in friction stir welded 2195-T8 aluminium—Part I: experiments. *Int J Fatigue* 33:1417–1425
6. Altenkirch J, Steuwer A, Peel M, Richards DG, Withers PJ (2008) The effect of tensioning and sectioning on residual stresses in aluminium AA7749 friction stir welds. *Mater Sci Eng, A* 488:16–24
7. Lombard H, Hattingh DG, Steuwer A, James MN (2009) Effect of process parameters on the residual stresses in AA5083-H321 friction stir welds. *Mater Sci Eng, A* 501:119–124
8. Sun T, Reynolds AP, Roy MJ, Withers PJ, Prangnell PB (2018) The effect of shoulder coupling on the residual stress and hardness distribution in AA7050 friction stir butt welds. *Mater Sci Eng, A* 735:218–227
9. Heideman R, Johnson C, Kou S (2010) Metallurgical analysis of Al/Cu friction stir spot welding. *Sci Technol Weld Joining* 15(7):597–604
10. Badarinarayan H, Yang Q, Zhu S (2009) Effect of tool geometry on static strength of friction stir spot-welded aluminum alloy. *Int J Mach Tools Manuf* 49(2):142–148
11. Özdemir U, Sayer S, Yeni Ç, Bornova-Izmir (2012) Effect of pin penetration depth on the mechanical properties of friction stir spot welded aluminum and copper. *Mater Test IN Join Technol* 54(4):233–239
12. Vashista M, Paul S (2012) Correlation between full width at half maximum (FWHM) of XRD peak with residual stress on ground surfaces. *Phil Mag* 92(33):4194–4204. <https://doi.org/10.1080/14786435.2012.704429>

# Effect of Chip Treatment on Chip-Based Billet Densification in Solid-State Recycling of New Aluminium Scrap



A. Wagiman, Mohd Sukri Mustapa, S. Shamsudin, Mohd Amri Lajis, R. Asmawi, M. A. Harimon, Farazila Yusof and Mohammed H. Rady

**Abstract** In solid state recycling of new aluminium scrap, processes prior to hot extrusion play an important role in order to obtain free-defect microvoid extrudates. The microvoid is formed due to air entrapment that came from porous chip-based billet. In this work, chip-based billet made from annealed and non-annealed chip was investigated to determine the effect of annealing on density, void pattern and hardness. AA6061-T651 chips were prepared as annealed and non-annealed and then compacted in die. The billets density and appearance were measured and visually inspected. Density measurement found that billet made from annealed chip has the highest relative density of 96.9%. Visual inspection and microstructure examination disclose that voids are present in the billet for both types of chip in which non-annealed chip is more obvious. The voids has distributed in homogeneously along the axial and vertical due to pressure gradient. The pressure gradient also affects the hardness distribution. The effect of strain hardening is more obvious at the peripheral compared to the centre. The average hardness of annealed chip is 49.5 HV0.1 while non-annealed chip recorded 89.5 HV0.1. In general, annealing treatment before compaction had softened the chip, reduced the hardness and strength, permitted large plastic deformation and improved billet density .

**Keywords** Solid state recycling · Chip treatment · Densification · Cold compact · Chip-based billet

---

A. Wagiman · M. S. Mustapa (✉) · S. Shamsudin · M. A. Lajis · R. Asmawi · M. A. Harimon  
Sustainable Manufacturing and Recycling Technology, Advanced Material Manufacturing Center (SMART-AMMC), Universiti Tun Hussein Onn Malaysia, Parit Raja, Malaysia  
e-mail: [sukri@uthm.edu.my](mailto:sukri@uthm.edu.my)

F. Yusof  
Department of Engineering Design and Manufacture, University of Malaya, Kuala Lumpur, Malaysia

M. H. Rady  
Mechanical Engineering Department, University of Wasit, Kut, Iraq

## 1 Introduction

Solid state recycling is an alternative process for sustainable aluminium processing [1]. The process can be carried out with various severe plastic deformation (SPD) techniques. Until today, many techniques including direct hot extrusion [2, 3] and indirect [4], hot press forging [5], rolling [6], cold compact [7] have been investigated in transforming aluminium scrap into finished or semi-finished product. In solid state recycling using hot extrusion, the process can be accomplished after undergoing several processing steps. The steps may include chip segregation, comminution, cleaning, cold compact, sintering and hot extrusion process.

Microvoid defect is always associated with solid state aluminium recycling when using SPD process [8]. The defect was found to become crack initiation point when the material was subjected to static and dynamic load [9]. The present of microvoid had reduced the strength and ductility of the recycled aluminium. The microvoid was formed in the extrudates due to entrapped air [10]. The entrapped air may result from the usage of porous chip-based billet. Therefore, in order to produce free void defect extrudates, the process prior to hot extrusion such as cold compaction plays an important role.

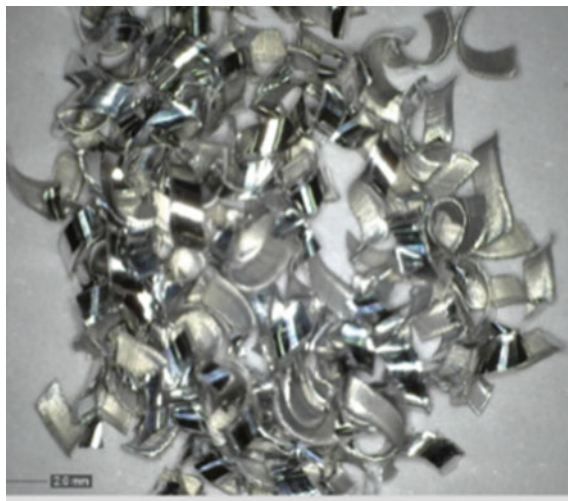
The void in the chip-based billet can be determined from the density. The closer the density to the theoretical density of the aluminium, the lesser the void develops in the chip based billet. The density of the chip-based billet is influenced by several factors including compaction technique, compaction pressure and time. Previous researchers have worked out to produce billet with high density by introducing various strategies. Tokarski [11] found that single layer compaction at 240 MPa produces chip-based billet with relative density as high as 77%. Additionally, Hasse [12] found that compacting the chip at 303 MPa produces green billet with the density of 82%.

In order to improve the density, Misiolok [13] has introduced the multi-layer cold compaction. He found that the density of multi-layer compaction is higher than the single layer. However, the chip-based billet was easily cracked at the interlayer due to poor consolidation at the interface between the former and subsequent layer. This is because the compaction process has developed strain hardening at the former layer. The strain hardening makes the subsequent chip unable to diffuse into the former layer. In addition, spring back may occur during the compaction. It is because the chip has a distinctive level of strain hardening and residual stress that was developed during the machining process [14]. Therefore, high pressure is required to obtain a shear strain that is enough to break the aluminium oxide on the chip surface. However, higher operating pressure will reduce tool life and increase operation cost.

Annealing treatment on the chip before compaction process is an alternative to reduce the strength of the chip. The technique has been introduced by Samuel [15] and also applied by Kore [16]. Samuel concluded here is no doubt that the annealing treatment can soften the aluminium chip and improve the density of the chip-based billet. However, research works explaining the effect of annealing on density, void distribution and hardness are seldom reported. Therefore, this research is carried out to determine the effect of annealing on density, void distribution and hardness. The work compared the responses obtained from both type chip based billet.

**Table 1** Mechanical properties of AA6061-T651

Ultimate strength (MPa)	Yield stress (MPa)	Elongation (%)	Hardness vickers (HV)
319	287	10.5	104

**Fig. 1** Aluminium AA6061-T651 chips

## 2 Methods

Artificial aluminium chip of AA6061-T651 was generated using MAZAK 3-axis CNC milling machine from slab to simulate the industrial aluminium scrap. This type of aluminium was selected because of it has been widely used in industry for engineering application. Table 1 tabulated the chemical composition and mechanical properties of the aluminium.

The machining process was performed at the cutting condition of side cut end mill, 10 mm cutting tool diameter, 345 mm/second cutting speed, 1 mm feed per tooth and 1 mm depth of cut. An oil-water emulsion was used as a coolant during the cutting. This cutting condition produced elemental chip as shown in Fig. 1.

The chips were collected, dried and cleaned in an ultrasonic acetone bath for 30 min to remove the oil-water emulsion that is fouled on the chip surface. The clean chips were dried in the furnace oven at 100 °C and held at 1 h to vaporize the acetone and water. Two types of chips, annealing and without annealing were prepared. The annealing process is carried out by heating the chip in the furnace. The chips were heated at 500 °C and held at 10 min. The chips then were immediately left to cool down naturally in the air for 10 min. Within this time, the chip has reached the ambient temperature of 26–28 °C.

Four samples of semi-finished billet with the length of  $25 \pm 1$  mm were produced. In order to obtain desired billet length, a few trials were carried out at a different weight of chip. To form the chip-based billets, the chips were filled in the 30 mm diameter cylindrical mould cavity and pressed. The plunger exerted on the top surface of the chips was forced to compact the chips in the cavity using the press machine. The semi-finished billets were produced according to two different pressure levels, 50 bar and 150 bar. The compaction process was carried out at ambient temperature.

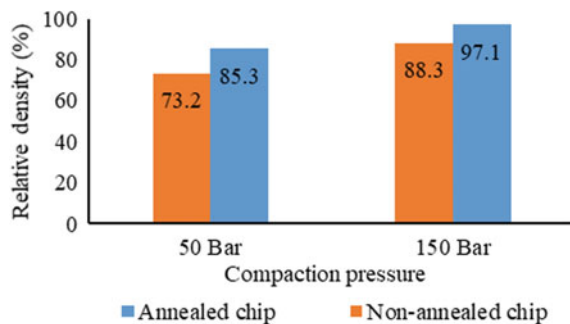
The resultant chip-based billets were inspected using Dynalite image capture. The billet density was calculated by dividing the mass of the billet by the volume. The relative density (RD) was calculated by dividing the measured density with an as-received density of AA6061-T651 ( $2700 \text{ mm}^3/\text{Kg}$ ). The microhardness was performed in accordance with ASTM E348 with the indentation load and time of 0.1 kgf and 10 s respectively.

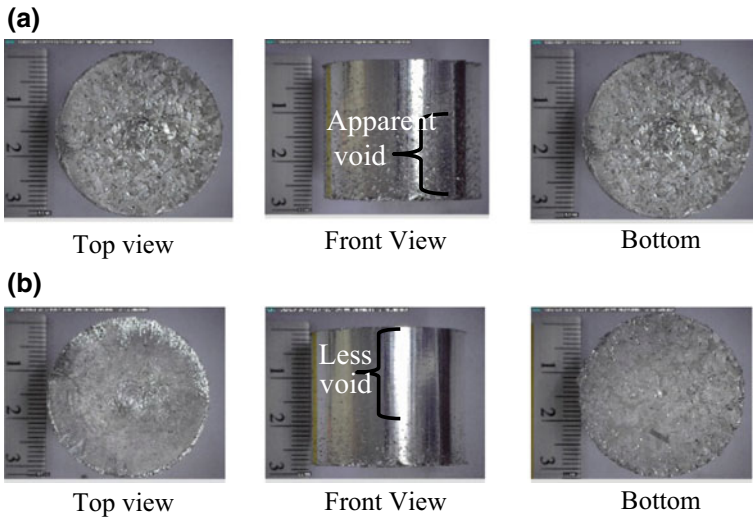
### 3 Results

The chip-based billet produced from the non-annealed chip and compacted at 50 bar pressure resulted in a relative density of 73.2%. Meanwhile, annealing treatment on chip before compaction improves the billet density to 84.4%. The same pattern is also obtained when the chip compacted at 150 bar. The billet relative density is improved from 88.3 to 96.9%. Figure 2 shows the comparison of the chip-based billet density of different compaction pressures and chips.

Visual inspection on the chip-based billet observed that the black dot appearing on the surface of the billet is a void (as shown in Fig. 3). The void is an empty space that mechanically developed during the compaction process. Chip-based billet with a relative density of 88.3% exhibited more voids if compared with the billet that has 96.9% relative density. The voids distributions along the vertical are inhomogeneous. It is more apparent on the bottom area and become vague toward the top. Obviously, the voids distributions determine that the top area is denser than the bottom area.

**Fig. 2** Chip-based billet relative density with different compaction pressure and chip treatment

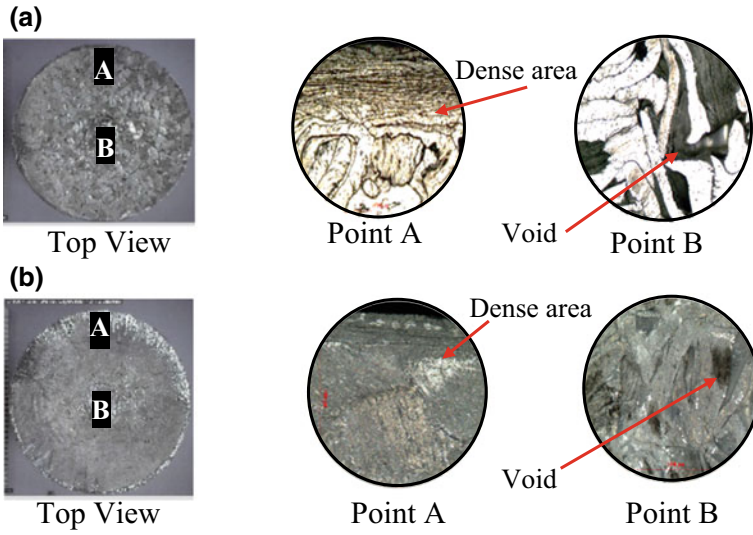




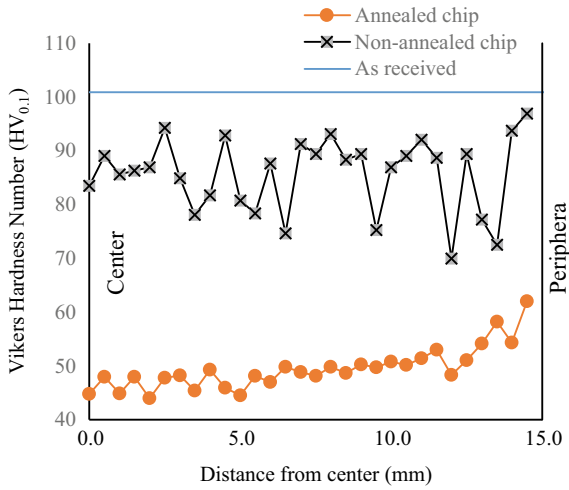
**Fig. 3** Chip-based billet (compacted at 150 bar), **a** non-annealed, **b** annealed

Microstructure examination on the top surface plane reveals that the densification trend varies from the peripheral to the centre of the billet. As shown in Fig. 4, for both types of chip, point A is denser than point B. In point A, the dense area is about 0.6 mm from the peripheral. Chips thinning were observed in this area in which the thickness of the chip had reduced from an average of 0.5 mm in original condition to less than 0.1 mm. No voids were observed in the point A. However, in point B, the voids are more noticeable when the distance reduces toward the centre.

Microhardness test carried out on the top plane of the annealed chip-based billet reveal that the hardness distribution varies along the radii. As shown in Fig. 5, the hardness number is lower at the centre and rises as the radii increases toward the edge surface. The hardness value at the centre is 40 HV<sub>0.1</sub>. The highest value of 62 HV<sub>0.1</sub> is recorded near the surface edge. On average, the annealed chip based billet resulted in 49.5 HV<sub>0.1</sub>. However non-annealed chip based billet responded indifferently. Except for point near the surface edge, other locations resulted in lower hardness number without an obvious trend. The highest hardness number of 97 HV<sub>0.1</sub> is recorded at the surface edge. For the rest, hardness values appear inconsistent within the range of 67 HV<sub>0.1</sub> to 93 HV<sub>0.1</sub> without obvious decreasing or increasing trend toward the surface edge. The average hardness number of the non-annealed chip is 89.5 HV<sub>0.1</sub>. This value is nearly one time higher than the annealed chip but less than the hardness value of the as-received material which is 105 HV<sub>0.1</sub>.



**Fig. 4** Chip-based billet macrostructure (compacted at 150 bar), **a** non-annealed chip, **b** annealed chip



**Fig. 5** Microhardness distribution of annealed and non-annealed chip-based billet

## 4 Discussions

The density of chip-based billet produced from the uniaxial compaction is depends on the given axial pressure and the yield stress properties of the chip. Higher pressure exerted on the chip resulted in higher density. However, when the chip based billet has achieved its deformation resistance, an increase in pressure resulted in negligible density improvement [13, 17]. Annealing treatment on the chips improves the billet density. In this work, chip annealed at 500 °C, held within 10 min and then compacted with 150 bar pressure resulted in a relative density of 96.9%. The value is 9% higher than the non-annealed chip. The density is increased because the annealing has softened the chip and facilitated the plastic flow into the empty space between the chip [15].

Annealing chip by heating above the solvus temperature of about 500 °C has recrystallized the structure and produced homogeneous solid solution, allowing dissolution second phase and eliminating the segregation of the alloys [18]. The heated aluminium chips that were immediately exposed to the air has rapidly cooled to the room temperature. It is because the chips have an enormous surface area to volume ratio which permit rapid heat dissipation. The energy associated with the material that has enormous surface area to volume ratio is different compared to the conventional bulk [19]. The rapid cooling of the chip has limited the atom diffusion process towards potential nucleation, thus enabling the formation of supersaturated solid solution of aluminium. The formation of this phase may reduce the yield stress to about 55 MPa [18]. This value is much lower than the yield stress of as-received material of 310 MPa.

The softened chip enables large plastic deformation, fragmenting the thin film of aluminium oxide on the surface and thus providing larger contact surface area within the virgin aluminium [8]. The condition permits more adjacent chip to consolidate among them and resulted in billet with high density. However, it may be hard to obtain 100% relative density as the uniaxial compaction of chips involved accumulation of vacancies or void through the bulk diffusion. The voids are an empty space between the adjunct chip boundary [20]. It was formed as a consequence of mechanical deformation. During the compaction, the plastic flow of the aluminium chip is unable to fill in space, leaving the space filled with entrapped air.

The voids formation along the vertical and radial were inhomogeneous. As found from the visual inspection on the surface appearance, the voids are more apparent on the bottom compared to the top side. Additionally, the void distribution is also inhomogeneous along the radii as found from microstructure examination. The findings show that billets compacted by uniaxial have density gradient along the vertical and radial. The variation in density is caused by differential stress distribution induced by applied compaction pressure. During compaction, the axial force from the applied compaction pressure is transmitted to the chip [21]. However, the force changes its reaction when the movement of chip achieved its limitation. At this condition, some



of the force transmitted to the die wall as radial force [22]. The reaction causes the force transmitted to the bottom chip is less than the upper chip due to interparticle friction and die wall friction. Therefore, the longer the distance from the plunger, the lower the force and the larger the distance from the centre the higher the reaction force.

Plastic deformation of the softened chip due to compaction had created a crystallographic defect. This defects impede the movement of dislocation, result in strain hardening and making the aluminium chip harder. The effect of strain hardening is more obvious at the die wall compared to the centre of the billet due to differential force distribution along the radii. The force at the die wall is higher than the centre due to the reaction of die wall friction. Therefore, higher hardness was recorded at the die wall compared to the centre.

Comparison of the hardness value of the annealed and non-annealed chip based billet shows a great difference. The annealing treatment had softened the chip and resulted in lowest average hardness of 49.5 HV<sub>0.1</sub>. The effect of homogeneity due to annealing treatment carried out before compaction resulted in more consistent hardness variation [18]. The large variation in non-annealed chip shows that the inhomogeneous structure of the non-annealed chip is still preserved although the chip had undergone cold compaction.

## 5 Conclusions

In comparison, annealing treatment performed on chips before compaction improved the relative density of the chip-based billet. The treatment had erased all hardening history, softened the chip, permitted large plastic deformation and resulted in greater billet density. Full density is hard to obtain since the deformation accumulates voids. Uneven void distribution due to differential force along the radial and vertical resulted in density gradient and hardness variation. The top area is denser than the bottom area. Meanwhile along the radii, the peripheral area is denser than the centre. High hardness was recorded at the peripheral and lower at the centre. On average, the hardness of annealed chip based billet was one time lower than non-annealed chip. The billet of non-annealed chip had large hardness variation compared to annealed chip.

**Acknowledgements** The authors would like to express their deepest appreciation to the Ministry of Higher Education Malaysia (MOHE), for funding this project through the Research Grant Schemes TIER 1 H085.

## References

1. Kadir MIA, Mustapa MS, Latif NA et al (2017) Microstructural analysis and mechanical properties of direct recycling aluminium chips AA6061/Al powder fabricated by uniaxial cold compaction technique. *Procedia Eng* 184:687–694
2. Güley V, Güzel A, Jäger A et al (2013) Effect of die design on the welding quality during solid state recycling of AA6060 chips by hot extrusion. *Mater Sci Eng, A* 574:163–175
3. Tekkaya AE, Güley V, Haase M et al (2012) Hot extrusion of aluminum chips. In: 13th international conference on aluminum alloys (ICAA13), pp 1559–1573
4. Behrens BA, Bouguecha A, Brunotte K et al (2016) Reprocessing of aluminum chips by hot backward extrusion. *Prod Eng* 10:375–382
5. Kuddus S, Mustapa MS, Ibrahim MR et al (2017) Microstructures and tensile characteristics on direct recycled aluminium chips AA6061/Al powder by hot pressing method. *Mater Sci Forum* 909:9–14
6. Chiba T Nakamura, Kuroda M (2011) Solid-state recycling of aluminium alloy swarf through cold profile extrusion and cold rolling. *J. Mater. Process. Tech.* 211:1878–1887
7. Kadir MIA, Mustapa MS, Mahdi AS et al (2017) Evaluation of hardness strength and microstructures of recycled Al chip and powder AA6061 fabricated by cold compaction method. In: *IOP Conference Series: Materials Science and Engineering*, p 165
8. Shamsudin S, Zhong ZW, Rahim SNA et al (2017) The influence of temperature and pre-heating time in extrudate quality of solid-state recycled aluminum. *Int J Adv Manuf Technol* 90:2631–2643
9. Wu S, Ji Z, Zhang T (2009) Microstructure and mechanical properties of AZ31B magnesium alloy recycled by solid-state process from different size chips. *J Mater Process Technol* 209:5319–5324
10. Dimos P, Karel K, Yelin D et al (2017) Solid state recycling of aluminium alloys via a porthole die hot extrusion process: Scaling up to production. In: *AIP Conference Proceeding*, vol 1896, pp 2–8
11. Tokarski T, Wedrychowicz M, Wiewiora M (2015) Light metals chips recycling by plastic consolidation. *Key Eng Mater* 641:24–29
12. Haase M, Tekkaya AE (2015) Cold extrusion of hot extruded aluminum chips. *J Mater Process Tech* 217:356–367
13. Misiolek WZ, Haase M, Ben N (2012) CIRP annals—manufacturing technology high quality extrudates from aluminum chips by new billet compaction and deformation routes. *CIRP Annals—Manufacturing Technology* 61:239–242
14. Jomaa W, Songmene V, Bocher P (2014) Surface finish and residual stresses induced by orthogonal dry machining of AA7075-T651. *Material* 7:1603–1624
15. Samuel M (2013) A new technique for recycling aluminium scrap. *J Mater Process Technol* 135:117–124
16. Kore AS, Nayak KC, Date PP (2017) Formability of aluminium sheets manufactured by solid state recycling. *IOP Conf Ser J, Phys* 896
17. Kadir IA, Mustapa MS, Ibrahim MR et al (2017) Microstructures and characteristics of solid state recycling aluminium chips AA6061/Al-SiC composites fabricated by cold compaction method. *AIP Conf Proc* 1846
18. Ambriz WRR, Jaramillo D (2014) Mechanical behavior of precipitation hardened aluminum alloys welds. *Light Metal Alloys Applications INTECH* 35–59
19. Singh M, Lara S, Tlali S (2016) Effects of size and shape on the specific heat, melting entropy and enthalpy of nanomaterials. *J Taibah Univ Sci* 11:922–929
20. Ferreira LFP, Gatamorta F, Bayraktar E et al (2017) Manufacturing of low cost composites with porous structures from scrap aluminium (AA2014) chips. *Conf Proc Soc Exp Mech Ser* 7:233–240

21. Fruhstorfer J, Aneziris CG (2017) Influence of particle size distributions on the density and density gradients in uniaxial compacts. *Ceram Int* 43:13175–13184
22. Michrafy A, Dodds JA, Kadiri MS (2004) Wall friction in the compaction of pharmaceutical powders: measurement and effect on the density distribution. *Powder Technol* 148:53–55

# The Effects of Rotational Tool Speed on Mechanical Properties of Bobbin Friction Stir Welded AA1100



Siti Noor Najihah Mohd Nasir, Mohammad Kamil Sued  
and Muhammad Zaimi Zainal Abidin

**Abstract** Bobbin friction stir welding (BFSW) is a solid state welding which joined the workpieces through the frictional heat generated by the non-consumable rotating tool. The influence of rotational speed on the AA1100 were studied by employing different rotational speeds ranging from 700 to 1100 rpm and the welding speed was fixed at 150 mm/min. All the weld samples were defect-free. The result found that as the rotational speed increased, the width of softened zone became large. The maximum tensile strength of the weld sample exhibited at value of ~92 MPa with the joint efficiency of 85.5% using rotation speed of 800 rpm and welding speed of 150 mm/min.

**Keywords** Bobbin friction stir welding · Mechanical properties · AA1100

## 1 Introduction

Friction stir welding (FSW) is a joint process that provides a great potential to weld material without melting the parent material. This welding technique allows the material be softened and joined through frictional heat generated by the action of the tool that rotated and traversed along the line of joint. Due to low heat input, it allows the FSW to have lower energy consumption compared to the metal inert gas welding (MIG) and tungsten inert gas welding (TIG) [1]. This process has been classified as an environmentally benign process [2] and is categorised as a solid state process.

One of the endeavours of FSW processes that improve the weldment of the conventional FSW is known as bobbin friction stir welding (BFSW). The improvement of this welding technique is based on the tool configuration called as bobbin tool. Having an extra shoulder that holds the bottom surface of the workpiece allows the BFSW process to eliminate the downforce [3, 4], avoiding the incomplete penetra-

---

S. N. N. M. Nasir (✉) · M. K. Sued · M. Z. Z. Abidin  
Advanced Manufacturing Centre, Fakulti Kejuruteraan Pembuatan, Universiti Teknikal Malaysia  
Melaka, Hang Tuah Jaya, 76100 Durian Tunggal, Melaka, Malaysia  
e-mail: [najihahnasir92@gmail.com](mailto:najihahnasir92@gmail.com)

© Springer Nature Singapore Pte Ltd. 2020  
M. Awang et al. (eds.), *Advances in Material Sciences  
and Engineering*, Lecture Notes in Mechanical Engineering,  
[https://doi.org/10.1007/978-981-13-8297-0\\_36](https://doi.org/10.1007/978-981-13-8297-0_36)

337

tion defect and providing uniform mechanical properties by through-thickness weld [5] besides having better energy consumption [6]. With these promising advantages, the main challenge is for weld to be formed when using BFSW [7]. Initiation of bond is challenging, hence defects such as open tunnel and excessive flash are produced. Although conventional FSW and BFSW are similar, the additional shoulder at the bottom provides significant process sensitivity required to be understood. With the absence of tool tilt angle and plunge (axial) force that are not feasible for BFSW, the pressure and heat are maintained from the compression load [8] and spindle speed. Zhou et al. [9] found that the increase of rotational speed on the AA6061-T6 weld increased tensile strength while further increases dropped the tensile strength of the weld. Subsequently, Wang et al. [10] claimed that the increase of rotational speed on AA2198-T851 changes the hardness profile from U-shaped to W-shaped. Heat generation is proportionate to the increase of spindle speed. For material that is soft and has high thermal conductivity, the role of heat is significant to the success of the bond. High thermal conductivity will cause fast heat dissipation hence high heat source is required. However, the heat influences the mechanical properties degradation.

In this paper, the impact of spindle rotation is being investigated in term of mechanical properties of the weld. The study focuses on pure Aluminium alloy grade in order to investigate the sensitivity of the heat to the joint strength. Through literatures, the influence of the rotational speed is focussing more on joining Aluminium alloy 2000 and 6000 series rather than other series of aluminium alloys. Thus, this study is important for impact study and widens the application of BFSW.

## 2 Methodology

The base material used for this study is a 6 mm thick AA1100 plate with the dimension of 140 mm long by 140 mm wide. For each welding trial, the AA1100 plates were clamped on the jig and were butt welded using the CNC milling machine and a bobbin tool. During the welding, the welding speed was fixed at 150 mm/min. The rotation speed was varied from 700 to 1100 rpm at an interval of 100 rpm and thus giving a total of 5 welding trial runs.

The bobbin tool used in this study comprised of a tool pin and two shoulders namely upper shoulder and lower shoulder. The diameter of the tool pin is 10 mm and has a smooth cylindrical shape with three flat features on it. Both shoulders have the diameter of 25 mm. The upper shoulder is featureless while the lower shoulder has a taper with 5°. The taper helps to prevent the formation of the flash occurring on the weld and helps to facilitate the material flow from the advancing side to the retreating side of the welding. Figure 1 shows the experimental setup in this study.

After welding, the weld samples were cross sectioned for mechanical testing. The microhardness testing was conducted on polished sample with the load of 200 g for 10 s dwell time using a semiautomatic Vickers (Mitutoyo) hardness machine. The microhardness profiles were measured at the middle thickness layer of weld

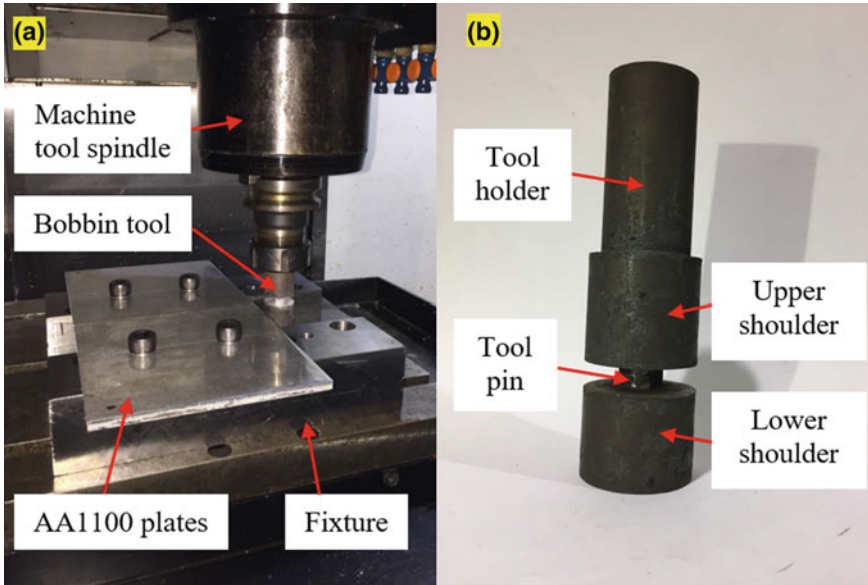


Fig. 1 a Experimental setup and b bobbin tool

sample with 1 mm spacing indentation distance. For transverse tensile testing, the weld samples were conducted following the standard of ASTM E8-04.

### 3 Results and Discussions

In this study, the mechanical testing result is by means of microhardness and tensile test. Figure 2 displayed the middle thickness hardness profile at different rotational speed. From the figure, all the weld sample exhibited the W-shape hardness profile corresponding to the four zones namely stir zone (SZ), heat affected zone (HAZ), thermo-mechanically affected zone (TMAZ) and base material (BM). The average hardness of the base material (BM) was in the range of 38–42 Hv. The hardness of each zone drops compared to the hardness of BM due to the thermal softening effect that gave the heat input during the welding. As the rotational speed increased from 700 to 800 rpm, the width of the softened zone became larger. For the case of the high rotational speed of 1100 rpm, the hardness decreased progressively at ~28 MPa at the edge of the SZ and slightly increased by ~33.7 MPa at the centre of SZ. Referring to Fig. 2, the maximum hardness in the SZ region was ~35 MPa achieved by the sample welded at the rotational speed of 700 rpm and welding speed of 150 mm/min. The lowest hardness was ~27–29 MPa at the advancing side of the weld.

The transverse tensile strength and elongation result for all weld samples are highlighted in Fig. 3. The average ultimate tensile strength (UTS) for the base material was

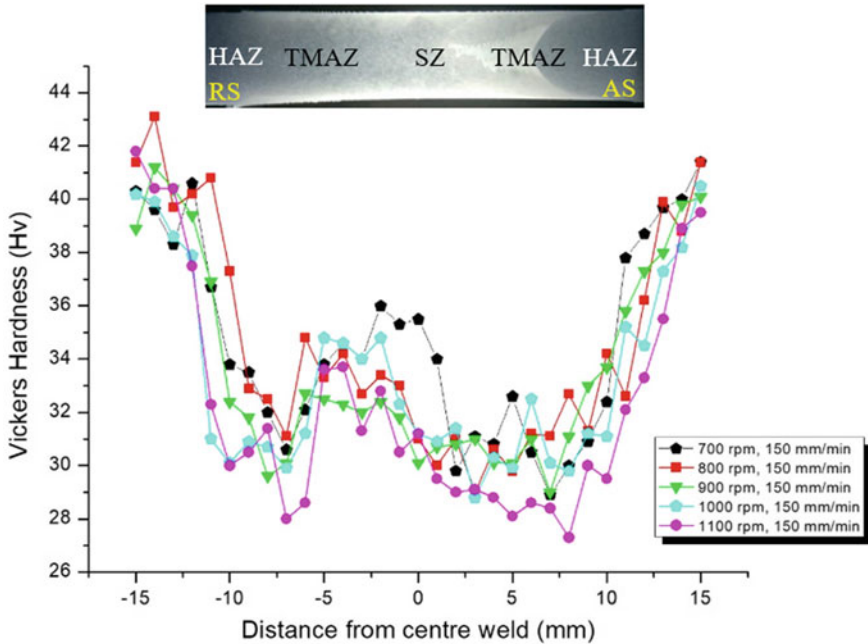


Fig. 2 Hardness profile for all welded samples

107.6 MPa. The highest UTS achieved by the weld sample was joined at rotational speed of 800 pm and welding speed of 150 mm/min at value of ~92 MPa with the joint efficiency of 85.5%. High tensile strength was due to the dislocation movement of the smaller grains that have higher resistance to localized plastic deformation [11]. From Fig. 3a, the tensile strength of the weld sample first increased with the increase of rotation speed from 700 to 800 rpm and then slightly decreased, maintaining the tensile strength at ~90 MPa from 900 to 1100 rpm. Although more heat input is produced by increasing the rotational speed, somehow this does not influence the tensile properties of the AA1100 weld but it does influence the elongation of the weld sample.

Referring to Fig. 3b, the lowest elongation exhibited by the sample is welded at rotational speed of 700 pm and welding speed of 150 mm/min. The increase of rotational speed increases the elongation of the weld sample. All the weld samples having the necking behaviour and the fracture location happened on HAZ near the boundary of TMAZ on the advancing side of the weld. These findings were in agreement with [9, 12, 13]. Fracture location at the advancing side is due to the stirring of material flow from the advancing side (AS) to the retreating side (RS). Material flow from the AS was stirred to fulfil the RS of the weld which influence the strength of the weld properties.

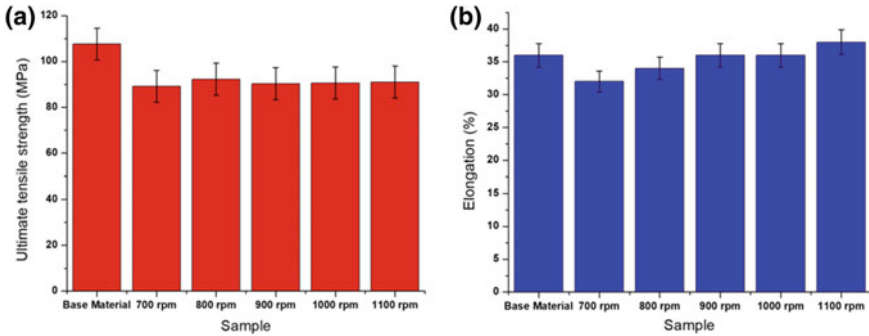


Fig. 3 Result of a ultimate tensile strength and b elongation

### 4 Conclusion

The AA1100 has been successfully bobbin friction stir welded and the mechanical properties have been clarified in details. On the basis of the present study, the following conclusions can be drawn;

- (1) The hardness profile of all weld samples exhibited the W-shape. As the rotational speed is increased, the width of softening zone becomes larger. The maximum hardness at SZ was exhibited by the sample welded at rotational speed of 700 pm and welding speed of 150 mm/min.
- (2) The AA1100 sample welded at rotational speed of 800 rpm and welding speed of 150 mm/min had the highest UTS of 92 MPa with 85.5% joint efficiency. There was no change in UTS as the rotational speed increased from 900 to 1100 rpm because the AA1100 had reached the optimal strength at 800 rpm. On the other hand, the elongation of sample welded at rotational speed of 800 pm and welding speed of 150 mm/min was the lowest compared to the base material.

**Acknowledgements** The author would like to thank the Universiti Teknikal Malaysia Melaka (UTeM) for the research grant of PJP/2017/FKP/H18/S01525.

### References

1. Kumar A, Gautam SS, Kumar A (2014) Heat input and joint efficiency of three welding processes TIG, MIG and FSW using AA6061. *Int J Mech Eng Robot Res* 1:89–94
2. Sued MK, Pons D, Lavroff J et al (2014) Design features for bobbin friction stir welding tools: development of a conceptual model linking the underlying physics to the production process. *Mater Des* (1980–2015) 54:632–643
3. Martin J, Wei S (2015) Friction stir welding technology for marine applications. *Friction Stir Weld Process VIII*:219–226
4. Longhurst WR, Cox CD, Gibson BT et al (2017) Development of friction stir welding technologies for in-space manufacturing. *Int J Adv Manuf Technol* 90(1–4):81–91



5. Skinner M, Edwards RL (2003) Improvements to the FSW process using the self-reacting technology. *Mater Sci Forum* 426–432:2849–2854
6. Sued MK, Samsuri SSM, Kassim MKAM et al (2018) Sustainability of welding process through bobbin friction stir welding. *IOP Conf Ser Mater Sci Eng* 318(1):012068
7. Nasir SNNM, Sued MK, Shamsharhadi MI (2018) Effect of unfitting bobbin friction stir welding parameters on aluminium alloy 5052. In: *Mechanical engineering research day*
8. Sued MK, Pons D, Lavroff J (2014) Compression ratio effects in bobbin friction stir welding. In: *10th international symposium on friction stir welding*
9. Zhou L, Li GH, Liu CL et al (2016) Effect of rotation speed on microstructure and mechanical properties of self-reacting friction stir welded Al–Mg–Si alloy. *Int J Adv Manuf Technol* 89(9–12):3509–3516
10. Wang FF, Li WY, Shen J et al (2015) Effect of tool rotational speed on the microstructure and mechanical properties of bobbin tool friction stir welding of Al–Li alloy. *Mater Des* 86:933–940
11. Yutaka S, Hiroyuki K (2001) Distribution of tensile property and microstructure in friction stir weld of 6063 aluminum. *Metall Mater Trans A* 32A:3023–3031
12. Hou JC, Liu HJ, Zhao YQ (2014) Influences of rotation speed on microstructures and mechanical properties of 6061-T6 aluminum alloy joints fabricated by self-reacting friction stir welding tool. *Int J Adv Manuf Technol* 73(5–8):1073–1079
13. Liu HJ, Hou JC, Guo H (2013) Effect of welding speed on microstructure and mechanical properties of self-reacting friction stir welded 6061-T6 aluminum alloy. *Mater Des* 50:872–878

# Investigation on Oil Absorption and Microstructural Properties of Polyethylene Composites Reinforced with Post-agricultural Waste Fillers



M. B. Mohd Salahuddin, N. A. Noor Emilia Adila  
and M. A. T. Intan Syafinaz

**Abstract** Conventional plastic made from polyethylene (PE) is not able to absorb excess oil from the fried food due to its nature to resist water and oil. As a result, oil inside fried food plastic packaging will be accumulated and will affect the freshness and shelf life of the product. To address this issue, polyethylene incorporated post-agricultural waste filler which is rice husk (RH) and rice husk ash (RHA) is produced. Five levels of filler loading which are 10, 15, 20, 25, and 30 in weight percent were incorporated into the PE to produce RH-PE and RHA-PE composites. Tests were performed to evaluate the oil absorption and microstructural properties of the composites. The results showed that the addition of fillers at any loading percentages resulted in significant improvement on the oil absorption of the composites as compared to control sample which is PE. The RH-PE and RHA-PE composites with 25% of fillers were found to possess the best oil absorption property as compared to other compositions. An increase in the loading of fillers would lead to some large agglomeration, high amount of spaces between rice husk and polyethylene and subsequently allow more oil to be absorbed into the composite. It proved that R RH-PE and RHA-PE composites with optimum composition have a great potential to be a good oil absorbent material.

**Keywords** Polyethylene composite · Rice husk · Rice husk ash · Agricultural waste · Oil absorption

## 1 Introduction

Fried food products are generally known to be undesirable due to oil absorbed during the frying process. It requires a longer time to toss the oils before it can be served to the consumer. In food industry, fried food is omit packed into plastic before its oil can

---

M. B. Mohd Salahuddin (✉) · N. A. Noor Emilia Adila · M. A. T. Intan Syafinaz  
Department of Process and Food Engineering, Faculty of Engineering, University Putra Malaysia,  
43400 Serdang, Selangor, Malaysia  
e-mail: [salahuddin@upm.edu.my](mailto:salahuddin@upm.edu.my)

© Springer Nature Singapore Pte Ltd. 2020  
M. Awang et al. (eds.), *Advances in Material Sciences and Engineering*, Lecture Notes in Mechanical Engineering,  
[https://doi.org/10.1007/978-981-13-8297-0\\_37](https://doi.org/10.1007/978-981-13-8297-0_37)

343

be fully tossed or vacuumed. Since time is very important in any production process, fully tossing the oil from fried food will require a longer time. Conventional plastic in the market, made from polyethylene (PE), is not able to absorb excess oil from the fried food due to its nature to resist water and oil. As a result, oil will be accumulated inside the plastic and will affect the freshness and shelf life of the product. Although using paper can be an alternative to absorb oil, utilization of this absorbent material will add to the overall production cost.

To date, research on the oil absorption property of polyethylene composite, particularly cooking oil, is rather limited. Most of the researches conducted focused on crude oil including research reported by Aboul-Gheit et al. [1], who conducted a study on absorption ability of waste plastic for spilled oil from seawater and Atuanya et al. [2], who studied the oil absorption properties of porous polyurethane foams based on recycled poly(ethylene terephthalate).

In order to enhance the oil absorption property of PE, post-agricultural waste filler including rice husk (RH) and rice husk ash (RHA) was reinforced into the PE. Utilization of rice husks as possible sorbent materials for oil spills has been discussed in several studies. Kumagai and Matsuo [3] studied the use of carbonized rice husk on the absorption of oil and found that 1 g of rice husk absorbed 6.7 g of heavy oil omit which indicates their usefulness as an adsorbent for oil spill cleanup. In a study conducted by Thompson et al. [4], acetylation of rice husks using N-bromosuccinimide (1% NBS) as a catalyst for one hour and 3.5 h increased the crude oil sorption from 1.9 to 8.2 g/g and 10.3 g/g, respectively. Chuayjuljit et al. [5] found that the addition of RHA silica to LDPE film modifies the film blocking behavior.

Although researches on oil absorption of PE and RH or RHA have been long conducted, however, research on rice husk-based polyethylene (RH-PE) and rice husk ash-based polyethylene (RHA-PE) composites on oil absorption using cooking oil is not well established. Therefore, this research aims to produce a plastic material made of polyethylene which is able to absorb oil from fried food when the food is packed inside the plastic. The objective of this study is to determine the effect of different loading of RH and RHA on the oil absorption and the microstructural properties of RH-PE and RHA-PE composite. Results from the test were compared and the potential of RH and RHA as post-agricultural waste filler in PE was elucidated.

## 2 Materials and Experimental Details

### 2.1 Materials

Rice husk (RH) and rice husk ash (RHA) were obtained from *Maerotech Sdn. Bhd.* RH is brown in color and slightly heavier and thicker compared to RHA. Low-density polyethylene (LDPE) was obtained from *Mylab Scientific Sdn. Bhd.*

**Table 1** Sample composition of RH-PE and RHA-PE composites

RH-PE composite		RHA-PE composite	
PE (%wt)	RH (%wt)	PE (%wt)	RHA (%wt)
100	0	100	0
90	10	90	10
85	15	85	15
80	20	80	20
75	25	75	25
70	30	70	30

## 2.2 Sample Preparation

Sample composites were prepared by weighing the materials based on the weight ratio as shown in Table 1. The actual mass of the fillers and binder was increased by 5% to account for wastage during the manufacturing process. RH or RHA and LDPE were mixed using Brabender Internal Mixer. The mixer was heated up at 130 °C for a period of 5 min at the preheating stage. The RH or RHA and LDP were poured into the mixer and allowed to be stirred at a speed of 50 rpm for 10 min. Once the mixer stopped, the front plate was opened to collect the polyethylene composites. The composites were pressed using a hot plate presser to obtain a thin sheet composite. The thickness of all samples was  $1 \pm 0.05$  mm.

## 2.3 Oil Absorption Test

The oil absorption capacity was determined by first weighing the sample before it was immersed into the oil. Once immersed in the oil, the samples were stored at room temperature. The samples were weighed again on day 2, 4, 6, 8 and 10 to determine the amount of oil absorbed. The oil absorption capacity was calculated using Eq. 1 where  $m_{\text{final}}$  is sheet weight after dipping in the oil and  $m_{\text{initial}}$  is initial sheet weight.

$$OAC(g/g) = \frac{m_{\text{final}} - m_{\text{initial}}}{m_{\text{initial}}} \times 100 \quad (1)$$

After oil absorption capacity was measured, the samples were wrapped using aluminum foil, placed under steel weight (1 kg) for 1–2 min and were then weighed again. The oil retention capacity was calculated using Eq. 2 where  $m_{\text{final}}$  is sheet weight after dipping in the oil and  $m_{\text{initial}}$  is sheet weight after pressing.

$$ORC(\%) = \frac{m_{\text{final}} - m_{\text{initial}}}{m_{\text{final}}} \times 100 \quad (2)$$

## 2.4 Microstructural Analysis

Scanning Electron Microscope (SEM) was carried out using a Hitachi S-3400N machine to observe the surface of the sample composites.

## 3 Result and Discussion

### 3.1 Fillers and PE Microstructures

Figure 1a, b shows SEM images of RH and RHA, respectively. The image of RH shows rough surface along with some granules as compared to RHA, and the same result was obtained by Kunal et al. [6]. The outer surface of RH is composed of dentate rectangular elements, which are mainly comprised of silica in which it is coated with a thick cuticle and surface hairs. The middle part and inner epidermis contain a small amount of silica [7]. Jauberthie et al. [8] reported that the presence of amorphous silica is concentrated at the surface of the rice husk and not within the husk itself.

RHA was found to be solid in nature with amorphous forms as with cristobalite and trace crystalline quartz [9]. Crystalline and amorphous forms of silica are obtained based on temperature range and duration of the burning of the husk [10]. The amorphous forms of silica are composed of silica tetrahedral arranged in a random three-dimensional network without regular lattice structures. The structure is open with holes in the network where electrical neutrality is not satisfied, and the specific surface area is high due to the disordered arrangement. This helps to increase the reactivity due to large area available for reaction to take place [11].

Morphological images of PE are shown in Fig. 2. It can be seen that the surface of the film is smooth which indicates a strong intermolecular bonding between the

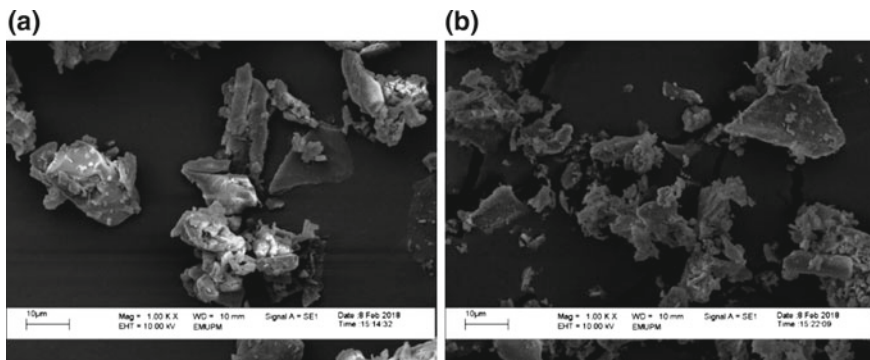
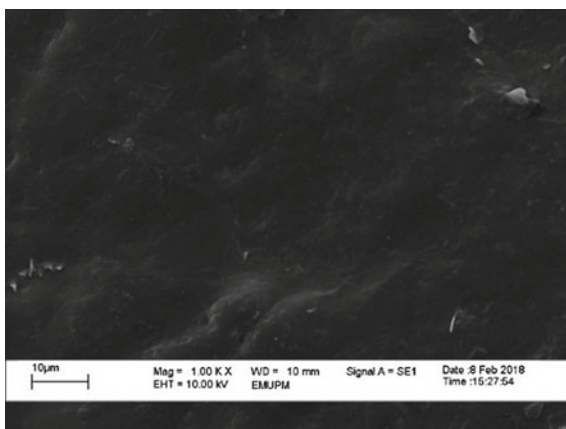


Fig. 1 SEM micrographs of a rice husk b rice husk ash

**Fig. 2** SEM micrographs of polyethylene film



fine particles of PE. A similar result was obtained by Wang et al. [12]. According to Ozaltin et al. [13], PE exhibits a homogenous, relatively smooth surface morphology with a minor uniform fiber-like feature stem. Ali et al. [14] also found that low-density PE films were smooth and plain after curing. However, the surface roughness increased after the degradation process.

### ***3.2 Effects of RH Loading on Oil Absorption of RH-PE Composites***

Result for each composite showed different absorption rate as in Fig. 3 with 0% omit filler (100% PE) acting as a control. Composites contained filler loading of 25, 20 and 10% appeared to have omit good, moderate and poor oil absorbent, respectively. It was observed that mass of oil uptake is increased with an increase in filler loading. However, a further increase in filler loading, which is above 25%, does not give a significant difference to the rate of oil sorption capacity. This result is in agreement with Idris et al. [15]. He found that the efficiency of oil sorption capacity depends on the filler loading.

The effect of contact time on the sorption capacity of RH-PE composite was studied. Based on Fig. 3, RH-PE composite with 25% filler showed the best oil absorption performance. The absorption capacity increases with the contact time within the first 10 min. The high rate of oil uptake may be attributed by the presence of vacant voids on the sorbents surface. However, after 20 min, less vacant voids were available to be occupied due to the repulsive forces between the solute molecules on the solid and bulk phases. Therefore, the oil uptake achieves equilibrium [16]. Time for RH-PE composite to reach equilibrium is 30 min and omit good absorbent is able to absorb oil up to 25%. Similar result was reported by Kenes et al. [17].

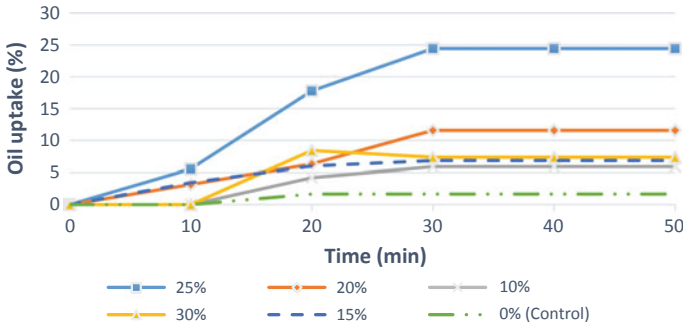


Fig. 3 Effect of RH loading on oil absorption properties of RH-PE composites

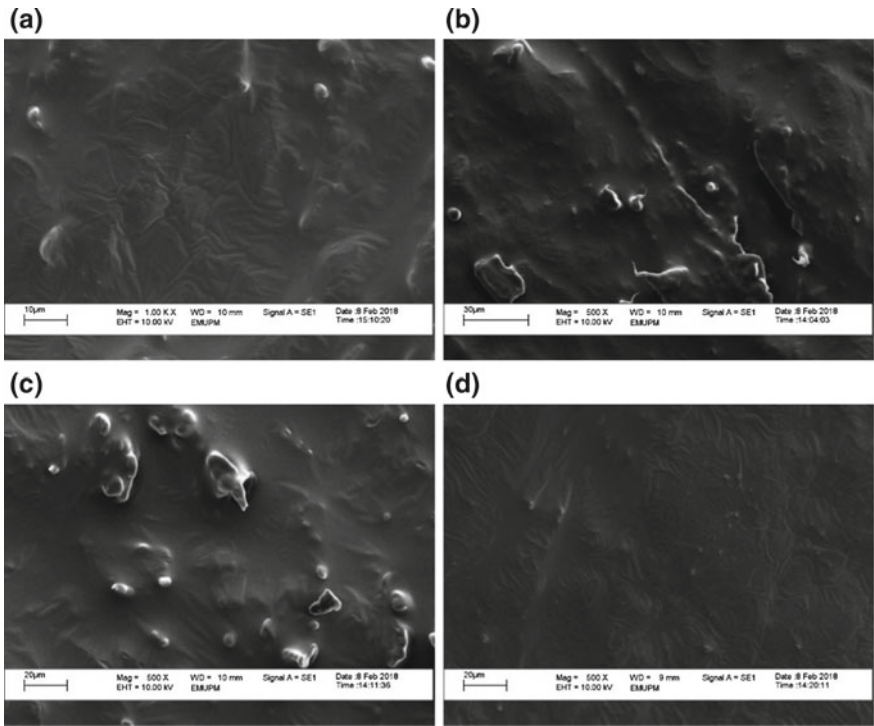


Fig. 4 a Polyethylene film after oil absorption test, b Good, c Moderate, and d Poor oil absorbance property of RH-PE composite

Figure 4a shows SEM images of PE film after oil absorption test. There is no significant difference as compared to the sample before the oil absorption test. It shows that the smooth plastic surface without any cellulose-based fiber is not a good absorbent. Figure 4b–d show results for the RH-PE composite with different RH loadings.

The SEM micrographs in Fig. 4 revealed that RH-PE composite contained numerous pores which are able to transport and hold oil. The pores vary in sizes and are distributed over the present silica craters. The spiky whitish materials are silica bodies, and underneath are perforations, which aid oil absorption [15]. Higher amount of spaces between rice husk and polyethylene may allow more oil to be absorbed into the composite. It indicates that higher filler content in the composite resulted in a higher percentage of oil uptake.

### 3.3 Effects of RHA Loading on Oil Absorption of RHA-PE Composites

Figure 5 shows the relationship between total oil uptake and time taken to reach equilibrium for five different compositions of RHA-PE composites. RHA-PE composite with filler loading of 25% appeared to be a good oil absorbent, filler loading of 20 and 10% was found to have a moderate and poor oil absorption capacity, respectively. From the result, it can be concluded that the RH-PE composite has better oil absorption capacity as compared to that of RHA-PE composite.

The total mass of oil uptake increases due to the availability of more active areas on the surface of the composites which allow for more oil absorption activity to take place. After attaining an optimum sorbent dose, the equilibrium between sorbate, which is the oil, and sorbent, which is the composite, at the operating conditions was achieved [16].

A decrease in the particle size of RHA may probably be the reason for lower oil absorption capacity. Previous research found that the oil absorption was improved with an increase in the particle size of natural organic sorbents. Generally, grinding the sorbents caused damage to the particles and destroyed the pores, thus the sorbent was unable to hold more oil on the surface and the absorption rate was reduced [16].

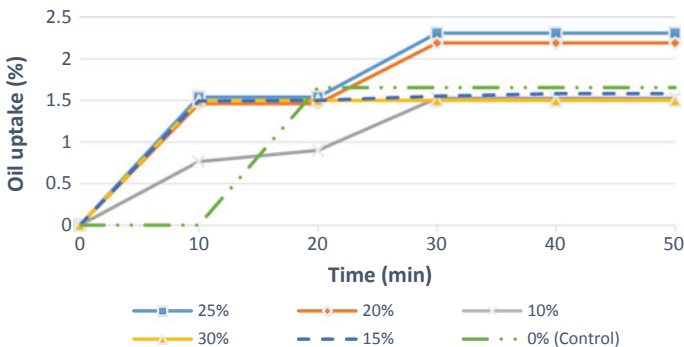
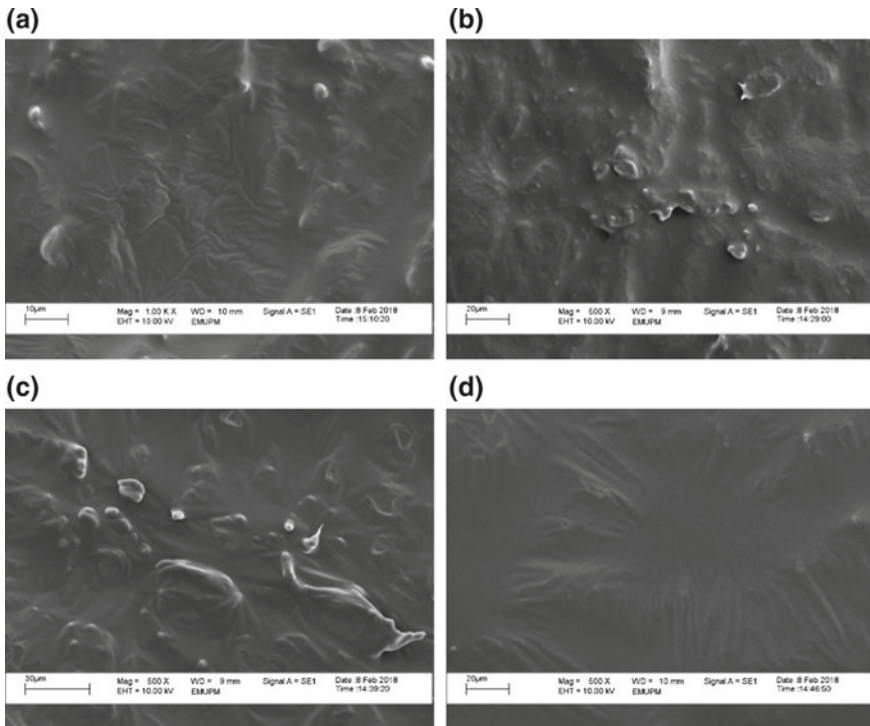


Fig. 5 Effect of RHA loading on oil absorption properties of RHA-PE composite





**Fig. 6** a Polyethylene film after oil absorption test, b Good, c Moderate, and d Poor oil absorbance property of RHA-PE composite

Figure 6b–d show the magnification images of SEM for RHA-PE composite with different filler loading. An increase in the oil sorption capacity was found to be influenced by a decrease in the particle size of the filler. This may probably be due to an increase in surface area of the filler. On the other hand, with the increase in particle size of RHA, the oil sorption properties decreased. The reason for this behavior might be due to the accumulation of small particles on each other, which resulted in plugging the pores and capillaries present between fibers and the polymer [18].

## 4 Conclusion

Samples of rice husk-based polyethylene (RH-PE) and rice husk ash-based polyethylene (RHA-PE) were prepared based on the experimental design and tested for oil absorption and microstructural properties. Omit overall, RH-PE and RHA-PE composites with 25% of fillers (RH and RHA) are the best samples which possess the best

oil absorption property. Based on the results obtained from the test, the addition of fillers showed significant improvement on the properties of the composites. Although further increase in filler loadings at 30% resulted in a decrease of the property value of the RH-PE composites, the total oil uptake is still above the control sample. For the microstructural property of RH-PE and RHA-PE composites, higher amount of fillers resulted in a less homogenous composite mixture while lower amount of fillers made the structure appears more homogeneous and the matrix system become denser. Based on the results from oil absorption test, an increase in the content of fillers would lead to some larger agglomerates due to the formation of hydrogen bonds among the abundant hydroxyl groups and adsorbed water on their surface. Higher amount of spaces between rice husk and polyethylene may allow more oil to be absorbed into the composite. It indicates that higher filler content in the composite resulted in a higher percentage of oil uptake. From the results, it proved that RH-PE and RHA-PE composites with optimum composition have a great potential to be a good oil absorbent material.

**Acknowledgements** Appreciation is given to Universiti Putra Malaysia (UPM) for funding this research study under the Geran Putra—IPM (9583800).

## References

1. Aboul-Gheit AK, Khalil FH, Abdel-Moghny T (2006) Adsorption of spilled oil from seawater by waste plastic. *Oil & Gas Sci Technol* 61(2):259–268
2. Atuanya CU, Olaitan SA, Akuga CC, Onukwuli OD, Menkiti MC (2013) Effect of rice husk filler on mechanical properties of polyethylene matrix composite. *Int J Curr Res Rev* 5(15):111
3. Kumagai S, Matsuo Y (2013) Composite produced from rice husk and chopped carbon fiber without using any binders. *Ind Crops Prod* 43:640–647
4. Thompson NE, Emmanue GC, Adagadzu KJ, Yusuf NB (2010) Sorption studies of crude oil on acetylated rice husks. *Arch Appl Sci Res* 2(5):142–151
5. Chuayjuljit S, Kunsawat C, Potiyaraj P (2003) Use of silica from rice husk ash as an antiblocking agent in low-density polyethylene film. *J Appl Polym Sci* 88(3):848–852
6. Kunal B, Bahurudeen A, Mohammed Haneefa K, Mahalingam B (2015) Microstructural characterization of rice husk and residual ash for the production of superior blended concrete. *Int J Res Eng Technol* 4(13):327–332
7. Bronzeoak G (2003) Rice husk ash market study—a feasibility study internal report. UK Companies, EXP 129, DTI/Pub., URN 03/668, UK
8. Jauberthie R, Rendell F, Tamba S, Cisse I (2000) Origin of the pozzolanic effect of rice husks. *Constr Build Mater* 14(8):419–423
9. Shinohara Y, Kohyama N (2004) Quantitative analysis of tridymite and cristobalite crystallized in rice husk ash by heating. *Ind Health* 42(2):277–285
10. Papohunda C, Akinbile B, Shittu A (2017) Structure and properties of mortar and concrete with rice husk ash as partial replacement of ordinary Portland cement—a review. *Int J Sustain Built Environ*
11. Ilochonwu CE, Onyenanu IU, Atanmo PN (2015) Extraction of high purity silica from rice husks ash for reduction to silicon
12. Wang Y, Wang C, Zhang Z, Xiao K (2017) Effect of nanoparticles on the morphology, thermal, and electrical properties of low-density polyethylene after thermal aging. *Nanomaterials* 7(10):320

13. Ozaltın K, Lehocký M, Humpolíček P, Pelková J, Sába P (2016) A new route of fucoidan immobilization on low density polyethylene and its blood compatibility and anticoagulation activity. *Int J Mol Sci* 17(6):908
14. Ali SS, Qazi IA, Arshad M, Khan Z, Voice TC, Mehmood CT (2016) Photocatalytic degradation of low density polyethylene (LDPE) films using titania nanotubes. *Environ Nanotechnol Monit Manag* 5:44–53
15. Idris J, Eyu GD, Mansor AM, Ahmad Z, Chukwuekezie CS (2014) A preliminary study of biodegradable waste as sorbent material for oil-spill cleanup. *The Sci World J*
16. Razavi Z, Mirghaffari N, Rezaei B (2015) Performance comparison of raw and thermal modified rice husk for decontamination of oil polluted water. *CLEAN–Soil Air Water* 43(2):182–190
17. Kenes K, Yerdos O, Zulkhair M, Marat T, Yربول T (2014) Rice husk ash for oil spill cleanup. *Appl Mech Mater* 446:447
18. El-Din GA, Amer AA, Malsh G, Hussein M (2017) Study on the use of banana peels for oil spill removal. *Alexandria Eng J*

# The Analytical Study of Stress Concentration Factor in an Infinite Plate at Various Temperatures



Nirav P. Patel, Dharmendra S. Sharma and Rahul Singh Dhari

**Abstract** This article presents the analytical investigation of stress concentration factor around the circular and square hole in an infinite carbon/epoxy plate at four different temperatures of 23, 60, 90, and 120 °C. The micromechanics model is executed in conjunction with a complex variable approach to calculate the stress distribution around these cut-outs considering biaxial and uniaxial loading. The carbon fibers are assumed to be thermal insensitive materials and elastic properties of epoxy are defined at various temperatures. The influences of temperatures, fiber angles and stacking sequence on maximum stress concentration factor are stated. The results show that the values of the stress concentration factor are highly affected by these parameters. The present article will serve as a tool for designers who wish to study the behavior of composites at various temperatures.

**Keywords** Complex variable method · Circular hole · Square Hole · Stress concentration · Temperature

## 1 Introduction

Carbon-based composite materials are widely used in various applications such as aerospace, transportation aircraft, military aircraft, helicopter, marine, and medical fields because of its superior strength, stiffness, formability and weight properties [1]. These types of composites are usually subject to various levels of thermal environments that deal with different temperatures. The structural behavior of these materials significantly changes due to variation in temperatures [2]. Considering experimental

---

N. P. Patel (✉) · R. S. Dhari  
Department of Mechanical Engineering, School of Technology, Pandit Deendayal Petroleum University, Gandhinagar 382007, Gujarat, India  
e-mail: [nirav.npp@gmail.com](mailto:nirav.npp@gmail.com)

D. S. Sharma  
Mechanical Engineering Department, Faculty of Technology and Engineering, The M. S. University of Baroda, Vadodara 390002, Gujarat, India

© Springer Nature Singapore Pte Ltd. 2020  
M. Awang et al. (eds.), *Advances in Material Sciences and Engineering*, Lecture Notes in Mechanical Engineering,  
[https://doi.org/10.1007/978-981-13-8297-0\\_38](https://doi.org/10.1007/978-981-13-8297-0_38)

results, Li et al. [3] stated that failure and damage behavior of composites varied with the loading and temperatures. Recently, Pan et al. [4, 5] have also studied the dynamic response of 3-D braided composites under different temperatures using a thermomechanical coupled constitutive model based on finite element analysis. Majority of studies dealt with the finite element analysis based calculation in various applications of damage mechanics. However, because of the significance of composites in various design applications, laminated fiber reinforced composites containing through cut-outs have been the matter of extensive study [6–9]. Hole/cut-outs are the unavoidable member of any components and the material properties prominently degrade due to the presence of these holes in any structural element. The behavior becomes even more intricate if the material is at various levels of temperature. The analytical modeling of composite laminated materials with a cut-out considering various loading are becoming an interesting domain of research.

Ever since Kirsch [6] addressed the issue of stress concentration in metallic plates, many researchers have described the analytical study of stress field around various cut-outs. Muskhelishvili [7] established the complex variable method to solve the problems of stress concentration in isotropic materials which is employed and altered by Lekhnitskii [8] and Savin [9]. This method [7] has also been extended to infinite composite plate subjects to in-plane [10–14] and bending loading [15, 16]. Majority of these studies present the stress analysis for regular cut-outs. However, few researchers [17, 18] have also attempted to calculate the stresses around the complex geometrical hole for isotropic [17] and anisotropic [18] media. They [10–18] concluded that the stress distribution around cut-outs was significantly affected by elastic properties, hole orientation, loading, fiber angles and stacking sequences. Hence, these parameters act as the governing parameters on which the performance of composite depends. The greatest benefit of working with composites is that their properties can be organized in a well-ordered manner.

The governing of parameters may not be appropriately truthful without considering the effect of constituent parameters such as fiber and matrix properties, and volume fraction. It is familiar that the elastic properties of a lamina depend upon the individual properties of fibers and resins. Micromechanics is a commanding method that can be used to evaluate precisely of the whole property of a unidirectional continuous composite lamina. The bridging model developed by Huang [19] is widely used micromechanical method to determine the elastic properties of lamina using constituent properties of fiber, matrix and volume fraction. Huang model [19] is also extended to strength and temperature based calculation and results are validated with experimentation [20, 21]. This bridging model is also implemental in the application where the behavior of composites studied for impact analysis [4, 5]. However, to the best of author's knowledge, there are rare articles that executed the bridging model to stress concentration problems. Yeh [22] calculated the stress concentration for composite wing at three temperature levels using constant strain approach and experimentation. The articles on analytical investigation of the effect of temperature on stress concentration are also limited.

The implementation of temperature based bridging model in conjunction with complex variable approach to study the stress concentration around a cut-out in

infinite composite plate is the primary upshot of the present work. Here, the carbon/epoxy plate containing circular and square hole is considered for the study. The plate is considered to be infinite and at various temperatures of 23, 60, 90, and 120 °C. The stress concentration factor is calculated using complex variable approach and temperature effects are introduced in the bridging model. The values of stress concentration factor are reported for various biaxial and uniaxial loading at different temperatures. The present model is also extended to symmetric laminated plates in addition to an orthotropic lamina.

## 2 Mathematical Formulations

The infinite homogeneous laminated plate containing a cut-out is considered, which is in equilibrium as a result of forces at the edges. The thickness of the plate is very small, and plane stress condition is applied. In the symmetric laminated composite plate, all layers are orthotropic and perfectly bonded together. For this laminate, the effective stiffness coefficient is written in the following form:

$$a_{ij} = \frac{2}{h} \sum_{k=1}^{n/2} Q_{ij}^{tk} t_k, [Q_{ij}^{tk}]_k = [T]_k^{-1} [Q_{ij}^k]_k [T]_k, Q_{ii(i=1,2)}^k = \frac{E_{ii}}{1 - \nu_{12}\nu_{21}},$$

$$Q_{12}^k = \frac{\nu_{12}E_{22}}{1 - \nu_{12}\nu_{21}}, Q_{66}^k = G_{12}, \quad (1)$$

where,  $a_{ij}$  is the stiffness coefficient of a laminate,  $Q_{ij}^{tk}$  and  $Q_{ij}^k$  are the transformed and on-axis stiffness coefficients of a lamina,  $t_k$  is the thickness of each layer, and  $E_{ij}$ ,  $\nu_{ij}$ ,  $G_{ij}$  ( $i, j = 1, 2, 6$ ) are the elastic properties of lamina. These elastic properties of lamina can be calculated from the bridging model [19–21]. Considering unidirectional fiber composite, the stress increment in the matrix  $\{d\sigma_i^m\}$  can be related with fiber  $\{d\sigma_i^f\}$  and henceforth, the equation of increment in stresses in lamina  $\{d\sigma_i\}$  and compliance matrix can be written in terms of volume fraction ( $V_f$ ) [19–21]:

$$\{d\sigma_i^m\} = [A_{ij}] \{d\sigma_i^f\}, \{d\sigma_i\} = V_f \{d\sigma_i^f\} + V_m \{d\sigma_i^m\},$$

$$[S_{ij}] = \left( V_f [S_{ij}^f] + V_m [S_{ij}^m] [A_{ij}] \right) (V_f [I] + V_m [A_{ij}])^{-1}, \quad (2)$$

where,  $[A_{ij}]$  is bridging matrix which represents the load sharing by fiber and matrix. Based on these values (Eq. 2), the elastic properties of a lamina can be calculated as below [19–21]:

$$E_{11} = V_f E_{11}^f + V_m E^{Tm}, \nu_{12} = V_f \nu_{12}^f + V_m \nu^{Tm},$$

$$\begin{aligned}
 E_{22} &= \frac{(V_f + V_m A_{11}^T)(V_f + V_m A_{22}^T)}{(V_f + V_m A_{11}^T)(V_f S_{22}^f + V_m A_{22}^T S_{22}^{Tm}) + (V_f V_m A_{12}^T)(S_{21}^{Tm} - S_{21}^f)}, \\
 G_{12} &= \frac{G_{12}^f G^{Tm} (V_f + V_m A_{66}^T)}{V_f G^{Tm} + V_m A_{66}^T G_{12}^f}, S_{ii(i=1,2)}^f = 1/E_{ii}^f, S_{12}^f = -\nu_{12}^f/E_{11}^f, \\
 S_{66}^f &= 1/G_{12}^f, A_{11}^T = \frac{E^{Tm}}{E_{11}^f}, A_{22}^T = \beta + (1 - \beta) \frac{E^{Tm}}{E_{22}^f}, \\
 A_{12}^T &= \frac{(S_{12}^f - S_{12}^{Tm})(A_{11}^T - A_{22}^T)}{(S_{11}^f - S_{22}^{Tm})}, A_{66}^T = \alpha + (1 - \alpha) \frac{G^{Tm}}{G_{12}^f}, \tag{3}
 \end{aligned}$$

where,  $\alpha$  and  $\beta$  is varying from 0 to 1. It is assumed that the carbon fiber is thermal insensitive (temperature-independent) [4, 5] and the matrix is sensitive to temperature that means the values of compliance coefficients of the matrix is written as a function of temperature:

$$S_{ii(i=1,2)}^{Tm} = 1/E_{ii}^{Tm}, S_{12}^{Tm} = -\nu_{12}^{Tm}/E_{11}^{Tm}, S_{66}^{Tm} = 1/G_{12}^{Tm}, \tag{4}$$

where, the values of elastic parameters of the matrix are evaluated at various temperatures using experimentation. The elastic properties of a lamina in Eq. (1) are computed from Eq. (3). Using Hooke’s law, Airy’s stress function and strain-displacement compatibility condition, the following characteristic equation is obtained:

$$a_{11}\kappa^4 - 2a_{16}\kappa^3 + (2a_{12} + a_{66})\kappa^2 - 2a_{26}\kappa + a_{22} = 0. \tag{5}$$

where,  $a_{ij}$  is calculated from Eq. (1). Introducing the  $\kappa_j (j = 1..4)$  [roots of Eq. (5)] to complex functions of complex variable method [7] and presenting Airy’s stress function in terms of complex functions:

$$\begin{aligned}
 \sigma_x &= 2\text{Re}[\kappa_1^2 \phi'(w_1) + \kappa_2^2 \psi'(w_2)], \\
 \sigma_y &= 2\text{Re}[\phi'(w_1) + \psi'(w_2)], \\
 \tau_{xy} &= -2\text{Re}[\kappa_1 \phi'(w_1) + \kappa_2 \psi'(w_2)]. \tag{6}
 \end{aligned}$$

$\phi(w_1)$  and  $\psi(w_2)$  are the Muskhelishvili’s stress functions [7] which are the functions of  $w_j (j = 1, 2)$ .  $w_j (j = 1, 2)$  are the mapping functions used to transfer area external to a given cut-out to the area outside the unit circle:

$$\begin{aligned}
 z^C &= \omega_j(\zeta) = \frac{c}{2} [(1 - i\kappa_j)(\zeta) + (1 + i\kappa_j)(\zeta^{-1})] (j = 1, 2), \\
 z^S &= \omega_j(\zeta) = \frac{c}{2} [(1 - i\kappa_j)(\zeta - 0.167\zeta^{-3}) + (1 + i\kappa_j)(\zeta^{-1} - 0.167\zeta^3)] \tag{7}
 \end{aligned}$$

where,  $z^C$  and  $z^S$  are the mapping functions of circle and square hole. The values of stress functions  $\phi(w_1)$  and  $\psi(w_2)$  in Eq. (6) can be obtained by considering method of superposition:  $\phi(w_1) = \Phi_1(w_1) + \Phi_2(w_1)$ , and  $\psi(w_2) = \Psi_1(w_2) + \Psi_2(w_2)$ . The values of  $\Phi$  and  $\Psi$  can be evaluated from the following relations:

$$\begin{aligned} \Phi_1(w_1) &= \int B dw_1, \Psi_1(w_2) = \int (B^* + C^*) dw_2, \\ \Phi_2(\zeta) &= \frac{i}{4\pi(\kappa_1 - \kappa_2)} \int_{\gamma} (\kappa_2 f_1^0 - f_2^0) \frac{t + \zeta}{t - \zeta} \frac{dt}{t}, \\ \Psi_2(\zeta) &= \frac{-i}{4\pi(\kappa_1 - \kappa_2)} \int_{\gamma} (\kappa_1 f_1^0 - f_2^0) \frac{t + \zeta}{t - \zeta} \frac{dt}{t}, \end{aligned} \tag{8}$$

where,  $B, B^*, C^*$  are obtained by putting the stress values at infinity [23] in Eq. (6). The  $\gamma$  is the boundary of the unit circle in  $\zeta$  plane, and  $f_{1,2}^0$  are the boundary conditions obtained on the periphery of the cut-out:

$$f_1^0 + i f_2^0 = -2\{\text{Re}[\kappa_1 \Phi_1(w_1) + \kappa_2 \Psi_1(w_2)] + i \text{Re}[\Phi_1(w_1) + \Psi_1(w_2)]\}. \tag{9}$$

By inserting values of Eq. (8) into Eq. (6), the values of stresses around a circular and square hole can be obtained. The normalized tangential stresses can be computed by applying transformation relations.

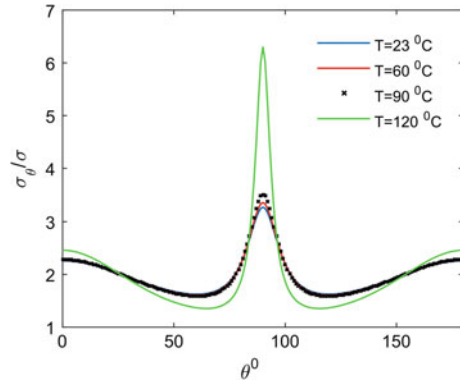
### 3 Results and Discussions

The objective of the present work is to study the effect of plate temperatures on the stress concentration around the circular and square hole. The symmetric laminated carbon/epoxy plate subjected to biaxial and uniaxial loading is considered for the study. The temperature dependent elastic properties of the laminate are calculated from Eq. (1) (based on Eq. (3–4)) that are finally inserted in the form of stress functions in Eq. (6). The normalized tangential stresses ( $\sigma_\theta/\sigma$ ) is calculated by transforming stresses of Eq. (6). The material properties of carbon fiber (thermal insensitive) are  $E_{11}^f = 243, E_{22}^f = 13.8, G_{12}^f = 23.1, G_{23}^f = 5.4$ (GPa),  $\nu_{12}^f = 0.29, \nu_{23}^f = 0.28$  and  $\nu_f = 0.6$  while, the elastic properties of epoxy resin is considered to be temperature dependent. The temperature dependent properties of matrix are adopted from the work of Pan et al. [24]: Temperature ( $^{\circ}\text{C}$ ) = [23, 60, 90, 120];  $E_{11,22}^{Tm} = [2.035, 1.891, 1.687, 0.3851]$ ; GPa;  $G_{12}^{Tm} = [0.765, 0.711, 0.635, 0.1447]$ ; GPa; and  $\nu_{12}^{Tm} = [0.33, 0.33, 0.33, 0.33]$ . Based on these temperature based elastic properties, the properties of laminate are calculated.

Considering the case of an orthotropic carbon/epoxy lamina (fiber angle =  $0^{\circ}$  from Y-axis) subjected to biaxial loading and containing a circular hole, the values of normalized tangential stress are obtained around the periphery of the circular hole.



**Fig. 1**  $\sigma_\theta/\sigma$  around circular hole in carbon/epoxy plate subjected to biaxial loading



**Table 1** The effect of fiber orientation and temperature

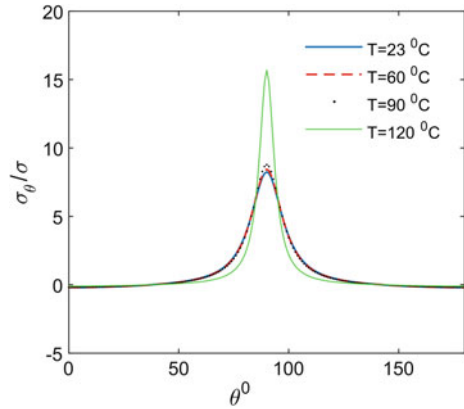
Fiber	23 °C	60 °C	90 °C	120 °C
0°	8.24	8.45	8.78	15.69
45°	4.91	5.00	5.16	10.52
90°	2.46	2.46	2.48	9.39

The values are computed for four plate temperatures (23, 60, 90, 120 °C) and the stress pattern is found to be symmetrical from the X-axis of the circular hole. Hence, the stress distribution is plotted with respect to various temperatures as shown in Fig 1. It can be observed from the figure that the values of  $\sigma_\theta/\sigma$  is increased as the temperature of the plate is increased. The maximum values of  $\sigma_\theta/\sigma$  are 8.2438 at 23 °C, 8.4450 at 60 °C, 8.7751 at 90 °C and 15.6934 at 120 °C. There is no change in stress distribution pattern as the temperature changes.

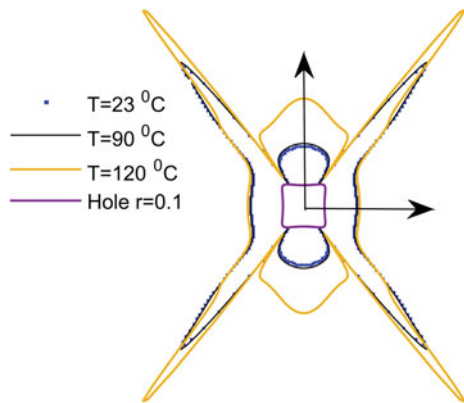
Similarly, the same carbon/epoxy plate (fiber angle=0°) containing circular hole is considered with uniaxial-X loading condition. The  $\sigma_\theta/\sigma$  is plotted for this case and presented in Fig 2. The maximum values are listed in Table 1 for fiber angle = 0°. The stress pattern is symmetric and different compared to biaxial loading but remains the same at various temperatures. The values of maximum  $\sigma_\theta/\sigma$  can be affected by variation in fiber angles. Table 1 reports these values at different fibers and temperatures. The values of stress concentration are greatly affected by varying fibers along with temperature. The stress concentration is increased as temperature increased for specific fiber angle but, 90° fiber performs best among all fibers at all considered temperatures and loading. Hence, one can control the fiber angle at various temperatures to reduce the stress concentration. An attempt has also been made to study the effect of temperature in carbon/epoxy plate containing a square hole. The plate is subjected to biaxial loading and fiber angle is considered to be at 0° (Fig 3). The same observation can be made as circular hole problem. The maximum values of  $\sigma_\theta$  are 6.3032 $\sigma$  at 23 °C, 6.4440  $\sigma$  at 60 °C and 9.0607  $\sigma$  at 90 °C.

In addition to the orthotropic case, the present methodology can be extended to the symmetric laminated composite. The cases of carbon/epoxy with cross play

**Fig. 2**  $\sigma_\theta/\sigma$  around circular hole in carbon/epoxy plate subjected to uniaxial-X loading



**Fig. 3**  $\sigma_\theta/\sigma$  around square hole (biaxial)

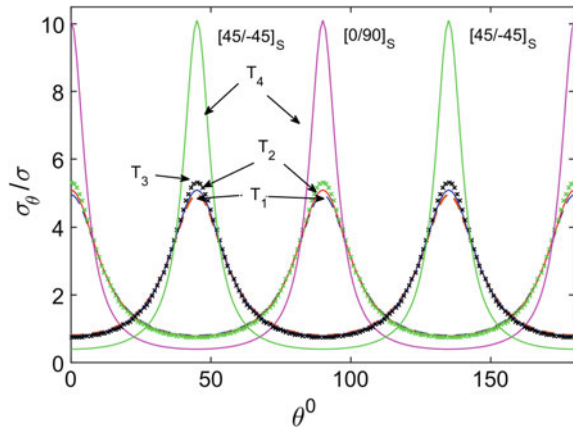


**Table 2** The maximum  $\sigma_\theta/\sigma$  for carbon/epoxy plate (circular hole)

Sequence	23 °C	60 °C	90 °C	120 °C
[0/90] <sub>s</sub>	5.946	6.085	6.311	11.103
[45/-45] <sub>s</sub>	3.502	3.577	3.705	6.505

([0/90]<sub>s</sub>) and angle ply (45/-45)<sub>s</sub> laminated composite plate are considered with a circular hole and biaxial loading. The stress distribution is found to be symmetrical and plotted in Fig. 4. The maximum values of both cases remain to be same as this is a biaxial loading case with a circular hole inside a plate. The stress pattern for [0/90]<sub>s</sub> carbon/epoxy plate (circular hole and 23 °C) subjected to biaxial loading case is found to be similar to results of Ukadgaonker and Rao [15] (Fig. 8 for Graphite/Epoxy). This stress pattern validates the methodology presented in this article. Similarly, for the uniaxial-X loading case, the maximum  $\sigma_\theta/\sigma$  is reported in Table 2. The performance of angle-ply is good compared to cross ply laminate. The proper choice of stacking sequence/fiber angle may lead to reduction in stress concentration for specific temperatures.

**Fig. 4**  $\sigma_\theta/\sigma$  around circular hole (biaxial)



## 4 Conclusions

The methodology to investigate the temperature effect on stress concentration is presented in this article by the conjunction of micromechanical bridging model with the complex variable method. The methodology can be valid for lamina and symmetric laminated composites and the upright solution is obtained from this method. The values of stress concentration factor are greatly affected by temperature. This is due to changes in elastic properties of the matrix that leads to final degradation of elastic properties of a lamina/laminate. In addition to this, the behavior of a composite can be tailor-made by selecting proper fiber angle/stacking sequence because the variations in these properties tend to decrease the stress concentration at various temperatures. The present methodology can be useful to designer who needs to study the stress concentration in composites at different temperatures.

## References

1. Fitzer E (ed) (2012) Carbon fibers and their composites: based on papers presented at the international conference on Carbon Fiber Applications, Springer Science & Business Media, Brazil, 5–9 Dec 1983
2. Fitzer E (1988) Composites for high temperatures. *Pure Appl Chem* 60(3):287–302
3. Li D, Sen Zhao CQ, Ge TQ, Jiang L, Huang CJ, Jiang N (2014) Experimental investigation on the compression properties and failure mechanism of 3D braided composites at room and liquid nitrogen temperature. *Compos Part B Eng* 56:647–659
4. Pan Z, Sun B, Gu B (2016) Thermo-mechanical numerical modeling on impact compressive damage of 3-D braided composite materials under room and low temperatures. *Aerosp Sci Technol* 54:23–40. <https://doi.org/10.1016/j.ast.2016.03.027>
5. Zhang W, Gu B, Sun B (2017) Thermal-mechanical coupling modeling of 3D braided composite under impact compression loading and high temperature field. *Compos Sci Technol* 140:73–88

6. Kirsch G (1898) Die theorie der elastizitat und die bedurfnisse der festigkeitslehre, vol 42. Springer
7. Muskhelishvili NI (1962) Some basic problems on the mathematical theory of elasticity (English translation by Radok JRM), 2nd edn. Noordhoff International Publishing
8. Lekhnitskii SG (1968) Anisotropic plates (Translation by the Second Russian Edition by Tsai SW and Cheron T)
9. Savin GN (1961) Stress concentration around holes. Pergamon Press, New York
10. Sharma DS (2014) Stress distribution around polygonal holes. *Int J Mech Sci* 78:177–182
11. Rezaeepazhand J, Jafari M (2010) Stress concentration in metallic plates with special shaped cutout. *Int J Mech Sci* 52:96–102
12. Ukadgaonker VG, Rao DKN (1999) Stress distribution around triangular holes in anisotropic plates. *Compos Struct* 45:171–183
13. Sharma DS, Patel NP, Trivedi RR (2014) Optimum design of laminates containing an elliptical hole. *Int J Mech Sci* 85:76–87
14. Patel NP, Sharma DS (2018) An analytical investigation of the best stacking sequence of a symmetric laminated composite plate weakened by a hole. *Math Mech Solids*. <https://doi.org/10.1177/1081286518797158>
15. Ukadgaonker VG, Rao DKN (2000) A general solution for stresses around holes in symmetric laminates under inplane loading. *Compos Struct* 49:339–354
16. Patel NP, Sharma DS (2015) Bending of composite plate weakened by square hole. *Int J Mech Sci* 94–95:131–139
17. Batista M (2011) On the stress concentration around a hole in an infinite plate subject to a uniform load at infinity. *Int J Mech Sci* 53:254–261
18. Patel NP, Sharma DS (2017) On the stress concentration around a polygonal cut-out of complex geometry in an infinite orthotropic plate 179:415–436
19. Huang ZM (1999) Micromechanical strength formulae of unidirectional composites. *Mater Lett* 40:164–169
20. Huang ZM, Zhou YX (2013) Correlation of the bridging model predictions for triaxial failure strengths of composites with experiments. *J Compos Mater* 47:697–731
21. Huang ZM, Liu L (2014) Assessment of composite failure and ultimate strength without experiment on composite. *Acta Mech Sin Xuebao* 30:569–588
22. Yeh HL (1989) Stress concentration of the composite material used by the X-29A forward-swept wing aircraft under various temperature levels. In: Marshall IH (ed) *Composite Structures* 5. Springer, Dordrecht
23. Gao XL (1996) A general solution of an infinite elastic plate with an elliptic hole under biaxial loading. *Int J Press Vessel Pip* 67:95–104
24. Pan Z, Gu B, Sun B (2015) Numerical analyses of thermo-mechanical behaviors of 3-D rectangular braided composite under different temperatures. *The J Text Inst* 106(2):173–186

# Performance Evaluation of EFB Biomass Supply Chain for Electricity Power Generation Based on Computer Simulation: Malaysia Case Study



Seyed Mojib Zahraee, Ainul Akmar Mokhtar, Ali Toloioe  
and Nurul Afiqah Mohd Asri

**Abstract** Malaysia is one of the largest countries that has the largest palm oil plantation size in the world. Despite the enormous amount of palm biomass in the state, the use of biomass as fuel for power generation remains low. One of the most significant crises in energy supply from the biomass is to utilize it efficiently and effectively by considering lower cost of the supply chain and the process to change the biomass into useful energy source. In this paper, computer simulation is used to develop a model form current situation of empty fruit bunches (EFB) biomass Supply chain in Perak sate of Malaysia based on Arena software. The results found that, there are sixteen potential palm oil sites that had been analysed and met all the criteria of the case study according to their existing palm oil capacity, distance to the nearest power plant and minimum palm oil produced. The model had also been run with two different scenarios by decreasing the number of labour and increasing the number of trucks. First scenario showed that by decreasing the labors, output is decreased from 4.59 to 4.336 ton/ha. In contrast, cycle time, value added (VA) time and other time are increased near 15, 25 and 15% respectively. Additionally, the final results based on the second scenario claimed that by assigning two truck, the output of the process is increased 23% (from 4.59 to 6.02 ton/ha) compared to current situation as well as the time cycle of the whole process is increased from 7.2 to 8.95 h because of an increase in VA and Other time (34 and 23%).

**Keywords** Biomass supply chain · Empty fruit bunches · Computer simulation · Arena software

---

S. M. Zahraee (✉) · A. A. Mokhtar · N. A. Mohd Asri  
Department of Mechanical Engineering, Universiti Teknologi PETRONAS, 32610 Bandar Seri  
Iskandar, Perak, Malaysia  
e-mail: [s\\_mojib\\_zahraee@yahoo.com](mailto:s_mojib_zahraee@yahoo.com)

A. Toloioe  
Department of Industrial and Manufacturing Systems Engineering, Kansas State University,  
Manhattan, USA

© Springer Nature Singapore Pte Ltd. 2020  
M. Awang et al. (eds.), *Advances in Material Sciences  
and Engineering*, Lecture Notes in Mechanical Engineering,  
[https://doi.org/10.1007/978-981-13-8297-0\\_39](https://doi.org/10.1007/978-981-13-8297-0_39)

## 1 Introduction

Global warming (GW) has become one of most crucial problems in the world. International communities have been attempting to reduce greenhouse gases (GHG) that are accelerating GW. Hence, the development of renewable and sustainable energy sources play a leading role in the current global policies to decrease GHG generation, especially in replacing fossil fuels [1]. Biomass is a renewable and versatile energy source used in combined heat and power (CHP) generation and transportation systems [2]. In the past decade, the number of countries exploiting biomass for the production of energy has increased rapidly, thus making biomass an attractive and promising option compared to other renewable energy sources [3]. It may be used for energy production at different scales, including large-scale power generation, CHP, or small-scale thermal heating projects at governmental, educational or other institutions [1]. Recently, governments around the world such as the United States, Brazil, Malaysia and many other European countries have tried to increase the commercialization process of the biomass industry. Malaysia is the world's second largest palm oil producer with 38% of the global market, and is the largest palm oil exporter, consisting of about 88% of the market's palm oil in 2011 [1]. Oil palm biomass emerges as a potential major contributor to renewable energy as the government has now shifted from conventional energy sources such as coal, oil and gas to promoting renewable energy sources in order to increase energy security [4]. One of the most significant crises in energy supply from the biomass is to utilize it efficiently and effectively by considering lower cost of the supply chain and the process to change the biomass into useful energy source. There are many advantages in using biomass to generate power, but several barriers have affected its efficiency such as quality and cost, feedstock availability, transportation cost, handling and stock, as well as logistic efficiency system [5]. All these factors have significant effects on the biomass supply chain efficiency. Regarding the EFB supply chain in Perak state, there are some conflicting decisions on the selection of supplier, location, routes and technologies in the production. One of the operational challenges is the feedstock unavailability [6]. Furthermore, EFB also consists of high moisture content [4]. Transporting wet biomass residues to the production site after the harvesting process is unfavourable since it is costly with increasing distance. Furthermore, due to the moisture content of the EFB, it requires to undergo a drying process to prevent biodegradation, which also increases the cost of the production and investment of the technologies and equipment. Besides, due to the high cost of biomass technologies, most small developers and plantation owners are unable to afford them thus the biomass itself is not fully implemented in Malaysia [7]. This paper aims at evaluating the performance of EFB supply chain in Perak state of Malaysia by comparing current situation and different scenarios using computer simulation.

## 2 Literature Review

### 2.1 *Application of Computer Simulation in Biomass Supply Chain*

It has been pointed out that simulation is a useful and compressive method due to its capability and flexibility in simulating and evaluating complicated dynamic systems, considering the uncertainty and variability in the system [8]. There are four types of simulation tools, namely spreadsheet simulation, system dynamics, discrete-event simulation, and business games [9]. In order to simulate complex stochastic systems, discrete-event simulation is the most effective tool [10, 11]. Discrete-event simulation has received a considerable amount of attention among investigators to model and evaluate biomass supply chain because of its time-dependency and stochasticity of biomass supply chain [12]. A few more simulation investigations have been conducted on other agricultural productions such as corn grain by Arinze et al. [13] and Sokhansanj et al. [14]. They applied the simulation modeling to investigate the changes in the quality of potash fertilizer and alfalfa cubes during storage and transport. Ravula et al. [15] used the discrete-event simulation model on the transportation system of cotton gin in order to schedule the trucks in the biomass logistic system. It should be noted that all these models, IBSAL and SHAM included, did not provide a schedule and plan that satisfied the daily demand. Zhang et al. [16] created a simulation model to study the woody residue supply chain. To achieve this goal, a simulation model of the biofuel supply chain was constructed using the Arena software by considering the graphical user interface. This model included the basic supply chain activities such as biomass harvesting/processing, on-site storage, and transportation. The delivery feedstock cost, GHG emissions, and energy consumptions were considered as the performance measurements to evaluate this model. In addition, discrete-event simulations were applied to estimate the work time cost for managerial organizational task for each of the supply chain [17]. From the reviewed literatures, it can be found that the simulation modeling is a useful method to evaluate the supply chain by examining different scenarios and circumstances. This paper tries to fill the research gap for Malaysia as the case of study by developing simulation model of the EFB biomass supply chain in Perak state in order to assess the current situation and propose a suitable scenario of EFB supply chain performance.

## 3 Materials and Methods

### 3.1 *Case Study*

Maju Intan Biomass Power Plant, Teluk Intan in Perak sate of Malaysia has been selected as the case study. As for the transportation limitation, it is not applicable in

Perak to transport biomass residue by using train, thus the transport is being limited to main road only and the distance from biomass site to power plant is being measured on road. There are sixteen potential locations of biomass sites based on the following criteria:

1. Location is within 2 km of a main road, 2. Location is within a society size of a minimum of 500 (population), 3. Area of the plantation is a minimum of 1000 ha, 4. Location is within 1 km of nearest rivers or lake (water source), 5. The moisture content of oil palm frond is less than 75%. In Perak there is only one biomass power plant that includes the following criteria: 1. Located within the state; Perak, 2. Generating capacity of the electricity is 12.5 MWh daily, 3. Use 100% EFB as primary fuel in electricity generation, 4. Daily demand of EFB is 500 ton.

Perak consists of two main transportations which are by road and by rail. Unfortunately, the railway is not being implemented in transporting palm oil residue due to shared railways with the Electric Train Service (ETS) and Keretapi Tanah Melayu Berhad (KTMB), and lower density of palm oil residue can be transported by truck. Therefore, the transportations of EFB are as follows: 1. All transportations are done by road, 2. Transportation distance from the plantation area to the power plant are measured by using rectilinear distance, 3. Biomass residues are being delivered by using truck with diesel oil consumption, 4. Minimum truck capacity is 3 ton.

Figure 1 shows the map of state of Perak that indicates sixteen potential locations of biomass plantation and the power plant.

### 3.2 Data Collection

As for the data collection, there will be data collection for cycle time. There are several data that have been collected which are the load truck, transportation and unload truck processes.

The transportation distance from harvesting area to biorefinery station is based on the sixteen potential locations of the harvesting area. The distance is based on rectilinear distance that had been taken by using Google Map only. Therefore, from the distance, the transportation time can be calculated as the average speed of a truck in Malaysia is 65 km/h [18]. The time taken can be calculated using formula below. The transportation time for each harvesting area is as in Table 1.

$$T_{\text{transport}} = di/60 \text{ km/h} \quad (1)$$

The cycle time of the processes were collected at two randomly selected harvesting areas. For unloading of the truck process, it only happened at biorefinery station which for this case study is Maju Intan Biomass Power Plant.



**Fig. 1** Map of state of Perak



**Table 1** Transportation time based for each potential harvesting area

Harvesting area	$d_i$ (km)	$T_{transport}$ (h)
Pengkalan Hulu	280	4.307692
Gerik	236	3.630769
Selama	227	3.492308
Larut	175	2.692308
Sungai Siput	118	1.815385
Chemor	102	1.569231
Ipoh	87.9	1.352308
Beruas	88.1	1.355385
Manjung	87.8	1.350769
Parit	75.1	1.155385
Tanjung Tualang	56.6	0.870769
Kampung Gajah	34.1	0.524615
Tapah	44.5	0.684615
Bagan Datoh	46.7	0.718462
Teluk Intan	8.1	0.124615
Slim river	61.5	0.946154

### 3.3 Simulation Model Development

One of the most significance parameters for developing a computer simulation is collecting the desired data. “stop watch” method is applied for collecting some needed data. After collecting the data related to duration of all of activities, a probability distribution function is fitted to every activity since the variability of the activities. Having determined the different resources involved in the production process along with their relationship and their duties and also the fitting probability distribution of each data sample of activity duration, the simulation model is developed [19]. The simulation model of the EFB supply chain in Perak is developed by using Arena Software and it consists of four sub-models which are: 1. Initialization Sub-Model, 2. Harvesting Area Sub-Model, 3. Bio refinery Sub-Model and 4. Daily Biomass Processing Sub-Model. There are some considerations that need to be taken such as delivered feedstock cost, inventory and delay, and waiting time. For the delivered feedstock cost, it includes the labour cost, loading and unloading cost, transportation cost and storage cost [16]. On the other hand, for the waiting and delay time, some data have been taken on the randomly selected harvesting area of EFB and the value used is based on the expression of beta of the data collection.

As for the flow of the model, it starts with the raw material which is the EFB from the harvesting area. The daily demand of biomass feedstock is one of the main influences at the biorefinery and it had been prescribed inside the sub-model. Every day, there will be a production target issued. As for the parameter, it has been set with the approximation of 35 ton of biomass per area. If the demand has met the requirement, no further process needed while if it is not, there will be some processes that need to be done. Then, since the working days are only applied during the weekdays, there will be a decision of what day in the process. If the day is weekend, there will be a delay of 1 day and the loop will go back to the decision making until it is not weekend. The process will continue checking the inventory of the EFB in the harvesting area. If the inventory exceeds 3 ton, it will proceed to the transportation process. If it is not, there will be a harvesting process that needs to be done in order for enough raw material to be transferred to the biorefinery area. After the transportation is done, there are also some extra processes such as unloading the truck that need to be considered. This model will simulate the time taken for 3 ton of EFB to be transferred to the biorefinery area. Figure 2 shows the operational component of the whole process. The model is run for 8 h daily which is the appropriate working hours in Malaysia and also being run for 30 days to get more accurate data by taking the average result. The simulation model developed can be shown in Fig. 3.

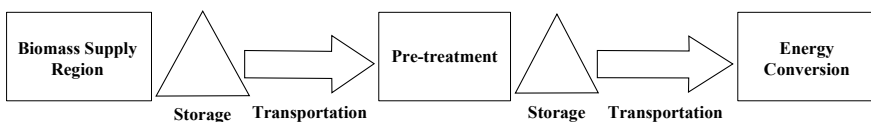


Fig. 2 Operational component of an EFB biomass supply chain

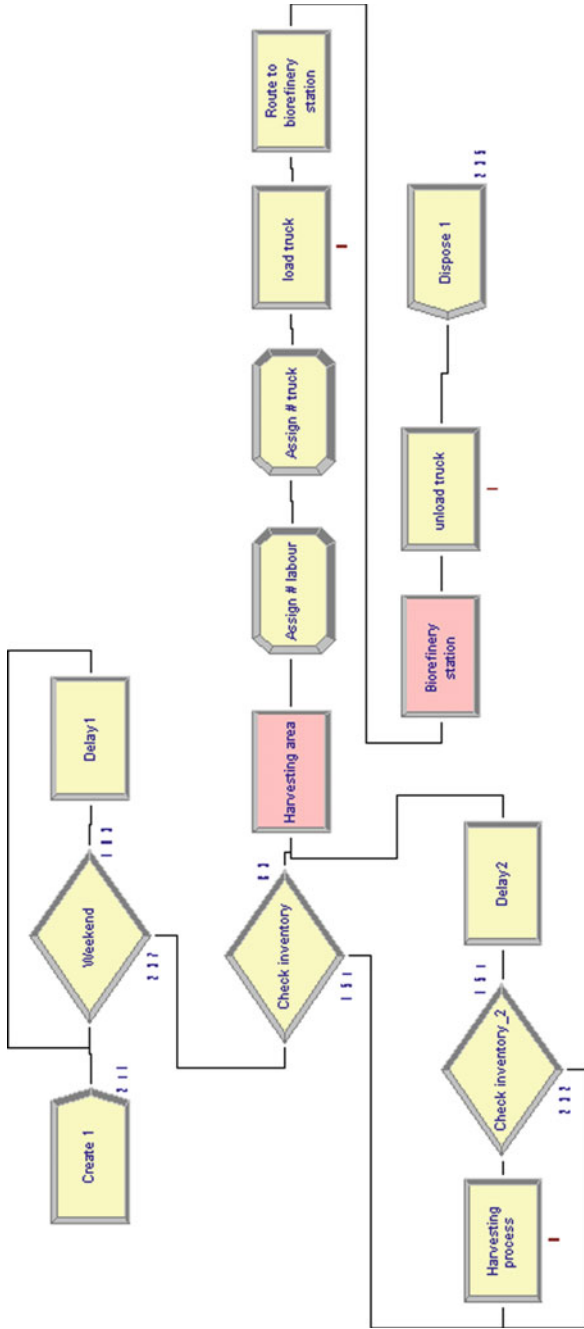


Fig. 3 Logic view of simulation model

**Table 2** Validation result of the simulation model

Items	Actual data	Simulated data	Achievement ratio (%)
Output (EFB)	4.42 ton/ha	4.59 ton/ha	96
Average of total cycle time	7.68 h	7.211943 h	93

### 3.3.1 Validation of Model

After simulating the cycle time for the whole process, starting from harvesting area to the power plant site by using Arena Simulation model, some information including number of orders, number of product outputs and process actual cycle time that were available for one week (5 working days) were added for the model validation. After gathering the information, they were compared to the obtained results of the simulation and the final finding is revealed in the Table 2. As shown in the below, the results are accurate up to approximation of 90%. However, these results depend on some considerations such as the 8 h of working per day, data taken is based on average of several readings and depending on the product availability due to harvesting.

## 4 Results and Discussion

For the main output, the simulation model estimates the total time for the process of 3 ton of EFB starting from the harvesting process until the transportation time. There will be no stumpage and harvesting cost to be calculated since it is assumed that every harvesting area will need the same amount of cost. The start date of the simulation is on 28th October 2017 until 28th November 2017, 30 days in total and 240 h total which is 8 h daily.

The total processing time is calculated by the functions below:

$$\text{Total Processing Time} = \text{VA time} + \text{Wait time} + \text{Transfer time} + \text{other time} \quad (2)$$

where: “VA Time: value added time; which is accumulated when an entity incurs a delay at a value-added process.” “Wait time: accumulated when the entity incurs a delay at a process that has been assigned as wait.” “Transfer Time: accumulated when the entity incurs a delay at a process that has been assigned as wait.” “Means, when the raw material needs to be transferred from one place to another.” “Other Time: accumulated when there is other process.” The Average Total Processing Time, VA time, Wait Time, Transfer Time and Other Time are then computed from the simulation as shown in Table 3.

While for the total cost, it can be calculated by using functions below:

**Table 3** Data output for processing time (hours)

Harvesting area	Wait time (h)	Transfer time (h)	VA time (h)	Other time (h)	Total (h)
Pengkalan Hulu	0.3429	4.30769	2.4407	3.5918	10.68309
Gerik	0.3249	3.63077	2.4043	3.9494	10.30937
Selama	0.3333	3.49231	2.4644	4.1333	10.42331
Larut	0.3368	2.69231	2.501	3.4477	8.977808
Sungai Siput	0.3287	1.81539	2.4934	3.5378	8.175285
Chemor	0.3174	1.56923	2.5559	3.6164	8.058931
Ipoh	0.3385	1.35231	2.5882	3.3231	7.602108
Beruas	0.3371	1.35539	2.5442	3.0909	7.327585
Manjung	0.3385	1.35077	2.5882	3.3231	7.600569
Parit	0.3204	1.15539	2.378	3.00471	6.858495
Tanjung Tualang	0.2996	0.87077	2.1914	2.8194	6.181169
Kampung Gajah	0.3205	0.52462	2.5058	3.7683	7.119215
Tapah	0.3268	0.68462	2.4094	3.1169	6.537715
Bagan Datoh	0.3372	0.71846	3.2316	3.3394	7.626662
Teluk Intan	0.3333	0.12462	2.5897	2.6016	5.649215
Slim river	0.3234	0.94615	2.3379	3.3362	6.943654

$$\text{Total Cost} = \text{Transportation Cost} + \text{Labour Cost} + \text{Harvesting Cost} \quad (3)$$

Where for transportation cost, it will include the estimated diesel cost and toll cost that will be determined from the model simulation. It is estimated that per litre of diesel can travel up to 14.16 km and the price of the diesel is estimated to be 2.20 Ringgit (RM) per litre. Therefore, the equation for the transportation cost is as below:

$$\text{Transportation Cost} = (di/14.16 \text{ km}) * 2.2 \text{ RM} \quad (4)$$

The labour cost depends on the other time that had been computed by the model. The rate for the labour for both in site and transportation is estimated to be 8 RM per hour. The equation is as below:

$$\text{Labour Cost} = (\text{Transfer time} * 8.00 \text{ RM}) + (\text{other time} * 8.00 \text{ RM}) \quad (5)$$

Since the harvesting cost can be assumed similar for each area, it is neglected. The result from the simulation can be shown in Table 4.

**Table 4** Data output for process cost (RM)

Harvesting area	Diesel (RM)	Tol (RM)	Labour cost (RM)	Total cost (RM)
Pengkalan Hulu	43.50282486	23.4	63.195936	130.10
Gerik	36.66666667	10	60.641352	107.31
Selama	35.26836158	19.8	61.004864	116.07
Larut	27.18926554	19.8	49.120064	71.16
Sungai Siput	18.33333333	10	42.82548	67.33
Chemor	15.84745763	10	41.485048	57.33
Ipoh	13.65677966	6	37.403264	57.06
Beruas	13.68785311	2.5	35.57028	51.76
Manjung	13.64124294	0	37.390952	51.03
Parit	11.6680791	0	33.28076	44.95
Tanjung Tualang	8.793785311	0	29.521352	38.32
Kampung Gajah	5.298022599	0	34.34332	39.64
Tapah	6.913841808	0	30.41212	37.33
Bagan Datoh	7.255649718	0	32.462896	39.71
Teluk Intan	1.258474576	0	21.80972	23.07
Slim river	9.555084746	15.8	34.258832	59.61

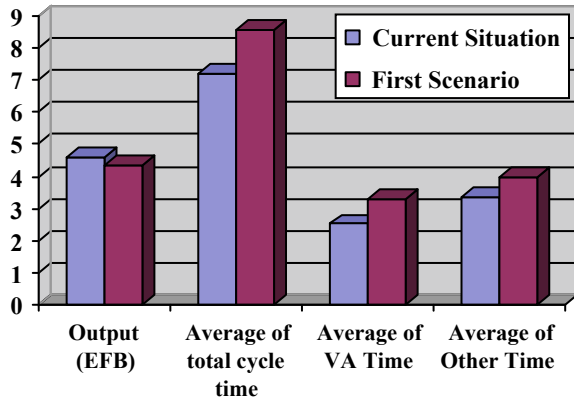
## 4.1 What-IF Analysis

After simulating the cycle time and cost analysis of the supply chain, the obtained results indicated the lack of proper balance and production control in the supply chain. Afterwards, the results were evaluated with real data and its validity was tested. Therefore, the supply chain is evaluated with different scenarios to improve the current situation of the model. Two different scenarios had been run in one month period with 8 h of production daily and discussed below.

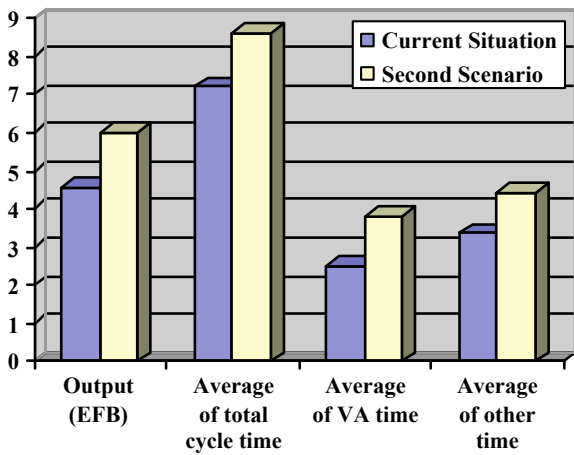
### 4.1.1 First Scenario

From the current situation, the number of labours assigned to the process is three. Therefore, in this scenario, it is assumed the labour is decreased due to leave or unavailability. After that the simulation was run, the results are shown in Fig. 4. According to the Fig. 4, it shows the decrease in output and increase in total cycle time. As for the cycle time, compared to the actual simulation model, the VA time and other time affected the most and increase the total time (25%). While for the transfer time and delay time, they are not affected due to no labour is required for the processes.

**Fig. 4** Comparison between current situation and first scenario



**Fig. 5** Comparison between current situation and second scenario



**4.1.2 Second Scenario**

In the second scenario, it is suggested to add two trucks to the process. All the parameters from the actual model are remained as constant; the number of labour is three and the route from harvesting area to the power plant is based on the actual data. From the simulation of the second scenario, the output of the process is increased (23%) compared to actual simulation while for the time cycle of the whole process is increased (20%) due to an increase in VA and Other time (34 and 23%). It is because from the load and unloading truck process, there will be double work that needs to be done by two trucks instead of one. The results are shown in Fig. 5.

## 5 Conclusion

In this study, a supply chain model of EFB product in Perak state of Malaysia has been designed and analyzed using Arena Simulation Software in order to facilitate the investigation of a wide of conditions that promise profitable biomass utilization. The model considers key activities of the supply chain, including biomass harvesting/processing, transportation, onsite storage and, the distance from the harvesting areas to the power plant that is only based on feasible roads using rectilinear distance by Google Map. The model is evaluated using two key performance indicators: total cost and process time. After running and analyzing the simulation model, it was concluded that the cycle time of the whole processes had been decreased and the output also increased compared to the actual data. In order to do the sensitivity analysis, two scenarios were run and compared. First scenarios showed that by decreasing the labors, output is decreased from 4.59 to 4.336 ton/ha. In contrast, cycle time, VA time and other time are increased near 15, 25 and 15% respectively. Additionally, the final results based on the second scenario claimed that by assigning two trucks, the output of the process is increased 23% (from 4.59 to 6.02 ton/ha) compared to current situation as well as the time cycle of the whole process is increased from 7.2 to 8.95 h because of an increase in VA and Other time (34 and 23%). Future study can be done by assessing more scenarios of the model such as increasing the number of station and reducing the truck capacity. Moreover, simulation modeling cannot be used as an optimization approach. However, using mathematical methods can be a powerful tool in determining the best alternatives from a set of available scenarios regarding criteria about biomass inventory, location, size of facilities, and delivered biomass.

## References

1. Zahraee SM, Khalaji Assadi M, Saidur R (2016) Application of artificial intelligence methods for hybrid energy system optimization. *Renew Sustain Energy Rev* 66:617–630
2. Rentizelas AA, Tolis AJ, Tatsiopoulos IP (2009) Logistics issues of biomass: the storage problem and the multi-biomass supply chain. *Renew Sustain Energy Rev* 13:887–894
3. Farouk H, Zahraee SM, Atabani A et al (2017) Optimization of the esterification process of crude jatropha oil (CJO) containing high levels of free fatty acids: a Malaysian case study. *Biofuels*:1–8
4. Zahraee SM, Khalaji Assadi M (2017) Applications and challenges of the palm biomass supply chain in Malaysia. *12(20):5789–5793*
5. Iakovou E, Karagiannidis A, Vlachos D et al (2010) Waste biomass-to-energy supply chain management: a critical synthesis. *Waste Manag* 30:1860–1870
6. Umar MS, Jennings P, Urmee T (2014) Generating renewable energy from oil palm biomass in Malaysia: The feed-in tariff policy framework. *Biomass Bioenergy* 62:37–46
7. Tan Z, Chen K, Liu P (2015) Possibilities and challenges of China's forestry biomass resource utilization. *Renew Sustain Energy Rev* 41:368–378
8. Zahraee SM, Golroudbary SR, Hashemi A et al (2014) Simulation of manufacturing production line based on Arena. *Adv Mater Res* 933:744–748



9. Shahpanah A, Poursafary S, Shariatmadari S et al (2014) Optimization waiting time at berthing area of port container terminal with hybrid genetic algorithm (GA) and artificial neural network (ANN). *Adv Mater Res* 902:431–436
10. Zahraee SM, Rezaei G, Shahpanah A et al (2014) Performance improvement of concrete pouring process based resource utilization using taguchi method and computer simulation. *Jurnal Teknologi* 69:17–24
11. Zahraee SM, Hatami M, Rohani JM et al (2014) Comparison of different scenarios using computer simulation to improve the manufacturing system productivity: case study. *Adv Mater Res* 845:770–774
12. Ebadian M, Sowlati T, Sokhansanj S et al (2011) A new simulation model for multi-agricultural biomass logistics system in bioenergy production. *Biosys Eng* 110:280–290
13. Arinze E, Sokhansanj S, Besant R et al (2001) Effects of material and environmental conditions on caking and breakage of potash fertilizer products during storage, shipment and handling. *The Int J Storing Handling Process Powder* 13:45–54
14. Sokhansanj S, Khoshtaghaza H, Schoenau G et al (2003) Heat and moisture transfer and quality changes in containerized alfalfa cubes during transport. *Trans-Am Soc Agric Eng* 46:423–434
15. Ravula PP, Grisso RD, Cundiff JS (2008) Cotton logistics as a model for a biomass transportation system. *Biomass Bioenerg* 32:314–325
16. Zhang F, Johnson DM, Johnson MA (2012) Development of a simulation model of biomass supply chain for biofuel production. *Renew Energy* 44:380–391
17. Windisch J, Roser D, Mola-Yudego B et al (2013) Business process mapping and discrete-event simulation of two forest biomass supply chains. *Biomass Bioenerg* 56:370–381
18. Hamzah A, Abdul Manap AR, Voon WS (2012) Heavy commercial passenger vehicle service life in Malaysia, MIROS MRev 01
19. Zahraee SM, Rohani JM, Wong KY (2018) Application of computer simulation experiment and response surface methodology for productivity improvement in a continuous production line: case study. *J King Saud Univ-Eng Sci* 30(3):207–217

# Effect of Thermal Cycling on Thermal Conductivity of Powder Injection Moulded MWCNT Reinforced Copper Matrix Composites



Faiz Ahmad, Masdi Mohammad, A. S. Muhsan, Muhammad Ali, A. Naseer, M. Aslam and M. R. R. Malik

**Abstract** Thermal management of electronics is a great challenge to achieve optimum performance. Nano materials provide a pathway to increase thermal conductivity but nano particles uniform dispersion in the matrix is very difficult. This study focuses on dispersion of functionalized multi-walled carbon nano tubes in copper to improve thermal conductivity of copper. Copper/Carbon Nano Tubes (CNTs) composites were developed via powder injection moulding. Feedstock was compounded using Z-blade mixer and defect free green parts were produced by injection moulding. Binder was removed by solvent and thermal means followed by sintering in argon at 1050 °C. Thermal conductivity and reliability tests were performed on sintered nano composite specimen at various temperatures. Results showed good dispersion of CNTs in copper and thermal conductivity measured was 550–580 w/m.k. A decrease of 27–37% in thermal conductivity was recorded during thermal cycling of sintered composite and the reduced thermal conductivity value is still 80% higher than pure copper.

**Keywords** Metal matrix composites · Feedstock · Metal injection molding · Thermal cycling · Sintering · Thermal conductivity

## 1 Introduction

The Thermal management of electronic devices is very important to achieve their optimum performance. These devices are in our daily use applications such as cellular

---

F. Ahmad (✉) · M. Mohammad · A. S. Muhsan · M. Ali · A. Naseer  
Department of Mechanical Engineering, Universiti Teknologi PETRONAS, Seri Iskandar,  
Malaysia  
e-mail: [faizahmad@utp.edu.my](mailto:faizahmad@utp.edu.my)

M. Aslam  
Centres of Excellence in Science and Applied Technologies, Islamabad, Pakistan

M. R. R. Malik  
Mechanical Engineering Department, COMSATS, Sahiwal, Pakistan

© Springer Nature Singapore Pte Ltd. 2020  
M. Awang et al. (eds.), *Advances in Material Sciences and Engineering*, Lecture Notes in Mechanical Engineering,  
[https://doi.org/10.1007/978-981-13-8297-0\\_40](https://doi.org/10.1007/978-981-13-8297-0_40)

phone, computer, television and LED light. Copper alloys and aluminium alloys are frequently used for thermal management of electronic devices due to their low cost [1]. Silver and gold are highly thermal conductive metals but their use in thermal management is restricted due to their high cost [2]. Recent development in electronics has increased current density that increases temperature. An improper means of heat dissipation causes failure of devices [1, 3]. Therefore, a highly thermal conductive and low cost material is required to meet the present and future challenges in thermal management.

Copper is a relatively low cost material and has high thermal conductivity of 360–390 W/m.k as compared to other metals. Recent developments of carbon nanotubes (CNTs) have attracted scientists due to their unique properties for development of new materials with enhanced performance. There are several processing techniques reported in the literature for improving thermal conductivity of copper by reinforcing CNTs and diamond [4–7]. The published literature has reported thermal conductivity of copper produced by metal injection moulding (MIM) 325–335 W/m.k. The reinforcement of CNTs in copper reduces thermal conductivity due to non-uniform dispersion. Therefore, uniform dispersion of CNTs in copper matrix is a great challenge to achieve high thermal conductivity. CNTs tend to agglomerate due to higher surface area and associated Van der Waals forces [8, 9]. The CNTs possess porosity and act as discontinuities due to agglomeration that result in lower properties [10–12]. The clustering of CNTs deteriorates the electrical, thermal and mechanical properties of nano-composites as reported in several studies. Therefore, many processes have been developed to improve the dispersion. Most of the techniques have been used for polymer nano composites and few have been reported for dispersion of CNTs in metal matrix composites [11, 13, 14], however, their results did not show improvement in thermal conductivity. The CNTs dispersion techniques are divided into physical and chemical approaches with several methods in each class. A physical approach was reported by Hagen Muellera et al. to improve the dispersion of CNTs that result in improved properties [15, 16]. Kyung et al. dispersed CNTs homogenously in copper matrix by another technique of molecular level mixing [17, 18]. Uniform dispersion of CNTs in metal matrix composites is still challenging due to low wettability of CNTs and matrix because of density difference [19]. In this study, a technique for dispersion of MWCNTs in copper powder is developed.

## 2 Materials and Methods

### 2.1 Raw Materials

Copper powder produced by gas atomization was used in this study. The powder was supplied by Sandvik Osprey LTD, UK. Functionalized Multi-walled Carbon Nano tubes (MWCNTs) were purchased from Nano Sky, USA. The MWCNTs purity ranges from 95 to 98% with ash contents  $\leq 0.2\%$  wt and attached with  $-\text{COOH}-$

**Table 1** Percentage ingredients of binder

Feedstock	Component	Component wt%	Feedstock vol. %
Powder loading	Cu	51.5	59
	CNT	7.5	
Binder content	PW	70	41
	PE	25	
	SA	5	

functional group. Copper powder and MWCNTs were characterized by Field Emission Electron Microscope for their size and microstructure. Binder system consists of three components such as paraffin wax (PW) as major binder, polyethylene (PE) to provide green strength and stearic acid (SA) as surfactant. The binders were purchased from Titan Pet chem. Sdn. Bhd, Johor, Malaysia.

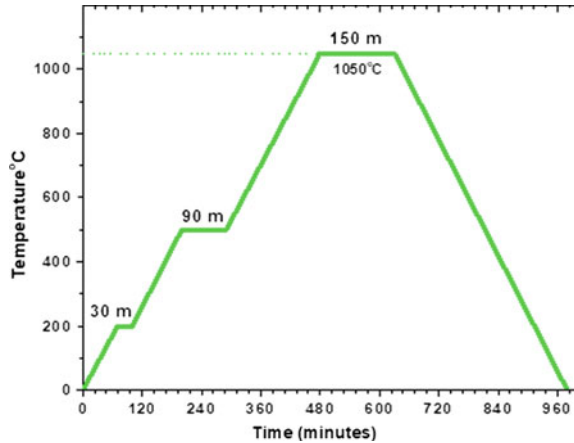
## 2.2 Dispersion of MWCNTs and Feedstock Preparation

The functionalized MWCNTs were dispersed in a viscous media prepared using PW diluted with n-heptane solvent by magnetic stirrer. One gram of MWCNTs were mixed with 250 ml of PW/Heptane solution and agitated for 60 min using magnetic stirrer. This was followed by sonication process to ensure uniform dispersion of MWCNTs in PW solution and dried at 50 °C for 2 h. The dried mixture was mixed with stearic acid at 60 °C in a Z-blade mixer for 30–45 min at 50 rpm. This was followed by the addition of copper powder in the mixture to coat the copper powder with wax and stearic acid. Then the temperature was raised to 160 °C and PE was added in the mixture and mixed for another 40–45 min. The feedstock was cooled slowly and converted into pellet form. The prepared feedstock with powder loading and binder percentage are fully described in Table 1.

## 2.3 Powder Injection Moulding

A vertical injection moulding machine (MCP-100KSA) was employed to produce test samples. The feedstock of Cu/MWCNTs was injected into mould cavity via heated barrel at 160 °C temperature and 4 MPa pressure. After filling the mould cavity, solidified component was removed.

**Fig. 1** An integrated thermal debinding and sintering cycle



## 2.4 Debinding and Sintering of Copper/CNT Parts

Binder was removed in two steps such as solvent and thermal debinding. Solvent debinding was done using n- heptane solution at 70 °C for 4 h to dissolve PW and SA. Thermal debinding process was done using a box furnace followed by sintering in argon atmosphere. In this process, the temperature was increased from ambient to 200 °C using a heating rate of 3 °C/min and held for 30 min. Then temperature was increased to 500 °C and held for 90 min to ensure a complete removal of the binder component from the moulded samples. After that, temperature was raised to 1050 °C and held for 150 min. The heating rate of 3 °C/min was used throughout the whole process of thermal debinding and sintering. Integrated thermal debinding and sintering cycle are described in Fig. 1.

## 2.5 Thermal Conductivity Measurement

Thermal conductivity of the sintered parts was measured using a NETZSCH model LFA 447 Nano Flash™ Germany. This works according to international standards ASTM E-1461, DIM EN 821 and DIN 30905. Specimens of 12.7 mm diameter and 3 mm thickness were prepared to obtain accurate results as shown in Fig. 2. In this technique, the temperature rise on the back face of the sample is measured using an In-Sb detector. Thermal conductivity was measured at 50, 100, 150, 200 and 250 °C to study the effects of temperature.



**Fig. 2** Test samples for thermal conductivity measurement

## ***2.6 Thermal Cycling of Sinter Copper-CNT Composites***

Sintered test samples of dimensions length: 60 mm, width: 60 mm, thickness: 3 mm were used for reliability test. Qualmark HAWQ Accelerated reliability testing machine was used at 25, 50, 75, 100 and 125 °C temperatures and all the tests were carried for 500 thermal cycles. Another reliability test was conducted at a constant temperature of 180 °C for 100 h [20–24].

## **3 Results and Discussion**

### ***3.1 Characterization of Cu and MWCNTs***

The copper powder was regular in shape with particle  $> 22 \mu\text{m}$  as described in Fig. 3a. The purity of the powder was up to 99.95%. MWCNTs are of 30 nm in diameter and 20–30  $\mu\text{m}$  in length as shown in Fig. 3b. The MWCNTs purity ranges 95–98% with ash contents  $\leq 0.2\%$  wt and attached with  $-\text{COOH}-$  functional group [25].

The functional group  $-\text{COOH}-$  attached to the multi-walled carbon nanotubes was confirmed by Fourier-transform infrared spectroscopy (FTIR) as described in Fig. 4. The purpose of this group attachment is to enhance the bonding between copper and CNT to improve thermal conductivity.

### ***3.2 Dispersion of MWCNTs in PW and Copper***

The dispersion of MWCNTs was examined in the mixture of PW/CNTs and their images are taken from our prior work [26]. Figure 5a shows a dried mixture of

MWCNT/PW and Fig. 5b described dispersed CNTs in the mixture. It can be clearly seen that the CNTs are homogeneously dispersed throughout the matrix of PW.

The dispersion of CNTs in the sintered samples was characterized by FESEM. Dispersion of CNTs and bonding of CNTs with copper particles are described in Fig. 6.

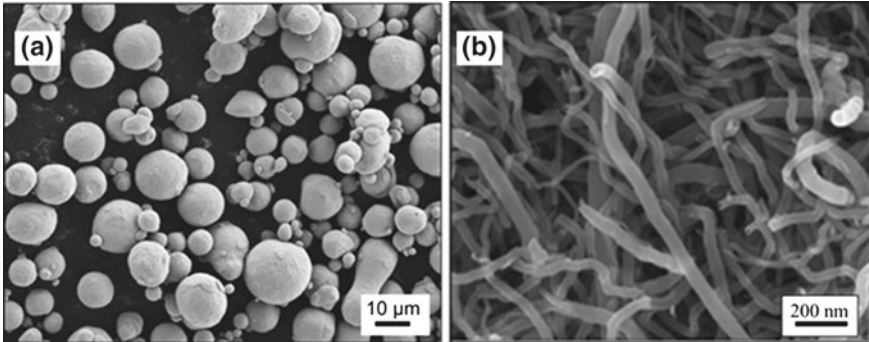


Fig. 3 FESEM image of a copper powder, b functionalized MWCNTs

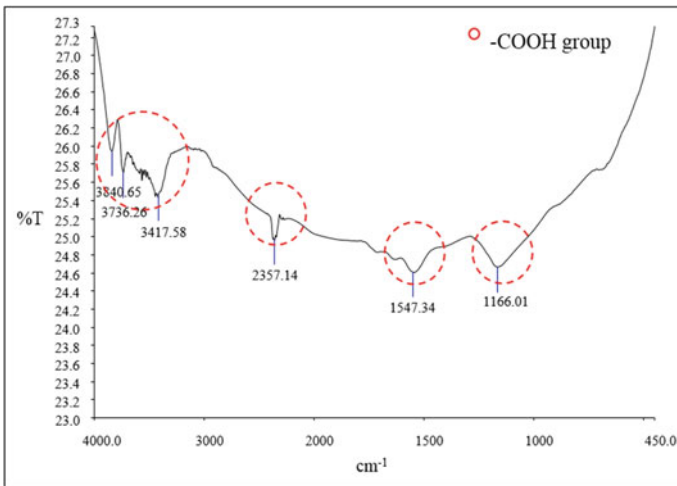
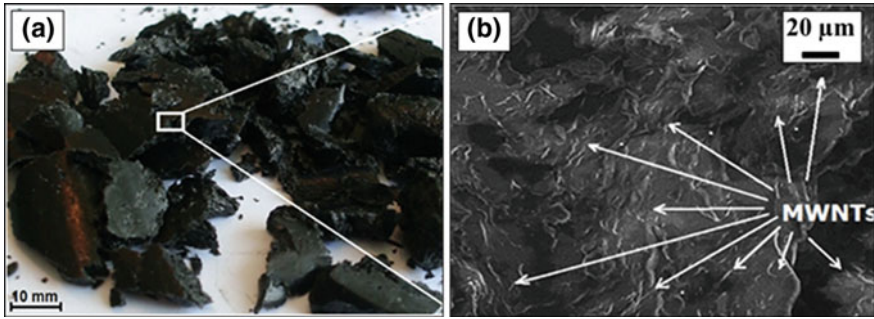
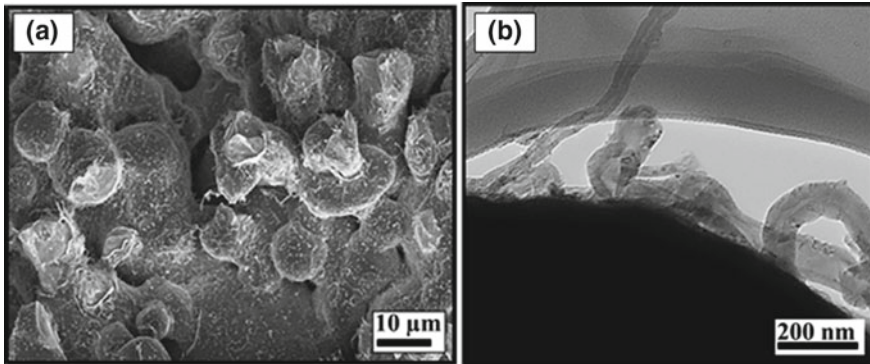


Fig. 4 FTIR test for MWCNTs



**Fig. 5** **a** PW after dispersion, **b** FESEM image of MWCNTs after dispersion [26]



**Fig. 6** FESEM image of **a** Copper/CNT bonding, **b** dispersion of CNTs

### 3.3 *Effects of Thermal Cycling and Temperature on Thermal Conductivity*

The maximum thermal conductivity of MWCNTs reinforced Copper composite was measured 550–580 W/m.k. The reliability test was conducted for 500 thermal cycles at various temperatures to analyse the performance of the sintered composite. The basic value of thermal conductivity used was in the range of 550–580 W/m.k. Thermal conductivity values measured after 500 cycles were approximately 26% less compared to the base value as described in Fig. 7. Furthermore, it was noticed that the colour of the samples was changed to light greenish after reliability test as shown in Fig. 8. The change in colour is due to oxidation of the test samples.

The thermal conductivity reliability test was conducted by holding the test sample at higher temperature with prolong time. The results of the test conducted for 100 h at 180 °C is described in Fig. 9. The decrease in thermal conductivity was calculated using a base value of test sample without thermal cycling. An average decrease of 37% in thermal conductivity was recorded for all tested samples. The physical



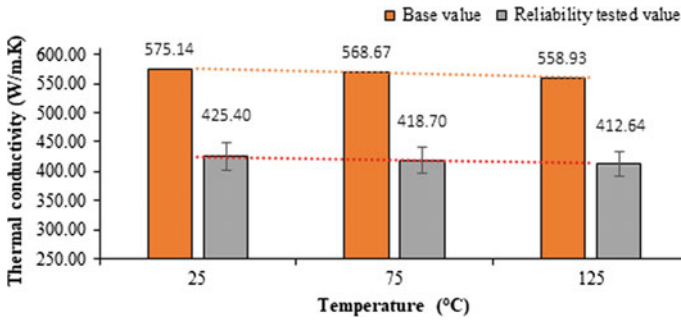


Fig. 7 Variation of thermal conductivity with temperature after 500 thermal cycles



Fig. 8 Physical appearance of Cu-CNT samples after reliability testing for 500 thermal cycles

appearance of the samples was also changed to dark colour due to oxidation as shown in Fig. 10.

### 3.4 Cost Comparison of Heat Sinks Produced by Various Techniques

A summary of cost comparison of copper composites heat sink produced by various techniques is presented in Table 2. Table shows the value of thermal conductivities and cost per 100 gm. This comparison shows that copper-MWCNTs reinforced heat

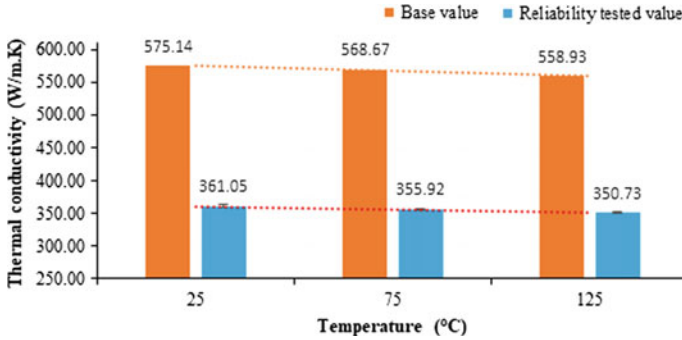
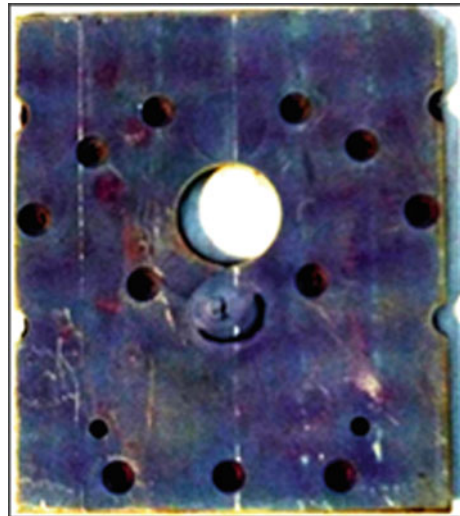


Fig. 9 Variation of thermal conductivity after holding samples for 100 h at 180 °C

Fig. 10 Physical appearance of Cu-CNT samples after holding at 180 °C for 100 h



sink produced by MIM has the highest values at very competitive cost. MIM has several advantages, in term of re-cycling of feedstock, dimensional accuracy and elimination of several post sintering operations available in powder metallurgy.

## 4 Conclusion

The following conclusions are drawn by the current study,

1. Uniform dispersion of MWCNTs was achieved in the copper matrix via a new dispersion technique and feedstock of copper-CNTs was prepared
2. Defect free green test samples of heat sink were injection moulded and sintered in controlled atmosphere successfully.

**Table 2** Comparison of copper heat sink materials prices developed by different techniques

Properties	Wrought C11000	Cast C81100	Cast C83400	SPS Cu/Diamond	SPS Cu/CNTs	MIM of Cu/CNTs
Density (g/cm <sup>3</sup> )	8.9	8.9	8.7	8.9	8.6	8.5
Thermal conductivity (W/m.k)	330–375	340–350	180–190	110–120	250–330	380–400
Net-shape compatibility	Low	Low	Low	Medium	Medium	High
Cost/100 g (USD)	40	22	13	40	35	15

3. High thermal conductivity was achieved in the sintered copper/CNT composites. Thermal conductivity achieved is higher than pure copper.
4. Thermal conductivity reliability test was conducted for sintered Copper/CNTs composites at different parameters. An average thermal conductivity degradation of 26% from baseline at 500 thermal cycles and 37% degradation at constant temperature (180 °C) were achieved.

**Acknowledgements** Authors are thankful to Centre for Advanced Functional Materials, Universiti Teknologi PETRONAS and Ministry of Science, Technology and Innovation (MOSTI) for funding pre-commercialization Techno fund of Nano composites for electronic industry.

## References

1. Tong XC (2011) Advanced materials for thermal management of electronic packaging, vol 30. Springer Science+business
2. Jiang G, Diao L, Kuang K et al (2013) Advanced thermal management materials. Springer
3. Zweben C (1992) Metal-matrix composites for electronic packaging. JOM 44:15–23
4. Chu K, Wu Q, Jia C et al (2010) Fabrication and effective thermal conductivity of multi-walled carbon nanotubes reinforced Cu matrix composites for heat sink applications. Compos Sci Technol 70:298–304
5. Abyzov AM, Kidalov SV et al (2012) High thermal conductivity composite of diamond particles with tungsten coating in a copper matrix for heat sink application. Appl Therm Eng 48:72–80
6. Guillemet T, Geffroy PM et al (2012) An innovative process to fabricate copper/diamond composite films for thermal management applications. Compos A Appl Sci Manuf 43:1746–1753
7. Bakshi SR, Lahiri D, Agarwal Arvind et al (2010) Carbon nanotube reinforced metal matrix composites—a review. Int Mater Rev 55:41–64
8. Wang H (2009) Dispersing carbon nanotubes using surfactants. Curr Opin Colloid Interface Sci 14:364–371
9. Peigney A, Laurent C, Flahaut E et al (2010) Specific surface area of carbon nanotubes and bundles of carbon nanotubes. Carbon 39:507–514
10. Yu J, Grossiord N, Koning CE et al (2007) Controlling the dispersion of multi-wall carbon nanotubes in aqueous surfactant solution. Carbon 45:618–623

11. Tan H, Jiang LY, Huang Y et al (2007) The effect of van der Waals-based Interface cohesive law on carbon nanotube-reinforced composite materials. *Compos Sci Technol* 67:2941–2946
12. Thostenson ET, Ren Z, Chou TW et al (2001) Advances in the science and technology of carbon nanotubes and their composites a review. *Compos Sci Technol* 61:1899–1912
13. Huang YY, Terentjev EM (2012) Dispersion of carbon nanotubes: mixing, sonication, stabilization, and composite properties. *Polymers* 4:275–295
14. Balani K, Bakshi SR et al (2007) Role of powder treatment and carbon nanotube dispersion in the fracture toughening of plasma-sprayed aluminum oxide/carbon nanotube nanocomposite. *J Nanosci Nanotechnol* 7:3553–3562
15. Haggemueller R et al (2000) Aligned single wall carbon nanotubes in composites by melt processing methods. *Chem Phys Lett* 330(3–4):219–225
16. Advani SG (2007) Processing and properties of nanocomposites. World Scientific Publishing Co. Pte. Ltd, 596224, Singapore
17. Kim KT, Eckert J, Liu G et al (2011) Influence of embedded carbon nanotubes on the thermal properties of copper matrix nano composites processed by molecular-level mixing. *Scr Mater* 64:181–184
18. Gao XP, Zhang Y, Chen X, Pan GL, Yan J, Wu F (2004) Carbon nanotubes filled with metallic nanowires. *Carbon* 42(1):47–52
19. Nyberga E, Millerb M, Simmonsa K et al (2004) Microstructure and mechanical properties of titanium components fabricated by a new powder injection molding technique. *Mater Sci Eng*
20. Turner MD (2010) A practical application of quantitative accelerated life testing in power system engineering. *IEEE Trans Reliab* 59:91–101
21. Stephenson LD, Heffron A, Mehnert et al (2015) Prediction of long term degradation of insulating materials. The U.S. Army Engineer Research and Development Center (ERDC), Washington, DC
22. Meeker WQ, Escobar LA, Lu CJ (1999) Accelerated degradation tests: modeling and analysis. Digital Repository, Iowa State University
23. Carlsson B, Möller K, Köhl M (2004) The applicability of accelerated life testing for assessment of service life of solar thermal components. *Sol Energy Mater Sol Cells* 84:255–274
24. Corporation R (2015) Accelerated life testing reference. Relia Soft Corporation Tucson, Arizona
25. Ahmad F, Raza MR, Muhsan AS (2013) Preparation and fiber fracture of metal matrix composite feed-stock for powder injection molding. *Int J Powder Metall* 49
26. Muhsan AS, Ahmad F (2014) Homogeneous distribution of carbon nanotubes in copper matrix nanocomposites fabricated via combined technique. *Nanosci Nanotechnol Lett* 06:865–874

# Bending Forces and Hardness Properties of Ti6Al4V Alloy Processed by Constrained Bending and Straightening Severe Plastic Deformation



Wambura Mwiriyeni Mwita  and Esther T. Akinlabi

**Abstract** This paper presents an investigation on bending forces and hardness properties of Ti6Al4V alloy sheets processed by constrained bending and straightening (CBS) severe plastic deformation (SPD) technique. CBS was proposed as a continuous SPD process of metals enhanced with homogeneous mechanical properties such as strain and hardness. A physical model for the CBS process was designed and fabricated. Ti6Al4V alloy samples were annealed for stress relief and ductility improvement. Alloy samples were then subjected to CBS process at 20, 10 and 5 mm feed lengths for 1 and 2-passes. Values of bending forces and micro-hardness on samples were determined. Results showed that magnitude and homogeneity of induced strain at 5 mm feed were higher than those at 20 and 10 mm feeds. The maximum average values of bending force and hardness were observed at 10 mm feed and 2-pass as 18296 N and 377.8 HV respectively. The hardness increased by 16.3% over that of annealed samples.

**Keywords** Constrained bending and straightening · Severe plastic deformation · Strain homogeneity

## 1 Introduction

Various severe plastic deformation (SPD) techniques to process titanium alloys with enhanced desired properties for structural engineering and biomedical applications are widely reported in the literature [1, 2]. SPD enhanced properties in material include grain refinement, improved tensile strength, hardness, wear, corrosion resis-

---

W. M. Mwita (✉) · E. T. Akinlabi

Department of Mechanical Engineering Science, Faculty of Engineering and the Built Environment, University of Johannesburg, Po Box 524, APK 2006, Johannesburg, Republic of South Africa  
e-mail: [mwita\\_wa@yahoo.com](mailto:mwita_wa@yahoo.com)

E. T. Akinlabi  
e-mail: [ETakinlabi@uj.ac.za](mailto:ETakinlabi@uj.ac.za)

© Springer Nature Singapore Pte Ltd. 2020  
M. Awang et al. (eds.), *Advances in Material Sciences and Engineering*, Lecture Notes in Mechanical Engineering, [https://doi.org/10.1007/978-981-13-8297-0\\_41](https://doi.org/10.1007/978-981-13-8297-0_41)

tance and biocompatibility [3, 4]. SPD is loading the material with a hydrostatic stress; as a result, plastic shear strains are accumulated in material with negligible change of sample dimensions [5]. Accumulated plastic strains increase grain boundaries by alteration of coarse grains into fine grains. Resulting grain size can be in the range of ultra-fine (100 to <1000 nm) or nano scale (<100 nm) [6, 7]. High pressure torsion (HPT), equal channel angular pressing (ECAP), asymmetric rolling (AR), accumulative roll bonding (ARB) and repetitive corrugation and straightening (RCS) are among the successful SPD processes reported in the literature [8–11]. However, most of these processes are still at experimental stage, they are performed with discrete cycles on limited size and geometry specimens, good examples are HPT and ECAP processes [12]. Improved models from these techniques for continuous process of bulky specimens have been reported in the literature, for instance, Continuous-HPT [13], Incremental-HPT [14], Incremental-ECAP [15, 16] and ECAP-Conform [3]. AR and ARB processes are competitive for implementation as continuous SPD processes due to the simplicity of the rolling facility required. However, currently these methods are mainly applicable to samples of rectangular sections. ARB processed samples have also been associated with risks of unreliable interfacial bonding and grains contamination during repeated cutting and stacking of sheet laminates [17, 18]. Induced strain heterogeneity in the deformed samples has been another serious drawback of most SPD processes, good examples are HPT [14, 19, 20] and RCS [21, 22] processed samples. Strain heterogeneity results to non-uniformity of enhanced mechanical and microstructure properties. RCS is the SPD technique where material is deformed with shear bending strains via repeated bending and flattening. An RCS discontinuous process tool is represented in Fig. 1. Considering the sample (Fig. 1) in the bending state, the inclined hatched planes are most strained while the horizontal unhatched planes are least strained. During flattening, the inclined planes continue deforming while the horizontal planes remain relatively un-deformed. The strains heterogeneity due to un-even deformation can remain in material regardless of the number of RCS passes performed. Improved RCS models on strain homogeneity have been reported, examples are RCS-Rolling [23], Groove Pressing (GP) [21, 24], Constrained Groove Pressing (CGP) [25, 26] and Constrained Groove Pressing-Cross Rotation (CGP-CR) [27, 28] discontinuous processes. It can be concluded that adaptation of SPD techniques reported in the literature to the industrial scale continuous process of bulk metals with homogeneous properties still remain a challenge that need more research. In this paper, CBS method is proposed for SPD of metals, bending forces, induced strain and hardness properties of Ti6Al4V processed by CBS are investigated. The CBS basically originates from RCS and is expected to provide continuously SPD of metals enhanced with homogeneous microstructure and mechanical properties. A detailed discussion on CBS process operation, the developed model tool and the model test procedures are presented in Chap. 2.

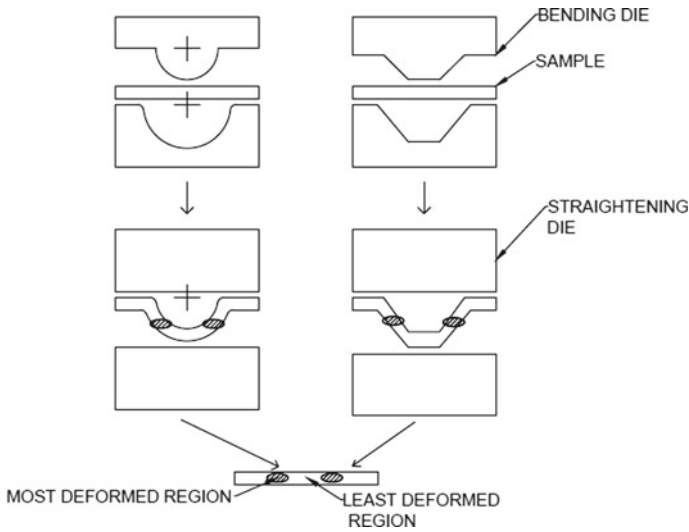


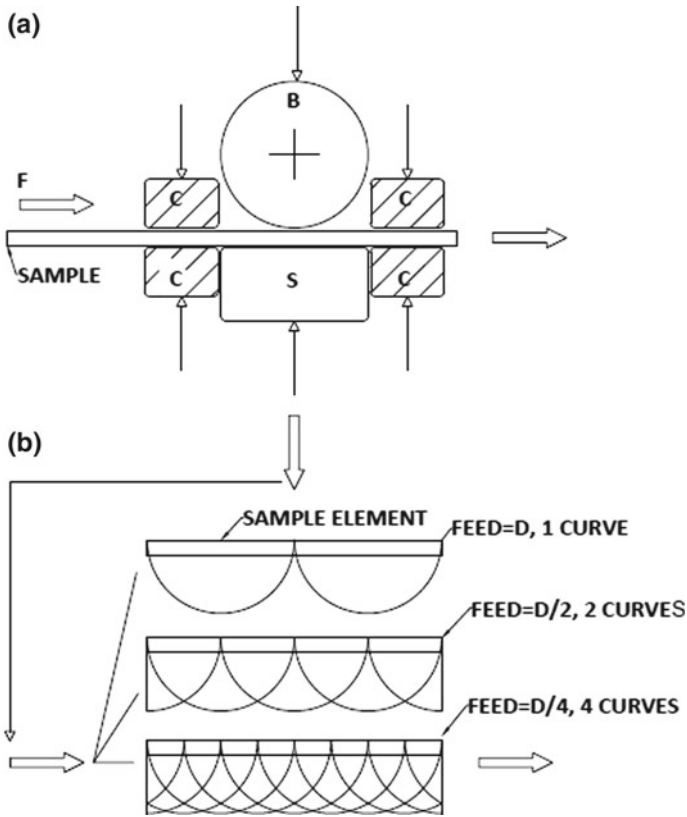
Fig. 1 An RSC discontinuous process tool-bending and straightening the sample

## 2 Method and Materials

### 2.1 The Principle of CBS Process

CBS process (Fig. 2a) is performed by bending and flattening of the constrained sheet then moving it at a specified length known as feed. A complete CBS pass is achieved when the process is done over the whole length of the sheet at a constant feed. Basically, the CBS consists of the bending roller B of diameter D, flattening roller S, constraining brackets C and the feed system F. In this study, constraining of the sample during bending was enhanced by manually tightening the nuts on two pairs of bolts. Feeding was done by loosening the nuts on bolts and sliding the sample forward at a selected feed. Loosening the nuts kept the sample in unconstrained state hence reduced contact friction and feed forces. Figure 2b represents sample longitudinal elements of length 2D and the resulting bending paths at feeds D, D/2 and D/4 respectively. Figure 2b theoretically shows that the values of effective strain and overlapping bending paths (strain homogeneity) are dependent on both decreased feed F and bending roller size D. Applying the Von Mises-energy criterion, the effective strain for a sheet of rectangular section bent and then flattened with a semi-circular roller is given by Eq. (1) [29]:

$$\epsilon_{eff} = N \frac{4}{\sqrt{3}} \ln \left( \frac{R + T}{R + 0.5T} \right) \tag{1}$$



**Fig. 2** a Principle of CBS b Number of induced bending curves (paths) in the sample versus feed length for one pass [30]

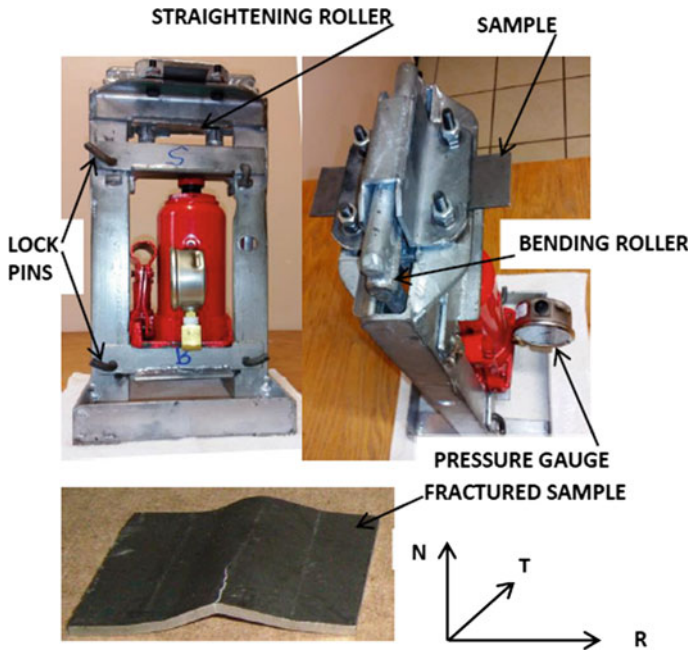
$R$  = radius of the roller =  $D/2$ ,  $T$  = thickness of sheet and  $N$  = number of passes. Introducing to Eq. (1) the number of plastic bending paths per pass,  $Z$ , where  $Z = D/F = 2R/F$ ,  $F =$  feed,  $0 < F \leq 2R$ , therefore the effective strain in the sheet processed with CBS is given by Eq. (2):

$$\epsilon_{eff} = N \frac{R}{F} \frac{8}{\sqrt{3}} \ln \left( \frac{R + T}{R + 0.5T} \right) \tag{2}$$

### 2.2 CBS Tool and Test Procedure

A model tool for CBS was designed and fabricated in the workshop. The tool was used to perform CBS on Ti6Al4V titanium alloy sheets. The tool and the deformed





**Fig. 3** Assembly of the CBS model tool with a deformed sample represented in the rolling (R), normal (N) and transverse (T) directional axes

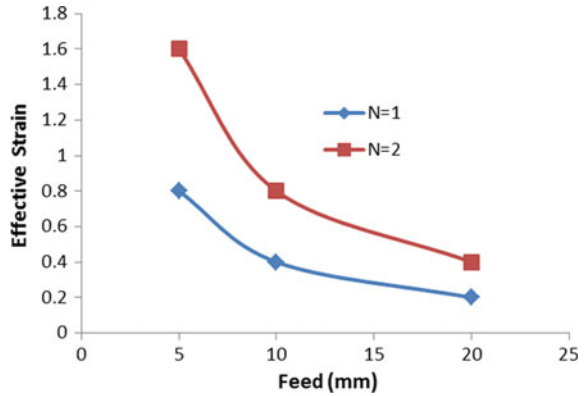
**Table 1** (a) Ti6Al4V chemical composition and tensile properties (b) CBS tool parameters

(a)		(b)	
Composition C (0.02), Fe (0.12), N (0.018), O (0.1), H (0.003), Al (5.9), V (4.1), Others (<0.4) and Ti (balance)		Sample dimensions (L, W, T) (mm)	153, 41, 2
Yield strength, TY (MPa)	Max 886	Bending roller diameter, D (mm)	20
Tensile strength, TS (MPa)	Max 950	Feed lengths, F (mm)	5, 10, 20
% Elongation to fracture	10–13	Number of passes, N	1, 2

sample are presented in Fig. 3. CBS tool design parameters and Ti6Al4V alloy material properties are presented in Table 1.

A 10 tone hydraulic jack equipped with 6000 psi/41.37 MPa (1 psi = 0.0068947 MPa) pressure capacity reading gauge (Model-G2517L) was used to provide bending and flattening forces. Activated jack provided either bending or flattening force by a pair of lock pins on flattening and bending sliding brackets respectively

**Fig. 4** Effective strain versus feed length at pass N



(see Fig. 3). The bending force on the sample generated by the hydraulic jack was calculated using Eq. (3) as:

$$f = PA \quad (3)$$

$f$  = force (N),  $P$  = pressure in the hydraulic jack (MPa) and  $A$  = cross section area of the jack large piston. The diameter of the jack piston was measured as 35 mm.

Prior to the CBS process, a total of fifteen (15) Ti6Al4V alloy samples were annealed to improve ductility and release residual stresses. Samples were heated in the furnace to a temperature of 550° C for two hours and left to cool in the furnace. CBS process was performed on two (2) samples at room temperature for each of feeds ( $F = 5, 10$  and  $20$  mm) and passes ( $N = 1, N = 2$ ) respectively. To avoid excessive bending, all samples were equally deformed with a plastic bending depth of 2 mm, which was less than 10 mm (radius  $R$  of the bending roller). The depth was measured from un-deformed sheet surface to deformed groove surface along the center of the bending roller. After the CBS process, sub size samples of length 20 mm and width 10 mm were cut from deformed samples along the rolling direction on the R-T plane (Fig. 3). The samples were mounted, ground with SiC, MD Largo discs and diamond suspension then polished with OPS solution. The micro hardness (in Vickers) on the samples were determined at intervals of 2 mm using a digital hardness tester at 9.8 N (1 kgf) indentation load and 15 s dwell time. For each feed length  $F$  and pass number  $N$ , average values of bending force and hardness were calculated and magnitudes of theoretical induced strains were determined using Eq. (2). Results for bending strain, CBS bending forces and micro hardness are presented in Figs. 4, 5 and 6.

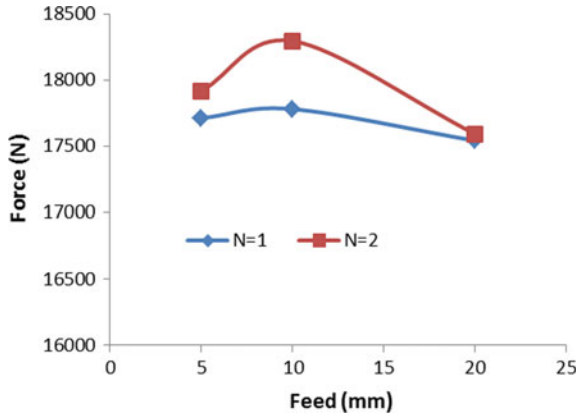


Fig. 5 Bending force versus feed length

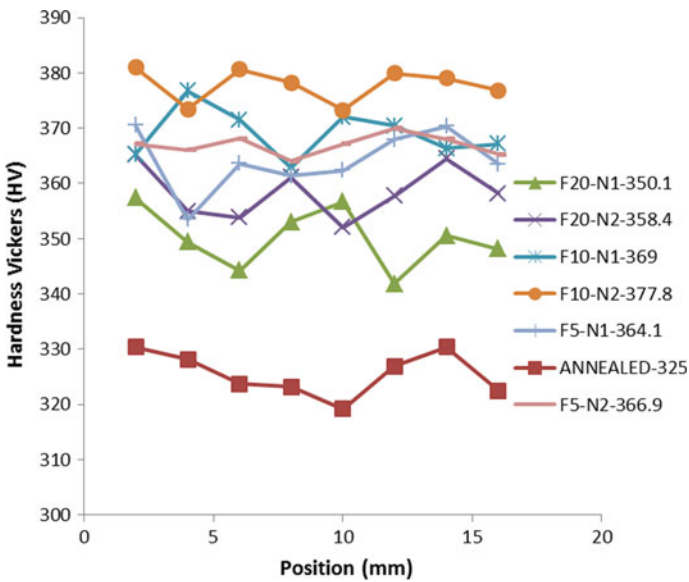


Fig. 6 Hardness (HV) distribution and mean values on samples R-T planes at various feed length F, pass N

### 3 Discussion of Results

Results (Fig. 4) show that induced strain is exponentially dependent on decreased feed and increased passes. Decreasing the feed from 20 to 5 mm increases the induced strain by 300%. A high increase of induced strain at reduced feed is due to the increased deformation (bending) paths in samples which also improve strain homo-

generity. Equation (2) also shows that the bending roller with smaller radius is more effective and induces more plastic strains. Results in Fig. 5 show that in first and second passes respectively, bending forces (17780 and 18296 N) were slightly higher at 10 mm feed than those (17542 and 17593 N) at 20 mm feed, then they decreased to (17712 and 17917 N) at 5 mm feed. Results in Fig. 6 showed that the average hardness values on samples increased with number of passes and reduced feed length from 325 HV for annealed samples to a maximum of 377.8 HV (about 16.3% increase) at 10 mm feed and 2-pass. Then, the average hardness reached a saturation point and decreased to 366.9 HV at 5 mm feed and 2-pass. It was also observed that hardness homogeneity improved with the increase of passes and decreased feed length. The best hardness homogeneity was observed on samples processed at 5 mm feed and 2-pass. The increase of bending force, strain and hardness of CBS processed samples as compared to annealed samples were attributed by induced plastic strain that resulted to strain hardening strengthening of material. Even though theoretical values of induced strains at 5 mm feed were higher than those at 10 mm feed, the bending force and hardness at 5 mm feed were lower than those at 10 mm feed. The reason for this could be samples strain hardening limit and onset of material yielding at 5 mm feed. In this work, the CBS process was performed on samples at a maximum of two passes. An attempt to perform CBS beyond two passes resulted to samples with developed surface cracks and fractures (see Fig. 3). The cold working process, geometric parameters of the bending roller and constraining blocks could have limited the number of passes and magnitude of induced strain.

## 4 Conclusion

In this paper bending force, strain and hardness of Ti6Al4V severely deformed by CBS process were investigated. Results showed that the magnitude and homogeneity of effective strain, bending force, and hardness were dependent on the number of passes, the feed length and the diameter of the bending roller. The CBS processed samples showed improved homogeneous strain and hardness properties. The study has shown that CBS is a potential continuous SPD process for bulky length metals. However, more research is needed to investigate effectiveness of this process on the microstructural, tensile and other properties. The CBS process can be improved by applying efficient mechanically/electronically controlled mechanisms for bending, flattening, constraining and feeding.

**Acknowledgements** This study was funded by the University of Johannesburg, the Global Excellent Statue (GES-2018) Scholarship.

## References

1. Elias CN, Meyers MA, Valiev RZ, Monteiro SN (2013) Ultrafine grained titanium for biomedical applications: an overview of performance. *J Mater Res Technol* 2(4):340–350. <https://doi.org/10.1016/j.jmrt.2013.07.003>
2. Fernandes DJ, Elias CN, Valiev RZ (2015) Properties and performance of ultrafine grained titanium for biomedical applications. *Mater Res* 18(6):1163–1175. <https://doi.org/10.1590/1516-1439.005615>
3. Polyakov AV, Semenova IP, Valiev RZ (2014) High fatigue strength and enhanced biocompatibility of UFG CP Ti for medical innovative applications. In: IOP conference series: materials science and engineering, vol 63, pp 1–6. <https://doi.org/10.1088/1757-899x/63/1/012113>
4. Segal VM (1995) Materials processing by simple shear. *Mater Sci Eng A* 197:157–164. [https://doi.org/10.1016/0921-5093\(95\)09705-8](https://doi.org/10.1016/0921-5093(95)09705-8)
5. Tsuji N, Saito Y, Utsunomiya H, Tanigawa S (1999) Ultra-fine grained bulk steel produced by accumulative roll-bonding (ARB) process. *Scr Mater* 40(7):795–800. [https://doi.org/10.1016/S1359-6462\(99\)00015-9](https://doi.org/10.1016/S1359-6462(99)00015-9)
6. Valiev RZ, Estrin Y, Horita Z, Langdon TG, Zehetbauer MJ, Zhu Y (2016) Producing bulk ultrafine-grained materials by severe plastic deformation: ten years later. *JOM* 68(4):1216–1226. <https://doi.org/10.1007/s11837-016-1820-6> [Online]
7. Mishnaevsky L et al (2014) Nanostructured titanium-based materials for medical implants: modeling and development. *Mater Sci Eng R Rep* 81(1):1–19. <https://doi.org/10.1016/j.mser.2014.04.002>
8. Estrin Y, Vinogradov A (2013) Extreme grain refinement by severe plastic deformation: a wealth of challenging science. *Acta Mater* 61(3):782–817. <https://doi.org/10.1016/j.actamat.2012.10.038>
9. Lugo N, Llorca N, Cabrera JM, Horita Z (2008) Microstructures and mechanical properties of pure copper deformed severely by equal-channel angular pressing and high pressure torsion. *Mater Sci Eng A* 477(1–2):366–371. <https://doi.org/10.1016/j.msea.2007.05.083>
10. Tsuji N, Saito Y, Lee SH, Minamino Y (2003) ARB (accumulative roll-bonding) and other new techniques to produce bulk ultrafine grained materials. *Adv Eng Mater* 5(5):338–344. <https://doi.org/10.1002/adem.200310077>
11. Polkowski W (2016) Differential speed rolling: A new method for a fabrication of metallic sheets with enhanced mechanical properties. In: Glebovsky V (ed) *Progress in metallic alloys*. InTech, pp 111–126 [Online]. <https://doi.org/10.5772/64418>
12. Mwita WM, Akinlabi ET, Sanusi KO (2018) Performance and prospects of severe plastic deformation for effective biomedical titanium alloys. *J Mod Mater* 5(1):8–23 [Online]. <https://doi.org/10.21467/jmm.5.1.8-23>
13. Edalati K, Lee S, Horita Z (2012) Continuous high-pressure torsion using wires. *J Mater Sci* 47(1):473–478. <https://doi.org/10.1007/s10853-011-5822-z>
14. Hohenwarter A (2015) Incremental high pressure torsion as a novel severe plastic deformation process: processing features and application to copper. *Mater Sci Eng A* 626:80–85. <https://doi.org/10.1016/j.msea.2014.12.041>
15. Gzyl M, Rosochowski A, Boczkal S, Olejnik L, Katimon MN (2016) Producing high-strength metals by I-ECAP. *Adv Eng Mater* 18(2):219–223. <https://doi.org/10.1002/adem.201500363>
16. Qarni MJ, Sivaswamy G, Rosochowski A, Boczkal S (2017) Effect of incremental equal channel angular pressing (I-ECAP) on the microstructural characteristics and mechanical behaviour of commercially pure titanium. *Mater Des* 122:385–402. <https://doi.org/10.1016/j.matdes.2017.03.015>
17. Hai B, Yu L, Lu C, Tieu AK, Li HJ, Godbole A (2016) Special rolling techniques for improvement of mechanical properties of ultra fine-grained metal sheets: a review. *Adv Eng Mater* 18(5):754–769. <https://doi.org/10.1002/adem.201500369>
18. Yu H, Tieu AK, Lu C, Godbole A (2014) An investigation of interface bonding of bimetallic foils by combined accumulative roll bonding and asymmetric rolling techniques. *Metall Mater Trans A* 45(9):4038–4045 [Online]. <https://doi.org/10.1007/s11661-014-2311-4>

19. Wang CT, Fox AG, Langdon TG (2014) An investigation of hardness homogeneity and microstructure in pure titanium processed by high pressure torsion. *Mater Sci Forum* 783–786:2701–2706. <https://doi.org/10.4028/www.scientific.net/MSF.783-786.2701>
20. Shahmir H, Nili-Ahmadabadi M, Langdon TG (2014) Shape memory effect of NiTi alloy processed by equal-channel angular pressing followed by post deformation annealing. In: IOP conference series: materials science and engineering, vol 63, no 1, pp 1–9. <https://doi.org/10.1088/1757-899x/63/1/012111>
21. Fong S, Danno A, Tan MJ, Wah Chua B (2015) Effect of deformation and temperature paths in severe plastic deformation using groove pressing on microstructure, texture, and mechanical properties of AZ31-O. *J Manuf Sci Eng* 137(5):16–26. <https://doi.org/10.1115/1.4031021>
22. Solhjoei N, Varposhty AR, Mokhtarian H, Manian A (2014) A comparative study to evaluate the efficiency of RCS and CGP processes. *Indian J Sci Res* 1(2):563–572
23. Mirsepasi A, Nili-Ahmadabadi M, Habibi-Parsa M, Ghasemi-Nanesa H, Dizaji AF (2012) Microstructure and mechanical behavior of martensitic steel severely deformed by the novel technique of repetitive corrugation and straightening by rolling. *Mater Sci Eng A* 551(November):32–39 [Online]. <https://doi.org/10.1016/j.msea.2012.04.073>
24. Ghazani MS, Vajd A (2014) Finite element analysis of the groove pressing of aluminum alloy. *Model Numer Simul Mater Sci* 4:32–36. <https://doi.org/10.4236/mnsms.2014.41006>
25. Shin DH, Park JJ, Kim YS, Park KT (2002) Constrained groove pressing and its application to grain refinement of aluminum. *Mater Sci Eng A* 328(1):98–103. [https://doi.org/10.1016/S0921-5093\(01\)01665-3](https://doi.org/10.1016/S0921-5093(01)01665-3)
26. Kumar GVP, Niranjana GG, Chakkingal U (2011) Grain refinement in commercial purity titanium sheets by constrained groove pressing. *Mater Sci Forum* 683:233–242. <https://doi.org/10.4028/www.scientific.net/MSF.683.233>
27. Khodabakhshi F, Abbaszadeh M, Mohebpour SR, Eskandari H (2014) 3D finite element analysis and experimental validation of constrained groove pressing-cross route as an SPD process for sheet form metals. *Int J Adv Manuf Technol* 73(9–12):1291–1305. <https://doi.org/10.1007/s00170-014-5919-z>
28. Moradpour M, Khodabakhshi F, Eskandari H (2018) Microstructure–mechanical property relationship in an Al–Mg alloy processed by constrained groove pressing-cross route. *Mater Sci Technol*, 1–15. <https://doi.org/10.1080/02670836.2017.1416906>
29. Thangapandian N, Balasivanandha Prabu S, Padmanabhan KA (2016) Effects of die profile on grain refinement in Al–Mg alloy processed by repetitive corrugation and straightening. *Mater Sci Eng* 649:229–238. <https://doi.org/10.1016/j.msea.2015.09.051>
30. Mwita WM, Akinlabi ET, Sanusi KO (2018) Constrained bending and straightening—a proposed method for severe plastic deformation of metals constrained bending and straightening—a proposed method for severe plastic deformation of metals. In: IOP conference series: materials science and engineering, vol 423, pp 1–6. <https://doi.org/10.1088/1757-899x/423/1/012169>

# Studies on Silica Produced from Original and Firing Rice Husk



Nur Saadah Zainal, Zaleha Mohamad, Mohd Sukri Mustapa,  
Nur Azam Badarulzaman and Abdullah Zulfairis Zulkiffi

**Abstract** Silica can be found in rice husk. The objective of this paper to investigate the composition of silica from the combustion of the rice husk. To get the silica, the rice husk was thoroughly washed and went for a chemical treatment. Then, the firing rice husk took place at temperature of 1000 °C for 2 h. This sample was studied and omit named as a C3. Then, this sample was compared to the original rice husk that has not been fired and has undergone to chemical treatment. The characteristics of material in both samples can be obtained by using Scanning electron microscopy (SEM) and x-ray diffractometer (XRD). The SEM for an original rice husk showed that the surface of the material was uneven, highly roughened and ridged while omit the C3 sample showed the crystallize shape has been formed. The properties of both materials have been showed more specifically by using XRD. The result showed that the silica contained in original rice husk was 67.1% and C3 was 98.7%. Thermogravimetric analysis (TGA) was only tested on sample C3 where the result showed the energy of organic compound lost was at 1000 °C was 0.00217 mg/min.

**Keywords** Rice husk · Firing · Silica · XRD · SEM · TGA

---

N. S. Zainal · Z. Mohamad (✉) · M. S. Mustapa · N. A. Badarulzaman  
Faculty of Mechanical and Manufacturing Engineering, Universiti Tun Hussein Onn Malaysia  
(UTHM), Johor, Malaysia  
e-mail: [zaleha@uthm.edu.my](mailto:zaleha@uthm.edu.my)

N. S. Zainal  
e-mail: [whaddup17@gmail.com](mailto:whaddup17@gmail.com)

M. S. Mustapa  
e-mail: [sukri@uthm.edu.my](mailto:sukri@uthm.edu.my)

N. A. Badarulzaman  
e-mail: [azam@uthm.edu.my](mailto:azam@uthm.edu.my)

A. Z. Zulkiffi  
Nano Siltech Sdn Bhd, Selangor, Malaysia  
e-mail: [zulfairis@kenafshoppe.com](mailto:zulfairis@kenafshoppe.com)

## 1 Introduction

To reduce omit agricultural waste, an organic source is the most environmentally preferable [1]. Aside from the affordability, this feature is particularly sustainable. Appropriately, one of the most practical waste materials in the world omit as of now that has been highly demanded is rice husk due to its high availability [2]. From that total amount, over 97% of the husk was generated in the developing countries, including Malaysia. According to the statistics compiled by the Malaysian Ministry of Agriculture, 408,000 metric tonnes of rice husk are produced in Malaysia each year [3]. Besides, the most significant characteristics of rice husk is lower cost. The production faces a low production cost because of there is no need to revitalize the rice husk [4].

The existence of natural silica omit can be extracted from diverse natural sources such as shell, sand and rice husk omit but among of them, rice husk has a high potential to produce silica after going through a few processes. After that, the contain of silica can be up to more than 80% [5]. Apart from the use of silica in the field of health, silica is also widely used in the development industry. In view of the fact that the surface area of the silica particles affect the mobility of water within concrete, segregation and bleeding of concrete are virtually eliminated [6]. Other than that, benefits inherent in silica concrete allow for custom-tailoring concrete placement methods, such as very high cohesive workability, ability of fluid concrete to hold slope and or long distance pumping of concrete. To gain that percentage, combustion or firing process can be used. Aside from that, omit chemical treatment also could be help to remove the metallic impurities such as iron (Fe), manganese (Mn), calcium (Ca), sodium (Na), potassium (K) and magnesium (Mg) by undergoing treatment with hydrochloric acid (HCl). The chemical treatment and firing could lead to change of microstructure of silica from amorphous to crystalline state [7]. At lower firing temperature, the amorphous can be detected in rice husk ash. The crystallization state of silica can be seen after firing more than 500 °C [8].

## 2 Material and Method

The rice husk has been obtained by Nano Siltech Sdn. Bhd (Selangor, Malaysia). It has been washed with tap water to remove unwanted substances and other contaminants. To produce sample C3, the rice husk was then omit dried out for 48 h under the sun to make it dry completely. Next, the washed rice husk went for the chemical treatment where the rice husk was treated with hot acid at 60 °C with hydrochloric acid at concentration of 0.5 M for 30 min with constant stirring. After the acidic solution was drained off, the rice husk was rinsed with distilled water until it was free from acids. The next process was continued with filtering and drying in air-oven at 110 °C for 24 h. After that, the firing process took place by using furnace at 1000 °C for 2 h with heating rate of 5 °C/min.



Therefore, both sample were finally formed after going through sieving process by passing through 63  $\mu\text{m}$ . Lastly, both samples (original and C3) were distinguished by using Scanning electron microscopy (SEM), X-ray diffractometer (XRD) and Thermogravimetric analysis (TGA) to find the silica obtained [9].

### **3 Characterization**

#### **3.1 Scanning Electron Microscopy (SEM)**

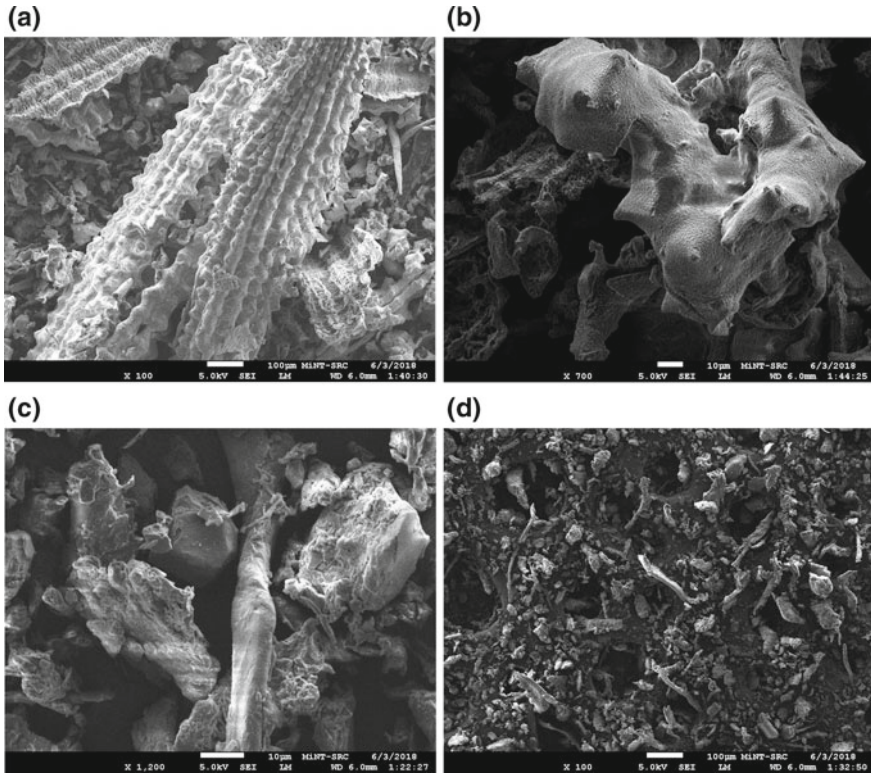
The morphology of original rice husk and C3 samples were confirmed by using scanning electron microscopy (SEM). At first, the samples were coated to keep away from the charging effects and to acquire a sharp and clear image. FESEM JSM 6701F (JOEL) model was used to run the testing. The compositions of both were also obtained by using electron dispersive spectroscopy (EDS) that has been attached with the machine.

#### **3.2 X-Ray Diffractometer (XRD)**

The mineralogical and the element that existed in both samples can be managed by using XRD system. Samples were scanned for 2 h from  $2\theta$  ranging from  $10^\circ$  to  $90^\circ$ . The EVA™ Software was used to analyze and record the structural pattern of the samples.

#### **3.3 Thermogravimetric Analysis (TGA)**

The thermogravimetric analysis was performed on a Linseis Thermobalance simultaneous thermal analysis (STA). The sample involved was only for C3. C3 Sample with weight of 15.1 mg was heated at heating rates of  $5^\circ\text{C}/\text{min}$  from  $20^\circ\text{C}$  to  $1000^\circ\text{C}$ .



**Fig. 1** **a** The micrographs of an original rice husk under the particle distribution indicated a large scale from 0.030 to 100  $\mu\text{m}$ . **b** The micrographs of an original rice husk under the particle distribution indicated a large scale from 0.030 to 10  $\mu\text{m}$ . **c** The micrographs of C3 sample under the particle distribution indicated a large scale from 0.030 to 10  $\mu\text{m}$ . **d** The micrographs of C3 sample under the particle distribution indicated a large scale from 0.030 to 100  $\mu\text{m}$

## 4 Result and Discussion

### 4.1 Scanning Electron Microscopy (SEM) Analysis of Rice Husk

Figure 1a, b show the micrographs of an original rice husk sample at large scale from 0.030 to 10  $\mu\text{m}$  and 0.030 to 100  $\mu\text{m}$ . It was observed that the sample was highly at amorphous silica state. According to Feng et al., the firing temperature definitely has to be more than 700  $^{\circ}\text{C}$  to obtain of silica in crystalline state. The surface of the material also was uneven, highly roughened and ridged.

According to the SEM micrograph of sample C3, Fig. 1c, d show the particle distribution indicated a large scale from 0.030 to 10  $\mu\text{m}$ . All figures show that the

**Table 1** Compound contained in an original rice husk sample

Element	Mass (%)	Compound	Mass (%)
O	40.40		
Si	31.40	SiO <sub>2</sub>	67.10
S	2.80	SO <sub>3</sub>	7.00
K	0.00	K <sub>2</sub> O	0.00
Fe	0.60	Fe <sub>2</sub> O <sub>3</sub>	0.80
Zn	0.60	ZnO	0.80
Other	27.00	Other	24.30
Total	100.00	Total	100.00

crystallized shape has been formed and the surface of the material had a few tiny spots and some of the surface was smoother than the original rice husk. This micrographs also proved that if we fire the rice husk more than this temperature, crystalline phase will change to tridymite which will lead to quartz, which is the form of glass [10].

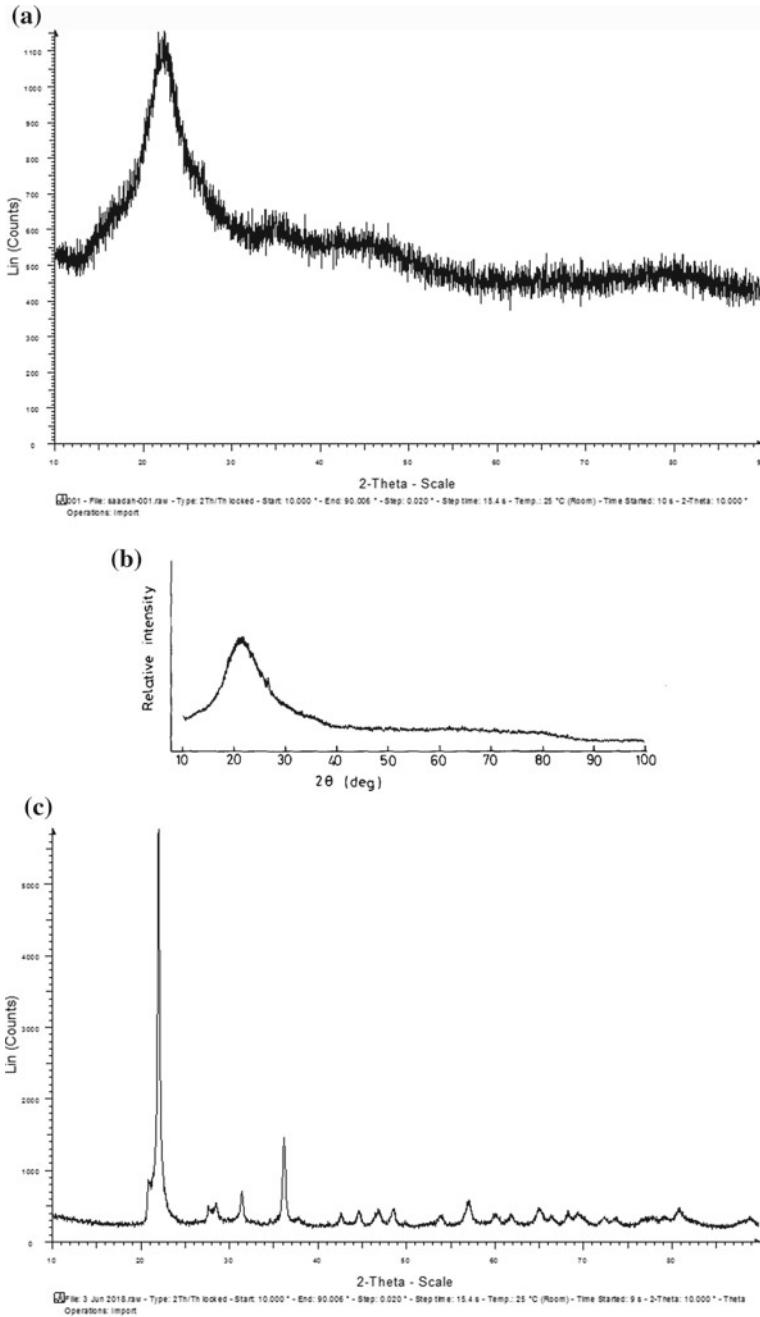
### 4.2 X-Ray Diffractometer (XRD)

Figure 2a shows the pattern performed by XRD for an original rice husk sample. The sample was omit completely at an amorphous state. This was proved by the appearance of single diffuse broad peak at about  $2\theta = 24.00^\circ$ . Other impurities have also not been identified. Figure 2b shows the pattern performed by XRD from Ikram and Akhter for an original rice husk sample. The single diffuse broad peak showed was at about  $2\theta = 22.00^\circ$  [11].

Figure 2c shows the pattern performed by XRD for sample C3. At the temperature of 1000 °C the crystalline structure of silica was formed. This is indicated by the appearance of a few diffuse broad peaks at about  $2\theta = 23^\circ$  to  $81^\circ$ . Figure 2d shows the pattern performed by XRD from [12] for an original crystalline silica sample. The single diffuse broad peak showed at about  $2\theta = 14.00^\circ$ – $110.00^\circ$  [12].

This crystalline structure omit happens when hinders eutectic reaction with silica by removed the alkali metals. Thus, the optimization of combustion temperature of rice husk is necessary to hinder the crystallization of silica [13].

The results in Tables 1 and 2 were obtained using XRD analysis. It shows that the percentage of silica oxide was contained of 67.1% in original rice husk sample while in C3 sample, the percentage of silica contained was 98.7%. It indicates that silica values increased with temperature.



**Fig. 2** **a** XRD patterns of an original rice husk sample. **b** XRD patterns of an original rice husk sample from [11]. **c** XRD patterns of sample C3 at 1000 °C. **d** XRD patterns of sample C3 at 1000 °C from [12]

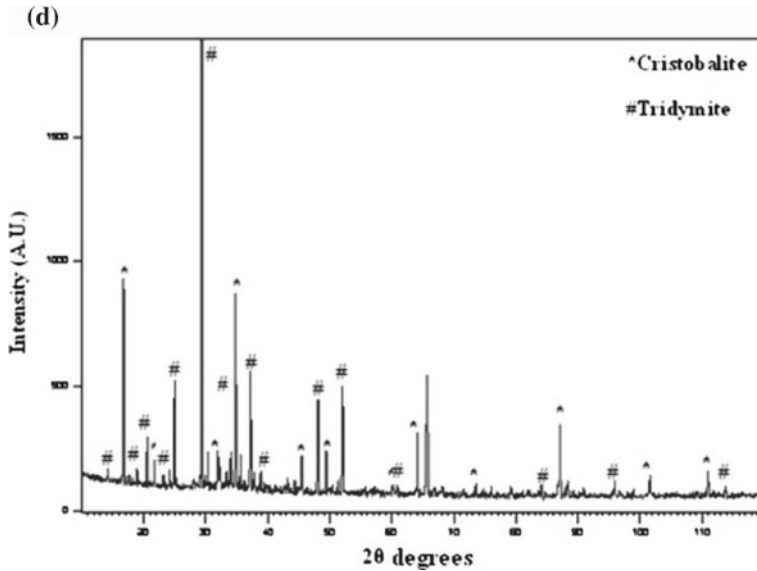


Fig. 2 (continued)

Table 2 Compound contained in C3 sample

Element	Mass (%)	Compound	Mass (%)
O	53.00	Excess	-0.90
Mg	1.30	MgO	2.20
Si	45.70	SiO <sub>2</sub>	98.70
Total	100.00	Total	100.00

### 4.3 Thermogravimetric Analysis (TGA)

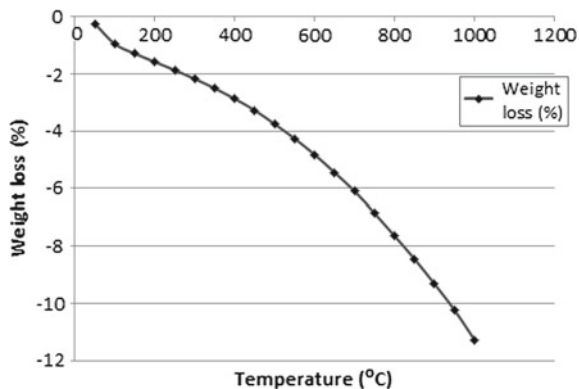
TGA analysis was used to measure the amount of mass change of a material that occur in response to the programmed temperature changes. The changes in the mass can be caused by a variety of processes such as decomposition, degradation, sublimation, vaporization, adsorption, desorption, oxidation, and reduction (Fig. 3).

From Table 3 omit in the first stage, the initial weight loss occurred at the range of 50–150 °C with weight loss of -0.25 to -1.29 mg/°C effects from loss of water and other unwanted substances. The second stage showed a huge weight loss of about -10.23 to -11.27 mg/°C which happened at 950–1000 °C. Both results showed an amorphous state. This process happened because of thermal decomposition of hemicellulose and cellulose; a major organic component in the rice husk. Previous study said that omit 50–360 °C are the least stable temperature as components of rice husk and cellulose decomposed between 275 and 350 °C [14].

**Table 3** Weight loss in sample C3

Temperature (°C)	Weight loss (mg/°C)
50	-0.25
100	-0.95
150	-1.29
200	-1.58
250	-1.87
300	-2.17
350	-2.50
400	-2.87
450	-3.27
500	-3.75
550	-4.26
600	-4.82
650	-5.45
700	-6.10
750	-6.85
800	-7.64
850	-8.45
900	-9.32
950	-10.23
1000	-11.27

Figure 3 shows the graph of weight loss in terms of percentage against the temperature starting from 50 to 1000 °C. From the observation, high amount of percentage of weight loss in sample C3 leads to high temperature.

**Fig. 3** Thermogravimetry analysis (TGA) curves of sample C3

## 5 Conclusions

Through acid treatment of hydrochloric acid (HCl) and firing process at 1000 °C for 2 h, the silica can be obtained from the rice husk. From the analysis, by firing the rice husk at temperature of 1000 °C, the resulted n crystalline state. Through the findings, it was found that high amount of silica in crystalline state could be produced by increasing the temperature of firing and soaking time, and amount of acid during treatment, prior to combustion.

**Acknowledgements** The authors would like to thank University Tun Hussein Onn Malaysia (UTHM), short term Grant No. U961 and Nano Siltech Sdn Bhd for sponsoring this work.

## References

1. Dies RW (2001) Development of a ceramic water filter for Nepal. Thesis, University of British Columbia, Canada
2. Chuah TG, Jumariah A, Azni I, Katayon S, Choong SYT (2015) Rice husk as a potentially low cost biosorbent for heavy metal and dye removal: an overview. *Desalination* 175:305–316
3. Noor Syuhadah S, Rohasliney H (2012) Rice husk as biosorbent: A Review. *Health Environ J* 3(1):89–95
4. Azab AMM (1992) Ph.D. Thesis, Cairo University
5. Onajah A, Amah AN, Echi IM (2012) Polymorphs of crystalline silica from rice husk ash. *J Basic Phys Res*, 73–75
6. Buhler ER (2007) Two decades of ready-mixed high performance silica fume concrete. *NRMCA Concr Tech Forum*, 15–19
7. Boateng AA, Skeete DA (1990) Incineration of rice husk for use as a cementitious material: the Guyana experience. *Cem Concr Res*, 795–802
8. Bakar RA, Yahya R, Gan SN (2016) Production of high purity amorphous silica from rice husk. *Procedia Chem* 19:189–195
9. Feng Q, Sugita S, Shoya M, Yamamichi H, Isojima Y (2002) Thermal decomposition of hydrochloric acid treated rice husk and properties of its product. *J Soc Inorg Mater Jpn* 9:505–510
10. Ismail NAA, Azmi MA, Ahmad S, Taib H (2014) Effect of husk firing temperature on synthesis of silica SiO<sub>2</sub>. In: International conference on x-rays and related techniques in research & industry, 183–184
11. Ikram N, Akhter M (1988) X-ray diffraction analysis of silicon prepared from rice husk ash. *J Mater Sci*, 2379–2381
12. Deshmukh P, Bhatt J, Peshwe D, Pathak S (2012) Determination of silica activity index and XRD, SEM and EDS studies of amorphous SiO<sub>2</sub> extracted from rice husk ash. *Indian Inst Met*, 63–70
13. Mann S (2011) Principles and concepts in bioinorganic materials chemistry. Oxford University Excess on Demand, pp 17–27
14. Shen Y, Zhao P, Shao Q (2014) Porous silica and carbon derived materials from rice husk pyrolysis char. *Microporous Mesoporous Mater* 188:46–76



# Industrial Applications of Bamboo in Ghana



D. R. Akwada and Esther T. Akinlabi

**Abstract** The concerns for the use of environmentally friendly, renewable and sustainable materials have led to the discovery of bamboo as an alternative to timber. Industrial utilisation of bamboo for structural works and biofuel in the country is on the rise. Its use for structural works and biofuel application has attracted many researchers and engineers in the country due to the rapid depletion of forest timbers in recent years. Other factors influencing bamboo industrial application in Ghana include its excellent mechanical properties in compression, tensile, stiffness, and its high load bearing qualities making it an alternative material for timber. Even though there is a high industrial application of bamboo in the country, there is little literature to cover its full industrial usage considering its mechanical characteristics and environmental friendliness. The study aims to investigate the industrial usage of bamboo's in the country through a thorough review of existing literature on the areas and the future trends of this resourceful material. There are several industrial uses of engineering bamboo as a resourceful material, but for the sake of this work, five current areas of its applications are being considered; bicycle, house, furniture, biofuel, laminate lumber and its carvings for some traditional Ghanaian artefacts. The study further looks at the future areas of industrial developments of bamboo resources in the country. With the abundance of bamboo in the country, its industrial use could be developed and use as commercialised sustainable raw material for industries in Ghana not only for construction and biofuel but also for other industrial uses.

**Keywords** Application · Bamboo · Industries · Properties · Sustainable

---

D. R. Akwada (✉) · E. T. Akinlabi  
Department of Mechanical Engineering Science, University of Johannesburg, Johannesburg,  
South Africa  
e-mail: [rich.akwada@gmail.com](mailto:rich.akwada@gmail.com)

© Springer Nature Singapore Pte Ltd. 2020  
M. Awang et al. (eds.), *Advances in Material Sciences and Engineering*, Lecture Notes in Mechanical Engineering,  
[https://doi.org/10.1007/978-981-13-8297-0\\_43](https://doi.org/10.1007/978-981-13-8297-0_43)

## 1 Introduction

There is a high interest in recent years, on the utilisation of bamboo as an alternative material to timber since it is readily available, cheap, excellent mechanical property and require less energy to process culm compared to steel, concrete and wood [1–3]. Its mechanical properties are exceptional, closely correlated with specific gravity, density, having the highest flexibility and weight ratio compared to concrete, steel and timber but light in weight [4]. The strength and the stiffness increase with a specific gravity especially in tensile parallel to the grain [3]. According to Ahmad and Kamke [5], bamboo is an anisotropic material which exhibits an excellent mechanical strength in the three cardinal directions which includes its transverse, longitudinal and radial directions but each varies accordingly.

The bamboo plant is a type of grass with its microstructure being significantly higher than timber, and a heterogeneous consisting of small dense cellulose fibre bonded in a less dense lignin matrix [6, 7]. Bamboo cellulose is arranged sideways the culm length enhancing its flexural, rigidity and tensile strength to the maximum [4]. It belongs to the Gramineae/Procea family, and therefore it is not classified as a tree, but as a grass [1, 6]. It is a renewable and a sustainable plant with about 75 genera and more than 1500 species worldwide [3, 8]. Bamboo matures for harvest within 3–5 years and is regenerative compared to soft and hardwood which takes 30–70 years [1, 4, 6, 9]. Some bamboo species may grow tall in a couple of weeks with a speed of 50 cm while other species surge skyward as fast as 8 inches in one-day and reach a final height of (20–40 m) in Monsoon climates. Bamboo has its nature as a hollow tube with thin walls but harder to join pieces compared to soft and hardwood [3]. Another, characteristics differentiating bamboo culm features from soft/hardwood is that its culms are smooth in their outer skin because of silica presences at the skin due to the absence of bark [6]. Furthermore, bamboo grass is divided into rhizomes and culms being the most two sections the plant with rhizome being the section underground, and the top section which is woody is the culm for industrial wood production.

It releases about 36% more oxygen and sequesters out the same percentages of CO<sub>2</sub> from the air [3, 10]. Bamboo is abundantly found in tropical countries and widely distributed across the globe including Africa, Asia, and America's as it has seen rapid growth for industrial application [3, 7]. Bamboo can be grouped into two (2) distinct types; herbaceous type (food and medicine) and woody type (industrial wood) [11]. Bamboo fibre is a superior competitor to synthetic and other natural fibres as a reinforcing material in both polymer and laminate composite [3]. The study aims to investigate areas of bamboo industrial uses and future areas of application in Ghana as raw material.

### ***1.1 Bamboo as an Alternative Raw Material for the Wood and Biofuel Industries***

The forest reserves in Ghana has suffered an over-exploitation in recent years from wood and timber companies for their processes [12]. Most of these companies in the country have indiscriminately exploited the natural reserves for exports to other foreign countries and the local market. Also, the challenge of a declining timber species in the forest is fast affecting the wood manufacturing firms in Ghana. These challenges and other factors have led to searching for other regenerative and environmentally friendly resources as an alternative raw material to help in sustaining the timber industries in Ghana [13]. The current trend of industrial bamboo application is for structural works and this has raised interest in processing by wood processing firms, Ghana bicycle initiative, building construction, architecture, furniture and biochar firms in Ghana.

For centuries, bamboo has traditionally been used in Ghana for different purposes ranging from being used for building temporal houses and as reinforcement in buildings. Other uses include its applications as furniture, bridges, poles, weapon, fencing, and as a source of fuel, mostly unprocessed. However, its characteristics of being a renewable and sustainable material have drawn the attention of wood processing and biofuel firms in Ghana to explore its potential as a raw material for products. Some bamboo products include strand woven bamboo, ply bamboo, bamboo laminate lumber, bamboo floor tiles and bamboo biofuels (pallet, briquette and charcoal).

### ***1.2 Bamboo as an Industry Engineering Raw Material***

In Ghana, there are about seven common bamboo species known with several other foreign species introduced into the country [2]. Most of these species though were also introduced some decades ago, they are considered as indigenous which include *Bambusa bambos*, *Bambusa vulgaris*, *Bambusa arundinacea*, *Bambusa pervariabilis*, *Oxythenanthera abyssinica*, and *Dendrocalamus strictus* [3]. The foreign species grown on a pilot basis is in selected areas, and these include *Gigantochloa albociliata*, *Bambusa edulis*, *Dendrocalamus brandisii*, *Guadua angustifolia*, *Guadua chacoensis*, *Dendrocalamus strictus* *Dendrocalamus membrenaceous*, and *Dendrocalamus latiflorus* [3]. Furthermore, these species were distributed to some selected institutions and non-governmental organisations to multiply and monitor their growth conditions and adaptability in Ghana. There are high yield varieties of bamboo used for biomass products in the country ranging from the pellet, briquette to charcoal. The bamboo biomass industrial application is an essential energy source for rural dwellers and as a vital source of energy for small firms in rural areas as a renewable energy source. A recent study by Akinlabi et al. [3], indicates a new trend of companies utilising the bamboo culm for manufacturing of bicycles, processing

of the culms by the wood firm into a laminated board, ply bamboo, furniture and as resource materials for polymer composite manufacturing on a small scale using simple equipment. Another area of high industrial application is the building and construction industry for constructing houses [14]. Finally, bamboo could serve as an alternative raw material to timber in industries, applying appropriate technology in its cultivation through to processing [3].

## 2 Methods

The present section outlines a comprehensive review of related published articles to identify the areas of industrial bamboo applications in Ghana. There is a detailed description of the various areas of application and its future trend of application. The various species of bamboo were identified in the country, and their trend of application through evaluations of their mechanical properties was studied.

### 2.1 *Bamboo Mechanical Properties*

Bamboo is a unique non-forest resource with excellent mechanical characteristics in its culms which includes high compressive, shrinkage, resistibility, tensile, strength and elasticity make it a potential multi-functional material for structural applications [3]. The constituents of bamboo culms are aligned axially with its tensile strength being effective on the outer edge of the culm making it a versatile vascular bundle. The mechanical strength of bamboo fibres along the culm height are of varying properties. On the other hand, the compressive strength in bamboo culms increases with height but the bending strength is the inverse to the compressive strength. Furthermore, the shrinkage property of bamboo culms is higher compared to that of hard/softwood when moisture is lost from the culms. The shrinkage process occurs across the entire length of the culms with a shrinkage percentage ranging from (10–17%), and the thickness of the wall is also about 15–18%. The property of high silicate acid by bamboo makes it have an abnormal flame resistibility. The excellent elastic properties of bamboo make it a suitable designing and building material for countries or areas with quakes. Furthermore, bamboo had a relatively low weight hence, easy to transport and utilised across the globe [3, 15].

### 2.2 *Industrial Uses of Bamboo's*

According to Vogtländer [16], industrial utilisations of bamboo range from structure works, biomass, textiles, foods, medicines, pulp and paper making. A study by Akinlabi et al. [3], indicates that wood processing companies in Ghana are shifting

from usage of traditional timber as their raw material to a new trend of utilising bamboo culms. Wood companies are processing laminated bamboo lumber board and furniture on a small scale using simple equipment by chemically treating the culms to enhance its properties. The most innovative industrial application of bamboo in Ghana is in bicycles production. The frames of bicycles are produced from the culm of bamboo, and other accessories such as the tyres, sprockets, chains and the brakes are then joined to make it complete. Trained youth are urged to go into self-entrepreneurship to produce the bamboo bicycles. In another area, engineered bamboo is used for architecture works, furniture, houses, and bridges. The use of bamboo as biofuel is gaining the most significant attention from the industry since it is a sustainable fuel resource. Industrial application of bamboo charcoal, briquette and pellet have been identified as an essential alternative energy source of solid fuel from a non-forest wood in Ghana due to its characteristic of growing at a faster rate and being a cheap material to use.

### **2.2.1 Engineered Bamboo Products**

There are several products that are produced from engineered bamboo culms. The commonly produced items from culms of bamboo in the wood industry include laminate or lumber, and these are produced by splitting the culms into smaller units (Fig. 1a). The split bamboo culms are further processed and used as a reinforcement in thermoplastics or thermosets through other techniques to bond them to form a composite having unique properties. Examples of products and applications of engineered bamboo products include furniture, parts of aerospace and automotive cars, construction of bridges, furniture works, household items, and for structural works, frames of electronic gadgets and automobile works, aerospace industry and so on [3, 17]. The industrial processing of timber can be adapted and used for processing of bamboo (Fig. 1b, c). The bamboo laminates are used for structural applications [18].

### **2.2.2 Bamboo Construction**

Bamboo studied. In the construction industries of Ghana, full culm as well as engineered bamboo, are used as materials for structural members of houses and bridges, ceilings and floor tiles. Applications of whole bamboo culm for construction of canopy and footbridge as well as an engineered bamboo for construction of the house are as shown (Fig. 2a, b, c). Bamboo species in Ghana at present has been developed into bamboo-based panels which are used in structural application such as mat-plybamboo, bamboo lumber board, bamboo particleboard made from bamboo. The bamboo-based composite is a suitable alternative material for prefabrication due to its excellent mechanical property advantages.

Development of panel products based on bamboo strips and fibre polymer is gaining importance in the Ghanaian industry as these panel products resemble wood.

Bamboo laminates and fibre polymers could replace timber in many applications in the construction of houses, and other structural applications.

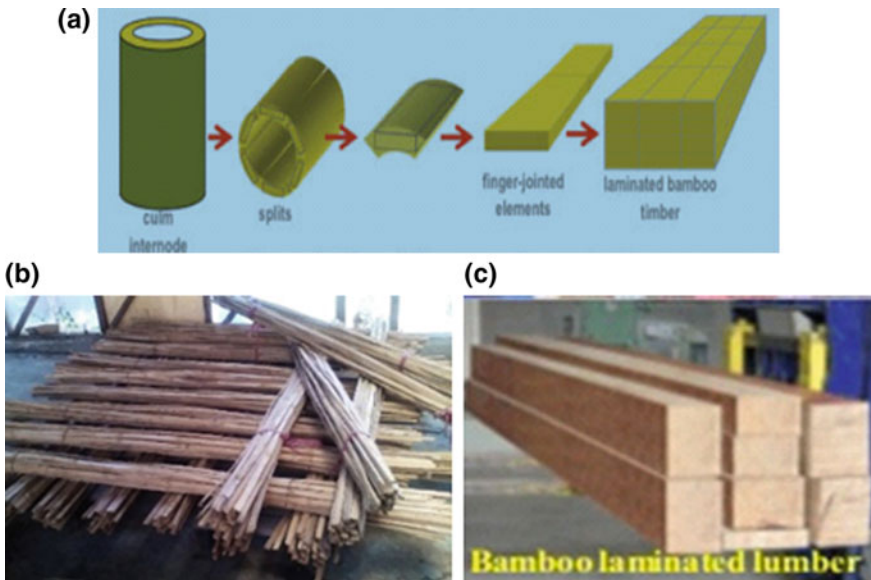
### 2.2.3 Bamboo Furniture

Bamboo usage for furniture works applies to tables and chairs, cupboards, window and door frames where the whole culm or engineered bamboo could be used as shown in (Fig. 3a, c).

### 2.2.4 Bamboo Handicrafts

The adoption and utilisation of engineered bamboo to produce handicraft artefacts in the Ghanaian industrial have been very innovative as bamboo has adopted an industrial raw material for traditional woodcarvers to produce several artworks for the local and the international market (Fig. 4a, b, c).

The application of bamboo as a raw material in handicrafts works has also seen a significant increase due to material availability, its environmental friendliness, being cheap, and biodegradable [23].



**Fig. 1** a Stages of processing bamboo laminate lumber, b Bamboo bundle strips, c Laminate Lumber Source [3, 19]

### 2.2.5 Bamboo Biofuel

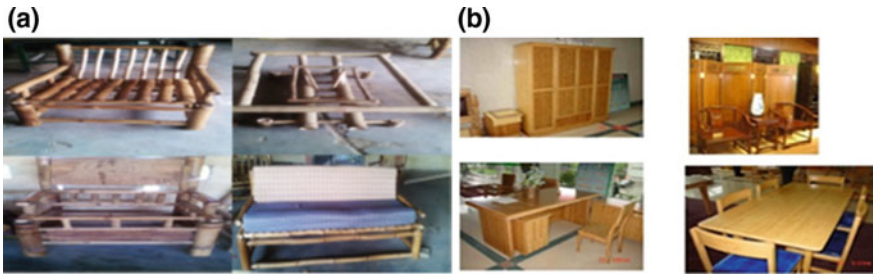
The recent development and utilisation of bamboo as a solid fuel are gaining extensive attention for commercial application in Ghana. The high cost of soft/hardwood for fuel, the prevailing global environmental challenges associated with fossil fuels and the need for a sustainable energy has led to the search of alternative sources of biofuel energy. The quest to have a sustainable biofuel energy has contributed to the development of innovative techniques which are currently being used to produce different types of biofuels. The use of bamboo culm as a biofuel does not require the culms to be fully grown, dry, or has high-moisture content and is transformed into fuels such as charcoal, pellet and briquette through several techniques. These techniques include the pyrolysing bamboo to produce charcoal and briquettes as well as crushing of the culm to produce pellet (Fig. 5a, b, c).

Activated bamboo charcoal and briquette are considered as an efficient biofuel alternative fuel derived from a non-forest plant in the country possessing unique characteristics rate of growing faster. The production of the pellet from bamboo is more economical and viable as it makes use of all its parts without any waste.



**Fig. 2** a Bamboo canopy structure for realisation, b Bamboo walking Bridge, c Bamboo Houses. Source [20, 21]



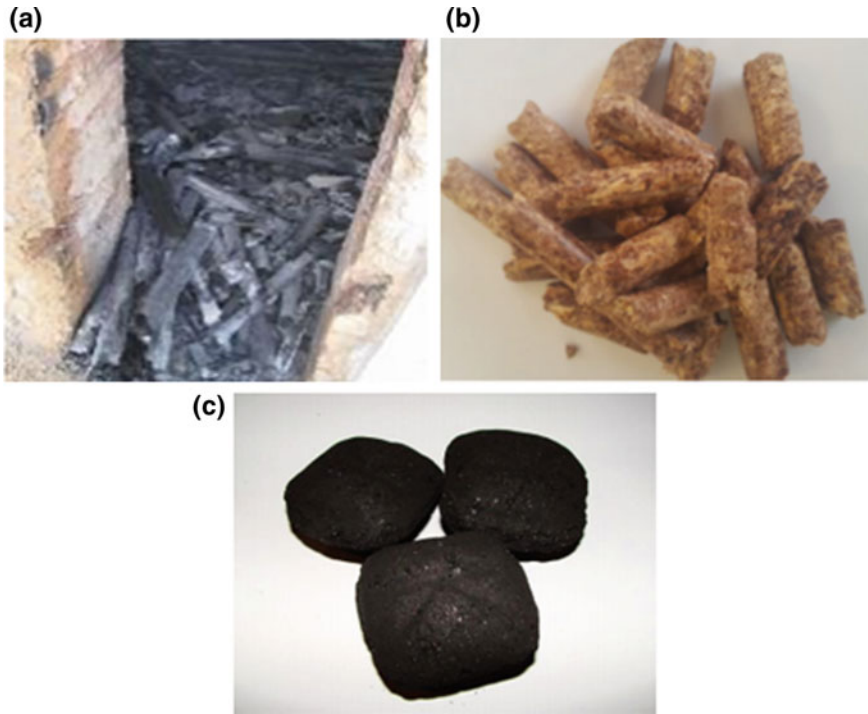


**Fig. 3** a Manufacture of furniture with Whole full bamboo culm, b Manufacture of furniture with engineered bamboo laminate. *Source* [3]



**Fig. 4** a Traditional Stool made from bamboo, b Ekuaba doll made from bamboo, c Oware made from bamboo. *Source* [22]





**Fig. 5** a Bamboo charcoal, b Bamboo pellet, c Ball bamboo Briquette. *Source* [23, 24]

### 2.2.6 Bamboo Application in Electrical and Automobile Industries

The strides in the cultivation of bamboo in recent years in Ghana for manufacturing of bicycles is significant and one of the most innovative utilisations in the country because bamboo is readily available and a cheap natural resource to utilised in the transport industries (Fig. 6 a, b). The bamboo bicycle is less costly in its production using simple machines and tools compared to the conventional steel and alloy produced bicycles. Its production does not require a high cost of electricity, equipment and tools. The utilisation of bamboo for manufacturing of bicycle in the country has focused on empowering local artisans and training of the youth to get into self-entrepreneurship with the aim of supplying the local and international market with the produced bicycles by exporting them across west Africa sub-regions and the world at large. The use of bamboo culms as a raw material for the manufacturing of bicycles, tricycles and other vehicle parts is due to its excellent shock resistance characteristics. The utilisation of bamboo for the manufacturing of bicycles serves as an income generation to rural farmers, artisans, consumers and companies who engages in its plantation and utilisation to produce bamboo products. Commercial bamboo farmers and artisans contribute immensely to the development of this indus-



**Fig. 6** **a** Bamboo bicycle, motorbike, interior and exterior deco of vehicles and tyres. **b** Bamboo used for the case of electronic gadgets phone, keyboard, mouse and monitor. *Source* [3, 25]

try through the process, management, harvesting, and transport which significantly influence the quality of the final manufacturing of bamboo products.

### 3 Future Industrial Developments

The future trend of industrial bamboo utilisation is to explore and develop its full potentials for structural works by developing new materials with different properties and products including strand woven bamboo (SWB), bamboo article board (BPB), bamboo mat board (BMB) through experiments with bamboo composites. Industrial bamboo needs the appropriate treatment and usage of modern equipment to process the above boards. The future utilisation is to extend the application of bamboo to other industrial sectors in the country include the pharmaceutical, shoe, electronic, textile, modern construction, transport, pulp and paper, food and fishing industries with other sectors to be implemented.

Another future initiative is the commercialised bamboo charcoal application as it possesses high absorptive properties which remove toxic and harmful gases and substance from formaldehyde, ammonia, and benzene which accumulates from room air. Activated bamboo char possesses a high volume of porosity which serves as an advantage for its utilisation to decrease humidity as it absorbs moisture from the humid air in a room or an environment. Industrial production of bamboo charcoal is beneficial for commercial utilisation to absorb toxic and accumulated odours in humid spaces like bedrooms, vehicles, bathrooms, living room, kitchens, and prevent fungus growth in shoes as well as in cloths. The activated bamboo carbon has the industrial advantage of binding all toxic gases from an environment where there is a high level of toxic gases including carbon dioxide, benzopyrene, carbon monoxide and nicotine. Bamboo charcoal in a refrigerator help to absorb all ethylene produced from fresh vegetables, fish and meat while in the refrigerator by lengthening their stay and keeping them fresh. Activated bamboo carbon and extracted vinegar from bamboo can be used as an advance ingredient to produce products for skin care.

Activated bamboo carbon has an excellent skin cleansing property. Also, the extracted vinegar from bamboo possesses an excellent skin nourishment as an additive in soaps.

Finally, the future development of bamboo charcoal or activated carbon industrially is to utilise its numerous advantages by putting it close to electrical gadgets which include laptop, computers, radio, television, and mobile phone, to dissipate all electromagnetic waves. Also, its industrial application can be extended to the fishing and farming industry where bamboo charcoal or activated charcoals are fed into the pool to keep the water clean and healthier for the fishes. Also, its industrial application can be considered in crop farming to aid in the enrichment of the soil for gardening and for commercial cultivation of plants as they grow in the soil with significant exposure to air with enhanced moisture conditions of the soil.

## 4 Conclusions

Bamboo has multiple industrial applications by using the whole bamboo or laminated lumber which ranges from:

- i. Building and construction, wood processing, aviation, automobile, electronics, furniture, handcraft, pulp and paper, textiles, food, medicine and many others.
- ii. Its industrial application could either be the use of the whole culm or the engineered bamboo. The engineered bamboo is the processed culm into various laminate lumbers, and fibre reinforced polymer composite use for manufacturing of complex parts and shapes due to the excellent mechanical properties possess by bamboo.

The bamboo application is gradually finding its root into:

- iii. automobile and electrical industry for the exterior, and interior decoration as well as frames of bicycles which is fast growing across the country.

It has been observed that bamboo application in the wood and timber industry of Ghana is on the rise for the manufacturing of various bamboo laminated and polymer products such as:

- iv. Bamboo chipboard or flakeboard, plybamboo, oriented-strand board (OSB), elastomer-based biocomposite, thermoplastic-based bamboo composite and thermoset-based bamboo composite. The traditional wood carving artisans also use bamboo culm or engineered bamboo laminate for their works.

In the biomass industry, bamboo is seen as a sustainable source of fuel with its application in the production of solid fuels such as:

- v. Bamboo charcoal, pellet and briquette are produced through several techniques, using mature, immature, dry, or high-moisture content culms.
- vi. From the study, it has been discovered that industrial bamboo charcoal is a the potential raw material for dissipation of electromagnetic waves from all

electronic gadgets, and as odour remover in refrigerators, cars, washrooms, and as ingredients for skin care products.

Bamboo serves as an alternate industrial engineering material to timber with multiple areas of application and having a high prospect for industrial developments in the future. The current focus of wood or timber companies in Ghana are now adapting to the processing of bamboo laminate lumbers from bamboo culms for structural works. Hence the need for modern equipment for processing.

Finally, the government of Ghana must help to commercialise bamboo industrial usage across the manufacturing and design of structures through scientific research and advanced technology.

## References

1. Kushwaha PK, Kumar R (2013) Studies on water absorption of bamboo-epoxy composites: effect of silane treatment of mercerised bamboo. *J Appl. Polym Sci* 115:1846–1852, 2010. <https://doi.org/10.4186/ej.17.1.61>
2. Akwada DR, Akinlabi ET (2018) Bamboo application in infrastructure development of Ghana. In: Conference on infrastructure development and investment strategies for Africa
3. Akinlabi ET, Anane-Fenin K, Akwada DR (2017) Bamboo: the multipurpose plant. Springer International Publishing, Cham, Switzerland, pp 1–147
4. Akwada DR, Akinlabi ET (2016) Economic, Social and Environmental Assessment of Bamboo for Infrastructure Development. In: 5th International conference on infrastructure development in Africa July in Johannesburg, South Africa
5. Ahmad M, Kamke FA (2005) Analysis of Calcutta bamboo for structural composite materials: physical and mechanical properties. *Wood Sci Technol* 39:448–459
6. American Bamboo Society (2014) Official Website, ABS, BAMBOO, Bamboo.org. (n.d.). Retrieved from <http://www.bamboo.org/index.php> on 12th August 2015
7. Gratani L, Crescente MF, Varone L, Fabrini G, Digiulio E (2008) Growth pattern and photosynthetic activity of different bamboo species growing in a botanical garden of Rome. *Flora* 203:77–84
8. Mulligan H, Ramage M (2013) Tomorrow's material today: from data to design in engineered bamboo. *World Archit* 12:39–43
9. Bayerl T, Geith M, Somashekar AA, Bhattacharyya D (2014) Influence of fibre architecture on the biodegradability of FLAX/PLA composites. *Int Biodeterior Biodegradation* 96:18–25. <https://doi.org/10.1016/j.ibiod.2014.08.005>
10. Vogtländer JG, van der Velden NM, Van der Lugt P (2014) Carbon sequestration in LCA, a proposal for a new approach based on the global carbon cycle; cases on wood and bamboo. *Int J Life Cycle Assess* 19:1323
11. Tara Sen HN, Jagannatha R (2011) Application of sisal, bamboo, coir and jute natural composites in structural upgradation. *Int J Innov Manag Technol* 2(3)
12. Marfo E (2010) Chainsaw milling in Ghana: context, drivers and impacts. Tropenbos International, Wageningen, The Netherlands
13. FAO (2015) Global forest resources assessment. Desk Reference. Food and Agriculture Organisation of the UN, Rome
14. Owusu FW, Tekpetey SL, Appiah-Kubi E, Pentsil S (2014) Bamboo utilisation for greener construction and future in Ghan. In: MSETI/CSIR-FORIG proceedings of a first bamboo colloquium held at CSIR -FORIG, Fumesua, Kumasi, Ghana, 29–30 April 2014
15. Klaus D (2002) Bamboo as a building material, in IL31 Bambus, Karl Kramer Verlag Stuttgart 1992. Contributions from the seminar: design with bamboo, RWTH Aachen SS, 2001

16. Vogtländer JG (2011) Life cycle assessment and carbon sequestration—bamboo products of MOSO international. Delft University of Technology
17. Xiang Z (2010) China's bamboo industry booms for greener economy. China English News. [http://news.xinhuanet.com/english2010/china/2010-07/18/c\\_13402777.htm](http://news.xinhuanet.com/english2010/china/2010-07/18/c_13402777.htm). Global Edition, July 18
18. van der Lugt P (2008) Design interventions for stimulating bamboo commercialization: Dutch design meets bamboo as a replicable model. Delft, Netherlands: VSSD; 2008
19. Yue Y (2012) The bamboo value chain in China and the importance of research for value chain development. In: International centre for bamboo and rattan, SFA China. The 9th WBC, Antwerp, Belgium. 12 Apr 2012
20. Van der Lugt P, Vogtländer J, Brezet H (2009) Bamboo, a sustainable solution for Western Europe design cases, LCAs and land-use. INBAR Technical Report No. 30
21. <https://www.designindaba.com/articles/creative-work/large-bamboo-canopy-sheltering-Ghanaian-artists>. Retrieved on the 25th Aug 2018
22. Asmah AE, Daitey ST, Steiner R (2016) Locally produced laminated bamboo lumber: a potential substitute for traditional wood carving in Ghana
23. Yu D, Tan H, Ruan Y (2011) A future bamboo-structure residential building prototype in China: life cycle assessment of energy use and carbon emission. Energy Build 40(10):2638–2646
24. FORIG (2014) Bamboo biomass energy—a partnership between Ghana, Ethiopia, China and INBAR, First National Forestry Conference 17th September 2014 FORIG-Kumasi, Ghana
25. <https://ourworld.unu.edu/en/riding-towards-sustainable-development-on-bamboo>

# Mechanical and Physical Properties of Bamboo Species in Ghana



D. R. Akwada and Esther T. Akinlabi

**Abstract** The call by United Nations for environmentally friendly, renewable and sustainable materials in recent years has led to the research into bamboo utilisation as an industrial raw material since it possesses exceptional mechanical properties making it a suitable alternative to timber in a structural application. There have been several reported literature types of research on this material for the past three decades. However, in Ghana, little literature on the mechanical and physical properties has been establishing, leading to its industrial neglect for centuries. However, because of the rapid depletion of forest timbers in recent years, many researchers are looking into its potential for industrial uses in the country. The study aims to investigate the mechanical and physical properties of two selected bamboo species most common in Ghana namely *Bambusa vulgaris* (green type) and *Dendrocalamus strictus*. A mechanical and physical test was conducted on the selected species to identify each property. The mechanical testing includes tensile, compression, flexural, and the physical properties include density, aesthetic and morphology to examine the distinctions in their culms. The results showed that the density of the two selected culms species of bamboo for this work shows variation in the range of 0.53–0.79 g/cm<sup>3</sup>. The two species of bamboo culms selected has a structural morphology being hollow in nature and consists of a vessel surrounded by fibres as well as having root system either sympodial or monopodial. The average tensile, compression, and flexural strength of *Bambusa vulgaris* (green type) and *Dendrocalamus strictus* are 253.69, 88.57, 106.07 and 235.59, 84.17, 115.33 N mm<sup>-2</sup>, respectively. The best mechanical performance was found in *Bambusa vulgaris*. The two-bamboo species possess excellent mechanical properties in tensile compression and flexural indicating its application in structural works and an alternative to timber in the country.

**Keywords** Bamboo · Construction · Environment · Mechanical properties · Physical properties

---

D. R. Akwada (✉) · E. T. Akinlabi  
Department of Mechanical Engineering Science, University of Johannesburg, Johannesburg,  
South Africa  
e-mail: [rich.akwada@gmail.com](mailto:rich.akwada@gmail.com)

© Springer Nature Singapore Pte Ltd. 2020  
M. Awang et al. (eds.), *Advances in Material Sciences and Engineering*, Lecture Notes in Mechanical Engineering,  
[https://doi.org/10.1007/978-981-13-8297-0\\_44](https://doi.org/10.1007/978-981-13-8297-0_44)

## 1 Introduction

The Bamboo possesses high mechanical properties with an advantage over other natural composite materials used for structural works in compression, tensile strength, and stiffness making it an alternative material to timber [1]. Bamboo is cheap, readily available, has excellent strength properties and less energy is used in the processing of its culm compared to wood, steel and concrete [1–5]. Bamboo yields good quality fibres which are exciting candidates for structural applications [1]. Bamboo fibre is a superior competitor to synthetic and other natural fibres as reinforcing the material in both polymer and laminate composite [3, 6]. Bamboo mechanical properties are exceptional, having the highest flexibility and weight ratio compared to concrete, steel and timber but light in weight [2]. According to Ahmad and Kamke [7], bamboo culms are anisotropic material with excellent mechanical strength in its 3 cardinal directions varying in the radial, transverse and longitudinal directions. Because of its excellent mechanical properties, there is an increasing interest by wood processing firms and structural engineers from the country regarding its processing and application as a raw material and alternative to timber. In recent years, most culms are used as scaffolds in construction sites, furniture, traditional carvings and construction of houses in its areas of habitation [8]. However, its full application has been undermined because of little knowledge of its mechanical properties, and cultural influence is some of the factors hindering its industrial applications for structural works.

The factors which determine bamboo culm ability to withstand shocks and loads include the moisture content and strength. The required content of moisture content for a bamboo to possess excellent mechanical strength to be utilised as an alternative wood without being susceptible to fungus attack 16% or less [9]. However, in terms of air-dried culms, the appropriate standard for moisture content which help to determine the mechanical strength of the bamboo culms is 12% [1]. Bamboo's durability differs from species as well as age difference. In a study conducted by Ghavami [10], it was stated that lifespan of bamboo is dependent on several factors which includes the techniques of harvesting and the processed methods. Those bamboo culms which are treated with or without chemicals can have a product's lifespan up to approximately 15–20 years or more depending on where its application functions but with the treated culms, it can stay up to 50 years or more depending on where it is applied [10]. Bamboo mechanical strength dependent factors such as age differences, species type, culms diameter and thickness of culm wall as species. Bamboo culms suitability as an industrial engineering material for structural works is determined by the type of species after harvesting. Bamboo harvested at a matured age possesses the most exceptional strength and is suitable for high load bearing components. Furthermore, the compressive strength of bamboo culms increases with respect to its height which runs through the inner part through to the outer section of the plant culms [1, 11]. This study aims to explore the bamboo culm mechanical and physical properties of the various species that could be convenient for industrial utilisation. More so, due to call by the centre for scientific research institute of Ghana and the engineers' association

to conventionalise bamboo in the country for commercial usage, a national code and standards are required for its utilisation as a structural engineering material.

## 1.1 Bamboo

The bamboo plant is classified as a grass and not tree belonging to the family of Gramineae/Process [1]. The transverse structure of a culm is determined anatomically by the counts of several vascular bundles, shape, and size arrangement [1]. Bamboo culm is a hollow tube with thin walls made up of vascular bundles shape also being hollow [12]. The culm's tissue comprises of parenchyma and vascular bundles made of vessels and fibre. The culms of bamboo obtain their mechanical strengths such as flexural, compressive, tensile and rigidity from the arrangement and direction of cellulose fibres arranged along the length of the culm [5]. Bamboo possesses two unique characteristics making it distinct from other grasses in this family. Firstly, it has a hardback which serves as a protective agent against any external forces though it has not barked [13]. Lastly, the existence of silica properties smoothens the bark coating of the bamboo culm [13]. The bamboo plant is a type of grass with its microstructure being significantly more than timber, and a heterogeneous consisting of small dense cellulose fibre surrounded in a less dense lignin matrix [3, 14].

Bamboo culms mature for harvest within 3–5 years and are regenerative compares to soft and hardwood which takes 30–70 years [5, 13, 15, 16]. Some bamboo species may grow tall in a couple of weeks with a speed of 50 cm while other species grows as fast as (2/3) foot in a day and reach a final height of (20–40 m) in Monsoon climates. Bamboo is a renewable and sustainable plant with about 75 genera and more than 1500 species worldwide [1, 17]. It releases about 36% more oxygen and sequesters tons of CO<sub>2</sub> from the atmosphere [3, 8, 18]. It is abundantly found in tropical countries and widely distributed across the globe including Africa, Asia and Latin and South America where the demand for its industrial application has seen rapid growth [1, 15]. Bamboo is distributed across the ten regions of Ghana with the tropical zone inhabiting the highest quantity of species which occurs naturally or is being cultivated commercially [8]. Bamboo can be grouped into two (2) distinct types; herbaceous type (food and medicine) and woody type (industrial wood) [5].

## 2 Materials and Methods

### 2.1 Materials

The selected bamboo species for the study are *Bambusa vulgaris* (green type), and *Dendrocalamus strictus*, which were harvested from Central, Western, Ashanti, and Brong-Ahafo regions of Ghana. The species were water treated and air-dried for one



month to attain a moisture content of 12% and further treated for furniture? or other artefacts using boric acid and gasoline, which help to increase the lifespan of bamboo and to give it resistance against fungus attack.

## ***2.2 Mechanical Test***

The test specimen of bamboo species was cut into average length, width and thickness from the culm. The three tests conducted include tensile, compression and flexural using ISO 22157 part 1 [2019]. A universal testing machine (Instron 3366) 10 kN was used for the tensile, compression and flexural strength for the two species of bamboo.

### **2.2.1 Tensile Test**

Tensile tests specimen was cut and prepared in accordance with ISO 22157 Part 2 [19] in a ‘dogbone’ shape extracted from the bamboo culm. The samples for the experiment were radially cut from the culms to acquire the dogbone like shape in order not to distort the fibre orientation which is parallel to culms. A load of 0.01 mm/s could tension the load subjected under it to determine the tensile strength in the culms. Figure 2a illustrates the tensile test setup procedures to follow when testing for samples with fibre orientation arranged parallel to bamboo’s grain.

### **2.2.2 Compression Test**

Compression test was conducted using ISO 22157 Part 2 [20] involving the two selected species samples, subjected to a constant compressive load at a steady rate of 0.01 mm/s with maximum load reading being recorded.

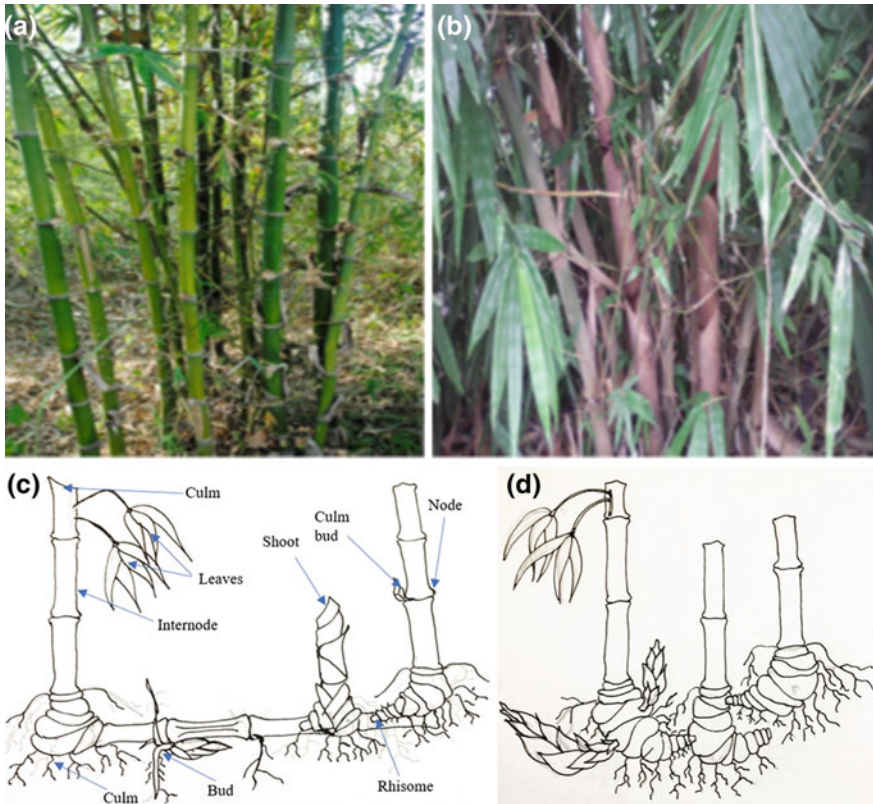
### **2.2.3 Flexural Properties**

The flexural test was carried out according to ISO 22157 Part 2 [20] using the universal testing machine at the same crosshead speed.

## ***2.3 Physical Properties***

Morphologically, bamboo species have similar anatomy made up of two sections, the upper section (culms) and the bottom (rhizome). The bottom part which is known as ‘rhizome’ is the part beneath the soil, and the top section which is the culm com-

prises of the node, internode, branch, sheath, leaves, flowers, and seeds. Bamboo culm walls thickness and fibre density have significant effects on the plant as the thickness gets reduced with respect to height while fibre density increases. Bamboo plant species are distinguishable by their essential topographies, the nature of culm growth, culm colour, leaves and diameter variation (Fig. 1a–d). Furthermore, morphologically bamboo can be distinguished by their root system either sympodial (clumpy) or monopodial (running) respectively [21]. However, the most dominant species colour is green, with others being yellow, purple-brown and striped. Bamboo culms properties have a direct correlation with its density and also dependent on the fibre contained within the culm, varying (0.5–0.9). However, this properties are higher within the outer layer of culm wall than the inner layer. Density affects the properties of the culms whereby it has also been established that density gets highest starting from base of culm to the top with the maximum density at nodes. The less the presences of parenchyma cells in the culm indicates of a higher density and mechanical strength within the culms more especially at the nodes of the culms.



**Fig. 1** a, b Variations in culm colour and leaves, c, d clumpy culm and running culm

### 3 Results and Discussions

#### 3.1 Tensile Test

The tensile test parallel to culm's grain was performed on the sample species, with each sample of specimens having been treated and with water, gasoline and allowed to season to the required air drying. Results of the tensile strength between the two-selected species *Bambusa vulgaris* and *Dendrocalamus strictus* are shown in Tables 1 and 2, like 250.7, 261.16, 249.20 and 243.88, 227.55, 235.35 N/mm<sup>2</sup> respectively. The maximum and higher average strength of *Bambusa vulgaris* culm was obtained in the middle portion with strength values of 261.16 N mm<sup>-2</sup> while *Dendrocalamus strictus* recoded the lowest strength as 227.55 N mm<sup>-2</sup>. The results of the two-bamboo species exhibited similar tensile strength with the highest tensile strength result occurring at the top portion of the culms.

From the two-species used for this study, there is a similarity in the failure of both species after the tensile test, and this is shown in Fig. 2, indicating tension and shear parallel to the grain of the culm.

In conclusion, *Bambusa vulgaris* has a higher overall average tensile strength of 253.69 N mm<sup>-2</sup> with *Dendrocalamus strictus* having the least 235.59 N mm<sup>-2</sup>.

#### 3.2 Compression Test

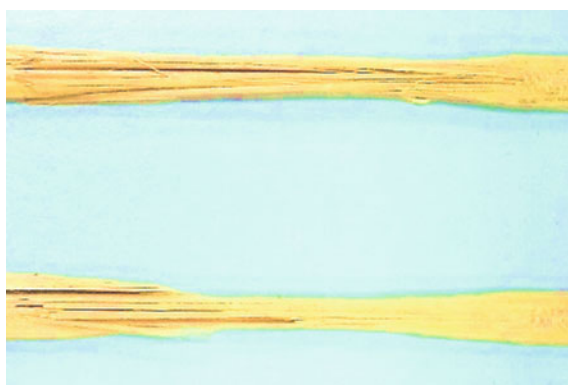
The compressive strength test of selected specimens of bamboo was presented in Table 3. The test was conducted parallel to culm's grain on the selected sample species, with each sample of specimens having been treated with water and chemicals

**Table 1** Data obtained from tensile tests of *Bambusa vulgaris*

Culm part	Samples	Area (mm <sup>2</sup> )	Tensile strength (N mm <sup>-2</sup> )	Average tensile strength (N mm <sup>-2</sup> )
Top	1	60.01	249.01	250.7
	2	60.42	251.31	
	3	60.30	251.79	
Middle	1	64.10	262.09	261.16
	2	63.27	260.28	
	3	63.91	261.12	
Bottom	1	68.91	247.99	249.20
	2	70.60	248.73	
	3	69.23	250.87	
The overall average tensile strength of <i>Bambusa vulgaris</i>				<b>253.69</b>

**Table 2** Data obtained from of *Dendrocalamus strictus*

Culm part	Samples	Area (mm <sup>2</sup> )	Tensile strength (N mm <sup>-2</sup> )	Average tensile strength (N mm <sup>-2</sup> )
Top	1	91.22	239.91	243.88
	2	91.11	241.07	
	3	90.33	250.65	
Middle	1	98.11	233.39	227.55
	2	97.57	228.94	
	3	98.76	220.32	
Bottom	1	123.11	220.63	235.35
	2	130.29	242.08	
	3	128.22	243.35	
The overall average tensile strength of <i>Dendrocalamus strictus</i>				<b>235.59</b>

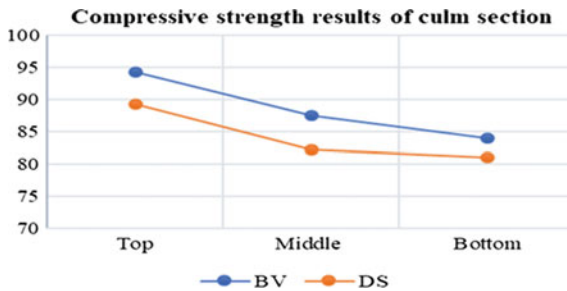
**Fig. 2** Shows nature of failure in culm specimen after tensile test

to prevent it from fungi attacks as well as being allowed to season airy to the required 12% moisture content. Results between the two-selected species *Bambusa vulgaris* and *Dendrocalamus strictus* are recorded in Table 3. It has been observed from Table 3 that average compressive test results of *Bambusa vulgaris* (BV) and *Dendrocalamus strictus* species was high at the top section, and the middle portion was next with the high values with the least being obtained at the bottom as shown in Fig. 3. The results obtained for both species show low and weak values at the bottom section of the culms when compare to those taken from the top portion. The distinction in the values of the culms along the length is an indication to show that compressive strength increases with height with the top section having the maximum strength and the bottom with the least.

The outcome of these results is due to the variation in culms properties along the length which can be related to many vascular bundles that are present in the various sections of the culms. It is because transporting of plant nutrients/food to

**Table 3** Data obtained from the compressive test on both species of bamboo

Culm part	Samples parts	Area (mm <sup>2</sup> )	Average compressive strength (N mm <sup>-2</sup> )	Overall average compressive strength (N mm <sup>-2</sup> )
<i>Bambusa vulgaris</i>	Top	3632.2	94.28	88.57
	Middle	5027.2	87.45	
	Bottom	5809.6	83.98	
<i>Dendrocalamus strictus</i>	Top	5281.7	89.32	84.17
	Middle	5675.2	82.16	
	Bottom	6362.6	81.04	



**Fig. 3** Shows the compression strength at various sections of the culm

all parts of the bamboo is performed by the vascular bundles during plant lifetime. The outcome from the experiment on both species shows that indirectly, the vascular bundle influences the content of fibres in the culms either decreasing or increasing with the former occurring at the bottom due to increment in size of the vascular bundle at the base. In conclusion, *Bambusa vulgaris* has a higher overall average compressive strength of 88.87 N mm<sup>-2</sup> with *Dendrocalamus strictus* having the least.

### 3.3 Flexural Test

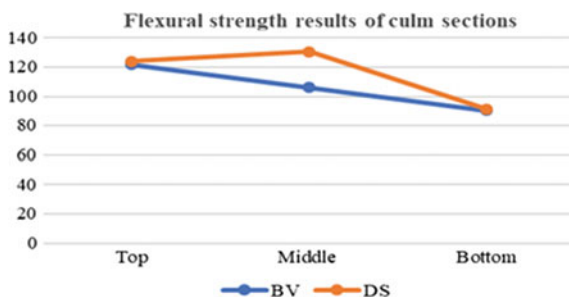
The data of the flexural strength test was reported in Table 4 for the selected sample specimen. The results revealed that increased flexural strength goes with an increase in vascular bundles present in the section of the culm.

It was observed from Table 4, that the average flexural strength of *Dendrocalamus strictus* (DS) was high at the middle section as 130.56 N mm<sup>-2</sup>, followed by the top and the bottom being the least as shown in Fig. 4. From the two-species used for this study, there is a similarity in the failure of both species after the flexural test, and this is shown in Fig. 5, indicating flexibility and shear parallel to the grain.

**Table 4** Flexural strength of bamboo species

Culm part	Samples parts	Area (mm <sup>2</sup> )	Average flexural strength (N mm <sup>-2</sup> )	Overall average flexural strength (N mm <sup>-2</sup> )
<i>Bambusa vulgaris</i>	Top	70	121.71	106.07
	Middle	98	106.07	
	Bottom	101.50	90.42	
<i>Dendrocalamus strictus</i>	Top	72	124.11	115.33
	Middle	72.8	130.56	
	Bottom	112	91.31	

**Fig. 4** Shows the flexural strength of BV and DS



**Fig. 5** Shows the nature of failure in culm after flexural test of the two species



In the case of *Bambusa vulgaris*, the highest flexural strength is from the top, middle and the bottom as the least. Specimens taken from the bottom of both culms show slight weakness. In conclusion, *Dendrocalamus strictus* has a higher overall average flexural strength of 115.33 N mm<sup>-2</sup> with *Bambusa vulgaris* having the least at 106.07 N mm<sup>-2</sup>.

## 4 Conclusions

From the derived experimental data on the selected bamboo species from Ghana, it has been determined that both *Bambusa vulgaris* and *Dendrocalamus strictus* exhibited excellent test results in mechanical and physical properties and these are outlined below:

- i. Both species have their culm morphology being green in colour.
- ii. Both species have their roots system being sympodial (clumpy) in nature.
- iii. Both species increases in mechanical strength when moisture content decrease in their culm to 12% dryness.
- iv. As density increases, their mechanical properties also increase in the culm.
- v. The selected bamboo species considered for the study *Bambusa vulgaris* and *Dendrocalamus strictus* presented in this study has exhibited excellent mechanical strength in tensile, compressive and flexural.
- vi. *Bambusa vulgaris* show an overall tensile, compressive and flexural strength of 253.69, 88.57, and 106.07 N mm<sup>-2</sup>, respectively.
- vii. *Dendrocalamus strictus* species shows an overall tensile, compressive and flexural strength as 235.59, 84.17, and 115.33 N mm<sup>-2</sup>, respectively.
- viii. The data obtained from the various mechanical test accounts for an excellent mechanical strength property for both selected species with other attributes making it an environmentally friendly and suitable material for green construction.
- ix. From experimental results gathered with the mechanical characterisation, *Bambusa vulgaris* species has outstanding mechanical properties possessing excellent compressive and tensile strength compared with *Dendrocalamus strictus* having the highest flexural strength.
- x. According to Akinlabi et al. [1], the mode failure in bamboo culms is distinct from soft/ hardwood which possesses knots and rays which through the length of its stem can withstand less stress.
- xi. The tensile and compressive strength of a bamboo can be compared with steel and wood respectively though slightly lower in terms of absolute outcome.
- xii. The test results for the selected species will be useful to the structural engineers for further analysis and design of buildings in the country.
- xiii. The outcome of results of both *Bambusa vulgaris* and *Dendrocalamus strictus* species shows an excellent mechanical strength giving an indication that their application in structural development practically is suitable and therefore they are recommended for commercial structural engineering industries in Ghana.
- xiv. Bamboo has several advantages over other conventional material as it enhances the conservation of the environment and has the prospects of serving as infrastructural material and alternative in the constructional and building industries of Ghana as well as the West African sub-region.

## References

1. Akinlabi ET, Anane-Fenin K, Akwada DR (2017) Bamboo: the multipurpose plant. Springer International Publishing, Cham, Switzerland, pp 1–147
2. Akwada DR, Akinlabi ET (2018) Bamboo application in infrastructure development of Ghana. In: Conference on infrastructure development and investment strategies for Africa, Livingstone, Zambia, DII-2018, 14–16 July
3. Dittenber DB, Gangarao HVS (2012) A critical review of recent publications on the use of natural composites in infrastructure. *Comput Part A Appl Sci Manuf* 43:1419–1429
4. Chattopadhyay SK, Khandal RK, Uppaluri R, Ghoshal AK (2011) Bamboo fibre reinforced polypropylene composites and their mechanical, thermal, and morphological properties. *J Appl Polym Sci* 119:1619–1626
5. Mulligan H, Ramage M (2013) Tomorrow's material today: from data to design in engineered bamboo. *World Archit* 12:39–43
6. Vogtländer DR, van der Velden NM, van der Lugt P (2014) Carbon sequestration in life cycle assessment, a proposal for a new approach based on the global carbon cycle; cases on wood and bamboo. *Int J Life Cycle Assess* 19:1323
7. Ahmad M, Kamke FA (2005) Analysis of Calcutta bamboo for structural composite materials: physical and mechanical properties. *Wood Sci Technol* 39:448–459
8. Akwada DR, Akinlabi ET (2015) Bamboo used in construction—how sustainable is it? In: International conference on infrastructure development and investment strategies for Africa, Livingstone, Zambia, DII-2015
9. Wakchaure MR, Kute SY (2012) Effect of moisture content on physical and mechanical properties of bamboo. *Asian J Civ Eng (Building Housing)* 13(6):753–763
10. Ghavami K (2008) Bamboo: low cost and energy saving construction materials. In: International conference on modern bamboo structures, no 8
11. Sattar MA, Kabir MF, Bhattacharjee DK (1990) Effect of age and height position of muli (*Melocanna baccifera*) and borak (*Bambusa balcooa*) on the physical and mechanical properties. *Bangladesh J Forestry Sci* 19(1 and 2):29–38
12. American Bamboo Society (2014) Official website, ABS, BAMBOO, Bamboo.org. Retrieved from <http://www.bamboo.org/index.php> on 12 Aug 2015
13. Waite M (2009) Sustainable textiles: the role of bamboo and the comparison of bamboo textile properties. *J Text Apparel Technol Manage* 6(2):1–21
14. Gratani L, Crescente MF, Varone L, Fabrini G, Digiulio E (2008) Growth pattern and photosynthetic activity of different bamboo species growing in a botanical garden of Rome. *Flora* 203:77–84
15. Kushwaha PK, Kumar R (2010) Studies on water absorption of bamboo-epoxy composites: effect of silane treatment of mercerised bamboo. *J Appl Polym Sci* 115:1846–1852. <https://doi.org/10.4186/ej.17.1.61>
16. American Bamboo Society, ABS (2002) Bamboo as a raw material. [www.Bamboo.org/generalinfoPages/BambooAsMaterial.html](http://www.Bamboo.org/generalinfoPages/BambooAsMaterial.html)
17. Akwada DR, Akinlabi ET (2016) Economic, social and environmental assessment of bamboo for infrastructure development. In: 5th international conference on infrastructure development in Africa July in Johannesburg, South Africa
18. Tara Sen HN, Jagannatha R (2011) Application of sisal, bamboo, coir and jute natural composites in structural upgradation. *Int J Innovation Manage Technol* 2(3)
19. ISO/TR. 22157-1 (2004) Bamboo—Determination of physical and mechanical properties—Part 1: requirement, pp 1–8
20. ISO/TR 22157-2 (2004) Bamboo—Determination of physical and mechanical properties—Part 2: laboratory manual, p 28
21. Sharma B, Gattoo A, Bock M, Mulligan H, Ramage M (2014) Engineered bamboo: state of the art. In: Proceedings of ICE construction materials, 1–11 Apr



# In-Process Cooling in Friction Stir Welding of Aluminium Alloys—An Overview



Olatunji P. Abolusoro and Esther T. Akinlabi

**Abstract** Friction stir welding (FSW) is a welding technique that has found extensive use in the joining of aluminium alloys for many applications. During FSW welding, severe plastic deformation occurs due to the stirring actions of the tool which generates heat on the workpiece. The thermal cycle set up at the weld region causes deterioration of precipitates by coarsening or dissolutions. The resultant mechanical properties of the weld region, therefore, become lesser than that of the base metal. Efforts have been made by various researchers to address this challenge through in-process cooling using different cooling fluids such as cryogenic, slush ice, water, compressed air and liquified nitrogen to control the temperature during FSW so as to enhance the mechanical behavior of the welds. The in-process cooling approach was generally reported to have improved the mechanical and corrosion behavior of welded joints as a result of fine and stable microstructures obtained at the weld zone. This paper reviewed the research efforts in this direction. The authors and their investigations and findings have been briefly summarized and the influence of these cooling media on tensile, microstructures and corrosion behavior has been highlighted. The overall aim of this review paper is to provide comprehensive requisite knowledge of the current state of research on in-process cooling in FSW of aluminium alloys with a view to exposing further areas of research interest in this aspect of FSW.

**Keywords** Aluminium · Friction stir welding · In-process cooling · Microstructures · Tensile strength

---

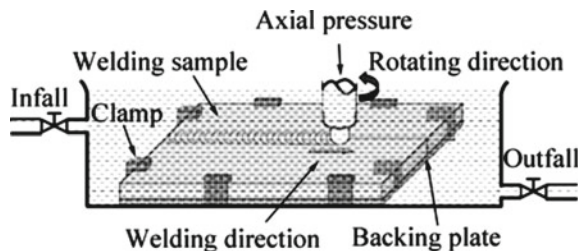
O. P. Abolusoro (✉) · E. T. Akinlabi  
Department of Mechanical Engineering Science, University of Johannesburg, Kingsway Campus,  
524, Auckland Park, Johannesburg, Gauteng 2006, South Africa  
e-mail: [abolusoroolatunji@yahoo.com](mailto:abolusoroolatunji@yahoo.com)

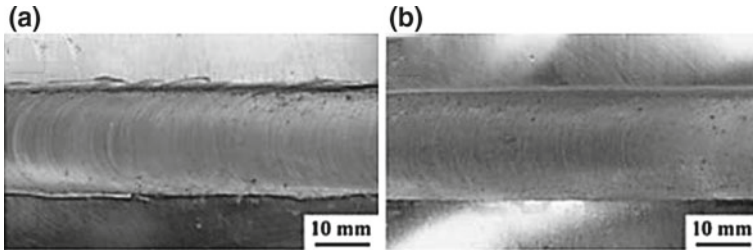
© Springer Nature Singapore Pte Ltd. 2020  
M. Awang et al. (eds.), *Advances in Material Sciences and Engineering*, Lecture Notes in Mechanical Engineering,  
[https://doi.org/10.1007/978-981-13-8297-0\\_45](https://doi.org/10.1007/978-981-13-8297-0_45)

## 1 Introduction

Friction stir welding is a modern solid-state welding method that started in 1991 at the welding institute in UK. It has been used extensively to weld low-temperature alloys such as aluminium, magnesium copper etc. Recent development has seen this welding technology being used to join steel, plastics, and other materials. However today, it has been predominantly used to join aluminium alloys. FSW involves a rotating tool made up of shoulder with a protruded part known as the pin. During welding, the tool is pressed against the workpiece surface to be joined. As the tool rotates and traverses the workpiece joint surface, heat is produced by the frictional movements of the rotating tool on the workpiece. This heat softened the material interface and plastically deformed the workpiece joint region and melted them together. Although FSW heat input is generally not high, the thermal cycle that occurred during welding could lead to coarsening or dissolution of grain precipitates [1–8]. The consequence of this grain reorientations is that the three major zones of the weld i.e. nugget zone (NZ), heat affected zone (HAZ) and thermo-mechanically affected zone (TMAZ) become softened thereby lowering the tensile strength of the joints than those of the base materials. Therefore, for the joints to be more efficient, temperature control during the welding becomes imperative. Various cooling media to control temperature during FSW of aluminium alloys have been investigated by researchers. Such media apart from the natural cooling air, include water, liquid nitrogen, cryogenic, compressed air and ice. In process cooling in friction stir welding with water can be done by immersing the rotating tool and the workpiece in water as shown in Fig. 1 [3–6, 8–13]. In some cases, the water may be sprinkled between the rotating tool and the workpiece interface [7, 12, 14, 15]. The temperature control achieved through in-process cooling during friction stir welding affects the microstructural evolutions and grain refinement of the joint. These changes considerably depend on the type of cooling media employed [10]. Figure 2 shows typical surface morphologies of in-process cooling in friction stir welding of 2014Al-T6 using the same process parameter for air cooled and water-cooled welds. In-process cooling in friction stir welding of aluminium alloys have recently attracted the attention of researchers in view of the importance of aluminium as one of the most widely used engineering materials in industries. This paper reviewed the available literatures on in-process cooling of friction stir welded joints of aluminium alloys.

**Fig. 1** Schematic diagram of underwater friction stir welding [3]





**Fig. 2** Surface morphologies of FSW 2014Al-T6 using the same process parameter. **a** Air cooled weld, **b** water cooled weld [10]

## 1.1 Investigations and Findings

Investigations and findings from various authors have been summarized in this section. Table 1 contains various authors, their focus, findings and conclusions on in-process cooling in FSW.

## 2 Summary

Based on the focus, findings and conclusions of the authors as highlighted in Table 1, the cooling effects of the various media considered on tensile strength, hardness, microstructures and corrosion can be summarized below.

### 2.1 Cooling Effects on Tensile Strength

Most of the effects of water cooling in FSW investigated were carried out by submerged or underwater welding [3–6, 8–13] however, very few cases of water being sprayed on the tool-workpiece interface and water heat sink were also reported [7, 12, 14, 15]. Most of the author's findings agreed and confirmed that tensile strength is enhanced by in-process water cooling. Other cooling methods like compressed air and liquid nitrogen, slush ice, rock salt with ice were also reported to enhance tensile strength in FSW of aluminium alloys. However, water and ice were reported to perform better than the other cooling media [14, 18]. This was generally attributed to the reduction of heat generated due to the cooling media during the welding which led to discontinuous smaller grain sizes of precipitates and narrow heat affected zones. Although many of the author's findings and conclusions followed this trend but there are few reports on tensile behavior of underwater FSW of some aluminium alloys on the contrary [10].

**Table 1** Summary of findings on in-process cooling in friction stir welding of aluminium alloy

References	Authors	Focus	Findings and conclusions
[9]	N. D. Ghetiya and K. M. Patel	FSW of AA2014-T4 aluminium alloy fully immersed in water. Experiment and modeling	Box-Behnken experimental designs and ANOVA (Analysis of variables) used agreed with the experimental outcome of improvement of 75% in the tensile strength of base materials of the friction stir aluminium alloy fully immersed in water. This was attributed to discontinuous smaller grain sizes of precipitates
[10]	Z. Zhang, B. L. Xia, Z. Ma	FSW of 2014-T6 aluminium alloy done underwater and air-cooling conditions	Low hardness zone was observed in both cooling methods at the advancing and retrieving sides of the weld. Tensile strength of the natural air-cooled welds increased as the welding speed goes higher, however, cooling underwater has no influence on the tensile and hardness properties of the welds
[3]	H. J. Liu, H. J. Zhang, Y. X. Huang, L. Yu	Mechanical behaviour of submerged friction stir welding of 2219 aluminium alloy	Improvement of tensile strength was observed, however, plasticity degenerates. Hardness was lower in the submerged welding at the nugget zone but greater in other zones
[14]	C. Sharma, D. K. Dwivedi, P. Kumar	Tensile behavior of friction stirs welded AA7039 with natural air-cooling during welding and cooling employing water, liquified nitrogen and compressed air	Hardness was higher with the three in-process cooling media. However, water cooling performed better in tensile strength than the other two cooling methods and those without in-process cooling. All the cooling processes generally alter the fracture locations to nugget zone from heat affected zone

(continued)

**Table 1** (continued)

References	Authors	Focus	Findings and conclusions
[4]	H. J. Zhang, H. J. Liu, L. Yu	Cooling effects of water on heat affected zone of underwater FSW of 2219-T6 aluminium alloy	Water improves the hardness of the HAZ. This was due to a reduction in precipitate hardening and narrow zone as a result of the cooling effects of water
[5]	Y. Zhao, K Yan, S. Jiang, S. Yang, Z. Lu	Under water and air-cooling friction stir welding of 6013 and AZ31 aluminium alloy and magnesium alloy respectively	The joint integrity of welds with water cooling was better than that of air cooling. However, the hardness in the air was higher than that of water
[6]	Z. Zhang, Z. Y. Ma, B. L. Xiao	Effects of high speed on the mechanical behaviour of FSW of 2219-T6 under in-process water and air-cooled conditions	The welds produced under both cooling conditions were good at high speed. However, air cooling led to lower hardness zone while water cooling had no significant effects on hardness. The tensile behavior of water-cooled welds was slightly better and the post weld artificial aging used improved the hardness for all the joints at all welding speeds. This was due to the formation of Al <sub>2</sub> Cu <sub>2</sub> in the low hardness and stir zone
[7]	W. F. Xu, J. S. Yao, J. H. Liu, G. H. Luan, D. L. Chen	Enhancing ductility and strength through in-process water and air cooling of FSW of 2219 aluminium alloy	Water cooling enhanced the ductility and strength of the welds but lowered the hardness of the weld than those obtained in air cooling
[8]	S. Sree Sabari, S. Malarvizhi, V. Balasubramanian	Rotational speed influence and underwater cooling behaviour of FSW of AA2519-T87	Higher tensile strength was observed at lower rotational speed in water submerged welds. This was due to a reduction in heat produced, greater grain boundary of precipitates and narrow hardness spread zone

(continued)

**Table 1** (continued)

References	Authors	Focus	Findings and conclusions
[11]	H. J. Liu, H. J. Zhang, L. Yu	Welding speed influence on the mechanical and microstructural behavior of water submerged friction stir welding of 2219 aluminium alloy	High welding speed led to the degeneration of precipitates at TMAZ which resulted to narrow and soft zone with higher hardness value. Tensile tests of welds at lower welding speed fractured at heat affected zone while those at higher speeds fractured at TMAZ
[12]	S. Sinhmar, D. K. Dwivedi	Corrosion and mechanical behaviour of sprayed water and natural air-cooled during friction stir welding of 2014 aluminium alloy	Water cooled welds exhibit greater hardness at HAZ than natural air-cooled welds. Tensile and yield strength, as well as resistance to corrosion, were also higher in the water-cooled welds than the air-cooled welds. This was due to discontinuous smaller grain sizes of precipitates in the weld zone
[15]	Q. Wang, Y. Zhao, K. Yan, S. Lu	Corrosion study of water submerged friction stir welding of 7055 aluminium alloy	Underwater joint exhibit better resistance to corrosion than the normal joint and the base metal. This was attributed to blockage of corrosion path in the underwater joint as a result of MgCu <sub>2</sub> distributions in the matrix
[13]	Deepti Jaiswala, Ratnesh Kumar, Raj Singhb, Sunil Pandey, Rajesh Prasad	Cooling media effects on mechanical behavior of FSW of 1060 aluminium alloy	The optimum parameter used for air-cooled welding was also applied for underwater welding. There was improvement in the impact and tensile strength. This was due to narrow HAZ resulting from heat reduction by the cooling water

(continued)

**Table 1** (continued)

References	Authors	Focus	Findings and conclusions
[16]	Jamshidi Aval Hamed	Heat input influence during FSW and post-weld aging time on mechanical behavior and microstructure of AA7075-AA5086	Heat sink made of copper with water tunnels to rapidly cooled the workpiece during the FSW was used. The result showed an increase in tensile strength, decrease in residual stresses, smaller grain size and narrowed softened region compared to samples without heatsink cooling
[17]	Khosro Bijanrostami and Reza Vatankhah Barenji	Effects of submerged friction stir welding of 6061-7075 on hardness and grain size. Experiment and modeling	The empirical model used predicted the experimental values obtained considerably. Fine grain size and greater hardness were obtained at reduced rotational speed and higher travel speed. The grain boundaries mechanism and its influenced dislocations were attributed to this behavior
[18]	Ashish Jacob, Sachin Maheshwari, Arshad Noor Siddiquee and Namrata Gangi	Enhancement of strength and microstructure through in process cooling using water, slush ice, and crushed ice added with rock salt during FSW of 7475	The cooling led to substantially fine grains at the stir zone and significantly increased mechanical behavior of the weld. Ice water cooling gave exceptionally stable microstructures
[19]	L. Fratini, G. Buffa, R. Shivpuri	In process cooling effects on mechanical and microstructural behavior of AA7075 during FSW using water as cooling medium	The cooling improved joint strength and narrowed the softened zone. There was a slight difference in hardness between the naturally cooled and water-cooled welds
[20]	M. Jariyaboon, A. J. Davenport, R. Ambat, B. J Connolly, S. W. Williams, D. A. Price	Cryogenic cooling effects on corrosion behavior of FSW AA7010-T7651	Intergranular corrosion occurred at HAZ with and without cooling but cooling narrowed the HAZ. Cryogenic cooling has no influence on anodic reaction but showed greater cathodic reaction in the nugget zone

## **2.2 *Effects on Hardness***

The effects of in-process cooling on hardness profile have not been fully established from the reviewed literature. Hardness depends on the type of aluminium alloys being joined together and materials movement and mixing during the welding. The hardness across the three zones of the weld varies irrespective of cooling methods employed.

## **2.3 *Effects on Corrosion***

Better corrosion resistance was equally reported to have been observed in underwater friction stir welds than the natural air-cooled friction stir welds. The same reasons for better tensile strength and hardness have been ascribed to this [12, 15]. However, increase in cathodic reactivity was reported in cryogenic cooling [20].

## **2.4 *Effects on Microstructures***

Analysis of cooling effects on microstructure during friction stir welding revealed the evolution of fine grain structures with smaller sizes in the nugget zone as a result of cooling brought about by the water during plastic deformation of the materials at the joint interface [3–18].

## **3 *Conclusions***

An overview of in-process cooling in friction stir welding of aluminium alloys have been discussed in this paper. Underwater or sprayed water, heat sink with water, compressed air, cryogenic and liquid nitrogen cooling during friction stir welding and their effects on tensile strength, hardness, microstructures and corrosion resistance of welded joints have been highlighted. The reports from various authors considered in this review affirmed the improvement in mechanical properties and corrosion of welds carried out with in-process cooling and therefore made it a desirable process for improving friction stir weld joints of low temperature alloys like aluminium. The improvement on mechanical behavior was generally linked to inhibition of coarsening of strengthening precipitates by the various cooling media. The heat input to the weld region as a result of the cooling is just sufficient enough for the required bonding and therefore hindered abnormal grain growth that could result from high heat input. However, the effects of this on wear and corrosion has not been fully reported. Also, the in-process cooling applications to high temperature alloys in friction stir



welding still calls for investigations. Future research could focus more on wear and corrosion behavior of the in-process cooling welds. This is a gap that seems yet to be fully reported. Investigations on effects of other cooling media different from the ones discussed above on mechanical properties, microstructures, wear and corrosion behaviour of different grades and series of aluminium alloys for both similar and dissimilar FSW could be explored. The research could also be extended not only to other low-temperature alloys such as copper, magnesium etc. but also to high-temperature alloys like steel.

## References

1. Akinlabi ET, Akinlabi SA (2012) Effect of heat input on the properties of dissimilar friction stir welds of aluminium and copper. *Am J Mater Sci* 2(5):147–152
2. Takayama Y, Akutsu Y, Choshiro N, Kato H, Watanabe H (2010) Temperature measurement during friction stir welding of dissimilar aluminum alloys, pp 0–5
3. Liu HJ, Zhang HJ, Huang YX, Yu L (2010) Mechanical properties of underwater friction stir welded 2219 aluminum alloy. *Trans Nonferrous Met Soc China (English Ed)* 20(8):1387–1391
4. Zhang HJ, Liu HJ, Yu L (2012) Effect of water cooling on the performances of friction stir welding heat-affected zone. *J Mater Eng Perform* 21(7):1182–1187
5. Zhao Y, Jiang S, Yang S, Lu Z, Yan K (2016) Influence of cooling conditions on joint properties and microstructures of aluminum and magnesium dissimilar alloys by friction stir welding. *Int J Adv Manuf Technol* 83(1–4):673–679
6. Zhang Z, Xiao BL, Ma ZY (2015) Enhancing mechanical properties of friction stir welded 2219Al-T6 joints at high welding speed through water cooling and post-welding artificial ageing. *Mater Charact* 106:255–265
7. Xu WF, Liu JH, Chen DL, Luan GH, Yao JS (2012) Improvements of strength and ductility in aluminum alloy joints via rapid cooling during friction stir welding. *Mater Sci Eng A* 548:89–98
8. Sree Sabari S, Malarvizhi S, Balasubramanian V (2016) Characteristics of FSW and UWFSW joints of AA2519-T87 aluminium alloy: effect of tool rotation speed. *J Manuf Process* 22:278–289
9. Ghetiya ND, Patel KM (2015) Prediction of tensile strength and microstructure characterization of immersed friction stir welding of aluminium alloy AA2014-T4. *NOPR NISCAIR Publ Res J Indian J Eng Mater Sci IJEMS* 133–140
10. Zhang Z, Xiao BL, Ma ZY (2014) Influence of water cooling on microstructure and mechanical properties of friction stir welded 2014Al-T6 joints. *Mater Sci Eng A* 614:6–15
11. Liu HJ, Zhang HJ, Yu L (2011) Effect of welding speed on microstructures and mechanical properties of underwater friction stir welded 2219 aluminum alloy. *Mater Des* 32(3):1548–1553
12. Sinhmar S, Dwivedi DK (2017) Enhancement of mechanical properties and corrosion resistance of friction stir welded joint of AA2014 using water cooling. *Mater Sci Eng A* 684:413–422
13. Jaiswal D, Kumar R, Singh R, Pandey S, Prasad R (2014) Influence of cooling media on mechanical properties of friction stir welded 1060 aluminium alloy, no 4, pp 54–57
14. Sharma C, Dwivedi DK, Kumar P (2012) Influence of in-process cooling on tensile behaviour of friction stir welded joints of AA7039. *Mater Sci Eng A* 556:479–487
15. Wang Q, Zhao Y, Yan K, Lu S (2015) Corrosion behavior of spray formed 7055 aluminum alloy joint welded by underwater friction stir welding. *Mater Des* 68:97–103
16. Hamed JA (2017) Effect of welding heat input and post-weld aging time on microstructure and mechanical properties in dissimilar friction stir welded AA7075–AA5086. *Trans Nonferrous Met Soc China (English Ed)* 27(8):1707–1715

17. Bijanrostami K, Vatankhah Barenji R (2017) Underwater dissimilar friction stir welding of aluminum alloys: elucidating the grain size and hardness of the joints. *Proc Inst Mech Eng Part L J Mater Des Appl* 1–13
18. Jacob A, Maheshwari S, Siddiquee AN, Gangil N (2018) Improvements in strength and microstructural behaviour of friction stir welded 7475 aluminium alloy using in-process cooling. *Mater Res Express* 5(1):1–12
19. Fratini L, Buffa G, Shivpuri R (2010) Mechanical and metallurgical effects of in process cooling during friction stir welding of AA7075-T6 butt joints. *Acta Mater* 58(6):2056–2067
20. Jariyaboon M, Davenport AJ, Ambat R, Connolly BJ, Williams SW, Price DA (2010) Effect of cryogenic cooling on corrosion of friction stir welded AA7010-T7651. *Anti-Corros Methods Mater* 57(2):83–89

# Experimental Investigation of the Effect of Inclination Angle on Heat Pipe Thermal Performance Using Cu-Nanofluids



Thaw Zinn Lynn, Aklilu Tesfamichael Baheta and Suleiman Akilu

**Abstract** In this paper, thermal performance of a heat pipe has been studied experimentally using 50 nm copper nanoparticles deionized water and acetone based nanofluids. The effect of nanoparticle concentrations (0.5 and 1%) on thermal resistance of heat pipe was investigated. Moreover, the effect of angle of inclination on thermal performance of the heat pipe was examined and the average temperature distribution of the heat pipe was recorded too. Regardless of the nanofluid type used, results showed that when the nanoparticles concentration increases, the evaporator section temperature drops whereas the condenser section temperature increases. Furthermore, for the same heat input, the higher the particle concentration, the less the thermal resistance was. It was also observed that the thermal performance of the heat pipe is best at 75° and 45° angles for deionized water based nanofluid and acetone based nanofluid, respectively.

**Keywords** Nanofluids · Concentration · Inclination angle · Thermal resistance · Performance

## 1 Introduction

The cooling requirements of today's high performance technological devices have exceeded the limits and capabilities of conventional heat pipes. So, different strategies are explored to improve the heat transfer efficiency of heat pipe. A heat pipe is a passive and advanced heat-transfer technology for efficient heat exchange and low thermal resistance delivery. As a closed system, the device operates on the two-phase fluid flow by relocating thermal energy through continuous cycles of evaporation and condensation. Most widely used applications for heat pipes include the heating, ventilation, and air-conditioning (HVAC), automotive, aerospace, and

---

T. Z. Lynn · A. T. Baheta (✉) · S. Akilu  
Department of Mechanical Engineering, Universiti Teknologi PETRONAS, 32610 Bandar Seri Iskandar, Tronoh, Perak, Malaysia  
e-mail: [aklilu.baheta@utp.edu.my](mailto:aklilu.baheta@utp.edu.my)

© Springer Nature Singapore Pte Ltd. 2020  
M. Awang et al. (eds.), *Advances in Material Sciences and Engineering*, Lecture Notes in Mechanical Engineering,  
[https://doi.org/10.1007/978-981-13-8297-0\\_46](https://doi.org/10.1007/978-981-13-8297-0_46)

electronic systems. Conventional heat pipes, depending on the type of application, exist in several designs as mesh wick, micro-grooved, oscillating, thermosyphon and sintered wick [1]. Among all these different types, thermosyphon is considered the simplest form of the existing heat pipes. It has three different sections which are evaporating, adiabatic and condensing. In the evaporating section, working fluid is transformed into a vapour phase with the addition of heat from the source. The vapour is caused to travel across the pipe to the condenser section due to density differences between the vapour and fluid. Moreover, the difference in wall temperature allows the vapour to condense, releasing the latent heat that was absorbed by the vaporization process, and then transforms back to liquid by the influence of gravity. Therefore, phase-change and vapours diffusion are important processes inside the heat pipe that help to remove the unwanted heat without any work input.

Many parameters can influence the performance of heat pipes (pipe material, working fluid and wick structure, etc.). Since thermal performance of heat pipe may be driven by phase-change fluid properties, researchers have prioritized nanofluids over conventional working fluid mediums like water, oil, or alcohols. Nanofluid refers to a suspension of nano-size particles in conventional fluids. It is a promising option for heat transfer applications that is concerned with enhancement of thermal conductivities or heat transfer coefficients. A number of studies have reported on the thermal and heat transfer characteristics of various nanofluids in the recent past. Copper and aluminium oxide nanofluids are frequently used in experimental investigations [2, 3]. Nevertheless, aluminium oxide nanofluid gives better performance than copper oxide nanofluid. Moraveji and Razvarz [2] examined the outcome of water-based alumina nanofluid in a circular heat pipe with constant heat flux. They stated that heat transfer coefficient inside the tube was boosted by increasing concentration of nanoparticles. Furthermore, heat transfer deteriorated with increasing diameter of particles and axial location. Xuan and Li [4] studied the heat transfer performance of nanofluids in a circular pipe with constant heat flux. They found out that convective heat transfer rate by using nanofluids upsurge with the nanoparticles volume fraction. The increase in Reynolds number leads to an improvement of turbulent heat transfer coefficient inside the tube. Noie et al. [5] investigated the heat recovery enhancement inside a heat pipe by using the aluminium oxide nanofluid under the conditions of different power inputs. A performance increase of 15% was achieved using nanofluid compared to pure water as the working fluid. Humnic and Humnic [6] conducted an experiment on the thermal performance of iron oxide/water nanofluids and observed 42% enhancement in heat transfer enhancement at 5.3% volume concentration. Additionally, the authors noted that heat transfer rate was affected by the nanoparticle concentration, inclination angle, operating temperatures.

According to the discussions above, utilizing nanofluid inside heat pipe can provide higher thermal performance instead of pure water as a working medium. To date, several studies applied aqueous-based metal oxides nanofluids, however research on metallic nanofluids are scarce in the literature. Copper (Cu) nanoparticles are attractive materials for thermal engineering application due to the advantage of high thermal conductivity when compared to metal oxides. Therefore; the current study aims to assess the performance of heat pipe charged with Cu/water nanofluids for

0, 0.5 and 1.0% weight concentrations. Finally, the results are compared with the thermal performance of the DI-water and acetone laden heat pipe system.

## 2 Experimental

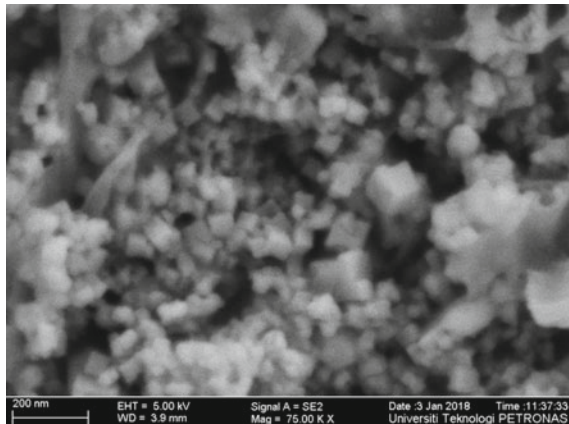
Copper (Cu) nano-powder with 50 nm nominal average diameters was procured commercially from US Research Nanomaterials Inc, USA. The base liquids acetone was obtained from R&M Chemicals, Malaysia and Milli-Q water purification system was used to obtain deionized water in the lab. The morphological characterization of the Cu powder was undertaken using scanning electron microscopy, SEM (SEM, Zeiss LEO, Germany). As shown in Fig. 1, the Cu particles are roughly spherical shape.

Preparation method of the nanofluids comprised of two main steps. First, nanofluids at the desired concentrations were produced by dispersing the nanoparticles in the base fluid. Equation (1) was used to determine the weight of powder to be added in the base liquid for the desired nanofluid concentrations of 0.5 and 1.0 wt%, respectively as follows:

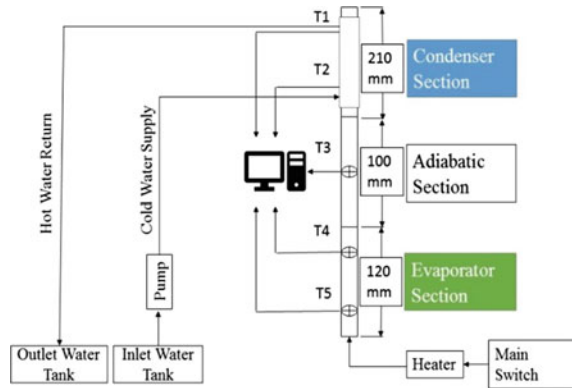
$$\varphi = \frac{w_{np}}{w_{np} + w_{bf}} \cdot 100 \quad (1)$$

where,  $\varphi$  is the weight concentration,  $w_{np}$  is the weight of nanoparticles, and  $w_{bf}$  is the weight of base liquid. The second step was disrupting the mixture to break up the agglomerates using mechanical stress ultrasonic probe (Labsonic M, Sartorius AG, Germany) operated at 250 W and 24 kHz for 2 h. No dispersant was used in the preparation process to prevent affecting thermo-physical properties of the nanofluids. The dispersion stability was examined through the observation of

**Fig. 1** SEM image of Cu nanoparticles



**Fig. 2** Schematic for heat pipe test rig system



nanofluid sample containers with the naked eye. All nanofluid maintains good stability without agglomeration for more than 48 h.

A schematic illustration of the experimental apparatus is shown in Fig. 2. The setup consists of test section, DC power supply, cooling water loop, and multi-channel data gathering system. The test section is a copper tube with total length of 430 and 14.8 mm diameter positioned vertically with three sections; evaporation, adiabatic and condensation of 120, 100, and 210 mm, respectively. The evaporation and adiabatic sections were insulated with fiberglass to minimize the heat loss to the surrounding. Heating of the evaporator is facilitated by an electrical heater with a DC power input of 350 W. In the cooling water loop system, a flow meter was used to regulate the rate of the coolant flow, while simultaneously the storage tanks ensure the constant supply of cooling water to the condenser section. The temperature of the tank was maintained constant by using a refrigeration system. Six k-type ( $\pm 0.1$  °C accuracy) were used to measure the temperature distribution along the wall of the heat pipe. Two of these were placed each on the evaporator and condenser section, while the remaining two detect the inlet and the outlet temperature for the cooling water. All the experimental data was recorded with a computer controlled data acquisition system (LABVIEW, National Instruments Inc, USA).

The operating procedure of the heat pipe required filling the amount of the working medium to be used about 2/3 of the total volume of the evaporator section. After filling the heat pipe with the working medium, the tube must be closed at both ends by means of ball valves to avoid leakage during the testing process. The cooling water to the condensing area was turned on by using the centrifugal pump. The pump flow rate display on the rotameter can be controlled by the glove valve. Furthermore, the chilling water supplied to the cooling water tank needed to circulate at the same time to control the rise in temperature of the coolant. Finally, the heating process to the evaporator began by controlling the supplied current and voltage to the device and these took between 20 and 25 min to attain steady heat supply. Once steady state heat supply condition to the evaporator reached, the temperature distribution at various locations was recorded. Experiments were conducted with different input

power values (0.2–2.8 W), and inclination angles (0, 15, 30, 45, 60, 75, 90°) at constant flow rates of 0.33 l/min.

The amount of heat supplied to the evaporator is given by the magnitudes of current and voltage used expression:

$$Q_{in} = IV \tag{2}$$

The thermal resistance between the evaporator and the condenser section is evaluated from temperature differences between the evaporating section and condensing section and the supplied heat load as follows:

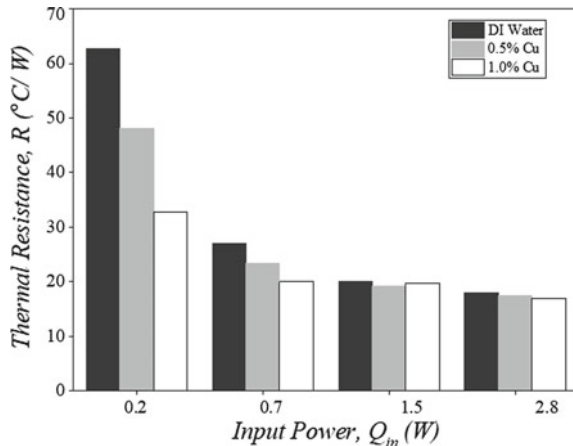
$$R = \frac{(T_e - T_c)}{Q_{in}} \tag{3}$$

### 3 Results and Discussion

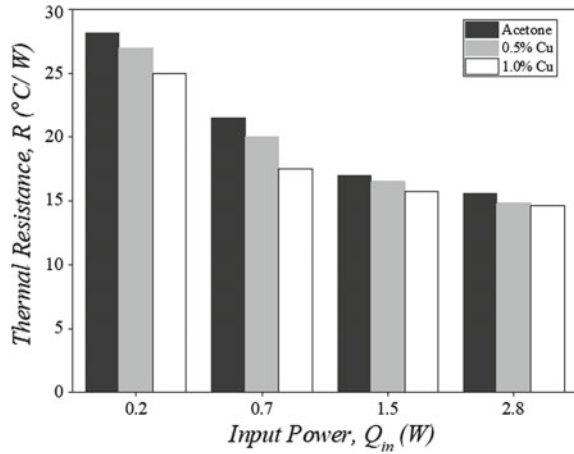
In Figs. 3 and 4, thermal resistance of the heat pipe changed by the increase in values of nanoparticles concentration in the working medium. There are two data sets, one with pure water versus water nanofluid and another with pure acetone versus acetone nanofluid. In both figures, with increased in nanoparticles concentration in the working medium, the thermal resistance of the heat pipe declined. This happened because of the development of the vapor bubble on the heat pipe’s interior wall. It also means that when nanoparticles were added to the working medium, the chance of developing larger vapor bubble on the heat pipe’s inside wall became less and that made the thermal resistance to drop in the heat pipe.

Analysis of thermal resistance changes by different angles of inclinations was done at 1.5 kW input power. From Figs. 5 and 6, it is examined that thermal resistance of

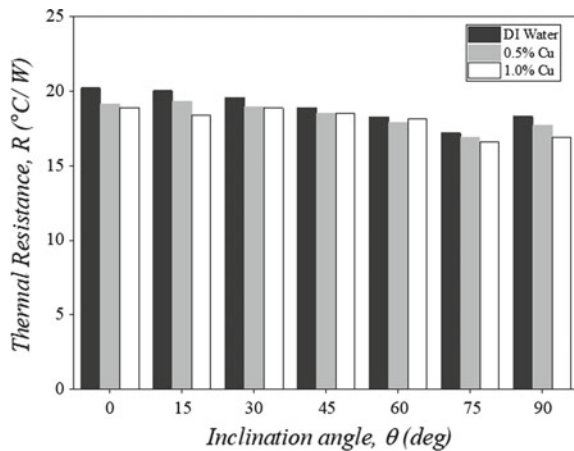
**Fig. 3** Effects of various input powers and nanoparticles concentration on thermal resistance of heat pipe (Deionized water as base fluid)



**Fig. 4** Effects of input powers and nanoparticles concentration on thermal resistance of the heat pipe (Acetone as base fluid)



**Fig. 5** Effects of angles of inclinations and nanoparticles concentration on thermal resistance of the heat pipe (Deionized water as base fluid)

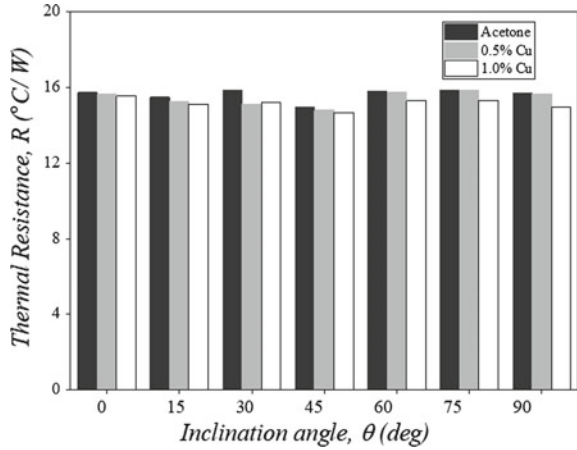


the heat pipe declined gradually with the rise in inclination angles. It is because of the significant effect of gravitational force on flowing the working medium between the condenser and evaporator. It kept decreasing and reached the lowest thermal resistance values at 75° angle for the deionized water based nanofluids and at 45° angle for the acetone base nanofluids. Then, it started to increase for both nanofluids. This is because when a liquid film started to develop on the inner wall of the condenser section, the thermal resistance tends to increase.

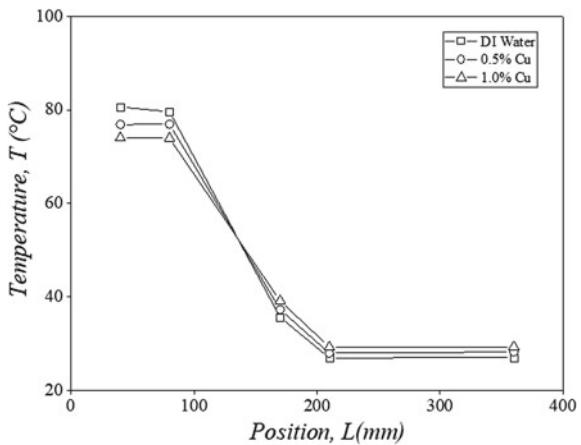
From Fig. 7, it is examined that the temperature distribution at the evaporator section which are 40 and 80 mm positions, gradually decreases when the nanoparticles were introduced in the base working medium. In the condenser section (210 and 360 mm positions), the temperature distribution increases nanoparticles volume concentration in the working medium. It is because nanoparticle has higher thermal conductivity which led to the evaporation of the working medium as it absorbed heat



**Fig. 6** Effects of various angle of inclinations and nanoparticles concentration on thermal resistance of heat pipe (Acetone as base fluid)



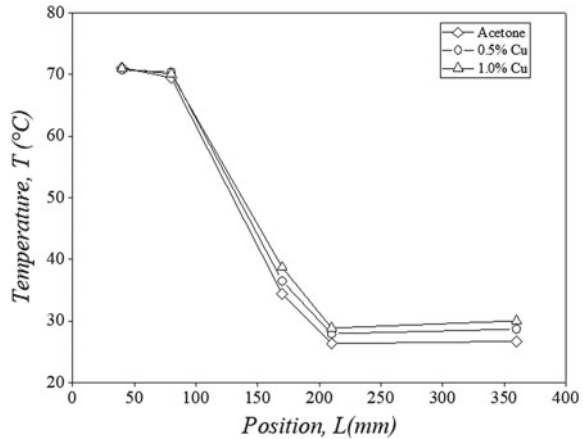
**Fig. 7** Temperature distribution along the heat pipe (Deionized water as base fluid)



quickly from the evaporator area and rapidly transferred heat to the condensing area. Therefore, the overall temperature differences of the heat pipe decreased when the working mediums have higher nanoparticles concentration and as a result, thermal resistance decreased.

From Fig. 8, it is observed that the temperature distribution at the condenser section (210 and 360 mm positions) followed the same nature as the deionized water based nanofluids. However, there was no significant temperature difference in the evaporator section (40 and 80 mm positions). It is because of the lower boiling point of the acetone. When a liquid reaches its boiling point, it does not matter which amount of heat supply to the liquid, the final temperature will not increase unless there is pressure control setting in the heating system.

**Fig. 8** Temperature distributions along the heat pipe (Acetone as base fluid)



## 4 Conclusions

From the experiments of the heat pipe, it is concluded that thermal resistance decreases with the increase in power supply to the evaporator. When nanoparticles are dispersed to the working medium, the temperature of the evaporator wall drops and at the condenser increases which leads to lower thermal resistance and heat pipe thermal performance improve. When the inclination angle increases, thermal resistance of the heat pipe decreases and then increases. Furthermore, the best thermal performance for deionized water based nanofluid is  $75^\circ$  angle whereas for acetone based nanofluid is  $45^\circ$  angle.

**Acknowledgements** The authors would like to thank Universiti Teknologi PETRONAS (UTP) for providing all the necessary supports and financial support, grant number URIF 0153AA-G01, for this research.

## References

- Jouhara H, Chauhan A, Nannou T, Almahmoud S, Delpach B, Wrobel LC (2017) Heat pipe based systems—advances and applications. *Energy* 128:729–754
- Moraveji MK, Razvarz S (2012) Experimental investigation of aluminum oxide nanofluid on heat pipe thermal performance. *Int Commun Heat Mass Transfer* 39:1444–1448
- Zeinali Heris S, Etemad SG, Nasr Esfahany M (2006) Experimental investigation of oxide nanofluids laminar flow convective heat transfer. *Int Commun Heat Mass Transfer* 33:529–535
- Xuan Y, Li Q (2003) Investigation on convective heat transfer and flow features of nanofluids. *J Heat Transfer* 125:151–155
- Noie S, Heris SZ, Kahani M, Nowee S (2009) Heat transfer enhancement using  $\text{Al}_2\text{O}_3$ /water nanofluid in a two-phase closed thermosyphon. *Int J Heat Fluid Flow* 30:700–705
- Huminc G, Huminc A (2011) Heat transfer characteristics of a two-phase closed thermosyphons using nanofluids. *Exp Thermal Fluid Sci* 35:550–557

# Biodegradability Characterization of Cotton Waste Planting Bag Prototype



Muhammad Farid Shaari, Harris Mubashir Mohamad Isa, Azrin Hani Abdul Rashid, Norshuhaila Mohamed Sunar, Salwa Mahmood, Najib Ismail, Angzzas Sari Mohd Kassim and Noraini Marsi

**Abstract** Currently, polymer-based planting bag is utilized in agriculture industry, either in nursery or commodity plantations. Due to environmental concerns, biodegradable type planting bag had been introduced globally. One of the proposed biodegradable planting bag is made from cotton waste. However, the feasibility of cotton type biodegradable planting bag is still under studies due to its mechanical properties. Hence, this research is conducted to characterize the cotton waste planting bag by differentiating the quantity of the binders. Cotton waste planting bag are made from nonwoven cotton waste fabric and starch (*amylum*) as matrix binder between the cotton fibres to enhance the nonwoven fabric strength. In this research, three samples were developed with 20, 30 and 40% starch concentration. Each of these sample underwent three testings which were the bursting test, water vapour permeability test and biodegradability test. The biodegradability test was analysed by observing the physical properties by using video analyser for visual inspection of the cotton waste planting bag after being buried in the soil for 60 days. The results showed that less starch concentration cotton waste planting bag has lower bursting force resistance but higher water vapour permeability. The average weight and the thickness of the cotton waste planting bag was extremely reduced within 60 days after being buried in the soil with not much difference between the three studied samples.

**Keywords** Biodegradability · Planting bag · Cotton waste · Natural fibre

---

M. F. Shaari (✉) · H. M. M. Isa · A. H. A. Rashid · N. M. Sunar · S. Mahmood · A. S. M. Kassim · N. Marsi  
Faculty of Engineering Technology, Universiti Tun Hussein Onn Malaysia (Pagoh Campus),  
84600 Muar, Johor, Malaysia  
e-mail: [mdfarid@uthm.edu.my](mailto:mdfarid@uthm.edu.my)

N. Ismail  
NBI Global Infinity, Melaka, Malaysia

© Springer Nature Singapore Pte Ltd. 2020  
M. Awang et al. (eds.), *Advances in Material Sciences and Engineering*, Lecture Notes in Mechanical Engineering,  
[https://doi.org/10.1007/978-981-13-8297-0\\_47](https://doi.org/10.1007/978-981-13-8297-0_47)

## 1 Introduction

The publisher, Demand on plastics had increased tremendously since few decades ago. As reported in *PlasticsEurope Annual Report 2017–2018* [1], the demand for plastics in agriculture industry, mostly the polyethylene type for Europe was 3.3% from the entire demand in 2016. On the other side, it was recorded that 8.4 million tonnes of plastics waste were collected to be recycled inside or outside the European Unions (EU). Globally, approximately 6300 million metric tonnes of plastic waste had been recorded in 2015, whereas only 9% had been recycled and 79% had been accumulated in landfills or natural environment [2]. Agriculture plastic waste generates about 615 tonnes of waste per year in Europe [3]. Almost half of this amount is dominated by polyethylene. Polyethylene material is used to protect cultivations, which includes greenhouses roofing, mulching, small tunnels, packaging, planting bag and many more. In plantation commodities industries such as palm oil and rubber or small scale nurseries, polyethylene planting bag is used to contain the plant from seedling phase to mature phase before being transplanted permanently in the soil. The polyethylene planting bag cannot be planted together with the plant in the ground because it affected the root growth as well as contaminating the soil. Thus, it will be removed during the transplanting process.

The increasing demand for these commodities and other commercial plants has increased the usage of the planting bag and eventually, it also contributes to the plastic waste increment. The introduction of biodegradable planting bag has been seen as one of the practical solution for the plastic pollutant problem. There are few types of biodegradable planting bags that have been applied in commercial plantations such as those made from paper, biodegradable plastics and fabrics [4, 5]. One of the potential biodegradable planting bags is nonwoven fabric type planting bag. The increasing cotton waste from textile industries has led to the utilization of cotton waste as the base for fabric type planting bag [6]. However, the weak bonding between cotton fibres has contributed to low mechanical properties. Hence, this research is conducted to determine the potential mechanical properties of the cotton waste planting bag through characterization process. The characterization of the cotton waste planting bag was performed based on three different binder concentrations. All the samples underwent few tests which are the bursting test, water vapour permeability test and biodegradability test. The details of the sample preparation and testing are described in section two of this article. The observations and results are discussed in section three. Finally, all the findings are summarized in the conclusion.

## 2 Methods

### 2.1 *Mechanical Properties*

The major requirements of mechanical properties for planting bags include the tensile strength, penetration strength, water absorption rate and water permeability. Tensile strength is important for planting bag because of its ability to withstand the load of soil/media and the plant. Furthermore, planting bag needs to endure the excessive load that will come during watering, root growing and in some cases fruit that will grow in soil, for instance potatoes. Penetration strength is required to measure how strong the cotton waste planting bags are able to resist the root penetration. In fact, this character must be contradict to the strength quality. A good planting bag must have low penetration resistance force to ensure the roots are growing well under the ground. High penetration resistance force limits the fine growth for the plant roots and will reduce the crops production. Water vapour permeability is a critical factor to ensure a certain amount of water could pass through the planting bag. Too much permeability allows more water to be drained out from the roots, thus the plant will have insufficient water. Low water permeability blocks the water out from the plant thus it will affect the plant growth. The mechanical properties depend on the production process of the planting bag. There are few influential factors such as fibre lengths, type of fibres, type of binders and manufacturing process. In this research, the cotton waste fibres with average uniform fibre length had been applied.

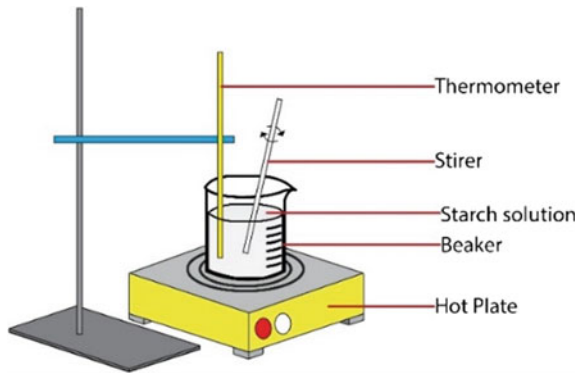
### 2.2 *Sample Preparation*

Cotton waste planting bag was developed from non-woven fabric process. Cotton waste fibres were placed on a conveyor which led to the opener. The opener opened the tuft of cotton waste fibres and separated any bulk fibre before it entered into the hopper. In the air circulating hopper, the fibres were totally disentangled and the fibres were then delivered to the carding roller. The carding roller eliminated any impurities and short fibres to make the fabric web. Then the fabric entered the needle punching process to become the non-woven fabrics. In this research, the cotton waste was purchased from Golden Gate Technologies Company. This cotton waste was derived from used cotton cloths, fabrics and garment factory. Figure 1 depicts the non-woven fabric formation in the non-woven processes. Figure 2 illustrates the process of making starch binder. This process is important to set up the three different cotton waste planting bag fabric samples based on the binder concentration. The binder concentration were 20, 30 and 40%.

The concentration percentage was determined by the weight ratio of the starch and water. 20% binder concentration consists of 0.4 g starch and 20 ml water. The weight of the starch mass measured using Mettler Toledo digital balance, model TLE3002E. The combination of starch and water was mixed in a beaker and heated up to 300 °C

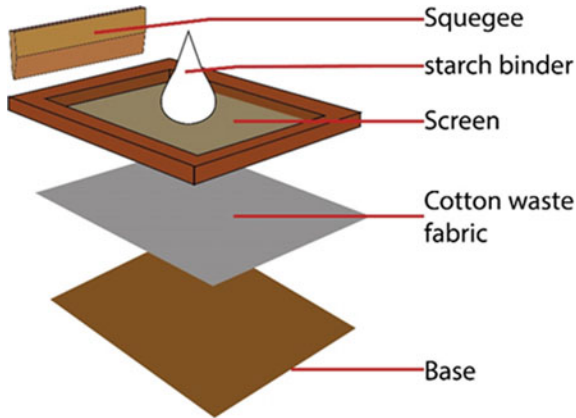


**Fig. 1** Non-woven process



**Fig. 2** Starch preparation

on the hot plate (model Thermo Scientific Cimarec; SP131635). During the heating process, the solution was continuously stirred for 10–15 min, until it became a thick binder. The binder solution temperature had increased up to 73 °C after it changed the viscosity. The binder was used to bind the cotton waste fibres into the non-woven fabric using squeegee and screen (Fig. 3). Heat press machine was used for the thermal application on the fabric binder cure.



**Fig. 3** Lay-up process for fabric sample fabrication

### 2.3 *Bursting Test*

Bursting test was conducted to determine the bursting strength performance of the cotton waste fabric sample. The bursting strength performance relates to the penetration resistance of the fabrics which is essential for the root growth after plantation. The fabric sample bursting strength was tested using a bursting tester machine (model SDL) according to the ASTM D 3786 testing method. Five samples were tested for each sample category. The bursting strength was measured in kgf, converted from the applied pressure. All the tests were performed under standard atmospheric conditions where the ambient temperature was approximately  $20 \pm 2$  °C and relative humidity was  $65 \pm 2\%$ . According to the standard, the test area for the fabric sample was  $10 \text{ cm}^2$  and the tested diameter was 35.7 mm. The fabric sample was clamped on the testing area and air flow that came from the bottom of the testing machine platform deformed the rubber diaphragm. The deformed rubber diaphragm transferred the generated force to the fabric into a semi dome shape until the fabric burst. The pressure where the fabric sample started to burst was measured and recorded. The bursting test was also applied to the polyethylene planting bag as reference.

### 2.4 *Water Vapour Permeability Test*

Water vapour permeability (WVP) properties is one of the crucial factors in determining cotton waste planting bag prototype as it represents the ability of transferring perspiration. It indicates the breathability of the planting bag against the traditional poly planting bag. The water vapour permeability test was conducted using the SDL Atlas Water Vapour Permeability Tester. This tester applied the cup method, which refers to the BS 7209 standards. In this method, the loss in the weight of water con-

tained in an airtight manner over the top of a cup was measured and recorded. The dishes with inner diameter of 8.2 cm was filled with 46 ml of distilled water. On the top of the dish, a triangular support was placed to maintain certain distance between the bottom of the specimen and water surface, at approximately 10 mm gap. On top of the triangular support, the circular nonwoven specimen was placed with the ring casing.

The technique compared the rate of water mass transfer through the fabric from eight cups, two of them covered with reference fabric and the other six with test samples. The weight of the cups was first measured at the start of the test and periodically after a certain time interval with a balance that has a resolution of 0.01 g to determine how much water was lost from each cup. The difference in water loss between the cup covered with a standard fabric and one with the test fabric enabled the study of the relative rates of moisture movement through the test fabrics, so that the moisture vapour permeability of the test specimen can be calculated. The WVP index (Eq. 1) was calculated by expressing the WVP of the fabric as a percentage of the WVP of reference, as shown below:

$$WVP = \frac{24 \times M}{A \times T} \text{ g/m}^2/6 \quad (1)$$

where  $M$  is the loss in mass (g);  $T$ , the time interval (h);  $A$ , the internal area of the cup  $\text{m}^2$ , and  $A$  is calculated by using the following equation:

$$A = \frac{\pi d^2}{4} \times 10^{-6} \quad (2)$$

## 2.5 Biodegradation Test

Generally the degree and rate of aerobic biodegradability of a textile waste in the environment determine the extent to which and period over which waste may be mineralized. This test method determines the degree of aerobic biodegradation of the fabric samples used for the developed planting bag by measuring the evolved carbon dioxide as a function of time that the textile waste is exposed to soil. This method was carried out based on [7] in their previous works. In this research, the biodegradation test was performed by referring to the ASTM D5988-03 standard. Small pieces of the cotton waste fabrics samples (dimensions 76.2 mm  $\times$  76.2 mm  $\times$  4 mm) were buried 70 mm deep under the ground. The average atmosphere temperature was  $30 \pm 5$  °C and relative humidity (RH) was 40–80% daily as recorded in Pagoh, Johor, Malaysia. The fabric samples were collected after 30 and 60 days of burial. The samples were collected, cleaned and dried in the oven at  $25 \pm 5$  °C for 24 h. The weight loss was calculated using Eq. (3).

$$\text{Weight loss(\%)} = \frac{W_{\text{initial}} - W_{\text{final}}}{W_{\text{initial}}} \times 100 \quad (3)$$



where the  $W_{initial}$  is the initial weight of the fabric sample and  $W_{final}$  is the final weight of the fabric samples. The thickness of the fabric samples were measured using the Vernier calliper. The obtained fabric samples structure was also investigated by using the video analyser (model Mesdan 2000 Code 250D).

### 3 Results and Discussion

#### 3.1 Bursting Test

Figure 4 shows the result of bursting test for all cotton waste planting bag samples. Fabric sample with 40% concentration has the highest bursting stress in average, which is 12.4 kgf, followed by fabric sample with 30% concentration (12.2 kgf) and the fabric with 20% concentration has 12.1 kgf bursting force. The value shows that the binder concentration percentage has higher bursting strength. More starch concentration in the binder helps to enhance the physical and mechanical properties of the cotton waste fabric by increasing the binding force among the cotton fibres. However, the bursting force of all three fabrics samples shows no distinctive difference. On average, each of the fabric samples has 0.1–0.2 kgf difference. From the experiment result, the recorded bursting force for polyethylene planting bag was 13 kgf. The bursting force difference between the 40% starch concentration fabric sample and the polyethylene planting bag sample was almost 40% in percentage value.

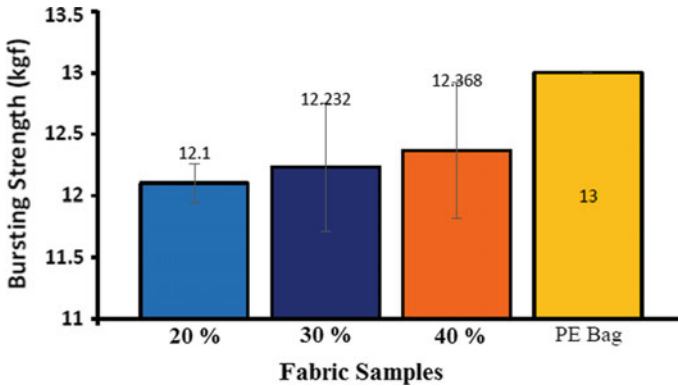


Fig. 4 Bursting strength results

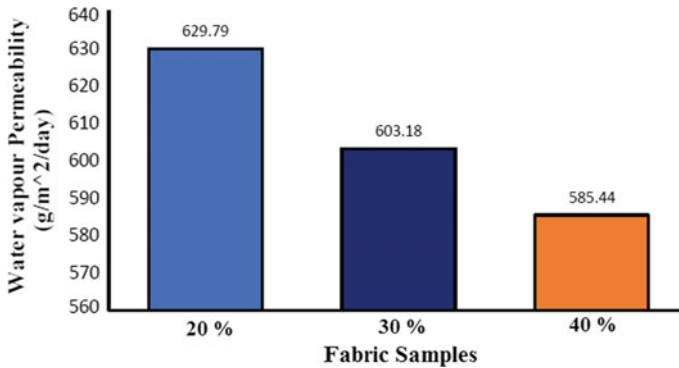


Fig. 5 Water vapour permeability results

### 3.2 Water Vapour Permeability Test

The WVP test results are exhibited in Fig. 5. Fabric sample with 20% starch concentration has the highest water vapour permeability value at approximately 630 g/m<sup>2</sup> per day, followed by fabric sample with 30% starch concentration (603 g/m<sup>2</sup> per day). Fabric sample with 40% starch concentration has the lowest water permeability value. This is because fabric sample 20% starch concentration has less binding strength that allows the water molecules to pass through it. Fabric with 40% starch concentration has the lowest water vapour permeability because it has more starch concentration, which increased the binding force of the cotton fibres thus reducing the capability of the water molecules to pass through it. As the starch binder is also made from water, water molecules have weak influence on the binder. With the addition of external force or increasing the level of acidity, the binder strength will deteriorated. Water vapour permeability is vital for plant's root to breathe and grow, but the amount of water that pass through the fabric must be sustained or controlled to avoid the soil from losing its humidity or accumulating a lot of water.

### 3.3 Biodegradation Test

In biodegradation test, the cotton fabric samples have lost their weight, approximately from 50 to 60% from their initial weight after 60 days. Figure 6 depicts the trend of fabric sample weight that declined in 60 days for all samples. Generally, the results present that all fabric samples show extreme weight loss in 60 days but less weight loss within the first 30 days. Fabric sample with 20% starch concentration in its binder has the highest weight loss with 57.87%, and fabric sample with 40% starch concentration has the lowest weight loss, 55.54% from its initial weight. As shown in Fig. 7, the weight loss for the fabric samples is matching to the thickness

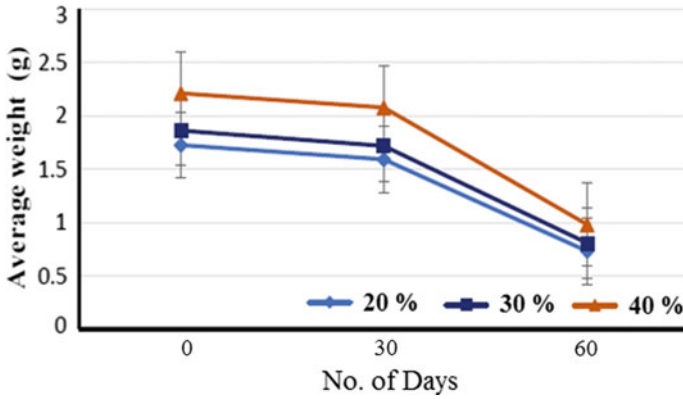


Fig. 6 Average weight in 60 days burial

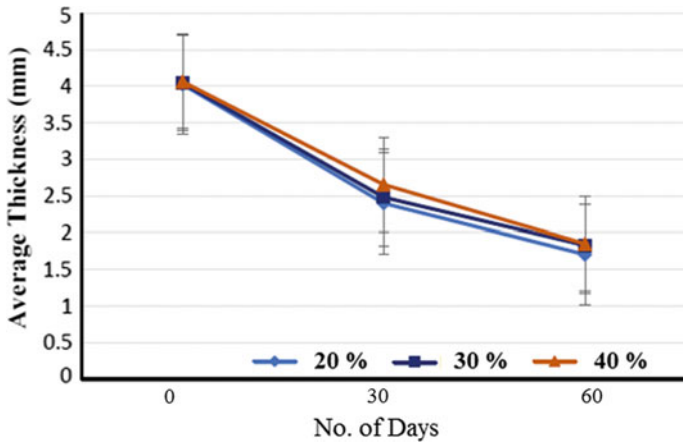
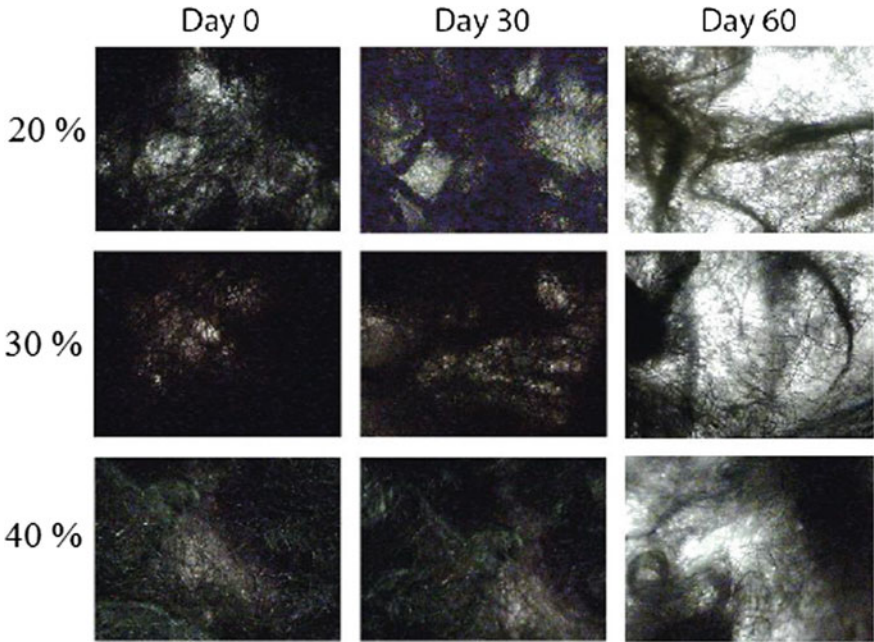
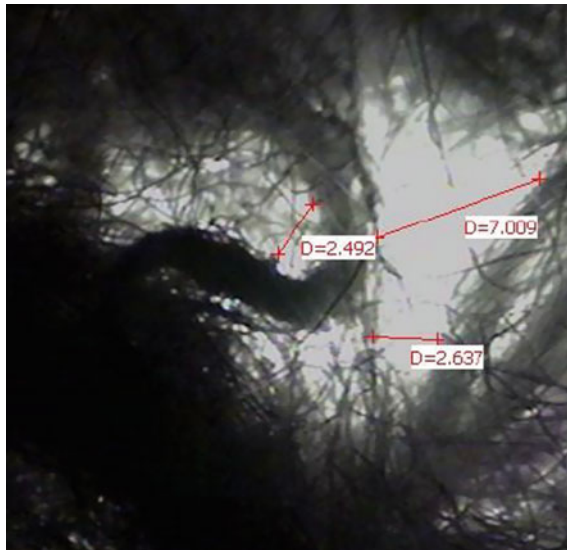


Fig. 7 Average thickness of the samples in 60 days burial

loss of the fabrics samples. Using the video analyser, the observations on fabric sample structure are recorded in Fig. 8. These results support the data presented in Fig. 6 where the fabric sample weight loss and thickness reduction is clear. In the 60th day, the amount of bonded cotton waste fibres had been reduced and it can be observed in the white area (porosities) in Fig. 9. Less starch concentration fabric sample shows more porosities. The porosities are non-uniformly distributed across the fabric sample area, due to the underground erosion process or cotton waste fibres uneven distribution during fabric fabrication process. The porosities length varies between 2 and 7 mm. Figure 10 shows lime plant root penetration after two months period, without burying in the ground.



**Fig. 8** Fabric sample structure at different burial period



**Fig. 9** Measurement of pores



**Fig. 10** Root penetration in 60 days for lime plant

## 4 Conclusions

The usage of non-woven cotton waste fabric as biodegradable planting bag is feasible and has a bright potential to be applied in agriculture sectors. However, the characterization works on the mechanical properties of the fabrics must be continued with other parameters, such as the acidity of soil, water erosion and other chemicals concentration in the soil. This research had contributed vital information for the development of cotton waste biodegradable planting bag. Currently, the bursting strength for 20–40% starch concentration shows no much difference and ranges between 12.1 and 12.4 kgf. The water vapour permeability value had obvious variations among the tested samples. Within 60 days, the quantity of fabrics materials deteriorated and biodegraded with the soils tremendously. This shows that the cotton waste biodegradable planting bag is practical to be applied in actual plantation environment.

**Acknowledgements** This The author would like to compliment Universiti Tun Hussein Onn Malaysia (UTHM) for sponsoring this project under TIER 1 Grant (H086) and providing the research facilities. The author would also address compliment and appreciation to Mr. Najib bin Ismail, owner of NBI Global Infinity company for allowing the project to take place in their plantation area.

## References

1. PlasticsEurope (2018) Annual Review 2017–2018. PlasticsEurope
2. Geyer R, Jambeck, JR Law KL et al (2017) Production, use, and fate of all plastics ever made. *Sci Adv* 3:1–5
3. Bos U, Makishi C, Fischer M et al (2008) Life cycle assessment of common used agricultural plastic products in the EU. *Acta Hort* 801:341–350
4. Nikolic MAL, Gauthier E, Colwell JM, Halley P, Bottle SE, Laycock B, Truss Rowan et al (2017) The challenges in lifetime prediction of oxodegradable polyolefin and biodegradable polymer films. *Polym Degrad Stab* 145:102–119
5. Wu CS et al (2012) Polyactide-based renewable composites from natural products residues by encapsulated film bag: characterization and biodegradability. *Carbohyd Polym* 90(10):583–591
6. Nam S, Slopek R, Wolf D, Warnock M, Condon BD, Sawhney P, Gbur E, Reynolds M, Allen C et al (2015) Comparison of biodegradation of low-weight hydroentangled raw cotton nonwoven fabric and that of commonly used disposable nonwoven fabrics in aerobic Captina silt loam soil. *Text Res J* 86(2):155–166
7. Li L, Frey M, Browning KJ et al (2010) Biodegradability study on cotton and polyester fabrics. *J Eng Fiber Fabr* 5(4):42–53

# Surface Modification of Ti4Al6V Alloy by Laser Cladding with 17-4PH Stainless Steel Powder



Esther T. Akinlabi and Abiodun Bayode

**Abstract** Surface treatment using laser assisted processes such as laser cladding are amongst the fastest growing research areas. Laser cladding has become a more sustainable material processing route with the development of more powerful and improved gas and solid state lasers. This technology is a single step process that is capable of improving the reliability of metal components in a variety of applications and also used for component repair. In this study, 17-4 precipitation hardening stainless steel powder was deposited on commercially pure Titanium alloy substrate by laser cladding. The influence of process variable on clad integrity and mechanical property was investigated. The laser power was varied between 1000–1400 W, while other associated process variables were fixed at constant values. The study revealed that increasing the laser power resulted in improved clad quality and no significant relationship was observed between laser power and microhardness of the specimens.

**Keywords** Laser cladding · Mechanical properties · Precipitation hardening · Process parameter · Surface treatment

## 1 Introduction

The Metal alloys are extensively used in the manufacturing of critical components for various applications and industries. Components made from these alloys are often exposed to severe environment and conditions in service which can lead to material loss or degradation. The application of the appropriate surface engineering procedure can enhance reliability, performance and also expand their area of application. Chrome plating, thermal spraying, carburizing, and various laser assisted alloying

---

E. T. Akinlabi · A. Bayode (✉)  
Department of Mechanical Engineering Science, University of Johannesburg, Auckland Park  
Kingsway Campus, Johannesburg 2006, South Africa  
e-mail: [reachabey@gmail.com](mailto:reachabey@gmail.com)

E. T. Akinlabi  
e-mail: [etakinlabi@uj.ac.za](mailto:etakinlabi@uj.ac.za)

© Springer Nature Singapore Pte Ltd. 2020  
M. Awang et al. (eds.), *Advances in Material Sciences and Engineering*, Lecture Notes in Mechanical Engineering,  
[https://doi.org/10.1007/978-981-13-8297-0\\_48](https://doi.org/10.1007/978-981-13-8297-0_48)

processes are some common surface modification techniques that are available and have been successfully applied to improve material properties such as wear, erosion, corrosion and bio-compatibility [1–3]. In recent times, laser processing methods like laser cladding have seen increased utilization for industrial applications with the development of more powerful and versatile lasers. Furthermore, laser cladding also offers exceptional benefits like minimal dilution and warping, material flexibility, improved bond strength, short processing time and component repair [4, 5].

Laser cladding belongs to the group of additive technology which combines a high power laser, automated material delivery and motion system. The process involves using the laser to weld the coating material on the surface of the component. The clads formed are usually relatively thin but can be increased by varying processing parameters such as powder flow rate and laser power [6–8]. The coating is metallurgically bonded to the substrate and the bulk properties of the base material are generally unaffected. This technology can be used to modify most metal surfaces provided that the feedstock is compatible and available in either wire or powder form [9–11]. Powder cladding is more popular than wire coating mainly because more alloys are readily available in powder compared to wire despite being costlier to produce than the later. Several metallic and non-metallic alloys have been successfully used as cladding material. Ceramics such as borides and carbide are amongst the most widely used coating material [12–17], however, metals like Iron and Nickel based alloy are presently being investigated as substitutes [9, 18, 19]. In addition, there is a growing interest for bimetallic components with different properties in opposite directions for potential use in the automotive and medical industry [20].

However, the consolidation of dissimilar materials using this technology presents some unique challenges such as the formation of unwanted intermetallic phases, solidification cracking and porosity [21]. In this present study, 17-4PH powder was deposited on commercially pure Titanium grade 5 substrate to improve its properties. The effect of process condition on clad integrity and hardness were investigated.

## 2 Experimental

### 2.1 Materials

The powder used was gas atomized 17-4PH stainless steel powder with particle sizes ranging between 44–90  $\mu\text{m}$ . A rectangular Titanium plate of type Ti6Al4V with dimension of 102 mm  $\times$  102 mm  $\times$  7.45 mm was used as the substrate. The surface of the substrate was roughened with a sand blaster and cleansed with acetone before the actual cladding operation. The chemical compositions of the powder and substrate are listed in Tables 1 and 2 respectively.



**Table 1** Chemical composition of the 17-4PH powder

Element	C	Nb	Si	Mn	Cu	Ni	Cr	Fe
Composition (wt%)	0.01	0.32	0.70	0.90	4.0	4.4	16.4	73.7

**Table 2** Chemical composition of the Ti6Al4V substrate

Element	H <sub>2</sub>	N <sub>2</sub>	C	Fe	O <sub>2</sub>	V	Al	Ti
Composition (wt%)	0.006	0.01	0.03	0.12	0.17	3.7	5.98	89.98

**Table 3** Process parameters used for cladding

Sample No.	Power (W)	Scan speed (m/s)	Beam diameter (mm)	Powder flowrate (rev/min)	Gas flowrate (rev/min)
S1	1000	0.5	2	2	2
S2	1200	0.5	2	2	2
S3	1400	0.5	2	2	2

## 2.2 Laser Cladding Process

The experiment was carried out using a 3 kW Nd:YAG laser with a coaxial deposition head attached to a three axis Kuka robot. Argon was used for both powder delivery and shielding gas. During processing, the substrate was stationary while the deposition head moved linearly. Several specimens with a series of clads with a 50% ratio were made by varying the laser power between 1000–1400 W. The laser beam diameter was maintained at 2 mm. A detailed descriptions of the process parameters used are listed in Table 3.

## 2.3 Material Characterization Procedure

After the laser cladding, specimens were cross-sectioned and prepared for characterization in accordance to the standard metallurgical preparation of Titanium [21]. Metallographic specimens were etched using Kroll's reagent (100 ml H<sub>2</sub>O, 3 ml HF and 5 ml HNO<sub>3</sub>) before observation under an Olympus optical microscope (BX51M). Microhardness measurements were conducted with a Vickers hardness indenter with a load and a dwell time of 500 g and 15 s respectively.

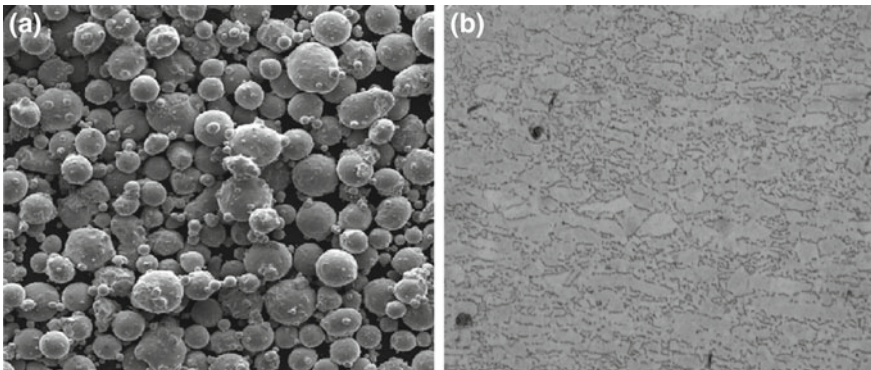
### 3 Results and Discussion

#### 3.1 Parent Material Analysis

The 17-4PH stainless steel powder particles are spherical in shape with a number of satellites agglomerated with the larger particles as seen in Fig. 1a. The micrograph does not show any indication of internal porosity in the powder, which suggests that the particles have very limited porosity or very small sized pores. Figure 1b shows the micrograph of the as received Ti6Al4V substrate. The microstructure consists of fine lamellar  $\alpha$ -phase in a  $\beta$ -phase matrix. The dark parts observed in the micrograph represent the alpha grains, while the lighter part is the beta grains.

#### 3.2 Macrostructural Examination of the Specimens

The cross-sectional view of the laser clad samples produced with different laser powers is shown in Fig. 2. Examination of the micrographs revealed that two of the three samples are characterized by macroscopic cracking (Fig. 2a, b). The cracks observed in samples S1 and S2 produced with laser power of 1000 and 1200 W respectively, were initiated at the substrate/clad interface and propagated all the way to the top of the clad. These cracks can be attributed to high residual stresses induced in the structure during solidification because of the difference in coefficient of thermal expansion (CTE) between the Ti6Al4V substrate and 17-4PH clad. The cracks observed in sample S2 is less severe than that of sample S1, while sample S3 produced with the highest power laser is crack free (Fig. 2c). This seems to suggest that the formation of cracks is linked to the laser power employed. This was anticipated as increasing the laser power, increases the surface area, temperature



**Fig. 1** Micrograph of (a) 17-4PH powder and (b) Ti6Al4V substrate

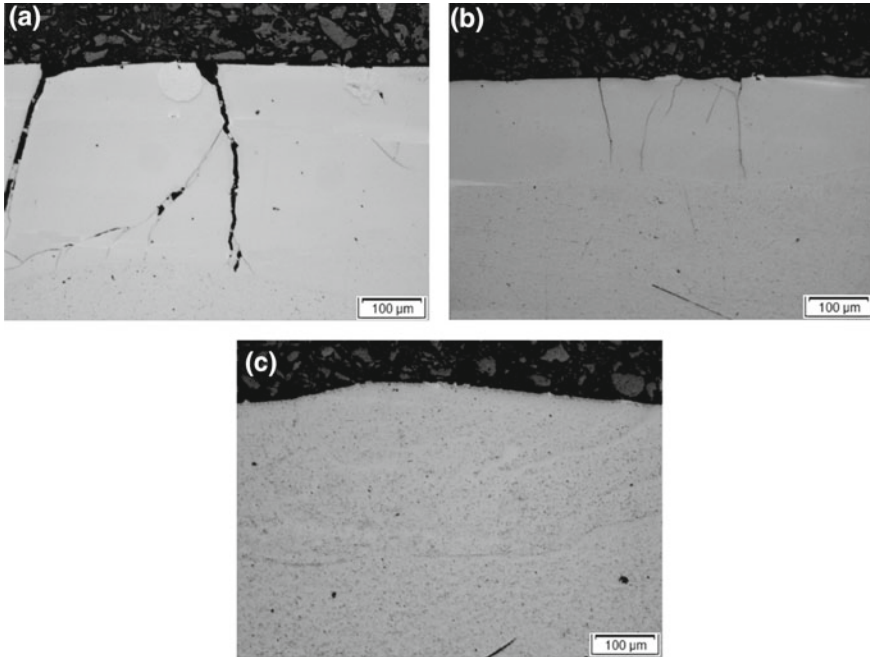


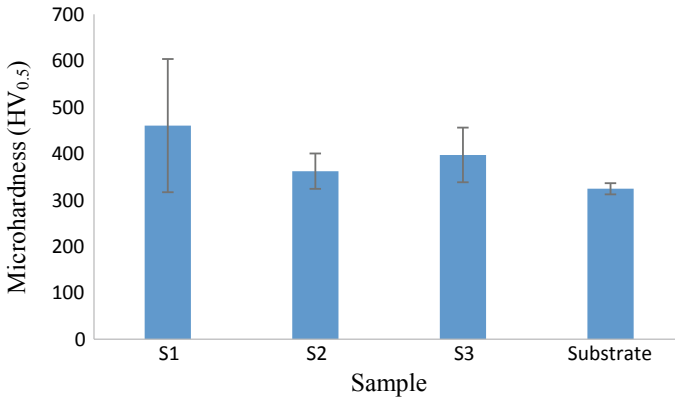
Fig. 2 Optical micrographs of sample **a** S1, **b** S2 and **c** S3

and cooling rate of the melt pool, which results in a decrease in residual stress [22]. Furthermore, cracks could have also been caused by the precipitation of brittle intermetallic phases such as TiNi, Ti<sub>2</sub>Ni, Cr<sub>2</sub>Ti and Fe–Ti which are typically formed in the melt pool when Ti alloy is bonded with steel [18, 19, 23, 24].

### 3.3 Microhardness Profiles

Figure 3 shows the average microhardness of all the fabricated samples measured perpendicular to the interface.

Sample S1 had the highest average hardness value of 460 HV<sub>0.5</sub> (with a peak hardness of about 605 HV<sub>0.5</sub>), while sample S2 recorded the lowest mean microhardness of about 361 HV<sub>0.5</sub>. Comparing the modified surfaces and the substrate, it is clear that laser cladding with the 17-4PH alloy induced some hardness as the average microhardness of all the samples were higher than that of the pure Ti4Al6V substrate (324.2 HV<sub>0.5</sub>). However, no clear trend was observed between the microhardness profiles and the laser powers. The increase in microhardness could be attributed to the precipitation of intermetallic and martensitic phases in the clads.



**Fig. 3** Average microhardness profiles of the clads

## 4 Conclusions

Laser cladding of 17-4PH stainless steel powder on Ti4Al6V alloy was conducted and the evolving properties were characterised. Varying levels of success were achieved with the cladding operation, macroscopic cracks were observed in two of the three samples produced, mainly as a result of residual stresses induced by differences in the thermal properties of the materials. Improvement in the integrity of the clad was observed with increment in the laser power. A noticeable increase in the microhardness was also observed. Further studies need to be conducted to determine corrosion resistance, solidification behavior and phase composition of the structure and also optimize the system for a typical engineering application.

**Acknowledgements** The authors wish to acknowledge the bursary received from the National Research Foundation (NRF), Pretoria, South Africa. In addition, we recognize the Rental Pool Program of National Laser Centre, Council of Scientific and Industrial Research (CSIR), Pretoria, South Africa for their support to this study.

## References

1. Mishra SK (2002) Advanced techniques for surface engineering of industrial materials
2. Liu X, Chu PK, Ding C (2004) Surface modification of titanium, titanium alloys, and related materials for biomedical applications. *Mater Sci Eng R Rep* 47(3–4):49–121
3. Vineet S, Vikas C (2014) A review of surface modification techniques in enhancing the erosion resistance of engineering components. *Int J Res Mech Eng Technol* 4:92–95
4. Sun S, Liu Q, Brandt M et al (2012) Microstructure and mechanical properties of laser cladding repair of AISI 4340 steel. In: 28th international congress of the aeronautical sciences, pp 1–9
5. Gibson I, Rosen DW, Stucker B (2010) Additive manufacturing technologies: rapid prototyping to direct digital manufacturing

6. Shukla M, Mahamood RM, Akinlabi ET et al (2012) Effect of laser power and powder flow rate on properties of laser metal deposited Ti6Al4V. *World Acad Sci Eng Technol Int J Mech Aerosp Ind Mech Manuf Eng* 6(11):2475–2479
7. Erinoshio MF, Akinlabi ET, Pityana S (2014) Effect of powder flow rate and gas flow rate on the evolving properties of deposited Ti6Al4V/cu composites. *Adv Mater Res*, 1016
8. Akinlabi ET, Mahamood RM, Shukla M et al (2012). Effect of scanning speed on material efficiency of laser metal deposited Ti6Al4v
9. Cheng FT, Lo KH, Man HC (2004) A preliminary study of laser cladding of AISI 316 stainless steel using preplaced NiTi wire. *Mater Sci Eng, A* 380(1–2):20–29
10. Syed WUH, Pinkerton AJ, Li L (2005) A comparative study of wire feeding and powder feeding in direct diode laser deposition for rapid prototyping. *Appl Surf Sci* 247(1–4):268–276
11. Syed WUH, Pinkerton AJ, Li L (2006) Combining wire and coaxial powder feeding in laser direct metal deposition for rapid prototyping. *Appl Surf Sci* 252(13):4803–4808
12. Mahamood RM, Akinlabi ET, Shukla M et al (2014) Characterization of laser deposited Ti6Al4V/TiC composite powders on a Ti6Al4V substrate
13. Obadele BA, Popoola OM (2012) Effects of TiC-particulate distribution in AISI 304L stainless steel matrix. *Dig J Nanomater Biostruct* 7(3):1245–1252
14. Jiang WH, Kovacevic R (2003) Fabrication of laser deposited TiC/steel matrix composite coatings. In: *Proceedings of the 14th solid freeform fabrication symposium*, 4–6 Aug, UT Austin, Austin, TX
15. Ravnikar D, Mrvar P, Medved J et al (2013) Microstructural analysis of laser coated ceramic components TiB<sub>2</sub> and TiC on aluminum alloy EN AW-6082-T651. *Strojniški vestnik-J Mech Eng* 59(5):281–290
16. Lifang C, Zhang Y, Likai S (2007) Microstructure and formation mechanism of titanium matrix composites coating on Ti-6Al-4V by laser cladding. *Rare Met* 26(4):342–346
17. Attar H, Bönisch M, Calin M et al (2014) Selective laser melting of in situ titanium–titanium boride composites: processing, microstructure and mechanical properties. *Acta Mater* 76:13–22
18. Chen JM, Chun G, Zhou JS (2012) Microstructure and tribological properties of laser cladding Fe-based coating on pure Ti substrate. *Trans Nonferr Metals Soc China* 22(9):2171–2178
19. Sahasrabudhe H, Harrison R, Carpenter C et al (2015) Stainless steel to titanium bimetallic structure using LENS™. *Addit Manuf* 5:1–8
20. Tan L, Baumgartner R, German R (2001) *Advances in powder metallurgy and particulate materials*. Metal Powder Industries Federation, Princeton, NJ, pp 4–191
21. ASTM E3-11 (2011) *Standard guide for preparation of metallographic specimens*, ASTM International, West Conshohocken, PA
22. Wu AS, Brown DW, Kumar M et al (2014) An experimental investigation into additive manufacturing-induced residual stresses in 316L stainless steel. *Metal Mater Trans A* 45(13):6260–6270
23. Bhanumurthy K, Kale GB (1993) Reactive diffusion between titanium and stainless steel. *J Mater Sci Lett* 12(23):1879–1881
24. Ghosh M, Chatterjee S, Mishra B (2003) The effect of intermetallics on the strength properties of diffusion bonds formed between Ti–5.5Al–2.4V and 304 stainless steel. *Mater Sci Eng A* 363(1–2):268–274

# Characterisation of Hardened Thermo-Mechanical Treated Reinforcement Bars



V. Musonda and Esther T. Akinlabi

**Abstract** Thermo-mechanically treated (TMT) reinforcement bars (rebars) are key materials in the construction industry by virtue of their high strength, high ductility and a host of other properties such as bendability and weldability. Characterisation of the TMT rebar is one fundamental requirement used to evaluate typical features, which include and not limited to the hardness and the uniformity of the martensite rim. Extensive and excellent work by other co-workers have so far been conducted on the characterisation of rebars. This study, however, aims at taking the efforts made by other co-workers further. Therefore, macrostructural analysis was conducted on the low carbon steel rebars in transverse and longitudinal sections respectively. The results indicate that, the uniformity of the hardened case of martensite for these rebars was within the 20–30% threshold with the average area of martensite ( $A_M$ ) being 29%. Interestingly, Pearlite colonies, comprising ferrite lamellae and cementite were revealed in the microstructure. It was observed that, the two phases were aligned alternately and parallel to each other. This alignment is due to their common growth direction during the transformation of pearlite. In addition, quantitative analysis by scanning electron microscope (SEM) revealed annealing and mechanical twins, the latter of which is symbolic of the material deforming at extremely high strain rates especially during hot rolling. The properties obtained in mechanical twinning are remarkable and worthy reporting about.

**Keywords** Characterization · Martensite · Uniformity · Hardness · Pearlite-ferrite · Macrostructure · Microstructure · SEM · Bendability · Weldability · Mechanical twins

---

V. Musonda (✉) · E. T. Akinlabi

Department of Mechanical Engineering Science, University of Johannesburg, Auckland Park Kingsway Campus, P.O. Box 524, Johannesburg 2006, South Africa  
e-mail: [musondachandi@gmail.com](mailto:musondachandi@gmail.com)

V. Musonda

Department of Mechanical Engineering, School of Engineering, The University of Zambia, Great East Road Campus, P.O. Box 32379, Lusaka, Zambia

© Springer Nature Singapore Pte Ltd. 2020

M. Awang et al. (eds.), *Advances in Material Sciences and Engineering*, Lecture Notes in Mechanical Engineering, [https://doi.org/10.1007/978-981-13-8297-0\\_49](https://doi.org/10.1007/978-981-13-8297-0_49)

473

## 1 Introduction

Thermo-mechanically treated (TMT) reinforcement bars have been in use mainly owing to their superior tensile and ductility properties. This has also been due to the demand for low cost re-enforcement steel bars, which can guarantee a maximum yield point [1]. The reinforcement of concrete structure requires that, the steel and concrete, while acting together, will withstand the forces induced. The bonding between the two materials is guaranteed because the properties for thermal expansion for both materials is almost the same. Steel has excellent bendability property, and this makes it suitable for reinforcing concrete structures. There are direct benefits of using TMT bars to the customer and these include reduced total weight of re-enforcement bars per unit weight of concrete. This leads to reduced cost, reduced work force for re-enforcement bar fabrication and lower transportation costs.

Hot rolled TMT reinforcement bars pass through the water-cooling chamber after exiting from the finishing mill stand at a temperature of 850 °C. The bars are then superficially quenched for a very short dwell time (< 1 second). During this step, the bars are surface hardened, resulting into a hard martensite rim. The core of the bar, however, remains hot after the cooling process is over. The hardening effect on the surface is due to the remaining heat from the core. Subsequently, the surface is self-tempered into martensite and bainite. The bars are then transferred to the cooling bed where the surface temperature drastically drops to below 200 °C within ten seconds [2, 3]. This results into an equalisation temperature of ≈600 °C after air-cooling before settling to room temperature. At this stage, the residual austenite is transformed to a tough ferrite and pearlite core but in a refined and ductile form. It is this type of structure, which determines the ductility of the bars.

The martensitic transformation during the fast cooling is instantaneous as it happens very quickly [4]. The change in temperature is the driving force in the transformation during cooling. This transformation is spontaneous and occurs once the difference in the chemically free energies is equal to the difference in the critically free energy  $\Delta G_{M_s}$  [5, 6]. This moment, however, should relate to the  $M_s$ -temperature. Empirically,  $M_s$  temperature is also related to the chemical composition and Eq. (1) as articulated by Eichelman and Hull's study [7], has been widely used in this relationship.

$$M_s(^{\circ}\text{C}) = 1302 - 42(\% \text{Cr}) - 61(\% \text{Ni}) - 33(\% \text{Mn}) - 28(\% \text{Si}) - 1667(\% [\text{C} + \text{N}]) \quad (1)$$

Conversely, when the transformation of martensite is through the applied stress, then it is also possible to reach the critical value of  $\Delta G_{M_s}$  for temperatures exceeding the  $M_s$ -temperature, [6]. The temperature, nevertheless, can increase and reduce the variance in the chemical free energies. This can also lead to the nucleation of martensite by plastic deformation. If the variance becomes too small then the transformation will cease. The temperature, at which such changes occur, is referred to as the  $M_d$ -temperature. This is the temperature below which martensite will form during deformation [6, 7]. Several empirical equations relating to the  $M_d$ -temperature are available, and one of the most used is that of Angel [7]

$$M_d(30/50)(^{\circ}\text{C}) = 413 - 9.5(\% \text{Ni}) - 9.2(\% \text{Si}) - 13.7(\% \text{Cr}) \\ - 8.1(\% \text{Mn}) - 18.5(\% \text{Mo}) - 462(\% [\text{C} + \text{N}]) \quad (2)$$

In Eq. (2),  $M_d(30/50)(^{\circ}\text{C})$  is the temperature at which  $\alpha'$ , 50 vol.% is formed. This happens when 30% true strain is achieved during deformation. The elements in the composition are expressed in wt%. The amount of  $\alpha'$  also depends on the stress state during deformation [7]. Although Eqs. (1) and (2) may apply to austenitic stainless steels, they are still valid for other series of steels empirically. While the transformation of martensite is taking place, mechanical twins can also form within the austenite grains by deformation due to the hot rolling of steel [6, 8]. This usually happens in deformed steels with high manganese content. These twins play an important role in mechanical properties such as high strength and elongation when deformed [6, 8]. The deformation mechanism is associated with stacking fault energy (SFE) and mechanical twinning occurs at SFE roughly in the range 18–24 mJ/m<sup>2</sup>. To transform austenite to martensite, a range of 12–18 mJ/m<sup>2</sup> SFE is required. Formation of annealing twins depends on inherent plastic deformation. During the thermal and nucleation process, the shape of annealing twins is not affected [9–12]. In addition, the formation of twins depends on the reduction of the energy associated with twinning at the grain boundary [11]. The difference between annealing and mechanical twins is that, mechanical twins have sharp ends and have shaped lens. Annealing twins, however, are flat without sharp ends [10].

The sensitivity to temperature and strain rate in twinning is lower when compared to the effect of dislocation slip [6, 13]. However, subdivision of grains in mechanical twinning is likely and this can increase the barriers to slip (see Fig. 2 zone B). This promotes the storage of dislocations as the latter accumulates. Twins also help in decreasing the work-hardening rate during plastic deformation. To achieve the critical twinning stress ( $\sigma_T$ ) required for occurrence of twins, the critical stress must be reached. The critical twinning stress required is as shown in Eq. (3) [6, 14].

$$\sigma_T = \frac{2\gamma_{SFE}}{b} \frac{1}{SF} \quad (3)$$

In Eq. (3),  $\sigma_T$  is the critical twinning stress,  $\gamma_{SFE}$  is the SFE,  $b$  is the Burgers vector and the Schmidt Factor is represented as SF. According to the survey conducted [6, 13] about the measurements on most metals, the  $\sigma_T$  is not sensitive to temperature. This observation, however, has attracted a lot of debates about the findings on sensitivity. Other findings have recorded positive sensitivity and vice versa. However, co-workers [15] as reported in [6], proposed the critical twinning stress equation as shown in Eq. (4):

$$\sigma_T = K \dot{\epsilon}^{1/m+1} e^{\frac{Q}{(m+1)RT}} \quad (4)$$

In Eq. (4),  $m$  is a constant,  $K$  is a parameter,  $Q$  is the activation energy,  $T$  is the temperature and  $R$  is the gas constant.



## 2 Experimental Procedure

### 2.1 Materials Preparation

TMT high strength 650 MPa rebars were used in this experiment. The as received Y32 mm and Y16 mm were cut and prepared for polishing and etching. The Y32 mm samples were prepared for macrostructure analysis while the Y16 mm rebar samples were prepared for microstructural analysis.

### 2.2 Chemical Composition

The elemental compositions of the steel bars used in this work for Y32 mm and Y16 mm low carbon steels comprised (wt%: Y32): 0.18C, 0.6Mn, 0.33Si, 0.023S, 0.015P, 0.135Cr, 0.10Ni, 0.02Mo, 0.33Cu, 0.001 V, 0.003Al and 0.006 Ti on average. For Y16 mm (wt%): 0.23C, 0.8Mn, 0.25Si, 0.022S, 0.002P, 0.13Cr, 0.08Ni, 0.01Mo, 0.28Cu, 0.002 V, 0.002Al, and 0.005Ti. The carbon equivalent ( $C_{eqv}$ ) for these compositions was 0.38% on average. An Optical Emission Spectrometer (OES) was used to obtain these elements.

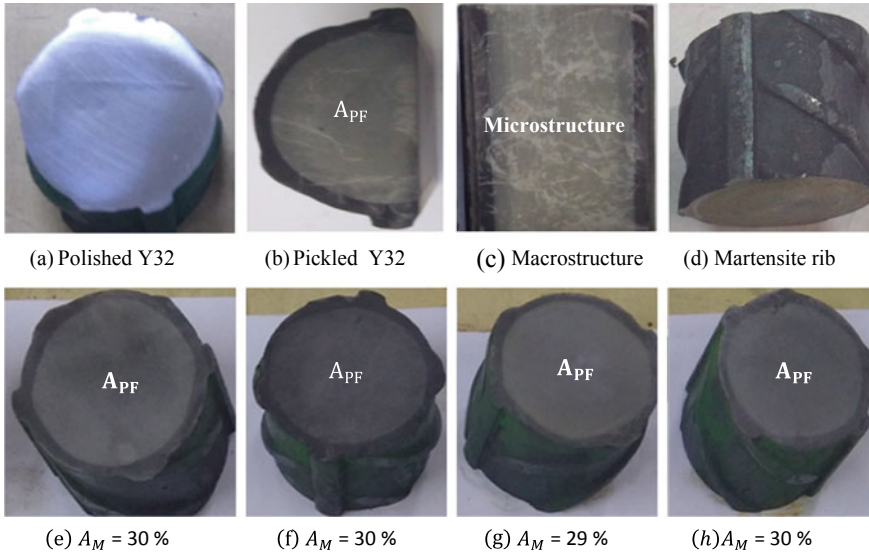
### 2.3 Metallography

Metallographic specimen preparation for microstructural analysis was conducted according to the standard guide ASTM E3-11 [16]. Upon completion of grinding and polishing, transverse and longitudinal sections of the samples were etched in 2% Nital solution for microstructure examination. A 5-min pickling using 5% Nital solution was used on samples for macrostructure characterisation [17].

## 3 Results and Discussion

### 3.1 Macrostructure Characterisation

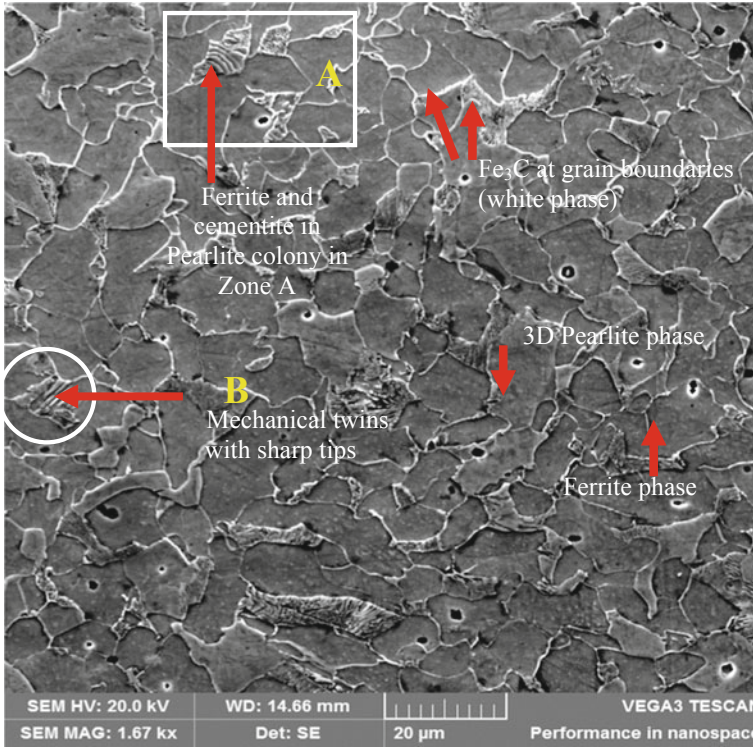
Typical cross-sectional macrostructure for thermally hardened rebars were analysed for uniformity of the martensite case. This is characterised by a uniform concentric cross-section of hardened case and a soft core at the centre. Figure 1a–h show the polished and etched macrographs of Y32 mm TMT rebars. The macrographs show a distinct surface layer of martensite (dark grey) followed by the core of the rebar (inner light grey circle) comprising pearlite and ferrite. Figure 1e–h further show



**Fig. 1** Macrographs of Y32 mm rebar polished and etched samples

the variation in martensite case areas with an average martensite area  $A_M = 29\%$ . Another interesting feature is the macrostructure revealed in Fig. 1c, which shows the microstructure of pearlite and ferrite visible with unaided eye after a 5 min pickling using 5% Nital solution. The lighter phases in the microstructure are the three-dimensional crystals of pearlite colonies, while the dark grey phase is the ferrite phase. Figure 1b is an etched transverse half section of the sample with uniform martensite rim.

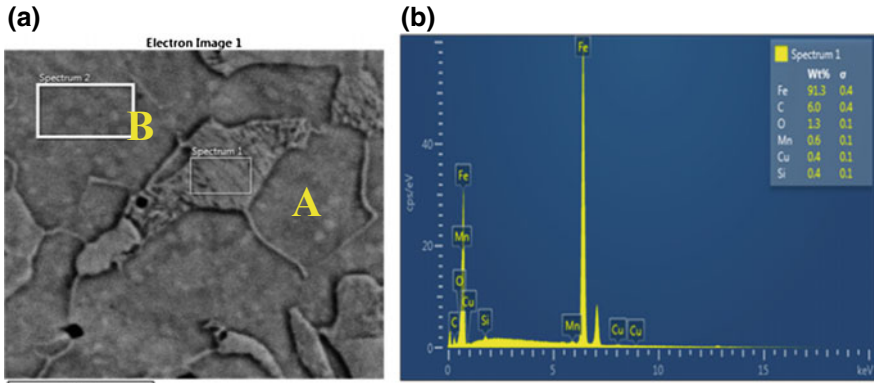
The proportion of the hardened periphery to the bar cross-section will vary according to the grade and size. A good quality quenched and self-tempered (Q & ST) steel shall have martensite area ( $A_M$ ) of about 20–30% of total cross sectional area ( $A_T$ ) [17, 18]. First, the total cross sectional area ( $A_T$ ) was determined without considering the area of ribs. Then, the area of pearlite-ferrite layer ( $A_{PF}$ ) was determined. The area of martensite layer for each specimen was then estimated as  $A_M = (A_T - A_{PF})$ . The  $A_M$  of tested specimens were found to vary between 28 and 30%. Such rebars are ideal for civil construction [19]. The proportion of the hardened case of rebar, which is over-quenched, is almost 60% of the  $A_T$  area of the rebar. This type of rebar, however, falls out of the required 20–30% threshold [19]. From the results of the macrostructure obtained for all the rebar samples, the martensite rim is within the 20–30% threshold with an average  $A_M$  of 29%. This is mainly due to the quality control measures taken during manufacturing.



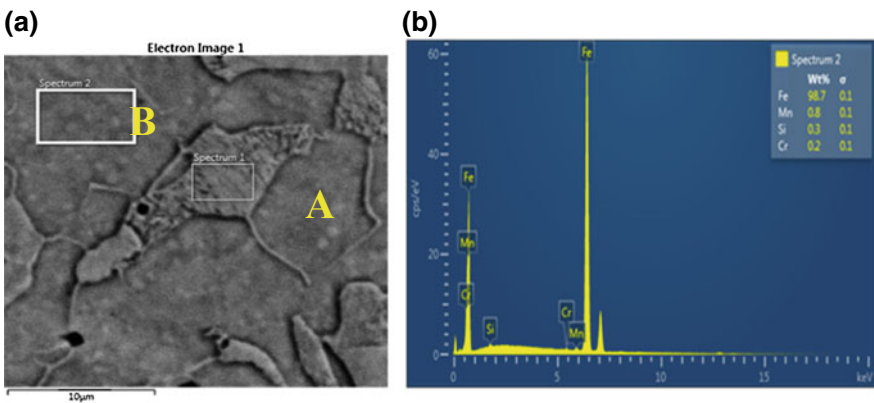
**Fig. 2** SEM micrographs for Y16 mm rebar showing ferrite and cementite in pearlite colony in zone A and mechanical twins in zone B

### 3.2 Microstructure Characterisation

Quantitative analysis of the microstructure was performed using VEGA 3 TESCAN Oxford Instruments X-Max 50 mm<sup>2</sup> SEM with energy dispersive x-ray spectroscopy (EDS). Figure 2 shows the pearlite colony of cementite and ferrite lamellae in zone A, aligned parallel to each other due to a common growth during the transformation in a Y16 mm rebar. Mechanical twins with sharp ends were also revealed as indicated in zone B. At the grain boundaries, Fe<sub>3</sub>C showing a white phase were also revealed in the microstructure. Figure 3a shows SEM-EDS image for Y16 mm rebar. The image reveals the pearlite colony of ferrite lamellae and cementite at spectrum 1 (Zone A) and the corresponding elemental composition for spectrum 1. Similarly, Fig. 4 shows SEM-EDS image for Y16 mm rebar. The image also reveals ferrite phase at spectrum 2 (Zone B) and the corresponding elemental composition for spectrum 2.



**Fig. 3** SEM-EDS images for Y16 mm rebar **a** SEM image of pearlite colony of ferrite lamellae and cementite at spectrum 1 (Zone A), **b** corresponding elemental composition for spectrum 1



**Fig. 4** SEM-EDS images for Y16 mm rebar **a** SEM image of ferrite phase at spectrum 2 (Zone B), **b** corresponding elemental composition for spectrum 2

### 4 Conclusion

In this study, characterisation of rebars has revealed that, mechanical properties can be affected by the non-uniformity of martensite area ( $A_M$ ). From the construction perspective; bendability and weldability of rebars are inevitable characteristics, which rebars should possess. Mechanical twins also contribute to the transformation of austenite to martensite when appropriate SFE is applied. Twins are part of the grains in the microstructure and they should not be regarded as grains themselves. Microstructure characterisation has also revealed that, the manganese content (wt% 0.6–0.8) was high enough to facilitate formations of twins in the Y16 mm rebar

as demonstrated in the SEM-EDS spectrums. Over and above, the quality control measures taken during the manufacturing process of the TMT bars have a significant impact on characterization of rebars.

**Acknowledgements** We sincerely thank Kafue Steel Plant at Universal Mining and Chemical Industries Limited in Zambia for the support rendered during our research.

## References

1. Prabir C, Shylamoni P, Roshan A (2004) Characterization of steel reinforcement for RC structures: an overview and related issues. *Indian Concr J*
2. Musonda V, Akinlabi ET, Jen TC (2017) Optimum temperature of hot rolled reinforced bars at the cooling bed. *IOP Conf. Series Mater Sci Eng* 225:012297. <https://doi.org/10.1088/1757-899x/225/1/012297>
3. Kabir IR, Islam MA (2014) Hardened case properties and tensile behaviours of TMT steel bars. *Am J Mech Eng* 2(1), 8–14
4. Haasen P (1996) *Physical metallurgy*, third edn. Cambridge University Press
5. Marshall P (1984) *Austenitic stainless steels—microstructure and mechanical properties*. Elsevier applied science publisher Ltd.
6. Wedberg D (2013) *Modelling of high strain rate plasticity and metal cutting*. Doctoral Thesis, Printed by Universitetsstryckeriet, Luleå. <http://tu.diva-portal.org/smash/get/diva2:999147/FULLTEXT02.pdf>. Accessed on 28 Aug 2018. ISBN 978-91-7439-670-6 (print), ISBN 978-91-7439-671-3 (pdf)
7. Eichelmann GJ, Hull FC (1953) The effect of composition of spontaneous transformation of austenite to martensite in 18–8-type stainless steel. *Trans ASM* 45, 77–104
8. Hedström P (2005) *Deformation induced martensitic transformation of metastable stainless AISI 310*. Licentiate thesis, Department of Applied Physics and Mechanical Engineering, Luleå University of Technology, Luleå
9. Muhammad M (2013) *The influence of grain size on the mechanical properties of Inconel 718*. Thesis, Department of Management and Engineering (IEI) Division of Engineering materials Linköping University, SE-58183 Linköping, Sweden. <http://www.diva-ortal.org/smash/get/diva2:779274/FULLTEXT01.pdf>. Last accessed 28 Aug 2017
10. Sourmail T, Opendacker P, Hopkin G, Bhadeshia HKDH (n.d) *Annealing twins, metals and alloys*. University of Cambridge
11. Dash S, Brown N (1963) An investigation of the origin and growth of annealing twins. *Acta Metall* 11(9):1067–1075
12. Jin Y, Bernacki M, Roher GS, Rollett AD, Lin B, Bozzolo N (2013) Formation of annealing twins during recrystallization and grain growth in 304L austenitic stainless steel, In: 5th international conference on recrystallization and grain growth, May 5, in Sydney, Australia
13. Meyers MA, Vöhringer O, Lubarda VA (2001) The onset of twinning in metals: a constitutive description. *Acta Mater* 49:4025–4039
14. Byun TS (2003) On the stress dependence of partial dislocation separation and deformation microstructure in austenitic stainless steels. *Acta Mater* 51:3063–3071
15. Talonen J, Hänninen H (2007) Formation of shear bands and strain-induced martensite during plastic deformation of metastable austenitic stainless steels. *Acta Mater* 55:6108–6118
16. ASTM E3-11 (2011) *Standard guide for preparation of metallographic specimens*
17. Sooraj Nair AO, Gokul PR, Sethuraj R, Nandipati S, Radhakrishna GP (2015) Variations in microstructure and mechanical properties of thermo-mechanically-treated (TMT) steel reinforcement bars. *Research Gate*. Accessed on 30 Aug 2018
18. Markan RK (2005) *Steel reinforcement for India—relevance of quenching and tempering technology*. *Steel World*, 4–9

19. Visvanathan CS, Prasad LN, Radhakrishna, Nataraja HS (2004) Sub-standard rebars in the Indian market: an insight. *Indian Concr J* 78(1):52–55

# Application of Fuzzy Control Charts: A Review of Its Analysis and Findings



Hidayah Razali, Lazim Abdullah, Termimi Ab Ghani and Nazim Aimran

**Abstract** Statistical process control is a technique for controlling processes to distinguish causes of variation and signal the need for corrective actions. Fuzzy control charts are more sensitive than traditional one hence, its provide better quality products. Thus, this article provides a comprehensive review of numerous fuzzy control charts that can help other researchers to extract key points of each paper in a minimum time. In brief, this paper has two objectives, which are to classify the types of application of fuzzy control chart (type 1 and type 2 fuzzy control chart) and to identify the past and current developments in the fuzzy control chart for the last five years. Based from the results, most of the researcher studied type 1 fuzzy  $u$  control charts and only few of them used the type 2 control charts.

**Keywords** Fuzzy control chart · Type 1 fuzzy control chart · Type 2 fuzzy control chart

## 1 Introduction

Quality has always been an integral part of virtually all products and services in our life. Nowadays, quality has become one of the most important consumer decision factors in the selection among competing products and services [1]. The introduction of methods in quality control and improvement had been evolutionary developed since the decades of 1700 [2], specifically statistical methods for quality control and improvement are divided into three major areas which are statistical process control, design of experiments and acceptance sampling. Statistical process control

---

H. Razali (✉) · N. Aimran  
Faculty of Computer & Mathematical Sciences, Universiti Teknologi MARA (UiTM), Shah Alam, Malaysia  
e-mail: [hidayah3849@ns.uitm.edu.my](mailto:hidayah3849@ns.uitm.edu.my)

L. Abdullah · T. A. Ghani  
School of Informatics & Applied Mathematics, Universiti Malaysia Terengganu (UMT), Terengganu, Malaysia

is a technique for controlling processes to distinguish causes of variation and signal the need for corrective actions [2]. In statistical process control, the most important tool that is useful in the process of monitoring technique is control chart. Control charts helps to distinguish the products that are less or more than the control limits.

Reviews of the control charts can be retrieved from journals studied by Sabegh et al. [3]. However, they only analyse type-1 fuzzy control charts and the data are from 2014 and before. In the concept of quality control, it seems that most of these reviews are not really updated since it covers 2014 and before. In fact, nowadays, researcher had already studied the type-2 fuzzy control charts which are more advanced than type 1 control charts.

This paper aims to get a clearer picture of statistical process control tools, models, methods and information needed about the fuzzy control charts. We include the distribution of articles that are related to fuzzy control charts from the last five years which is from year 2014 until 2018. In brief, we have two objectives which are (1) to classify the types of application of fuzzy control chart (type 1 and type 2 fuzzy control chart) and (2) to identify the past and current developments in the fuzzy control chart.

## 2 Type-1 Fuzzy Control Chart

Nowadays, fuzzy control charts had been well known and being used widely. Fuzzy theory is one of the most applicable tools which academia have employed to deal with uncertainty [4]. In fact, the use of a fuzzy approach in the design of control charts has allowed to improve the performance of traditional control charts, as well as enabled a simple approach for the design of control charts for linguistic variables with multinomial distributions for both, the univariate case and the multivariate case [5]. The development of control chart is not only to monitor the central tendency of the process, but it will also indicate the degree of fuzziness of the data itself [2].

### 2.1 Fuzzy Attribute Control Chart

A research by Darestani et al. [4] studied the development of fuzzy  $u$  control chart for monitoring defects in the format of a case study. The purpose of the research was to investigate the attributes of fuzzy  $U$  control chart. The result was grouped into four categories which are “in control”, “out of control”, “rather in control”, “rather out of control”. A case study for monitoring defects had been done to the data from the supply chain of the automotive industry to control the average number of defects in devices of 25 subgroups to identify the number of defects. As a result, the definition of fuzzy numbers for each type of defect sensitivity and the unit could be classified into the four groups (as hypothesized before) which represents the actual quality of the products [4].



In 2014, Erginel [6] studied a process in monitoring the attribute data that comprises of  $p$  control charts and  $np$  control charts. Based from previous literature review, the researches configured the transformation techniques at the decision stage but in this study, the fuzzy control charts were constructed using rules. Hence, fully fuzzy control chart had been introduced first based on constant sample size and variable sample size. Again, Erginel [7] investigated the fuzzy  $p$  control chart. In the study, the methodology used to construct the fuzzy  $p$  control chart was based on median transformation method for both constant and variable sample size was proposed by using alpha-cuts [7]. In 2016, Hou et al. [8] studied the attribute control chart construction based on fuzzy score number in China. The method was built a control chart based on fuzzy score number, describe the design of nonconformity judging criteria and analyse the type selection of fuzzy numbers. On the other hand, Truong et al. [9] analysed the fuzzy  $u$  chart for sustainable manufacturing in the Vietnam textile dyeing industry in 2017 to monitor the fuzzy average number of nonconformities per unit.

Besides, a research conducted by [9] used fuzzy  $u$  control chart based on fuzzy rules and evaluated its performance using fuzzy operating characteristics (OC) curve. The study aims to apply fuzzy spectrum in collecting the vague data and to employ the fuzzy  $u$  chart in variable sample sizes using fuzzy rules. The researcher used fuzzy operating characteristic (FOC) curve to investigate the performance of the fuzzy  $u$  control chart. A practical example was illustrated to investigate the efficiency of the proposed approach by comparing the performances of control charts. As a result, the probability of the type II error for the crisp chart was more than the same amount for the fuzzy chart and the efficiency of the fuzzy chart was more that the crisp chart [9]. Next, Chang et al. [10] investigated the multilevel control chart and fuzzy set theory to monitor inpatient falls. They used  $u$  control chart to monitor the adverse events relating to falls, severity of fall injuries to develop multilevel control charts and applies fuzzy set theory to determine the severity falls. The researcher also combined a multilevel control charts, fuzzy set theory and warning lines concept.

## 2.2 Fuzzy Variables Control Chart

Fuzzy variable control charts are usually necessary to monitor both the mean value of the quality characteristics and its variability.

Darestani and Nasiri [11] studied the fuzzy  $\bar{X}$  and  $s$  control chart and process capability indices in normal data environment. The study aimed to discuss the issue of measuring the quality characteristics that practitioners sometimes face with uncertainties and linguistic variables by using the fuzzy theory [11]. The researcher analysed the fuzzy formulation of the process capability indices (PCI) to state whether the production process can produce items within the specification limits predetermined by the customer. Besides, the researcher also measured both triangular fuzzy numbers (TFNs) and trapezoidal fuzzy numbers (TrFNs) stages. On the other hand, Shu and Wu [12] studied the fuzzy  $\bar{X}$  chart and  $R$  control chart based on fuzzy dominance

approach. The researcher proposed fuzzy  $\bar{X}$  and  $R$  chart whose fuzzy control limits were obtained on the basis of the results of the resolution identity, a well-known theory in the fuzzy set field.

A research by Shu et al. [13] studied the fuzzy  $s$  control charts in 2017. They integrated fuzzy set theories to establish the fuzzy charts under a general variable sample size condition. At first, the resolution identity principle was exerted to erect the sample statistics and control limits fuzzy numbers (SSFNs and CLFNs), where the sample fuzzy data were unified and aggregated through statistical and non-linear programming manipulations. Then, the fuzzy logic was enacted to categorize process conditions with intermittent classifications between in control and out of control processes. Kaya et al. [14] investigated the analysis and control of variability by using fuzzy individual control chart. The research aimed to develop two new fuzzy control charts for individual measurements (FCCIM) namely fuzzy individual control chart for (FICC) and fuzzy moving range control chart for (FMRCC) with fuzzy control rules in determining the variability of the process. Return volatility in the Borsa Istanbul-30index (BIST-30) had been analysed and a fuzzy control chart for individual measurement (FCCIM) had been proposed to be used in determining and controlling the variables for the BIST-30 index. The detection of changes in a process within shortest time provides significant benefits in terms of cost and quality hence it gives much importance for the investors [14].

### 2.3 Other Fuzzy Control Chart

Aside from the attribute and variables control chart, there are Cumulative Sum (CUSUM) control chart, multilevel control charts, Exponentially Moving Average (EWMA) control chart and multinomial control chart.

It is not feasible to use such an approach of the traditional control chart to monitor the fuzzy control chart when the data is composed of integral-valued fuzzy [12]. This study aimed to propose the designed standardized fuzzy control chart for interval-valued fuzzy data set. The datasets of vegetable price from January 2009 to September 2010 were obtained from Council of Agriculture, Executive Yuan. Based from the analysis, they proved that the simpler approach to construct the standardized interval-valued chart based on traditional standardized control chart was easy and straightforward to be used. In fact, the control limit of the designed standardized fuzzy control chart was an interval with (lower control limit (LCL), upper control limit (UCL)) that consists of the conventional range of classical standardized control chart.

Azadeh et al. [15] introduced a unique fuzzy multi-control approach for continuous quality improvement in a radio therapy department. Each radiation beam was divided into many sub fields with a modulated intensity and the quality control modelling for IMRT is a desirable area for the researchers. The researcher concluded that each criterion out of fuzzy control chart zone was necessary for implementation plan to avoid the patient from danger due to out of control feature and the improve-

ment was very beneficial to all industries, especially in sensitive industries. Besides, [16] developed a fuzzy multivariate CUSUM control chart to monitor multinomial linguistic quality characteristics. Therefore, Hotelling's  $T^2$  chart (F- $T^2$ ) and fuzzy multivariate exponentially weighted moving average (F-EWMA) control chart had been used to monitor the processes. In the paper, a fuzzy multivariate cumulative sum control chart (F-MCUSUM) was developed by using the fuzzy set theory. The case study used data from the food industry to show that the applicability of the proposed approach and the interpretation of the out of control signals were improved better than the conventional multivariate control charts.

In another research, fuzzy exponentially weighted moving average (FEWMA) control chart for univariate data was investigated to decrease the number of false decisions by providing flexibility on the control limits. Sample data included uncertainties from the measurements systems and environmental conditions, fuzzy numbers and or linguistic variables could be used to capture these uncertainties [17]. The researcher used data about production process of plastic buttons that are produced by small scale enterprise operating in clothing industry in Turkey as a real application.

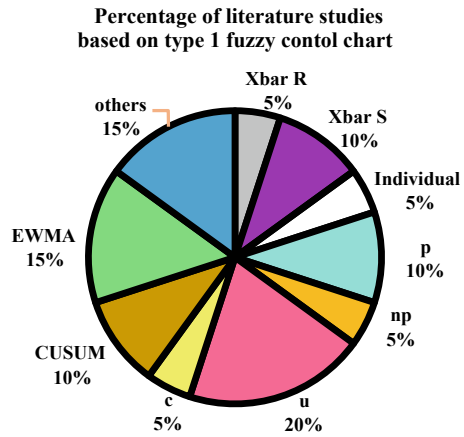
Erginel and Şentürk [18] studied the fuzzy EWMA and fuzzy CUSUM control charts in Turkey. Classical Exponentially Weighted Moving Average (EWMA) and Cumulative Sum (CUSUM) control charts have the ability of detecting small shifts in the process mean but they are not capable to capture any uncertainty of incomplete data. Wibawati et al. [19] studied the fuzzy multinomial control chart and its application in Indonesia. The chart used was based on binomial distribution and each item was classified based on more than two categories such as very bad, good and very good. The control limit of the control chart obtained multinomial distribution and the chart was being applied to the data glass and they were compared with multinomial  $p$  control chart [19].

### 3 Type-2 Fuzzy Control Chart

Type 2 fuzzy set theory captures ambiguity that associates the uncertainty of membership functions by incorporating foot prints and models high level uncertainty. Once the process monitoring tools have detected an assignable causes, this cause is removed to bring the process back into control.

In 2018, Erginel et al. [20] monitored fraction nonconforming in process with interval type-2 fuzzy control chart. The researcher used interval type-2 fuzzy nonconforming control chart to handle more uncertainties in the process. In fact, the interval type-2 fuzzy  $p$  control chart was developed into the literature for the first time. Besides, Senturk and Antucheviciene [21] studied the interval type-2 fuzzy control charts for a number of nonconformities control chart. The application was implemented into the data of packaging process of the food sector and the data were collected from 18 samples as interval type-2 fuzzy numbers from the process because of the imprecise collecting methodology, and the limits of interval type-2 fuzzy  $c$  control charts were calculated. After that, the proposed fuzzification method was

**Fig. 1** Literature studies based on type 1 fuzzy control chart. Based from the pie chart, we can conclude that majority of the researcher studied fuzzy  $u$  control charts which is 20%, followed by, EWMA and others chart, which is 15% respectively. The least fuzzy control chart that had been studied is the  $\bar{X}$  and  $R$  chart,  $np$  chart, individual chart and  $c$  chart which is by 5% respectively



applied to the fuzzy control limit and as a result, the best decision had been made for the food company.

A research by Teksen and Anagün [22] investigated type 2 fuzzy control charts using likelihood and defuzzification methods. Previous research showed that the use of type 1 fuzzy sets was used widely, however it showed that much of the data used in the daily life cannot be expressed by type 1 fuzzy control charts but they could be expressed by type 2 fuzzy control charts. The study aimed to use type 2 fuzzy sets in  $c$  control charts as a new approach and they compared it with the classical control charts.

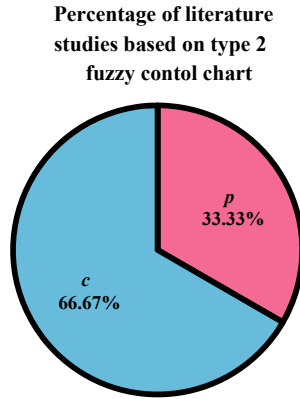
### 4 Analysis and Findings

After we reviewed the journals related to fuzzy control charts, we analyse the case studies based on the type of control chart (Figs. 1, 2).

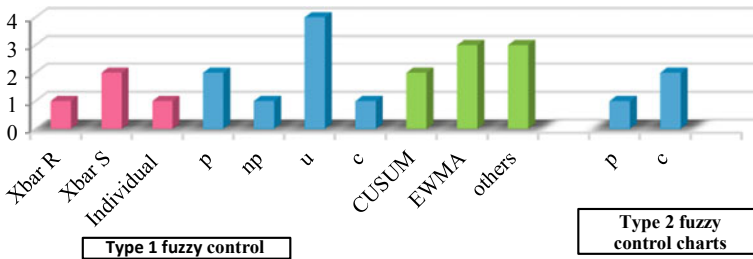
Based on the Fig. 3, we can see that Attributes control charts are more popular than Variables control charts in both type 1 and type 2 fuzzy control charts. In Type 1 control charts,  $u$  chart is being studied most followed by  $p$  chart and both  $np$  and  $c$  chart.

### 5 Conclusion

This study analysed published articles in leading scientific journals for the last 5 years which is between 2014 until 2018. Some limitations may exist since the findings are based on papers published in academic journals and journals that are not well-known are not being included in this study. For Sects. 2 and 3, they help readers to have



**Fig. 2** Literature studies based on type 2 fuzzy control chart For type-2 fuzzy control charts, *c* control charts had been studied twice and *p* chart had been studied once. Many other control charts are not being investigated yet



**Fig. 3** Comparison between literature studies based on type 1 and type 2 fuzzy control charts

a good overview of Type 1 and Type 2 fuzzy control charts based on attribute and variable charts.

## 6 Future Research

Based on the analysis, we can conclude that majority of the researcher had analysed type 1 fuzzy control charts compared to type 2 fuzzy control charts. In fact, the highest number of control charts that had been investigated is Attributes control chart. Hence, future researcher can study type 2 fuzzy control charts and other types of fuzzy sets such as intuitionistic fuzzy sets, hesitant fuzzy sets or neutrosophic fuzzy sets.

## References

1. Montgomery DC (2013) *Statistical quality control*, 7th edn. Wiley, Singapore
2. Cheng C.-B. (2005) Fuzzy process control: construction of control charts with fuzzy numbers. *Fuzzy Sets Syst* 154(2):287–303
3. Sabegh, MHZ, et al (2014) A literature review on the fuzzy control chart; Classifications & analysis. *Int J Supply and Operations Manag* 1(2):167–189
4. Darestani SA et al (2014) Development of fuzzy u control chart for monitoring defects. *Int J Qual Reliab Manag* 31(7):811–821
5. Fernandez MNP (2017) IEEE, fuzzy theory and quality control charts. In 2017 IEEE international conference on fuzzy systems. IEEE, New York
6. Erginel N (2014) Fuzzy rule-based p and np control charts. *J Intell Fuzzy Syst* 27(1):159–171
7. Erginel N (2008) Fuzzy  $\bar{p}$  control chart. In: World scientific proceedings series on computer engineering and information science 1; computational intelligence in decision and control—proceedings of the 8th international FLINS conference
8. Hou SW, Wang H, Feng SX (2016) Attribute control chart construction based on fuzzy score number. *Symmetry-Basel* 8(12):13
9. Truong K-P, et al (2017) The fuzzy U-chart for sustainable manufacturing in the Vietnam textile dyeing industry. *J Symmetry* 9(116)
10. Chang C-M et al (2016) Multilevel control chart and fuzzy set theory to monitor inpatient falls. *J Bus Res* 69(6):2284–2288
11. Darestani SA, Nasiri M (2016) Fuzzy  $X^{\bar{}}-S$  control chart and process capability indices in normal data environment. *J Qual Reliab Manag* 23(1):2–24
12. Shu M-H, Wu H-C (2011) Fuzzy  $X^{\bar{}}$  and R control charts: Fuzzy dominance approach. *Comput Ind Eng* 61(3):676–685
13. Shu M-H, et al (2017) Fuzzy  $X^{\bar{}}$  and S control charts: a data-adaptability and human-acceptance approach. *J Complex* 2017:17
14. Kaya I, Erdogan M, Yıldız C (2016) Analysis and control of variability by using fuzzy individual control charts. *J Appl Soft Comput* 51:370–381
15. Azadeh A et al (2016) A unique fuzzy multi-control approach for continuous quality improvementradio therapy department. *Qual Quant* 50:2469–2493
16. Ghobadi S et al (2015) Developing a fuzzy multivariate CUSUM control chart to monitor multinomial linguistic quality characteristics. *Int J Adv Manuf Technol* 79(9–12):1893–1903
17. Şentürk S, Erginel N, Kaya İ, Kahraman C (2014) Fuzzy exponentially weighted moving average control chart for univariate data with a real case application. *Applied Soft Computing* 22:1–10
18. Erginel N, Senturk S (2016) Fuzzy EWMA and fuzzy CUSUM control charts. In Kahraman C, Kabak O (eds) *Fuzzy statistical decision-making: theory and applications*. Springer Int Publishing Ag: Cham, pp 281–295
19. Wibawati et al (2016) Fuzzy multinomial control chart and its application. In: Yasin M, Harun SW (eds) 5th international conference and workshop on basic and applied sciences. Amer Inst Physics, Melville
20. Erginel N, Şentürk S, Yıldız G (2018) Monitoring fraction nonconforming in process with interval type-2 fuzzy control chart. *Adv Intell Syst Comput*, 701–709
21. Şentürk S, Antucheviciene J (2017) Interval type-2 fuzzy c-control charts: an application in a food company. *Informatica* 28 (2):269–283
22. Teksen HE, Anagün AS (2018) Type 2 fuzzy control charts using likelihood and defuzzification methods. *Adv Intell Syst Comput*, 405–417

# Fracturing Parameters in Petroleum Reservoirs and Simulation



Amani J. Majeed, Ahmed K. Alshara, A. M. Al-Mukhtar  
and Falah A. Abood

**Abstract** The increasing demand for crude oil makes it necessary to consider factors that increase the productivity of the reservoirs. One of these factors is fracture that is found naturally or produced hydraulically, where the fracture improves reservoir flow and connectivity. The most common characteristics of naturally fractured reservoirs (NFRs) are the fractures directionality. In this review, the most important characteristics and parameters that affect the fracture have been explained. In addition, the simulations of the fracture phenomena have been cleared. The difference among the models that solved the fracture problems are; discrete fracture model (DFM), dual porosity model (DPM), embedded discrete fracture model (EDFM), and hybrid models DP and EDFM (DP + EDFM) are shown with characteristics of each model. The present study focused on the shape factor and the direction of the fracture to show their effects on the performance of the petroleum reservoir. In addition, the review of general important parameters for the fractured reservoirs has been presented.

**Keywords** Rock mechanics · Fractured reservoirs · Fracture parameters · Fracture simulation

---

A. J. Majeed  
Petroleum Engineering Department, University of Basra, Basra, Iraq

A. K. Alshara  
Civil Engineering Department, University of Misan, Amarah, Iraq

A. M. Al-Mukhtar (✉)  
College of Engineering, University of Warith Alanbiyaa, Karbalaa, Iraq  
e-mail: [almukhtar@hotmail.de](mailto:almukhtar@hotmail.de)

VFF, TUBA Freiberg, 09599 Freiberg, Germany

F. A. Abood  
Mechanical Engineering Department, University of Basra, Basra, Iraq

## 1 Introduction

All petroleum reservoirs contain natural fractures due to the earth layers stress. The man-made fractures result from drilling activities and increase in pore pressure during the injection operations. The naturally fractured reservoir (NFR) is a randomly located fracture networks in earth layers. The injection and production practices caused a redistribution of the earth stresses [1, 2]. Characteristics of fracture networks such as shape, dimensions, orientations, rocks properties of fracture matrix, etc. They are important in order to enhance the productivity of the reservoir. For fractured reservoirs, obtaining the right data and forecasting the reservoir performance is much more difficult than for the conventional reservoir. Naturally fractured reservoirs (NFRs) characterized are difficult for the engineers to predict because of the constructions of the fractures and nature of rocks and fluid (phases, wettability, capillary, etc.). It is important to establish some basic criteria for recognizing the fractures, since the fractures are an important element in performance of NFR. Fractures occur in preferential directions, determined by the direction of regional stress [3]. This is usually parallel to the direction of nearby faults or folds. Nevertheless, in the case of faults, they may be perpendicular to the fault or there may be two orthogonal directions. This study summarizes the main characteristics and parameters that effect on the fluid flow within the fractured reservoirs. It also includes a thorough review of the fractured reservoir simulation modeling, and models that deal and solve the fracture problems.

## 2 Reservoir Fracture Parameters

The researchers show that natural fracture permeability and density are the most common parameters [4]. The fractures have high permeability than the matrix. Therefore, they provide a quick flow. Many parameters are considered to characterize the fractured reservoir [5]. Some of these parameters related to the properties of rock and some others related to the fractures. The properties of fracture (porosity, relative permeability, intensity, conductivity, orientation, and size of fractures) can be estimated directly from core analysis or by well logging methods [6, 7].

In 1986, a new method for modeling NFR was developed to describe the effect of capillary pressure and gravity forces in fractured reservoirs [8].

In addition, many papers studied the effect of interporosity function and shape factors [9–11]. The shape factor is one of the important parameters in a dual porosity system, which describes the fluid transportation between matrix blocks and fractures [12]. Nevertheless, this parameter is not used in a single porosity matrix block as it is a single piece of rock [13]. This factor is proposed by Warren [14], and Kazemi [15] in double porosity concept. In 1976, Kazemi et al. extended the Warren and Root's shape factor to be used for two phases and three dimensional NFR [16]. However, in 1989, they proposed that Kazemi's shape factor is not accurate, and the most



accurate pressure distribution has been obtained if they multiplied this parameter with some factors [17, 18]. In 1985, it was concluded that by increasing the surface area, the imbibitions recovery rate increases [19]. Since that time, the shape factor has been discussed stormily for modeling fractured reservoir [20–24]. In 2012, it was explained that the hydraulic conductivity in the fracture has been affected by the fracture toughness [25]. They proposed a new method to simulate the flow in a real fracture.

Fracture porosity and fracture permeability have a major effect on fluid flow in many NFR [26]. These properties can be estimated by using a well test analysis [27]. Hydraulic fracturing in some low-permeability reservoirs is instrumental to increase and achieve an economic production rate. Modeling complex coupled with transient and dynamic processes found in geo-systems require increasingly high-resolution models for a more precise and qualified validation and evaluation [28].

Recently, in 2012, the fractured permeability have been estimated with more reliability if image log data and well test analysis were integrated together [26]. The resistance of the material against fracture can be measured in the lab or in the field [29]. There is a significant complexity in numerical simulation fracturing and multiple phases flow. A significant number of researches during the last 50 years described the fracturing in laboratories [30].

In 2016, [31] a study has noted that dual porosity-dual permeability simulation of the water-flood process is inaccurate if all fractures have been taken in calculate shape factor. Therefore, they suggested that the shape factor used in dual porosity-dual permeability water-flood or enhanced oil recovery simulations or in homogenization should be based only on the sub-network that carries almost all the injected fluid.

In 2017, a new analytical solution was developed for interporosity flow functions and shape factors between the fracture and matrix block in the NFR [32]. Their new method is able to provide more accurate parameters for compressible fluid productivity prediction and the more reasonable theoretical basis for the correct interpretation of well testing has been introduced.

### 3 Fractured Reservoir Simulation

Fractures have a great effect on the fluid within the reservoir. To simulate the flow in the fractured reservoir, the dual porosity models have been used widely [4, 33–38]. At that time, they stated that the dual porosity model gave a sufficient precision for a practical purpose [37]. The porosity and permeability are high in the fractured reservoir. Therefore, the single porosity model cannot be used in such cases.

In 1960, dual porosity was established [39]. In former time, the dual continuum modeling was the conventional method for simulating fractured reservoir [40]. None of them, neither dual continuum nor dual porosity could provide an accurate solution [41]. Discrete fracture methods were better than dual continuum and others because it models the fluid flow in individual fracture [41]. Nevertheless, the disadvantaged,

and limitations due to the time consuming and high computational cost for the above numerical methods have been stated in Ref. [4].

Several studies assumed transient interporosity flow for modeling [42–44]. The fracture of the basement reservoir was introduced by Lefranc et al. [45], Suardana et al. [46] and Gupta et al. [47].

In 2014, Huang et al. [48] used the mimetic finite difference method to develop a new numerical scheme for the discrete-fracture model. They explained that their new method provides a highly accurate approximation of the velocity field. In addition, a robust and efficient numerical approach has been implemented for the two-phase flow simulation in discrete-fractured media, if the mimetic finite difference and finite volume methods were combined. Their approach is applicable for both 2D and 3D discrete-fracture systems.

However, in 2017, it has been proposed that the results are not as accurate as compared with discrete fracture models [41]. The most accurate results have been obtained if a discrete fracture model with dual porosity and dual permeability (DPDP) were integrated together [41]. The exemplary results are presented in Fig. 1. Obviously, different models have been used to simulate the oil production in a low-permeability oil reservoir. Their workflow contained five vertical wells. Four of these wells hold at the corners of the reservoir, while the water injection from one well holds at the center. As shown in this Fig. 1, the dual porosity method gives a less accuracy among all other considered models, while high accuracy was achieved when embedded discrete fracture method was applied.

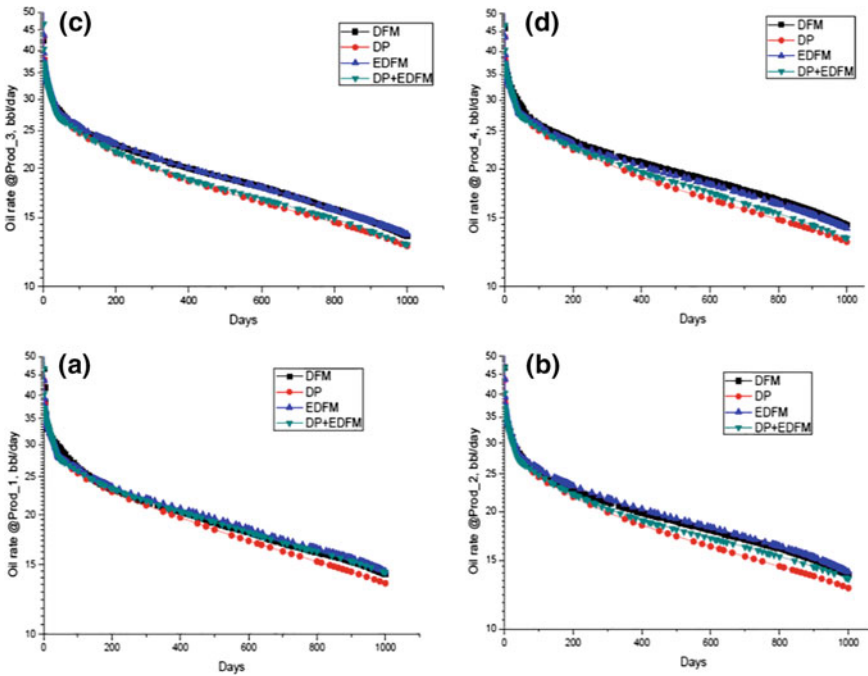
The fracture networks were simulated also by extended FEM (XFEM) method based on the stress intensity factor (SIF) [49]. This approach is criticized as it is time consuming. Therefore, the crack propagation based on energy criterion was used instead [49].

Simulation of fractures in rocks and reservoirs like in metals can be done in terms of the SIF and fracture mechanics approach. This approach is essential, and can be used to understand the behavior of the reservoir. Simulating the fracturing process in rock using Franc2D was carried out [50, 51]. Fracture mechanics and SIF calculations for metal structures can be found [50–52].

SIFs were calculated using a Franc2D program from Cornell University Fracture Group [53], which needs less effort than a 3D model. The fracture propagation in 2-D requires a series of fracture analysis. The author published few works using Franc2D that can be considered as the extended case studies [54–57].

The flow model through the naturally fractured was presented in Ref. [58]. Hence, streamlines and contour have been shown. The flow is controlled between the matrix (crack networks) and fracture by hydraulic conductivity [58].

Finally, the fracture in reservoir with both categories (naturally and hydraulic) needed more attention and investigation.



**Fig. 1** Comparison between different models: **a** well “Prod\_1” oil rate, **b** well “Prod\_2” oil rate, **c** well “Prod\_3” oil rate, **d** well “Prod\_4” oil rate, and, **e** field cumulative oil [41]

## 4 Conclusions

In the above-mentioned reviews, it has been concluded that the models and simulation of the fractured reservoir are still developing. However, discrete fracture model gives a more accurate simulation when comparing with dual-continuum models. Moreover, for a large scale and for a complex fracture network in shale oil reservoirs, high accuracy simulation can be achieved when it is integrated with embedded discrete fracture model and dual continuum models. Finally, to get an integrated model for any fractured reservoir, all parameters may affect on the fluid flow in the fracture zone or affect on the porous zone as well, and these must be considered. In this issue, we discussed some important parameters of the unconventional reservoir. Moreover, importantly many parameters that affect on the performance of fractured petroleum reservoirs such as shape, dimensions, orientations of fracture, etc., were detected and discussed.

## References

1. Abushaikh AS, Gosselin, OR (2008) Matrix-fracture transfer function in dual-media flow simulation: REVIEW, comparison and validation. In: Europec/EAGE conference and exhibition
2. Bratton T et al (2006) The nature of naturally fractured reservoirs. *Oilfield Rev* 4–23
3. Ouenes A, Richardson S, Weiss WW (1995) Fractured reservoir characterization and performance forecasting using geomechanics and artificial intelligence. In: SPE annual technical conference and exhibition
4. Han X et al (2013) The optimal design of hydraulic fracture parameters in fractured gas reservoirs with low porosity. In: Proceedings of the 2nd international conference on computer science and electronics engineering
5. Golf-Racht TD (1982) Fundamentals of fractured reservoir engineering
6. Cinco-Ley H (1996) Well-test analysis for naturally fractured reservoirs. *J Pet Technol* 48(01):51–54
7. Mavor MJ, Cinco-Ley H (1979) Transient pressure behavior of naturally fractured reservoirs. In: SPE California regional meeting
8. Litvak BL (1986) Simulation and characterization of naturally fractured reservoirs. In: Reservoir characterization, Elsevier, pp 561–584
9. Matthews CS, Russell DG (1967) Pressure buildup and flow tests in wells. *Soc Pet Eng AIME* 130–133
10. Sarma P, Aziz K (2004) New transfer functions for simulation of naturally fractured reservoirs with dual porosity models. In: SPE annual technical conference and exhibition
11. Bourbiaux B, Granet S, Landereau P, Noetinger B, Sarda S, Sabathier JC (1999) Scaling up matrix-fracture transfers in dual-porosity models: theory and application. In: SPE annual technical conference and exhibition
12. Dershowitz B, LaPointe P, Eiben T, Wei L (1998) Integration of discrete feature network methods with conventional simulator approaches. In: SPE annual technical conference and exhibition
13. Firoozabadi A, Thomas LK (1990) Sixth SPE comparative solution project: dual-porosity simulators. *J Pet Technol* 42(06):710–763
14. Warren PRJE (1963) The behavior of naturally fractured reservoirs. *Trans Soc Pet Eng AIME* 228:245–255
15. Kazemi H (1969) Pressure transient analysis of naturally fractured reservoirs with uniform fracture distribution. *Soc Pet Eng J* 9(04):451–462
16. Kazemi H, Merrill LS Jr, Porterfield KL, Zeman PR (1976) Numerical simulation of water-oil flow in naturally fractured reservoirs. *Soc Pet Eng J* 16(06):317–326
17. Ueda Y, Murata S, Watanabe Y, Funatsu K (1989) Investigation of the shape factor used in the dual-porosity reservoir simulator. In: SPE Asia-Pacific conference
18. Coats KH (1989) Implicit compositional simulation of single-porosity and dual-porosity reservoirs. In: SPE symposium on reservoir simulation
19. Torsaeter O, Silseth JK (1985) The effects of sample shape and boundary conditions on capillary imbibition. In: North Sea Chalk symposium, Stavanger
20. Panek LA (1985) Estimating fracture trace length from censored measurements on multiple scanlines. In: Proceedings of the international symposium on fundamentals of rock joints, Björkliden, pp 15–20
21. Rouleau A, Gale JE (1985) Statistical characterization of the fracture system in the Stripa granite, Sweden. *Int J Rock Mech Mining Sci Geomech Abstr* 22(6):353–367
22. Rives T, Razack M, Petit J-P, Rawnsley KD (1992) Joint spacing: analogue and numerical simulations. *J Struct Geol* 14(8–9):925–937
23. Lee SH, Lough MF, Jensen CL (2001) Hierarchical modeling of flow in naturally fractured formations with multiple length scales conventional finite difference on the basis of their length ( $l_f$ ) relative to the finite difference grid size ( $l_g$ ), fractures are classified as belonging to on. *Water Resour Res* 37(3):443–455

24. Pirker B (2008) A new approach for modeling dual porosity reservoirs using recovery curves (na)
25. Liu QQ, Fan HG (2012) The characteristics and estimation of flow through a single rough-walled fracture. *J Hydrodyn* 24(3):315–322
26. Bahrami H, Rezaee R, Hossain M (2012) Characterizing natural fractures productivity in tight gas reservoirs. *J Pet Explor Prod Technol* 2(2):107–115
27. Saidi AM (1987) Reservoir engineering of fractured reservoirs: fundamental and practical aspects. Total Edition Presse, Paris. Total
28. Kemmler D, Adamidis P, Wang W, Bauer S, Kolditz O (2005) Solving coupled geoscience problems on high performance computing platforms. In: International conference on computational science, pp 1064–1071
29. Malin SC (2005) In situ stress determination in unsaturated soils using hydraulic fractures. Clemson University
30. Murdoch LC, Richardson JR, Tan Q, Malin SC, Fairbanks C (2007) Reply to the discussion by Au and Yeung on ‘forms and sand transport in shallow hydraulic fractures in residual soil’ *Can Geotech J* 44(12) :1474–1475, 1476–1478
31. Gong J, Rossen WR (2016) Shape factor for dual-permeability fractured reservoir simulation: effect of non-uniform flow in 2D fracture network. *Fuel* 184:81–88
32. He Y, Chen X, Zhang Y, Yu W (2017) Modeling interporosity flow functions and shape factors in low-permeability naturally fractured reservoir. *J Pet Sci Eng* 156(March):110–117
33. Douglas J, Hensley JL, Arbogast T (1991) A dual-porosity model for water flooding in naturally fractured reservoirs. *Comput Meth Appl Mech Eng* 87(2):157–174
34. Dykhuizen R (1990) A new coupling term for dual-porosity models. *Water Resour Res* 26(2):351–356
35. Zimmerman RW, Chen G, Hadgu T, Bodvarsson GS (1993) A numerical dual-porosity model with semianalytical treatment of fracture/matrix flow. *Water Resour Res* 29(7):2127–2137
36. Gerke HH, Van Genuchten MT (1993) A dual-porosity model for simulating the preferential movement of water and solutes in structured porous media. *Water Resour Res* 29(2):305–319
37. Douglas Jr V, Arbogast T (1990) Dual porosity models for flow in naturally fractured reservoirs. *Dyn Fluids Hierarchical Porous Media* 177–221
38. Li W, Dong Z, Lei G (2017) Integrating embedded discrete fracture and dual-porosity, dual-permeability methods to simulate fluid flow in shale oil reservoirs
39. Barenblatt G, Zheltov I, Kochina I (1960) Basic concepts in the theory of seepage of homogeneous liquids in fissured rocks [strata]. *J Appl Math Mech* 24(5):1286–1303
40. Moinfar A, Varavei A, Sepehrnoori K, Johns RT (2013) Development of a novel and computationally-efficient discrete-fracture model to study IOR processes in naturally fractured reservoirs. In: SPE improved oil recovery symposium, pp 1–17
41. Li W, Dong Z, Lei G (2017) Integrating EDFM and dual porosity method to simulate fluid flow in shale oil reservoir. In: SPE/IATMI Asia Pacific oil & gas conference and exhibition
42. Pruess K, Narasimhan TN (1982) Practical method for modeling fluid and heat flow in fractured porous media. Lawrence Berkeley Lab, CA, USA
43. Serra K, Reynolds AC, Raghavan R (1983) New pressure transient analysis methods for naturally fractured reservoirs (includes associated papers 12940 and 13014). *J Pet Technol* 35(12):2–271
44. Streltsova TD (1983) Well pressure behavior of a naturally fractured reservoir. *Soc Pet Eng J* 23(05):769–780
45. Lefranc M, Farag S, Souche L, Dubois A (2012) Fractured basement reservoir characterization for fracture distribution, porosity and permeability prediction. *Aapg* 41106:#41106
46. Suardana M, Samodra A, Wahidin A, Sule MR (2013) Identification of fractured basement reservoir using integrated well data and seismic attributes: case study at Ruby Field, North West Java Basin. In: Proceedings of AAPG annual convention and exhibition, Pennsylvania, Pittsburg
47. Gupta SD, Chatterjee R, Farooqui MY (2012) Formation evaluation of fractured basement, Cambay Basin, India. *J Geophys Eng* 9(2):162–175

48. Huang Z, Yan X, Yao J (2014) A two-phase flow simulation of discrete-fractured media using mimetic finite difference method. *Commun Comput Phys* 16(3):799–816
49. Zhao H, Wang X, Wang W, Mu E (2018) A simulation method based on energy criterion for network fracturing in shale gas reservoirs. *J Nat Gas Sci Eng* 52:295–303
50. Al-Mukhtar AM, Merkel B (2015) Simulation of the crack propagation in rocks using fracture mechanics approach. *J Fail Anal Prev* 15(1):90–100
51. Al-Mukhtar AM (2017) Fracturing in HDR geothermal system. *Adv Eng Forum* 20:57–60
52. Al-Mukhtar AM (2014) Performance of the subsurface hydraulics in a doublet system using the ThermoGIS calculator. *J Geogr Geol* 6(3):90
53. Cornell Fracture Group (2010) “FRANC2D Version 3.2 [Online]. Available [http://www.cfg.cornell.edu/software/franc2d\\_casca.htm](http://www.cfg.cornell.edu/software/franc2d_casca.htm). Accessed 07 July 2013
54. Al-Mukhtar AM (2011) Fracture mechanics method of welded components under cyclic loads: Fatigue life calculations and simulation. Südwestdeutscher Verlag für Hochschulschriften
55. Al-Mukhtar A, Biermann H, Hübner P, Henkel S (2009) Fatigue crack propagation life calculation in welded joints. In: CP2009, pp 391–397
56. Al-Mukhtar A, Biermann H, Henkel S, Hübner P (2010) Comparison of the stress intensity factor of load-carrying cruciform welded joints with different geometries. *J Mater Eng Perform* 19(6):802–809
57. Al-Mukhtar AM, Biermann H, Hübner P, Henkel S (2010) Determination of some parameters for fatigue life in welded joints using fracture mechanics method. *J Mater Eng Perform* 19(9):1225–1234
58. van Harmelen A, Weijermars R (2018) Complex analytical solutions for flow in hydraulically fractured hydrocarbon reservoirs with and without natural fractures. *Appl Math Model* 56:137–157

# A Modelling of Stereo Matching Algorithm for Machine Vision Application



Rostam Affendi Hamzah, A. F. Kadmin, S. F. Abd Gani, N. Mohamood, A N. A. Jahari, T. M. F. T. Wook and S. Salam

**Abstract** Stereo matching algorithm is a part of machine vision research area. The most challenging issue for stereo matching algorithm is to get an accurate corresponding point on the low texture region. Hence, this article proposes an algorithm utilizing the Sum of Absolute Differences (SAD), gradient matching and Bilateral Filter (BF) to increase the accuracy on this region. The combination of SAD with Red, Green and Blue (RGB) channels differences and gradient matching could improve the matching accuracy on the low texture region. Furthermore, the use of edge preserving filter such as BF that is capable to refine and remove the remaining noise on the final result. This filter is robust against high contrast and brightness. Based on the experimental analysis using standard benchmarking dataset from the Middlebury, the proposed work in this article achieves good accuracy on the low texture region. The comparison is also conducted with some established methods where the proposed framework performs much better.

**Keywords** Sum of absolute differences · Bilateral filter · Stereo matching algorithm · Stereo vision

## 1 Introduction

A disparity map is the map produced by stereo matching process. This map contains depth information which will be used by many applications such as virtual reality [1], 3D surface reconstruction [2], face recognition [3] and robotics automation [4, 5]. There are short or wide baseline [6] range of applications using the stereo vision sensor. Fundamentally, the triangulation principle is used to get the depth estimation based on the pixel information on the disparity map. Hence, the matching

---

R. A. Hamzah (✉) · A. F. Kadmin · S. F. Abd Gani · N. Mohamood · A. N. A. Jahari · T. M. F. T. Wook · S. Salam  
Fakulti Teknologi Kejuruteraan Elektrik Dan Elektronik, Universiti Teknikal Malaysia Melaka, 76100 Durian Tunggal, Melaka, Malaysia  
e-mail: [rostamaffendi@utem.edu.my](mailto:rostamaffendi@utem.edu.my)

© Springer Nature Singapore Pte Ltd. 2020  
M. Awang et al. (eds.), *Advances in Material Sciences and Engineering*, Lecture Notes in Mechanical Engineering, [https://doi.org/10.1007/978-981-13-8297-0\\_52](https://doi.org/10.1007/978-981-13-8297-0_52)

process is one of the challenging jobs in stereo vision research areas. Fundamentally, multiple stages were developed by Szeliski and Scharstein [7] to construct a stereo correspondence or matching algorithm. First, the matching cost computation is used to calculate the matching points between two images. Second, the cost aggregation stage reduces the noise after matching cost process. The third step is to normalize the disparity values on each pixel of image. This stage is also recognized as the process of optimization and disparity selection. Last step is known as enhancement final results stage.

In stereo matching algorithm development, local [8–10] and global [11] methods are listed as two major approaches in optimizing the disparity map. Local approach uses local contents or support windows in computing the disparity map. Most of the local-based implementations are using support windows such as fixed window [12, 13], adaptive window [14], convolution neural network [15] and multiple window [16]. Generally, this method applies Winner-Takes-All (WTA) strategy in their third stage of optimization stage [17–19]. Local method has fast running time and low computational complexity. In [20], the RANSAC plane fitting technique was used to increase the efficiency at the final stage of the algorithm development. This method works on low textured regions but unable to correctly determine the edges of object detection. Wrong plane fitting assumptions makes incorrect disparity estimation. Usually, local-based method shows low precision on the low texture region because there is a possibility that improper window sizes are selected during the matching process. Thus, one of the challenges for researches is to overcome this problem.

Fundamentally, global method processes the disparity map based on the Markov Random Field (MRF) technique. The MRF uses energy minimization function such implemented in [12, 21] by using Belief Propagation (BP) and Graph Cut (GC) respectively. These techniques use energy minimization function for all pixels on an image. They calculate from current point to the nearest pixels of disparity map using maximum flow and cut the minimum energy flow. Base on their methods, the computational requirement is very high because it counts every pixel individually. Hence, the global methods require long execution time since they use the iterative technique for each disparity estimation. The local-based method is selected in this article. The first stage of the proposed work is implemented using SAD [22] and gradient matching. Then the BF is utilized at the second and the last stage where the BF is strong against the low texture regions [23]. The Winner Takes All (WTA) strategy [24] is executed at the optimization stage. Next section describes about the propose framework, then followed by experimental analysis section. The last part is a conclusion of the proposed work in this article.

## 2 Methods

Based on Fig. 1, a flowchart of the proposed work in this paper starts with the matching process at STEP 1. This step uses SAD with gradient matching to get preliminary result of disparity map. The combination should be able to increase the



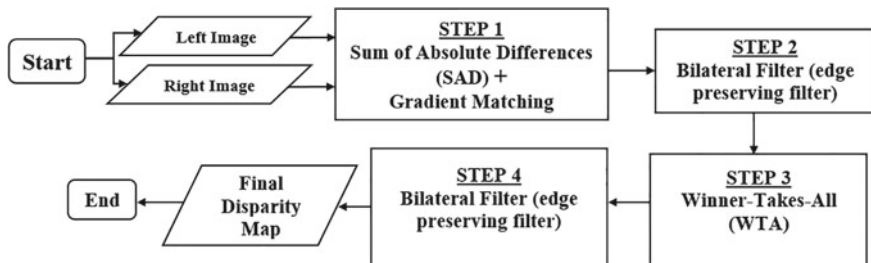


Fig. 1 A framework of the proposed algorithm

effectiveness on the low texture region. Then, the BF is used at STEP 2 to filter the noise and preserved the object’s edges. After that the WTA strategy is implemented at STEP 3 by selecting the minimum disparity value in an image. The last stage in the framework uses the BF to filter out the remaining noise to obtain the final disparity map.

### 2.1 Matching Cost Computation

This stage produces preliminary differences of disparity value. The function used at this stage must be robust and strong against the low texture region. Normally, the mismatch between stereo pair pixels is high at this stage. Hence, this work uses the combination of SAD and gradient matching to improve the accuracy on the low texture region. The input images are in Red, Green and Blue (RGB) channels. The SAD function of the left image  $I_l$  and  $I_r$  is presented by Eq. (1):

$$SAD(x, y, d) = \sum_{(x,y) \in w} |I_l^i(x, y) - I_r^i(x - d, y)| \tag{1}$$

where  $(x, y, d)$  represent the coordinates of disparity  $d$ ,  $w$  is the SAD window size and  $i$  denotes the RGB channels of left and right images. Fundamentally, the differences are scaled in pixels based intensity values. The gradient component for matching process contains the magnitude differences from each image. There are two directions to be calculated which are the vertical direction  $G_y$  and horizontal direction  $G_x$ . The equation of the directions are given by Eqs. (2) and (3):

$$G_x = [1 \ 0 \ -1] * I \tag{2}$$

$$G_y = \begin{bmatrix} 1 \\ 0 \\ -1 \end{bmatrix} * I \tag{3}$$

where  $*$  is the convolution operation and  $I$  is the input image. Using both of the gradient components, the gradient magnitude  $m$  of  $G_x$  and  $G_y$  is given by Eq. (4):

$$m = \sqrt{G_x^2 + G_y^2} \quad (4)$$

The gradient matching kernel is given by cost  $G(x, y, d)$  which is given by Eq. (5):

$$G(x, y, d) = |m_l(x, y) - m_r(x - d, y)| \quad (5)$$

where the coordinates pixel of interest's denotes as  $(x, y)$  and  $d$  represents the disparity value. The matching cost computation function  $MC(x, y, d)$  at this step is the combination of  $SAD(x, y, d)$  and  $G(x, y, d)$  which is provided in Eq. (6):

$$MC(x, y, d) = SAD(x, y, d) + G(x, y, d) \quad (6)$$

## 2.2 Cost Aggregation

The local-based method requires this stage to filter out the preliminary differences after the step of matching cost computation. Hence, this stage is very important to minimize the error due to matching uncertainties on the low texture region. The proposed work at this stage utilizes the BF where this filter efficiently removed the noise and preserved the object edges. The formulation of BF is given by Eq. (7):

$$WM_{p,q}^{BF} = \sum_{q \in w_B} \exp\left(-\frac{|p - q|^2}{\sigma_s^2}\right) \exp\left(-\frac{|I_p - I_q|^2}{\sigma_c^2}\right) \quad (7)$$

where  $q$  and  $w_B$  are the neighbouring pixels and BF support window respectively,  $p$  is the positions of pixel  $(x, y)$  in the filter windows. The  $\sigma_c$  equals to the color law of similarity factor and  $\sigma_s$  describes a spatial adjustment factor. The  $I_p - I_q$  denotes the Euclidean distance in color space and  $p - q$  is the spatial Euclidean interval. The function of this stage is formulated by Eq. (8).

$$C(x, y, d) = WM_{x,y,q}^{BF} MC(x, y, d) \quad (8)$$

## 2.3 Disparity Optimization

Generally, every image contains a set of disparity values. This stage utilizes the WTA strategy which uses minimum disparity value for every location on the disparity

map. Hence, the WTA is the most suitable approach to be used in this article. The formulation of the WTA is given by Eq. (9):

$$d_{x,y} = \arg \min_{d \in D} C(x, y, d) \quad (9)$$

where  $C(x, y, d)$  represents the data of aggregation step and  $D$  denotes a set of valid disparity values for an image. There are some invalid pixels still remaining on the disparity map. Hence, this invalid disparity will be treated at the next step to increase the accuracy.

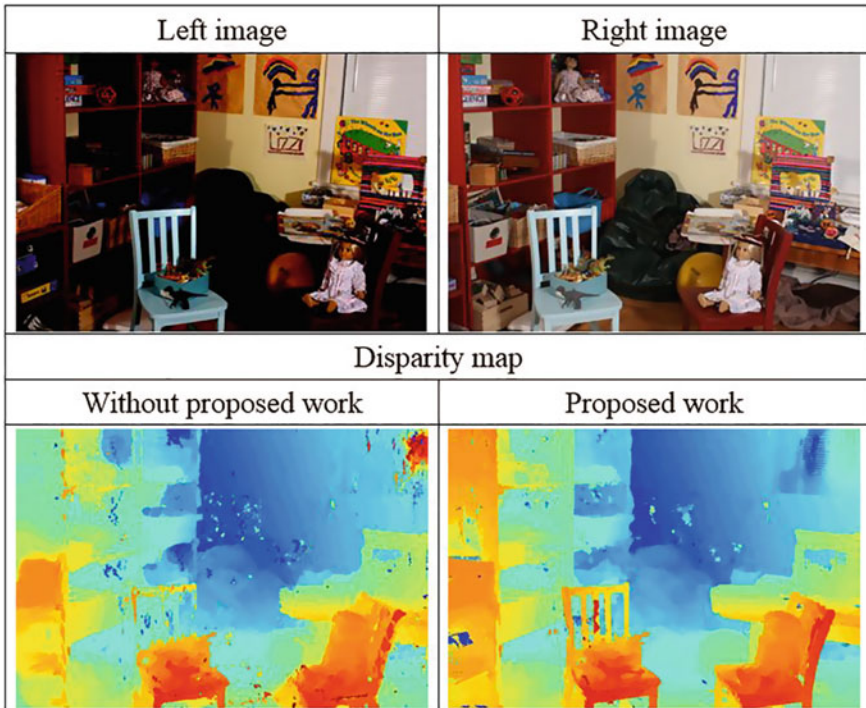
## 2.4 Refinement Stage

This stage consists of several continuous processes. It starts with occlusion handling, invalid pixels filling process and smoothing the final disparity map. The occlusion region comprises of invalid pixels which are detected by left-right consistency checking process. Then, these invalid pixels are replaced by valid pixel values using fill-in process. Generally, after this process, there are many unwanted pixels or some artifacts on the disparity map. Hence, the final step is to smooth the final disparity map using BP. The parameters of BP are similarly used as implemented at cost aggregation step. The BF kernel is given by Eq. (10).

$$WM_{p,q}^{BF} = \sum_{q \in w_B} \exp\left(-\frac{|p-q|^2}{\sigma_s^2}\right) \exp\left(-\frac{|I_p - I_q|^2}{\sigma_c^2}\right) \quad (10)$$

## 3 Results and Analysis

The platform used in this section for experimental analysis is a personal computer with Windows 10, 8G RAM and i5, 3.2 GHz processor. The dataset uses a standard benchmarking evaluation system from the Middlebury [25]. This dataset contains 15 training and testing images with online submission. The parameters for this article are  $(w, \sigma_s, \sigma_c, w_B)$  with the values of  $(7 \times 7, 17, 0.3, 13 \times 13)$ . Figure 2 shows the Playroom image (i.e., left and right) with high contrast and brightness from the Middlebury training dataset. Fundamentally, these two images are difficult to be matched due to different pixel values at the same corresponding point. However, the proposed algorithm in this article correctly determined the disparity location. The disparity level is assigned at precise position where the contours of object distance are well-recognized. The chair, a toy and the books on the book rack are well recovered and reconstructed based on the different disparity levels. It shows that the proposed work is robust against the input images with different characteristics.

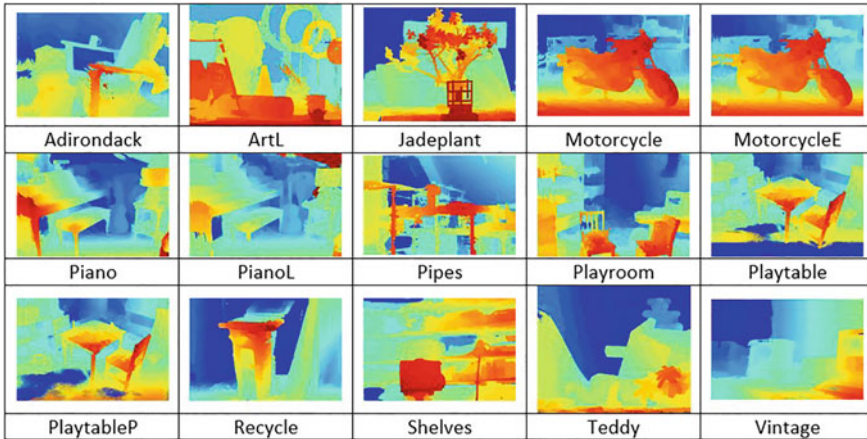


**Fig. 2** The disparity map result of the Playroom stereo image with high contrast and brightness

This figure also shows the comparison result of the Playroom image before (i.e., without the proposed work) and after using the proposed work. The image without the proposed work contains high noise and the disparity values are incorrectly estimated. Edges and shapes of the Playroom disparity map are distorted compared with the proposed work. The result of the proposed work is more accurate which displays low noise and is capable to improve the object shapes. Furthermore, it also reconstructed efficiently the low texture areas (i.e., background and chair surfaces) which increases the accuracy on the disparity map result. It shows that the proposed framework is able to estimate capably the low texture area and edge discontinuities.

Figure 3 shows the final disparity images of the Middlebury dataset based on the quantitative results in Table 1. The color scheme used on the disparity maps are based on the results provided by the Middlebury online submission. The red color indicates the object surface is closer to the stereo camera. The darkest blue shows the objects are farther away from the stereo sensor.

Table 1 is the results from the online submission as shown in the Middlebury quantitative database. Based on these tables, the proposed work is more precise than the work in [17–19, 26–28] for *nonocc* error. The weight average error is 6.54% where there are 15 training images as shown in Fig. 3 (Adirondack, ArtL, Jadeplant,



**Fig. 3** Disparity map results of the training Middlebury dataset

**Table 1** The quantitative results of *nonocc* and *all* errors from the Middlebury

Algorithms	Weight average (% <i>nonocc</i> error)	Weight average (% <i>all</i> error)
Proposed algorithm	6.54	9.73
SNCC [26]	6.97	10.40
ELAS [27]	7.22	10.60
MPSV [17]	8.81	12.30
ADSM [18]	8.95	12.70
DoGGuided [19]	12.00	22.30
BSM [28]	13.40	23.50

Motorcycle, MotorcycleE, Piano, PianoL, Pipes, Playroom, Playtable, PlaytableP, Recycle, Shelves, Teddy and Vintage). Additionally, for the *all* error attribute in the same table, the proposed work produces the lowest average error with 9.73%. The results in this table are followed by SNCC, ELAS, ADSM, MPSV, DoGGuided and BSM.

The competitiveness of the proposed work is shown by these two tables where the results are the lowest average error produced compared with recently published works in the Middlebury database. Additionally, real stereo images from the KITTI [29] are also utilized to verify the capability of the proposed algorithm. The KITTI images are more challenging and contain complex structures such as large untextured regions, plain color surfaces, shadow and high different contrast and brightness regions. Figure 3 shows the disparity map results of four KITTI training images using the proposed algorithm. The results display accurate disparity estimation for all images. The cars, trees, signage and a cyclist are well-recovered with accurate disparity level. It shows that the proposed algorithm is also capable to work with complex stereo images of real environment (Fig. 4).



**Fig. 4** The sample results of the KITTI training dataset from image number #000004\_10-#000007\_10 using the proposed algorithm

### 4 Conclusion

An accurate stereo matching algorithm was presented in this article. The framework used the combination of SAD using block matching technique based on RGB color differences and gradient matching at the first stage. Then, the second and the last stage utilized an edge-preserving filter which is able to further reduce the noise based on the standard quantitative benchmarking dataset. The dual BF used in the framework increased the accuracy and is robust against the different brightness and contrast on the images. Furthermore, the proposed framework is competitive with some established algorithms in the Middlebury database as shown in Table 1. It proves that the proposed work in this article can be applied as a complete algorithm in machine vision applications.

**Acknowledgements** This work was supported by the Universiti Teknikal Malaysia Melaka with the grant number (PJP/2018/FTK(13C)/S01632).

## References

1. Vedamurthy I, Knill DC, Huang SJ et al (2016) Recovering stereo vision by squashing virtual bugs in a virtual reality environment. *Phil Trans R Soc B* 371(1697):20150264
2. Hamzah RA, Ibrahim H, Hassan AH (2016) Stereo matching algorithm for 3D surface reconstruction based on triangulation principle. In: International conference on information technology, information systems and electrical engineering (ICITISEE), pp 119–124
3. Winarno E, Harjoko A, Arymurthy AM (2016) Face recognition based on symmetrical half-join method using stereo vision camera. *Int J Electr Comput Eng* 6(6):2818
4. Hasan AH, Hamzah RA, Johar MH (2009) Range estimation in disparity mapping for navigation of stereo vision autonomous vehicle using curve fitting tool. *IJVIPNS* 9(9):5–9
5. Budiharto W, Santoso A, Purwanto D et al (2011) Multiple moving obstacles avoidance of service robot using stereo vision. *TELKOMNIKA (Telecommun Comput Electron Control)* 9(3):433–444
6. Xi HX, Cui W (2013) Wide baseline matching using support vector regression. *TELKOMNIKA (Telecommun Comput Electron Control)* 11(3):597–602
7. Scharstein D, Szeliski R (2002) A taxonomy and evaluation of dense two-frame stereo correspondence algorithms. *Int J Comput Vision* 47(1–3):7–42
8. Yang Q (2012) A non-local cost aggregation method for stereo matching. In *IEEE Conference on Computer Vision and Pattern Recognition (CVPR)* 1402–1409
9. Hosni A, Rhemann C, Bleyer M et al (2013) Fast cost-volume filtering for visual correspondence and beyond. *IEEE Trans Pattern Anal Mach Intell* 35(2):504–511
10. Hamzah RA, Kadmin AF, Hamid MS et al (2018) Improvement of stereo matching algorithm for 3D surface reconstruction. *Sig Process Image Commun* 65:165–172
11. Richardt C, Kim H, Valgaerts L, Theobalt C et al (2016) Dense wide-baseline scene flow from two handheld video cameras. In: *Fourth international conference on 3D vision (3DV)*, pp 276–285
12. Liang Q, Yang Y, Liu B (2014) Stereo matching algorithm based on ground control points using graph cut. In: *International congress on image and signal processing (CISP)*, pp 503–508
13. Yang Q, Ji P, Li D et al (2014) Fast stereo matching using adaptive guided filtering. *Image Vis Comput* 32(3):202–211
14. Kowalczyk J, Psota ET, Perez LC (2013) Real-time stereo matching on CUDA using an iterative refinement method for adaptive support-weight correspondences. *IEEE Trans Circuits Syst Video Technol* 23(1):94–104
15. Zbontar J, LeCun Y (2015) Computing the stereo matching cost with a convolutional neural network. In: *Proceedings of the IEEE conference on computer vision and pattern recognition*, pp 1592–1599
16. Hirschmüller H, Innocent PR, Garibaldi J (2002) Real-time correlation-based stereo vision with reduced border errors. *Int J Comput Vision* 47(1–3):229–246
17. Bricola JC, Bilodeau M, Beucher S (2016) Morphological processing of stereoscopic image superimpositions for disparity map estimation. *Hal-01330139* 1–17
18. Ma N, Men Y, Men C (2016) Accurate dense stereo matching based on image segmentation using an adaptive multi-cost approach. *Symmetry* 8(12):159
19. Kitagawa M, Shimizu I, Sara R (2017) High accuracy local stereo matching using DoG scale map. In: *IAPR international conference on machine vision applications (MVA)*, pp 258–261
20. Hamzah RA, Kadmin AF, Ghani SF et al (2017) Disparity refinement process based on RANSAC plane fitting for machine vision applications. *J Fundam Appl Sci* 9(4S):226–237
21. Wu SS, Tsai CH, Chen LG (2016) Efficient hardware architecture for large disparity range stereo matching based on belief propagation. In: *IEEE international workshop on signal processing systems (SiPS)*, pp 236–241
22. Hasan AH, Hamzah RA, Johar MH (2009) Disparity mapping for navigation of stereo vision autonomous guided vehicle. In: *International conference of soft computing and pattern recognition*, pp 575–579

23. Hamzah RA, Rahim RA (2010) Depth evaluation in selected region of disparity mapping for navigation of stereo vision mobile robot. In: IEEE symposium on industrial electronics & applications (ISIEA), pp 551–555
24. Hamzah RA, Ghani SF, Din A (2012) Visualization of image distortion on camera calibration for stereo vision application. In: International conference on control system, computing and engineering (ICCSCE), pp 28–33
25. Daniel S, Richard S (2018) Middlebury Stereo evaluation—version 3. Accessed Sept 2018. <http://vision.middlebury.edu/stereo/eval/references>
26. Einecke N, Eggert J (2013) Anisotropic median filtering for stereo disparity map refinement. In VISAPP, pp 189–198
27. Geiger A, Roser M, Urtasun R (2010) Efficient large-scale stereo matching. In: Asian conference on computer vision, pp 25–38
28. Zhang K, Li J, Li Y et al (2012) Binary stereo matching. In: International conference on pattern recognition (ICPR), pp 356–359
29. Menze M, Geiger A (2015) Object scene flow for autonomous vehicles. In: Proceedings of the IEEE conference on computer vision and pattern recognition, pp 3061–3070



# Machinability Performance of RBD Palm Oil as a Bio Degradable Dielectric Fluid on Sustainable Electrical Discharge Machining (EDM) of AISI D2 Steel



Said Ahmad, Richard Ngalie Chendang, Mohd Amri Lajis, Aiman Supawi and Erween Abd Rahim

**Abstract** Dielectric fluid plays a very significant role in any electrical discharge machining (EDM) operation. Hence, a proper selection of dielectric medium is an important consideration for EDM performance. This study is to investigate the usability and performance of bio degradable oil based dielectric fluid in comparison with conventional dielectric fluid when EDM machining of AISI D2 steel by using copper as a tool electrode. Peak current,  $I_p$  up to 12 A and pulse on-time,  $t_{on}$  up to 150  $\mu$ s were selected as the main parameters. Refined, Bleached and Deodorised (RBD) Palm oil (cooking oil) and kerosene were used as dielectric fluid. Their influence on the machinability such as material removal rate (MRR), electrode wear rate (EWR), and surface roughness (Ra) were experimentally investigated. The result shows that omit the highest  $I_p = 12$  A and the lowest  $t_{on} = 150$   $\mu$ s yields the highest MRR for both palm oil and kerosene dielectric fluid, respectively. The improvement of MRR for palm oil as dielectric fluid is about 158.56% when compared to kerosene at the same parameter setting. Meanwhile, machining by using palm oil and kerosene at  $I_p = 6$  A and  $t_{on} = 150$   $\mu$ s yields the lowest EWR and Ra respectively. However, the value of EWR and Ra for palm oil is slightly higher compared to kerosene. In the case of machinability, bio-dielectric fluid which is palm oil shows a significant potential for its performance in EDM machining of AISI D2 steel.

**Keywords** Palm oil · Electrical discharge machining · AISI D2 steel

---

S. Ahmad

Faculty of Mechanical and Manufacturing Engineering, Precision Machining Research Center (PREMACH), Universiti Tun Hussein Onn Malaysia, 86400 Parit Raja, Johor, Malaysia

R. N. Chendang (✉) · M. A. Lajis · A. Supawi · E. A. Rahim

Faculty of Mechanical and Manufacturing Engineering, Universiti Tun Hussein Onn Malaysia, 86400 Parit Raja, Johor, Malaysia

e-mail: [richardngaliechendang@gmail.com](mailto:richardngaliechendang@gmail.com)

© Springer Nature Singapore Pte Ltd. 2020

M. Awang et al. (eds.), *Advances in Material Sciences and Engineering*, Lecture Notes in Mechanical Engineering, [https://doi.org/10.1007/978-981-13-8297-0\\_53](https://doi.org/10.1007/978-981-13-8297-0_53)

509

## 1 Introduction

Electrical discharge machining (EDM) is a non-conventional material removal process which is widely used to produce dies and moulds, finishing part for many industries such as aerospace and automotive industry, and surgical components [1]. Therefore, EDM is mainly used to machine difficult-to-machine material and high strength temperature resistant alloys which are difficult to create by conventional machining [2]. This machine also has the advantage of being able to machine difficult geometries in small batches or even on job shop basis. This process can be successfully employed to machine electrically conductive parts of their hardness, shape and toughness [3]. However, there are a lot of technology that have been devoted to improve machining capabilities but environmental sustainability is not one of their main concerns. To address this problem, one relative new technique is used to improve the sustainability concern of EDM by using sustainable EDM.

EDM is made up of components which are electrode and workpiece, immersed in dielectric fluid during machining. Dielectric fluid plays an important role as it concentrates the plasma channel over the machining area and also acts as carrier for debris [4]. The dielectric fluid used in EDM is a pollutant to the environment and causes carcinogenic problem to the operator in long term usage. In order to create a sustainable environment in manufacturing practice, using bio degradable oil based dielectric fluid in EDM is the most sustainable dielectric fluid for environmental concerns.

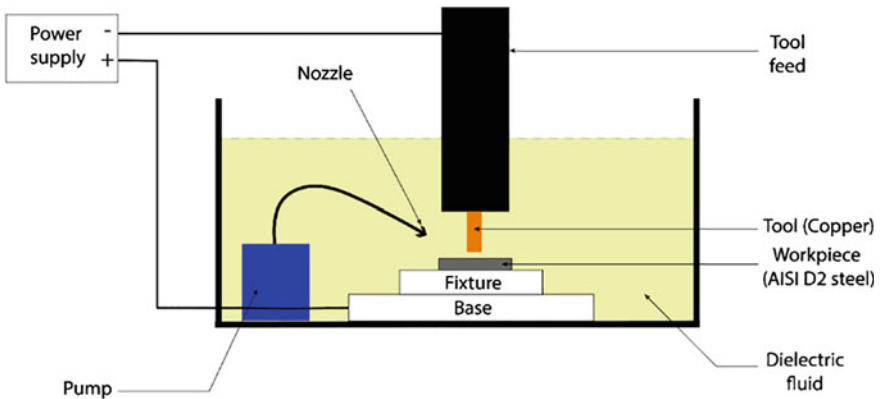
In addition, bio degradable oil based dielectric fluid in EDM process is applied in industry at very slow pace due to the fundamental issues of this new development. In addition, this machining mechanism are still not well understood [3]. In order to enhance the performance of EDM, it is desirable to choose a suitable dielectric during EDM operation. Currently, there is a research using bio-dielectric from palm oil and *Jatropha curcas* oil extracted in order to introduce a sustainable machining method. However, to apply bio-dielectric fluid in EDM, the operation requires further study and research. This study focuses on the effect of using bio-dielectric fluid to the machinability of AISI D2 steel in EDM process.

## 2 Experimental Methods

This topic reviews the method that was used in this research. The details of this research were described technically through the process that had been carried out.

**Table 1** Properties of dielectric fluid used in this research

Dielectric fluid	Density (kg/m <sup>3</sup> )	Viscosity (at 40 °C)	Flash point (°C)	Specific heat (kJ/kg C)	Thermal conductivity (W/mC)
Palm oil	870	40.27	154	1.872	0.163
Kerosene	730	5.42	65	2.01	0.130



**Fig. 1** Schematic diagram of the machine setup for this research

## 2.1 Experimental Setup and Details

The experiment work has been performed on the Computer Numerical Control (CNC) Sodick High Speed EDM die sink AQ55L (3 Axis Linear) machine. There are two different types of dielectric fluid used: palm oil as bio degradable oil dielectric fluid and kerosene as conventional dielectric fluid. The properties of these dielectric fluids are as shown in Table 1.

For the case of experimental work by using palm oil as a dielectric fluid, a custom made tank was used to conduct the experiment. Figure 1 shows the schematic diagram of the machine setup. A pump was placed into the tank to do the flushing process during the machining. Bio-oil such as palm oil has good properties in terms of low price, ease to use, abundant availability and higher sustainability impact index. Other than that, it has characteristic that can be reusable and does not cause harm to the environment and the operator’s health that handles the machine [5].

The workpiece material used for this research is AISI D2 steel. This steel has excellent wear resistance and high compressive strength. The dimension of workpiece used for machining is 40 mm × 30 mm × 10 mm. The composition properties of workpiece material is shown in Table 2. While cylindrical copper electrode of 10 mm diameter is selected for this experiment. Copper electrode is commonly used as electrode in EDM process due to its high thermal conductivity [6]. Copper electrode

**Table 2** AISI D2 steel workpiece material composition

Element	C	Si	Mn	Mo	Cr	Ni	V	Co	Fe
Composition (%)	1.5	0.3	0.3	1.0	12	0.3	0.8	1.0	Balance

**Table 3** Copper electrode material composition

Element	C	Al	Si	S	P	Zn	Mn	Ni	Pb	C
Composition (%)	99.58	0.006	0.002	0.035	0.052	0.25	0.002	0.023	0.02	0.028

**Table 4** Experimental condition on EDM machining of AISI D2 steel

Parameters	Details
Workpiece material	AISI D2 steel
Electrode material	Copper
Peak current, $I_p$ (A)	6, 9, 12
Pulse on-time, $t_{on}$ ( $\mu$ s)	50, 100, 150
Pulse off-time, $t_{off}$ ( $\mu$ s)	50
Voltage, V	120
Electrode polarity	Positive (+ve)
Depth of cut (mm)	1.5

material composition is shown in Table 3. Then, Table 4 shows the experimental condition and parameters setting for the research.

## 2.2 Responses

Machinability study of this research focuses on three major responses: material removal rate (MRR), electrode wear rate (EWR) and surface roughness (Ra). They are defined as follows.

MRR was calculated by the volume of workpiece loss per machining time and the unit is  $\text{mm}^3/\text{min}$ . Where,  $m_w$  is the mass loss of the workpiece (g),  $\rho_w$  is the density of the workpiece ( $0.0077 \text{ g/mm}^3$ ) and  $t$  is the machining time (min).

$$\text{MRR} = \frac{m_w}{\rho_w t} \quad (1)$$

EWR was measured according to the volume of electrode wear per machining time and the unit is  $\text{mm}^3/\text{min}$ . Where,  $m_e$  is the mass loss of the electrode (g),  $\rho_e$  is the density of the electrode ( $0.0088852 \text{ g/mm}^3$ ) and  $t$  is the machining time (min).

$$\text{EWR} = \frac{m_e}{\rho_e t} \quad (2)$$

The weights of the electrodes and workpieces before and after machining need to be measured in order to obtain MRR and EWR. The changes in weight from the tool electrode or workpiece are suspected to be small. Thus, omit more decimal points are better to eliminate the possibilities of large error. For this analysis, Shimadzu weight balance measurement was used. The maximum weight can be measured is 210 g until five decimal point accuracy. However, for this study, the decimal point of the weight balance is set to 4 decimal point. Mitutoyo SJ-400 Surface Roughness Tester was used to measure the average surface roughness, Ra of the machining surface.

### 3 Results and Discussion

The focus of this experiments is to study the effect of peak current,  $I_p$  and pulse on-time,  $t_{on}$  on the machinability performance of AISI D2 steel by using bio degradable oil as a dielectric fluid and kerosene as conventional method in subject to the selected responses.

#### 3.1 Material Removal Rate (MRR)

In order to achieve a better economical production, a higher MRR is desirable. There are several factors that need to be considered to ensure the results gained are useful in increasing the productivity in EDM operation. The most important factor to increase the speed of the machining is due to how much the volume of the material can be removed per time taken.

In Fig. 2, comparative response behavior shows influence of  $I_p$  and  $t_{on}$  on MRR. It was observed that the MRR increases with increase of  $I_p$  and  $t_{on}$  for both dielectric fluids: palm oil and kerosene. The highest and the lowest MRR for both dielectric are located at  $I_p=12$  A,  $t_{on}=150$   $\mu$ s and  $I_p=6$  A,  $t_{on}=150$   $\mu$ s respectively. At high  $I_p=12$  A, the intensity of energy release during sparking is proportionally increased whereby higher temperature produced by the spark, melts more material [7]. Therefore, it is able to generate more sparking, thereby affecting the increase of MRR. Meanwhile, the increasing of  $t_{on}$  has led to a slight decrease in MRR at the  $I_p=6$  A of palm oil and all conditions of  $I_p$  by using kerosene. This is due to the electrode which does not properly flush away and the debris from the machining process remains at working surface, resulting in arching [8]. By comparing the MRR, palm oil has higher MRR than kerosene. This is due to the density and viscosity of palm oil that generate better confinement which produced higher MRR. Sparking is proportionally increased due to the viscosity and flash point of the palm oil that is higher than kerosene [9]. The improvement is about 158.56% at the same parameter setting which are  $I_p=12$  A and  $t_{on}=150$   $\mu$ s respectively.

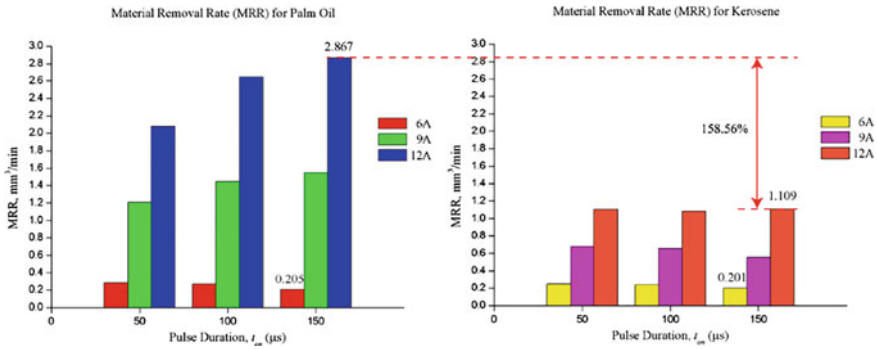


Fig. 2 Effect of MRR on palm oil and kerosene dielectric fluid

### 3.2 Electrode Wear Rate (EWR)

In EDM process, spark generated causes high speed electron strike onto the surface of softer electrode resulting into erosion of electrode surface. This erosion alters the geometry and dimension of the electrode and the cavity produced as well. Hence, minimum EWR is desirable to achieve better dimension and size. Also due to this erosion, the electrode needs frequent dressing, increasing the loss of electrode material and omit the electrode cost.

Figure 3 shows a comparative of response behavior of influence of control parameters condition. Result of EWR for palm oil which is EWR, increase with the increment of  $I_p$  from 6 to 12 A on each  $t_{on}$ . This is due to high discharge current which leads to high spark energy causing more material removal from the workpiece and the tool electrode which affect the increase of EWR [10]. The highest and the lowest EWR for palm oil are located at  $I_p= 12$  A and  $I_p= 6$  A on  $t_{on}= 150 \mu$ s respectively. A similar trend was observed in kerosene dielectric fluid at  $t_{on}= 50 \mu$ s and  $t_{on}= 150 \mu$ s from 6 to 12 A. However, at  $t_{on}= 100 \mu$ s, the EWR increased from  $I_p= 6-9$  A but slightly decreased when  $I_p= 12$  A was applied. The highest and the lowest EWR for kerosene are located at  $I_p= 12$  A,  $t_{on}= 50 \mu$ s and  $I_p= 6$  A,  $t_{on}= 150 \mu$ s. As a comparison, kerosene has lower EWR than palm oil at similar parameter setting which is at  $I_p= 12$  A,  $t_{on}= 150 \mu$ s.

### 3.3 Surface Roughness (Ra)

Ra is used to analyse the quality of surface machine by EDM process. The analysis is used to investigate the relationship between  $I_p$  and  $t_{on}$  in this research. For good accuracy, low wear and high service life, low Ra is desired. Responds trend under influence of control parameter on Ra are shown in Fig. 4.

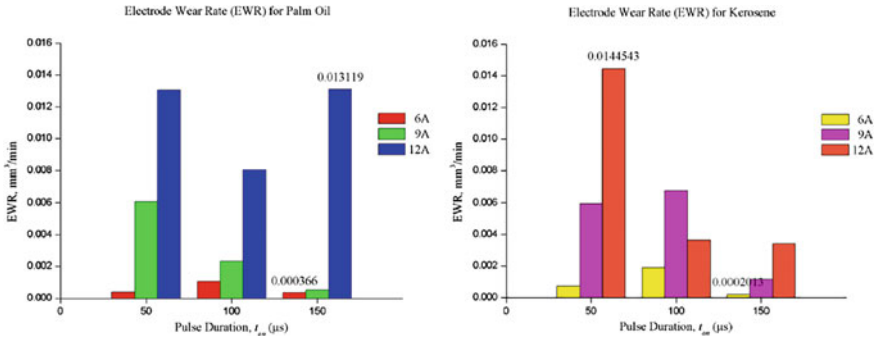


Fig. 3 Effect of EWR on palm oil and kerosene dielectric fluid

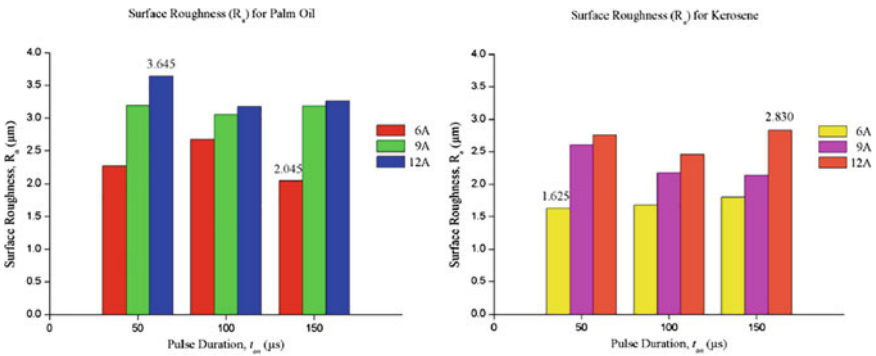


Fig. 4 Effect of Ra on palm oil and kerosene dielectric fluid

Figure 4 shows the responds trend between  $I_p$  and  $t_{on}$  for both dielectric fluids used. At higher value of  $I_p$ , the spark impinges on the surface with more intensity to remove the material. The impact force results in formation of wider crater and generates coarse surface. Based on Fig. 4, the trend of Ra is increased with increasing of  $I_p$  from 6 to 12 A. This is due to the high density of plasma channel and higher breakdown voltage results into higher spark energy which causes deeper penetration in work surface to remove the material [9]. Furthermore, higher  $t_{on}$  results in more sparks that extends the melting and evaporation of material resulting in a wider crater [3]. However, according to the result, an increasing of  $t_{on}$  was directly proportional with increment of Ra. This shows that the  $t_{on}$  surely effects on the Ra [11]. This is due to the  $I_p$  which Ra at the highest was at the  $t_{on}= 150 \mu s$ . Based on Fig. 4, the lowest Ra is at  $I_p= 6 A$  and  $t_{on}= 50 \mu s$  for kerosene while the highest Ra is at  $I_p= 12 A$  and  $t_{on}= 50 \mu s$  for palm oil. As a comparison in overall, kerosene has lower Ra compared to palm oil.

## 4 Conclusions

By using RBD palm oil as a bio degradable dielectric fluid, a comparison of its usability and performance with kerosene dielectric fluid at different setting parameters have been studied. From the analysis, the following conclusions could be drawn:

- (a) The peak current,  $I_p$  and pulse on-time,  $t_{on}$  are the most contributing factors that improve the MRR. The MRR increased as  $I_p$  and  $t_{on}$  increased. The result shows the highest of MRR for palm oil is 2.867 mm<sup>3</sup>/min at  $I_p = 12$  A while the highest for kerosene is 1.109 mm<sup>3</sup>/min at  $I_p = 12$  A. The improvement of using bio degradable oil as dielectric fluid is 158.56% compared to conventional dielectric fluid which is kerosene.
- (b) The result shows that the introduction of palm oil that acts as dielectric fluid helps to enhance the machining speed. It was found that while using palm oil, the time of machining process is shorter compared to kerosene.
- (c) The EWR was increased with increasing of  $I_p$ , but inversely proportional with  $t_{on}$ . The lowest EWR of palm oil is 0.0003660 mm<sup>3</sup>/min obtained at  $I_p = 6$  A and  $t_{on} = 150$   $\mu$ s. For kerosene, the lowest is 0.0002013 mm<sup>3</sup>/min obtained at  $I_p = 6$  A and  $t_{on} = 150$   $\mu$ s.
- (d) The highest  $I_p$  is not recommended for Ra. The Ra is increased with the increasing of the  $I_p$ . According to the result, increasing the  $t_{on}$  is directly proportional with the increment of Ra for bio degradable oil as dielectric fluid. The lowest and the highest Ra value were obtained when bio degradable oil was used as dielectric fluid at  $I_p = 6$  A and  $t_{on} = 150$   $\mu$ s whereby  $I_p = 12$  A and  $t_{on} = 50$   $\mu$ s, with value 2.045 and 3.645  $\mu$ m respectively. However, it is showing a decrease of Ra when increasing of the  $t_{on}$  for the kerosene. The lowest and the highest Ra value were obtained when kerosene was used as dielectric fluid at  $I_p = 6$  A and  $t_{on} = 50$   $\mu$ s whereby  $I_p = 12$  A and  $t_{on} = 150$   $\mu$ s, with value 1.625 and 2.83  $\mu$ m respectively.
- (e) By comparing the performance of palm oil and kerosene as dielectric fluid, the result within selected parameters shows that the palm oil has a good potential to be used as a dielectric fluid. In the case of machinability study, palm oil has achieved higher MRR and lower EWR but higher Ra in comparison with kerosene.

**Acknowledgements** The authors would like to thanks to the Universiti Tun Hussein Onn Malaysia by supporting this research under the funding of TIER 1 Grant U871.

## References

1. Muthramalingam T, Mohan B (2015) A review on influence of electrical process parameters in EDM. Arch Civ Mech Eng 15(1):87–94
2. Dhirendra NM, Bhatia A, Rana V (2013) Study on electro discharge machining (EDM). Int J Eng Sci 3(2):24–35



3. Kansal HK, Singh S, Kumar P (2007) Technology and research developments in powder mixed electric discharge machining (PMEDM). *J Mater Process Technol* 184(1–3):32–41
4. Choudhary SK, Jadoun RS (2014) Current advanced research development of electric discharge machining (EDM): a review. *Int J Res Advent Technol* 2(3):2321–9637
5. Paper C, Jaipur T (2016) Investigating feasibility of waste vegetable oil for sustainable EDM investigating feasibility of waste vegetable. *J Mater Process Technol* 18(3):38–51
6. Tzeng YF, Lee CY (2001) Effects of powder characteristics on electro-discharge machining efficiency. *Int J Adv Manuf Technol* 17(8):586–592
7. Harlal SM, Nitesh K (2016) Investigating feasibility of waste vegetable oil for sustainability EDM. Department of Mechanical Engineering, Malaviya National Institute of Technology, Jaipur, India
8. Pey Tee KT, Hosseinnezhad R (2013) Pulse discrimination for electrical discharge machining with rotating electrode. *Mach Sci Technol* 17(2):292–311
9. Valaki JB, Rathod PP, Sankhavara C (2016) Investigations on technical feasibility of *Jatropha curcas* oil based bio dielectric fluid for sustainable electric discharge machining (EDM). *J Manuf Process* 22:151–160
10. Bharti PS, Maheshwari S, Sharma C (2010) Experimental investigation of inconel 718 during die-sinking electric discharge machining. *Int J Eng Sci Technol* 2(11):6464–6473
11. Lajis MA, Ahmad S (2015) Machinability performance of powder mixed dielectric in electrical discharge machining (EDM) of inconel 718 with copper electrode. *Int J Mech Mech Eng* 15(04):37–52

# Handling Phase Ambiguity in Full Spectrum from FFT



Nabam Teyi and Sandeep Singh 

**Abstract** Condition monitoring of rotating machines essentially utilises frequency domain analysis of the vibration signals, to expose features otherwise hidden in the time domain. Generally, full spectrum of the frequency domain obtained from Fast Fourier Transform (FFT) is used for analysis. The FFT process introduces a phase ambiguity in the harmonics due to random selection of the span of the time domain signal used for decomposition. As the span of the time domain signal cannot be determined a priori; such that phase ambiguity is not introduced, alternate methods are required to remove this ambiguity. A phase compensation based on the FFT of the multi harmonic complex reference signal in unison with the vibration signal may be used for this purpose. This paper presents a mathematical background and a practical way for its implementation. Though the example presented in the paper is based on applications related to rotating shaft, the methodology is generic and applicable to all fields of application where, the phase of the harmonics obtained from FFT are important.

**Keywords** Fast Fourier Transform · Full spectrum · Phase correction · Phase compensation

## 1 Introduction

Frequency domain analysis of the vibration signals emanating from a machinery is a key tool in the diagnosis and prognosis of the machinery condition. Of the many frequency domain tools available for the purpose, Fast Fourier Transform (FFT) is commonly employed to obtain the frequency spectrum of the time domain vibration signal, principally due to the simplicity and speed of its implementation. In configurations where the vibration signals are available along two orthogonal

---

N. Teyi · S. Singh (✉)

Department of Mechanical Engineering, North Eastern Regional Institute of Science and Technology, Nirjuli 791109, Arunachal Pradesh, India  
e-mail: [sandeep@nerist.ac.in](mailto:sandeep@nerist.ac.in)

© Springer Nature Singapore Pte Ltd. 2020

M. Awang et al. (eds.), *Advances in Material Sciences and Engineering*, Lecture Notes in Mechanical Engineering, [https://doi.org/10.1007/978-981-13-8297-0\\_54](https://doi.org/10.1007/978-981-13-8297-0_54)

519

directions, the pair of signals can be handled as a single complex signal. The FFT of such signals contain asymmetric positive and negative frequencies, making essential the use of the whole spectrum of frequencies (commonly termed as *full spectrum*) to draw a conclusion about the condition of the machinery from which the vibration signals were taken.

In rotor dynamic applications, full spectrum presents a special opportunity to analyse the nature of the rotor vibration which is generally characterized by positive and negative whirls, corresponding to the positive and negative frequencies in the full spectrum. As early as 1993, researchers have identified the need and importance of full spectrum analysis in rotating machines condition monitoring, for instance [1]. In this paper the minimal hardware requirement for obtaining the orbit plot and full spectrum were elaborated. The author explained the generation of an ellipse with rotating vectors. A single frequency elliptical orbit could be constituted from a particular positive (forward) and negative (reverse) vibration frequency components of a full spectrum.

Most of the rotor faults present an overlapping dynamics, many features of one fault are common to that of the other fault. Availability of the full spectrum helps in identification of complex faults such as rubs, preloads, misalignments, shaft cracks and many others. Unique faults like high friction rubs generating reverse frequency components can be identified using the full-spectrum; which is not identifiable otherwise. A shaft crack is commonly identified from  $2\times$  component. Also, there is a phase change in both  $1\times$  and  $2\times$  vectors. A complete list of faults identifiable from the frequency components is available in [2].

Many advanced mathematical approaches have been attempted to extract more and more of the information available in the vibration signals, for instance, to study the non-stationary vibration in large machines, some researchers integrated the techniques of Wigner Distributions (WD) and Short Period Fourier Transforms (SPFT) with the full-spectrum [3]. In the new generation Bently Nevada packages such as ADRE (Automated Diagnostics for Rotating Equipment) and WDM (Windows Data Manager), full spectrum analysis capabilities are inbuilt. In context to these packages, Goldman and Muszynska briefed applications of the full spectrum to rotating machinery diagnostics [4]. This paper explained many aspects of the full spectrum analysis, some are detailed as follows. The full spectrum is capable of displaying the correlation between vibration patterns from different transducers, which is generally hidden in a single sided spectrum information. At a glance, the full-spectrum plot indicates whether the rotor orbit is forward or reverse in relation to the direction of shaft rotation.

The use of the full multi-spectra was made by Tuma and Bilos [5] to study the fluid induced instability of rotor systems with journal bearings during the run up and coast down operations. The whirl frequency component and fluid induced instability components were identified. The Full-spectrum generated by the orbit decomposition has been used for the detection of rotor crack and misalignment [6] by some authors.

Though a number of methods are available to obtain the full spectrum of the time domain signal as detailed in [4], the FFT based full spectrum analysis is relatively easy to implement. In spite of this fact, the FFT based full spectrum analysis suffers

an operational lacuna—it gives rise to phase ambiguity if the span of the time domain signal used for frequency decomposition is not chosen in a particular way.

## 2 Problem Definition

The standard FFT implementation works on the concept of representing the time domain signal with the cosine and sine harmonics of integral frequencies such that the time integration of sum of these harmonics with due consideration of amplitude and phase is able to reconstruct the original time domain signal. Since the cosine and sine harmonics are available on factoring, representation of the individual FFT harmonics in complex form is possible with cosine terms taken as real and sine terms as imaginary. So, the FFT process outputs a complex result. If the time domain signal is representable by all cosine or sine harmonics only, the FFT will output the result with imaginary part zero or the real part zero respectively. In all other generic cases, the output will be complex. The modulus and angle of this complex number is the amplitude and phase of the particular harmonic. While the phase of the harmonic carries information of the shape of the time domain signal, information of the size (magnitude) of the time domain signal, is carried by the amplitude. FFT is a linear process but not shift invariant, hence with shift of the time domain signal, the amplitude of the harmonics remains unaltered but the phase changes. This necessitates passing the time domain signal to the FFT algorithm, starting at time instants such that the initial zero condition of the physical system are met. In rotor dynamic application, this requirement translates to instants such that  $\omega t = 0, 2\pi, 4\pi, \dots$ , where  $\omega$  is the rotor spin speed and  $t$  is the time instant. This is necessary for maintaining consistency between the mathematical formulations and physical behavior of the system under investigation. For all practical purposes, it is not possible to capture signal in the aforesaid manner.

The discrepancy in phase of the harmonics due to random instants of picking the time domain signal can be compensated, by making suitable correction in the phase. A complex reference signal composed of harmonics expected in the main signal can be implemented for this purpose.

## 3 Phase Correction Algorithm

For the time domain signal starting at different instants, phase correction can be made with the help of a complex reference. A multi harmonic quadrature reference signal can be implemented. Along with the time domain vibration signal, this multi harmonic quadrature reference signal is also passed through the FFT algorithm. All the signals are picked starting at the same time instant. For the vibration signals the amplitude and phase are both important for machine condition analysis, for the reference signal only the phase shift is useful. The phase shift of individual harmonic

of the reference signal is the amount of phase discrepancy added in the frequency domain of the vibration signal. Thus, for correction of phase, the phase shift of the reference harmonics should be subtracted from the phase of the vibration harmonics.

The output of an FFT process is an array of complex numbers as discussed in the preceding section. In polar form, this complex array can be written in terms of the magnitude and angle of the individual entries. The FFT converts the time domain complex vibration signal  $v$  to frequency domain in the following form:

$$r(t) \xrightarrow{\text{FFT}} |R_i| \angle \gamma_i(\omega), \quad -\infty \leq i \leq \infty, \quad i \text{ limited to frequencies of interest} \quad (1)$$

Here,  $|R_i|$  is the magnitude and  $\gamma_i$  is the phase of the  $i$ th harmonic of the vibration signal. The multi-harmonic complex reference signal has the form

$$s(t) = \cos(i\omega t) + j \sin(i\omega t), \quad i = \dots - 1, 0, 1, \dots \quad (2)$$

The harmonics that are of importance in Eq. (1) only needs to be present in the reference signal, defined in Eq. (2). The FFT generates the frequency domain of the complex quadrature reference signal as

$$s(t) \xrightarrow{\text{FFT}} |s_i| \angle \lambda_i(\omega) \quad i = \dots - 1, 0, 1, \dots \quad (3)$$

Here,  $|s_i| = 1$  is the magnitude and  $\lambda_i$  is the phase of the  $i$ th harmonic of the complex reference signal upon FFT. In terms of the assumed system configuration, angle  $\lambda_i$  corresponds to the angle by which the  $i$ th harmonic of the vibration signal passed on to the FFT algorithm is shifted from true configuration. Subtracting this angle from the phase of  $i$ th harmonic of vibration signal, viz.  $\gamma_i$  compensates for the phase shift in the vibration harmonics obtained from full spectrum FFT. The vibration harmonics, duly compensated for the phase shift, take the form:

$$R_i = |R_i| \angle (\gamma_i - \lambda_i) \quad (4)$$

The vibration displacement harmonics obtained from Eq. (4) is a faithful representation of the time domain signal consistent with the conditions expressed in the preceding sections and can be used in machine condition monitoring programs, without ambiguity.

## 4 Numerical Example

If To demonstrate the applicability of the algorithm discussed above, a numerical example is presented, with the intention of ascertaining the amount of error present in the frequency domain on account of phase of the individual harmonic. To have several harmonics in the vibration signal, a cracked Jeffcott rotor with a small disc

**Table 1** Data used in simulation

Parameters	Values	
Disc mass, $m$	2	kg
Intact shaft stiffness, $k$	$7.6 \times 10^5$	$\text{Nm}^{-1}$
Additive crack stiffness, $\Delta k_\xi$	$3 \times 10^5$	$\text{Nm}^{-1}$
Viscous damping, $c$	76	$\text{Ns m}^{-1}$
Phase of unbalance, $\beta$	$10^\circ$	deg.
Shaft deflection, $\delta_x$	$2.6 \times 10^{-5}$	m
Disc eccentricity, $e$	240	$\mu\text{m}$

unbalance is considered. The equation of motion of the disc with crack located close to it is given as:

$$m\ddot{r} + c\dot{r} + kr = f_{cr}^c + f_{un}^c \tag{5}$$

Here,  $r = u_x + ju_y$  is the complex vibration displacement composed of  $u_x$  and  $u_y$  along the two orthogonal directions,  $m$  is the disc mass,  $c$  is the viscous damping and  $k$  is the stiffness of the shaft. The two forcing terms on the right hand are due to crack and the unbalance. The force term due to static deflection has been used to define the crack force thus not available explicitly in Eq. (5). For details and underlying assumptions in development of Eq. (5) and the simplifications that follows, Singh and Tiwari [7]) may be referred.

The crack force in terms of the static deflection  $\delta_x$  and crack stiffness  $\Delta k_\xi$  is expressed in complex form as

$$f_{cr}^r = \Delta k_\xi \delta_x \sum_{i=-n}^{+n} p_i e^{i\omega t} \tag{6}$$

Here  $p_i$  is the coefficient of the  $i$ th harmonic of the crack force excitation. In literature, it is sometimes referred to as the *participation factor* of the individual harmonic. The unbalance force is given as

$$f_{un}^c = me\omega^2 e^{j(\omega t + \beta)} \tag{7}$$

Here,  $e$  is the eccentricity and  $\omega$  is the shaft spin speed.

A Simulink model is implemented to execute the dynamics of crack, unbalance and the rotor according to Eq. (5). The model also contains a complex reference signal generator according to Eq. (2). The theoretical data used for simulation is summarized in Table 1.

The simulation is run for 5 s and the last 1 s data is retained for frequency domain decomposition. The complex vibration displacement history obtained from the simulation is used to define the frequency domain of the vibration displacement and

**Table 2** Phase (in degrees) of the various harmonics of vibration displacement and reference signal and the corrected phase

Harmonic number	Phase of vibration signal	Phase of reference signal	Corrected phase of vibration signal
0	0.0000	0.0000	0.0000
1	4.3232	0.3600	3.9632
2	-0.0312	0.7200	-0.7512
3	-0.1112	1.0800	-1.1912
5	179.3699	1.8000	177.5699
7	-2.5994	2.5200	-5.1194
-1	0.0038	-0.3600	0.3638
-3	-179.8888	-1.0800	-178.8088
-5	0.6301	-1.8000	2.4301

similarly, the multi harmonic complex reference time history is used to define the frequency domain of the reference signal. By the choice of the *crack excitation function*, different harmonics would be available in the frequency domain. In the present example, a rectangular switching crack excitation function has been used, thus forward harmonics at  $1\times, 2\times, 3\times, 5\times, 7\times$  and reverse harmonics at  $-1\times, -3\times$  and  $-5\times$  etc. are available. A DC valued harmonic will also be present. In ideal case, when the time domain signal is picked such that the consistency of the mathematical model and the physical phenomenon are maintained, as detailed in the previous section; all the harmonics of the reference signal shall register phase of zero. The phase of the reference signals other than zero is identified as the amount of phase ambiguity that has crept in into the phase of the vibration displacement harmonics. For a simulation run at 10 rad/s, the phase of the harmonics of vibration displacement, reference signal and the corrected phase are presented in Table 2.

From Table 2, it may be seen that the complex reference signal has undergone phase shift, which is indicative of phase ambiguity in the vibration displacement signal as well. The corrected phase is reported in the last column.

## 5 Practical Implementation

The need for implementation of phase compensation in physical measurement and signal acquisition are established in the present numerical example. For practical implementations of this algorithm, a quadrature reference signal will be required. This could be obtained by placing two reference generators orthogonal to each other; in place of only one, as in case of conventional reference generator. Since the reference generators generally form a spike of the signal, it carries multiple frequencies. Upon FFT of this quadrature reference signal, all the frequencies could be identified and

the phase of the harmonics of interest can be extracted for use in the phase correction algorithm as per Eq. (4).

## 6 Conclusions

For obtaining a faithful frequency domain of the time domain signal in rotating machines condition monitoring programs, a suitable phase correction is required so that the physical system and the numerical work has a consistency. The present paper presents a suitable method and a simple algorithm to accomplish this. To evidence the phase ambiguity arising out of the FFT process, a numerical example has been presented and the solution is deduced in form of an algorithm. At the end, some hints for practical implementation of the idea has been included.

## References

1. Southwick D (1993) Using full spectrum plots. *Orbit* 14(4):12–16
2. Muszynska A (1995) Vibrational diagnostics of rotating machinery malfunctions. *Int J Rotating Mach* 1(3–4):237–266
3. Lee CW, Han Y (1998) Use of directional Wigner distributions for identification of the instantaneous whirling orbit in rotating machinery. In: 7th ISROMAC, pp 22–26
4. Goldman P and Muszynska A (1999) Application of full spectrum to rotating machinery diagnostics. *Orbit* 17–21
5. Tuma J, Bilos J (2007) Fluid induced instability of rotor systems with Journal bearings. *Eng Mech* 14:69–80
6. Patel TH, Darpe AK (2011) Application of full spectrum analysis for rotor fault diagnosis. In: IUTAM symposium on emerging trends in rotor dynamics, vol 1011, pp 535–545
7. Singh S, Tiwari R (2015) Model-based fatigue crack identification in rotors integrated with active magnetic bearings. *J Vib Control* 1–21. <https://doi.org/10.1177/1077546315587146>



# A New Model for Predicting Minimum Miscibility Pressure (MMP) in Reservoir-Oil/Injection Gas Mixtures Using Adaptive Neuro Fuzzy Inference System



M. A. Ayoub, Mysara Eissa Mohyaldinn, Alexy Manalo, Anas. M. Hassan and Quosay A. Ahmed

**Abstract** One of the critical concerns in determining the effectiveness of Enhanced Oil Recovery (EOR) is the understanding and evaluation of the Minimum Miscibility Pressure (MMP). Minimum miscibility pressure is the lowest possible pressure required to attain the mixing of injected fluid and the hydrocarbons in the reservoir into one phase. It is believed that optimum recovery and better sweep efficiency could only be achieved by reaching this minimum pressure. MMP determination, however usually depends on reservoir condition, reservoir fluid composition, and injected gas properties. The reservoir fluid composition could be represented by the Molecular weight  $C_{7+}$ . However, Reservoir condition is represented by a reservoir temperature that affects MMP response. Selection of hydrocarbon gasses as the injection fluids is represented by the injected gas composition (Mole fraction  $C_2-C_6$ , and Mole fraction  $C_1$ ). Determination of the minimum pressure could be either through experimental or empirical approaches. The objective of this study is to provide an empirical correlation to estimate the MMP by using Adaptive Neuro-Fuzzy Inference System (ANFIS). To develop the model, a code is generated under MATLAB environment. A total of 177 data points have been used in training the proposed model while 98

---

M. A. Ayoub (✉) · Anas. M. Hassan  
Department of Petroleum Engineering, Universiti Teknologi PETRONAS (UTP), Seri Iskandar,  
32610 Tronoh, Perak, Malaysia  
e-mail: [abdalla.ayoub@utp.edu.my](mailto:abdalla.ayoub@utp.edu.my)

Anas. M. Hassan  
e-mail: [anas\\_17005873@utp.edu.my](mailto:anas_17005873@utp.edu.my)

M. E. Mohyaldinn · A. Manalo  
Department of Petroleum Engineering, Universiti Teknologi PETRONAS (UTP), Bandar Seri  
Iskandar, 32610 Tronoh, Perak, Malaysia  
e-mail: [mysara.eissa@utp.edu.my](mailto:mysara.eissa@utp.edu.my)

A. Manalo  
e-mail: [leyber\\_16000603@utp.edu.my](mailto:leyber_16000603@utp.edu.my)

Q. A. Ahmed  
Department of Petroleum Engineering, University of Khartoum, Khartoum, Sudan  
e-mail: [quosay@gmail.com](mailto:quosay@gmail.com)

data sets have been used for testing the model performance. The proposed ANFIS correlation is then being compared with other previously published correlations. The best model currently used by industry has scored an average absolute percent error (AAPE) equivalent to 15% while the proposed ANFIS model managed to score 4.12%. By using the new ANFIS model, the study was able to produce a reliable and accurate correlation for estimating Minimum Miscibility Pressure as compared to other previously tested correlations.

**Keywords** Artificial intelligence · Adaptive Neuro-Fuzzy inference system · Minimum miscibility pressure · Trend analysis

## 1 Introduction

Enhanced oil recovery, or EOR, (sometimes called tertiary recovery) is the application of various techniques to increase hydrocarbon recovery in marginal oilfields in which primary (natural drive) and secondary (water and gas flooding) recovery are not feasible anymore. There are three primary techniques of EOR: gas injection, thermal injection, and chemical injection. During any EOR operation, miscibility of the injected fluid is essential to maximize its application. Miscible injection is a proven, economically viable process that significantly increases oil recovery from many different types of reservoirs. [1, 2]. Although gas injection has been the subject of important research and development for more than 50 years, there are still some discrepancies in the interpretation of several laboratory data, and much progress still needs to be made to improve the estimation of the experimental data. There are many analytical and experimental methods used for calculating minimum miscibility pressure (MMP) in relation to certain points of temperature in the reservoir. Analytical methods are more practical compared to experimental in terms of time consumed and the cost of operation. Experimental methods are generally reliable because they could capture the complex interaction between flow and real phase behavior inside the porous medium. However, because they are expensive to conduct and take long time to obtain the result; only few utilize this method as compared to the Analytical one [3]. On the other hand, analytical method is dependent on good experimental data and accurate fluid characterization from Equation-of-State (EOS). Another drawback of the analytical models is that they do not adequately represent the physical system in the reservoir. To address this problem, a new model is developed using Adaptive Neuro-Fuzzy Inference System (ANFIS). The model was coded under MATLAB environment with a user-friendly and easy to use graphical user interface (GUI). One of the critical concerns in determining the effectiveness of Enhanced Oil Recovery (EOR) is the understanding and evaluation of the Minimum Miscibility Pressure (MMP). Minimum miscibility pressure is the lowest possible pressure required to attain the mixing of injected fluid and the hydrocarbons in the reservoir into one phase. It is believed that optimum recovery and better sweep efficiency could only be achieved by reaching this minimum pressure. MMP determination, however usu-

ally depends on reservoir condition, reservoir fluid composition, and injected gas properties. The reservoir fluid composition could be represented by the Molecular weight  $C_{7+}$ . However, Reservoir condition is represented by reservoir temperature that affects MMP response. Selection of hydrocarbon gasses as the injection fluids is represented by the injected gas composition (Mole fraction  $C_2$ – $C_6$ , and Mole fraction  $C_1$ ).

## 2 Model Development

Machine Learning models could achieve high precision, provided that the input data is carefully selected. There are many parameters that affect the MMP determination in reservoir-oil/injection gas mixtures. These are: reservoir condition, reservoir fluid composition, and injected gas properties. Reservoir condition is represented by reservoir temperature that is affecting MMP response. The reservoir fluid composition is represented by Molecular weight  $C_{7+}$  oil composition; however, the injection gas mixture is being represented by the Mole fraction  $C_2$ – $C_6$ , and the Mole fraction  $C_1$ .

### 2.1 Model Training and Testing

The Adaptive Neuro-Fuzzy Inference System (ANFIS) approach is selected to create the model. A thorough understanding of this approach is needed to update the model's parameters during training. This machine learning is a type of artificial neural network that is based on the fuzzy inference system by Takagi-Sugeno. It is an architecture that falls under hybrid neuro-fuzzy system. Neural network will be trained to learn and emulate the pattern of the input data sets for prediction MMP. A combination method from neural network and fuzzy logic provides idealistic prediction [4]. There are no definite rules to follow regarding the division of data for training and testing. The usual practice is that, if the data is very few, 50/50 is used, while if there is abundant data, 70/30 is used, although variations between the two norms of divisions could be applied leniently. In the present investigation, 177 data sets were used for training, while 98 data sets were used for testing. All data used in this study have been collected from published literature.

### 2.2 Model Testing and Validation

The performance of any machine learning (ML) model may not necessarily be better if compared with other correlations but is dependent on careful selection of its learning parameters [5, 6]. The proposed ANFIS model is then compared to other previous correlations; these are: Firoozabadi et al. [7], Sebastian and Lawrence [8],

Maklavani et al. [9], and Menouar [10] correlations. A refining process is needed to increase the accuracy and reliability of the model. The coefficient of correlation, as well as error analysis helps in evaluating the performance of the model. In refining ANFIS model, the following training options need to be optimized:

(i) *Clustering radii*

Clustering radius identifies the extent of influence of the cluster's centre. Various degrees of association used are assumed by changing the value of the radius. In this study, clustering radii is set to be 0.6.

(ii) *Learning step size*

To keep the learning process stable and optimize the model, a value of 0.0001 step size is selected.

(iii) *Increasing rate*

This option is to make the adapting quicker once the model is identified to learn effectively. If the measured error occurs in a consecutive decrease, the step size is scaled up by the same number of the decreased successive value. The chosen increasing rate for this study is 1.4.

(iv) *Decreasing rate*

This option is used to slow down the learning rate and make it more precise once the model appears to increase in error. The step size will be scaled down by the same number of steps once it detected that the error increases. In this model, the decrease rate applied is 15.

Trend analysis is employed in determining the validity of the model as well as the comparison with the selected correlations. Trend analysis is done by changing one parameter in an increasing interval while, other parameters were kept constant and plotting the result against the modelled MMP values from the code.

### **2.3 Error and Statistical Analysis**

Mathematical analysis is needed to calculate the percentage error of correlations and the developed model. The predicted result ( $MMP_{\text{predicted}}$ ) of the model would be compared to the actual ( $MMP_{\text{actual}}$ ) value to obtain the errors. This error is determined by utilizing the Average Percent Relative Error (APE), Average Absolute Percent Relative Errors (AAPE), Minimum Absolute Percentage Error equation ( $APE_{\text{min}}$ ), and Maximum Absolute Percentage Error equation ( $APE_{\text{max}}$ ). While for the statistical measurement, Standard Deviation (SD), Coefficient of Correlation (R), and Root Mean Square Error (RMSE), were utilized to evaluate the accuracy of the model.

### 3 Results and Discussion

There are 275 measured data of minimum miscibility pressure which were divided into training and testing purposes. The New model is developed and simulated. The following are the results.

#### 3.1 Trend Analysis

The trend analysis makes use of the maximum, minimum and average values of each parameter. The range of the data parameter chosen is plotted against a constant value of the other remaining parameters.

Through this process, the obtained trend line could be analyzed as to whether it follows the specified trend for that parameter.

Figure 1a shows the effect of temperature on MMP for various empirical correlations, while Fig. 1b shows the declining trend of temperature as generated by ANFIS model. This means that the ANFIS model corresponds to the temperature trend of the previously published correlations and models.

Figure 2a shows the change in MW of reservoir oil  $C_{7+}$  composition for various empirical correlations and models, whereas the second figure (Fig. 2b) shows the declining trend of MW  $C_{7+}$  composition as generated by ANFIS model. This again confirms that the ANFIS model corresponds to the MW  $C_{7+}$  composition trend of the previously used correlations and models.

Figure 3a shows the effect in change of MW of  $C_1$  (in gas mixture composition) on MMP for various empirical correlations, whereas the Fig. 2b shows the declining trend of MW of  $C_1$  composition as generated by ANFIS model. This verifies that the ANFIS model corresponds to the MW of  $C_1$  composition trend of the previous models and correlations.

#### 3.2 Error, Statistical and Graphical Analyses

These are the results of error analysis which are utilized in accordance with statistical calculations. The statistical parameters used for assessment are: coefficient of correlation, average absolute percentage relative error, root mean square error, average percent relative error, minimum or maximum absolute percent error, and standard deviation of error (Table 1).

The newly created ANFIS correlation shows a high positive coefficient of correlation both for training and testing phases. Based on the results of the errors, there is also a low error coefficient for SD, RMSE, AAPE, and APE, which suggest that the model would have low possibility of producing an error. In analyzing the results, graphical tools were also used to aid visualizing the performance and accuracy of

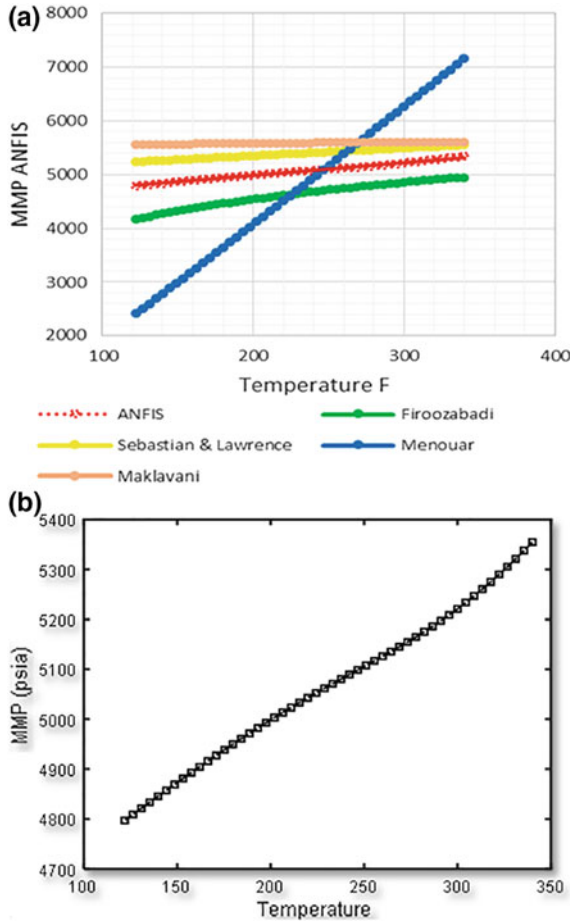


Fig. 1 Plot of temperature versus MMP

the proposed model. Cross plots and Error distribution are the two graphical analysis techniques which were applied in the analysis.

Based on result of testing data set, Fig. 5 yields a coefficient of correlation, R-value of 0.93881, which is higher compared to the training data set in Fig. 4. Similarly, this outcome means that the correlation between predicted MMP and measured MMP is accurate on the testing data sets. Even though the result obtained was high in coefficient of correlation, which is a decent marker to decide on the exactness of the model, other statistical measures should be considered to give a solid evidence that the ANFIS solution is more precise than other alternative models.

The frequency table of error distribution is a simple way to display the number of occurrences of an error the value occurs. As shown in the Fig. 6, a notable concentration of error occurs on the bar 6, which reaches up to 50 times. But looking at the

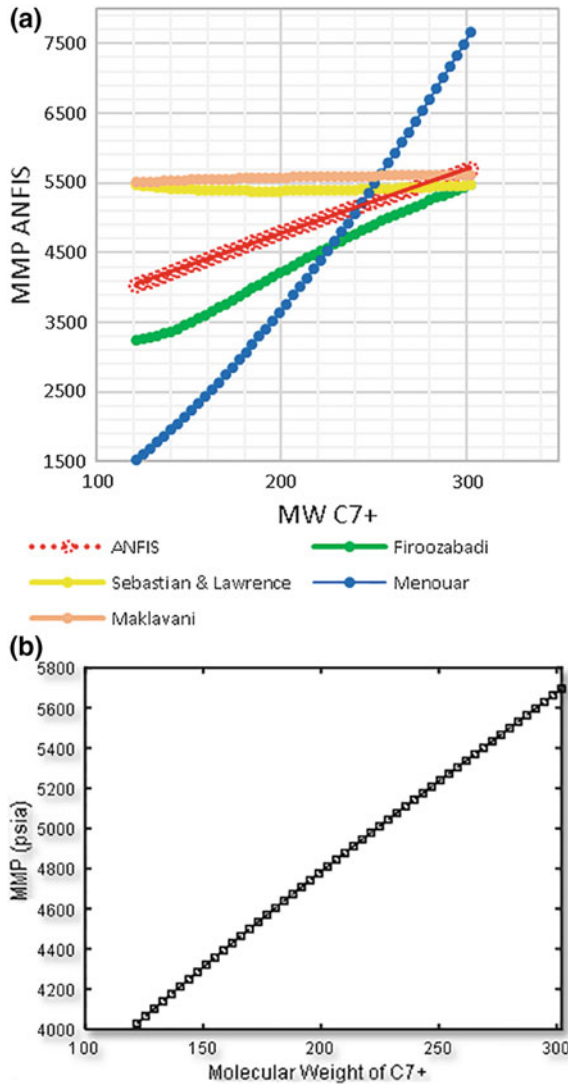


Fig. 2 Plot of MW C<sub>7+</sub> versus MMP

normal distribution curve, we could find that most of the errors are within the area and are near to the median value. Figure 7 shows the residual of errors of the model. Consistency of the model can be determined by generating the residual graph. Values of errors are distributed randomly on positive values as well as in negative values. Although a slight heteroskedasticity is observed near the smaller values, the overall randomness of points is observed throughout the whole plot. This means that the residuals do not contradict the linear assumption.

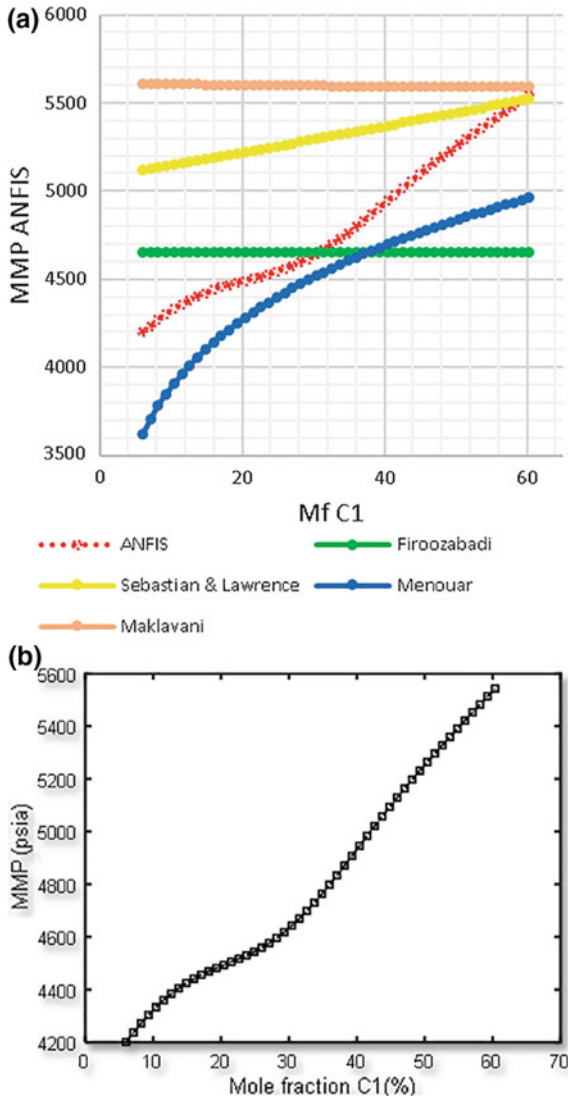


Fig. 3 Plot of Mf C<sub>1</sub> versus MMP

### 3.3 Comparison with Other Empirical Correlations

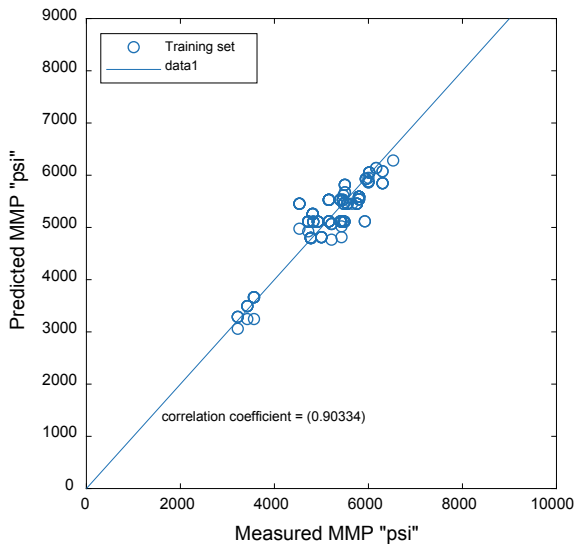
A summary of the statistical test used to evaluate the performance of the created ANFIS model and its comparison to other previous correlation models is shown on Table 2. Based on the test data results, the ANFIS performs well when it comes to coefficient of correlation, root mean square error, average percent relative error, and



**Table 1** Statistical analysis error for ANFIS model

Statistical parameters	Data sets	
	Training	Testing
Correlation coefficient (R)	0.9033	0.9388
Standard deviation error (SD)	6.0609	5.5526
Root mean square error (RMSE)	6.0534	5.5243
Maximum error ( $E_{max}$ )	20.3520	20.3520
Minimum error ( $E_{min}$ )	0.2415	0.2415
Average absolute percent relative error, AAPE	4.5940	4.1223
Average percent relative error, APE	-0.3430	-0.0287

standard deviation compared to other previous correlations. While all correlation models have positive high correlation, ANFIS was observed to have the highest coefficient of correlation of 0.9388, which means that it has achieved a stronger correlation to the actual MMP compared to other correlations. RMSE indicates the separation of data around zero deviation. This statistical measure determines the spread of deviation between the predicted and actual values. These deviations are called “residuals”. ANFIS was observed to have the lowest RMSE of 5.5243, this means that the value of the predicted data is more concentrated around the line of best fit as compared with other MMP correlations. The variability of predicted data points is measured through SD. The further the points are from the mean value,



**Fig. 4** Scatter plot of predicted ANFIS MMP versus Actual MMP (training)

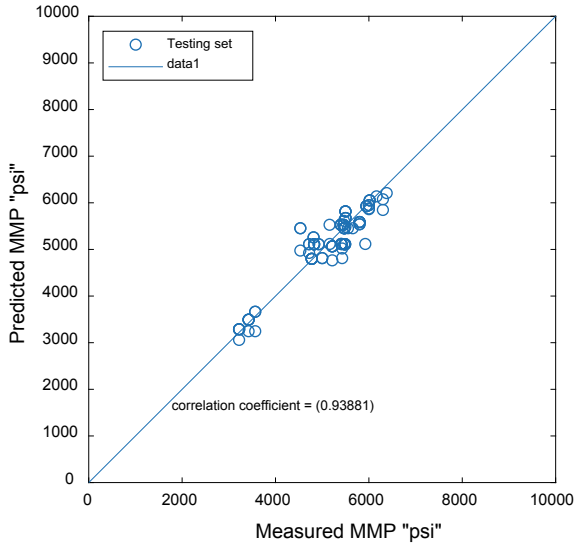


Fig. 5 Scatter plot of predicted ANFIS MMP versus Actual MMP (testing)

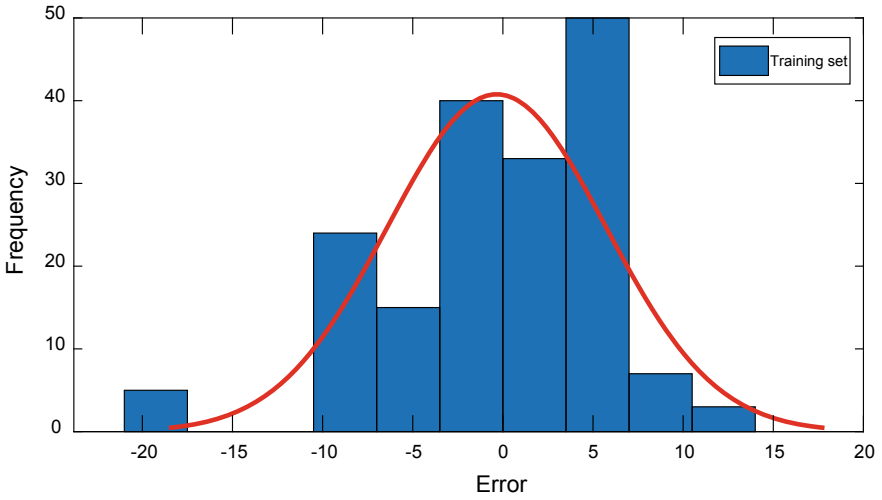
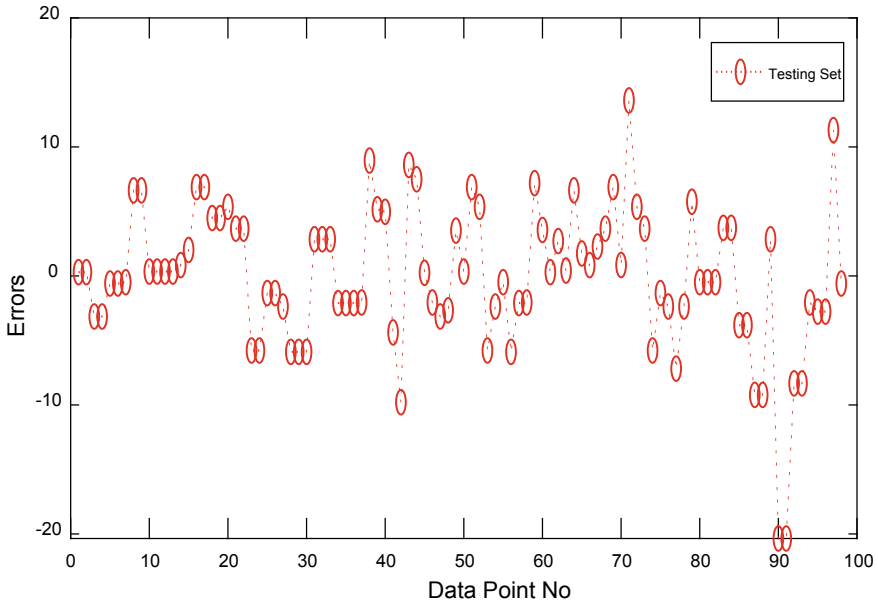


Fig. 6 Frequency distribution of Error



**Fig. 7** Residual error of data points

the larger the SD. Therefore, the lower the deviation, the better its performance is (refer to Tables 3, 4, 5 in Appendix 1 for Error Ranking). ANFIS was observed to have the lowest Absolute Percent Relative Error of 4.1223%, which means that it achieved lesser error compared to other correlations. AAPE values could be more clearly understood when shown graphically using  $x = y$  plot of predicted and actual measured value of MMP. Sometimes it is called the 45° best fit line.

As observed here, most of the points are not so much scattered and are following the matching trend line. The closer the point is to the line; the better accuracy the model has in predicting the values of MMP.

As seen in the graph, the data points here are also following the trend line, but it is more scattered compared to ANFIS plot in Fig. 8.

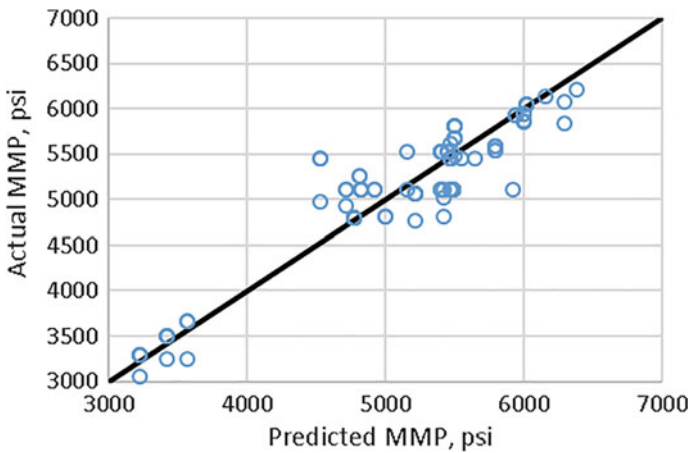
Figure 10 shows a less scattered plot of points, but the deviated trend of points is not following the matching trend line. This is the reason why the Sebastian and Lawrence has a relatively high AAPE value (Fig. 9).

As in the case of Sebastian and Lawrence, Fig. 11 for Maklavani’s model shows that the points are not scattered which causes its correlation coefficient to reach 0.9319; but at the same time the points do not follow the matching trend line, causing it to have a high AAPE and higher prediction error for the actual value of MMP, especially at the low-to-medium MMP values (Fig. 11).

The data point plotted in Fig. 12 show loosely-scattered trend and the trend is not directly noticeable. This is the reason why Menouar model has low coefficient of correlation of 0.61 and has relatively high AAPE of 27.87%.

**Table 2** Summary of statistical analysis and errors of ANFIS and other correlation model

Model Name		Proposed ANFIS model	Firoozabadi et al. [7]	Sebastian and Lawrence [8]	Menouar [10]	Maklavani et al. [9]
Statistical feature	Correlation coefficient (R)	0.9388	0.8286	0.8507	0.6100	0.9319
	Root mean square error (RMSE)	5.5243	9.5680	19.4689	37.6256	21.9151
	Maximum error ( $E_{max}$ ) average	20.3521	24.48	57.07	91.35	59.14
	Minimum error ( $E_{min}$ )	0.2415	0.18	0.12	0.24	0.07
	Average percent relative error, APE ( $E_r$ )	-0.0287	-1.7133	-6.9004	11.0316	-15.3029
	Absolute percent relative error, AAPE ( $E_a$ )	4.1223	6.7039	11.9236	27.8739	15.3552
	Standard deviation error (SD)	5.5527	9.4617	18.2987	36.1570	15.7680



**Fig. 8** Plot of data points of Actual versus Predicted ANFIS model

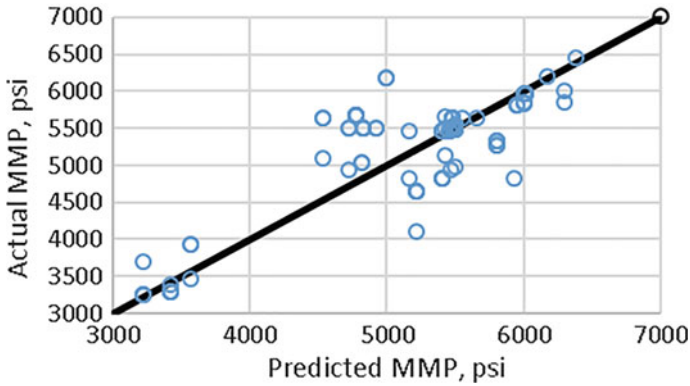


Fig. 9 Plot of data points of Actual versus Predicted Firoozbadi model

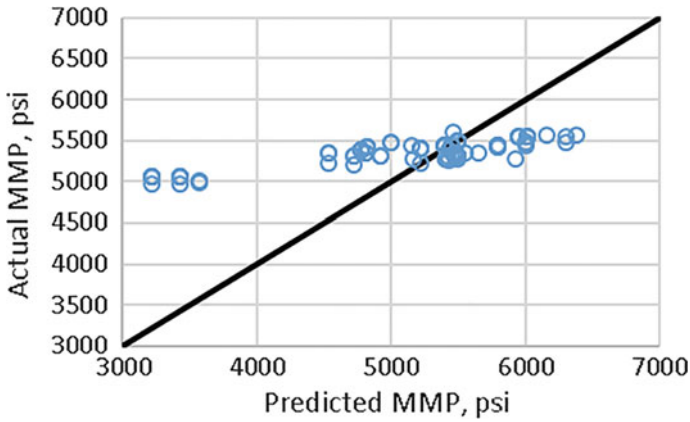


Fig. 10 Plot of data points of Actual versus Predicted Sebastian and Lawrence model

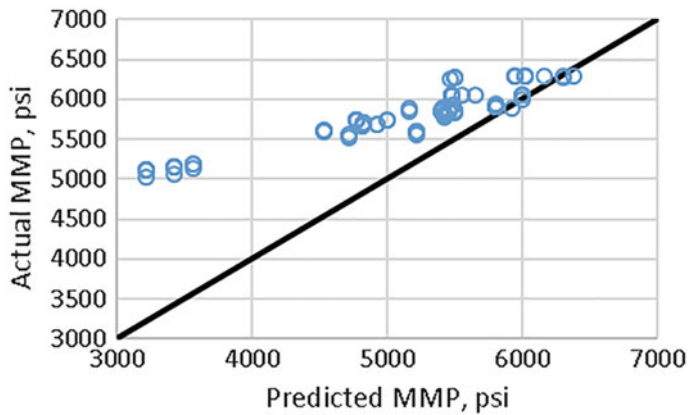


Fig. 11 Plot of data points of Actual versus Predicted Maklavani model

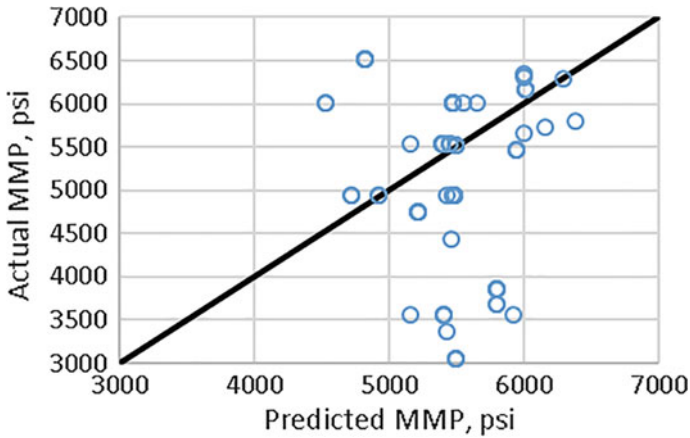


Fig. 12 Plot of data points of Actual versus Predicted Menouar model

### 3.4 GUI Graphical User Interface (GUI)

The development of the Graphical User Interface (GUI) was completed through MATLAB guide. In this GUI, there are ANFIS models which are operated by four input parameters. These prepared ANFIS models enable the client to choose any parameters and the GUI will consequently determine and generate the result which is the Minimum Miscibility Pressure. The Graphical User Interface (GUI) likewise enables the client to peruse and select any Excel record which contains the information and the GUI will read the chosen document (see Appendix 2).

## 4 Conclusion and Recommendation

In conclusion, the New proposed model for predicting Minimum Miscibility Pressure (MMP) for reservoir-oil/injection gas mixtures using ANFIS machine learning has satisfied all its objectives which are:

- (i) Developing a model which is coded in MATLAB software using backpropagation scheme.  
The code has been done and run through backpropagation scheme, and a Graphical User Interface (GUI) has been created accordingly. The model has been executed smoothly without syntax error detected.
- (ii) Utilizing Adaptive Neuro-Fuzzy Inference System (ANFIS) in determining the appropriate Minimum Miscibility Pressure (MMP).  
Using input data parameters, the ANFIS model was able to generate the minimum miscibility pressure required output data were automatically written and saved in an excel file.

- (iii) Training, Validating, and Testing the model performance by Trend analysis.
- The model has been trained using 177 data samples, and 98 data samples were used in the testing to validate the model output. The set of data conforms to the expected trend of each parameter which are increasing for Temperature and Molecular weight  $C_{7+}$ ; decreasing trend for Mole Fraction  $C_2-C_6$ ; increasing trend for Mole Fraction  $C_1$ ; and decreasing trend for Mole Fraction  $C_{2+}$ .
  - The model performance was checked, and it also conformed to the trend analysis for each parameter.
- (iv) Analyzing statistical and graphical results by comparing it to other correlations of MMP.
- The high correlation coefficient  $R$  of 0.93881 of the newly proposed ANFIS model proved that the predicted value of the model is closely associated with the actual measurements.
  - The low RMSE of 5.5243 exhibited by the proposed ANFIS model indicates that the model accurately fits the data. This proves that residual errors do not contradict with the linear assumption of the model.
  - With the comparison of the Average Absolute Percentage Error (AAPE), we could conclude that the ANFIS model generates less error and at the same time it matched closely to the actual measured values.
  - The difference between the Maximum and Minimum Errors for each model indicates that ANFIS model has more accurate prediction results.

Based on evaluation on the models, the ANFIS system was able to establish a better outcome of estimates. It is concluded that the proposed ANFIS model is more precise and dependable. Having an exact combination of training option and detailed techniques in refining the parameters, the model was able to perform better in estimating the Minimum Miscibility Pressure for reservoir-oil/injection gas mixtures. Since the error is reduced, EOR would be able to achieve its optimum recovery with lesser degree of uncertainty.

It is suggested to incorporate additional past correlations in the selection procedure to enhance the parameters screening and improving the new proposed model. Moreover, it is also recommended to use other types of Machine Learning Algorithms and compare their results with this study. It is also recommended to utilize the field information rather than reported experimental values in the literature since the outcomes of field data would be directly gathered from the field and is more realistically dependable.

**Acknowledgements** We would like to take this chance to express our heartfelt gratitude to Universiti Teknologi PETRONAS and University of Khartoum for providing the necessary fund and the support to complete this project. This project was fully sponsored by grant code center 0153AB-M60.

## Appendix 1

See Tables 3, 4 and 5.

**Table 3** RMSE ranking

Model name		ANFIS	Firoozabadi et al. [7]	Sebastian and Lawrence [8]	Maklavani et al. [9]	Menouar [10]
Statistical feature	<i>Root mean square error (RMSE)</i>	5.5243	9.5680	19.4689	21.9151	37.6256
Ranking		1st	2nd	3rd	4th	5th

**Table 4** SD ranking

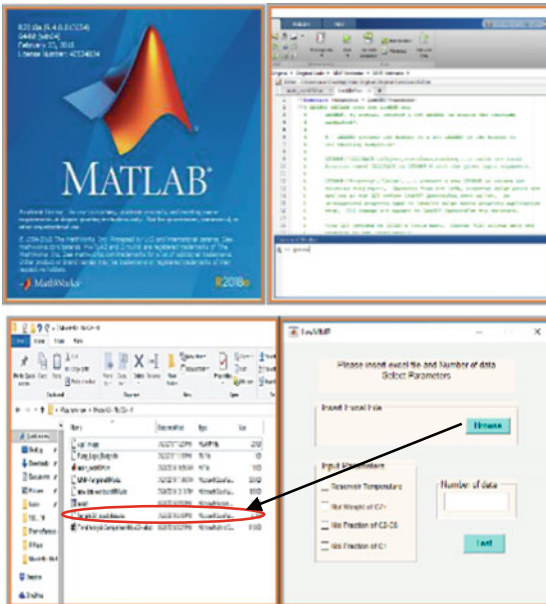
Model name		ANFIS	Firoozabadi et al. [7]	Maklavani et al. [9]	Sebastian and Lawrence [8]	Menouar [10]
Statistical feature	<i>Standard deviation error (SD)</i>	5.5527	9.4617	15.7680	18.2987	36.1570
Ranking		1st	2nd	3rd	4th	5th



**Table 5** AAPE ranking

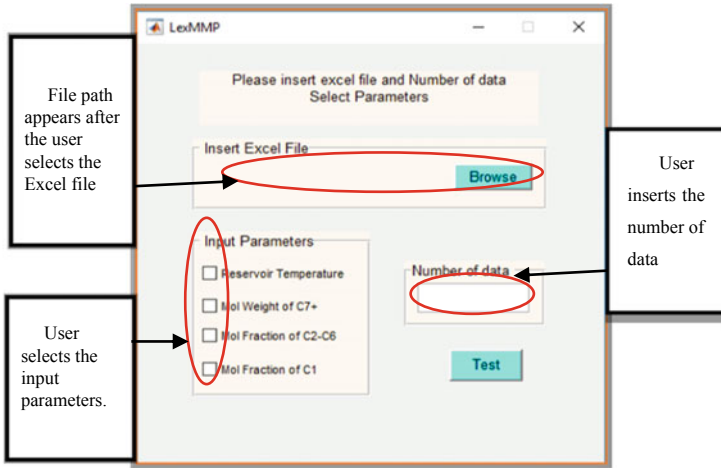
Model Name		ANFIS	Firoozabadi et al. [7]	Sebastian and Lawrence [8]	Maklavani et al. [9]	Menouar [10]
Statistical Feature	<i>Absolute percent relative error, AAPE (<math>E_a</math>)</i>	4.1223	6.7039	11.9236	15.3552	27.8740
Ranking		1st	2nd	3rd	4th	5th

## Appendix 2

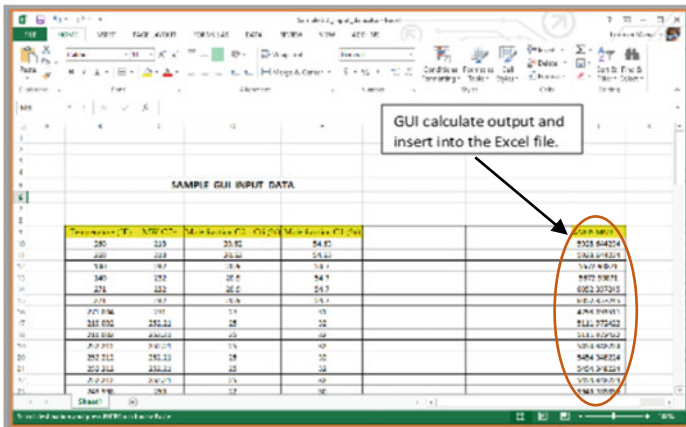


The figure on the left shows the Matlab opening window. The Graphical User Interface (GUI) likewise enables the client to peruse and select any Excel record which contains the information and the GUI will read the chosen document.

The figure here shows the GUI window and the panels and buttons together with the corresponding process executed by its function button.



The created GUI insert its predicted value on the excel file where the input data sheet was written.



## References

1. Mansour E, Al-Sabagh A, Desouky S et al (2016) Experimental approach of minimum miscibility pressure for CO<sub>2</sub> miscible flooding: application to Egyptian oil fields. Int J New Technol Res (IJNTR) 2:105–112
2. Zhang K, Seetahal S, Alexander D et al (2016) Correlation for CO<sub>2</sub> minimum miscibility pressure in tight oil reservoirs. In: SPE Trinidad and Tobago section energy resources conference

3. Johns R, Sah P, Solano R (2002) Effect of dispersion on local displacement efficiency for multicomponent enriched-gas floods above the minimum miscibility enrichment. *SPE Reservoir Eval Eng* 5:4–10
4. Mohandas K, Karimulla S (2001) Fuzzy and Neuro-fuzzy modeling and control of non linear systems. In: *Second international conference on electrical and electronics*
5. Al-Shammasi A (2001) A review of bubblepoint pressure and oil formation volume factor correlations. *SPE Reservoir Eval Eng* 4:146–160
6. Oloso MA, Hassan MG, Bader-El-Den MB et al (2017) Hybrid functional networks for oil reservoir PVT characterisation. *Expert Syst Appl* 87:363–369
7. Firoozabadi A, Khalid A (1986) Analysis and correlation of nitrogen and lean-gas miscibility pressure (includes associated paper 16463). *SPE Reservoir Eng* 1:575–582
8. Sebastian H, Lawrence D (1992) Nitrogen minimum miscibility pressures. In *SPE/DOE enhanced oil recovery symposium*
9. Maklavani A, Vatani A, Moradi B et al (2010) New minimum miscibility pressure (MMP) correlation for hydrocarbon miscible injections. *Braz J Pet Gas* 4
10. Menouar H (2013) Discussion on carbon dioxide minimum miscibility pressure estimation: an experimental investigation. In: *SPE Western Regional & AAPG Pacific Section Meeting 2013 joint technical conference*

# Design and Development of Apparatus for Evaluating Galling Resistance Test



Hemanta Doley, Sandeep Singh  and Nabam Teyi

**Abstract** In the present study, a custom made galling test setup has been developed and tested for use. The preliminary result obtained with mild steel specimens is presented. The present test configuration consists of two coaxially aligned hollow cylindrical specimen loaded along the longitudinal axis. The specimen holder is provided with an internal taper of  $3^\circ$  and specimen with an external taper of  $3^\circ$ , to ensure firm grip between the holder and the specimens. The test configuration adheres to American Society for Testing and Materials (ASTM) G196 standards, in which the resulting contacting surface is in the shape of annulus and there is uniform distribution of pressure. It was found that the results obtained through this setup are satisfactory and reproducible. The purpose of the present work is to design, develop and qualify a fixture for conducting galling tests.

**Keywords** Galling · G98 · G196 · Tribology · Wear

## 1 Introduction

Wear is defined as an alteration of a solid surface by progressive loss or progressive displacement of material due to relative motion between that surface and a contacting substance or substances [1]. This phenomenon is apparent among machinery components which are being rigorously used at extreme environments on routine basis in industries and accounts for catastrophic failure of the components. Galling is a form of adhesive wear which occurs when there is a relative sliding motion between conforming surfaces and under loading and no lubrication condition. American Society for Testing and Materials (ASTM) defines galling as a form of surface damage arising between sliding solids, distinguished by macroscopic, usually localized, roughening, and the creation of protrusions above the original surface; it is characterized by plas-

---

H. Doley · S. Singh · N. Teyi (✉)

Department of Mechanical Engineering, North Eastern Regional Institute of Science and Technology, Nirjuli 791109, Arunachal Pradesh, India  
e-mail: [nbtnerist@gmail.com](mailto:nbtnerist@gmail.com)

© Springer Nature Singapore Pte Ltd. 2020

M. Awang et al. (eds.), *Advances in Material Sciences and Engineering*, Lecture Notes in Mechanical Engineering, [https://doi.org/10.1007/978-981-13-8297-0\\_56](https://doi.org/10.1007/978-981-13-8297-0_56)

547

tic flow and may involve material transfer [1]. Due to the relative motion between the contacting surfaces, friction or plastic deformation is initiated and as a result induces pressure and energy in the contact zone. The elevation in the pressure increases the energy density and heat level, which leads to greater adhesion between the surfaces and initiates material transfer or plastic flow or both. Galling can often lead to complete seizure of the mated surfaces.

There are two international standards for galling test that are being commonly used: ASTM G98 [2] and G196 [3]. The significant difference between them is that, the former uses cylindrical flat on flat contact while the later uses matching annular surface. The reason for the annular shape is that minimum contact area and no part on the mating part has zero velocity. The G196 test method has shown to have higher repeatability than G98 test in determining the galling resistance [3]. The G98 test will likely remain the most used galling test while G 196 test is very expensive [4].

From the available literatures, it can be witnessed that many tribologists have tried different procedures to test galling resistance. Hummel [5] evaluated galling resistance, in which the mating couples experiences a line contact, where the stationary button was made to contact with a rotating cylinder. The threshold galling stress and the coefficient of friction between the button and the cylinder was determined. Hummel [6] developed a test method which overcomes several problems that are inadequate in the ASTM standard test method for galling resistance. In this, the specimen consisting of two hollow cylinders was aligned with a custom made alignment pin and loaded along their longitudinal axis. As a result, the contacting surface has a uniform stress distribution and zero sliding distance. He ascertained that galling phenomenon from non-galled to galled does not go through a step transition/single value but rather a stochastic process. Gurumoorthy et al. [7] developed a wear testing machine capable of testing both galling resistance as well as sliding wear behaviour at high stress level. Swanson et al. [8] studied the galling behaviour of two heat treated steels, AISI 1541 and AISI 8620 with the help of two different tests. One uses pin with a spherical tip loaded against the block and the pin is held stationary and the block is driven while another uses a button with a flat cylindrical base which is loaded against a flat rectangular block, where the button is rotated manually. The damage surface was measured by profilometer and the average of the maximum peak to valley distance was calculated and was used to quantify the amount of galling produced.

Olsson [9] studied the tribological characteristics of the die tool materials during the powder compaction process, through controlled base scratch test using a commercially available scratch tester and custom made aluminium sample holder instead of Rockwell C-diamond stylus. In this, the powder green body was attached to the sample holder, and the friction and material transfer characteristic of different couple was evaluated, using a normal load of 50 N and sliding velocity of 20 mm/min and sliding distance of 20 mm for 10 passes at ambient temperature and at no lubrication condition. Smith et al. [10] developed a cobalt free, stainless steel powder metallurgy hard-facing alloy, designed to replace the cobalt based hard-face alloy stellite-6, which exhibits comparable galling resistance up to 350 °C. The galling resistance was evaluated on ASTM G98 pin on block test at 343 °C, and the dam-

aged surface was studied using metallography and SEM. Siefert and Babu [11] tested materials as per ASTM G98, and attempted to quantify galling of the materials by examining under laser microscope and measuring the depth and surface roughness of the tested materials and comparing with as machined specimens. Wycliffe [12] studied the galling behaviour of 6061 aluminium alloys, Duralcan aluminium matrix composites with 20 vol.% of SiC and cast iron by mating reciprocating plate made of 6061 aluminium alloys or duralcan aluminium matrix composites or cast iron with cylinder mounted on an axle made of 52100 bearing steel or nodular iron, with contact stress below the yield stress of aluminium alloys.

## 2 Experimental Set-up

A custom made experimental apparatus was developed as per ASTM G98 and G196 standards. The setup ensures maintenance of constant compressive load between the test specimens without use of screw type loading mechanism and maintains rotatory motion over the other.

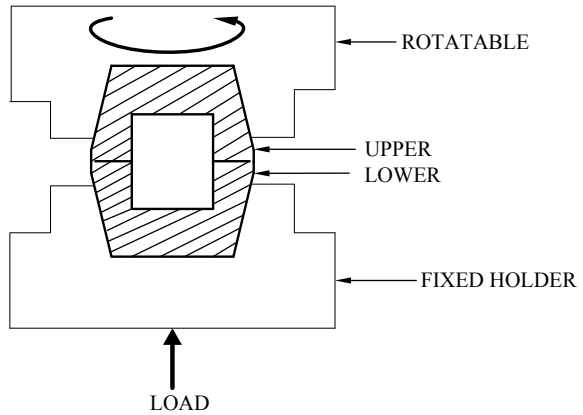
It consists of an upper and a lower holder which is fitted in the main cylinder with a through hole of varying diameter, which maintains the co-axiality and allows a rotary motion. A very limited axial movement is permitted and desired motion can be constrained wherever necessary. The motion of the lower holder can be constrained through a keyway designed along the periphery via a hole made through the main cylinder for the successful conduct of the galling test. The lower holder and upper holder have a through hole along its length through which the specimen can be de-assembled, using a small metallic rod. The upper holder rests in the upper part of the main cylinder and does not pass entirely through the hole. It is fitted with a thrust bearing which allows the maintaining of smooth, frictionless and uninterrupted rotary motion; while its axial movement is highly limited. The specimen is provided with an external taper and the holder with an internal taper of approximately  $3^\circ$ , so that when it is rotated upon loading—the specimen does not slip due to the friction between the tapering surfaces. A photograph of the set-up is presented in Fig. 1.

In the test apparatus, the button is held stationary and is loaded vertically upward through a class 1 lever system which consists of a fulcrum supported firmly on the base plate, a lever, a load concentrator and a fixed pulley from where the load hangs freely. The load is transferred through load concentrator made to contact with the block which is given a rotary motion manually through a handle from the top. Schematic diagram of the test procedure (tapers exaggerated for emphasis) is presented in Fig. 2.

**Fig. 1** The physical set up for testing for galling limit

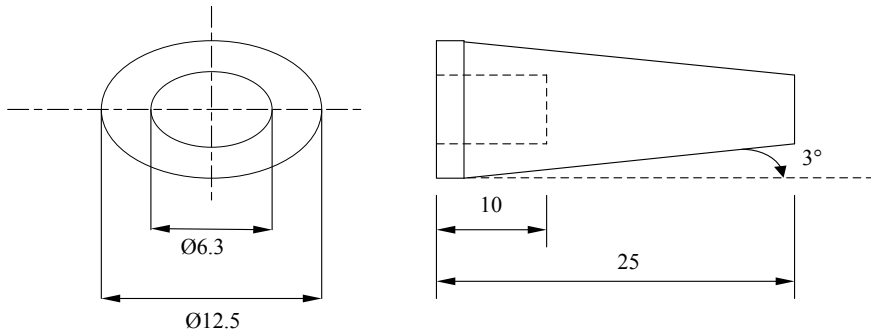


**Fig. 2** Schematic arrangement of the two test pieces



### 3 Experimental Procedures

Please read the Instructions to Authors documents carefully. Manuscripts that do not comply will be returned for correction. The following should be noted in particular. The specimens for the experiment were prepared as per ASTM G196 standards. The geometry of the test specimen is presented in Fig. 3. A commercially available mild steel rod of 16 mm was mounted in the lathe chuck and was centred. Facing operation was performed followed by turning operation and the diameter was reduced to 13 mm. The sample was further reduced to a diameter of 12.5 mm and a hole of 6.3 mm diameter with a hole length of 10 mm was drilled on the centre. An external taper of 3° for a length of 25 mm was given on the sample. The samples were cleaned in soap water solution to get rid of the dirt and grease and were wiped dry with tissue paper. The samples were mounted on the upper and lower holder and the lower specimen was constrained with an allen screw. The required load was applied through the



**Fig. 3** Dimensions of the specimens in mm

fulcrum which has a load concentrator at one of its end which is fitted beneath the lower holder and rotary motion was given through the rotating lever, completing one revolution within 10 s. The sample sets were taken out and examined with naked eyes, to see if there is material transfer between them. If that happened, then galling is said to have occurred.  $G_{50}$  was determined from the observation based on a series of experiments.  $G_{50}$  is defined as, the stress at which the probability of occurrence of galling on one or both of the test specimens is 50% [3].

The material used for the experiments was a commercially available mild steel with loads varied from 10.144 to 20.144 kg. The weight of the hanger was found to be 0.144 kg.

## 4 Results and Discussions

A test study on 29 pairs of commercially available mild steel specimens was conducted on the galling setup developed. The test was conducted at 10.144, 11.144, 12.144, 13.144, 14.144, 14.644, 15.144, 15.644, 16.144, 18.144 and 20.144 kg. The result of the study is presented in Table 1. From Table 1, it can be observed that from the load range of 16.144 to 20.144 kg, galling has been found to occur in all the specimens but the moment the loading is reduced to 14.144 kg, galling stopped occurring. So, we again started to increase the load through level of 0.5 kg. By increasing the load to 14.644 kg, galling was found to occur on few specimens but less than 50% of the tested specimens, so we again increased the load to 15.144 kg and still galling was found on few specimens, but less than 50% of the tested specimens. Upon further increase in the load to 15.644 kg, we found that six out of the nine specimens underwent galling, whereas the other three specimens did not show galling for the same load.

Hence, the  $G_{50}$  is found out to be at the load of 15.644 kg. As the occurrence of galling is examined through naked eye, determination of  $G_{50}$  value varies from



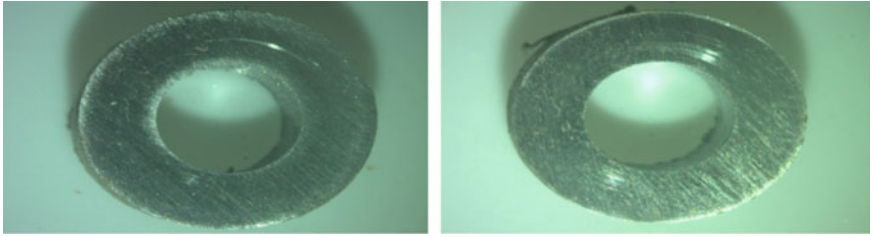
**Table 1** Replicates, loads and occurrence of galling

Sample No.	Weight (kg)	Occurrence of galling
1	10.144	No
2	11.144	No
3	11.644	No
4	12.144	No
5	13.144	No
6	14.144	No
7	14.144	No
8	14.144	No
9	14.144	No
10	14.644	Yes
11	14.644	No
12	14.644	No
13	14.644	No
14	15.144	Yes
15	15.144	No
16	15.144	No
17	15.144	No
18	15.644	Yes
19	15.644	Yes
20	15.644	No
21	15.644	Yes
22	15.644	No
23	15.644	No
24	15.644	Yes
25	15.644	Yes
26	15.644	Yes
27	16.144	Yes
28	18.144	Yes
29	20.144	Yes

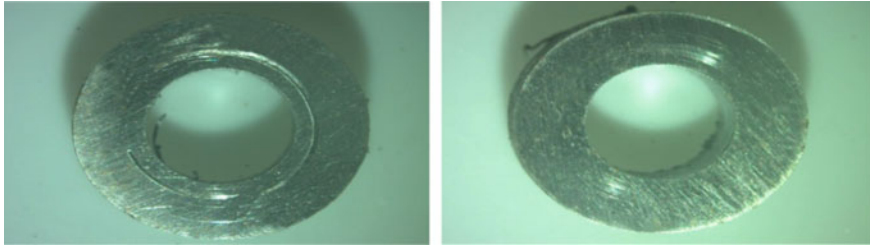
person to person. The force exerted by 15.644 kg on the mating samples is given by  $15.644 \times 9.81 \text{ N} = 153.468 \text{ N}$ .

This load is subjected over an area =  $\pi/4(\text{OD}^2 - \text{ID}^2)$ , where OD = Outer Diameter of the specimen and ID = Inner Diameter of the specimen.

$$= \pi/4(12.5^2 - 6.3^2) = 91.49 \text{ mm}^2$$



**Fig. 4** Specimens without galling



**Fig. 5** Specimens with galling

Therefore, the applied stress was calculated as applied force acting per unit area i.e.  $153.468/91.49 \text{ N/mm}^2 = 1.677 \text{ N/mm}^2$ .

Hence, the value of  $G_{50} = 1.677 \text{ N/mm}^2$  (Figs. 4 and 5).

## 5 Conclusions

In this paper, a design for a galling resistance test apparatus has been proposed and presented. This test fixture addresses all the features actually needed to conduct a test as ASTM-G196. In the present work reported here, the number of samples was low, with the increased number of samples, there may be a statistical spread developed which can help to determine the galling load. The results of the limited tests performed over a small range of loads, as presented in Table 1, indicate that the fixture as designed, has repeatability of the galling appearance. Hence, it is fit for use. The galling results presented show that the propensity for galling increases with load and transition from load leading to appearance of galling to those loads safe against galling; the transition is gradual.

## References

1. Standard Terminology Relating to Wear and Erosion, G40-17, ASTM standards
2. Standard Test Method for Galling Resistance of Materials, G98-17, ASTM standards
3. Standard Test Method for Galling Resistance of Materials Couples, G196-08 (Reapproved 2016), ASTM standards
4. Budinski KG, Budinski ST (2015) Interpretation of galling tests. *Wear* 332–333:1185–1192
5. Hummel SR (2001) New test method and apparatus for measuring galling resistance. *Tribol Int* 34:593–597
6. Hummel SR (2008) Development of a galling resistance test method with a uniform stress distribution. *Tribol Int* 41:175–180
7. Gurumoorthy K, Kamaraj M, Rao KP et al (2007) Development and use of combined wear testing equipment for evaluating galling and high stress sliding wear behaviour. *Mater Des* 28:987–992
8. Swanson PA, Ives LK, Whitenton EP et al (1988) A study of the galling of two steels using two test methods. *Wear* 122:207–223
9. Olsson M (2011) A new test method for measuring the galling resistance between metal powders and die tool materials in powder compaction. *Wear* 273:49–54
10. Smith R, Doran M, Gandy D et al Development of a gall-resistant stainless-steel hardfacing alloy. <https://doi.org/10.1016/j.matdes.2018.01.020>
11. Siefert JA, Babu SS (2014) Experimental observations of wear in specimens tested to ASTM G98. *Wear* 320:111–119
12. Wycliffe P (1993) Galling in aluminum alloys and Duralcan aluminum matrix composites. *Wear* 162–164:514–579

# A Method for the Quantification of Nanoparticle Dispersion in Nanocomposites Based on Fractal Dimension



K. Anane-Fenin, Esther T. Akinlabi and N. Perry

**Abstract** Dispersion quantification provides critical insight and towards understanding and improving the influence of nanoparticle dispersion on the behaviour of the nanocomposite at macro and nanoscale level. This study was precipitated by the limitations of most methods for quantifying dispersion to sufficiently handle issues regarding scalability, complexity, consistency and versatility. A quantity ( $D_0$ ) based on the variance of the fractal dimension was used to quantify dispersion successfully. The concept was validated using real microscopy images. The approach is simple and versatile to implement.

**Keywords** Dispersion · Fractal dimension · Variance · Nanocomposites · Nanoparticles

## 1 Introduction

There are several classifications of polymer composites, however, there is a growing interest in the application of polymer nanocomposites in multidisciplinary fields such as in drug delivery [1], purification systems [2], polymer biomaterials [3] and chemical protection [4]. Dispersion quantification is an important step required for the exploitation of the excellent properties and characteristics of nanocomposites such as mechanical, electrical properties, chemical stability and high aspect ratio [5–8]. The ability to manage the state of dispersion will lead to superior composites by manufacturers with optimised properties [9]. The Van der Waal forces within the individual nanoparticles are the primary cause of agglomeration [10] and therefore

---

K. Anane-Fenin (✉) · E. T. Akinlabi

Department of Mechanical Engineering Science, Faculty of Engineering and the Built Environment, University of Johannesburg, P.O. Box 524, Auckland Park 2006, Johannesburg, South Africa  
e-mail: [kwafen@gmail.com](mailto:kwafen@gmail.com)

N. Perry

Arts et Métiers ParisTech, CNRS, 12M Bordeaux, Esplanade des Arts et Métiers, Talence, France

© Springer Nature Singapore Pte Ltd. 2020

555

M. Awang et al. (eds.), *Advances in Material Sciences and Engineering*, Lecture Notes in Mechanical Engineering, [https://doi.org/10.1007/978-981-13-8297-0\\_57](https://doi.org/10.1007/978-981-13-8297-0_57)

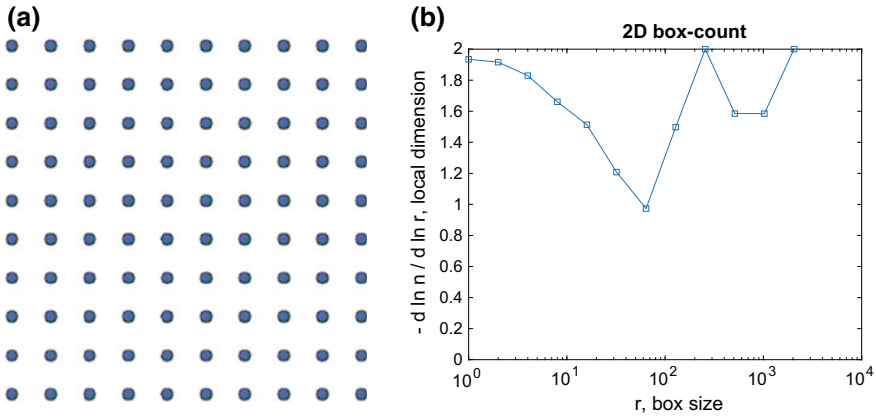
several dispersion techniques to overcome this challenge have been developed such as mechanical or high-speed stirring [11], sonication [12], high shear mixing or melting [13], incorporating surfactants or compatibilisers [9], solution processing, in - situ polymerisation processing, Coagulation Spinning and Electrospinning, Buckypaper-based Approaches, Layer-by-layer (LBL) Technique and Swelling Under Ultrasound Technique [10, 13].

The traditional convention for assessing dispersion of nanoparticles within the nanocomposite matrix is mainly through visual inspection using optical microscopy [14], Transmission electron microscope (TEM) [15], Scanning electron microscope (SEM) [15, 16] or Scanning probe microscope (SPM) [17]. These methods are mainly qualitative, and subjective in nature [18]. Quantitative methods are therefore necessary to overcome the limitations of visual inspection. Quantification provides a platform for correlating the effects of dispersion state on the properties of the composite material [9].

Some studies have been conducted to quantify dispersion within composites using random distribution determinants [19], dispersion characterisation using integration of probability density function (PDF) for estimating the statistical distribution of particle spacing [20], average distance between particles per unit volume. [15], application of Delaunay triangulation [21], the use of differential scanning calorimetry [22] and the quadrant methods [23–27]. A Fourier domain optical coherence tomography based on a static light scattering method was used for quantifying dispersion although it had major limitations such as sensitivity several external factors such as morphology and size of particles and inconsistency of results [28]. The study by Lillehei et al. [16], is one of the few researches that quantified dispersion using Minkowski functionals, fractal dimension and more specifically radial power spectral density (RPSD).

Traditionally, fractal dimension techniques have been widely used in analysing roughness [29] and multidisciplinary fields in of graphics and image analysis [30, 31]. Self-similarity is an important characteristic of fractal dimension approaches. There is a wide array of theorems in fractal dimension which applies to several images including grayscale and coloured images [29]. Gagnepain proposed a technique which was based on reticular counting of cells which was later improved by Voss [32] with the inclusion of probability theory. The linear interpolation was incorporated by Keller et al. [33, 34] to refine the box-counting method.

Several box counting approaches have been developed [35–37], however, in this study the method presented by Moisy [38] is adopted. The box-counting method is chosen because of its simplicity and compatibility. The variance of the calculated fractal dimension was used in formulating a dispersion quantity ( $D_0$ ) which successfully quantified concept models and later validated by real SEM images.



**Fig. 1** **a** Uniformly dispersed model. **b** Fractal dimension graph of the uniformly dispersed model

## 2 Materials

The experimental sample was manufactured using open cast moulding. The matrix was a thermosetting epoxy (Prime 20 LV Resin) and hardener (Prime 20 Slow Hardener) from Advanced Material technology (AMT). The reinforcement was titanium (IV) oxide nanoparticles (21 nm), acquired from Sigma Aldrich. Mechanical stirring was the dispersion technique adopted in dispersing 2 wt% fraction weight of the TiO<sub>2</sub> within the epoxy matrix. The plates were then cut using waterjet, cryofractured before the capturing of Scan electron Microscopy images at 15 kV and 5 μm.

## 3 Proof of Concept

### 3.1 Fractal Dimension Techniques

A technique for assessment of dispersion using the variance from the fractal dimension of the SEM images was developed. Firstly, five models of varying dispersion states were designed as shown in Fig. 1a (uniform dispersion), Fig. 2a (random dispersion), Fig. 3a (Cluster distribution) while Fig. 4a and Fig. 5a. have large agglomerates present. The fractal dimensions of the models were then obtained via an initial step of image segmentation to generate greyscale and black and white images for computation using the box-counting approach. As stated earlier, the box-counting technique was selected because of its simplicity and compatibility [29]. The MATLAB function developed by Moisy [38] for estimating fractal dimension is adopted for this study. Equation (1) is used for calculating the fractal dimension.

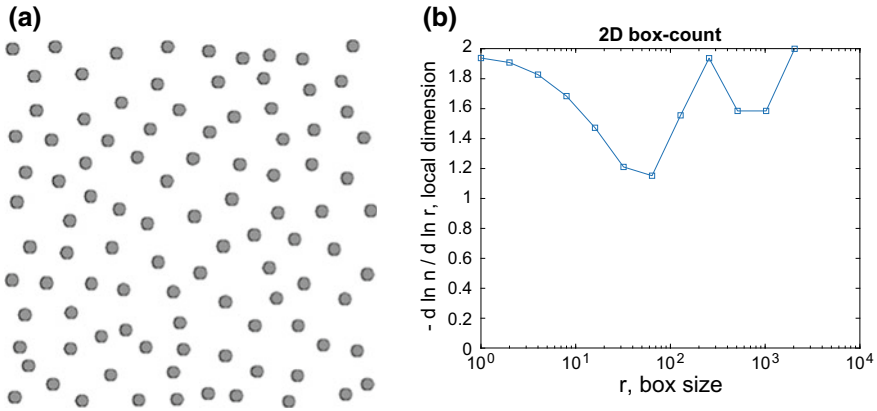


Fig. 2 a Randomly dispersed model. b Fractal dimension graph of the randomly dispersed model

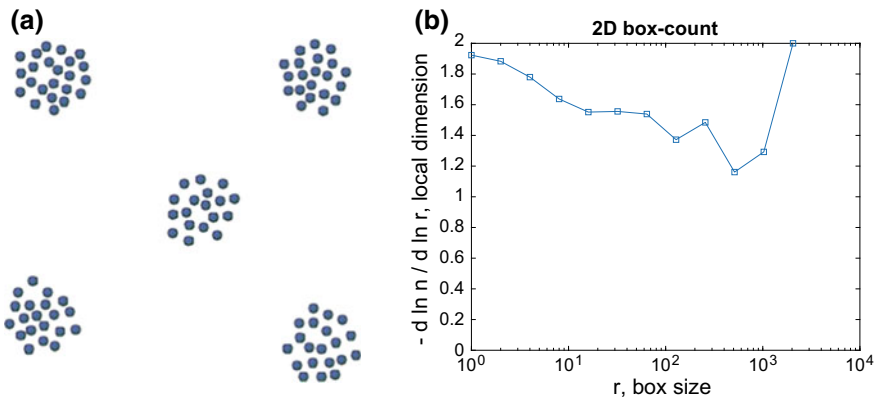
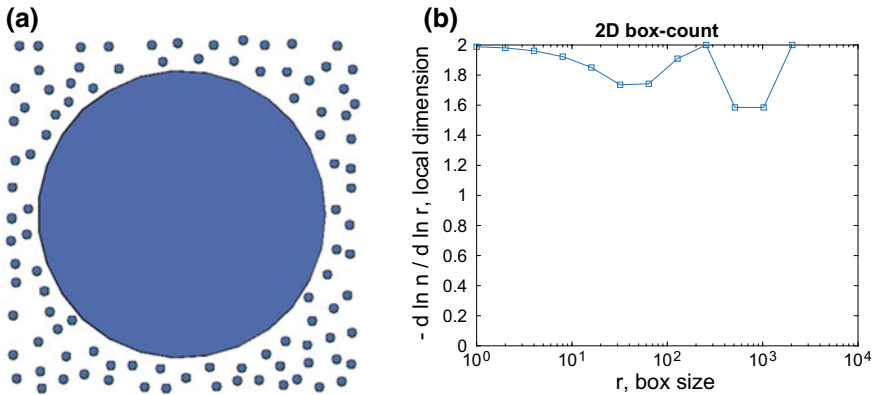


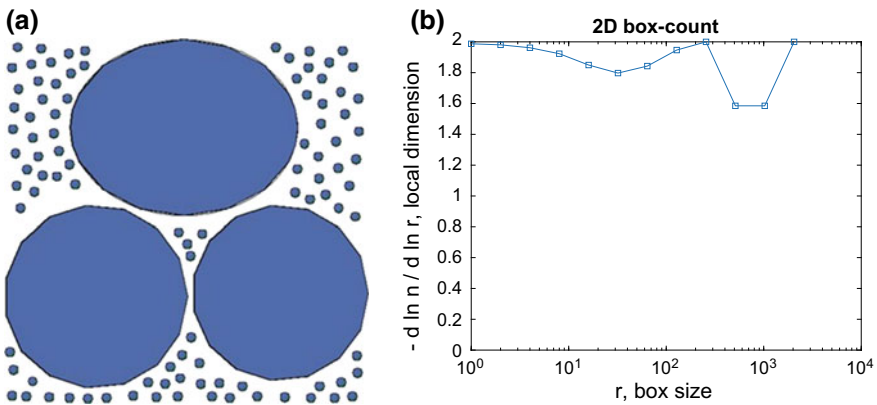
Fig. 3 a Cluster distribution model. b Fractal dimension graph of the cluster distribution model

$$D_f = - \frac{d \ln N}{d \ln R} \tag{1}$$

where  $D_f$  represents fractal dimension of a fractal set  $C$ , and  $N$  is the number of  $D$ -dimensional ( $D = 1, 2, 3$ ) boxes with size  $R$  required for covering the elements of set  $C$  which are nonzero.  $R = 1, 2, 4 \dots 2^P$ , where  $P$  is the smallest integer. A second order finite difference is used to calculate the derivative. Figures 1b, 2b, 3b, 4b and 5b. are the fractal dimension slope plots for the five models.



**Fig. 4** a One large agglomerate model. b Fractal dimension graph of the one large agglomerate model



**Fig. 5** a One three large agglomerate model. b Fractal dimension graph of the three large model

### 3.2 Dispersion Quantity

The variance for each model's  $D_f$  was then calculated as shown in Table 1. The Uniformly dispersed variance value was used to set the upper boundary limit for the rest of the dispersion states. This is due to the fact that a uniformly dispersed state may be considered as an ideal state in composite manufacturing. Therefore, from Table 1, the variance for uniformly dispersed is  $(S_{UD}^2) = 1.89 \times 10^{-1}$ . Since this is the ideal state a dispersion factor  $(f_D) = 1.0 \times 10^{-1}$  was carefully chosen. Equation (2) was formulated to quantify the state of dispersion.

$$D_0 = \left( \frac{S^2}{f_D} \right) \times 100\% \tag{2}$$



**Table 1** Fractal dimension, variance and dispersion of the concept models

Models	Fractal dimension ( $D_f$ )	Variance ( $S^2$ )	Dispersion (%)
Uniformly dispersed	$1.394 \pm 0.434$	$1.89 \times 10^{-1}$	100
Randomly dispersed	$1.425 \pm 0.315$	0.099	99.47
Clustered	$1.483 \pm 0.142$	0.020	20.03
One large agglomerate	$1.837 \pm 0.123$	0.015	15.17
Three large agglomerates	$1.877 \pm 0.084$	0.007	7.13

where  $D_0$  is the dispersion quantity and  $S^2$  is the variance of the fractal dimension of the sample. For the ideal situation,  $D_0 = 100\%$  represents a perfectly homogeneous system. The boundary condition set was  $0\% \leq D_0 \leq 100\%$ , whereas  $D_0 \rightarrow 100\%$  the homogeneity of dispersed particles. To ensure accuracy and consistency in obtained results, some assumptions and considerations were adopted. These include the use of an equal number of particles for each model and the conversion of all model images to  $1500 \times 1500$  pixels.

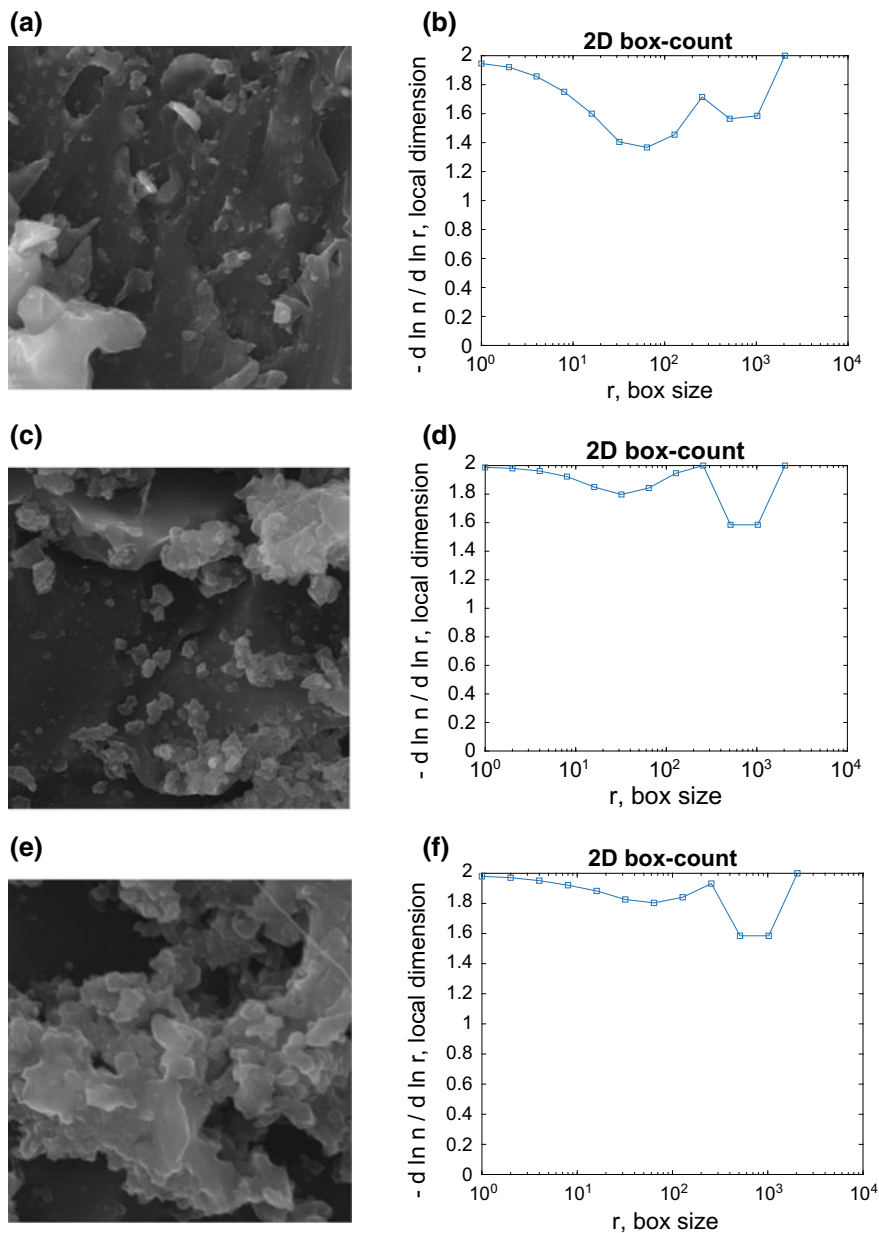
$$D_0 = \left( \frac{S^2}{f_D} \right) \times 100\% \quad (2)$$

A summary of the calculated dispersion quantities is presented in Table 1. The results reveal that, for uniform, random, clustered, one large agglomerate and three large agglomerates, the states of dispersion, were  $D_0 = 100, 99.47, 20.03, 15.17$  and  $7.135\%$  respectively. These results are consistent with visual assessment of the models.

## 4 Proof of Concept

The theoretical proof of concept has been established. However, this must be validated using real microscopy images. Therefore, three SEM Images captured using 15 kV at  $5 \mu\text{m}$  were used as test samples to ascertain the robustness and versatility of the method. All image resolutions were converted to  $1500 \times 1500$  pixels.

The proposed method was used to assess the state of dispersion for all the samples successfully. The summary of the obtained results is summarized in Table 2. The dispersion state for sample 1, 2 and 3 as shown in Fig. 6 was  $D_0 = 19.79, 11.74\%$  and  $1.95\%$  respectively. A visual assessment of all the images confirms that the distribution of particles in sample 1 is better than that in samples 2 and 3. Furthermore, the low degree of dispersion may be attributed to the large agglomerates resulting from using unfunctionalized  $\text{TiO}_2$  nanoparticles which resulted in poor interfacial properties between the matrix and nanoparticles [39]. Moreover, the viscosity of the matrix as well as the specific surface area of the particles significantly influenced the degree of dispersion and agglomeration [40, 41].



**Fig. 6** a Sample 1. b Fractal dimension graph of Sample 1, c Sample 2. d Fractal dimension graph of Sample 2. e Sample 3 and f fractal dimension graph of Sample 3

**Table 2** Fractal dimension, variance and dispersion of real samples

Real images	Fractal dimension ( $D_f$ )	Variance ( $S^2$ )	Dispersion (%)
Sample 1	$1.481 \pm 0.141$	0.0198	19.785
Sample 2	$1.706 \pm 0.108$	0.0117	11.744
Sample 3	$1.847 \pm 0.044$	0.0019	1.945

There are however some limitations to the current state of the proposed method. This method does not consider spacing between particles and define a quantity for the state of agglomeration.

## 5 Conclusions

A simple method for quantifying dispersion was formulated using the variance of the calculated fractal dimension. In theory, maximising  $D_0$  should improve dispersion. The technique is versatile and capable of analysing optical and electron microscopy images with a high degree of accuracy. The results can be used as a platform for introducing some measure of standardisation aimed at benchmarking dispersion quality. This new approach is suitable for analysis at varied scales such as the micro, meso and nano level. The new approach avoids the limitations of previous methods such as the over reliance on varied probability distribution functions and references. The dispersion quantity is easy to implement and execute and shows reliably consistent outputs that are very similar to visual assessments. The formulation ensures robustness and some level of sophistication without the complexity of other methods.

## References

1. DeLeon VH, Nguyen TD, Nar M, D'Souza NA, Golden TD (2012) Polymer nanocomposites for improved drug delivery efficiency. *Mater Chem Phys* 132:409–415
2. Cong H, Radosz M, Towler BF, Shen Y (2007) Polymer-inorganic nanocomposite membranes for gas separation. *Sep Purif Technol* 55:281–291
3. Hule R a, Pochan DJ. (2007) Polymer nanocomposites for biomedical applications. *MRS Bull* 32(4):354–358
4. Paul DR, Robeson LM (2008) Polymer nanotechnology: nanocomposites. *Polymer* 49:3187–3204
5. Dresselhaus MS, Dresselhaus G, Avouris P (2001) Carbon nanotubes. *Carbon nanotubes synthesis, structure, properties, and applications*. Springer 1–427
6. Iijima S (1991) Helical microtubules of graphitic carbon. *Nature* 354(6348):56–58
7. Meyer RR, Sloan J, Dunin-Borkowski RE, Kirkland AI, Novotny MC, Bailey SR et al (2000) Discrete atom imaging of one-dimensional crystals formed within single-walled carbon nanotubes. *Science* (80-) 289(5483):1324–1326

8. Smith BW, Monthieux M, Luzzi DE (1998) Encapsulated C60 in carbon nanotubes. *Nature* 396(6709):323–324
9. Esawi AMK, Morsi K, Sayed A, Taher M, Lanka S (2010) Effect of carbon nanotube (CNT) content on the mechanical properties of CNT-reinforced aluminium composites. *Compos Sci Technol* 70(16):2237–2241
10. Šupová M, Martynková GS, Barabaszová K (2011) Effect of nanofillers dispersion in polymer matrices: a review. *Sci Adv Mater* 3(1):1–25
11. Sandler J, Shaffer MSP, Prasse T, Bauhofer W, Schulte K, Windle AH (1999) Development of a dispersion process for carbon nanotubes in an epoxy matrix and the resulting electrical properties. *Polymer (Guildf)* 40(21):5967–5971
12. Huang YY, Terentjev EM (2012) Dispersion of carbon nanotubes: mixing, sonication, stabilization, and composite properties. *Polymers. Mol Divers Preserv Int* 4:275–295
13. Bensadoun F, Kchit N, Billotte C, Bickerton S, Trochu F, Ruiz E (2011) A study of nanoclay reinforcement of biocomposites made by liquid composite molding. *Int J Polym Sci* 2011:1–10
14. Rastogi R, Kaushal R, Tripathi SK, Sharma AL, Kaur I, Bharadwaj LM (2008) Comparative study of carbon nanotube dispersion using surfactants. *J Colloid Interface Sci* 328(2):421–428
15. Xie S, Harkin-Jones E, Shen Y, Hornsby P, McAfee M, McNally T et al (2010) Quantitative characterization of clay dispersion in polypropylene-clay nanocomposites by combined transmission electron microscopy and optical microscopy. *Mater Lett* 64(2):185–188
16. Lillehei PT, Kim J-W, Gibbons LJ, Park C (2009) A quantitative assessment of carbon nanotube dispersion in polymer matrices. *Nanotechnology* 20(32):32–57
17. Trionfi A, Scrymgeour DA, Hsu JWP, Arlen MJ, Tomlin D, Jacobs JD et al (2008) Direct imaging of current paths in multiwalled carbon nanofiber polymer nanocomposites using conducting-tip atomic force microscopy. *J Appl Phys* 104(8):28–37
18. Haslam MD, Raeymaekers B (2013) A composite index to quantify dispersion of carbon nanotubes in polymer-based composite materials. *Compos Part B Eng* 55(1):16–21
19. Clark PJ, Evans FC (1954) Distance to nearest neighbor as a measure of spatial relationships in populations. *Ecology* 35(4):445–453
20. Luo ZP, Koo JH (2007) Quantifying the dispersion of mixture microstructures. *J Microsc* 225(2):118–125
21. Bakshi SR, Batista RG, Agarwal A (2009) Quantification of carbon nanotube distribution and property correlation in nanocomposites. *Compos Part A Appl Sci Manuf* 40(8):1311–1318
22. Kim SH, Il Lee W, Park JM (2009) Assessment of dispersion in carbon nanotube reinforced composites using differential scanning calorimetry. *Carbon* 47(11):2699–2703
23. Kim D, Lee JS, Barry CMF, Mead JL (2007) Microscopic measurement of the degree of mixing for nanoparticles in polymer nanocomposites by TEM images. *Microsc Res Tech* 70(6):539–546
24. Gleason HA (1920) Society some applications of the Quadrat method. *Bull Torrey Bot Club* 47(1):21–33
25. Yazdanbakhsh A, Grasley Z, Tyson B, Abu Al-Rub RK (2011) Dispersion quantification of inclusions in composites. *Compos Part A Appl Sci Manuf* 42(1):75–83
26. Fan LT, Chen YM, Lai FS (1990) Recent developments in solids mixing. *Powder Technol* 61(3):255–287
27. Rhodes M (2008) Introduction to particle technology. *Chem Eng Process* 7:450
28. Broughton WR, Koukoulas T, Woolliams P, Williams J, Rahatekar SS (2013) Assessment of nanoparticle loading and dispersion in polymeric materials using optical coherence tomography. *Polym Test.* 32(7):1290–1298
29. Nayak SR, Mishra J, Palai G (2018) A modified approach to estimate fractal dimension of gray scale images. *Optik (Stuttg)* 161:136–145
30. Asvestas P, Matsopoulos GK, Nikita KS (1998) A power differentiation method of fractal dimension estimation for 2-D signals. *J Vis Commun Image Represent* 9(4):392–400
31. Lin KH, Lam KM, Siu WC (2001) Locating the eye in human face images using fractal dimensions. *IEE Proc Vis Image Sig Process* 148(6):413–421
32. Voss RF (1986) Characterization and measurement of random fractals. *Phys Scr* 13:27–32

33. Keller JM, Crownover RM, Chen RY (1987) Characteristics of natural scenes related to the fractal dimension. *IEEE Trans Pattern Anal Mach Intell* 9(5):621–627
34. Keller JM, Chen S, Crownover RM (1989) Texture description and segmentation through fractal geometry. *Comput Vis Graph Image Process* 45(2):150–166
35. Gagnepain JJ, Roques-Carmes C (1986) Fractal approach to two-dimensional and three-dimensional surface roughness. *Wear* 109(1–4):119–126
36. Chen W-S, Yuan S-Y, Hsieh C-M (2003) Two algorithms to estimate fractal dimension of gray-level images. *Opt Eng* 42(8):2452
37. Xu S, Weng Y (2006) A new approach to estimate fractal dimensions of corrosion images. *Pattern Recognit Lett* 27(16):1942–1947
38. Moisy F (2008) Fractal dimension using the “box-counting” method for 1D, 2D and 3D sets. Available from <https://www.mathworks.com/matlabcentral/fileexchange/13063-boxcount?focused=5083247&tab=example>
39. Ma PC, Siddiqui NA, Marom G, Kim JK (2010) Dispersion and functionalization of carbon nanotubes for polymer-based nanocomposites: a review. *Compos Part A Appl Sci Manuf* 41(10):1345–1367
40. Naguib HM, Ahmed MA, Abo-Shanab ZL (2018) Silane coupling agent for enhanced epoxy-iron oxide nanocomposite. *J Mater Res Technol* 7(1):21–28
41. Dalod ARM, Henriksen L, Grande T, Einarsrud M-A (2017) Functionalized TiO<sub>2</sub> nanoparticles by single-step hydrothermal synthesis: the role of the silane coupling agents. *Beilstein J Nanotechnol* 8:304–312

# Mode I Fracture Toughness of Optimized Alkali-Treated *Bambusa Vulgaris* Bamboo by Box-Behnken Design



Siti Amni Roslan, Mohamad Zaki Hassan, Zainudin A. Rasid,  
Nurul Aini Bani, Shamsul Sarip, Mohd Yusof Md Daud  
and Firdaus Muhammad-Sukki

**Abstract** Alkaline treatment is widely being used to treat natural fibres and it improves the fibre surface for better bonding with the polymer matrix. The aim of this study is to optimize the alkaline treatment variables such as sodium hydroxide (NaOH) concentration, soaking and drying time that influence the strength of natural fibres, including bamboo. In this study, Box-Behnken design (BBD) of the response surface method was employed to set an experimental parameter of alkaline treatment for the bamboo specimen. In order to investigate the effect of treatment conditions on crack propagation behaviour of the bamboo along the longitudinal direction, Mode I interlaminar fracture toughness ( $G_{IC}$ ) test was carried out. It can be suggested from the statistical analysis approach (ANOVA) that bamboo treated with 1 wt% concentration of NaOH is able to reach fracture toughness value up to  $365.86 \text{ J/m}^2$ , which differs by only 0.82% from the experimental finding. It is also shown that all proposed variables for treatment in this study i.e. the concentration of the NaOH is highly significant with the soaking and drying time.

**Keywords** Mode I · Fracture toughness · Chemical treatment · Optimisation · Box-Behnken design

---

S. A. Roslan · Z. A. Rasid

Malaysia-Japan International Institute of Technology, Universiti Teknologi Malaysia, Jalan Sultan Yahya Petra, 54100 Kuala Lumpur, Malaysia

M. Z. Hassan (✉) · N. A. Bani · S. Sarip · M. Y. Md Daud

Razak Faculty of Technology and Informatics, Universiti Teknologi Malaysia, Jalan Sultan Yahya Petra, 54100 Kuala Lumpur, Malaysia

e-mail: [mzaki.kl@utm.my](mailto:mzaki.kl@utm.my)

F. Muhammad-Sukki

Robert Gordon University Garthdee House, Garthdee Rd, Aberdeen AB10 7AQ, UK

© Springer Nature Singapore Pte Ltd. 2020

M. Awang et al. (eds.), *Advances in Material Sciences and Engineering*, Lecture Notes in Mechanical Engineering, [https://doi.org/10.1007/978-981-13-8297-0\\_58](https://doi.org/10.1007/978-981-13-8297-0_58)

565

## 1 Introduction

Natural fibres can simply be defined as non-synthetic fibres. They can be obtained from animal, plant or mineral resources. Among these types, the combination of plant-based fibres with polymer matrices to form natural fibre reinforced polymer composites (NFPCs) are extensively being employed. This is because their combination exhibited a great mechanical strength and stiffness to weight ratio [1]. The increase in the utilisations of NFPCs in the automotive industries [2], marine [3] and construction [4] are good demonstrations to this affirmation. Bamboo is one of the most researched natural fibres of late due to its specialties of having low density and high specific strength, which is up to 4 times higher than that of the mild steel. These two characteristics show that bamboo fibre is on par with glass fibre properties.

A major drawback from using natural fibres in polymeric composites is the incompatibility between the natural fibre and polymer matrix due to hydrophilic and hydrophobic interaction. The high moisture content in natural fibres makes them difficult to bond properly with the polymer matrix and thereby degrading the mechanical properties of NFPCs. Thus, chemical treatment on natural fibre is being promoted to increase the interfacial bonding compatibility between the fibre and polymer matrix [5]. Among the chemical treatments that have been obtained, alkaline treatment is frequently used. This method is carried out by immersing the natural fibre in a particular concentration of the alkaline solution, like sodium hydroxide (NaOH), for a certain period of time. It is reported that this treatment improves the strength of fibre and increases the surface roughness for better interlocking between fibre and polymer matrix [6, 7]. Jacob et al. [8] studied the effect of NaOH concentrations of 0.5, 1, 2, 4 and 10% on sisal fibre reinforced composites. They reported that the highest tensile strength composite laminate has been found at 4% of NaOH concentration tested at room temperature. In contrast, Mishra et al. [9] reported that sisal fibre reinforced polyester composites which were treated with 5% concentration of NaOH exhibited good tensile strength properties to those treated with 10% of concentration. They also highlighted that the higher alkali concentration would cause excess delignification of the natural fibre and thus weaken it. Zhang et al. [10] treated bamboo fibres with 4% concentration of NaOH for one hour. It was discovered that the treatment increased the effective surface area for better bonding of the fibre with the matrix by removing chemical components such as hemicellulose and lignin. They were observed from scanning electron microscope (SEM) images of the treated bamboo fibre surface seems to be smoother than those untreated fibres due to the removal of chemical components and impurities. Phong et al. [7] suggested that 1% concentration of NaOH treated on bamboo/epoxy laminate resulted in higher mechanical characteristics compared to 2 and 3% concentration. In their study, bamboo fibres were immersed in NaOH concentrations of 1, 2 and 3% for 10 h at 70 °C and allowed to dry for a day at 105 °C in the air circulation oven. It was found that bamboo fibre with 1% concentration of NaOH showed the highest tensile strength and Young's modulus among those treated with different concentrations. The result was in good agreement with Rao et al. [11] who reported that 1% concentration of NaOH is the

best to treat bamboo polymeric composite. On the contrary, few studies claimed that a higher NaOH concentration is the best in treating bamboo fibre and capable of removing excess moisture thoroughly. In spite of that, the NaOH concentration is the most dominant factor that gives effect on the natural fibre. In addition, treatment variables such as soaking time, drying period and temperature could also influence the end results.

Many attempts have been made, including applying of Box-Behnken design (BBD) in the optimization of chemical treatment for natural fibres, as conducted by Aly et al. [12] in NaOH treatment parameters of flax fibre. They reported that the BBD is an accurate tool for optimizing chemical treatment to obtain the outstanding mechanical properties of the fibre matrix composite. Vardhini et al. [13] employed BBD tool to determine the optimum treatment conditions in treating banana and kenaf fibres, where they found that treatment conditions of 11 g/L NaOH concentration, 2.5 h of treatment time and temperature of 90 °C are able to remove lignin from the banana fibre at higher rates. Thus, these previous works proved that the BBD is an efficient tool in optimization of work processes that involves more than two variables.

In this study, the Box-Behnken design (BBD) of the response surface method was employed to set an experimental design of alkaline treatment conditions for the bambusa vulgaris bamboo. Mode I interlaminar fracture toughness ( $G_{IC}$ ) test was conducted to investigate the effect of alkaline treatment conditions on crack propagation behaviour along the longitudinal direction of the bamboo. Three conditions are considered for the concentration of NaOH, soaking and drying time. The results are subsequently analysed statistically using the Analysis of Variance (ANOVA).

## 2 Experimental Method

The material and testing of the BBD experimental design conducted in this study is given in this section. Later, the  $G_{IC}$  analysis is explained.

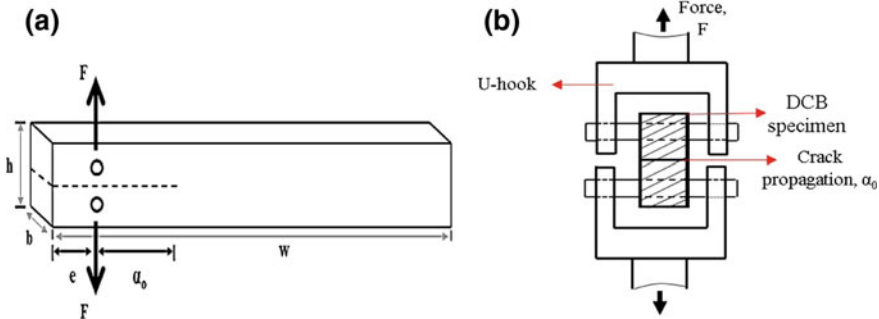
### 2.1 Box-Behnken Design Iteration

In order to determine the optimum chemical treatment condition, an experimental design composed of three variables was built using Box-Behnken design (BBD). Table 1 shows the design points for low, middle and high levels of each variable condition. This input data then was randomized and modelled by BBD using the Design-expert (6.0.8) software. It offers a total number of 17 experimental runs that consist of 12 runs and 5 replication runs of the centre point.



**Table 1** The initial setting of Box-Behnken design (BBD)

Factors/independent variables	Symbols	Coded and actual levels		
		Low (-1)	Middle (0)	High (+1)
Concentration of NaOH (%)	X <sub>1</sub>	1	2	3
Soaking duration (h)	X <sub>2</sub>	3	6	9
Drying duration (h)	X <sub>3</sub>	2	48	72



**Fig. 1** a Schematic diagram of DCB specimen b connected to U-hook following tensile test

## 2.2 Materials and Testing

The bamboo material that was used in this study belongs to bambusa vulgaris family. The raw bamboo was cut approximately 5 m above the ground. The age of bamboo was approximately four years old and taken from Jeli, Kelantan at the north-eastern state of Malaysia. Mode I testing specimens are prepared as a double cantilever beam (DCB) according to the ASTM D5528 standard [14]. The dimension of the DCB specimen is, longitudinal direction,  $w = 200$  mm; tangential direction,  $h = 20$  mm; and radial thickness,  $b = 9$  mm with initial crack length,  $\alpha_0 = 40$  mm. Two loading holes of 5 mm in diameter were made at the point crack initiation (about 20 mm before the end). Figure 1a shows a schematic diagram of the DCB specimen. After that, the specimens were chemically treated with an alkali solution. The concentration of this solution, which was sodium hydroxide (NaOH), was prepared by weight per volume (w/v) percentage. In order to obtain 1 wt% concentration of NaOH, 1 g of NaOH pellets was diluted in 100 ml of distilled water. After undergoing alkali treatment and drying process, an initial crack was cleaved along the middle-line of the bamboo DCB specimen parallel to grain by a stiff razor. Following that, the bamboo DCB specimen was fitted to the U-shaped hook steel which connected to a 10 kN load cell on a Shidmazu universal testing machine as illustrated in Fig. 1b.

### 2.3 $G_{IC}$ Analysis

According to the compliance method, the reciprocal slope from load-displacement traces is the corresponding compliance ( $C_i$ ) of the DCB specimen with a certain crack length ( $\alpha_i$ ). The relationship between  $C$  and  $\alpha$  can be described as stated in the following Eq. (1).

$$C = q\alpha^m \quad (1)$$

where  $q$  and  $m$  are the fitting coefficients of the compliance curve of the DCB specimen. So, after taking a logarithm of Eq. (1), the equation meets the linear model as stated in Eq. (2). Following the Mode I test, the results were analyzed and evaluated statistically using the Analysis of Variance (ANOVA).

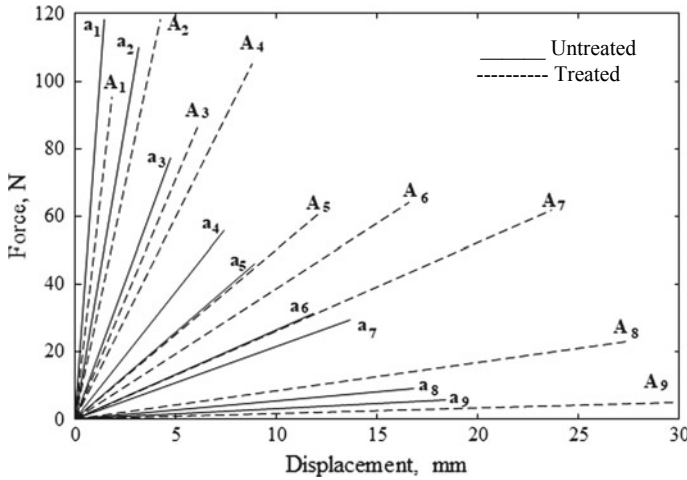
$$\lg C = \lg q + m \lg \alpha \quad (2)$$

## 3 Results and Discussions

Initially this section gives the results on the  $G_{IC}$  characteristic of the bamboo specimens based on the force-displacement plot. Following that the BBD analysis of  $G_{IC}$  for treated bamboo is conducted.

### 3.1 $G_{IC}$ Characterization of Bamboo DCB Specimen

Figure 2 depicts the force-displacement traces corresponding to different crack lengths,  $\alpha$ , of untreated and treated bamboo specimens. Here,  $a_1, a_2, a_3, \dots, a_9$  and  $A_1, A_2, A_3, \dots, A_9$  are the sum of the measured crack length,  $\alpha$ , for untreated and treated specimens respectively. It can be seen that the slope of traces for both conditions decreased with the increase of crack lengths. However, it seems that the treated specimen exhibited an inconsistent trend of force and displacement traces compared to untreated, in which the traces occasionally dropped on lower or higher forces with the larger of displacement. It can be proposed that the alkaline treatment has caused the crack surface to be rougher due to the forming of peaks and valleys. These peaks and valleys disrupted the distribution of applied force along the fibre and caused the load to concentrate on a particular point on the fibre. Thereby, it causes the specimen to yield at an uneven load. On the other hand, Islam [15] and Bledzki et al. [16] reported that alkali-treated fibre tends to break at a higher displacement value as a resultant of the softening of the inter-fibrils matrix. This softening effect has negatively affected the transfer of stress between the fibres, thus, disturbing the overall stress development in fibre during tensile deformation.



**Fig. 2** The typical force-displacement traces of untreated and treated bamboo ( $a_1 = 42$  mm,  $a_2 = 56$  mm,  $a_3 = 66$  mm,  $a_4 = 83$  mm,  $a_5 = 78$  mm,  $a_6 = 97$  mm,  $a_7 = 105$  mm,  $a_8 = 114$  mm,  $a_9 = 122$  mm)

### 3.2 The BBD Analysis of $G_{IC}$ for Treated Bamboo

The  $G_{IC}$  results of treated bamboo were further investigated using analysis of variance (ANOVA) in order to determine which variables significantly affect the  $G_{IC}$  value of treated bamboo. By applying a multiple regression analysis of the responses, the outcome proposed the highest order polynomial in which the additional terms were significant and the model was not aliased. Following that, backwards elimination method was applied to exclude insignificant terms automatically. The ANOVA for the reduced quadratic models summarized in the  $G_{IC}$  value, is shown in Eq. (3).

$$G_{IC} = 573.235 - 160.801X_1 - 14.743X_2 - 1.229X_3 + 27.696X_1^2 + 0.679X_2^2 + 0.033X_3^2 + 3.936X_1X_2 - 1.095X_1X_3 \tag{3}$$

Equation (3) represents the relationship between NaOH concentration ( $X_1$ ), soaking time ( $X_2$ ) and drying time ( $X_3$ ) towards  $G_{IC}$  value of treated bamboo. This equation was also used to generate predictions of the response for a given level of each variable. Table 2 depicts the predicted  $G_{IC}$  values using Eq. (8) and the experimental finding value. It is in good agreement between the yield predicted and the experimental responses, with a small difference in  $G_{IC}$  value measured as observed in Table 2. The percentages of error are also calculated to determine the precision of calculations. Here, the error percentage of each run is less than 4%, which is considered effective [17]. The bamboo treated with 1 wt% concentration of NaOH offers the fracture toughness value up to 365.86 J/m<sup>2</sup>, with 0.82% of error from the testing result. The  $G_{IC}$  value of treated bamboo specimens is declined with the increasing

**Table 2** The BBD analysis predicted and experimental  $G_{IC}$  values

Run	Independent variables								
	Coded values			Actual values			Exp.	Pred.	Err. (%)
	$X_1$	$X_2$	$X_3$	$X_1$	$X_2$	$X_3$			
1	0	+1	-1	2	9	24	186.1	182.4	2.03
2	0	0	0	2	6	48	205.6	208.4	1.33
3	0	-1	-1	2	3	24	270.8	272.5	0.64
4	0	0	0	2	6	48	207.1	208.4	0.59
5	0	+1	+1	2	9	72	163.9	169.9	3.51
6	+1	-1	0	3	3	48	185.0	184.3	0.40
7	0	0	0	2	6	48	207.6	208.4	0.38
8	0	-1	+1	2	3	72	264.1	260.1	1.54
9	-1	+1	0	1	9	48	251.3	252.0	0.29
10	+1	0	+1	3	6	72	142.7	143.6	0.62
11	0	0	0	2	6	48	208.7	208.4	0.15
12	-1	-1	0	1	3	48	362.8	365.8	0.82
13	-1	0	+1	1	6	72	356.9	354.0	0.80
14	-1	0	-1	1	6	24	314.8	313.9	0.28
15	0	0	0	2	6	48	212.9	208.4	2.15
16	+1	+1	0	3	9	48	120.7	117.7	2.55
17	+1	0	-1	3	6	24	205.7	208.6	1.37

NaOH concentration and soaking time. Again, the higher NaOH concentration and soaking time could worsen mechanical properties of fibre due to the softening effect and weakens the fibre. Longer drying time, however, has a positive correlation with the response. The model afterwards was inspected statistically using the  $F$ -test and regression coefficient,  $R^2$  for validity purposes.

Table 3 presents the results acquired following executing the analysis of variance (ANOVA). The significance of the coefficient terms is determined by the  $F$  and  $p$  values. As shown in Table 3, this regression model is highly significant with  $F$ -value of 551.22. The interactions among the NaOH concentration ( $X_1$ ), soaking time ( $X_2$ ) and the drying period ( $X_3$ ) with a probability value (“Prob > F” > 0.05) indicate that the model terms are highly significant. According to “Prob > F”, the most significant model terms that affect  $G_{IC}$  values of the treated bamboo are NaOH concentration ( $X_1$ ), soaking time ( $X_2$ ), drying time ( $X_3$ ), second-order NaOH concentration ( $X_1^2$ ), second-order soaking time ( $X_2^2$ ) and second-order drying time ( $X_3^2$ ). On the other hand, the interaction between NaOH concentration and soaking time ( $X_1 X_2$ ) and interaction between NaOH concentration and drying time ( $X_1 X_3$ ) are the subsequent significant factors in this study.

**Table 3** The ANOVA of quadratic model for alkaline treatment of bamboo

Source	SoS	DoF	MS	F-value	p-value (Prob > F)
Model	74816.17	8	9352.02	551.22	<0.0001 <sup>a</sup>
X <sub>1</sub> -C	49879.03	1	49879.03	2939.93	<0.0001 <sup>a</sup>
X <sub>2</sub> -S	16263.96	1	16263.96	958.62	<0.0001 <sup>a</sup>
X <sub>3</sub> -D	310.50	1	310.50	18.30	0.0027 <sup>a</sup>
X <sub>1</sub> <sup>2</sup>	3229.82	1	3229.82	190.37	<0.0001 <sup>a</sup>
X <sub>2</sub> <sup>2</sup>	157.64	1	157.64	9.29	0.0159 <sup>a</sup>
X <sub>3</sub> <sup>2</sup>	1513.41	1	1513.41	89.20	<0.0001 <sup>a</sup>
X <sub>1</sub> X <sub>2</sub>	557.67	1	557.67	32.87	0.0004 <sup>a</sup>
X <sub>1</sub> X <sub>3</sub>	2762.55	1	2762.55	162.83	< 0.0001 <sup>a</sup>
Residual	135.73	8	16.97		
LoF	105.61	4	26.40	3.51	0.1259 <sup>b</sup>
PE	30.12	4	7.53		
Cor total	74951.90	16			

<sup>a</sup> Significant <sup>b</sup>Not significant

X<sub>1</sub>-C X<sub>1</sub>-concentration; X<sub>2</sub>-S X<sub>2</sub>-soaking; X<sub>3</sub>-D X<sub>3</sub>-Drying; LoF Lack of Fit; PE Pure error; CT Correlation total; SoS Sum of square; DoF Degree of freedom; MS Mean square

### 3.3 Response Surface Plots

The predicted models can be visualized as two-dimensional (2D) contour plot and three-dimensional (3D) surface graph. Each plot shows the effects of two variables within the studied ranges, while the other variables are fixed at their zero-coded level value. In contour plots, the contour lines display the extent of the interactions between two independent variables. It is easy to spot the optimum levels and it is convenient for the user to present the shape of the response of a two-dimensional projection. The 3D-surface graph visualizes the tendency of each variable to influence the response in a graphical view. The curvature in the 3D graph is formed based on the quadratic dependence of response and parameters. Contour plot and response surface for the interaction effect of NaOH concentration (X<sub>1</sub>) and soaking time (X<sub>2</sub>) on  $G_{IC}$  values of bamboo at 48 h of drying time (X<sub>3</sub>) are presented in Fig. 3a, b.

The highest  $G_{IC}$  value of 365.86 J/m<sup>2</sup> was recorded at the lowest NaOH concentration and soaking time. The  $G_{IC}$  value dropped to the minimum when treated with the highest NaOH concentration for 9 h. Figure 3c, d presents the response surface and corresponding contour plots for the interaction effect of NaOH concentration (X<sub>1</sub>) and drying time (X<sub>3</sub>) on  $G_{IC}$  values of bamboo for 6 h of soaking time (X<sub>2</sub>). The highest  $G_{IC}$  value of 354.09 J/m<sup>2</sup> was recorded when treated with the lowest NaOH concentration and be dried at the maximum drying hour. However,  $G_{IC}$  value

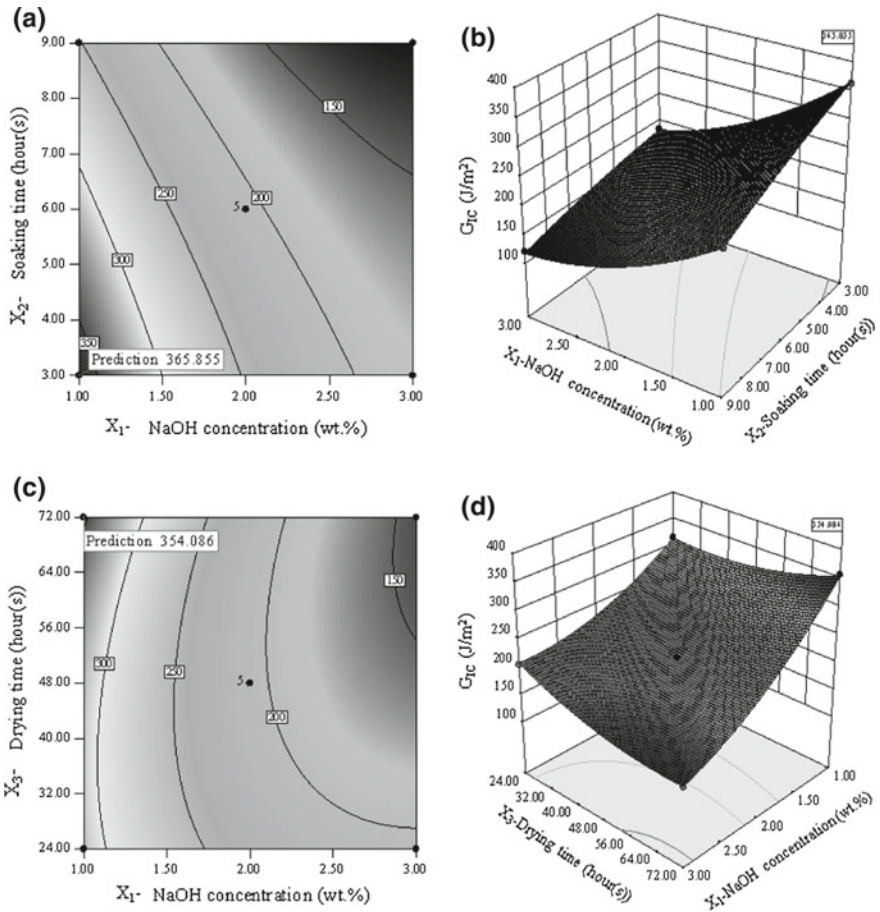


Fig. 3 The response surface plots of  $X_1X_2$  in 2D contour and 3D model

seemed to be dropped to 143.22 J/m<sup>2</sup> at the maximum NaOH concentration even though the soaking and drying time was kept in the same condition. Based on the finding, the proposed variables were found to significantly influence the  $G_{IC}$  values of treated bamboo. The analysis suggested that the bamboo needs to be treated with low NaOH concentration for a short soaking period and dried at a longer drying time to obtain the optimum  $G_{IC}$  value of bamboo at room temperature.

## 4 Conclusions

Based on Mode I test results, it was found untreated bamboo specimen exhibited greater  $G_{IC}$  values compared to the treated specimen. This may be attributed to

the softening effect caused by alkaline treatment which influences the stress transfer process along the specimen during the test. For treated bamboo, NaOH concentration ( $X_1$ ) was recorded as the most significant parameter that affected the  $G_{IC}$  values of bamboo. The highest  $G_{IC}$  value for treated bamboo was predicted at 365.86 J/m<sup>2</sup> when the bamboo was treated with 1 wt% concentration of NaOH for 3 h and dried for 72 h at room temperature (1wt%-3-72 h).  $G_{IC}$  value gradually dropped to 120 J/m<sup>2</sup> when the bamboo was treated to higher than 1 wt% concentration of NaOH. Such results may be influenced by the softening effect of alkaline treatment which disturbs the overall performance of the specimen during Mode I of loading.

**Acknowledgements** The appreciation is given to Universiti Teknologi Malaysia and Ministry of Higher Education under Fundamental Research Grant Scheme, R.K130000.7840.4F880 and ‘Geran Universiti Penyelidik’ (GUP) Tier 1, Q.K130000.2540.15H70 and Q.K130000.2540.16H95 for financially support provided throughout the course of this research project.

## References

1. Layth M, Ansari M, Grace P et al (2015) A review on natural fibre reinforced polymer composite and its applications. *Int J Poly Sci* 2015:1–15
2. Ashik K, Sharma R (2015) A review on mechanical properties of natural fibre reinforced hybrid polymer composites. *J Min Mat Char Eng* 3:420–426
3. Fragassa C (2017) Marine applications of natural fibre-reinforced composites: a manufacturing case study. In: Prodanović S, Milutinović M (eds) *Advances in applications of industrial biomaterials*. Springer International Publishing, 21–47
4. Fan M, Feng F (2016) *Advanced high strength natural fibre composites in construction*, 1st edn. Woodhead Publishing
5. Srinivas K, Lakshumu NA, Raju BA (2017) A review on chemical and mechanical properties of natural fibre reinforced polymer composites. *Int J Perform Eng* 13(2):189–200
6. Malenab J, Ngo S, Promentilla B (2017) Chemical treatment of waste abaca for natural fibre-reinforced geopolymer composite. *Materials* 10(6):579
7. Phong NT, Fuji T, Chuong B et al (2012) Study on how to effectively extract bamboo fibres from raw bamboo and wastewater treatment. *J Mat Sci Res* 1(1):144–155
8. Jacob M, Thomas S, Varughese T (2004) Natural rubber composites reinforced with sisal/oil palm hybrid fibres: tensile and cure characteristics. *J. App Poly Sc* 93(5):2305–2312
9. Mishra S, Mohanty A, Drzal L et al (2003) Studies on mechanical performance of biofibre/glass reinforced polyester hybrid composites. *Comp Sci Tech* 63(10):1377–1385
10. Zhang X, Wang F, Keer L (2015) Influence of surface modification on the microstructure and thermo-mechanical properties of bamboo fibres. *Materials* 8:6597–6608
11. Rao R, Varada R, Ramachandra R et al (2010) Flexural and compressive properties of bamboo and glass fibre-reinforced epoxy hybrid composites. *J Reinf Plas Comp* 29(10):1446–1450
12. Aly M, Hashmi J, Olabi A et al (2012) Optimization of alkaline treatment conditions of flax fibre using box-behnken method. *J Nat Fib* 9(4):256–276
13. Vardhini K, Murugan R, Selvi C et al (2016) Optimization of alkali treatment of banana fibres on lignin removal. *Ind J Fib Text Res* 41(1):156–160
14. American Society for Testing and Materials (ASTM) (2001) Standard test for Mode I interlaminar fracture toughness of unidirectional fibre-reinforced polymer matrix composites. Philadelphia, D 5528-01
15. Islam MS (2008) The influence of fibre processing and treatments on hemp fibre/epoxy and hemp fibre/pla composites. Doctor of Education Thesis, The University of Waikato, Hamilton, New Zealand

16. Bledzki AK, Fink HP, Specht K (2004) Unidirectional hemp and flax ep- and pp composites: influence of defined fibre treatments. *J App Poly Sci* 93(1):2150–2156
17. Montgomery DC (2005) *Design and analysis of experiments*, 6th edn. Wiley, New York



# A Preliminary Study of Additional Safety Mechanical Structure for Safety Shoe



Suhaimi Hassan, Mohd Sallehuddin Yusof, Zaidi Embong,  
Mohamad Zhairul Iqmal Jumari, Maznan Ismon, Hanis Zakaria,  
Mohammad Zulafif Rahim, Rosli Ahmad  
and Engku Mohd Nasri Engku Nasir

**Abstract** A confined space is a fully or partially enclosed space that is not primarily designed which has limited entrance or exit, or a configuration that can complicate first aid, rescue, evacuation, or other emergency response activities. The confined space can represent a risk for the health and safety of anyone who enters, due to one or more of the following factors like design, construction, location, the material or substances in it, work activities being carried out in it or the mechanical process and safety hazards present. Therefore, the objective of this research is to study additional safety mechanical structures for safety shoe by using the SolidWork software. SolidWork software analysis is popular among researchers as an alternative for experimental method to investigate the mechanical structure of the part and compo-

---

S. Hassan (✉) · M. S. Yusof · Z. Embong · M. Z. I. Jumari · M. Ismon · H. Zakaria ·  
M. Z. Rahim · R. Ahmad · E. M. N. E. Nasir  
Faculty of Mechanical and Manufacturing Engineering, Universiti Tun Hussein Onn Malaysia,  
86400 Batu Pahat, Johor, Malaysia  
e-mail: [suhaimihas@uthm.edu.my](mailto:suhaimihas@uthm.edu.my)

M. S. Yusof  
e-mail: [mdsalleh@uthm.edu.my](mailto:mdsalleh@uthm.edu.my)

Z. Embong  
e-mail: [zaidi@uthm.edu.my](mailto:zaidi@uthm.edu.my)

M. Z. I. Jumari  
e-mail: [zhairul.iqmal@gmail.com](mailto:zhairul.iqmal@gmail.com)

M. Ismon  
e-mail: [maznan@uthm.edu.my](mailto:maznan@uthm.edu.my)

H. Zakaria  
e-mail: [hanisz@uthm.edu.my](mailto:hanisz@uthm.edu.my)

M. Z. Rahim  
e-mail: [zulafif@uthm.edu.my](mailto:zulafif@uthm.edu.my)

R. Ahmad  
e-mail: [roslee@uthm.edu.my](mailto:roslee@uthm.edu.my)

E. M. N. E. Nasir  
e-mail: [emdnasri@gmail.com](mailto:emdnasri@gmail.com)

ment. In this present paper, an additional safety mechanism is considered to stimulate the safety shoe designed for confining space. From the preliminary result, maximum yield strength and displacement that applied at the additional safety structure of safety shoe are  $5.067e + 08 \text{ N/m}^2$  and  $3.895 \text{ e-}02 \text{ mm}$  respectively. The design is chosen which follows the safety shoes classes and standard. The result obtained in this study will prevent the workers from the hazard in confined space because of poor safety procedure during work.

**Keywords** Safety shoe · Mechanical structure · Design analysis

## 1 Introduction

Safety shoes were made with a protective reinforcement at the front which makes them quite durable. The reinforcement helped to protect the toes from falling objects or any kinds of compression [1]. They were normally installed with a sole plate at the main sole to prevent against punctures that could come from below. The reinforcement was normally made of steel hence they were sometimes known as steel toe cap shoes. These were originally meant for workers to help protect themselves during their work duty [2]. Before these shoes were invented, workers used to wear leather shoes or wooden clogs. Currently several other users including civilians and the military used these shoes. Various subcultures had adopted the use of the safety shoes. These shoes were very dangerous when it came to fights because of their sturdiness and also due to the steel toe [3].

The safety shoes had continued to develop to reflect the current fashions, unlike many other protective gadgets. The customers' expectations kept changing hence the manufacturers were forced to produce such shoes in a variety of styles [4]. Despite steel being the main material used for making reinforcement, the other composite materials or even plastic also could be used for the same purpose [5]. The popularity of the safety shoes is bound to come due to its importance in various industries.

Currently, safety footwear comes in assorted styles liked clogs and sneakers. Some were meant for formal purposes or engineers who work in sites that require protective footwear to be used. Due to the popularity of safety shoes, other brands which mainly featured in the fashion business, had diversified their market to target safety footwear industry [6].

Employers should provide industrial safety shoes to their worker if they are exposed to hazards such as objects falling from above and striking to the workers on the foot. Moreover, the workers working near exposed electrical conductors and others hazard situation or location might harm their foot [7]. Many countries all over the world are implementing tougher policies and standards in terms of work safety, so as to assure protection at the workplace. In Canada, for instance, the amount of feet injuries decreased by 60% since the use of safety shoes at work became compulsory [7].

**Table 1** Industrial safety shoes classes [9]

No.	Shoe classes	Description
1	Steel insole shoes	Designed to protect joint problem and keep foot stabilized and comfortable shoes
2	Metal instep footwear	To keeps feet protection from accidents or injuries at workplace. This type for industrial factories as it is designed to protect feet from sharp object or heavy material
3	Metatarsal shoes	Designed to protect the upper part of bones and feet. These shoes are designed for construction worker or job demands lifting of heavy object. The best shoe that protect feet and toe both externally and internally
4	Safety-toed shoes	Suitable for work in an environment where toes are risk. These shoes are made of steel, alloy or non-metallic toe caps that cover toe area and protect from hurt or damage
5	Electric hazard shoes	Specially designed for who work with high voltage machines, circuits, electricity, wiring etc. these ensure safety when worker exposed to electricity and high voltage circuits by reducing to receive an electric shock

In general, the importance of safety shoes at the workplace had several reasons. By wearing safety shoes at work is extremely important as 25% of disability applications worldwide are due to injured feet. In Malaysia, there are more than 2100 accidents at work were reported in the year 2017, which costs a lot of money to the companies [8].

There are several types of industrial safety shoes which usually distinguished by design. All these designs are specific to hazard situation or location depending on the type of hazard the workers are exposed to [9]. According to Occupational Safety and Health Administration (OSHA), there are 5 major types or classes of industrial safety shoe and the classes are shown in Table 1.

Any industrial of safety shoes maker would follow regulations standard set by the American National Standards Institute (ANSI) in order to keep the workers foot safe from any unwanted accident. Industrial safety shoe should function to resist diffusion by objects, absorb the shock of the heavy objects, water resistant, slow in burning and others [10].

There are several standards that related to the industrial safety shoe in order to standardize the safety and physical criteria of the industrial safety shoe. OSHA is an example of an institution or organization that related and in charge of the industrial safety shoe standard. OSHA is a regulatory agency that oversees the assurance of the safe and healthful working conditions for working men and women [11]. The standard is called OSHA standard for foot protection and information of this standard is shown in Table 2.

**Table 2** OSHA standard for foot protection [11]

No.	OSHA standard	Descriptions
1	1910.136(a)	General requirement
2	1910.136(a)(1)	The employer shall ensure that each affected employee uses protective footwear when working in areas where there is a danger of foot injuries due to falling or rolling objects
3	1910.136(a)(2)	The employer shall ensure that protective safety shoe are use of protective footwear will protect the affected employee from an electrical hazard, such as a static-discharge or electric-shock hazard, that remains after the employer takes other necessary protective measures
4	1910.136(b)	Criteria for protective footwear
5	1910.136(b)(1)	Protective footwear must comply with any of the following consensus standards
6	1910.136(b)(1)(i)	ANSI Z41-1999, "American National Standard for Personal Protection—Protective Footwear," which is incorporated by reference in § 1910.6
7	1910.136(b)(1)(ii)	ANSI Z41-1991, "American National Standard for Personal Protection—Protective Footwear," which is incorporated by reference in § 1910.6

## 2 Research Methodology

The research methodology process was started by mechanical designing of safety shoe structure. The mechanical design process was involved scanning existing safety shoe, conceptual design structure and material selection. Scanning process covered from image digitalizing until 3D surface model by using 3D Optical Digitalizing Machine. The image was edited from digitalizing to 3D surface model using Advanced Topometric Sensor (ATOS) optical measurement techniques software. Then, major editing was done by using SolidWork Modelling Software for some modification and redesign of industrial safety shoe structure.

Research mechanical structure design is an important element to meet the research project objective [12]. It is important to understand the design relationship in comparing design bench making and the strengths or weaknesses of other shoe designs.

Conceptual design is an early phase of the design process, where the broad outlines of function and form of something were articulated. Since this project's goal is to design a new additional mechanical safety structure, so the basic functionality need to be maintained to keep their functionality [13].

The material design specification is a document created during the problem definition activity in the early stage of the design process. The alloy steel material was chosen in the preliminary study for additional safety mechanical structure of safety shoe.

Sources of data and information in this research are mostly taken from previous research and journal patent design. Besides that, some research investigated the safety issue in workplace to prevent foots from any harm [14]. Various journals, patents, designs, proceeding papers, books, thesis and other information that could be trusted had been studied and referred in order to redesign the best structure safety shoe for industrial need. From this point, a general specification could be produced to meet the research project objective.

### 3 Preliminary Result and Analysis

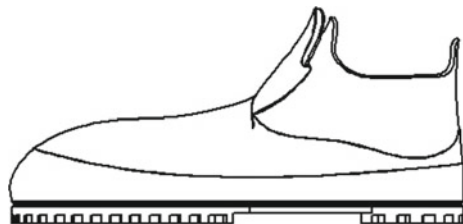
The design of additional safety mechanical structure of safety shoe had been analysed to adapt the design, match with the implementation environment, and design it for safety and performance [15]. The product design had been applied to show the model of the additional safety mechanical structure of the safety shoe with actual dimension. The existing safety shoe had been scanned by using 3D Optical Digitalizing Machine. Then, the scanned image was converted to engineering 3D drawing as shown in Figs. 1 and 2. The software used to apply this engineering drawing is a SolidWorks.

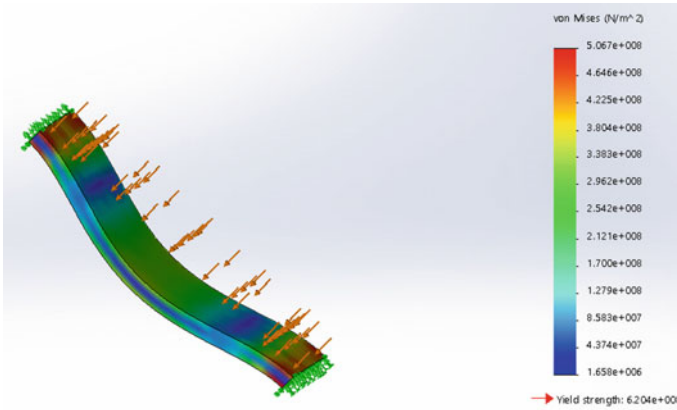
The engineering design drawing had been developed by considering the material selection and main components [16]. Some of the research processes involved in preparing this additional safety mechanical structure of safety shoe are scanning process, material selection, assembly and others. Detailed drawing showed the detailed part giving a complete and exact description of its form, dimensions, and construc-

**Fig. 1** Additional safety mechanism

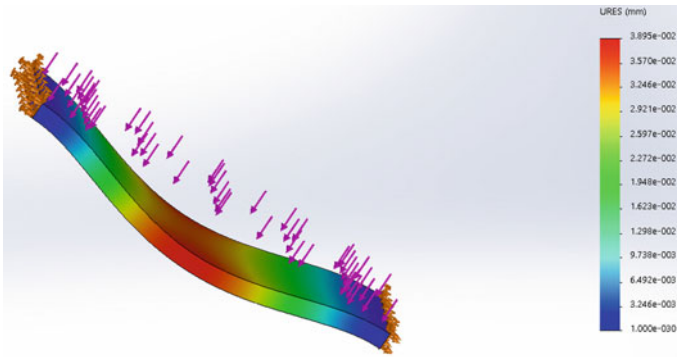


**Fig. 2** CAD drawing of safety shoe





**Fig. 3** The static analysis for alloy steel material



**Fig. 4** The displacement analysis for alloy steel material

tion. Analysis is carried out on the part of the safety structure. The simulation was aimed at studying the resilience of the safety structure so that the weakness of the additional safety structure and the quality of the safety shoe could be improved.

In this study, static analysis and displacement analysis were applied at the main parts of the additional safety mechanical structure of safety shoe. Static and displacement analysis are terms for simplifying analysis wherein the effected of an immediate changed to a system was calculated without respect to the longer-term response of the system to that change as shown in Figs. 3 and 4.

From both static and displacement analysis, the maximum yield strength and maximum displacement that applied at the alloy steel material as additional safety structure of safety shoe were  $5.067e + 08 \text{ N/m}^2$  and  $3.895 \text{ e-}02 \text{ mm}$  respectively. These results were used to support the alloy steel as one of the material analysis in designing additional safety structure of safety shoe. The result followed and adhered to the safety shoe standard which provided by OSHA for safety foot protection.

## 4 Conclusions

The research was done successfully to achieve its objective as preliminary study of additional safety structure of safety shoe. By scanning the existing safety shoe structure in 3D approach, this research is useful for future simulation where a new modification of safety shoe structure in could be edited using SolidWork software. The preliminary result of maximum yield strength and maximum displacement that applied at the additional safety structure of safety shoe were  $5.067e + 08 \text{ N/m}^2$  and  $3.895 e-02 \text{ mm}$  respectively which followed the safety shoes classes and standard. It is also important for workers who work in confined space. The outcome of this research can be used as guideline to help preventing accidents worker in the work place and creating a safe working environment.

**Acknowledgements** This project is supported by TIER 1 Grant (H197) Research Management Center and Faculty of Mechanical and Manufacturing Engineering (FKMP), Universiti Tun Hussein Onn Malaysia (UTHM), Ministry of High Education Malaysia.

## References

1. Kim IJ (2015) Wear observation of shoe surfaces: application for slip and fall safety assessments. *Tribol Trans* 58(3):407–417
2. Derler S, Kausch F, Huber R (2008) Analysis of factors influencing the friction coefficients of shoe sole materials. *Saf Sci* 46(5):822–832
3. Marpet MI (2002) Improved characterization of tribometric test results in Safety. *Science* 40(7–8):705–714
4. Norlander A, Miller M, Gard G (2015) Perceived risks for slipping and falling at work during wintertime and criteria for a slip-resistant winter shoe among Swedish outdoor workers. *Saf Sci* 73:52–61
5. Hassan S, Yusof MS, Maksud MI et al (2017) A study of PDMS printing plate for fine solid lines image in micro-flexographic printing process. *J Eng Appl Sci Medwell J* 12:5644–5649
6. Marr SJ Quine S (1993) Shoe concerns and foot problems of wearers of safety footwear. *Occup Med (Chic. Ill)* 43(2):73–77
7. National Safety Council (1970) 5 minute safety talk: dress for safety. *Ind Superv* 34(10):6–7
8. Sai SM, Halim ZA, Said F (2012) Workplace injuries in Malaysian Manufacturing Industries. *J Occup Saf Heal* 9(1):21–32
9. Chih-Wei Hsu CJL, Chang Chih-Chung (2008) A Practical guide to support vector classification. *BJU Int* 101(1):1396–1400
10. Mooren L, Grzebieta R, Williamson A et al (2014) Safety management for heavy vehicle transport: a review of the literature. *Saf Sci* 62:79–89
11. Chao EL, Henshaw JL (2013) *OSHA Ins* 55(12)
12. Hassan S, Rahim EA, Mohid Z et al (2013) Dynamic analysis of micro-milling machine. *Appl Mech Mater* 465–466:699–703
13. Yin RK (2009) *Case Study Res Design Meth* 5(5)
14. Liu L, Li KW, Lee YH et al (2010) Friction measurements on ‘anti-slip’ floors under shoe sole, contamination, and inclination conditions. *Saf Sci* 48(10):1321–1326

15. Davia-Aracil M, Jimeno-Morenilla A, Salas F (2016) A new methodological approach for shoe sole design and validation. *Int J Adv Manuf Technol* 86(9–12):3495–3516
16. Zhu L, Li M, Martin RR (2016) Direct simulation for CAD models undergoing parametric modifications. *CAD Comput Aided Des* 78:3–13



# Effect of Flow Regime on Total Interfacial Area of Two Immiscible Fluids in Microchannel Reactor Using VOF Model



Afiq Mohd Laziz and Ku Zilati Ku Shaari

**Abstract** The application of microfluidic in chemical processing, for example, the microchannel reactor has received much attention. This type of reactor can enhance the reaction efficiency due to high total interfacial area for the interaction of reactants in a multiphase reaction. The behavior of multiphase flow can create several different types of regimes such as segmented, annular, or droplet flow, depending on the flow conditions between the two immiscible liquids. The droplet flow has relatively higher total interfacial area than the annular flow. Depending on the total volumetric flow rate and volumetric ratio, the size of the microdroplet can be varied. In this study, the size of the microdroplet is investigated by varying the volumetric ratio of oil-to-methanol, O/M, and the total volumetric flowrate,  $Q_{\text{Total}}$ . Computational fluid dynamics (CFD) method using Volume of Fluid (VOF) model is implemented to predict the size of the microdroplet produced in the microchannel reactor. In addition, the model is first validated with the experimental data which showed good agreement between numerical and experimental results. It was found that the droplet size is decreasing as the total volumetric flow rate and oil-to-methanol ratio increases, which will increase the total interfacial area. In addition, droplet regime has the highest total interfacial area, while segmented regime has the lowest total interfacial area. This finding is useful especially in designing a microreactor that controls the size of droplet and maximizes the total interfacial area, overall enhancing the reaction process.

**Keywords** Computational fluid dynamics · Microchannel · Microfluidic · Microreactor · Volumetric ratio · Hydrodynamics · Channel geometry

## 1 Introduction

Microfluidic system is a system that is operating at a microscale level between 1 and 1,000  $\mu\text{m}$  size and the application is widely used especially in the perspective of chemical processes which include mixing, extraction, reaction, heat exchange and

---

A. M. Laziz · K. Z. K. Shaari (✉)  
Chemical Engineering Department, Universiti Teknologi Petronas, 32610 Bandar, Seri Iskandar, Malaysia  
e-mail: [kuzilati-kushaari@utp.edu.my](mailto:kuzilati-kushaari@utp.edu.my)

© Springer Nature Singapore Pte Ltd. 2020  
M. Awang et al. (eds.), *Advances in Material Sciences and Engineering*, Lecture Notes in Mechanical Engineering, [https://doi.org/10.1007/978-981-13-8297-0\\_61](https://doi.org/10.1007/978-981-13-8297-0_61)

585

separation [1, 2]. This technology has raised a lot of interest by researchers due to its advantages such as large surface area-to-volume ratio ( $s/v$ ), safe for potentially explosive reactions, point-of-use production, and good control of high exothermicity [3].

Furthermore, this technology has attracted attention as one of the process intensification strategies in producing biodiesel, especially in the transesterification process between vegetable oil and alcohol. The transesterification reaction process generally uses a variety of vegetable oil with methanol or ethanol, and homogeneous catalyst such as potassium hydroxide (KOH) or sodium hydroxide (NaOH) [4–7]. The objective is to improve biodiesel production by achieving faster reaction and maximizing yield of fatty acid methyl ester (FAME), which is the main product of biodiesel. Among many factors to achieve this objective are the reaction conditions such as the methanol-to-oil ratio, catalyst concentration, residence time, and temperature [8–11]. However, the factor that is seldom being discussed is the effect of hydrodynamics. Transesterification process is a multiphase reaction because both reactants are immiscible to each other and the reaction could be taking place either inside of one phase, or at the interface of the two phases. Csernica et al. [12] observed that the reaction is occurring inside the methanol phase, and the components of oil such as triglyceride, diglyceride, and monoglyceride, are transferred from oil phase into the methanol phase. This raises the question whether improving mass transfer could also significantly enhance the total reaction performance and FAME yield in microchannel reactor.

Two factors affecting the mass transfer are total interfacial area and the mass transfer coefficient. One way to study the mass transfer effect is by investigating the hydrodynamic properties of the flow itself. In multiphase flow, there are several flow regimes that exist. In the case inside a microchannel, the possible regimes are the droplet, slug/segmented, annular, and stratified flow [2]. These different regimes will affect the total interfacial area created inside the microchannel reactor. The factors that control the formation of these regimes are the hydrodynamic properties such as flow velocity and liquid properties such as density  $\rho$ , viscosity  $\mu$ , interfacial tension  $\gamma$ , and contact angle  $\theta$ .

In addition, the design of the microchannel inlets could affect the formation of the multiphase regimes. Most commonly used design for the study of the transesterification process are T-junction [4, 6, 7] and cross-junction microchannels [13]. Among these findings, different flow regimes have been observed from different authors. For example, Wan Ab Rashid et al. observed the segmented/slug flow in their microchannel of palm oil and methanol system [14], while Jamil et al. observed the droplet regime in their reaction between the mixture of castor and sunflower oil with methanol [5]. The stratified flow regime has been observed by Santana et al., in both experiment and simulation work, using their microchannel of sunflower oil and ethanol system [6].

To increase the production of biodiesel, one can increase the overall volumetric flow rate of the system which directly increases throughput. According to Guarjardo et al., it was observed that as the volumetric flowrate increases, higher oil conversions will be achieved compared to lower flowrates [15]. This observation may be a result

of the increase in recirculation intensity found in the droplet regime as have been described by Kurup et al. experimentally [16] and by Raimondi et al. numerically [17]. However, it is difficult to conclude this for the case of Guarjardo et al. because they did not report the observation from the flow regime properties of the multiphase system because the microchannel is made from stainless steel. The same authors also reported reducing at 50% methanol molar excess (1:4.5 oil:methanol ratio) and still achieving conversions up to 90% with 4 min residence time. This is considered good since most of the findings found in other authors [4–6] have excess of methanol between 1:6 up to 1:25 oil:alcohol molar ratio.

For the factor of total interfacial area, it can be explained in term of surface-to-volume ratio,  $s/v$ . High  $s/v$  indicated high surface area that can be used for mass transfer at the interface. Azam et al. have reported that as the diameter of microchannel decreases, the  $s/v$  value will increase, hence, increasing the oil conversion [4]. Therefore, it can be shown that the interfacial area effect contributes significantly in the reaction performance, especially in the multiphase flow system, such as in the transesterification process. In this study, the value of  $s/v$  will be investigated based on different oil-to-methanol ratios,  $O/M$ , and total volumetric flowrates,  $Q_{\text{Total}}$ , with respect to each flow regime created in these different flow conditions.

## 2 Methodology

### 2.1 Geometry Case Descriptions

Hydrodynamic of multiphase flow between two immiscible liquids of methanol and palm oil was studied for the application of transesterification process. No catalyst was used during the experiment to have a constant condition without any reaction factor. Two microchannel designs were used for preliminary analysis. The description and geometry of the designs are shown in Fig. 1. The main channel for T-junction has 500  $\mu\text{m}$  width and injected with oil, while the side channel has 250  $\mu\text{m}$  width and injected with methanol. As for the cross-junction, the main channel has 500  $\mu\text{m}$  width and injected with methanol, while the oil was injected from the two side channels with 250  $\mu\text{m}$  width. The dashed-line box in Fig. 1 indicates the observation area. The flow was assumed to be fully developed in this region.

### 2.2 Experimental Setup for Validation

The microchannel was fabricated based on Xurography method [18] using Graphtec® cutting plotter CE6000-60. The mold was fabricated using epoxy resin with the ratio between resin and hardener of 2:1. The microchannel was fabricated using polydimethylsiloxane (PDMS) from Dow Corning® Sylgard 184 with the ratio between PDMS and hardener of 10:1. The experimental setup for the validation is illus-

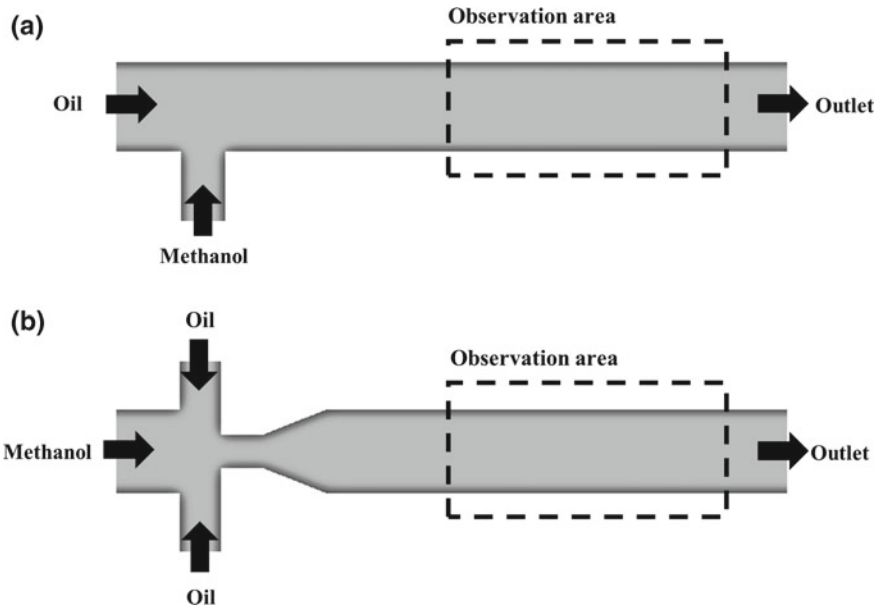


Fig. 1 Geometry description of the micro-channel for a T-junction and b cross-junction channel

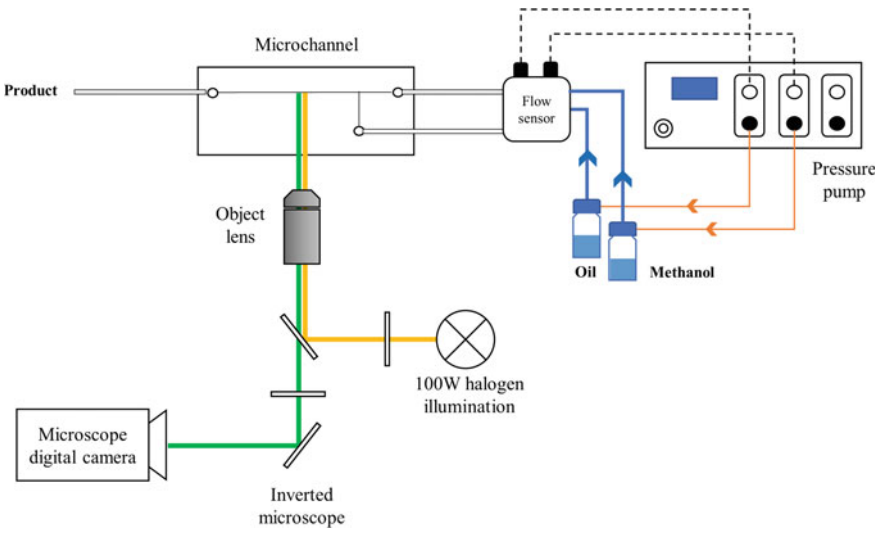


Fig. 2 Experimental setup used for the validation

**Table 1** Details of liquid properties at 25 °C

Parameter	Palm oil	Methanol
Density, $\rho$ (kg m <sup>-3</sup> )	909.15	785
Dynamic viscosity, $\mu$ (mPa s)	69.1	0.5495
Contact angle, $\theta$ (°) (oil in methanol at PDMS wall)	107	
Interfacial tension, $\gamma$ (mN m <sup>-1</sup> ) (between palm oil and methanol)	3.27	

trated in Fig. 2. The oil and methanol were pumped into the microchannel using the microfluidic pressure pump from Elveflow®. The liquid flow rate was measured using mass flow sensor connected to Elveflow system. The flow regimes inside the microchannel were observed using Olympus® inverted microscope IX53 equipped with 100 W halogen illumination, 2-40X objective lenses and DP22 microscope digital camera. The image captured by the camera is then processed using cellSens Dimension software to analyse the flow characteristics in the microchannel.

The methanol used was purchased from R&M Chemical® with analysis reagent standard. The oil used was cooking palm oil from Buruh® produced by Lam Soon Sdn Bhd. The details of the chemical properties can be described in Table 1. The density and viscosity were analysed using SVM 3000 from Anton Paar®. The interfacial tension and contact angle were measured using DataPhysics® OCA 20.

### 2.3 Simulation Setup and Boundary Conditions

The simulation was performed in Ansys Fluent version 17.2 using Volume of Fluid (VOF) model. The solver used was pressure-based and used transient mode, therefore, it was calculated iteratively with  $1 \times 10^{-5}$  s time step and the Courant number below 5 to have a conservative and stable convergent value along the simulation. Since the depth of the microchannel was 88  $\mu\text{m}$ , the confinement ratio between the channel width and depth is 5.7. Therefore, the simulation was sufficient to be performed in a two dimensions geometry. Preliminary works on the meshing study indicated that the simulation was highly mesh dependent, so, the simulation conducted used high meshing quality [19]. The mesh was created uniformly throughout the domain and had approximately 300 k quadrilateral cells. The maximum face area created amounted to approximately 10  $\mu\text{m}^2$  and the maximum aspect ratio was 6.25. The liquid properties used in the simulation were exactly according to the liquid property values from Table 1. Both liquids are incompressible Newtonian fluids, therefore, all the liquid properties were assumed to be constant. The oil was taken as the primary phase, while the methanol as the secondary phase. In the boundary condition, volume fraction of methanol equals to 1, while the oil equals to 0. The wall was assumed to have no slip condition. The adhesion function was activated to define the contact angle value to characterize the wetting properties between oil and methanol on PDMS

wall. The variable that changed in the simulation was the velocity at the methanol and oil inlet channels.

The VOF model estimates the separation of the phases by tracking the interface(s) between the phases [20]. It is accomplished by the solution of a continuity equation for the volume fraction of one (or more) of the phases. For the  $q$ th phase, this equation has the form as shown in Eq. (1), where  $\dot{m}_{qp}$  is the mass transfer from phase  $q$  to phase  $p$  and  $\dot{m}_{pq}$  is the mass transfer from phase  $p$  to phase  $q$ .

$$\frac{1}{\rho_q} \left[ \frac{\partial}{\partial t} (\alpha_q \rho_q) + \nabla \cdot (\alpha_q \rho_q \bar{V}_q) = \sum_{p=1}^n (\dot{m}_{pq} - \dot{m}_{qp}) \right] \quad (1)$$

A single momentum equation as shown in Eq. (2) is solved throughout the domain and the resulting velocity field is shared among the phases [20]. It is dependent on the volume fractions of all phases through the properties of  $\rho$  and  $\mu$ .

$$\frac{\partial}{\partial t} (\rho \bar{v}) + \Delta \cdot (\rho \bar{v} \bar{v}) = -\nabla p + \nabla \cdot [\mu (\nabla \bar{v} + \nabla \bar{v}^T)] + \rho \bar{g} + \bar{F} \quad (2)$$

The source term  $\bar{F}$  in Eq. (2) is for the surface tension term where in this study, the continuum surface force (CSF) model has been used. This model has been proposed by Brackbill et al. [21] and has been implemented such that the addition of surface tension to the VOF calculation results in a source term in the momentum equation. It can be shown that the pressure drop across the surface depends upon the surface tension coefficient,  $\sigma$ , and the surface curvature as measured by two radii in orthogonal direction,  $R_1$  and  $R_2$  in Eq. (3) below:

$$p_2 - p_1 = \sigma \left( \frac{1}{R_1} - \frac{1}{R_2} \right) \quad (3)$$

where  $p_1$  and  $p_2$  are the pressures in the two fluids on either side of the interface. In Ansys Fluent, a formulation of the CSF model is used, where the surface curvature is computed from local gradients in the surface normal at the interface. Equation (4) show the surface normal,  $n$  that is used to calculate the surface curvature, where  $\alpha_q$  defined as the gradient of the volume fraction of  $q$ th phase.

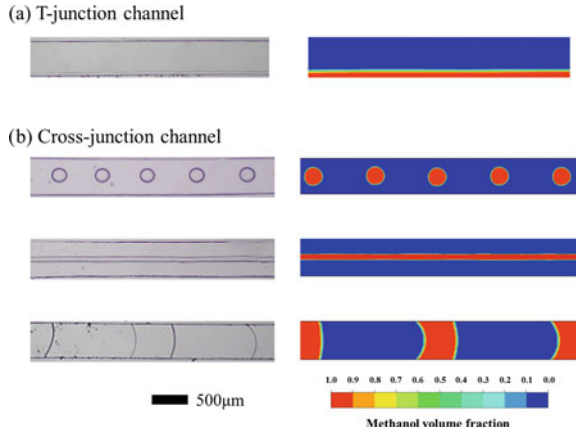
$$n = \nabla \alpha_q \quad (4)$$

### 3 Result and Discussion

#### 3.1 Preliminary Design Analysis and Validation

Two microchannel designs as shown in Fig. 1 were screened to observe the capability to create multiple flow regimes in the oil and methanol system. Figure 3 shows the

**Fig. 3** Comparison between experimental (left) and simulation (right) results at **a** T-junction, and **b** cross-junction micro channel



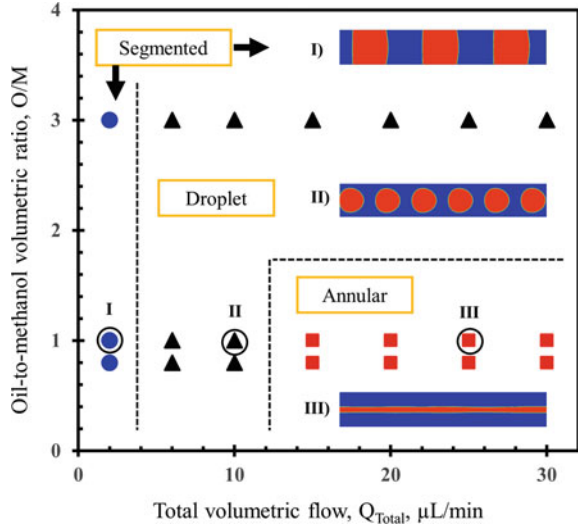
result for comparison between experiment and simulation. As illustrated, the result for T-junction channel created stratified flow regime at all flow conditions tested which include low and high total volumetric flow rate. With the inability to create multiple flow regimes, the T-junction will not be further investigated in the study of  $s/v$  analysis. In addition, other researchers have reported similar findings in their experimental work [7, 22, 23] supporting our conclusion.

Furthermore, for cross-junction channel, multiple regimes of multiphase flow occurred as shown in Fig. 3, which will be further discussed in the next section. In conclusion, the experimental results validated the simulation results showing good agreement for all multiphase regimes created.

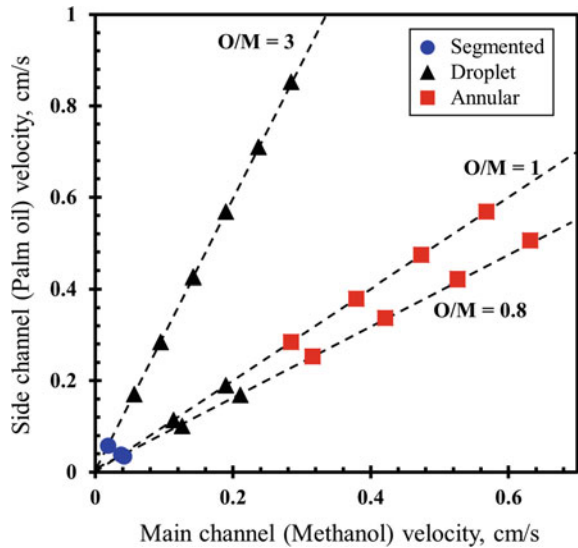
### 3.2 Flow Regimes in Cross-Junction Channel

Three different regimes were created using cross-junction channel: segmented, droplet and annular flow regime as shown in Fig. 4. Different regimes were created depending on two factors, total volumetric flow rate,  $Q_{Total}$ , and the oil-to-methanol volumetric ratio,  $O/M$ . The  $Q_{Total}$  was calculated based on both methanol and oil liquids in the microchannel after the junction. From this observation, the segmented flow regime was found at low  $Q_{Total}$ , below 4  $\mu\text{L}/\text{min}$ ; while the annular flow regime at high  $Q_{Total}$ , above 12  $\mu\text{L}/\text{min}$ . However, at  $O/M$  volumetric ratio of 3, the annular flow regime was not found, instead the droplet flow regime was created up until 30  $\mu\text{L}/\text{min}$ . It was observed that the droplet flow regime at  $O/M$  volumetric ratio of 3 will not maintain the droplet form infinitely. At very high  $Q_{Total}$  of 80  $\mu\text{L}/\text{min}$ , it was found that the flow regime started to form annular flow regime. This result is not shown in Fig. 3 due to insignificant findings for another  $O/M$  volumetric ratio at very high  $Q_{Total}$  of 80  $\mu\text{L}/\text{min}$ .

**Fig. 4** Different flow regimes created in cross-junction microchannel at different oil-to-methanol volumetric ratio



**Fig. 5** Factor of inlet velocity in creating different flow regimes



The same results from the flow regimes can also be described in terms of flow velocity conditions at respective inlet channels as shown in Fig. 5. The velocity value for both side channels of oil were identical to each other and the velocity value presented in Fig. 5 refers only to one of the side channels.

The velocity was calculated using the volumetric flow rate of respective liquids based on the controlled  $O/M$  volumetric ratio. At high  $O/M$  volumetric ratios, the velocity of oil at the side channels was higher than the velocity of methanol at the main channel. This is observed because volume of oil flowing at the side channels



at high O/M ratio is larger compared to lower O/M ratio. From this observation, it is interpreted that the annular flow regime occurred when the velocity of the main channel was higher or equal with the velocity of the side channels. The segmented flow, however, appeared at all volumetric ratios at relatively low  $Q_{\text{Total}}$  values.

In segmented flow regime, it is observed that the dispersed phase of methanol appeared to be wetting the wall as illustrated in the inset Fig. 4I. This creates a segmented shape that separates the phases between methanol and oil. Although the oil has higher wetting properties with the PDMS wall, the wetting difference by contact angle value was distinctly small which is  $107^\circ$ . Therefore, at low volumetric flow rate, it is possible that the methanol can wet the wall despite lower wetting properties from oil phase, hence forming a segmented flow regime. The observation differed at droplet flow regime. The dispersed phase in this regime did not wet the wall, therefore forming a droplet shape due to the surface tension of methanol acquiring the least surface area possible.

At O/M volumetric ratio of 3, the flow created a droplet regime even at relatively high flow rate. However, this was not observed for the lower O/M volumetric ratio of 1 and 0.8. At  $Q_{\text{Total}}$  higher than  $10 \mu\text{L}/\text{min}$ , the oil flow from the side channels did not break the methanol phase, hence creating a different flow regime of annular flow. It is concluded that a maximum value of  $Q_{\text{Total}}$  exists to give a droplet flow regime in the microchannel. In addition, higher O/M volumetric ratio could maintain the droplet flow regime at higher  $Q_{\text{Total}}$  value compared to the lower O/M volumetric ratio. While annular flow regime can be observed when the velocity of the methanol channel inlet is higher than the velocity of the side channel inlet.

### 3.3 Droplet Characteristic and $s/v$ Value

In this section, all flow cases at different  $Q_{\text{Total}}$  and O/M volumetric ratio are evaluated, but the droplet characteristics can only be described at the droplet flow regime and the results are shown in Fig. 6.

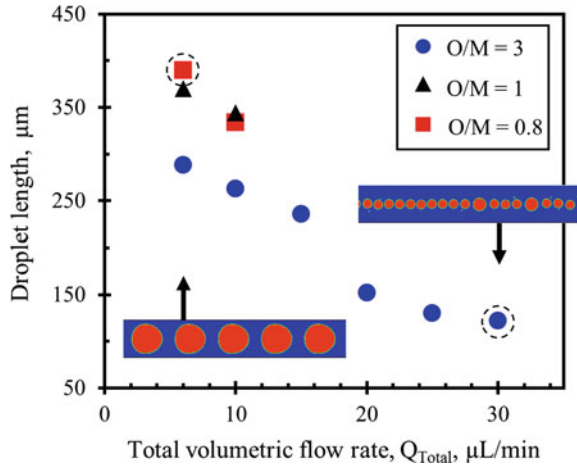
Due to the constant repetitive of droplet created, the calculation of single droplet was used to represent the general calculation of  $s/v$  ratio for the entire microchannel system. The measurement at the system domain where the  $s/v$  calculated can be described as in Fig. 7.

The shape of the droplet was taken as an ellipsoidal. The length and diameter were almost identical to each other, so the diameter value was not reported. The area of the droplet was calculated based on the ellipsoidal shape using Eq. (5)

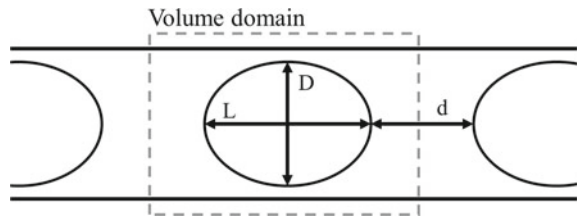
$$Area = 4\pi \left[ \frac{\left(\frac{1}{4}ab\right)^{1.6} + \left(\frac{1}{4}ac\right)^{1.6} + \left(\frac{1}{4}bc\right)^{1.6}}{3} \right]^{\frac{1}{1.6}} \quad (5)$$

where  $a$  is the droplet diameter,  $b$  is channel depth (constant at  $88 \mu\text{m}$ ), and  $c$  is the droplet length. The segmented and annular regimes volume was calculated based on

**Fig. 6** Droplet length at different  $Q_{Total}$  and O/M volumetric ratio



**Fig. 7** Measurement analysis where  $L$  is droplet length,  $D$  for droplet diameter and  $d$  for the distance between consecutive droplets



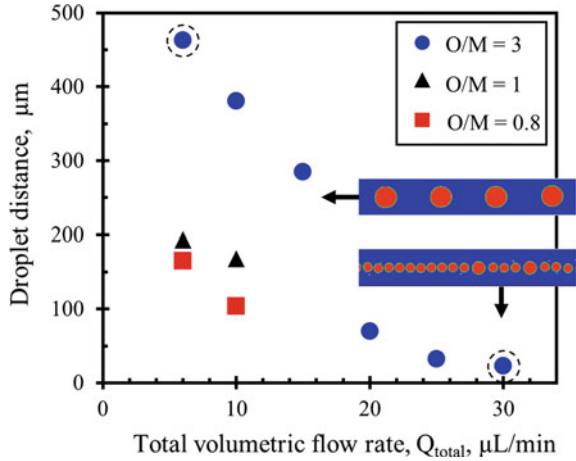
the rectangular shape. The area was calculated based on the area exposed to both phases between the oil and methanol.

In the droplet regime, it is observed that the size of droplet, in terms of droplet length, changes at different  $Q_{Total}$  and O/M volumetric ratios. From Fig. 6, it is observed that the droplet length decreased as the  $Q_{Total}$  and O/M ratio increased. From the data collected, there was less data points for O/M ratio 0.8 and 1 because, at higher  $Q_{Total}$  the regime was no longer in droplet regime. Another important observation was the distance between each droplet because this value will be used in the calculation of  $s/v$  ratio for each droplet size case. Figure 8 shows the distance behavior of the droplet at different flow conditions. In this finding, the droplet distance also decreased as the  $Q_{Total}$  increased, but, the O/M volumetric ratio decreased. According to Garstecki et al. [24], the break-up rate at the neck is dependent on the side flow velocity. Higher  $Q_{Total}$  means higher side flow velocity. Therefore, the break-up rate is faster creating smaller droplet and reducing the distance between the droplets.

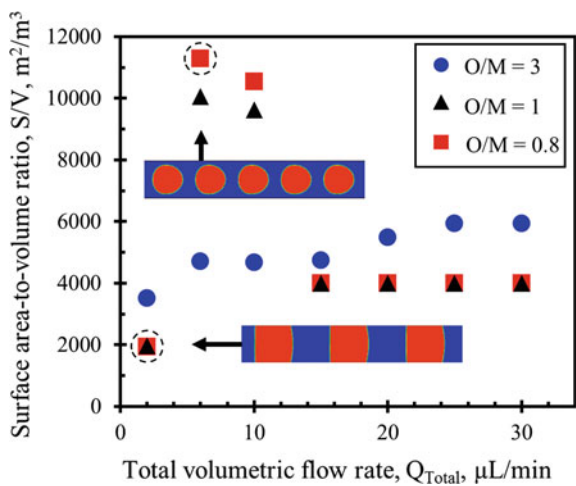
Based on the results, these values were used to calculate the surface area-to-volume ratio,  $s/v$  value. Figure 9 shows the  $s/v$  comparison for all flow regimes which include different sizes of droplet created by cross-junction microchannel.

It can be seen in the results that the segmented flow regime has the lowest  $s/v$  value because the area exposed for mass transfer is limited to the depth of the microchannel itself, which was kept constant at 88  $\mu\text{m}$ . The annular flow regime has a constant

**Fig. 8** Droplet distance at different  $Q_{Total}$  and O/M volumetric ratio



**Fig. 9**  $S/V$  value for all flow regimes and at different flow conditions



$s/v$  value at all  $Q_{Total}$  and O/M ratios because the area exposed to both phases are only a straight-line plane. The highest  $s/v$  value found was from the droplet regime and it varies from different  $Q_{Total}$  and O/M ratios due to the variation of size and distance between droplets at different flow conditions. The droplet regimes from low O/M volumetric ratio of 0.8 and 1 have higher  $s/v$  value compared to the  $s/v$  value from the high O/M volumetric ratio. The difference in  $s/v$  value is due to the factor of droplet size and the distance between the droplets. The size of the droplet affects the value of interfacial area, while the distance between the droplets affects the volume of the system domain. Bigger droplet size creates a bigger area compared to a smaller droplet. Longer distance between droplets also creates a larger volume domain. As shown in Fig. 6, droplets at lower O/M ratios have larger size droplets and shorter distance between the droplets, creating high interfacial area at a smaller

volume domain. Overall, this will create a high value of  $s/v$ . As for the droplet regime at high O/M ratio, the  $s/v$  value increases as the  $Q_{\text{Total}}$  increases. This was due to the decrease of distance between droplets which decreases the volume of system domain, although the droplet size was observed to decrease. Therefore, to obtain a high  $s/v$  value, the factor of distance between the droplets is observed to be more significant than the size of droplets.

It is concluded that the factors affecting the  $s/v$  value include the flow regime,  $Q_{\text{Total}}$ , and O/M volumetric ratio. The droplet flow regime has the highest  $s/v$  value that can reach up to  $11,000 \text{ m}^2/\text{m}^3$ , while the segmented flow regime has the lowest  $s/v$  value of  $2,000 \text{ m}^2/\text{m}^3$ . Furthermore, within the droplet regime, the flow at lowest O/M ratio of 0.8 has the highest  $s/v$  value but limited up to certain  $Q_{\text{Total}}$  due to the transformation of annular regime at higher  $Q_{\text{Total}}$ .

## 4 Conclusion

One way to increase the yield of reaction from two immiscible fluids is by enhancing the mass transfer between two immiscible phases of oil and methanol reactants. Surface area-to-volume ratio,  $s/v$  value can be used to evaluate the mass transfer performance because the transfer at multiphase flow occurs only at the interface. Factors affecting  $s/v$  value include the type of flow regimes, the total volumetric flow rate,  $Q_{\text{Total}}$ , and the oil-to-volume ratio, O/M. It is concluded that the segmented flow regime can be created at low  $Q_{\text{Total}}$  while annular flow regime can be created at high  $Q_{\text{Total}}$ . The droplet flow regime was found in between lowest and highest  $Q_{\text{Total}}$ , but depending on the O/M ratio, higher O/M ratio has a larger range of  $Q_{\text{Total}}$  to create droplet flow regime compared to lower O/M ratio. In addition, within the droplet flow regime, the droplet size decreases as the  $Q_{\text{Total}}$  and O/M decreases. The distance between droplet will also decrease as the  $Q_{\text{Total}}$  increases, while the O/M decreases. In term of  $s/v$  value, segmented flow regime has the lowest  $s/v$  while droplet regime created the highest  $s/v$  value. With this finding, it is understood that one can have various flow regimes inside microchannel reactor and its total interfacial area for reaction purposes. In addition, it is also useful in designing a suitable channel geometry where specific droplet size could be controlled by varying the inlet flow conditions.

**Acknowledgements** The authors would like to offer their gratitude to Universiti Teknologi PETRONAS, Malaysia for providing a conducive work environment and state-of-the-art research facilities.

## References

1. Huebner A, Sharma S, Srisa-Art M, Hollfelder F, Edel JB, DeMello AJ (2008) Microdroplets: a sea of applications? Lab Chip 8:1244

2. Antony R, Nandagopal MSG, Sreekumar N, Rangabhashiyam S, Selvaraju N (2014) Liquid-liquid slug flow in a microchannel reactor and its mass transfer properties—a review. *Bull Chem React Eng Catal* 9
3. Srinivasan R, Hsing I-M, Berger PE, Jensen KF, Firebaugh SL, Schmidt MA, Harold MP, Lerou JJ, Ryley JF (1997) Micromachined reactors for catalytic partial oxidation reactions. *AIChE J* 43:3059–3069
4. Azam NAM, Uemura Y, Kusakabe K, Bustam MA (2016) Biodiesel production from palm oil using micro tube reactors: effects of catalyst concentration and residence time. *Procedia Eng* 148:354–360
5. Jamil MF, Uemura Y, Kusakabe K, Ayodele OB, Osman N, Majid NMNA, Yusup S (2016) Transesterification of mixture of castor oil and sunflower oil in millichannel reactor: FAME yield and flow behaviour. *Procedia Eng* 148:378–384
6. Santana HS, Tortola DS, Reis ÉM, Silva JL, Taranto OP (2016) Transesterification reaction of sunflower oil and ethanol for biodiesel synthesis in microchannel reactor: experimental and simulation studies. *Chem Eng J* 302:752–762
7. Pontes PC, Chen K, Naveira-Cotta CP, Costa Junior JM, Tostado CP, Quaresma JNN (2016) Mass transfer simulation of biodiesel synthesis in microreactors. *Comput Chem Eng* 93:36–51
8. Xie T, Zhang L, Xu N (2012) Biodiesel synthesis in microreactors. *Green Process Synth* 1
9. Rashid WNA, Uemura Y, Kusakabe K, Osman NB, Abdullah B (2014) Synthesis of biodiesel from palm oil in capillary millichannel reactor: effect of temperature, methanol to oil molar ratio, and KOH concentration on FAME yield. *Procedia Chem.* 9:165–171
10. Aghel B, Rahimi M, Sepahvand A, Alitabar M, Ghasempour HR (2014) Using a wire coil insert for biodiesel production enhancement in a microreactor. *Energy Convers Manag* 84:541–549
11. Rahimi M, Aghel B, Alitabar M, Sepahvand A, Ghasempour HR (2014) Optimization of biodiesel production from soybean oil in a microreactor. *Energy Convers Manag* 79:599–605
12. Csernica SN, Hsu JT (2012) The phase behavior effect on the kinetics of transesterification reactions for biodiesel production. *Ind Eng Chem Res* 51:6340–6349
13. Santana HS, Silva JL, Taranto OP (2015) Numerical simulation of mixing and reaction of *Jatropha curcas* oil and ethanol for synthesis of biodiesel in micromixers. *Chem Eng Sci* 132:159–168
14. Rashid WNA, Uemura Y, Kusakabe K, Osman NB, Abdullah B (2013) Transesterification of palm oil in a millichannel reactor. *J Japan Inst Energy* 92:905–908
15. López-Guajardo E, Ortiz-Nadal E, Montesinos-Castellanos A, Nigam KDP (2017) Process intensification of biodiesel production using a tubular micro-reactor (TMR): experimental and numerical assessment. *Chem Eng Commun* 204:467–475
16. Kurup GK, Basu AS (2012) Field-free particle focusing in microfluidic plugs. *Biomicrofluidics* 6:022008
17. Di Miceli Raimondi N, Prat L, Gourdon C, Cognet P (2008) Direct numerical simulations of mass transfer in square microchannels for liquid–liquid slug flow. *Chem Eng Sci* 63:5522–5530
18. Lim C, Koh K, Ren Y, Chin J, Shi Y, Yan Y (2017) Analysis of liquid-liquid droplets fission and encapsulation in single/two layer microfluidic devices fabricated by xurographic method. *Micromachines* 8:49
19. Laziz AM, Shaari KZK (2017) CFD simulation of two phase segmented flow in microchannel reactor using volume of fluid model for biodiesel production. Presented at the (2017)
20. ANSYS Inc.: *Fluent 15.0 Theory guide*. Canonsburg, PA (2011)
21. Brackbill JU, Kothe DB, Zemach C (1992) A continuum method for modeling surface tension. *J Comput Phys* 100:335–354
22. Santana HS, Tortola DS, Silva JL, Taranto OP (2017) Biodiesel synthesis in micromixer with static elements. *Energy Convers Manag* 141:28–39
23. Santana HS, Amaral RL, Taranto OP (2015) Numerical study of mixing and reaction for biodiesel production in spiral microchannel. *Chem Eng Trans* 43
24. Garstecki P, Stone HA, Whitesides GM (2005) Mechanism for flow-rate controlled breakup in confined geometries: a route to monodisperse emulsions. *Phys Rev Lett* 94:164501

# Study on the Wear Influence for Recycled AA6061 Aluminum/ $\text{Al}_2\text{O}_3$ Utilizing the Face Central-Full Factorial Technique (FCFFT)



Huda M. Sabbar, S. Shamsudin, Mohammed Abdulridha Abbas, Muntadher S. Msebawi, Mohd Sukri Mustapa, Mohd Amri Lajis, Mohammed H. Rady and Sami Al Alim

**Abstract** The AA6061-T6 aluminum alloy is one of the widely spread alloys, used in different fields and most commonly in automotive industries. Due to high demand of this alloy, direct recycling plays a significant role to reduce the energy consumption and greenhouse gas emissions. The progressing of the product technology requires the mechanical properties of this alloy to be enhanced to meet the expressed requirements. Therefore, enhancement of the directly recycled aluminum alloy chips based matrix composite is crucial. This study focuses on the influences of *Preheating Temperature* (PHT), *Preheating Time* (PHti), and *Volume Fraction* (VF) on *Wear Mass Loss* (WML) property of the newly developed chip-based matrix composite. The result of *Analysis of Variance* (ANOVA) exhibits the considerable effect of PHT and VF on WML. The P-Value of all parameters was set at 5% significance level. This criterion revealed very strong interactions between PHT  $\times$  PHti, PHT  $\times$  VF, and PHT  $\times$  PHti  $\times$  VF respectively. The optimum values for PHT, PHti, and VF are 550 °C, 3 h, and 15% which revealed the optimum WML of 0.0014 and desirability of 0.9876. A response optimizer shows that as low as 0.0014 g wear mass loss can be possibly achieved. This optimum reading will deliver the best wear performance for the applications of *Aluminum Matrix Composites* (AMCs) in the wear demanded working environment.

**Keywords** Aluminum alloy AA6061 · Alumina · Hot extrusion · DOE · Wear test

## 1 Introduction

The dynamic nature and reusability of aluminum and its alloys have earned their place in recycling operation for further applications in various industries [1]. In

---

H. M. Sabbar (✉) · S. Shamsudin · M. A. Abbas · M. S. Msebawi · M. S. Mustapa · M. A. Lajis · M. H. Rady · S. Al Alim  
Faculty of Mechanical and Manufacturing Engineering, Universiti Tun Hussein Onn Malaysia, Batu Pahat, Johor, Malaysia  
e-mail: [hudasabbar86@gmail.com](mailto:hudasabbar86@gmail.com)

© Springer Nature Singapore Pte Ltd. 2020  
M. Awang et al. (eds.), *Advances in Material Sciences and Engineering*, Lecture Notes in Mechanical Engineering, [https://doi.org/10.1007/978-981-13-8297-0\\_62](https://doi.org/10.1007/978-981-13-8297-0_62)

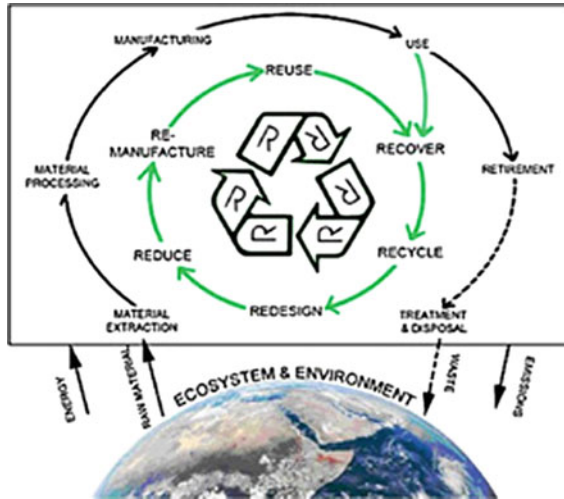


Fig. 1 Relationship between Six-R strategy within the ecosystem and environment [3]

direct recycling, the principal source of aluminum depends on chips that derived from various manufacturing processes [2]. The concept of recycling constitutes R-Strategy from the Six-R practices. This strategy consists of the following steps: redesign, reduce, remanufacture, reuse, recover, and recycle respectively. Figure 1 shows the evolution of different manufacturing concepts and their contributions to the ecosystem and the environment in general [3]. Today, sustainability remains one of the top priorities for green technology, targeted at supporting the economy and environment through recycling. In aluminum industry, one method to achieve this target is through the direct recycling by means of hot extrusion [4]. In contrast to the conventional recycling process where melting of scraps is mandatory, the hot extrusion is an innovative process targeted to utilize low energy and less labour intensive with improved mechanical properties [5]. *Aluminum Matrix Composites* (AMCs) has demonstrated better properties in comparison with the conventional aluminum alloy [6].

Ceramic particles strengthen AMCs and contribute to the increment of hardness, strength and wear resistance properties as well as reducing thermal expansion of the composites [7].  $Al_2O_3$  is considered to be among a good composite reinforced particle in the aluminum alloy matrix. This is made possible due to size difference between composite and matrix of the original composite which promotes a better composite [8]. This paper designates *Wear Mass Loss* (WML) as the principal response to quantify the wear resistance of AMCs. On the other and, the determination of WML of AMCs samples followed the procedures established in the works of Rahim et al., Alshmri et al., and Raghavendra et al. [5–13].

Table 1 indicates the terms used in the calculation of WML according to previous studies. This study investigates the effects of preheating time, temperature and vol-

**Table 1** Terms used for wear rate estimation

No.	Wear mass	Unit	Reference no.
1	Wear volume/sliding distance	mm <sup>3</sup> /m	[8]
2	Weight mass loss/distance	gm/s	[6]
3	Weights before wear test—weights after wear test	gm	[9, 10]

**Table 2** Composition of alloy AA6061 (BS EN 573-3: 2009)

Element	Mg	Si	Fe	Cu	Cr	Zn	Ti	Mn
% Present	0.8–1.2	0.4–0.8	≤0.7	0.15–0.4	0.04–0.35	≤0.25	≤0.15	≤0.15

**Table 3** Wear resistance of as receive alloy AA6061-T6

Wear mass loss (g)	Load (N)	Sliding speed (RPM)	Wear time (min)
0.0016	10	100	5

ume fraction of AMCs's on the WML property of the chip-based matrix composite material.

## 2 Experimental Setup

High-speed milling was utilized to machine aluminum blocks in order to mimic the industrial chip wastes. Smaller chip size was reported to lead to a greater deformability [9]. The average dimensions of the measured chips were 1.120 mm width × 3.20–3.50 mm length × 0.094 mm thickness and the estimated surface area was 23.63 mm<sup>2</sup>. The chemical compositions and the wear resistance of as-received AA6061 are shown in Tables 2 and 3.

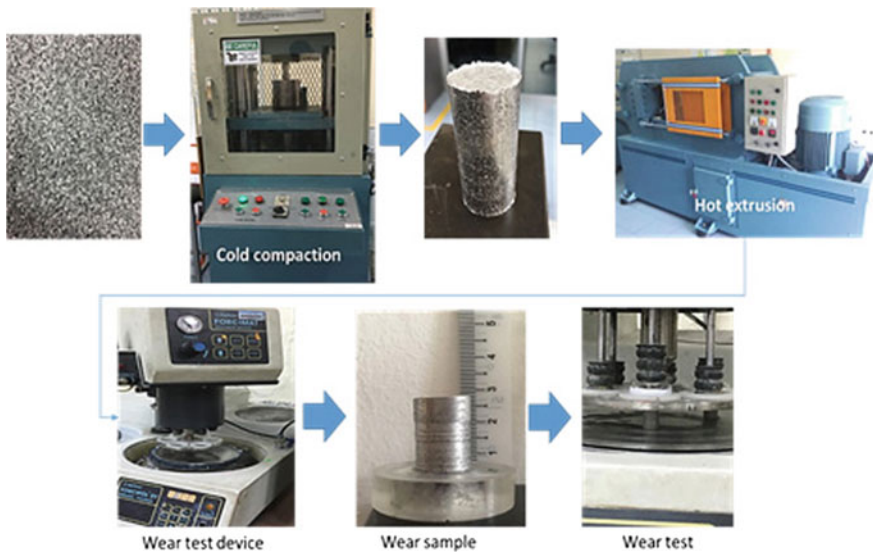
The chip cleaning was done as per ASTM G131-96, the standard practice applicable for cleaning materials via ultrasonic to remove impurities and dirt. Mixing of the composite was carried out by 3D planetary mixer to obtain a homogeneous mixture. The mixture was then filled up in a cylindrical container and compacted to produce billet with 80 mm height and 30 mm diameter by a cold press machine. Table 4 shows the designated conditions for chip-based billet extrusion. The sequence of the experiment is shown in Fig. 2. The ranges of temperature, preheating time and volume fraction of alumina powder selected were between 450–550 °C, 1–3 h/s, and 5–15% respectively. The maximum temperature was restricted to 550 °C because preheating to more than 550 °C will result in hot cracks on the surface of extruded product [11].

A ceramic heater was used to heat up the container and die. Graphite-based lubricant was added at the end of every extrusion cycle to reduce friction between inner surface of the die and container.



**Table 4** Parameter settings for hot extrusion process

Parameter	Value/type
Extrusion die	Round
Extrusion ratio, R	5.4
Billet diameter, $\phi$ (mm)	30
Extrusion speed (mm/s)	4.4
Container temp. ( $^{\circ}\text{C}$ )	300
Die temp. ( $^{\circ}\text{C}$ )	300
Preheating temp. ( $^{\circ}\text{C}$ )	450, 500, 550
Preheating time (h/s)	1, 2, 3
Volume fraction of $\text{Al}_2\text{O}_3$ (wt%)	5, 10, 15%

**Fig. 2** Preparation and testing

### 3 Experimental Design

Experiment was designed according to  $2^3$  full factorial design with two replicates. Three center points were included to investigate the linearity effect of the model. The selected parameters with their levels are shown in Table 5. Details of the experimental settings are presented in Table 4. Response in this study was wear mass loss of the extruded samples. The ASTM G99-17 was adopted for wear test. Load, sliding speed and wear time were fixed at 10 N, 100 RPM and 5 min respectively. Analysis of variance (ANOVA) was applied to study the nature of interactions between the input parameters. The results of DOE can provide a further insight of experimental direction for process optimization.

**Table 5** Process parameters and their levels used in the DOE

Parameter symbol	Parameter	Levels		
		Low (-1)	Center (0)	High (+1)
A	Preheating temp.	450	500	550
B	Preheating time	1	2	3
C	Volume fraction	5%	10%	15%

**Table 6** Results of the wear resistance

Sample	Std. order	Preheating temp. (°C)	Preheating time (h)	Volume fraction (%)	Wear mass loss (WML) (g)
S1	1	450	1	5	0.0045
S2	2	550	1	5	0.0056
S3	3	450	3	5	0.0083
S4	4	550	3	5	0.0017
S5	5	450	1	15	0.0072
S6	6	550	1	15	0.0080
S7	7	450	3	15	0.0134
S8	8	550	3	15	0.0015
S9	9	450	1	5	0.0040
S10	10	550	1	5	0.0048
S11	11	450	3	5	0.0090
S12	12	550	3	5	0.0029
S13	13	450	1	15	0.0070
S14	14	550	1	15	0.0084
S15	15	450	3	15	0.0141
S16	16	550	3	15	0.0012
S17	17	500	2	10	0.0061
S18	18	500	2	10	0.0062
S19	19	500	2	10	0.0060

## 4 Results and Discussion

Nineteen experimental runs in total were carried out as a result of full factorial design with three center points selection. The results of the experiments are shown in Table 6. The resulting high wear resistance came from the maximum preheating temperature and volume fraction. It was observed that the relationship between wear resistance and preheating temperature is linear. As the preheating temperature and volume fraction increased, the wear resistance becomes maximum. The discussions of the findings will rely on results of ANOVA of the full factorial design.

**Table 7** Results of analysis of variance

Source	DF	Seq SS	Contribution (%)	Adj SS	Adj MS	F-Val.	P-Val.
Model	7	0.000222	99.12	0.000222	0.000032	176.65	0
Linear	3	0.000095	42.42	0.000095	0.000032	176.38	0
PHT	1	0.00007	31.08	0.00007	0.00007	387.76	0
PHti	1	0	0.19	0	0	2.35	0.154
VF	1	0.000025	11.14	0.000025	0.000025	139.04	0
2-way interactions	3	0.000118	52.42	0.000118	0.000039	217.98	0
PHT × PHti	1	0.000108	48.22	0.000108	0.000108	601.53	0
PHT × VF	1	0.000009	3.88	0.000009	0.000009	48.4	0
PHti × VF	1	0.000001	0.32	0.000001	0.000001	4.02	0.07
3-way interactions	1	0.00001	4.28	0.00001	0.00001	53.45	0
PHT × PHti × VF	1	0.00001	4.28	0.00001	0.00001	53.45	0

#### 4.1 Analysis of Results

The ANOVA results indicate that the important terms that maximize the tensile strength in hot extrusion process of AMC are preheating temperature and volume fraction. The important of these two parameters are shown by  $p < 0.05$  in Table 7 and Pareto Chart as shown in Fig. 3. The remaining factors such as preheating time (B), interaction of preheating temperature and preheating time ( $A \times B$ ) and interaction of preheating temperature, preheating time and volume fraction ( $A \times B \times C$ ) are less significant than the two aforementioned parameters. The specimens extruded at the highest temperature and volume fraction resulted in highest wear resistance. Similarly, the joint effects between preheating time and temperature are responsible for significant effect on the wear results. An increase in temperature from 500 to 550 °C associated with an increment of volume fraction from 10 to 15% led to the considerable improvement in wear resistance. Furthermore, an inverse relationship was observed between wear resistance and volume fraction. This may be responsible for the low wear resistance recorded in all samples extruded at 450 °C with 5 vol.% of alumina. In general, higher reinforcement will lead to the lower wear resistance. These findings were similar as reported in Raghavendra and Rajesh [12–14].

For ANOVA, the main effects plot as shown in Fig. 4 clearly indicates that all center points are most likely close to the line connecting the average wear resistance. The average wear mass loss decreases as the preheating temperature increases and it behaves in the opposite manner for the volume fraction. This relationship is further established in the interaction plot presented in Fig. 5, whereby the similar trends were observed as shown in the main effects plot. This relationship demonstrates that

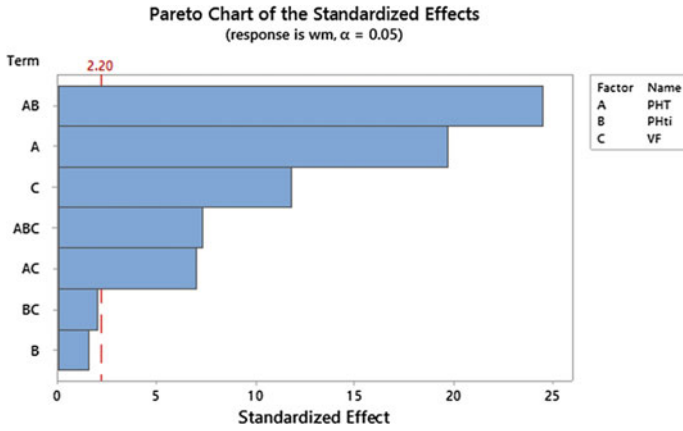


Fig. 3 Pareto chart shows the significant parameters

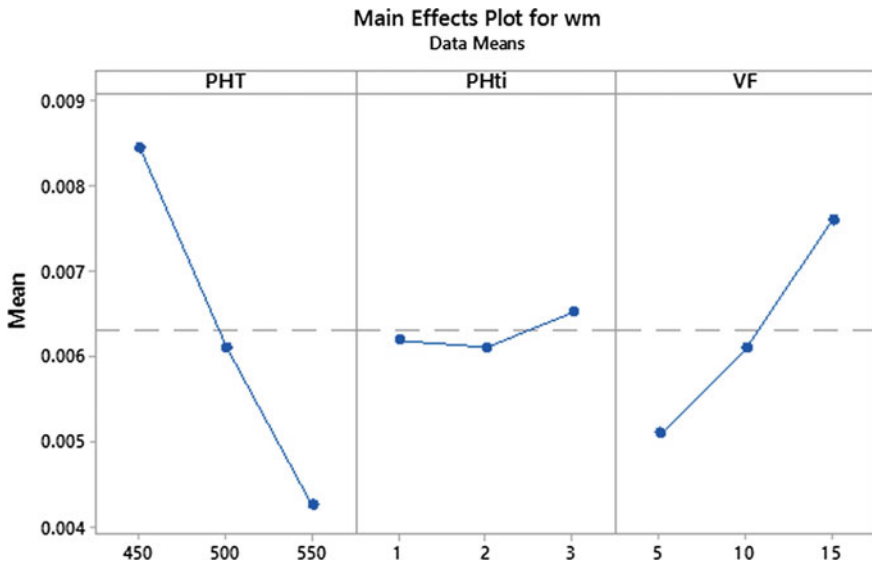


Fig. 4 Main effects plot for WM

an appropriate model for the observed data has been chosen and established. On the other hand, the curvature effect is insignificant towards the response as indicated in ANOVA results as shown in Table 7. Therefore, the linear model is sufficient to fit all the data because  $p > 0.05$  for the curvature term.

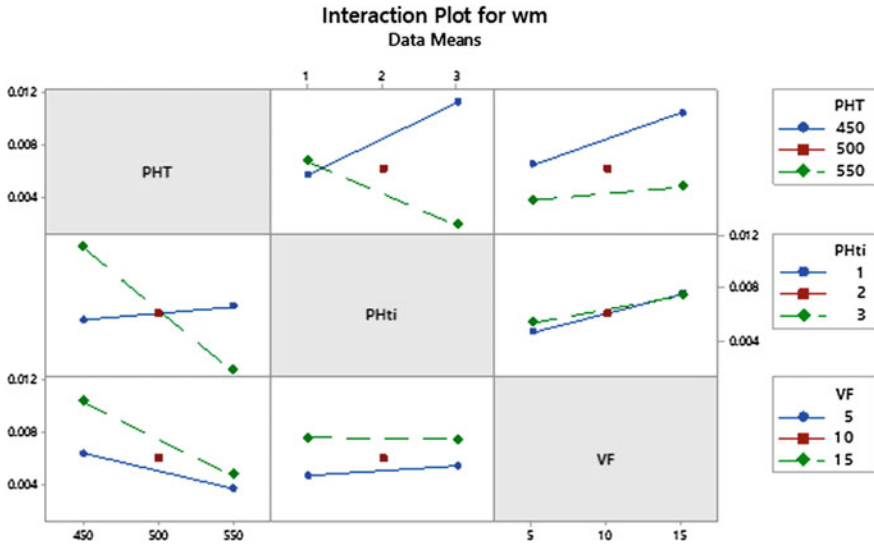


Fig. 5 Interaction plot for WM

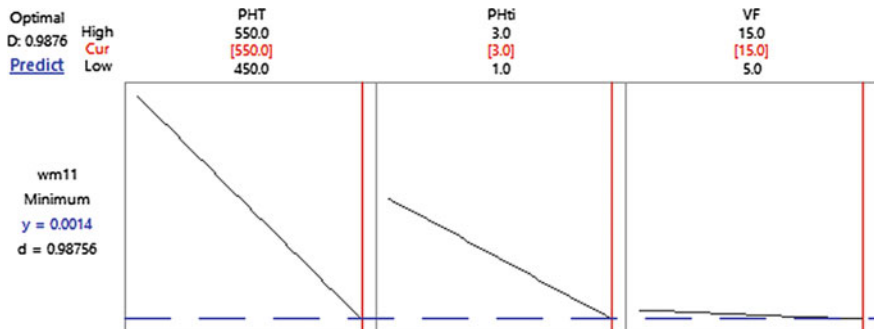


Fig. 6 Optimization plot

### 4.2 Response Optimizer

The objective of optimization is to reveal the optimum wear resistance. The analysis is based on “smaller is better” concept. It means lowest wear loss is considered as the optimum result [15]. The ramp function (optimal solution) is the response optimizer approach that finds application in locating which factors have effect on extrudates separately and their impact on the wear resistance. Figure 6 shows the results of response optimizer from (DOE) for wear resistance. Thus, to obtain the maximum wear resistance, the factors of PHT, PHTi and VT should be set at 550 °C, 3 h and 15 vol.% of alumina.

## 5 Conclusions

The preheating temperature and volume fraction are found to play the most important role in alumina powder reinforced chip-based matrix composite. The addition of micro alumina to aluminum alloy AA6061-T6 reduces the porosity and prevents further sliding of the aluminum atoms upon exposed to shear stresses. Increasing the preheating temperature increases the activation energy and promotes better homogenization within the chip-based AMC. The relationship between  $Al_2O_3$  and WML of the composite is inversely proportional whereby by increasing the  $Al_2O_3$ , it decreases the WML of the composite material.

**Acknowledgements** The authors would like to express deepest appreciation to the Centre for Graduate Studies, Universiti Tun Hussein Onn Malaysia (UTHM). Additional support was also provided by Sustainable Manufacturing and Recycling Technology, Advanced Manufacturing and Materials Center (SMART-AMMC), Universiti Tun Hussein Onn Malaysia (UTHM). In addition, a special appreciation goes to the Government of the Republic of Iraq for supporting the author throughout this study.

## References

1. Ab Rahim SN, Lajis MA, Ariffin S (2015) A review on recycling aluminum chips by hot extrusion process. *Procedia CIRP* 26:761–766
2. Samrendukumar S, Pulkool P, Chovatiya M, Prajapati B. Scrap management and redesigning plant layout
3. Jayal AD, Badurdeen F, Dillon OW Jr, Jawahir IS (2010) Sustainable manufacturing: Modeling and optimization challenges at the product, process and system levels. *CIRP J Manuf Sci Technol* 2(3):144–152
4. Shamsudin S, Zhong ZW, Ab Rahim SN, Lajis MA (2017) The influence of temperature and preheating time in extrudate quality of solid-state recycled aluminum. *Int J Adv Manuf Technol* 90(9–12):2631–2643
5. Rahim A, Nizam S, Lajis MA (2017) Effects on mechanical properties of solid state recycled aluminium 6061 by extrusion material processing. In: *Key engineering materials*, vol 730. Trans Tech Publications, pp 317–320
6. Shamsudin S, Lajis MA, Zhong ZW (2016) Evolutionary in solid state recycling techniques of aluminium: a review. *Procedia CIRP* 40:256–261
7. Alshmiri F, Atkinson HV, Hainsworth SV, Haidon C, Lawes SDA (2014) Dry sliding wear of aluminium-high silicon hypereutectic alloys. *Wear* 313(1–2):106–116
8. Radhika N, Balaji TV, Palaniappan S (2015) Studies on mechanical properties and tribological behaviour of LM25/SiC/Al<sub>2</sub>O<sub>3</sub> composites. *J Eng Sci Technol* 10(2):134–144
9. Zhou H, Guo QC, Lin PY, Zhang XL, Ren LQ (2008) Influence of H13 steel unit on wear behavior of vermicular cast iron. *Appl Surf Sci* 255(5):3394–3399
10. Niinomi M (ed) (2010) *Metals for biomedical devices*. Elsevier
11. Kondoh K, Luangvaranunt T, Aizawa T (2002) Solid-state recycle processing for magnesium alloy waste via direct hot forging. *Mater Trans* 43(3):322–325
12. Raghavendra N, Ramamurthy VS (2014) Effect of particle size and weight fraction of alumina reinforcement on wear behavior of aluminum metal matrix composites. *Int J Innov Res Sci Eng Technol* 3(4):11191–11198

13. Rajesh S, Krishna AG, Raju PRM, Duraiselvam M (2013) Statistical modeling and analysis of dry sliding wear of SiC reinforced aluminum MMCs. *Int J Surf Eng Interdiscip Mater Sci (IJSEIMS)* 1(1):57–70
14. Pramanik A (2016) Effects of reinforcement on wear resistance of aluminum matrix composites. *Trans Nonferrous Metals Soc China* 26(2):348–358
15. Praveen JED, Smart DR, Babu R, Gnanaprakash N. Investigations on dry sliding wear behaviour of LM13/SiC/Gr hybrid composites by response surface methodology

# Tensile, Flexural and Fracture Morphological Properties of Recycled Polypropylene (*rPP*) Filled Dried Banana Leaves Fibre (DBLF) Composites: Effects of DBLF Loadings



**Thinakaran Narayanan, Jeefferie Abd Razak, Intan Sharhida Othman, Noraiham Mohamad, Mohd Edeerozey Abd Manaf, Mazlin Aida Mahamood, Hazman Hasib, Mohd Muzafar Ismail and Ramli Junid**

**Abstract** Global interest to reduce the use and disposal of non-degradable plastic based product, has enticed the initiative to develop eco-friendly plastic based composites. Green product require degradability attribute while maintaining superior mechanical and physical properties, especially for packaging application. For such reason, some portion of thermoplastic was substituted with some portion of plant based natural fibre, for composite production. In this study, recycled waste polypropylene (*rPP*) was filled with dried banana leaves fibre (DBLF), for *rPP*/DBLF composites fabrication. The effects of DBLF fibre loadings (0, 10, 20, 30 and 40 wt%) towards the resulted mechanical, physical and fracture morphological properties of *rPP*/DBLF composites were studied. Local supply of dried banana leaves was grinded into 60  $\mu\text{m}$  of fibre length, and *rPP* was obtained from waste injection moulding scrapped and crushed beforehand into finer *rPP* particles. The *rPP*/DBLF composites were prepared through double steps compounding method using melting device (180 °C, 80 rpm, 30 min) followed by an injection moulding process (185 °C, 5 min of residence time). Later, produced *rPP*/DBLF composites were tested for their tensile strength (ASTM D638) and flexural strength (ASTM D790)

---

T. Narayanan · J. Abd Razak (✉) · I. S. Othman · N. Mohamad · M. E. Abd Manaf · M. A. Mahamood · H. Hasib

Advanced Manufacturing Centre, Fakulti Kejuruteraan Pembuatan, Universiti Teknikal Malaysia Melaka, Hang Tuah Jaya, 76100 Durian Tunggal, Melaka, Malaysia  
e-mail: [jeefferie@utem.edu.my](mailto:jeefferie@utem.edu.my)

T. Narayanan

Department of Mechanical Polymer, National Youth and High Skill Institute (IKTBN) Sepang, Bandar Baru Salak Tinggi, 43900 Sepang, Selangor, Malaysia

M. M. Ismail

Faculty of Electronic Engineering and Computer Engineering, Universiti Teknikal Malaysia Melaka, Hang Tuah Jaya, 76100 Durian Tunggal, Melaka, Malaysia

R. Junid

Faculty of Mechanical Engineering, Universiti Malaysia Pahang, 26600 Pekan, Pahang, Malaysia

© Springer Nature Singapore Pte Ltd. 2020

M. Awang et al. (eds.), *Advances in Material Sciences and Engineering*, Lecture Notes in Mechanical Engineering, [https://doi.org/10.1007/978-981-13-8297-0\\_63](https://doi.org/10.1007/978-981-13-8297-0_63)



performances. The relationships between the fracture morphology and composite strength was established through the observation of tensile fracture surfaces of the selected samples, under the Scanning Electron Microscope (SEM) observation. From the experimental work, interestingly it was found that, the tensile strength (TS) of *rPP*/DBLF composite has improved about +37.70% with 30 wt% of DBLF higher loading, while oppositely the maximum flexural strength (FS) had attained by 10 wt% of DBLF lower loadings, with only +22.60% of positive improvement, in comparison to unfilled *rPP* sample. Addition of DBLF into *rPP* prone to establish the strengthening outcome, but less stiffening effects. This could be explained by coarse DBLF particle morphology as observed by SEM, which encourage for mechanical interlocking with *rPP* for good matrix-filler interaction, that increased the TS, while better filler-filler segregation avoiding the filler domination which lowering the stiffness or FS. In overall, this study has successfully highlighted the potential of DBLF filler to enhance the properties of *rPP*, as another alternative of degradable plastic based composite for various promising applications.

**Keywords** *rPP* · DBLF · Degradable plastics · Tensile · Flexural · Fracture surfaces

## 1 Introduction

Thermoplastic materials have been increasingly used for various applications [1]. Due to their versatility, the usage of plastic based product are becoming boundless. This scenario has created serious after consumption and post-consumer issues on disposal and environmental pollution, due to plastic wastes. Value adding the waste into wealth are significantly crucial for balance eco-system sustainability. Among effective strategies are by manufacturing the composites or through blending with another polymeric phases, for enhanced performance of waste plastics. Nowadays, extensive research on filled plastic based composites development, has getting huge attention in dealing with plastic materials deficiency [2]. In this research, the plastic waste from injection moulding scrapped was utilized as matrix, which reinforced by plant based natural fibres incorporation.

Plant based natural fibres are feasible and plentiful replacement for expensive and non-renewable synthetic fibres [1, 2]. They possessed low cost, low density, non-toxicity, comparable strength and almost no waste disposal issues. Malaysia has rich diversity of plant based fibres including coconut coir fibres, kenaf fibres, palm oil empty fruit bunch, banana fibres and etc. The utilization of plant based fibre are very trendy in various engineering applications, such as automotive, construction and furniture industry [3]. The incorporation of natural fibres into recycled polypropylene (*rPP*) has tremendously increased the resulted tensile and flexural strength properties of produced composites [4]. In this study, dried banana leaves fibre (DBLF) was utilized as reinforcement filler for *rPP* from scrapped injection moulding wastes. In this study, the polypropylene scrapped was obtained from an injection moulding

operation, and was crushed into fine pellets by using an industrial crusher. Later, several compounding steps and hot compression method were utilized for *rPP*/DBLF composites fabrication.

Banana leaves are agricultural waste, rich in starch and cellulosic fibres content [4, 5]. Cellulosic based fillers have been of greater interest as they provides composites improved mechanical properties as compared than those containing non-fibrous fillers. The ripe banana leaf contains about 6–9% of dry matter protein, 20–30% of lignocellulose fibres and about 40% of starch content, alongside with 88% of moisture [6]. Banana tree produces huge amount of cellulosic waste which disposed into landfill. During biodegradation, they emitted about 20% of methane gaseous, forming major contributor of global warming [7]. In addition, DBL can be obtained for industrial purpose without any extra cost [8]. In this study, DBL was obtained from post-harvest of banana tree. The DBL was shredded by using a laboratory blender for conversion into DBLF powder. Hence, to understand the role of DBLF as newly discovered functional filler for polymer matrix composites, their loadings effects to the resulted physical, mechanical and fracture morphological of *rPP*/DBLF composites were studied in this preliminary research.

## 2 Materials and Methods

### 2.1 Raw Materials

Recycled polypropylene (*rPP*) are collected from scrapped injection moulding process in IKTBN Sepang. IKTBN Sepang is one of the premier technical institute focusing on skills development among Malaysian youth. The scrapped has been generated from teaching and learning activities held in the polymer processing laboratory. The *rPP* was initially virgin homopolymer polypropylene supplied by Titan PP Polymers (M) Sdn. Bhd. The polymer grade TitanPro 6331 was basically for general purpose of injection moulding process. The collected *rPP* scrapped was first screened and segregated for any contamination or impurities elimination. Later, the *rPP* was loaded into industrial crusher machine for shredding into finer particles or *rPP* granules. The process was repeated about two times to ensure *rPP* sizes homogeneity.

The dried banana leaves fibre were yielded from dry banana petiole of *musa acuminata sp.* species that grown wild at the reserved area located in IKTBN Sepang, Malaysia. The petiole was separated from dried banana leaves and was crushed using industrial blender and sieved into 60  $\mu\text{m}$  of length size with *Analysette 3* vibratory sieve shaker. The DBLF was further dried in a drying oven for 24 h at 80 °C for conditioning purpose, before incorporation with *rPP* by double steps of melt-blending process.

## **2.2 *rPP/DBLF Composites Preparation via Double Steps Melt-Blending Procedure***

Five formulation of *rPP/DBLF* composites with various DBLF loadings (0, 10, 20, 30 and 40 wt%) were prepared to understand the effects of different filler loadings or filler incorporation to the *rPP* based composites. The double-steps melt-blending approach was utilized to compound the *rPP/DBLF* composites. At the first step, the calibrated melting device was set into 180 °C and blending was held within 30 min at 80 rpm. Later, the second melt-blending step was followed by injection moulding into specific dimension and shape of samples for tensile and flexural tests, respectively. The moulding process was performed at 185 °C within five mins of residence period, using DKM-8188 Dakumar type injection moulding machine. Produced samples were conditioned at 80 °C within 24 h. in a drying oven, before performing the subsequent mechanical tests.

## **2.3 *Tensile Testing of rPP/DBLF Composites***

The tensile test for *rPP/DBLF* composites were performed in accordance to ASTM D638—Type 1. Dimension of tensile test sample was monitored within  $\pm 1.00$  mm of thickness, overall width of 19.00 mm and gauge length at 50.00 mm. The test was carried out at controlled atmosphere of  $22 \pm 2$  °C, at relative humidity of 60%. Testing was performed at 10 mm/min of cross-head speed by using a Universal Testing Machine (GoTech brand from South Korea). For each loadings, about five samples were tested for data averaging purpose. For the case of this study, only tensile strength (TS) response was analysed and presented, to represent the reinforcement effects of DBLF filler addition into *rPP* matrix.

## **2.4 *Flexural Testing of rPP/DBLF Composites***

The flexural test for *rPP/DBLF* composites were performed in accordance to ASTM D790—three point bending type. Dimension of flexural test sample was standardized into 127 mm  $\times$  12.70 mm  $\times$  3.20 mm, for length, width and thickness, respectively. The test was carried out at controlled atmosphere of  $22 \pm 2$  °C, at relative humidity of 60%. Testing was performed at 2.00 mm/mins of cross-head speed and resulting span to depth ration of 16:1, by using a Universal Testing Machine (GoTech brand from Taiwan). The distance of two support span was fixed at 100 mm. The width and depth of tested sample was measure to the nearest 0.03 mm at the centre of support span. For each loadings, about five samples were tested for data averaging purpose. For the case of this study, only flexural strength (FS) response was analysed and

presented, to represent the stiffness behaviour of resulted composites due to DBLF filler addition into *rPP* matrix.

## 2.5 Fracture Surface Morphological Observation of RPP/DBLF Composites

The fracture surfaces of the selected samples of *rPP*/DBLF composite based on TS experimental result was observed under the Scanning Electron Microscope (SEM) observation. At first, the fragment of fracture surface was cut and mounted onto the stub with carbon tape before being coated with gold-palladium (Au-Pd) thin conductive coating, using a sputter coater model Polaron E-1500, to eliminate the charging effects during observation. The fracture surface images were captured by using Zeiss Evo VPSEM at 7.00 kV accelerating voltage for 100 $\times$  of magnification power at secondary electron detection.

## 3 Results and Discussion

The main aim of this study is to evaluate the efficacy of DBLF filler in reinforcing and stiffening the *rPP* matrix for composite fabrication. For preliminary study stage, the effects of DBLF loadings were tested and evaluated. The DBLF reinforcing effect were represented by TS response, while stiffening effect was represented by FS response. Figure 1 has presented the resulted TS versus weight percentages of DBLF in *rPP* based composites. It was clearly found that, by adding the DBLF filler up to 30.00 wt% addition into *rPP* matrix, the TS was significantly increased up to +37.70% of positive improvement, in comparison to the unfilled *rPP* sample. This affirmative enhancement was due to special ability of DBLF to introduce the reinforcement effect into *rPP* matrix. The nature of rough and coarse DBLF texture morphology (Fig. 2), has encouraged the mechanical inter-locking between *rPP* matrix and DBLF filler.

This situation would promote the matrix-filler interaction due to establish interface and interphase interaction between both parties in *rPP*/DBLF composite bodies. Fluffy pocket morphology of DBLF, has promoted better *rPP* wetting for good mechanical inter-locking phenomena. During the tensile loading, this improve matrix-filler interaction, was molecularly strengthen the composite until resulting the increase TS value. Increasing the added DBLF content will further increase the cumulative strengthening effects due to the presence of DBLF in *rPP* matrix. However, this only could sustain at maximal 30.00 wt% of DBLF addition, whereby after then, about -33.10% of TS reduction was experienced by *rPP*/40.00 wt% DBLF composite. This lessening condition was accountable by worst agglomeration of DBLF, due to cumulative van der Waals forces interaction between DBLF surfaces

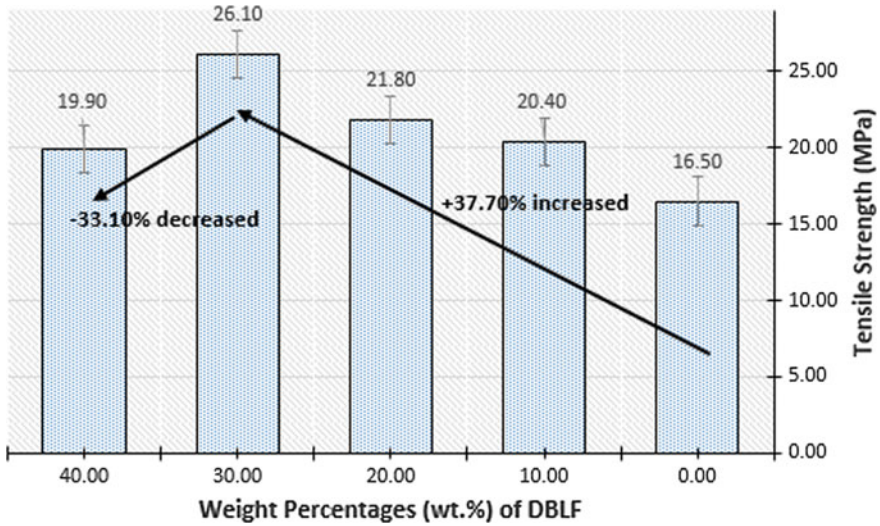


Fig. 1 TS versus wt% of DBLF in *rPP* based composites

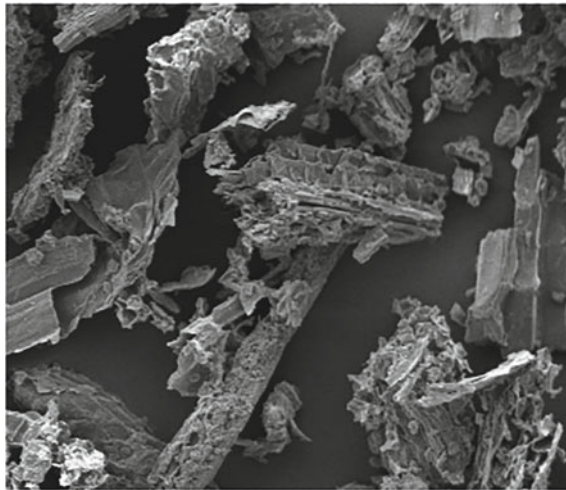
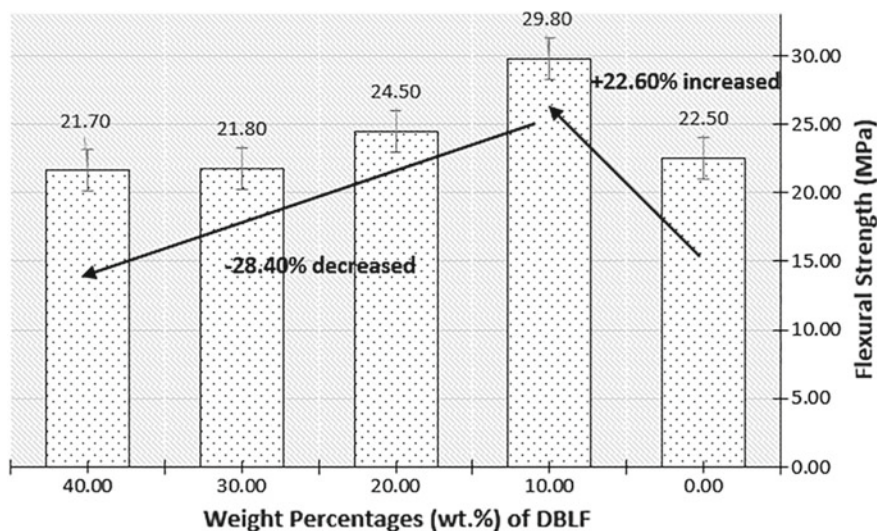


Fig. 2 Rough and coarse texture morphology of DBLF (100× mag)

at higher loadings. This factor hindered the homogenous force distribution, during the tensile event and un-wetted DBLF in the agglomerates has created voids, which prone to act as failure initiation sites, due to worst matrix-filler interaction [8]. Hence, the premature failure was mainly responsible for TS reduction, especially at higher DBLF loadings in *rPP* matrix based composites.

Next, Fig. 3 has shown the flexural strength (FS) plots versus the weight percentages of DBLF in *rPP* based composites. The three point bending type of flexural test



**Fig. 3** FS versus wt% of DBLF in *rPP* based composites

has primarily used to determine the stiffness behaviour of *rPP*/DBLF composites. This attribute, represent the ability of *rPP*/DBLF composites to resist the deformation due to flexural force loading. The higher the flexural strength, the higher the ability of produced composites to sustain the deformation, the higher the stiffness of the tested samples. Normally, the presence of the filler in the composite bodies, would enhanced the stiffness characteristic of the samples. However, it was not the case for this study. In this work, it has clearly found that, the presence of DBLF within *rPP* matrix bodies, just able to enhance the FS up to 10.00 wt% of DBLF addition, with about +22.60% of positive increment than the unfilled *rPP*. Later, by increasing the DBLF content addition up to 40.00 wt%, it has caused the FS property reduction down to -28.40%, in comparison with *rPP*/10.00 wt% DBLF composite. This phenomenon has basically opposite with the plots trend of TS properties of *rPP*/DBLF composites. These findings has proven that the DBLF added into *rPP* has efficient capacity to perform the reinforcing role but not to stiffen the *rPP*/DBLF composites. This has shown by improved TS response with oppositely decreased FS response, alongside with the increase of DBLF filler addition. The rough surface nature promotes interfacial inter-locking between DBLF surfaces with *rPP* matrix, that's improving the TS, but higher flexibility and deformability of DBLF has obstructed their efficacy to resist the load, which at the end limits the capability in stiffening the produced *rPP*/DBLF composites. Cumulative effects of this inability has shown further by decreasing performance of FS of *rPP*/DBLF composites at higher DBLF loadings. In addition, based on Fig. 2, it was also found that the morphological nature of DBLF was looked irregular, brittle, fragile and fluffy, which indicates weak characteristics of DBLF filler at higher loadings, to perform the stiffening function in composites



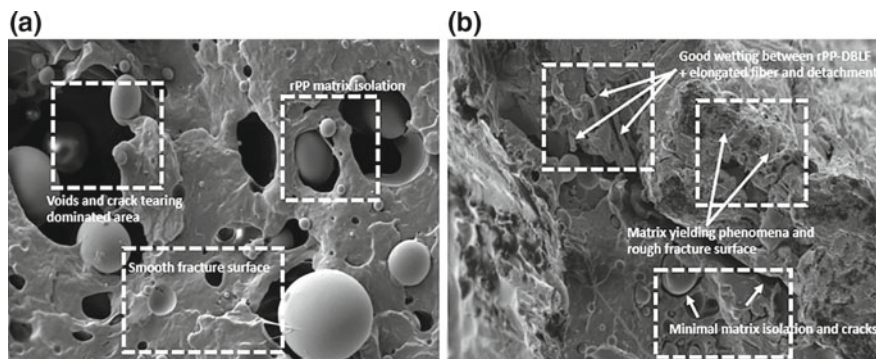
structure. The improvement of FS value at low loading addition has mainly contributed by better dispersion of DBLF within *rPP* matrix that responsible for better matrix-filler interaction, which later ease the distribution of homogeneous forces, during the flexural loading. This condition at least provide benefits for *rPP*/DBLF composites at 10.00 wt% of DBLF addition to resist the deformation, which at the end enhanced the stiffness value of FS. In overall, the DBLF added has suitable effect at higher loading (up to 30.00 wt%) to strengthen the *rPP*/DBLF composites, but only efficient at lower loading addition (up to 10.00 wt% only) to stiffen the resulted composites.

In the next section, the fracture morphological images as observed through the scanning electron microscope (SEM) for the selected tensile test sample of *rPP*/DBLF composite with 30.00 wt% of DBLF addition, was compared with unfilled *rPP* sample. Based on TS and FS results, unfilled *rPP* sample always possessed the lowest performance of strength and stiffness characteristics. Addition of DBLF at 30.00 wt% of percentages addition has successfully reinforced the TS, but was failed to stiffen the *rPP*/DBLF composite. Hence, for this part, the discussion has been made to clarify the inter-related phenomena which effects the variation of TS and FS response for this composite.

Based on the fracture morphology observation of an unfilled *rPP* sample, it was found that the applied tensile loading has revealed the brittle failure characteristic as proven by smooth pattern of fracture surface. This characteristic explained the lowermost performance of TS and FS, in comparison with *rPP*/DBLF type's composites samples. Smooth fracture surface indicates limited strength sustained by the *rPP* sample, prior of the failure due to tensile loading exposure. In addition, it was clearly observed the *rPP* matrix isolation due to the presence of aggravated voids and crack tearing phenomena. Matrix isolation, crack and voids occurrence are worsen by the force given during the tensile and flexural loadings. This situation, has limits the capability of *rPP* to sustain the tensile and flexural loads, during the testing which initiated the early premature failure.

However, for *rPP*/30.00 wt% DBLF composite, it was evidenced that from the TS test, this composite possessed the highest performance about 26.10 MPa (the highest). From the image (refer Fig. 4b), it was clearly shows that minimal matrix isolation and cracks has appeared in the fractured image. This condition explained the superior TS performance for this selected sample. Less matrix isolation and cracks sites, has eliminated or lessen the early premature failure possibility for produced composites. Matrix continuity of *rPP*/DBLF composite was evidenced by the matrix yielding phenomena and rough fracture surface, which explained the capability of load carrying capability of produced composite. At the end, as focused in the micrograph, good wetting between *rPP*-DBLF and several elongated DBLF fibre detachment, provides the reason for extraordinary TS improvement with the presence of 30.00 wt% of DBLF within the *rPP* matrix. Proven compatibility between *rPP* phase and DBLF filler phase, enhanced the matrix-filler interaction between them.

Finally, on the FS performance, some of the explanation on their properties reduction has been explained in the FS discussion part. Basically, the lessening phenomena of FS at higher DBLF filler addition was mainly due to the characteristic of DBLF



**Fig. 4** a Unfilled *rPP* SEM image; b *rPP*/30 wt% DBLF composite SEM image

filler itself, as explained beforehand. Hence, up to this stage, it is worth to mention that, DBLF filler are good for strengthening effect, but not for the stiffening purposes. For the final application, this finding should be well manipulated and applied. Observation via SEM provides valuable hints for understanding the TS and FS behaviour of produced *rPP*/DBLF composites. From this study, the morphological analysis has successfully explained the TS and FS properties variation from the experimental findings.

## 4 Conclusions

In conclusion, from this study, the effects of DBLF fibre loadings towards the resulted mechanical, physical and fracture morphological properties of *rPP*/DBLF composites were fully explored and understood. It was found that, about 30.00 wt% of DBLF addition has enough to enhance the TS, but not for FS which requires even lower percentage addition (only 10.00 wt%) for positive improvements. DBLF added was efficient for introducing the reinforcement effects but has failed to provide the stiffening improvement at higher DBLF loadings. In addition, the morphological inter-relationships between the characteristic of fracture surfaces and TS-FS responses was also established and able to provide further justification on DBLF quality as functional filler for composite development. In overall, this study has successfully highlighted the potential of DBLF filler to enhance the properties of *rPP*, as another alternative of degradable plastic based composite for various promising applications.

**Acknowledgements** Authors would like to extend their sincere appreciation to Ministry of Education, Malaysia (MOE) and Universiti Teknikal Malaysia Melaka (UTeM) for funding and supporting this research work under the FRGS research grant-FRGS/2018/FKP-AMC/F00381. Also, special thanks to Universiti Malaysia Pahang for co-researcher involvement under the fund—RDU1703321. Sincere thanks to Faculty of Manufacturing (FKP), UTeM and Mechanical Polymer Department, IKTBN Sepang, for extensive support on laboratory and facilities until the completion of this research works.



## References

1. Ramesh M, Sri Ananda Atreya T, Aswin US et al (2014) Processing and mechanical property evaluation of banana fibre reinforced polymer composites. *Proc Eng* 97:563–572
2. Yion S, Tuladhar R, Combe M et al (2013) Mechanical properties of recycled plastic fibres for reinforcing concrete. *Fibre Conc* 2013:1–10
3. Bolka S, Slapnik J, Rudolf R et al (2017) Thermal and mechanical properties of biocomposites based on green PE-HD and hemp fibers. *Contem Mater VIII-1*:80–90
4. Mohapatra D, Mishra S, Sutar N (2010) Banana and its by-product utilisation: an overview. *J Sci Ind Res* 69:323–329
5. Marikkar JMN, Tan SJ, Salleh A et al (2016) Evaluation of banana (*Musa sp.*) flowers of selected varieties for their antioxidative and anti-hyperglycemic potentials. *Int Food Res J* 23:1988–1995
6. Mukhopadhyay S, Fanguero R, Arpac Y et al (2008) Banana fibres—variability and fracture behavior. *J Eng Fibre Fabr* 3:39–45
7. Abd Razak J, Ahmad SH, Ratnam CT et al (2015) Effects of poly(ethyleneimine) adsorption on graphene nanoplatelets to the properties of NR/EPDM rubber blend nanocomposites. *J Mater Sci* 50:6365–6381
8. Kamarudin N, Abd Razak J, Norddin N et al (2018) Effect of filler loading on tracking and erosion of silicone rubber based composites under DC voltage. *Intel Mfg Mechtro. Lecture Notes in Mechanical Engineering*, pp 73–83. [https://doi.org/10.1007/978-981-10-8788-2\\_7](https://doi.org/10.1007/978-981-10-8788-2_7)
9. Batori M, Jabbari M, Akesson D et al (2017) Production of pectin-cellulose biofilms: a new approach for citrus waste recycling. *Int J Polym Sci* 2017:1–7

# Developing a Finite Element Model for Thermal Analysis of Friction Stir Welding (FSW) Using Hyperworks



Bahman Meyghani and Mokhtar Awang

**Abstract** The study undertakes a three-dimensional finite element analysis of the friction stir welding (FSW) process of 6061-T6 aluminium alloy. The analysis investigates the temperature distribution and the fundamental knowledge of the process with respect to temperature difference in the material to be welded. HyperMesh<sup>®</sup> and HyperView<sup>®</sup> solver have been used from Altair Hyperworks<sup>®</sup> to analyse the process. Different traverse and rotational speeds have been applied in the model. The results of the study create a better understanding for peak temperature distribution. In addition, the results illustrate that the peak temperature during welding increases as the rotational speeds rises and the effect of the transverse speed on the temperature is found to be insignificant. Finally, comparisons with some published papers has been done in order to compare the results of the different finite element packages and summarize the advantages and disadvantages of each software.

**Keywords** Friction Stir Welding · Thermal analysis · Temperature distribution · Heat Affected Zone · Hyperworks

## 1 Introduction

Friction Stir Welding (FSW) contains some stages including plunging, welding and retracting (plunging out). It needs to be mentioned that there are two significant causes for the heat generation in this process: friction force and plastic deformation ‘cold work’ [1–5]. There is a rotating, cylindrical, and non-consumable tool in FSW which has a pin and a shoulder (that can have different shapes). During the plunging of the tool inside the workpiece, the contact between the tool and the workpiece

---

B. Meyghani

Institute of Materials Joining, Shandong University, Jinan 250061, People’s Republic of China

M. Awang (✉)

Department of Mechanical Engineering, Faculty of Engineering, Universiti Teknologi

PETRONAS, 32610 Bandar Seri Iskandar, Perak Darul Ridzuan, Malaysia

e-mail: [mokhtar\\_awang@utp.edu.my](mailto:mokhtar_awang@utp.edu.my)

© Springer Nature Singapore Pte Ltd. 2020

M. Awang et al. (eds.), *Advances in Material Sciences*

*and Engineering*, Lecture Notes in Mechanical Engineering,

[https://doi.org/10.1007/978-981-13-8297-0\\_64](https://doi.org/10.1007/978-981-13-8297-0_64)

generates heat. In some cases, there is a dwelling step in order to assist in softening of the material, then the tool is ready to move across the welding seam and join the plates.

It should be mentioned that the ability of the tool for producing a good processed zone depends on the life of the tool [6]. One of the key parameters that affects the tool life is the heat generated during FSW. The range of temperature has been specified to ensure good material flow and good stirring of the materials [7]. Fehrenbacher et al. [7] reported that at the shoulder temperature of 515 °C, defects were come across in the welds for AA6061. Nevertheless, welding at above solidus temperature has led to the degradation in the weld quality, thus, indicating that local melting had occurred. In the contrary, at shoulder temperature of 533 °C, the welds performed a higher quality weld [7]. A decrement of the ultimate tensile strength of the welds were also reported once the solidus temperature was achieved during welding. Additionally, grain growth can also be enhanced during higher welding temperatures [7].

It needs to be mentioned that finite element methods are appropriate for investigating of the temperature behaviour during the process more in detail, save time and the manufacturing costs. Different finite element models have been used so far for modelling the process [8–12] including Eulerian [4], Lagrangian and Arbitrary Eulerian Lagrangian [9, 13] for welding of different materials [5, 14, 15]. Although, all of the above-mentioned studies have used refine mesh technique, however the distortion of mesh is still one of the most significant problems for modelling the FSW. To illustrate the issue, the deformation of the material during the process is large and this issue causes the distortion of mesh. The capability of the quick generation of high-quality mesh is one of the core competencies of HyperMesh®, therefore by using this software the mesh distortion problem can be solved. Moreover, the direct recording of the temperature in the nugget zone is difficult, however by employing finite element modelling the behaviour of the temperature inside the nugget zone can be investigated. Thus, the purpose of this study is to explore the peak temperature in the vicinity of the tool-workpiece by using high-performance finite element modelling commercial software Altair Hyperworks®. Finally, the findings have been validated and the model is confirmed by comparing the results with published papers.

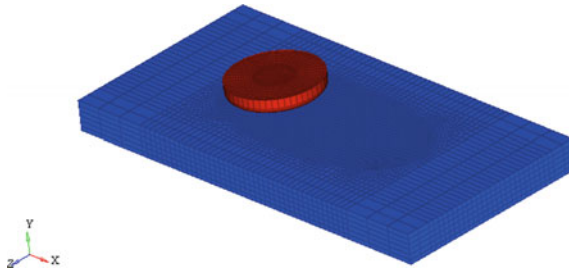
## 2 Methodology

### 2.1 Finite Element Model Descriptions

Aluminium 6061-T6 alloy is used for the plates and the tool material is steel H13. The dimension of the plate is 200 mm in length, 100 mm in width and 10 mm in thickness. The shoulder diameter is 18 mm and length of the pin is 6 mm. Figure 1a shows the tool description and Fig. 1b indicates the assembled model. It needs to be mentioned that the shoulder penetration depth inside the workpiece is set to be



**Fig. 1** **a** The tool, **b** the assembled model including the tool and the workpiece



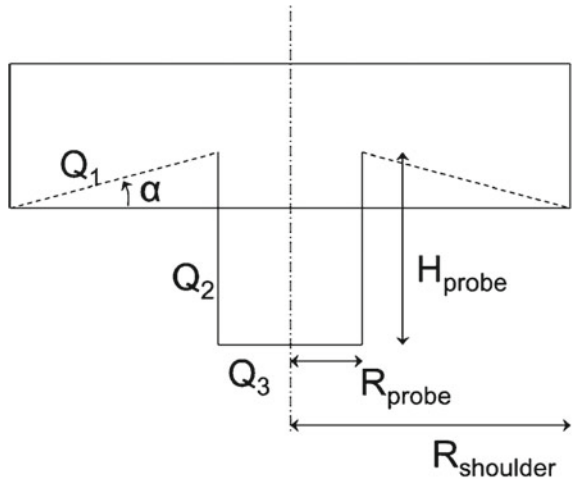
**Fig. 2** The explanation of the mesh for the workpiece and the tool

0.15 mm. Furthermore, different rotational (800, 1200 and 1600 RPM) and transverse velocities (40, 70 and 100 mm/min) have been applied to the model.

Three dimensional (3D) finite element thermo-mechanical analysis type is used for the simulation. The finite element assumptions are applied in the model such as temperature dependent values of the friction coefficient which is calculated by Meyghani et al. [3, 16, 17]. In addition, different temperature dependent material properties have been applied in the model [18] including thermal conductivity, specific heat and density. As can be observed in Fig. 2, CTD8RT element is selected for the welding, total number of nodes are 28,357 and the total number of elements are 23,832.

RADIOSS™ solver is established around 30 years ago. It has been used in different problems such as the crash of the automotive, drop and impact analysis, terminal ballistic, blast and explosion effects and high velocity impacts. It should be noted that, in all of the abovementioned problems, large plastic deformation is present. Moreover, in complex environments such as aerospace, defence companies, automotive, electronics, and R&D centres for understanding and predicting the behaviour of the design, HyperWorks® environment is used and this issue makes RADIOSS™ as an appropriate tool for designing and analysing the problem. Therefore, in this research Altair RADIOSS™ solver is employed in order to solve the problem, because this solver is a leading structural analysis solver and can be employed for highly non-linear problems under dynamic loadings.

**Fig. 3** FSW tool with a conical shoulder and a cylindrical unthreaded pin



### 2.2 Heat Generation Theoretical Background

Figure 3 shows the total heat generation at different areas of the tool [19] which are sub-divided into different components of the tool interface, including the generated heat at the shoulder bottom  $Q_1$ , at the pin side  $Q_2$  and at the tool pin bottom  $Q_3$ .

The general expression for the heat generation is defined as,

$$Q = \omega T_{total} \tag{1}$$

where  $\omega$  is the rotating velocity and  $T_{total}$  is the magnitude of the total torque which depends on different quantities: the force applied to the welding tool, the length of the lever arm linking the axis to the point of force application, and the angle between the lever arm and the force vector. The value of the torque is equal to,

$$T_{total} = \vec{r} \cdot \vec{F} \tag{2}$$

where  $r$  is the position vector and  $F$  is the force vector, therefore,

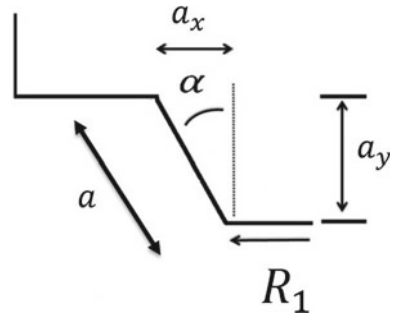
$$Q = \omega \vec{r} \cdot \vec{F} \tag{3}$$

According to the shear stress formula, the force vector is equal to,

$$\vec{F} = \vec{\tau} \cdot A \tag{4}$$

where  $\tau$  is the shear stress and  $A$  is the area of the tool that are involved in producing the friction force, including  $A_S$  which is the region of the shoulder bottom,  $A_{pb}$  which is the pin bottom area and  $A_{ps}$  which is the pin side region, therefore,

**Fig. 4** Schematic view of the tool and the pin side area



$$Q = \omega \vec{r} \cdot \vec{\tau} A \tag{5}$$

The formula for calculating average heat generation per unit area can be written as follows,

$$dQ = \omega \vec{r} \cdot \vec{\tau} dA \tag{6}$$

where  $dA$  can be written as,

$$dA = \vec{r} dr d\theta \tag{7}$$

Therefore, an integral can be summarized for calculating the generated heat in all areas, for example, for the shoulder bottom area ( $Q_1$ ), the value of the generated heat can be explained as follows,

$$Q_1 = \oint_{A_S} \omega \tau_0 dA_S = \int_0^{2\pi} \int_{R_1}^{R_S} \omega \tau_0 \cdot r^2 dr d\theta = \omega \tau_0 \frac{2}{3} \pi (R_S^3 - R_1^3) \tag{8}$$

For finding the heat generation at the pin side area, firstly the region of the pin side ( $A_{PS}$ ) which is explained in Fig. 4 needs to be investigated.

where  $a = \sqrt{a_x^2 + a_y^2}$ , in which  $a_x = R_2$  and  $a_y = H$ , where  $H$  is the pin height, therefore,  $(R_2 + H \tan \alpha) = A_{PS}$ . For the pin side area, the generated heat ( $Q_2$ ) is equal to,

$$\begin{aligned} Q_2 &= \oint_{A_{PS}} \omega \tau_1 dA_{PS} = \int_0^{2\pi} \int_0^H \omega \tau_1 (R_2 + H \tan \alpha)^2 dH d\theta \\ &= \omega \tau_1 \frac{2}{3} \pi (R_2^2 H + 3R_2 H^2 \tan \alpha + H^3 \tan^2 \alpha) \end{aligned} \tag{9}$$

The generated heat for the pin bottom area ( $Q_3$ ) can be calculated as,

$$Q_3 = \oint_{A_{pb}} \omega \tau_0 dA_{pb} = \int_0^{2\pi} \int_0^{R_2} \omega \tau_0 r^2 dr d\theta = \omega \tau_0 \frac{2}{3} \pi (R_2^3) \quad (10)$$

Finally, the total generated heat is denoted by gathering all generated heats in different areas, the shoulder bottom  $Q_1$ , the pin side  $Q_2$  and the pin bottom  $Q_3$  as follows,

$$Q_{total} = \oint_{A_S} \omega \tau_0 dA_S + \oint_{A_{pb}} \omega \tau_0 dA_{pb} + \oint_{A_{ps}} \omega \tau_1 dA_{ps}$$

$$Q_{total} = Q_1 + Q_2 + Q_3 \quad (11)$$

Therefore, the summarize of the above-mentioned values will be the overall amount of the produced heat during the process. It can be concluded that the geometry of the contact area, rotational velocity, the force and the shear stress will affect the generation of the heat during FSW.

### 3 Results and Discussion

A couple thermo mechanical finite element model is considered for the simulation. As can be observed in Fig. 5 the welding temperature is increased as the tool penetrates inside the plates. It is obtained that the temperature of the welding at the tool trailing edge is more than the other parts. Moreover, the temperature of the welding advancing side is always more than the temperature of the welding retreating side. This issue happens due to the difference in the conduction of the heat at different welding sides. To illustrate the issue, the solid material starts to move from the welding advancing side to the welding retreating side, therefore the movement of heat from the solid material which is located in the advancing side to another side causes difference temperature values. Furthermore, the results indicate that the slipping rate of the front side and the retreating side are lower than the back side and the advancing side.

It is also detected that the heat produces by the shoulder is more than the heat that is generated by the pin (Fig. 6), therefore the upper surface temperature is always higher than the bottom surface temperature (around 60 °C higher). In addition, it is observed that as the distance from the welding centre line increases the difference between the temperature of the upper and the lower surface is decreased.

The highest heat is generated inside the nugget zone (NZ) and the maximum heat dissipation is obtained from the NZ (happened close to the shoulder edge contact area). The contours of the gradient of the temperature at the upper surface in the horizontal-side (longitudinal side) is shown in Fig. 6, which verifies that the area contacted with the shoulder lateral surface is exposed to the higher temperature gradient effect.

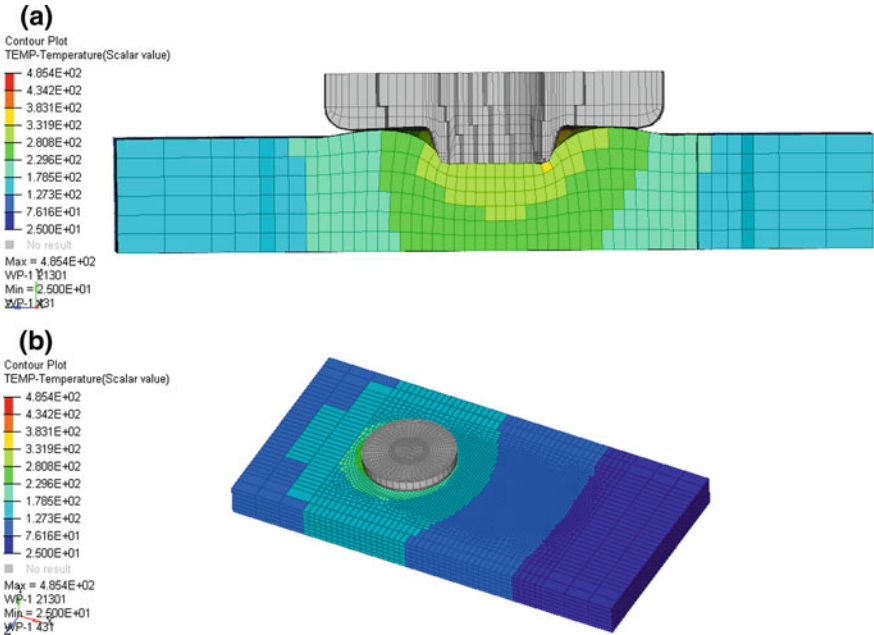


Fig. 5 The behaviour of the welding during the plunging step a cross section, b 3D view

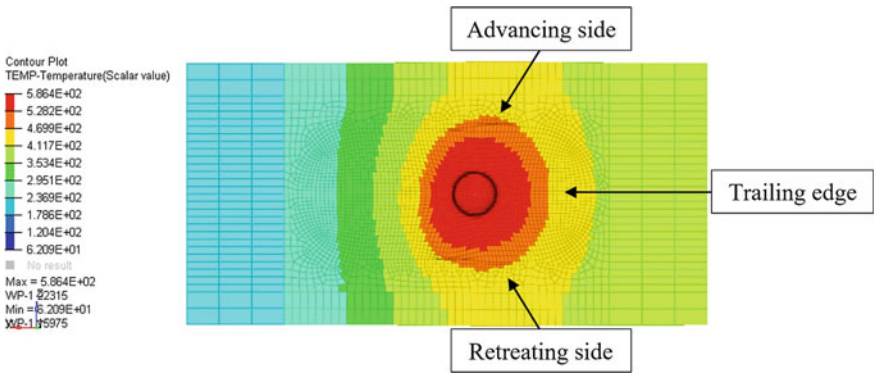
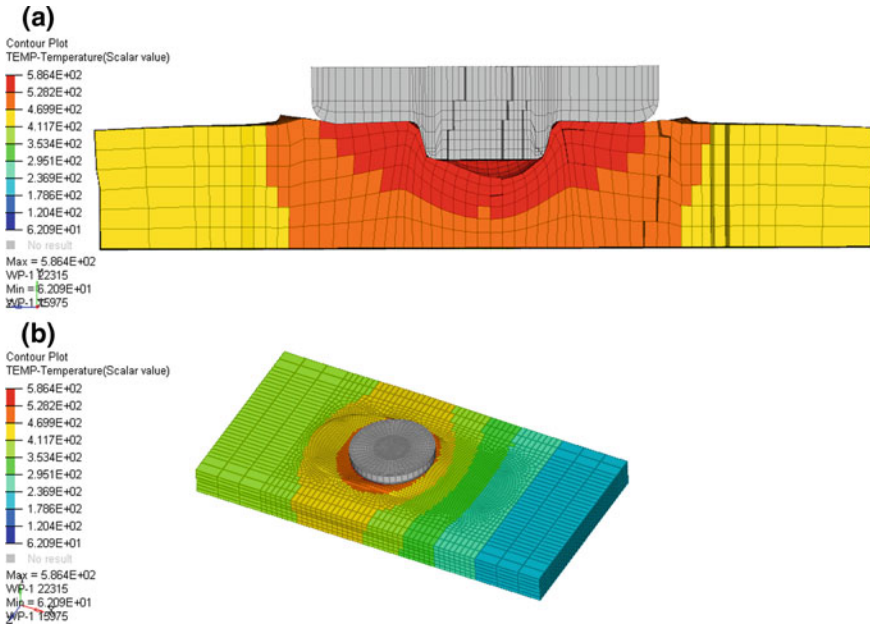


Fig. 6 Horizontal section of the welding

Figure 7 indicates that as the tool transfers across the vertical direction, the welding temperature increases. Besides, there is a “V” shape pattern for the temperature. The main reason for this pattern is due to the higher convection of the workpiece from the bottom surface. It needs to be noted that this matter affects the grain size of the thermo mechanical affected zone (TMAZ) and the heat affected zone (HAZ) [20]. In addition, an “onion ring” (bands of textures) structure is observed in the welding





**Fig. 7** Welding temperature distribution **a** cross section, **b** 3D view

area. The main reason of this kind of structure is the higher mixing of the material in the centre of the weld.

It is also observed that, temperature changes are highly influenced by the welding rotating speeds and the welding transverse movement. It was detected that, as the tool rotating speed is increased, the joint maximum temperature was also increased to 365 °C at the rotating velocity of 1600 RPM and the transverse velocity of 40 mm/min. Conversely, the welding temperature was decreased as the transverse speed increased [21–23]. Moreover, the differences of the temperature in the stirring zone were generally described as a quasi-steady behaviour, but as the distance from the welding centre line increases, the quasi-steady behaviour disappeared. Furthermore, the results showed that during all stages of the welding, the maximum temperature of the welding is less than the melting temperature of 6061-T6 aluminium alloy that is around 580 °C [24].

## 4 Conclusions

In this work finite element modelling of friction stir welding (FSW) is done in order to investigate the behavior of the heat. Altair® Software was used for modelling the process because of its powerful abilities in creating high quality mesh. From

the results it was investigated that, the heat produced by shoulder is higher (60 °C) and there is an asymmetrical pattern for the temperature and the temperature of the welding advancing side is higher around 30 °C. Moreover, at the constant transverse speed, when the rotational speed increased, temperature increased as well. Finally, the simulated model was validated with experiments and published papers and a good correlation between the results is achieved.

**Acknowledgements** The authors would like to acknowledge the financial support from Universiti Teknologi PETRONAS (UTP), Bandar Seri Iskandar, Perak Darul Ridzuan, Malaysia and the financial support from YUTP-FRG grant cost center 0153AA-H18. Moreover, the authors would like to thank Altair Engineering Sdn Bhd, Malaysia and professor Wallace Kaufman for their endless support and collaboration.

## References

1. Su H, Wu CS, Bachmann M, Rethmeier M (2015) Numerical modeling for the effect of pin profiles on thermal and material flow characteristics in friction stir welding. *Mater Des* 77:114–125
2. Meyghani B, Awang MB, Emamian SS, Mohd Nor MKB, Pedapati SR (2017) A comparison of different finite element methods in the thermal analysis of friction stir welding (FSW). *Metals* 7:450
3. Meyghani B, Awang M, Emamian S, Khalid NM (2017) Developing a finite element model for thermal analysis of friction stir welding by calculating temperature dependent friction coefficient. In: 2nd international conference on mechanical, manufacturing and process plant engineering, pp 107–126
4. Miles M, Nelson T, Gunter C, Liu F, Fourment L, Mathis T (2018) Predicting recrystallized grain size in friction stir processed 304L stainless steel. *J Mater Sci Technol*
5. Argesi FB, Shamsipur A, Mirsalehi SE (2018) Dissimilar joining of pure copper to aluminum alloy via friction stir welding. *Acta Metall Sinica (English Letters)* 31:1183–1196
6. Khandkar M, Khan JA, Reynolds AP (2003) Prediction of temperature distribution and thermal history during friction stir welding: input torque based model. *Sci Technol Weld Joining* 8:165–174
7. Fehrenbacher A, Duffie NA, Ferrier NJ, Pfefferkorn FE, Zinn MR (2014) Effects of tool–workpiece interface temperature on weld quality and quality improvements through temperature control in friction stir welding. *Int J Adv Manuf Technol* 71:165–179
8. Dialami N, Chiumenti M, Cervera M, de Saracibar CA (2015) Challenges in thermo-mechanical analysis of friction stir welding processes. *Arch Comput Method Eng* 1–37
9. Dialami N, Chiumenti M, Cervera M, Segatori A, Osikowicz W (2017) Enhanced friction model for friction stir welding (FSW) analysis: simulation and experimental validation. *Int J Mech Sci* 133:555–567
10. Su H, Wu C, Pittner A, Rethmeier M (2014) Thermal energy generation and distribution in friction stir welding of aluminum alloys. *Energy* 77:720–731
11. Meyghani B, Awang M, Emamian S (2016) A comparative study of finite element analysis for friction stir welding application. *ARPN J Eng Appl Sci* 11:12984–12989
12. Ansari MA, Samanta A, Behnagh RA, Ding H (2018) An efficient coupled Eulerian-Lagrangian finite element model for friction stir processing. *Int J Adv Manuf Technol* 1–14
13. Meyghani B, Awang M, Emamian S, Nor MKBM (2018) Thermal modelling of friction stir welding (FSW) using calculated young's modulus values. In: *The advances in joining technology*. Springer, pp 1–13
14. Sun Z, Wu C, Kumar S (2018) Determination of heat generation by correlating the interfacial friction stress with temperature in friction stir welding. *J Manuf Process* 31:801–811

15. Jaffarullah MS, Nur' Amirah Busu CYL, Saedon J, Armansyah MSBS, Jaffar A (2015) Simulation analysis of peak temperature in weld zones during friction stir process. *J Teknol* 76:77–81
16. Meyghani B, Awang M, Emamian S, Akinlabi E (2018) A comparison between temperature dependent and constant Young's modulus values in investigating the effect of the process parameters on thermal behaviour during friction stir welding: Vergleich zwischen den temperaturabhängigen und konstanten Elastizitätsmodulwerten in der Untersuchung der Prozessparameter auf die Wärmewirkung beim Rührreißschweißen. *Materialwiss Werkstofftech* 49:427–434
17. Meyghani B, Awang M, Emamian S (2017) A mathematical formulation for calculating temperature dependent friction coefficient values: application in friction stir welding (FSW). *Defect Diff Forum* 379:73–82
18. Su H, Wu C, Pittner A, Rethmeier M (2013) Simultaneous measurement of tool torque, traverse force and axial force in friction stir welding. *J Manuf Process* 15:495–500
19. Mishra RS, De PS, Kumar N (2014) Fundamentals of the friction stir process. In: *Friction stir welding and processing*. Springer, pp 13–58
20. Abdul-Sattar M, Tolephih MH, Jweeg MJ (2012) Theoretical and experimental investigation of transient temperature distribution in friction stir welding of AA 7020-T53. *J Eng* 18:693–709
21. Emamian S, Awang M, Hussai P, Meyghani B, Zafar A (2016) Influences of tool pin profile on the friction stir welding of AA6061. *ARP J Eng Appl Sci* 11:12258–12261
22. Emamian S, Awang M, Yusof F, Hussain P, Mehrpouya M, Kakooei S et al (2017) A review of friction stir welding pin profile. In: Awang M (ed) *2nd international conference on mechanical, manufacturing and process plant engineering*. Springer, Singapore, pp 1–18
23. Emamian S, Awang M, Yusof F, Hussain P, Meyghani B, Zafar A (2018) The effect of pin profiles and process parameters on temperature and tensile strength in friction stir welding of AL6061 alloy. In: *The advances in joining technology*. Springer, pp 15–37
24. Meyghani B, Awang MB (2018) Prediction of the temperature distribution during friction stir welding (Fsw) with a complex curved welding seam: application in the automotive industry. *MATEC Web Conference*, vol 225, p 01001